

Naphthalimide and Perylenimide Luminogens: Structure-Property Relationships for Sensing and Biomedical Applications

A Dissertation Submitted for the Degree of
Doctor of Philosophy

By

Mst Nasima Khatun

Roll No. 176122016



Department of Chemistry
Indian Institute of Technology Guwahati
December, 2023

Department of Chemistry

IIT Guwahati

PhD Thesis



**Naphthalimide and Perylenimide Luminogens:
Structure-Property Relationships for Sensing
and Biomedical Applications**

By

Mst Nasima Khatun

Supervisor

Prof. Parameswar Krishnan Iyer

December, 2023

**PhD
Thesis**

**Naphthalimide and Perylenimide Luminogens: Structure-
Property Relationships for Sensing Biomedical
Applications**

Mst Nasima Khatun





Dedicated to My Maa...



Indian Institute of Technology Guwahati

Department of Chemistry

Certificate

This is to certify that the work contained in the thesis entitled “**Naphthalimide and Perylenimide Luminogens: Structure-Property Relationships for Sensing and Biomedical Applications**” by **Mst Nasima Khatun**, a student of the Department of Chemistry at the Indian Institute of Technology Guwahati, for the award of the degree of Doctor of Philosophy, has been carried out under my supervision. This work has not been submitted for any other degree elsewhere.

December, 2023

IIT Guwahati

Parameswar Krishnan Iyer

Thesis Supervisor

Department of Chemistry

IIT Guwahati

Guwahati-781039, Assam, India.



Indian Institute of Technology Guwahati

Department of Chemistry

Statement

I hereby declare that the work presented in the thesis titled “**Naphthalimide and Perylenimide Luminogens: Structure-Property Relationships for Sensing and Biomedical Applications**” are the direct results of investigations conducted by me within the Department of Chemistry at the Indian Institute of Technology Guwahati, under the attentive guidance of Prof. Parameswar Krishnan Iyer. This work has not been previously submitted for the purpose of obtaining any degree elsewhere.

Consistent with the established practice of documenting my observations, appropriate acknowledgments have been rendered whenever the content of this work is rooted in the discoveries of my collaborators.

December, 2023

IIT Guwahati

Mst Nasima Khatun

Acknowledgments

I wish to express my deep gratitude to numerous individuals who have contributed to the fruition of this thesis in manifold ways: First and foremost, I extend my heartfelt appreciation to my parents and sisters, who have been an integral part of my vision, providing unwavering inspiration throughout every facet of my life. My heartfelt thanks go to my Maa, whose boundless love and moral strength have been my guiding light. I am truly grateful for everything and dedicate this Ph.D. Thesis to you, believing in your enduring presence and spiritual support.

A profound debt of gratitude is owed to my supervisor, Prof. Parameswar Krishnan Iyer, who has played an irreplaceable role in shaping my journey. Over the past five years, he has been a constant source of motivation, fostering fresh perspectives and igniting new possibilities in my life. His approach of turning serendipitous discoveries into innovative avenues, connecting ideas, and unveiling the implicit has propelled me forward and will continue to guide me in the years to come. I can never adequately convey what I owe to him.

My sincere acknowledgments extend to my doctoral committee members, Prof. Abu Taleb Khan, Prof. Manabendra Sarma, and Prof. Subhendu Sekhar Bagh, for their valuable time and insightful suggestions, which have enhanced my research endeavors.

I am grateful to my senior colleague, Dr. Niranjana Meher and Dr. Laxmi Raman Adil, whose diligent efforts in introducing me to basic experimental techniques and instrumentation have been invaluable. Although I later gravitated towards aggregation studies, I hold deep gratitude for his guidance during my early research phase and for the enriching experience of working together.

Special recognition is also due to Dr. Saravanan Sir, Dr. Anamika Dey and Dr. Debasis Barman for their guidance during the initial stages of my research journey. Engaging in scientific discussions with them has significantly contributed to my understanding and evaluation of various experimental and theoretical studies. Additionally, I must express my gratitude to the brilliant labmates from diverse backgrounds, whose shared insights and discussions have consistently refined and elevated my research. I thank Iyer Sir for orchestrating regular group meetings that have been invaluable learning platforms.

I extend my thanks to Prof. Sachin Kumar and Prof. Siddhartha Sankar Ghosh from the BSBE department at IITG for their collaboration on the biological aspects presented in Chapters 4 and 5. My appreciation goes to Satyendu Nandy for his remarkable effort in completing the work ahead of schedule. I also express my gratitude to Prof. Aditya Narayan Panda and Mohd. Qureshi from the Department of Chemistry, IITG, for their assistance in theoretical studies and preliminary synthetic procedures for my ongoing project.

My gratitude is incomplete without acknowledging the exceptional contributions of my lab seniors, who have not only introduced me to the lab's culture but also provided real-life lessons. I extend my gratitude to Dr. Radhakrishna Ratha, Dr. Anamika Kalita, Dr. Ashish Singh, Dr. Arvin Sain Tanwar, and Dr. M. Adil Afroz, among others, for their consistent support and motivation during my five years in the lab.

I am indebted to my fellow labmates and postdoctoral fellows who have provided unwavering camaraderie and support. My heartfelt thanks go to Paromita, Retwik, Biki Ji, Anwasha, Kabita, Anita, Rajdixit, Priyam, Debika, Tapashi, Soumalya, Dhiraj, HIRAK, Manab, Mayur, Mizanur, Sayantani, Srinivas, Sushant, Tamal, Mrinalini, Ramakrishnan, Himangshu, and Dr. Geetmani, Dr. Jupitara, Dr. Himani, and Dr. Muzafar. Their discussions and suggestions have been instrumental in shaping my work.

I reserve a special place of gratitude for my friends, whose unwavering support and encouragement have spurred me to give my best. Rupa, Biswanath, Araghni, Palak, Kisan, Rahul, Oindrilla, Mihir Da, Suwendu, Parth Pratim das and Abdus Saif thank you all for standing by me through thick and thin.

I offer my special acknowledgment to Soumalya and Ramakrishna for their pivotal role in numerous experimental studies, such as XPS and FESEM.

I am deeply thankful to all the teachers who have guided my journey from childhood, particularly Prof. Sabir Ahammed, Prof. Maidul, Prof. Hedayetullah Mir, and Khakon Sir. A special acknowledgment goes to Prof. Sabir Ahammed, who has consistently been a source of confidence and motivation throughout my life. Their unwavering support, guidance, and blessings have brought me to where I stand today.

I am indebted to friends from both my alma mater and IITG who have consistently offered moral support and extended their helping hands. I express my gratitude to my colleagues in the Department of Chemistry at IITG for their steadfast support.

I acknowledge the financial support from the Department of Science and Technology (DST), India; the Department of Electronics & Information Technology (DeitY), India; and the DST-Max Planck Society, Germany, which facilitated my research at IITG. I am grateful to the Department of Chemistry, Centre for Nanotechnology, and the Central Instruments Facility at IIT Guwahati for providing access to essential instruments.

Mst Nasima Khatun



Synopsis

Naphthalimides or Perylenimides are well-known classical fluorophores that have been extensively studied in various practical applications. However, traditional fluorescent materials habitually suffer from notorious aggregation caused quenching (ACQ) effect in their aggregated-state and limit their versatile real-world applications. The naphthalimides (**NI**) and perylenimides (**PI**) derivatives with electron withdrawing characteristics are planar aromatic cores and prone to strong π - π stacking interaction in their condensed state. In comparison to recognized propeller-shaped such as tetraphenylethylene (**TPE**), Triphenyl amine (TPA), or silole luminogens, the planar aromatic cores like **NI** and **PI** derivatives often experience notorious face-to-face π - π stacking interaction in their condensed state that dissipates its excited energy and leads to emission quenching significantly in their condensed state. However, the Chang group in 2011 first time stated aggregation-induced enhanced emission (AIEE) **NI** luminogens by substituting the peri-position of the rigid **NI** cores which extended the π -conjugation and made the molecules flexible which led to fluorescent nanoparticles in aqueous media. This is due to the 4th position substitution at the NI cores that weakens or distorts the face-to-face π - π stacking interaction between the naphthalimide cores in their condensed state. This leads to V-shaped NIs core and flexible molecular systems which subsequently restrict the non-emissive H-aggregations in their condensed state. This design strategy established that classical ACQphoric molecules could also be transformed into strong condensed state emitters by careful structural perturbation. In addition, the condensed state emissive property in luminogenic systems is principally dependent on the intermolecular interaction characteristics. Moreover, the strong intermolecular π - π stacking interactions among the **NI** and perylenimide cores could be easily fine-tuned and controlled by their structural orientation at their molecular level. This can be easily used to generate distinct supramolecular-assembly and photophysical properties. In recent years, the spontaneously formed multifunctional nano- and micro-supramolecular self-assembled systems have generated considerable interest among the scientific community. In particular, spontaneously formed fluorescent supramolecular self-assembly comprising of precise size and shape exhibits fascinating applications in optoelectronic and biomedical fields. However, **NI** derivatives are strong blue emitters and usually exhibit UV region absorptions up to the visible region. In comparison, perylene derivatives are highly conjugated molecules, having good electron mobility, high fluorescence quantum yields, and strong absorption in the visible region up to NIR/far-IR. It has high photostability, thermal stability, and good semi-conductivity, which are required for optoelectronic devices, sensing, and biomedical applications.¹ Abundant structural design, well-defined morphologies, facile device fabrication, and excellent optoelectronic

performances make these **PI** materials very promising in diverse fields. Motivated by the excellent properties and versatile applications of the **PI** materials, the **PI** core opens a new class of luminogenic materials in this area after the first exploration of the PI luminogen.

In this thesis, it has been unveiled that applying different design strategies of structural orientation in small organic ACQ fluorophoric systems is an effective yet simple technique to generate distinct condensed state emissive characteristics and supramolecular self-assembly behavior. Interestingly, unlike the molecularly dispersed state, the photophysical and morphological behavior of the small organic molecules is significantly dictated by their distinct intermolecular π - π stacking orientation of the planar aromatic core in their condensed state. Besides, the highly AIE/AIEE active fluorescent nano aggregates of **NI** and **PI** luminogens with specific receptor sites have gained significant attention to sense different toxic and bio-active analytes in aqueous media. Recently, Photodynamic therapy (PDT) due to its non-invasive and spatio-temporal behavior, has surpassed traditional techniques like surgery, chemotherapy, and radiotherapy for cancer treatment. AIE/AIEE **NI** and **PI** photosensitizers (PSs) with high brightness fluorescent nano aggregates are promising to the ablation of cancer cells or pathogens owing to their synergistic behavior like diagnostic and treatment in one platform. In other words, near-infrared (NIR) AIE/AIEE **PI** PSs have shown great potential to penetrate deep-tissue and win-win cooperation in the field of biomedical with negligible toxicity towards normal cells due to their low excitation energy. Overall, this thesis work emphasizes the exploration of the structure-property optimization of the **NI** and **PI** derivatives with sensing and biomedical applications.

The content of the thesis report entitled “**Naphthalimide and Perylenimide Luminogens: Structure-Property Relationships for Sensing and Biomedical Applications**” has been divided into five chapters as summarized below:

Chapter 1 briefly describes the need and discovery of condensed state emission as well as the types and mechanistic aspects of condensed state emission. This chapter demonstrates the importance, potential applications, and structural modulation in **NI** and **PI** luminogens as well as the concluding statement on this thesis work.

Chapter 2 demonstrates the influence of the pendant non-conjugated chain effect in PI on the electronic, thermal, and photophysical along with their morphology in their condensed state. This chapter also includes the OFET characteristics of the **PI** comprising of the long pendant alkyl chain.

Chapter 3 provides condensed state luminescence characteristics and supramolecular-assembly behaviors of the naphthalene substituted in **NI**. This chapter also unveils the 4-nitroaniline (class III toxic pesticides) detection on multiple platforms, which includes

aqueous media and the cost-effective simple and portable Whatman paper test strips based on-site solid state detection. The sensing mechanisms involved the receptor free inner filter effect (IFE).

Chapter 4 This chapter presents simple and precise molecular engineering of donor functional group targeting the imidazole group serves condensed state emission and supramolecular-assembly along with their high ROS generation characteristics could provide a new tool for the development of the new generation materials for the diverse futuristic application.

Chapter 5 We demonstrated the novel yet facile design strategy for the ACQ-to-AIEE transformation by simply tweaking the conformation into the functional group in **PNI** as well as the second comprehensive structural design of thiobased PS through S-atom engineering at carbonyl position in **PNI** (**PNIS**) with excellent potential in PDT in cancer cell.

The thesis concludes with distinct design strategies and fine-tuned condensed state characteristics, photosensitizing properties with future possibilities that could be promising tool for the small molecule based traditional fluorophores towards many unexplored potentials.

Chapter 1: Introduction

In this chapter, the need for the development of the condensed state emission of organic fluorescent materials, various types, applications as well and mechanistic aspects of the condensed state emission have been illustrated. Besides, multiplatform applications of **NI** and **PI** luminogens and their easy synthetic modulation on the **NI** and **PI** core to attain condensed state fluorescence in chromophoric systems have been discussed (**Figure S1**). A concluding remark on the complete thesis work has also been included here.

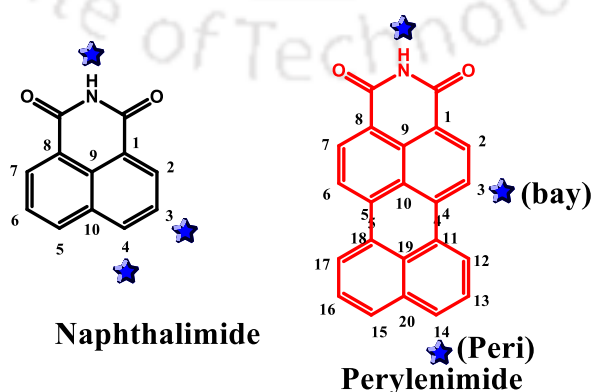
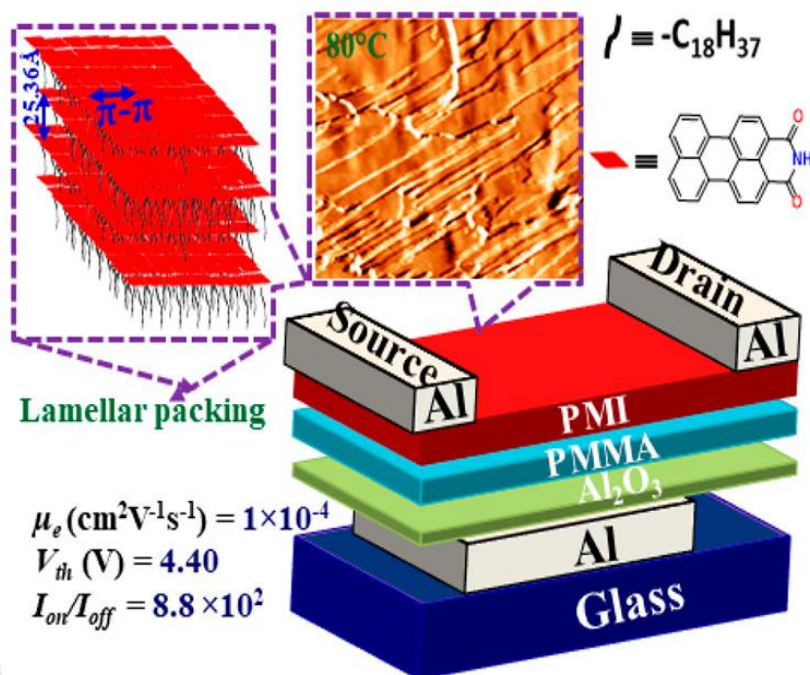


Figure S1. Chemical structure of the **NI** and **PI** core with their respective reactive site, where a wide variety of structural modulation can be observed to generate condensed state emission to this conventional fluorophore.

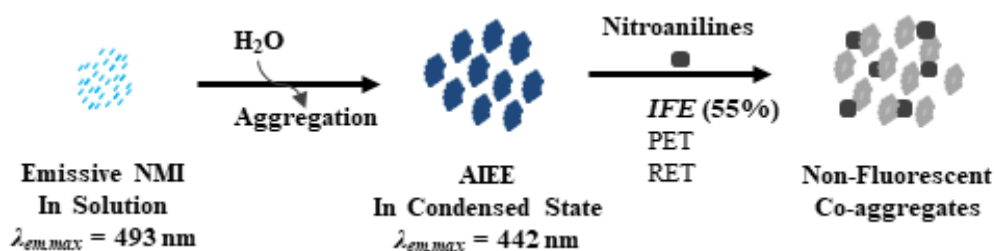
Chapter 2: Long Alkyl Chain Induced OFET Characteristic with Low Threshold Voltage in an n-Type Perylenimide Semiconductor

This work reports the fabrication of an n-channel OFET device using simple perylene monoimide (**PMI**) derivatives by introducing a nonconjugated long alkyl chain (octadecyl) at the imide position. To demonstrate the primary role of the long pendant chain in the generation of OFET characteristics, a series of electronically similar **PMI** congeners were synthesized with different alkyl chains namely, hexyl, 2-ethylhexyl, octyl, and octadecyl. It was observed that the insertion of the octadecyl chain can significantly manipulate the supramolecular self-assembly in **PMI-C18** with very good film-forming property, suggesting the prominent role of the pendant alkyl chain length in their condensed state intermolecular interaction. Along with the good film forming property, the long octadecyl chain at the imide position significantly improves the thermal, electrochemical, and photophysical properties, which help in generating OFET characteristics in **PMI-C18**, whereas other congeners do not show any device properties. With poly(methyl methacrylate) (PMMA) as the dielectric, top-contact bottom-gate n-channel OFET were fabricated on an economical glass substrate using these simple **PMI** derivatives. Among them, **PMI-C18** demonstrates OFET properties with electron mobility (μ_e) of $1 \times 10^{-4} \text{ cm}^2 \text{ V}^{-1} \text{ s}^{-1}$ and current on/off ratio ($I_{\text{on/off}}$) of 8.8×10^2 . Moreover, the threshold voltage (V_{th}) of 4.40 V obtained for **PMI-C18** was the lowest among all the reported perylene monoimide core based OFET devices. Besides, these **PMI** cores also demonstrated the influence of the alkyl chain on the photophysical, electronic, and electrochemical properties along with the molecular packing and charge transport behavior. Thus, such simple yet strategic synthetic manipulations in **PMIs** could contribute to the development of imide based materials for OFET applications.



Chapter 3: An Unprecedented Blueshifted Naphthalimide AIEEgen for Ultrasensitive Detection of 4-Nitroaniline in Water via “Receptor-Free” IFE Mechanism

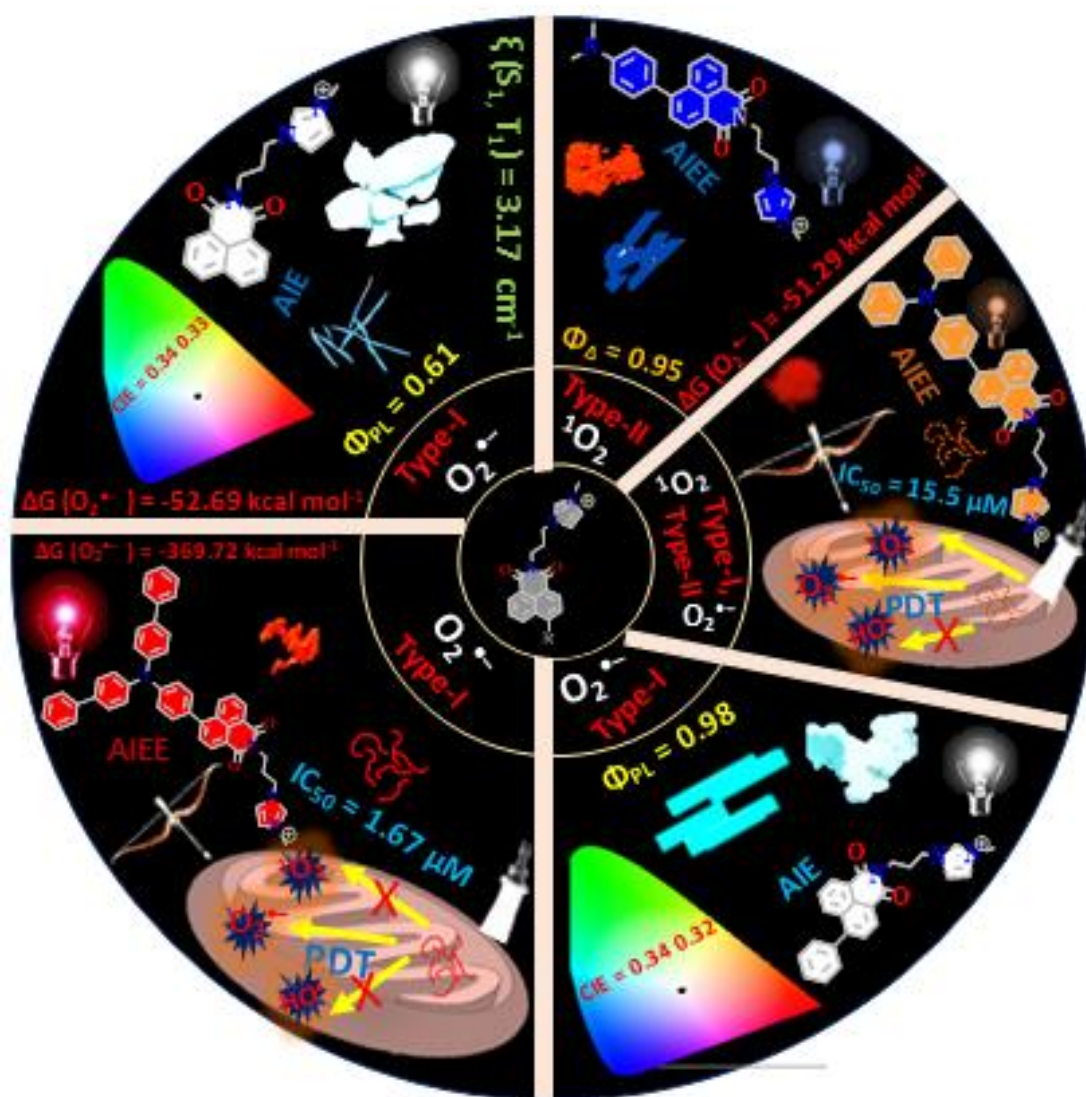
The development of a new naphthalene appended naphthalimide derivative (NMI) with aggregation-induced enhanced emission (AIEE) property for the sensitive detection of 4-nitroaniline (4-NA) in aqueous media is presented here. The newly designed naphthalimide AIEEgen has an exceptional blue-shifted condensed state emission that is devoid of any receptor site, accomplished ultrasensitive detection of 4-NA, which is one of the broad-spectrum pesticides that belong to the class III toxic chemical, at parts per billion level (LOD/36 ppb, $K_{sv}=4.1 \times 10^4 \text{m}^{-1}$) in water with excellent selectivity even in the presence of potentially competing aliphatic and aromatic amines. The reported probe is the first of its kind, demonstrating major advantages of receptor-free inner filter effect (IFE) mechanism for the sensitive detection of 4-NA using an AIEEgenic probe. Excellent sensitivity for 4-NA is also achieved on paper-based teststrip for low-cost on-site detection.



Chapter 4: Solid-State White Light, Excimer-based Photosensitization, and Type 1 Mitochondrion-Targeted Image-Guided Cancer Theranostics with Naphthalimides

An innovative design strategy manipulated donor functional units within the ionic naphthalimide (**NIC**) core, achieving exceptional photophysical, supramolecular assembly and photosensitization. 1-(3-(1,3-dioxo-1H-benzo[de]isoquinolin-2(3H)-yl)propyl)-3-methyl-1H-imidazol-3-ium (**HNIC**) and 1-(3-(1,3-dioxo-6-phenyl-1H-benzo[de]isoquinolin-2(3H)-yl)propyl)-3-methyl-1H-imidazol-3-ium (**PNIC**) exhibited solid-state white light-emissive properties. Moreover, high photoluminescence (Φ_{PL}) of 0.99 and singlet oxygen quantum yields (Φ_{Δ}) of 0.95 were exhibited by **PNIC** and **NNIC** in aqueous environments. This study showed specific type-I ROS production (superoxide, $O_2^{\bullet-}$) efficacy. A novel AIE mechanism in rigid aromatic systems and an excimer-based ROS production approach were also introduced, diverging from traditional donor-acceptor principles. **BNIC** exhibited highly specific mitochondrion-targeted photodynamic therapy, achieving a low IC_{50} of 1.67 μM without the need for an additional targeting ligand. This research showed various photosensitizers (type-I PSs: **HNIC**, **PNIC**, 1-(3-(6-(4-aminophenyl)-1,3-dioxo-1H-benzo[de]isoquinolin-2(3H)-yl)propyl)-3-methyl-1H-imidazol-3-ium (**ANIC**), and 1-(3-(6-(4-(di([1,1'-biphenyl]-4-yl)amino)phenyl)-1,3-dioxo-1H-benzo[de]isoquinolin-2(3H)-yl)propyl)-3-methyl-1H-imidazol-3-ium (**BNIC**), type-II PS: 1-(3-(6-(4-(dimethylamino)phenyl)-1,3-dioxo-1H-benzo[de]isoquinolin-2(3H)-yl)propyl)-3-methyl-1H-imidazol-3-ium (**NNIC**), and both type-I and type-II characteristics PS: 1-(3-(6-(4-(diphenylamino)phenyl)-1,3-dioxo-1H-benzo[de]isoquinolin-2(3H)-yl)propyl)-3-methyl-1H-imidazol-3-ium (**TNIC**), respectively). This design principle holds the potential to establish a novel platform for creating advanced and versatile materials for a wide range of practical

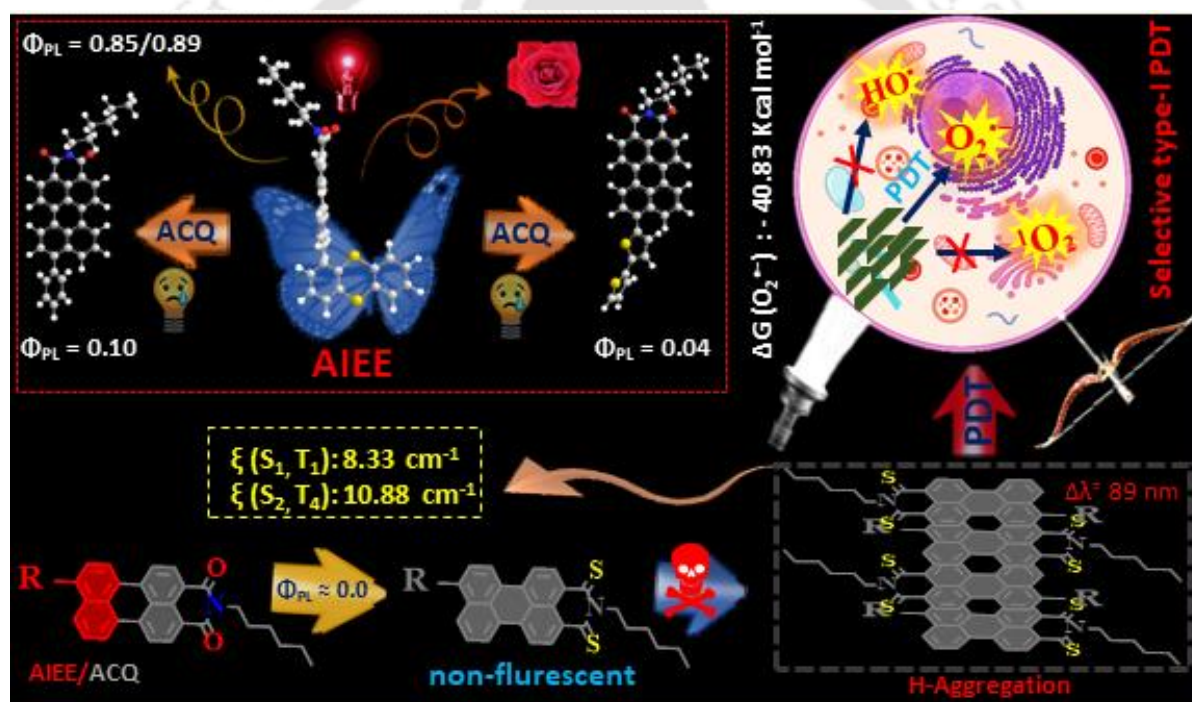
applications.



Chapter 5: Sulphur-Atom Positional Engineering in Perylenimide: Enhanced Properties and H-aggregation Unveiled Type-I Photodynamic Therapy

An innovative design strategy of placing sulfur (S)-atoms within pendant functional groups and carbonyl positions in conventional perylenimide (**PNI-O**) has been demonstrated to strategically investigate condensed state structure-property relationship and potential photodynamic therapy (PDT) application. Incorporation of simply S-atoms at the peri-functionalized perylenimide (**RPNI-O**) leads to AIEEgen, 2-hexyl-8-(thianthren-1-yl)-1H-benzo[5,10]anthra[2,1,9-def]isoquinoline-1,3(2H)-dione (**API**), which achieves a remarkable photoluminescence quantum yield (Φ_{PL}) of 0.85 in aqueous environments and established novel AIE mechanisms. Additionally, substitution of the S-atom at the carbonyl position in

RPNI-O leads to thioperlenimides (**RPNI-S**): 2-hexyl-8-phenyl-1H-benzo[5,10]anthra[2,1,9-def]isoquinoline-1,3(2H)-dithione (**PPIS**), 8-([2,2'-bithiophen]-5-yl)-2-hexyl-1H-benzo[5,10]anthra[2,1,9-def]isoquinoline-1,3(2H)-dithione (**THPIS**), and 2-hexyl-8-(thianthren-1-yl)-1H-benzo[5,10]anthra[2,1,9-def]isoquinoline-1,3(2H)-dithione (**APIS**), with distinct photophysical properties (enlarge spin-orbit coupling (SOC) and $\Phi_{PL} \approx 0.00$), and developed diverse potent photosensitizers (PSs). The present work has provided a novel SOC enhancement mechanism via pronounced H-aggregation. Surprisingly, the lowest singlet oxygen quantum yield (Φ_{Δ}) and theoretical calculations suggest the very specific type-I PDT for **RPNI-S**. Interestingly, **RPNI-S** efficiently produces superoxide ($O_2^{\cdot-}$) due to its remarkable lower Gibbs free energy (ΔG) values (**THPIS**: $-40.83 \text{ kcal mol}^{-1}$). The non-toxic and heavy-atom free very specific thio-based **PPIS** and **THPIS** PSs showed selective and efficient PDT under normoxia, which is very rare.



Future Aspects and Thesis Overview

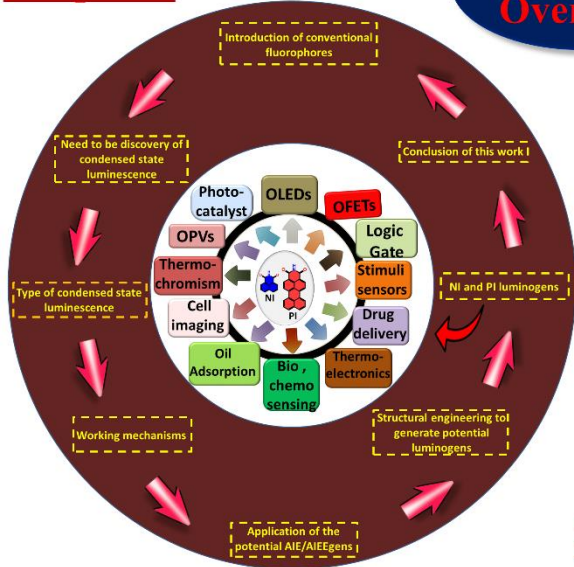
This research explores the potential of new **NI** and **PI** luminogens in various applications. NIs and PIs have garnered significant scientific interest due to their accepting nature, high fluorescence quantum yield, and unique photophysical properties. This work emphasizes a new class of luminogens called AIEgens, with particular promise for practical applications. Core luminogenic structures like TPE, HPS, and TPA are established standards, with TPA opening new avenues. Research groups have actively developed numerous AIE/AIEE-active

materials for diverse applications. **NIs** have gained attention due to their straightforward synthesis and utility in self-assembly studies, sensors, and biology. **PIs**, though less explored in sensing, have been studied extensively in LEDs and solar cells. Both hold promise for long-term bio-imaging due to their photostability and biocompatibility. **PIs'** tunable properties make them potential replacements for **NIs**. Asymmetric properties and π - π stacking interactions confer unique structure-property relationships. This research focuses on tailoring **NI** and **PI** condensed state emissions through structural manipulation and supramolecular assembly. The findings offer insights into diverse applications, including cancer therapy.

Chapter 1 introduces condensed state emission, highlighting **NIs** and **PIs'** potential and structural modulation. **Chapter 2** delves into the influence of pendant chains on **PI** electronic, thermal, and photophysical properties. **Chapter 3** explores naphthalene-substituted **NIs**, revealing their supramolecular assembly and pesticide detection capabilities. **Chapter 4** showcases the molecular engineering of donor groups for condensed state emission, supramolecular assembly, and ROS generation. **Chapter 5** presents strategies for ACQ-to-AIEE transformation in **PIs**, along with S-atom engineering for enhanced PDT in cancer cells.

In conclusion, this thesis offers diverse design strategies to fine-tune condensed state characteristics, and photosensitizing properties, and opens pathways to unexplored potential applications.

Chapter 1



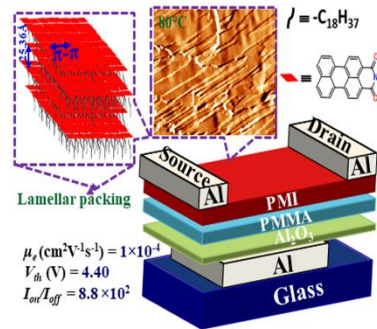
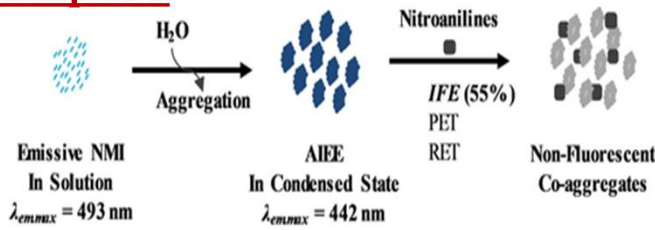
Thesis Overview

Chapter 4

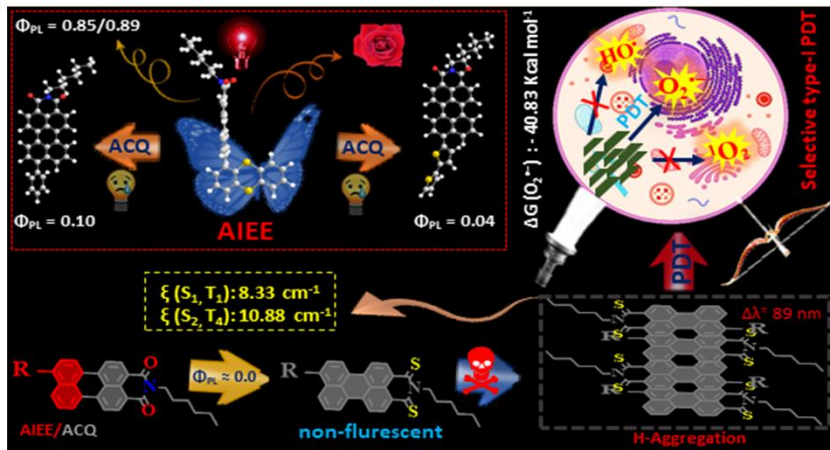


Chapter 2

Chapter 3



Chapter 5



Contents

Chapter 1	Introduction	01
1.1.	Classical Fluorophores and Need of Condensed State	01
1.2.	Discovery and Types of Condense State Emission	02
1.2.1.	Aggregation Induced Emission	03
1.2.2.	Aggregation Induced Emission Enhancement	03
1.2.2.	Dual-State Emission	04
1.2.3.	Crystallization Induced Emission	04
1.3.	Working Mechanisms	04
1.4.	Potential Application of the Condensed State Emitters	06
1.5.	Naphthalimide Luminogens	07
1.6.	Potential Applications of Naphthalimide Luminogens	09
1.7.	Structural Engineering to obtain Naphthalimide Luminogens	10
1.8.	Perylenimide Luminogems	13
1.9.	Potential Applications of Perylenimide Luminogens	14
2.0.	Structural Manipulation to Achieve Peryleneimide Luminogens	15
2.1.	Objective and Conclusions of the Thesis work	18
Chapter 2	Long Alkyl Chain Induced OFET Characteristic with Low Threshold Voltage in n-Type Perylene Monoimide Semiconductor	
	Abstract	23
2.1	Introduction	24
2.2	Experimental Section	27
2.2.1.	Materials and Instrumentations	27
2.2.2.	Substrate Cleaning technique	28
2.2.3.	Preparation of films for AFM, FESEM, XRD, POM and spectroscopic technique	28
2.2.4.	Preparation of Stock Solutions for optical study	28
2.2.5.	Theoretical Studies	28
2.2.6.	Synthetic procedures	28
2.3.	Results and Discussions	30
2.3.1.	Design, Synthesis, and characterization of PMI congeners	30
2.3.2.	Thermal, Photophysical, Electrochemical, and Theoretical Studies of PMI Congeners	30
2.3.3.	XRD analysis for interpretation of molecular Packing	35

2.3.4. Thin film morphology analysis in PMI congeners via AFM, FESEM and POM analysis	38
2.3.5. OFET device Fabrication and Characterization	41
2.4. Conclusions	44
References	45
Appendix	48

Chapter 3 An Unprecedented Blueshifted Naphthalimide AIEEgen for Ultrasensitive Detection of 4-Nitroaniline in Water via “Receptor-Free” IFE Mechanism

Abstract	62
3.1. Introduction	63
3.2. Experimental Section	64
3.2.1. Materials and Methods	64
3.2.2. Synthesis and characterization of Naphthalenemonoimide (NMI)	64
3.2.3. Preparation of Stock Solutions for Sensing	66
3.2.4. Time-resolved photoluminescence (TRPL) studies	66
3.2.5. Preparation of Test Strips	66
3.2.6. Preparation of FESEM sample	66
3.2.7. Preparation of surface area analyzer (BET) sample	66
3.2.8. Quantum Yield Calculations	66
3.2.9. Method for Limit of Detection (LOD) calculation	67
3.3. Results and Discussion	67
3.3.1. Design, Synthesis, and Characterization of NMI	67
3.3.2. AIEE in NMI with Exceptional Blue-shifted Emission	68
3.3.3. 4-NA Detection in Aqueous Medium	71
3.3.4. Selectivity Studies	72
3.3.5. Sensing Studies in Competitive Environment	73
3.3.6. Portable Test strips for Onsite Detection	73
3.3.7. The sensing mechanism of 4-NA detection	73
3.4. Conclusions	78
References	78
Appendix	79

Chapter 4 Solid-State White Light, Excimer-based Photosensitization, and Type 1 Mitochondrion-Targeted Image-Guided Cancer Theranostics with Naphthalimides

Abstract	98
4.1. Introduction	99
4.2. Experimental Section	101
4.2.1. Materials and Instrumentations	101
4.2.2. Preparation of the Test Solution	102
4.2.3. Preparation of FESEM samples	102
4.2.4. Theoretical Studies	102
4.2.5. Photoluminescence quantum Yield Calculations	103
4.2.6. Synthesis of RNIC derivatives	103
4.2.7. Computational studies	107
4.2.8. $^1\text{O}_2$ generation quantum yield Estimation	108
4.2.9. Reactive oxygen species (ROS) Generation/Mesurament	108
4.2.10. The Point of Zero Zeta Potential Evaluation	109
4.2.11. The Energy of the Valence Band and Conduction Band Calculations	110
4.2.12. Cell studies	110
4.2.12.1. Cell culture	110
4.2.12.2. Cell Imaging	110
4.2.12.3. Dark & Light Cytotoxicity Evaluated by MTT assay	111
4.2.12.4. Live/dead cell co-staining assay	111
4.3. Results and Discussion	112
4.3.1. Design, synthesis and characterization of RNIC derivatives	112
4.3.2. Photophysical Properties	113
4.3.3. ACQ to AIE transformation	116
4.3.4. EEM spectra	119
4.3.5. Supramolecular assembly modulate condensed state luminescence	121
4.3.6. SCXRD analysis	123
4.3.7. Electronic properties controlled the photophysical properties	124
4.3.8. Solid state white light emission	125
4.3.9. Theoretical Calculation	126
4.3.10. Singlet Oxygen (Type 2 ROS) Detection	128
4.3.11. Total ROS generation evaluation	128
4.3.12. Radical (Type 1 ROS) detection	129

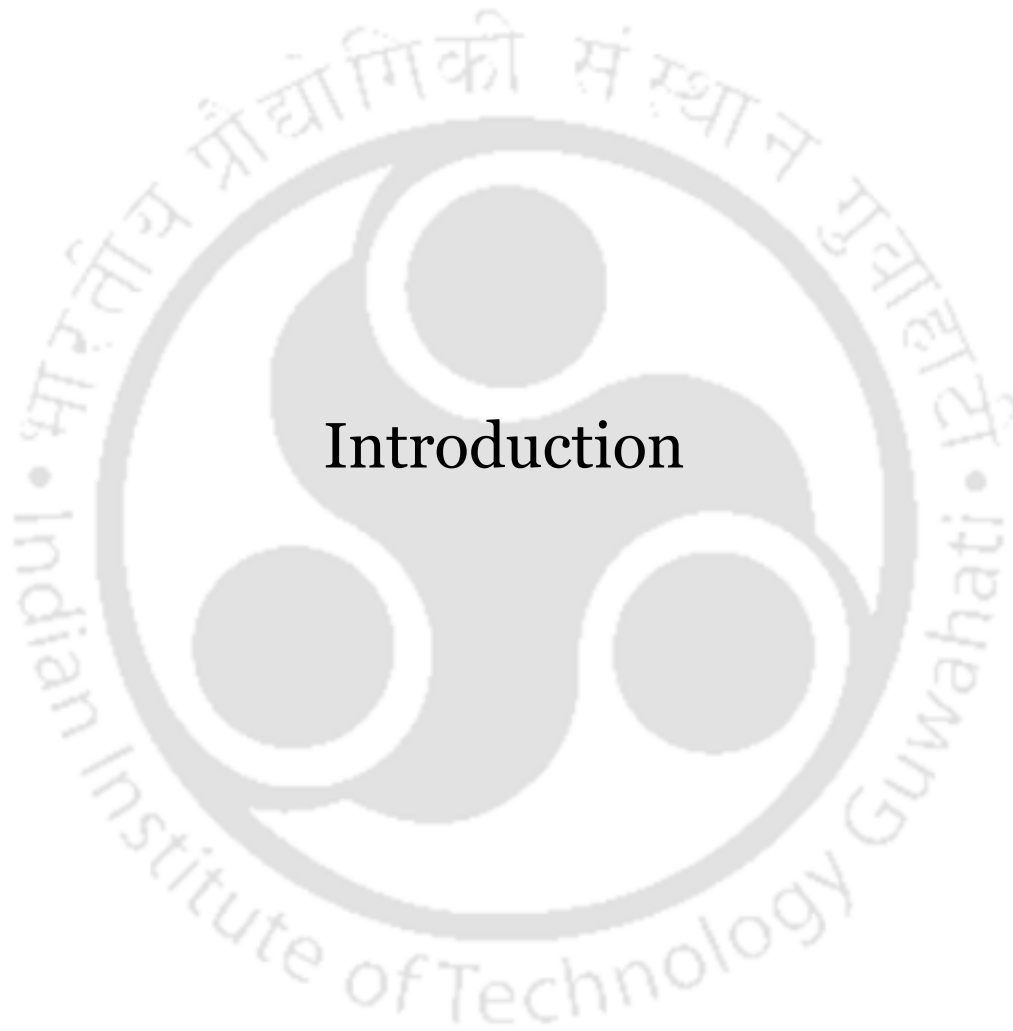
4.3.13. Mitochondria targeting cell imaging, and white light induced efficient PDT performances	131
4.3.14. Live cell/ dead cell co-staining and intracellular ROS generation	133
4.4. Conclusions	134
References	135
Appendix	137

Chapter 5 Sulphur-Atom Positional Engineering in Perylenimide: Structure-Property Relationships and H-aggregation Unveiled Type-I Photodynamic Therapy

Abstract	208
5.1. Introduction	209
5.2. Experimental Section	211
5.2.1. Materials and Instrumentations	211
5.2.2. Preparation of the Test Solution	212
5.2.3. Preparation of FESEM samples	212
5.2.4. Theoretical Studies	212
5.2.5. Photoluminescence quantum Yield Calculations	212
5.2.6. Synthesis of RPNI-O and RPNI-S derivatives	213
5.2.7. Computational studies	216
5.2.8. $^1\text{O}_2$ generation quantum yield Estimation	217
5.2.9. Reactive oxygen species (ROS) Generation/Mesurament	217
5.2.10. The Point of Zero Zeta Potential Evaluation	218
5.2.11. The Energy of the Valence Band and Conduction Band Calculations	218
5.2.12. Cell studies	219
5.2.12.2. Dark & Light Cytotoxicity Evaluated by MTT assay	219
5.2.12.3. Cellular Uptake	219
5.2.12.4. Live/dead cell co-staining assay	220
5.3. Results and Discussion	220
5.3.1. Design, synthesis and characterization of RPNI derivatives	220
5.3.2. Photophysical Properties	221
5.3.3. ACQ to AIE transformation	225
5.3.4. Excitation-emission matrix spectra	227
5.3.5. Supramolecular self-assembly	229
5.3.6. SCXRD analysis	231
5.3.7. Electronic properties driven the photophysical properties	233
5.3.8. Theoretical Calculation	234

5.3.9. Singlet Oxygen (Type 2 ROS) Detection	237
5.3.10. Total ROS generation evaluation	237
5.3.11. Type 1 ROS evaluation	238
5.3.12. Photodynamic therapy in vitro	241
5.3.13. Live cell/ dead cell co-staining and intracellular ROS generation	243
5.4. Conclusions	246
References	247
Appendix	252
Future Aspect and Thesis Overview	310
Publications	314
Patents	315
Awards	315
Conferences	316
Vitae	316





Introduction

1.1. Classical Fluorophores and Need of Condensed State Emitters

Organic luminescent materials have great potential due to their light emitting processes, which have prominently impacted several other high technological innovations and opened up numerous possibilities in the modern world. The development of luminescent materials is a hot topic in the scientific community. The Nobel Prize was awarded to the work on green fluorescent protein (GFP) in the year of 2008 is witness to this, which has resulted in great advances into the biological field due to its visualizing ability of biochemical processes and structures.¹ Theoretical perspective of the luminescent materials shows their promising practical applications in different physical states such as liquid, solid, and gaseous state. However, most of these classical fluorophores show complete quenching of their emission or reduced emission in a condensed state compared to their bright emission in a dilute solution.²⁻⁵ For example, Fluorescein in water (good solvent) in a completely dissolved state emits strongly, however, its emission intensity quenched progressively with a gradual increase of the acetone (poor solvent) in water and becomes almost non-fluorescent (Figure 1.1). This is due to the poor solubility in the acetone, which subsequently leads to a more pronounced local concentration quenching effect and this has been clearly noticeable above the 60% acetone fraction in water. In other words, fluorescence quenching of fluorescein with increasing volume fraction of acetone is more pronounced owing to its simple aggregate formation. In the aggregated-state, the planar aromatic core of the fluorescein exhibits strong intermolecular face-to-face π - π stacking interaction, which dissipates or consumes its maximum amount of excited energy and leads to non-fluorescent aggregate. Besides, fluorescein shows totally quenched emission in its powder form due to its prominent π - π stacking interaction in its condensed state. This type of fluorescence quenching phenomenon is termed as aggregation caused quenching (ACQ), which has been well-established for many years. Förster in 1954, discovered this concentration quenching (CQ) effect phenomenon.⁷ The fluorescent dyes almost often get quenched in their solution state and on increasing the concentration it leads to aggregate formation and this notorious physical CQ phenomenon have been most dominant. Bricks et al summarized this ACQ phenomenon in his book on Photophysics of Aromatic Molecules in 1970.⁸ The conventional fluorophores often exhibit totally quenched fluorescence due to the aggregate formation and this aggregate formation is more prominent in poor solvents even at lower concentrations as well as in solid state. Various real-world applications including fabrication of different optoelectronic devices like organic field effect transistors (OFET) and organic light-emitting diodes (OLED) requires the luminogenic materials in their condensed state (solid, thin-film or crystal state).¹ Besides, organic fluorophoric system have been extensively employed in biomedical field, where

luminogenic materials are applied in the physiological environments or in aqueous media. Although the polar functionality like sulphonic or carboxylic groups of the fluorophores increase the water solubility and leads to strong emission, they could quench fluorescence significantly in their aggregated state owing to the strong hydrophobicity of the planar aromatic cores which are prone to aggregate formation efficiently in aqueous media. Despite the various potential technological applications of the classical fluorophores, the notorious ACQ effect often leads to negative impact and prevents their wide varieties of real-world applications like OLED and biomedical field (Figure 1.1 and 1.2).^{1,9-11} Thus, the advancement of the condensed state emissive materials are considerably in high demand and of huge impact that could open up routes with many promises and high technological innovations along with many unexplored possibilities.

1.2. Discovery and Types of Condensed State Emission

Tang group discovered the aggregation-induced emission (AIE) behavior which has changed the insights of the aggregating materials.¹² Unlike the classical fluorescent dyes, which are non-fluorescent in a condensed state, the first discovered propeller-shaped AIEgen named as hexaphenylsilole (HPS) derivatives, exhibit strong emission in their aggregated or solid state. The generation of this new phenomenon of unconventional emitters are named as luminogens. In contrast to ACQ system, these AIEgens show emission when they are together (aggregate) and non-fluorescent in individual (solution state). Figure 1.2 presents some well-established condensed state emitters and conventional fluorophores. The condensed state luminescent property of the luminogen materials are dependent on their behavior at different states, and have been divided into many categories, and are discussed below subsequently.

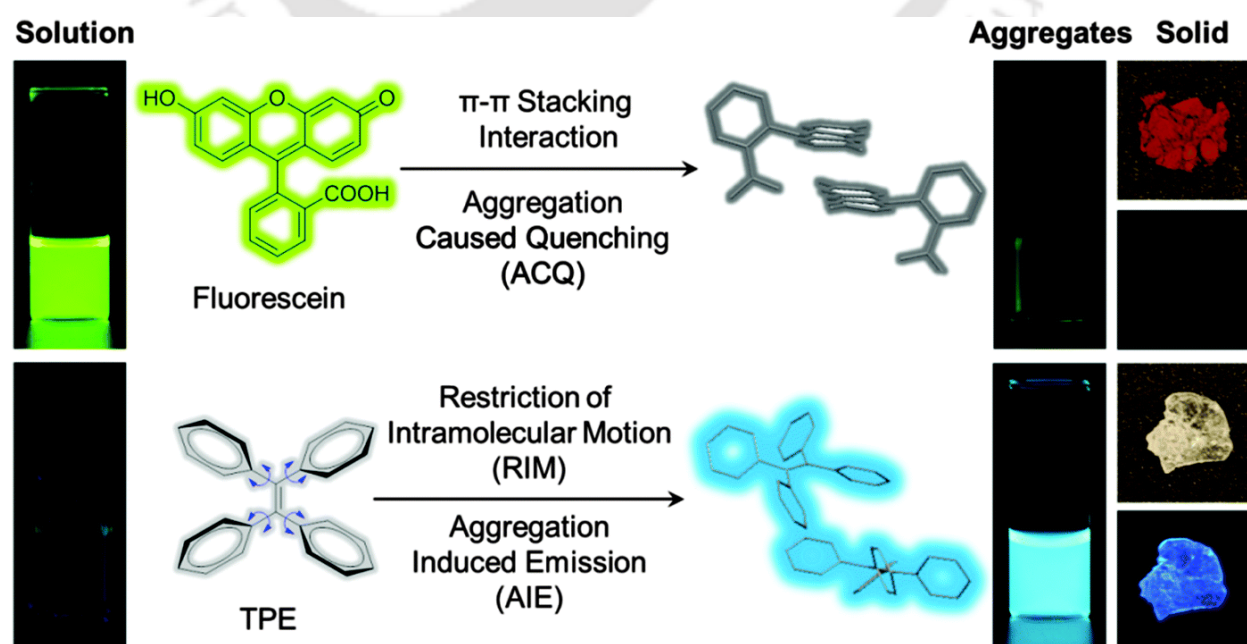


Figure 1.1. A classical fluorophore fluorescein exhibits strong emission in solution state and quench emission in their aggregated or solid state. The propeller-shaped tetraphenylethene (TPE) AIEgens shows strong emission upon aggregation as well as in the solid state. Adapted from Ref. 6 with permission from The Royal Society of Chemistry.

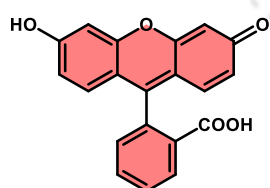
1.2.1. Aggregation-Induced Emission

In Figure 1.1, fluorescein shows strong emission in their dilute state such as in the good solvent and complete reduction of the emission in the poor solvent such as upon aggregation. Whereas, the non-planar tetraphenylethene (TPE) exhibits exactly opposite photophysical phenomenon to that of the fluorescein, which shows strong emission in the poor solvents due to the homogenous nanoaggregate formation. This type of completely opposite phenomenon of the molecules where non-fluorescent molecules display emissive characteristics in their aggregate state and completely quenched emission property in their solution station, are termed as aggregation-induced emission (AIE).

1.2.2. Aggregation Induced Emission Enhancement

In 2002 Park et al discovered another condensed state phenomenon termed as aggregation induced enhanced emission (AIEE), which is a subclass of the AIE.^{1,13} This class of molecules show strong emission both in solution state (good solvent) as well as in their aggregated-state (poor solvent). However, the emission of this class of molecules shows reduced emission upon increasing the poor solvent and emission turns back strongly due to the highly emissive nano-aggregate formation. This could be due to the J-aggregation and intramolecular planarization. This type of AIEE derivatives highlighted considerable attention owing to their both dilute state and condensed state emission.

Conventional Fluorophores (ACQphores)



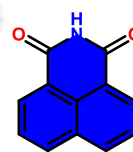
Fluorescein



Perylene

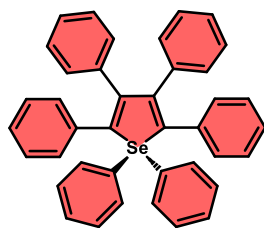


fi-TTE

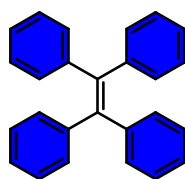


Naphthalimide

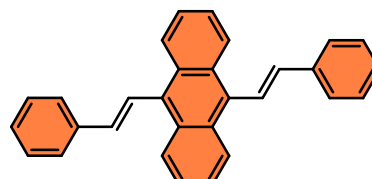
Condensed State Emitters (AIEgens)



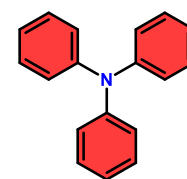
HPS



TPE



DSA



TPA

Figure 1.2. Chemical structures of few classical ACQphoric fluorophores and well-established condensed state emitters.

1.2.3. Dual-State Emission

Tang group developed another interesting phenomenon apart from the AIE and AIEE, termed as dual state emission (DSE), where like the AIEE luminogens it emit strongly both in solution state and condensed state.¹⁴ However, unlike the AIEE active materials, DSE materials show strong emission in all possible solvent fraction. The development of the DSE materials are in initial stage and exhibit distinct advantages compared to AIE, ACQ and AIEE materials.^{15,16}

1.2.4. Crystallization Induced Emission

Crystallization-induced emission (CIE), another concept in the field of the condensed state luminescent materials has also received potential attention. These CIE materials emit strongly in their crystalline state compared to their solid amorphous state or aggregated-state as well as solution state unlike the AIE/AIEE and DSE luminogenic materials, where the materials show intense emission in their aggregated-state or in their solid powder form. This notable CIE properties manipulate the luminescence characteristics by simply external stimuli such as cooling, heating and fuming processes between bright and dark state. Thus, this CIE phenomenon could find a promising attention for the novel application in rewritable optical media, chemosensors, and optical displays (Figure 1.3).^{17,18}

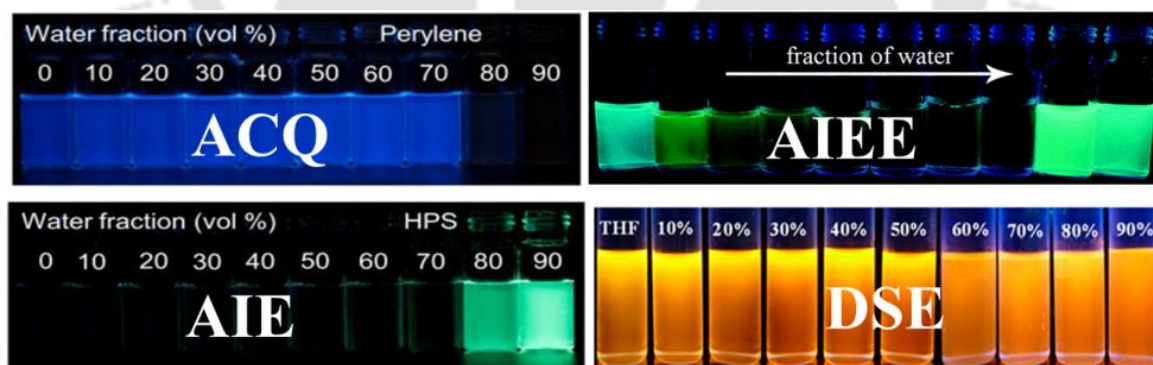


Figure 1.3. Schematic presentation of the ACQ, AIE, AIEE and dual-state emission behaviors of the luminescence materials.

1.3. Working Mechanisms

Many researchers have hypothesized various mechanistic insights of this remarkable condensed state phenomenon including J-aggregate formation, excited state intramolecular

proton transfer (ESIPT), conformational planarization, E/Z isomerization, and twisted intramolecular charge transfer (TICT),^{1,9} However, these mechanistic insights are not universalized due to their irrelevant application in all the discovered luminescence materials. Tang et.al in 2014, generalized these working mechanisms and depicted strong features concerning the condensed state emission properties.^{1,9} Herein, the restriction of intramolecular motion (RIM) has been hypothesized as a most convenient and reliable working mechanism for the condensed state luminescence materials, which has been proved via experimental and solid theoretical analysis. According to the fundamental physics, the organic molecules comprising of the rigid rotors could consume the maximum amount of the excited energy via the intramolecular dynamic rotation and vibrations lead to non-emissive or less emissive behavior in their solution state. Whereas, the molecules interlock themselves in their condensed state such as aggregated or solid state, which subsequently restrict their intramolecular rotation (RIR) and vibration (RIV) and relax via radiative decay pathways. It is also significantly important to declare that the intermolecular face-to-face π - π stacking interactions, which prominently leads to ACQ phenomenon via radiationless relaxation along with the red-shift has been often observed in most of the conventional fluorophores. Considering these scenarios, the designed approach of the well-explored AIEgens like TPE, HPS and TPA have been taken into most significant interest that their propeller-shaped conformations lead to strong emission in their condensed state due to its restriction of their intermolecular face-to-face π - π stacking interaction (Figure 1.4). This general technique can be promisingly employed to any different ACQ planar system to achieve the AIE/AIEE characteristics via simple structural perturbation by altering their planarity or avoiding their strong intermolecular π - π stacking interactions among the planar aromatic cores. Thus, various groups have proposed to develop various design strategies, which can be potentially applied to the existing inherent classical fluorophores to achieve the condensed state emission and unlock their versatile real-world applications.

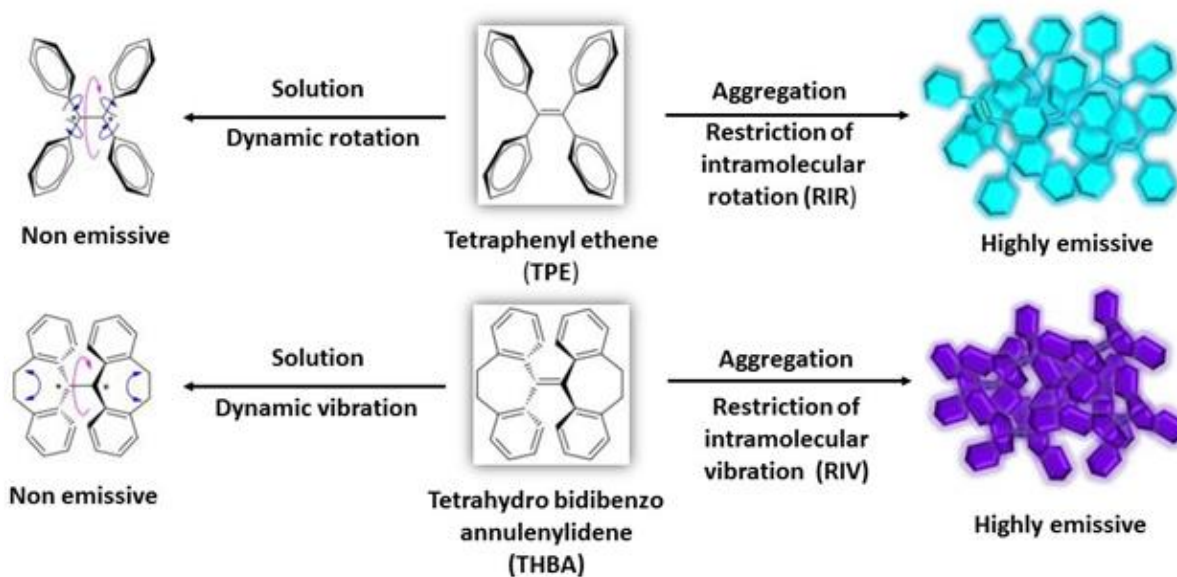


Figure 1.4. Graphical representation concerning the mechanistic insight of the condensed state emission.

1.4 Potential Applications of condensed state emitters

This up-to-date condensed-state emissive phenomenon has been extensively considered in the scientific interest owing to their broad applications including bio/chemosensors, electronic devices, biomedical such as cancer theranostics, image-guided therapy, and many more, which have been schematically illustrated in Figure 1.5.⁵

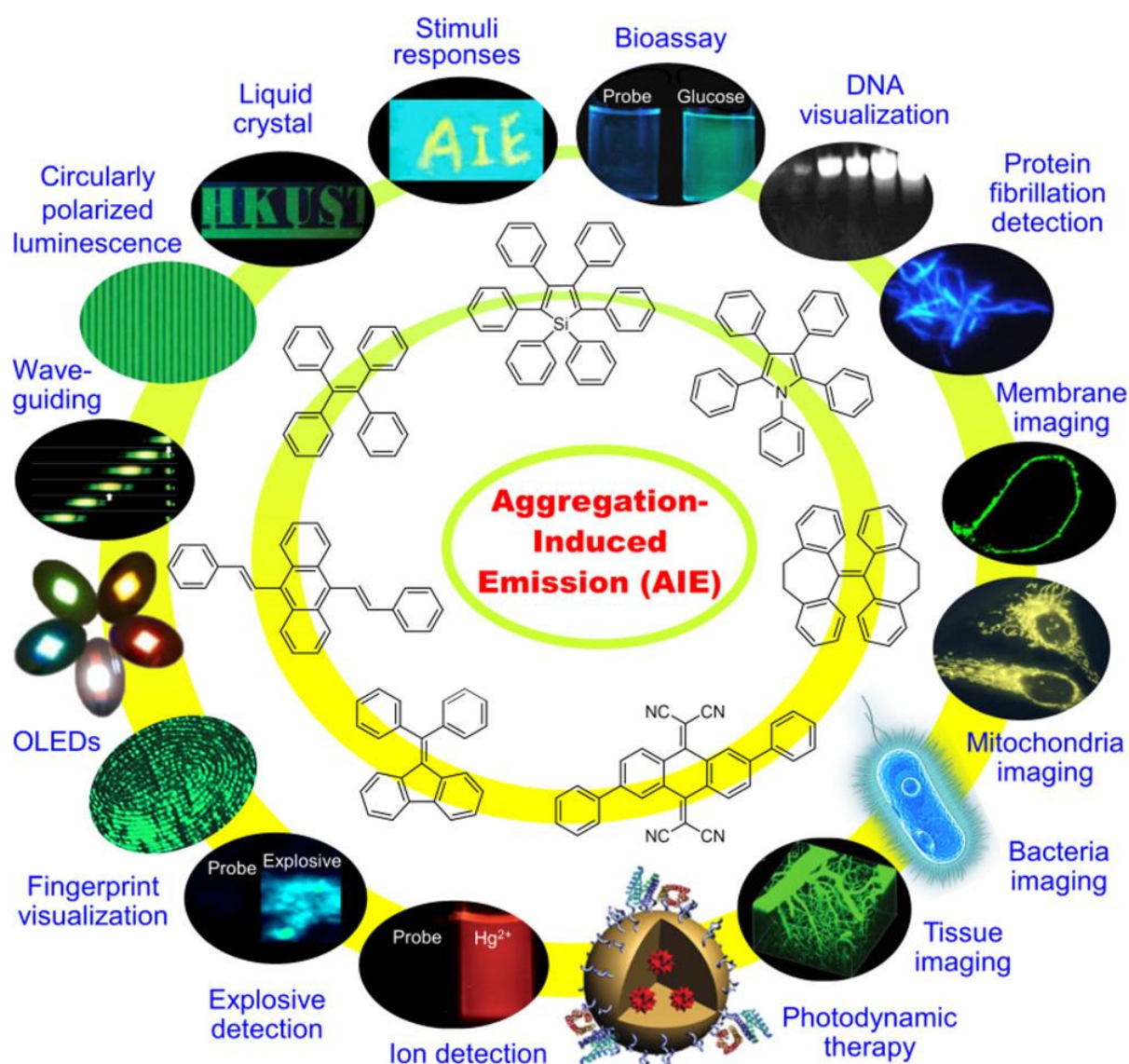


Figure 1.5. Graphical illustration of the various diverse real-world applications of condensed state emitters.

1.5. Naphthalimide Luminogens

In recent years, there has been significant development in a wide range of AIE/AIEE cores, particularly the well-established silole and TPE luminogen cores. However, there is currently growing interest in the utilization of new TPA cores as luminogenic cores. Additionally, researchers are continuously exploring the design of new AIE/AIEE luminogens or structural modifications of classical cores to expand their applications beyond the limitations imposed by the ACQ phenomenon.^{1,9} Traditional ACQ fluorophores like perylene and fluorescein have been successfully converted into condensed state emitters, showcasing their immense potential in optoelectronics and biomedicine.¹ The naphthalimide (NI) core has emerged as a versatile fluorophore with exceptional photophysical properties. It exhibits absorption in the UV-visible region and fluorescence emission in the visible to near-infrared (NIR) region, making it an excellent platform for studying biological systems.²⁰ NIs have found applications

in various fields such as fluorescent sensors, optoelectronic materials, laser dyes, and bioimaging, owing to their remarkable chemical, thermal, and quantum yield properties.^{19,21} Additionally, **NI** derivatives have demonstrated antitumor activity against both human and murine cells.²² Modifying the **NI** core with thiazole or poly thiazole groups has been employed in the development of antibiotics related to anticancer agents like bleomycin and photo nucleases.²³ Sulfonated **NI** derivatives have shown antiviral activity and selectivity towards the human immunodeficiency virus (HIV-1) in vitro.²⁴ Furthermore, bromination of the **NI** core at the third and fourth positions has exhibited a photochemotherapeutic inhibitory effect on the blood.²⁵ These diverse applications highlight the broad possibilities of **NI** derivatives in phototherapy, DNA-binding motifs, and anticancer agents.²⁶ Despite the wide range of applications for **NI** cores²⁷, their ACQ properties have limited their practical utility. In 2011, Chang et al. developed the first AIEE **NI** luminogens by substituting them with rigid aromatic groups, which extended the π -conjugation and led to the formation of flexible and nonplanar fluorescent nano aggregates. This contribution demonstrates that the highly emissive planar **NI** molecules in the solution state, where the molecules are isolated, exhibit dense intermolecular face-to-face π - π stacking interactions, resulting in quenched emission in their aggregated-state via H-aggregation. However, the substitution of the planar **NI** core with rigid planar aromatic groups restricts this H-type aggregation and exhibits strong fluorescence in their condensed state, while becoming weakly emissive or completely non-emissive in the solution state due to the dynamic rotation or vibration of the attached pendant rigid aromatic unit in the **NI** core. This example highlights the transformation of an ACQ molecule into an AIE/AIEE material by simply substituting the core, thereby breaking its planarity. Another approach involves incorporating the AIE unit into a polymeric chain to form AIE/AIEE polymers. The main objective of this structural engineering is to restrict the problematic face-to-face packing interaction of planar aromatic molecules in their aggregated or solid state.

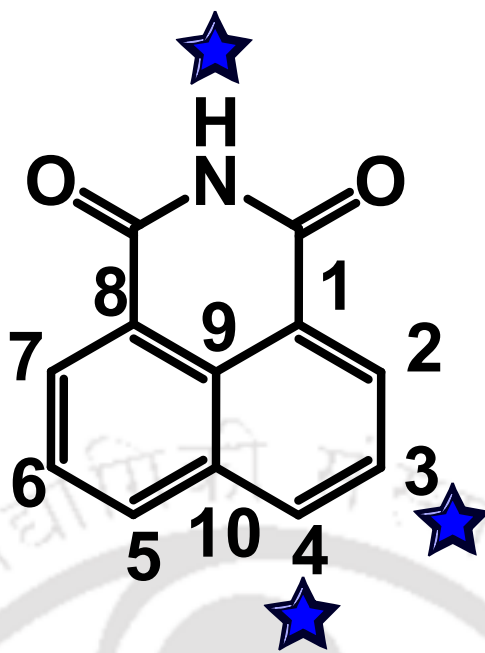


Figure 1.6. Illustration of NI core representative the most reactive positions (blue star).

1.6. Potential Applications of Naphthalimide Luminogens

Various research groups resolved the ACQ hurdle by distinct well-designed molecular engineering. To date, high fluorescence quantum yield in solid as well as aggregated-state NI derivatives have been reported by N-substitution or substitution at fourth position by the organic units, which unlocks many restricted areas with various possibilities (Figure 1.6).²⁸ These types of altered luminogens have been highly promising towards OLEDs as well as in living cells. Many condensed state emitters are habitually insoluble in aqueous media, which form stable emissive nanoaggregates in aqueous media. These kinds of stable and higher surface area aggregates comprising of inherent characteristics are highly essential for biomedical or biological application both in vitro and in vivo. Thus, it is clearly evident that NI derivatives exhibit wide versatility towards many applications from the past decade. The development of many AIE/AIEE NI condensed state emitters has demonstrated that the integration of concept of AIE/AIEE phenomenon leads to NI derivatives with huge versatility (Figure 1.7).²⁸

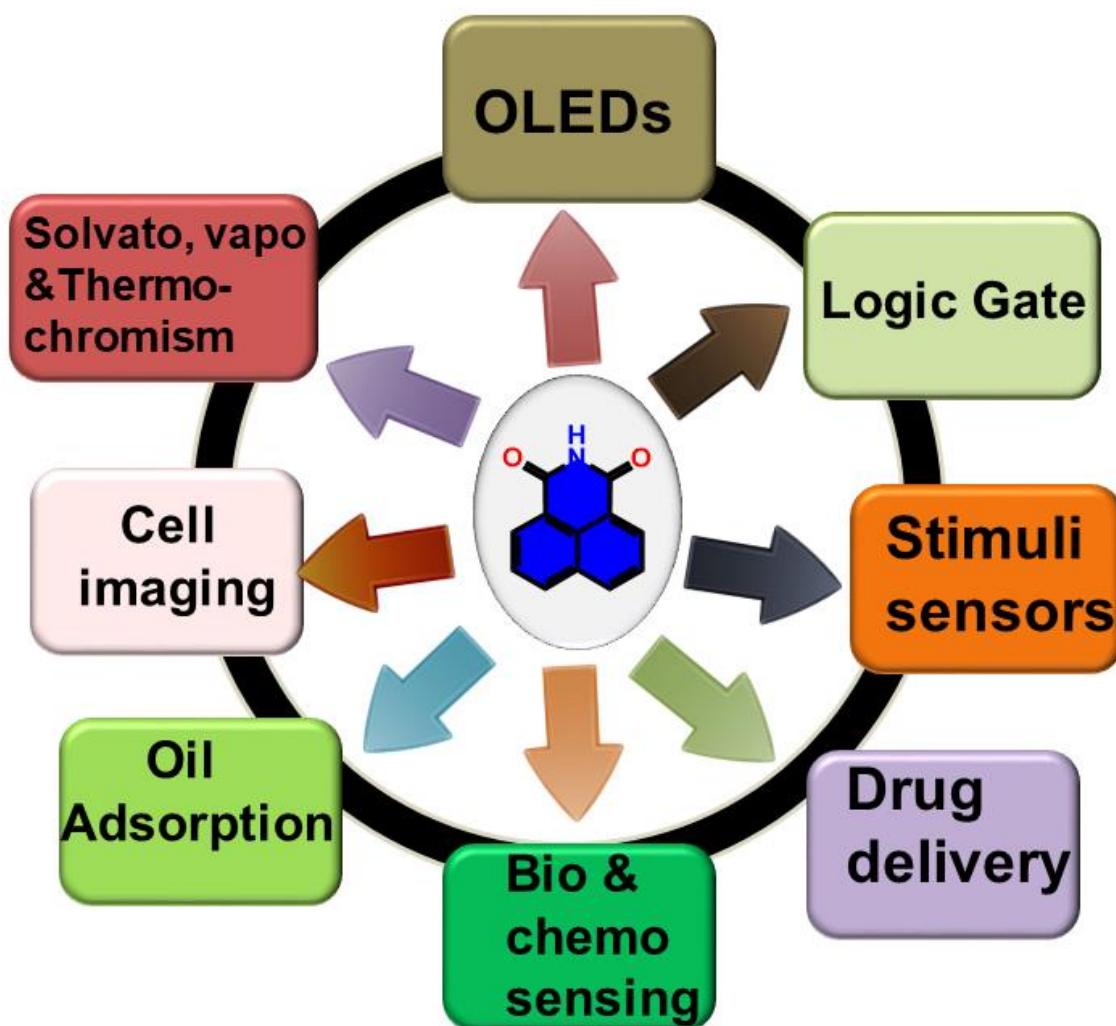


Figure 1.7. Possible technological applications of the AIE/AIEE active NIs.

1.7. Structural Engineering to obtain Naphthalimide Luminogens

1,8-naphthalic anhydride precursor have been easily functionalized in N-position via simply Gabriel phthalimide synthesis. Most of the literature has been well-explored that N-substitution via alkyl amine groups leads to imide linkage and improves the solubility in most of the organic solvents. However, it is a hurdle for most of the N-functionalized NI derivatives to overcome the π - π stacking interactions among the planar NI cores in their condensed state that leads to less efficient luminogens. These stacking interactions between the NI cores can be overcome by substitution at the alternative reactive position of the NI aromatic core (Figure 1.8).

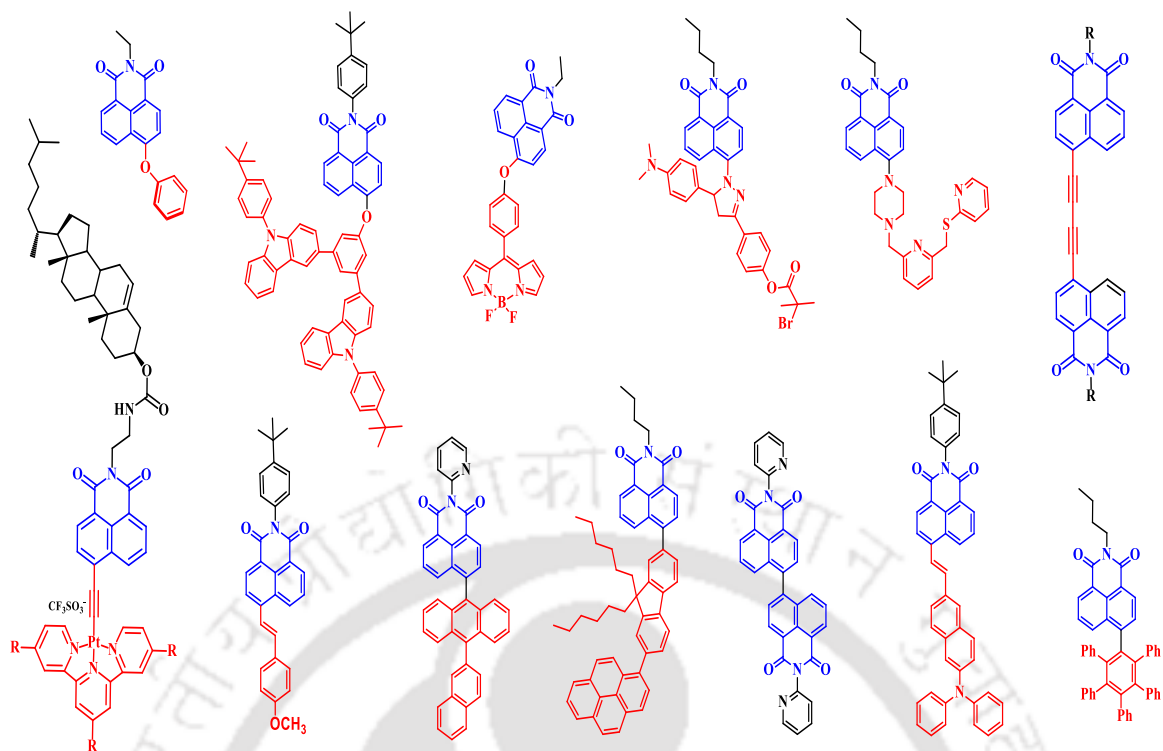
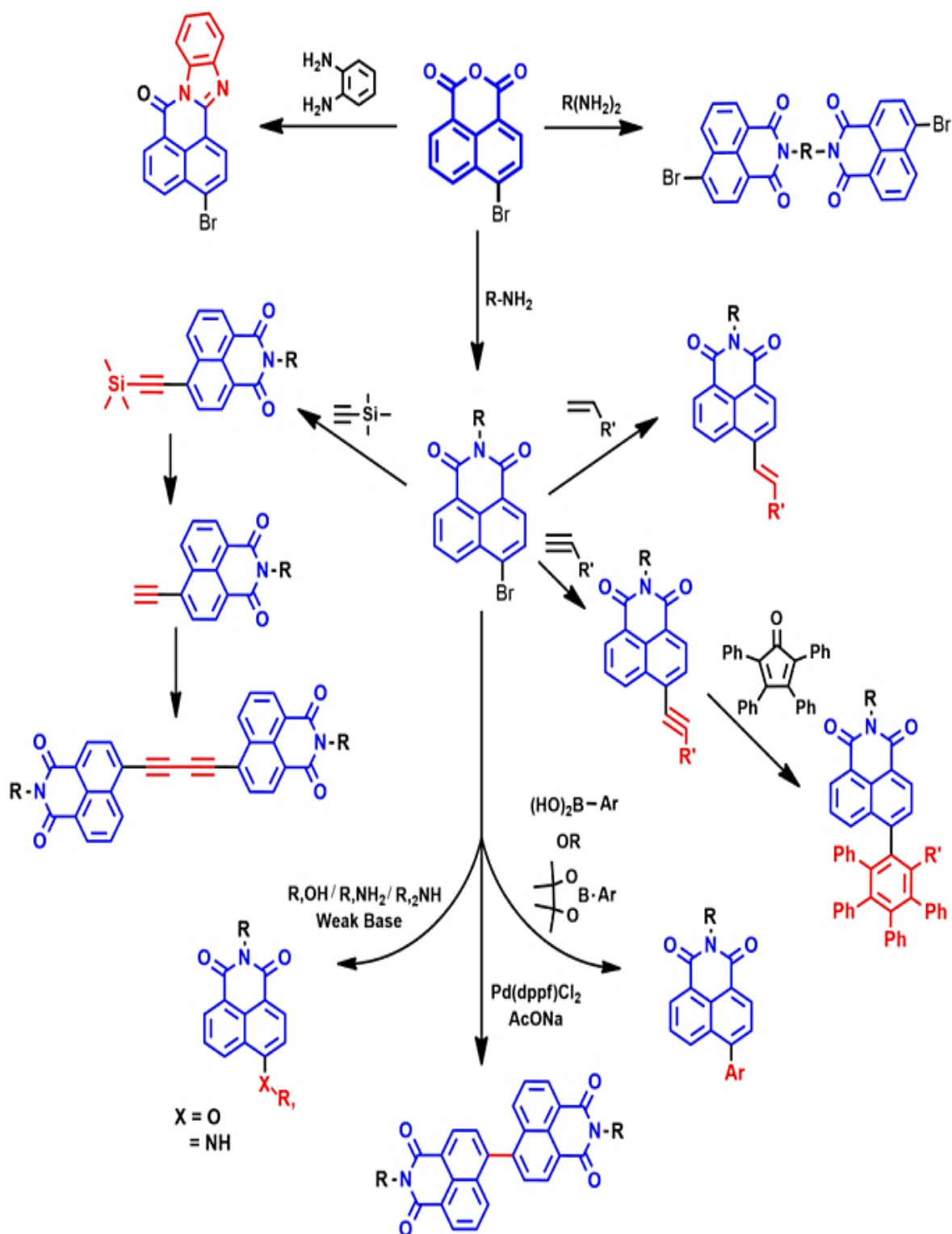


Figure 1.8. The chemical structures of some of well-established AIE/AIEE NI luminogens applied in multiple technological applications.²⁸



Scheme 1.1. Possible synthetic technique to achieve AIE/AIEE NIs.

The fourth position of the NI core are highly facile to substitute and can be easily tweaked via different synthetic techniques to generate condensed state emission like AIE/AIEE behaviors in classical NI cores. The different susceptible methods to generate this phenomenon which have evolved in several past decade, have been potted in Scheme 1.1.²⁸ The fourth position

substitution of the **NI** core leads to the most promising AIE/AIEE **NI** luminogens. Some well-explored core substitution **NI** condensed state emitters applied in multiple technological applications have been summarized in Figure 1.8.²⁸

1.8. Perylenimide Luminogens

Although peryleneimide (**PI**) derivatives exhibit excellent photophysical properties with absorption in the UV-visible region and the ability to tune emission up to the NIR region, their strong absorption and fluorescence emission in the visible region can be easily shifted to the red or NIR region in the condensed state.²⁹⁻³⁹ Moreover, **PI** derivatives are prone to intrinsic π - π stacking interactions between the perylene cores, which can be utilized to modulate their structural perturbation and result in distinct supramolecular self-assembly behavior in the condensed state. This exceptional photophysical behavior of **PI** derivatives surpasses that of **NI** derivatives and holds great significance in various biomedical applications. **PIs** demonstrate outstanding thermal, chemical, and photochemical stability in most organic solvents, along with high fluorescence quantum yield (QY) and high extinction coefficient, making them suitable for a wide range of applications such as organic light-emitting diodes (OLEDs), field-effect transistors (OFETs), and dye sensitizers in solar cells. Their absorption and emission maxima above 500 nm minimize autofluorescence in living cells.³⁰ However, **PIs** have poor water solubility, leading to weak or completely quenched emission, as well as detrimental face-to-face π - π stacking interactions between the perylene backbone, resulting in non-fluorescent or quenched emission characteristics in the condensed state. These limitations restrict the promising medicinal and biological applications of **PI** derivatives. Nevertheless, by introducing cationic, anionic, sulfonic acids, phosphonic acids, and functional groups like PEG (polyethylene glycol), dendritic carbohydrates, and polyglycerol dendrons at the imide or bay positions, the water solubility of **PIs** can be improved, overcoming the fluorescence quenching phenomenon. Water-soluble **PIs** exhibit tremendous biological applications, including DNA sensors, bioimaging, lysozyme sensors, tissue imaging, and many more, leveraging their intrinsic assembly formation properties.³⁸ Despite the broad applications of **PI** derivatives in optoelectronics and the biological field, their potential has been limited by the aggregation-caused quenching (ACQ) phenomenon resulting from strong π - π stacking interactions among the perylene cores. In 2018, different donor groups were functionalized at the bay position of the planar **PI** cores to disrupt the intrinsic π - π stacking interactions and enable condensed state emission characteristics. Additionally, tartaric acid-induced AIEE-active **PI** derivatives have been developed, exhibiting efficient supramolecular assembly and distinct chiral characteristics. The utilization of propeller-shaped TPE in **PIs** has been prevalent in generating AIE/AIEE characteristics. These TPE-induced NIR-emissive condensed state **PI** emitters have been reported, unlocking their potential for bio-imaging

applications. While the first generation of **PI** derivatives with two imide linkages has been extensively explored across various fields, the second generation with one imide linkage represents a new class of luminogens. In 2016, the Zhao group developed NIR-emissive AIE **PI** derivatives containing one imide linkage in aqueous media by N-functionalizing the planar perylenimide core with a 2,5-di-tert-butylphenyl group, which breaks planarity and overcomes π - π stacking interactions.³⁵ These water-soluble **PI** derivatives exhibit condensed state NIR emission and demonstrate phototherapy effects. They have also been employed as folate receptors targeting cancer cells in the condensed state. The excellent photophysical properties and large Stokes shift of **PI** derivatives unlock their versatile biological applications. Additionally, **PI** derivatives with one imide linkage exhibit less symmetry compared to those with two imide linkages, enabling easy structural modulation to disrupt planarity and overcome detrimental face-to-face dense π - π stacking interactions between the planar perylene cores (Figure 1.9).

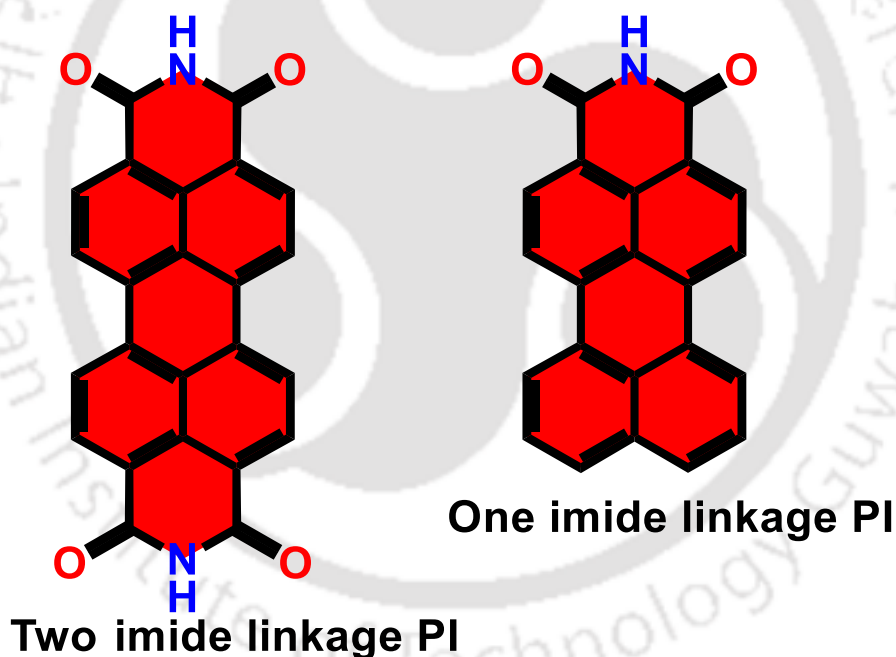


Figure 1.9. Chemical structures of two imide and imide linkage **PI** derivatives.

1.9. Potential Applications of Perylenimide Luminogens

Generally, low molecular weight small molecular systems are favored over polymeric system considering the easier synthetic procedures and structure modification.^{3,4} Herein, perylenimide core has been used over other conventional fluorophores due to easy synthetic procedures, modification and photophysical, optoelectronic properties can be tuned easily by simply destroying the notorious strong π - π stacking interaction among the planar aromatic

cores. Unlike the two imide linkage **PIs**, one imide linkage **PI** comprising of similar π - π stacking interaction with two imide linkage **PIs** shows easy structural manipulation due to its less symmetry compared to two imide linkage **PIs**. It is well witnessed that from the past decades, bulkier AIE lumigen core like TPE or HPS have been chosen to achieve AIE/AIEE behavior in two imide linkage planar **PIs**. Whereas, the asymmetry characteristics of the one imide linkage **PI** leads to its efficient condensed state emitter by easily tweaking its π - π stacking interaction via incorporating the small aromatic cores. Besides, the strong visible absorption, photostability, thermal stability and good thin-film forming characteristics triggers its versatile applications in optoelectronics like organic light emitting diode (OLED), OLET, photovoltaics, bioimaging with deep tissue penetrating, and sensory arrays (Figure 1.10).²⁹⁻³⁹

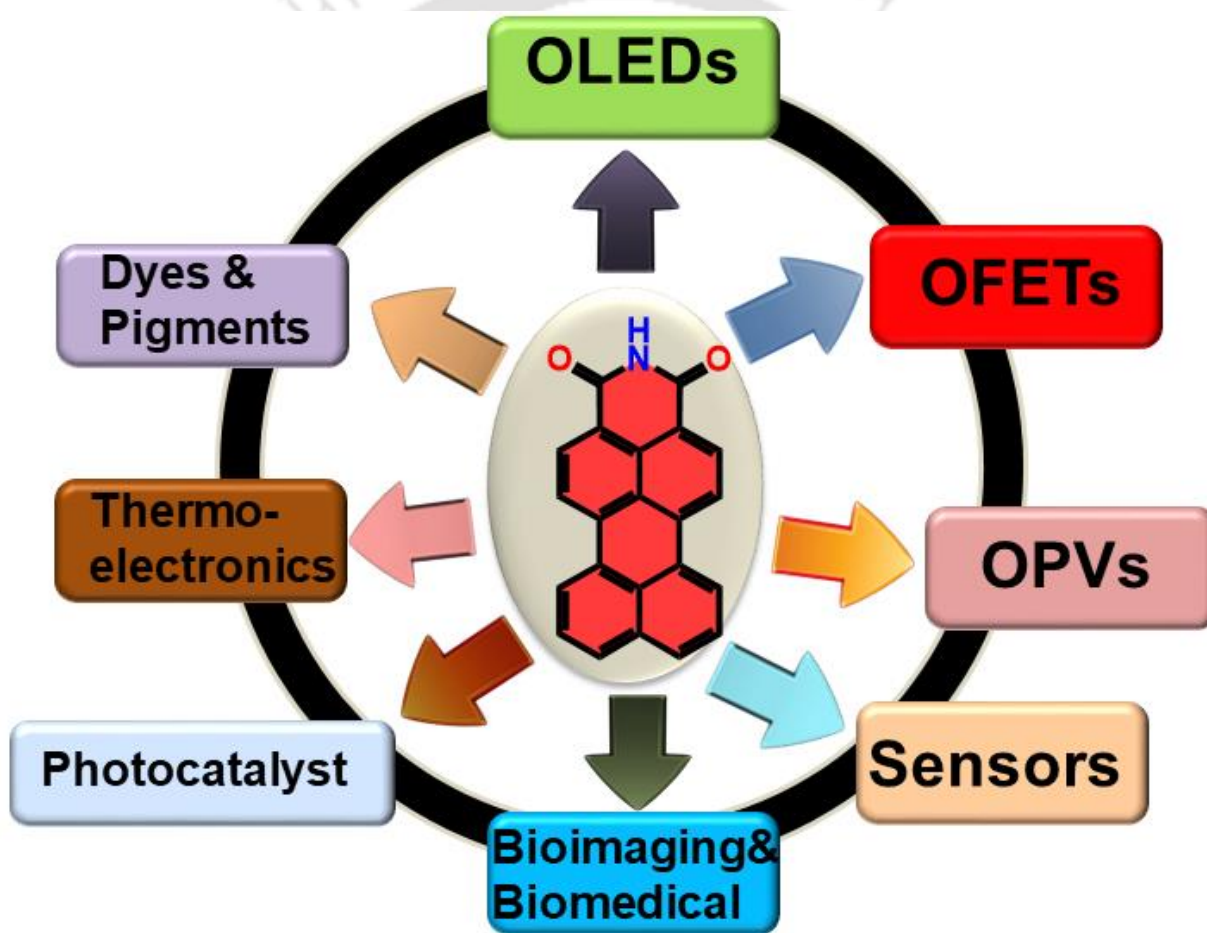


Figure 1.10. Schematic illustration of the wide-range applications of AIE/AIEE **PIs** condensed state emitters.

1.10. Structural Manipulation to Achieve Peryleneimide Luminogens

Perylene dianhydride precursors have been used to N-functionalize **PIs** via hydrothermal reaction procedures. Although, N-functionalization through alkyl chains at the imide position in **PIs** improve its solubility in most of the organic solvents, it is hurdle for most of the **PI** derivatives to break its planarity by destroying the notorious π - π stacking interaction between planar **PI** cores that leads to non-fluorescent or weak emissive condensed state emitters. This stacking interaction can be easily tweaked, which subsequently simply break its planarity by the functionalization at the bay (6/7 or 1/12) as well as peri (9/10) positions in **PIs** (Figure 1.11) and enhanced its condensed state emission property. The bay or peri position substitution in **PIs** leads to most efficient condensed state emitters. The general facile and susceptible structural engineering procedures have been depicted in Scheme 1.2. Along with some well-explored AIE/AIEE condensed state emissive **PIs** employed in wide varieties of real-world applications, some have also been summarized in (Figure 1.12).^{40,41}

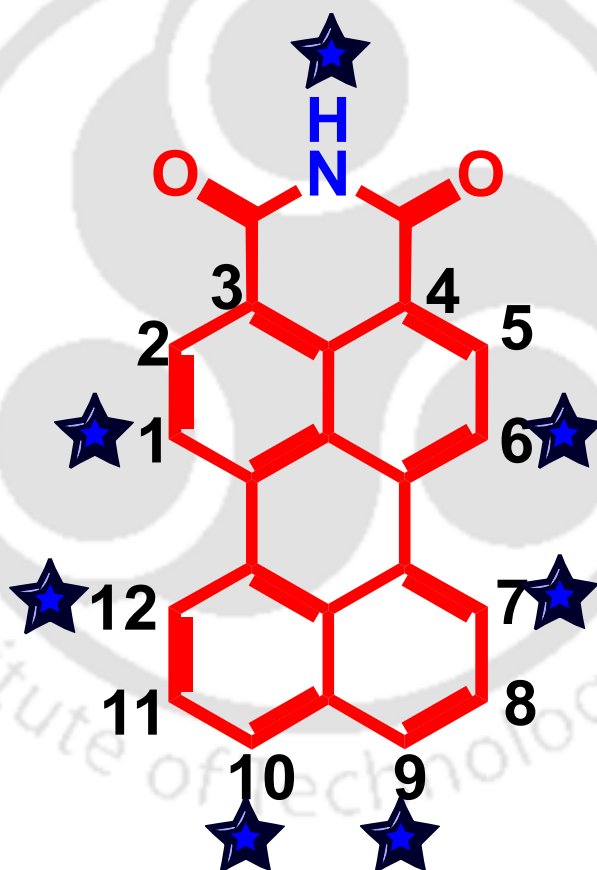


Figure 1.11: Graphical representation of **PI** core demonstrating the most reactive positions (blue star).

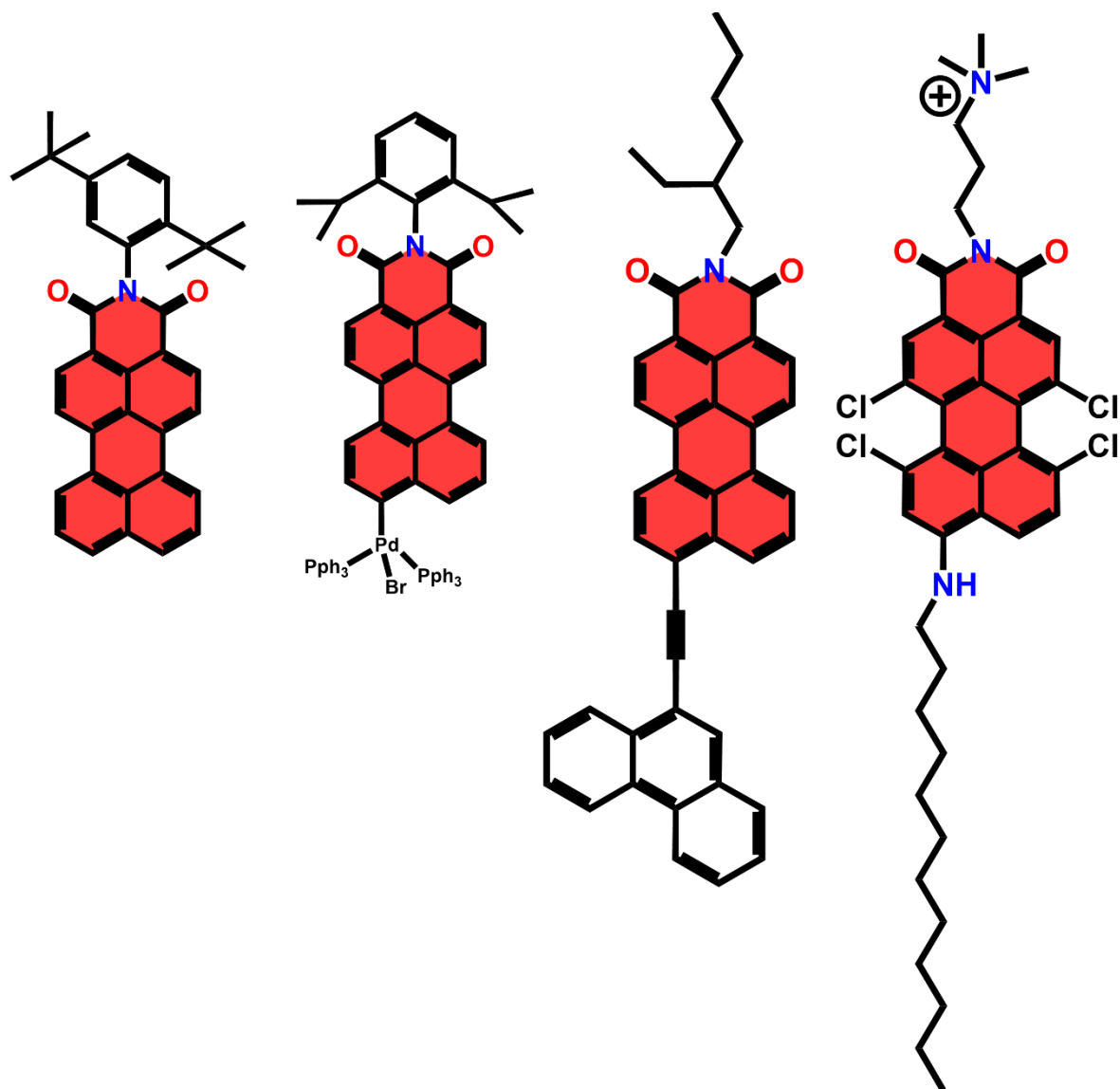
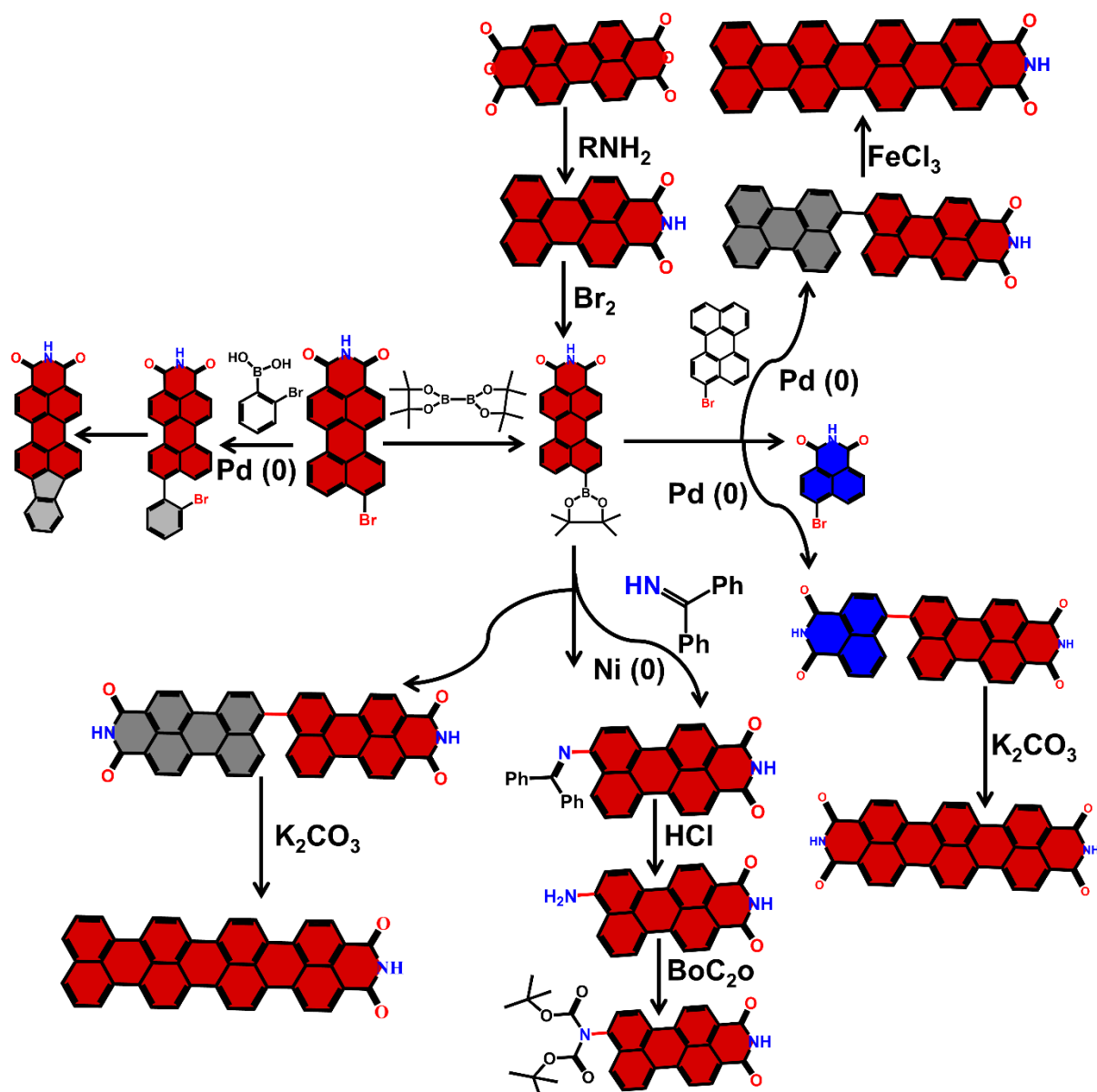


Figure 1.12. The chemical structures of some of the well-established AIE/AIEE PI luminogens are applied in multiple practical applications.



Scheme 1.2. Possible Synthetic route to achieve AIE/AIEE PIs.

1.11. Objective and Conclusion of the Thesis work

NI and **PI** materials are well-known acceptors and have been extensively studied in multiple platforms over the last several decades. They have received a significant interest among the scientific community due to its accepting nature and high fluorescence quantum yield. The **NI**s and especially **PI** based AIEgens highlight a new class of luminogens with huge promises for various practical applications. TPE and HPS are well-established standard and efficient luminogenic cores, whereas TPA opens a new luminogenic core in this area. Various research groups have been actively participating in this field and developed a large number of AIE/AIEE-active materials with their wide variety of applications.

NI luminogens have been extensively explored over the years after the first discovery due to its easy and simple synthetic route. The **NI** luminogens exhibit considerable attention in the supramolecular self-assembly studies, sensors and biological applications. Although, **PI** luminogens has been considered as new class of luminogenic materials in the areas of sensing and biological applications owing to its solubility issues in most of the organic solvents, **PI** materials has been extensively studied in the field of light-emitting diode and solar cells compared to **NI** derivatives. **NI** and **PI** luminogens are promising candidates for long-term bio-imaging and tracking in depth cellular activity owing to its photostability, biocompatibility and condensed state emissive characteristics. More importantly, **PI** luminogens could substitute the **NI** luminogens due to its higher wavelength region absorption and emission properties compared to **NI** AIEgens, and its condensed state luminescence characteristics that can be very easily fine-tuned upto NIR/IR region by simply tweaking of the π - π stacking interactions among the **PI** cores by structural perturbation at their molecular level. The asymmetric and electron withdrawing properties as well as those prone to π - π stacking interactions of the **NI** and **PI** have been recognized to have unique and distinct structure-property relationships. The structural conformation of the asymmetric **NI** and **PI** materials could be easily regulated by easily tweaking its π - π stacking interactions which extend their diverse applications towards many unexplored promises.

In this research area, different new strategies have been developed to switch ACQ/AIE phenomenon in **NI** and **PI** derivatives. This research work focused on the systematic tailoring and construction of the condensed state emission of the **NI** and **PI** by basic structural manipulation. In addition, supramolecular-assembly in **NI**s and **PI**s have been tuned by simple yet judicious structural perturbation. The photophysical properties and supramolecular-assembly behavior is greatly controlled by the intermolecular packing orientations of the **NI** and **PI** by the distinct magnitude of electronic constrains of the attached units. This strategy presents huge possibilities to monitor the biomedical applications of distinct self-assembly spontaneously achieved from the similar electronic motifs. Along with the distinct supramolecular assembly and condensed state properties, the photosensitizer characteristics of the **NI** and **PI** luminogens make them very promising candidates in image-guided photodynamic therapy towards cancer cell and various pathogens. Besides, NIR AIE **PI**s could emerge as a great potential for win-win cooperation in their application for biomedical fields.

The content of the thesis report entitled “**Naphthalimide and Perylenimide Luminogens: Structure-Property Relationships for Sensing and Biomedical Applications**” has been divided into five chapters as summarized below:

Chapter 1 briefly describes the need and discovery of condensed state emission as well as types and mechanistic aspects of luminogens. This chapter demonstrates the importance, potential applications and structural modulation in naphthalimide and perylenimide luminogens as well as the concluding statement on this thesis work.

Chapter 2 demonstrates the influence of the pendant non-conjugated chain effect in perylenimide on the electronic, thermal, photophysical along with their morphology in their condensed state. This chapter also includes the OFET characteristics of the perylenimide comprising of the long pendant alkyl chain.

Chapter 3 provides condensed state luminescence characteristics and supramolecular-assembly behaviors of the naphthalene substituted in naphthalimide. This chapter also unveils the 4-nitroaniline (class III toxic pesticides) detection on multiple platform, which includes in aqueous media and the cost-effective simple and portable Whatman paper test strips based on on-site solid state detection. The sensing mechanisms involved the receptor free inner filter effect (IFE).

Chapter 4 This chapter suggests the simple and precise molecular engineering of donor functional group with targeting imidazole group that serves as condensed state emission and supramolecular-assembly along with their highly ROS generation characteristics that could provide a new tool for the development of the new generation materials for the diverse futuristic application.

Chapter 5 demonstrated the novel yet facile design strategy for the ACQ-to-AIEE transformation by simply tweaking the conformation into the functional group in **PNI** as well as second comprehensive structural design of thiobased PS through S-atom engineering at carbonyl position in **PNI (PNIS)** with excellent potential for PDT in cancer cell.

The thesis concludes with distinct design strategies with fine-tuned condensed state characteristics, and photosensitizing properties with brief future possibilities that could be a promising tool for small molecule based traditional fluorophores towards many unexplored potentials.

References

- (1) Mei, J.; Leung, N. L. C.; Kwok, R. T. K.; Lam, J. W. Y.; Tang, B. Z. *Chem. Rev.* **2015**, *115*, 11718–11940.
- (2) Photonic Research Systems, http://www.prsbio.com/html/general_faq.html#q4; retrieved on May 15, **2014**.
- (3) Thomas III, S. W.; Joly, G. D.; Swager, T. M. *Chem. Rev.* **2007**, *107*, 1339-1386.
- (4) Hoeben, F. J. M.; Jonkheijm, P.; Meijer, E. W.; Schenning, A. P. H. J. *Chem. Rev.* **2005**, *105*, 1491-1546.
- (5) Bunz, U. H. F. *Chem. Rev.* **2000**, *100*, 1605-1644.
- (6) Chen, S.; Wang, H.; Hong, Y.; Tang, B. Z. *Mater. Horiz.* **2016**, *3*, 283-293.

- (7) Förster, T.; Kasper, K. Ein Konzentrationsumschlag der Fluoreszenz. *Z. Phys. Chem. (Muenchen, Ger.)* **1954**, *1*, 275-277.
- (8) Photophysics of Aromatic Molecules; Birks, J. B., Ed.; Wiley: London, **1970**.
- (9) Mei, J.; Hong, Y.; Lam, J. W. Y.; Qin, A.; Tang, Y.; Tang, B. Z. *Adv. Mater.* **2014**, *26*, 5429-5479.
- (10) Ma, X.; Sun, R.; Cheng, J.; Liu, J.; Gou, F.; Xiang, H.; Zhou, X. *J. Chem. Educ.* **2016**, *93*, 345-350.
- (11) Viglianti, L.; Leung, N. L. C.; Xie, N.; Gu, X.; Sung, H. H. Y.; Miao, Q.; Williams, I. D.; Licandro, E.; Tang, B. Z. *Chem. Sci.* **2017**, *8*, 2629-2639.
- (12) Luo, J. D.; Xie, Z. L.; Lam, J. W. Y.; Cheng, L.; Chen, H. Y.; Qiu, C. F.; Kwok, H. S.; Zhan, X. W.; Liu, Y. Q.; Zhu, D. B.; Tang, B. Z. *Chem. Commun.* **2001**, 1740-1741.
- (13) An, B. K.; Kwon, S. K.; Jung, S. D.; Park, S. Y. *J. Am. Chem. Soc.* **2002**, *124*, 14410-14415.
- (14) Chen, G.; Li, W.; Zhou, T.; Peng, Q.; Zhai, D.; Li, H.; Yuan, W. Z.; Zhang, Y.; Tang, B. Z. *Adv. Mater.* **2015**, *27*, 4496-4501.
- (15) Li, W. J.; Liu, D. D.; Shen, F. Z.; Ma, D. G.; Wang, Z. M.; Feng, T.; Xu, Y. X.; Yang, B.; Ma, Y. G. *Adv. Funct. Mater.* **2012**, *22*, 2797-2803.
- (16) Liu, Y. W.; Zhang, Y.; Wu, X. H.; Lan, Q.; Chen, C. S.; Liu, S. W.; Chi, Z. G.; Jiang, L.; Chen, X. D.; Xu, J. R. *J. Mater. Chem. C* **2014**, *2*, 1068-1075.
- (17) Dong, Y.; Lam, J. W. Y.; Qin, A.; Sun, J.; Liu, J.; Li, Z.; Sun, J.; Sung, H. H. Y.; Williams, I. D.; Kwok, H.-S.; Tang, B. Z. *Chem. Commun.* **2007**, 3255-3257.
- (18) Dong, Y.; Lam, J. W. Y.; Qin, A.; Li, Z.; Sun, J.; Sung, H. H. Y.; Williams, I. D.; Tang, B. Z. *Chem. Commun.* **2007**, 40-42.
- (19) Banerjee, S.; Veale, E. B.; Phelan, C. M.; Murphy, S. A.; Tocci, G. M.; Gillespie, L. J.; Frimannsson, D. O.; Kelly, J. M.; Gunnlaugsson, T. *Chem. Soc. Rev.* **2013**, *42*, 1601-1618.
- (20) Duke, R. M.; Veale, E. B.; Pfeffer, F. M.; Kruger, P. E.; Gunnlaugsson, T. *Chem. Soc. Rev.* **2010**, *39*, 3936-3953.
- (21) Chen, X. Q.; Wang, F.; Hyun, J. Y.; Wei, T. W.; Qiang, J.; Ren, X. T.; Shin, I.; Yoon, J. *Chem. Soc. Rev.* **2016**, *45*, 2976-3016.
- (22) Brana, M. F.; Castellano, J. M.; Moran, M. *Anti-Cancer Drug Des.* **1993**, *8*, 257-268.
- (23) M207. Brana, F.; Berlanga, J. M. C.; Roldan, C. M. DE patent 2318136 A1, **1973**.
- (24) Rideout, D.; Schinazi, R.; Pauza, C. D.; Lovelace, K.; Chiang, L. C.; Calogeropoulou, T.; Mccarthy, M.; Elder, J. H. *J. Cell. Biochem.* **1993**, *51*, 446-457.
- (25) Chanh, T. C.; Lewis, D. E.; Allan, J. S.; Sogandaresbernal, F.; Judy, M. M.; Utecht, R. E.; Matthews, J. L. *AIDS Res. Hum. Retroviruses* **1993**, *9*, 891-896.
- (26) Bailly, C.; Brana, M.; Waring, M. J. *Eur. J. Biochem.* **1996**, *240*, 195-208.
- (27) Lin, H. H.; Chan, Y. C.; Chen, J. W.; Chang, C. C. *J. Mater. Chem.* **2011**, *21*, 3170-3177.
- (28) Gopikrishna, P.; Meher, N.; Iyer, P. K. *ACS Appl. Mater. Interfaces* **2018**, *10*, 12081-12111.
- (29) Chen, S.; Slattum, P.; Wang, C.; Zang, L. *Chem. Rev.* **2015**, *115*, 11967-11998.
- (30) Li, C.; Wonneberger, H. *Adv. Mater.* **2012**, *24*, 613-636.
- (31) Yang, N.; Song, S.; Ren, J.; Liu, C.; Li, Z.; Qi, H.; Yu, C. *ACS Appl. Bio Mater.* **2021**, *4*, 5008-5015.
- (32) Li, C.; Yan, H.; Zhang, G.-F.; Gong, W.-L.; Chen, T.; Hu, R.; Aldred, M. P.; Zhu, M.-Q. *Chem. Asian J.* **2014**, *9*, 104-109.
- (33) Zhao, Q.; Zhang, S.; Liu, Y.; Mei, J.; Chen, S.; Lu, P.; Qin, A.; Ma, Y.; Sun, J. Z.; Tang, B. Z. *J. Mater. Chem.* **2012**, *22*, 7387-7394.
- (34) Kaur, S.; Kumar, M.; Bhalla, V. *Chem. Commun.* **2015**, *51*, 4085-4088.

- (35) Zhao, Q.; Li, K.; Chen, S.; Qin, A.; Ding, D.; Zhang, S.; Liu, Y.; Liu, B.; Sun, J. Z.; Tang, B. Z. *J. Mater. Chem.* **2012**, *22*, 15128-15135.
- (36) Zong, L.; Zhang, H.; Li, Y.; Gong, Y.; Li, D.; Wang, J.; Wang, Z.; Xie, Y.; Han, M.; Peng, Q.; Li, X.; Dong, J.; Qian, J.; Li, Q.; Li, Z. *ACS Nano* **2018**, *12*, 9532-9540.
- (37) Pal, K.; Sharma, V.; Sahoo, D.; Kapuria, N.; Koner, A. L. *Chem. Commun.* **2018**, *54*, 523-526.
- (38) Sun, M.; Müllen, K.; Yin, M. *Chem. Soc. Rev.* **2016**, *45*, 1513-1528.
- (39) Aryal, G. H.; Rana, G. R.; Guo, F.; Hunter, K. W.; Huang, L. *Chem. Commun.* **2020**, *56*, 13437-13440.
- (40) Avlasevich, Y.; Li, C.; Müllen, K. *Dyes. J. Mater. Chem.* **2010**, *20*, 3814-3826.
- (41) Costabel, D.; Skabeev, A.; Nabiyan, A.; Luo, Y.; Max, J. B.; Rajagopal, A.; Kowalczyk, D.; Dietzek, B.; Wächtler, M.; Görls, H.; Ziegenbalg, D.; Zagranyarski, Y.; Streb, C.; Schacher, F. H.; Peneva, K. *Chem. Eur. J.* **2021**, *27*, 4081-4088.



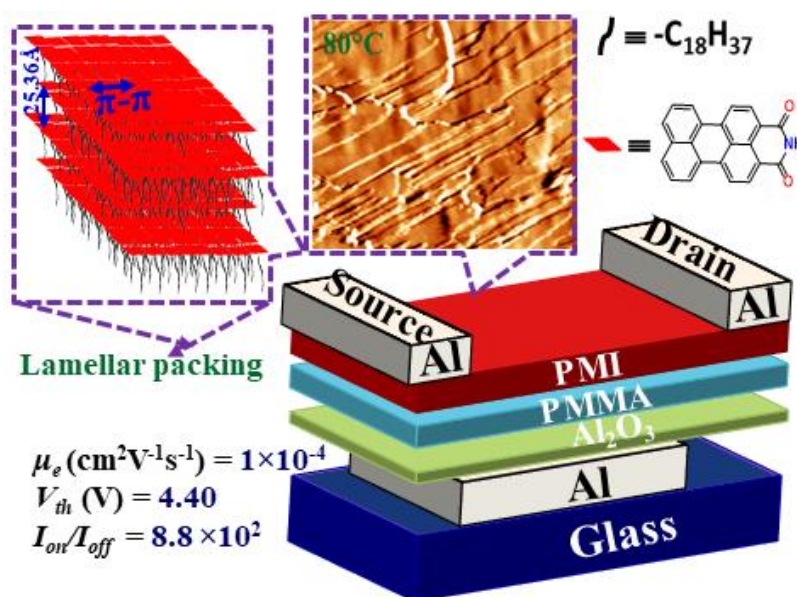
Long Alkyl Chain Induced OFET
Characteristic with Low Threshold Voltage
in n-Type Perylene Monoimide
Semiconductor

Khatun, M N.; Dey, A.; Meher, N.; Iyer, P. K.; *ACS Appl. Electron. Mater.* **2021**, *3*, 3575–3587

Abstract

This work reports the fabrication of n-channel OFET device using simple perylenemonoimide (**PMI**) derivatives by introducing a non-conjugated long alkyl chain (octadecyl) at the imide position. To demonstrate the primary role of the long pendant chain in the generation of OFET characteristics, a series of electronically similar **PMI** congeners were synthesized with different alkyl chains, viz; hexyl, 2-ethyl hexyl, octyl and octadecyl. It was observed that the insertion of the octadecyl chain can significantly manipulate the supramolecular self-assembly in **PMI-C18** with very good film-forming property, suggesting the prominent role of pendant alkyl chain length in their condensed state intermolecular interaction. Along with good film forming property, the long octadecyl chain at the imide position significantly improves the thermal, electrochemical, and photophysical properties, which help in generating OFET characteristics in **PMI-C18**, whereas other congeners do not show any device property. With poly(methyl methacrylate) (PMMA) as dielectric, top-contact bottom-gate n-channel OFET were fabricated on an economical glass substrate by using these simple **PMI** derivatives. Among them, **PMI-C18** demonstrates OFET properties with electron mobility (μ_e) of $1 \times 10^{-4} \text{ cm}^2 \text{ V}^{-1} \text{ s}^{-1}$ and current on/off ratio ($I_{on/off}$) of 8.8×10^2 . Moreover, the threshold voltage (V_{th}) of **4.40 V** obtained for **PMI-C18** was the lowest among all the reported perylene monoimide core based OFET devices. Besides, these **PMI** cores also demonstrated the influence of alkyl chain on the photophysical, electronic and electrochemical properties along with the molecular packing and charge transport behavior. Thus, such simple yet strategic synthetic manipulations in **PMIs** could contribute to the development of imide based materials for OFET applications.

Keywords: perylenemonoimide (**PMI**); n-type semiconductor; OFET; long alkyl chain; electron transport; threshold voltage.



2.1. Introduction

OFETs have received much attention owing to their portability, large-area fabrication compatibility, repeatability, low cost as well as high sensitivity and flexibility¹⁻³ OFETs have been successfully established as a robust alternative of inorganic transistors with significant commercial consideration, allowing their application in flexible displays,⁴ sensor devices,⁵⁻¹³ RFID (radio-frequency identification) tags¹⁴ and many more. Thus wide varieties of OFET active materials, including small molecules and conjugated polymers based on p-type (holes) and n-type (electrons) organic semiconductors, divided into two classes according to their charge transport abilities, have been developed.^{6,15-20} However, the n-channel semiconductor hasn't been much explored due to their poor electrical and environmental stability and lack of well-ordered molecular packing, which is a crucial parameter to influence the overall OFET device performance.²¹⁻²³ Therefore, n-channel organic semiconductors with ample air-stability and intended for the ambipolar semiconductors are of high demand for practical OFET device applications.

NDI, PDI and PMI derivatives comprising of extended π -conjugation have been well-known as a flexible class of n-type organic semiconductor due to their high electron affinity and high absorptivity, with excellent chemical, thermal as well as photochemical stability. They have been efficiently applied in the fabrication of different electronic devices including organic thin-film transistors (OTFTs), organic light-emitting diodes (OLEDs) and organic solar cells due to their low lying LUMO levels as well as efficient intermolecular π - π interactions, which endow multifunctional well-ordered self-assembly behavior.²⁴⁻³² However, due to the high threshold and operating voltage, OFET devices are limited to their broad industrial applications. Such limitations can be overcome by controlling the surface roughness and

morphology of the active layer. The growth of the organic semiconductors (OSCs) film and their crystalline alignment on the dielectric layers are highly prerequisite for attaining the high mobility.³³⁻³⁵ Herein, the V_{th} , is shown as one of the most important parameters in OFET device, which directly influences the charge trapping at the organic-dielectric interface. The low V_{th} decreases the power consumption along with the higher circuit operation speed. Thus, the construction of integrated transistors with low V_{th} is significantly important.³⁶

Among all the n-type rylene and related rylene diimides semiconducting materials such as NDI, PDI and **PMI**, a plenty of literatures are available for both NDI and PDI molecules studying the OFET characteristics, whereas the **PMI** core is relatively less explored in the OFET device performance due to the synthetic challenges. Perylene imide diones based materials were recently shown to have μ_e and V_{th} of $10^{-4} \text{ cm}^2 \text{ V}^{-1} \text{ s}^{-1}$ and 8 volt respectively.³⁷ Further, triperylene[3,3,3]propellane triimides materials were also reported for the OFET characteristics with the best values of μ_e and $I_{on/off}$ of $4.51 \times 10^{-3} \text{ cm}^2 \text{ V}^{-1} \text{ s}^{-1}$ and 5.7×10^6 respectively, however V_{th} were high as -5.2 volt (See the reference 3 of supporting information).

It can be witnessed that the nature of alkyl substitutions in molecules has strong influence on their intermolecular packing arrangement, roughness and alignment of crystalline packing, has been established as a robust parameter to control the morphology of organic molecules.^{34,38-43} Although the simple design strategy of alkyl chain substitutions at the imide position has negligible effect on the photophysical properties and electronic properties in the solution state, it has significant influence on the molecular packing, solid state ordering and thin-film microstructure, which subsequently influence the OFET device performances.^{39,44-51} It has been demonstrated that the alkyl side chain with appropriate chain length and branching position for semiconducting materials plays a crucial role in achieving efficient molecular packing, satisfactory layer continuity, and high film crystallinity, which results in excellent charge-transport properties and charge carrier mobilities.^{39,44-46} For example, the hole mobilities of isoindigo-based conjugated polymers have been significantly enhanced by choosing the appropriate branching position of branched alkyl chain.³⁹ Furthermore, the influence of the branched alkyl chain on the charge transport behavior and molecular packing, has resulted in enhanced electron mobility of solution processed OTFTs of naphthalimide derivatives.^{44,45} Molecular packing and self-assembly dependant n-channel OFET device showed good performances by simply substituting the long linear alkyl chain at the imide position of di(perylene bisimides) derivatives with the mobility and on/off ratio of $0.70 \text{ cm}^2 \text{ V}^{-1} \text{ s}^{-1}$ and 4×10^7 respectively.⁴⁹ Thiazolothiazole-thiophene copolymers have also

exhibited the influence of the short linear alkyl chain on the OFET device performances with field-effect-mobilities of $0.3 \text{ cm}^2\text{V}^{-1}\text{s}^{-1}$.⁵⁰

Herein, we designed a series of simple **PMI** based n-type organic semiconductors with varying pendant alkyl chains viz; hexyl, ethyl hexyl, octyl and octadecyl at the imide position for the fabrication of bottom-gate top-contact OFET device by thermal deposition technique (Figure 2.1). Among all the congeners, the long octadecyl chain containing **PMI-C18** showed promising OFET properties under vacuum with μ_e value of $1 \times 10^{-4} \text{ cm}^2 \text{ V}^{-1} \text{ s}^{-1}$ and I_{on}/I_{off} ratio of 8.8×10^2 at substrate temperature (T_{sub}) of $80 \text{ }^\circ\text{C}$, which can be attributed to its smooth homogenous crystalline microstructure and well-organized molecular arrangements over a large surface area. Notably, an unprecedented V_{th} of **4.40 V** has been achieved in the long alkyl chain substituted **PMI-C18** congener (Figure 2.1a). It was also important to mention that OFET characteristic with low threshold voltage in **PMI** congener has been induced for the first time by simply incorporating long alkyl chain at its imide position. Moreover, the influence of alkyl chain on the photophysical, electronic and electrochemical behavior as well as charge transport characteristics and molecular packing was also demonstrated for the first time here by tuning the alkyl chain length at the imide position of the **PMI** core.

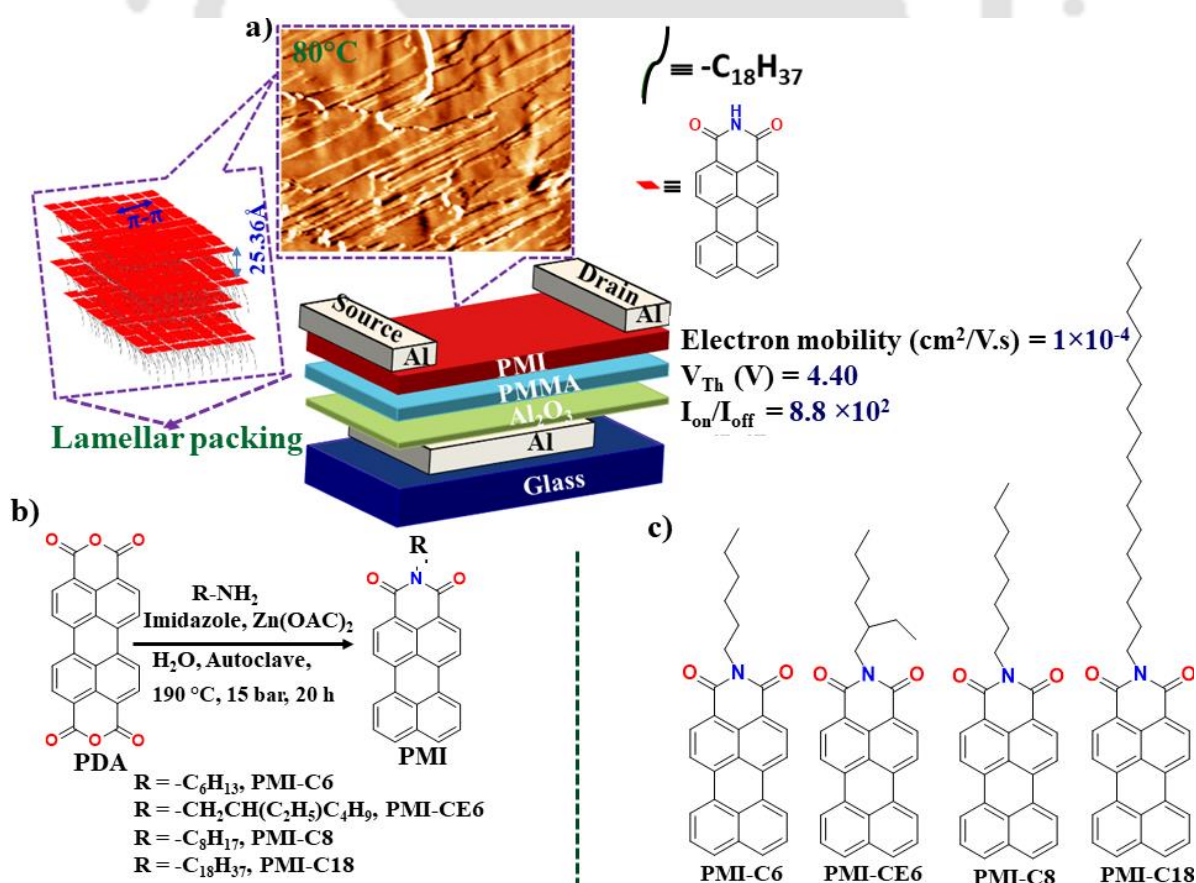


Figure 2.1. a) Graphical representation of **PMI-C18** congener with longer alkyl chain featuring induced intermolecular π stack overlap and appropriate structural molecular arrangements in thin-film promoting amended OFET performance. **b)** Synthetic procedure for the preparation of **PMI** congeners with different alkyl chain engineering from the commercially available Perylene-3,4,9,10-tetracarboxylic acid anhydride (PDA). **c)** The chemical structure of synthesized **PMI** congeners.

2.2. Experimental Section

2.2.1. Materials and Instrumentations:

All starting materials and reagents viz; 3,4,9,10-Perylene tetra carboxylic anhydride, all amines viz; hexyl, 2-ethyl hexyl, octyl and octadecyl respectively, zinc acetate, Imidazole, PMMA (MW = 996 000 g/mol) were purchased from Sigma Aldrich (India) as well as solvents were obtained from Northeast Chemicals and Zenith India. Milli-Q water was used for synthesizing all molecules. The chemicals and solvents obtained were of highly pure and used without any further purification. The probe were characterized by using NMR, IR spectroscopy and Mass spectrometry. The ^1H NMR (400 MHz) and ^{13}C NMR (100 MHz) spectra were obtained on Varian-AS400 NMR spectrometer. Mass spectra were obtained by using the MALDI-TOF spectrometry. Photoluminescence and UV/vis absorption spectra (solution and thin-film state) were recorded on a Horiba Fluoromax-4 spectrofluorometer using slit width of 3 nm and Perkin Elmer Lambda-25 spectrophotometer at 298 K. The theoretical calculations were carried out by DFT using the basis set of 6-31G/B3LYP, (+d, p). Electrochemical properties were recorded on a CH instruments model 700D series electrochemical workstation consisting of three-electrode systems, viz; glassy carbon as the working electrode, Ag/Ag⁺ as the reference electrode and platinum wire as the counter electrode respectively, and, as a supporting electrolyte 0.1 M tetra-n-butyl ammonium hexafluorophosphate (TBAP) in acetonitrile solution was used at a scan rate of 50 mV/s under an argon atmosphere. TGA (Thermogravimetric analysis) and X-ray diffraction (XRD) viz; Thin-film and powder XRD were carried out on thermogravimetric analyzer Mettler Toledo (model: TG/SDTA 851e) under the nitrogen flow at an heating rate of 20 °C min⁻¹ and Rigaku, Model: Micromax-007HF respectively. The samples for XRD (Thin-film and powder XRD) analysis were scanned in the 2-50° 2 θ range at a scan rate of 1.2° min⁻¹. Atomic force microscopy (AFM) and Field emission electron microscope (FESEM) images were collected by using agilent 5500 AFM/SPM microscope and Zeiss, Model: Sigma 300 field emission scanning electron microscope respectively. Optical microscopy images were taken at room temperature by using Leica polarizable optical microscope.

2.2.2. Substrate Cleaning technique

Glass slides were cut into 1 cm × 1 cm square substrates and dipped in piranha solution (3:1 H₂SO₄ : 30% H₂O₂) for approximately 45 min and then washed step by step with detergent, deionized water, acetone and isopropanol followed by sonication for 45 min each at room temperature. Finally the cleaned substrates were dried under the vacuum oven at 100 °C.

2.2.3. Preparation of films for AFM, FESEM, XRD, POM and spectroscopic technique.

The Thin films of **PMI** derivatives viz; **PMI-C6**, **PMI-CE6**, **PMI-C8** and **PMI-C18** were prepared by thermally depositing the each of the **PMI** OSC congeners at $T_{\text{sub}} = 80$ °C on the glass substrate under a base pressure of 10^{-6} mbar by keeping the thickness of the films of each were approximately 60 nm measured by Veeco Dektak 150 Surface Profilometer. Then the all microscopic viz; AFM, FESEM, POM as well as XRD and optical studies (Uv-vis spectroscopy study at thin film state) respectively were performed at room temperature.

2.2.4. Preparation of Stock Solutions for optical study

The stock solutions of each of the **PMI** congeners were prepared in THF solvent at a concentration of 1mM. The 9 μ L of stock solution was taken into 3 mL THF in a 3 mL quartz cuvette for each titration and the optical spectra for all the congeners were taken at a same concentration ($\lambda_{\text{ex, max}} = 477$ nm).

2.2.5. Theoretical Studies

Gaussian 09 package, B3LYP 6-31G (+d, p) basis set were used to evaluate the ground state optimized geometries along with HOMO/LUMO energy and molecular length of the all molecules (references 1,2 in AI).

2.2.6. Synthetic procedures

PMI derivatives with different chains viz, hexyl, 2-ethyl hexyl, octyl and octadecyl were synthesized via simply hydrothermal method. Perylene-3,4,9,10-tetracarboxylic acid anhydride (PDA) (2.54 mmol), amine (1.35 mmol), Zn (OAc)₂ dehydrate (1.72 mmol), imidazole (5g) and water (1ml) were taken in a teflon sleeve and mixed it properly until it forms homogenous mixture and placed in an hydrothermal autoclave reactor vessel at 15 bar pressure. The autoclave reactor was sealed, placed in an oven and the temperature was gradually increased to 190 °C for 20 h. The heat was turned off after 20 h and the reaction was cooled down to room temperature. The dark reddish crude product was extracted with

chloroform (200 ml) and water (50 ml) mixture at acidic pH, washed for four times with water, dried over Na₂SO₄, filtered, and concentrated via rotary evaporator. The resulting residue was purified by flash column chromatography (CHCl₃ as eluent) afforded the desired dark reddish compound (340 mg, 34% yield). The **PMI** derivatives with all amines were synthesized via repeating this same procedures.

Characterization of PMI-C6

¹H NMR (400 MHz, CDCl₃) δ 8.44 (d, *J* = 8.0 Hz, 2H), 8.29 (d, *J* = 7.5 Hz, 2H), 8.24 (d, *J* = 8.1 Hz, 2H), 7.80 (d, *J* = 8.0 Hz, 2H), 7.52 (t, *J* = 7.8 Hz, 2H), 4.14 – 4.09 (t, 2H), 1.70 (dd, *J* = 15.3, 7.4 Hz, 2H), 1.44 – 1.28 (m, 6H), 0.84 (t, *J* = 7.0 Hz, 3H). ¹³C NMR (101 MHz, CDCl₃) δ 163.86, 136.94, 134.35, 131.29, 130.90, 129.10, 127.75, 126.96, 126.73, 123.67, 120.83, 120.12, 40.49, 31.64, 28.19, 26.92, 22.58, 14.09. MALDI-TOF: calculated for C₂₈H₂₃NO₂: 405.17, Found: 404.950

Characterization of PMI-CE6

¹H NMR (400 MHz, CDCl₃) δ 8.28 (d, *J* = 8.1 Hz, 2H), 8.11 (d, *J* = 7.4 Hz, 2H), 8.04 (d, *J* = 8.0 Hz, 2H), 7.71 (d, *J* = 8.1 Hz, 2H), 7.43 (t, *J* = 7.8 Hz, 2H), 4.10 – 3.96 (t, 2H), 1.88 (dt, *J* = 13.1, 6.5 Hz, 1H), 1.37 – 1.19 (m, 8H), 0.89 (t, *J* = 7.4 Hz, 3H), 0.83 (t, *J* = 7.1 Hz, 3H). ¹³C NMR (101 MHz, CDCl₃) δ 164.27, 136.68, 134.05, 131.20, 130.67, 129.56, 129.05, 127.66, 126.82, 126.36, 123.35, 120.76, 119.91, 44.24, 38.02, 30.81, 28.90, 24.14, 23.11, 14.10, 10.83. MALDI-TOF: calculated for C₃₀H₂₇NO₂: 433.20, Found: 434.056

Characterization of PMI-C8

¹H NMR (400 MHz, CDCl₃) δ 8.55 (d, *J* = 8.0 Hz, 2H), 8.40 (d, *J* = 7.5 Hz, 2H), 8.37 (d, *J* = 8.1 Hz, 2H), 7.89 (d, *J* = 8.0 Hz, 2H), 7.61 (t, *J* = 7.8 Hz, 2H), 4.24 – 4.15 (t, 2H), 1.75 (dd, *J* = 7.5 Hz, 2H), 1.39 – 1.24 (m, 10H), 0.88 (t, *J* = 6.7 Hz, 3H). ¹³C NMR (101 MHz, CDCl₃) δ 163.86, 136.83, 134.28, 131.24, 130.69, 128.97, 127.85, 126.92, 123.41, 120.76, 119.91, 40.50, 31.85, 29.39, 29.26, 28.23, 27.25, 22.71, 14.08. MALDI-TOF: calculated for C₃₀H₂₇NO₂: 433.2042, Found: 434.056

Characterization of PMI-C18

¹H NMR (400 MHz, CDCl₃) δ 8.55 (d, *J* = 8.0 Hz, 2H), 8.40 (d, *J* = 7.6 Hz, 2H), 8.36 (d, *J* = 8.1 Hz, 2H), 7.88 (d, *J* = 8.1 Hz, 2H), 7.61 (t, *J* = 7.8 Hz, 2H), 4.22 – 4.17 (t, 2H), 1.77 (dd, *J* = 15.0, 7.2 Hz, 2H), 1.55 – 1.25 (m, 29H), 0.87 (t, *J* = 6.8 Hz, 3H). ¹³C NMR (101 MHz, CDCl₃) δ 163.89, 136.86, 134.29, 131.11, 130.73, 129.03, 126.90, 123.53, 120.87, 119.94, 40.62, 31.96,

29.70, 29.43, 29.35, 28.16, 27.15, 22.73, 14.27. MALDI-TOF: calculated for C₄₀H₄₇NO₂:573.3607 [M⁺], Found: 574.500.

2.3. Results and Discussions

2.3.1. Design, Synthesis, and characterization of PMI congeners

Four **PMI** congeners with varying non-conjugated pendant alkyl chains viz; hexyl, 2-ethyl hexyl, octyl, and octadecyl have been synthesized via one-step hydrothermal reaction procedure from the commercially available economical, reliable Perylene-3,4,9,10-tetracarboxylic acid anhydride (PDA) (Figure 2.1b, 2.1c).⁵² The different alkyl chains were intentionally incorporated here to observe the effect of chain length on their nature of intermolecular π - π stacking interactions and supramolecular self-assembly, which could strongly influence the OFET properties in these **PMIs**. The synthetic monomers were well characterized by MALDI, FTIR, nuclear magnetic resonance (¹H and ¹³C NMR) spectroscopy and their thermal, electrochemical and photophysical properties were investigated by thermogravimetric analysis (TGA), cyclic voltammetry (CV), photoluminescence (PL) and UV-vis spectroscopy. In addition, their supramolecular self-assembly was studied by atomic force microscopy (AFM), Polarized optical microscopy (POM), field emission scanning electron microscopy (FESEM), and X-ray diffraction (XRD) analysis. The detailed synthetic procedures, purifications, and associated spectra have been placed in the supporting information (Figure A2.1-A2.16). Moreover, the substitution of alkyl chain at the imide position of **PMI** core makes the molecules soluble in most of the organic solvents such as chloroform, dichloromethane (DCM), or chlorobenzene, which could enable the **PMI** congeners for large-area production and fabrication of printed electronic devices.

2.3.2. Thermal, Photophysical, Electrochemical, and Theoretical Studies of PMI Congeners

The thermal properties of any organic devices especially n-type organic thin-film transistors (OTFTs) has a significant role in device fabrication. The thermal behavior of all synthesized **PMI** congeners were carried out using TGA in the range of 19-800 °C at a heating rate of 10 °C min⁻¹ under nitrogen environment. All the four **PMI** congeners demonstrated excellent thermal stability, which favors the high-temperature deposition technique (Figure 2.2). From figure 2.2, it was demonstrated that the onset decomposition temperatures of **PMI-C6**, **PMI-CE6**, **PMI-C8** and **PMI-C18** at 5% weight loss were found to be 349 °C, 334 °C, 353 °C and 390 °C respectively. It was observed that **PMI-CE6** possess the lowest onset decomposition temperature, which could be due to the presence of branched alkyl chain. The branched ethyl hexyl chain in **PMI-CE6** can induce more steric hindrance around the

aromatic plane and that makes the molecules packed loosely by reducing their intermolecular π - π stacking interaction.^{32,42,53} Whereas, the onset decomposition temperature of other congeners increase steadily with increasing chain length and exhibit complete degradation temperature above 500 °C. It was witnessed that the presence of long alkyl chains provide higher thermal stability in these **PMI** congeners, which can be explained by their enhanced intermolecular π - π stacking interaction and has been discussed later.

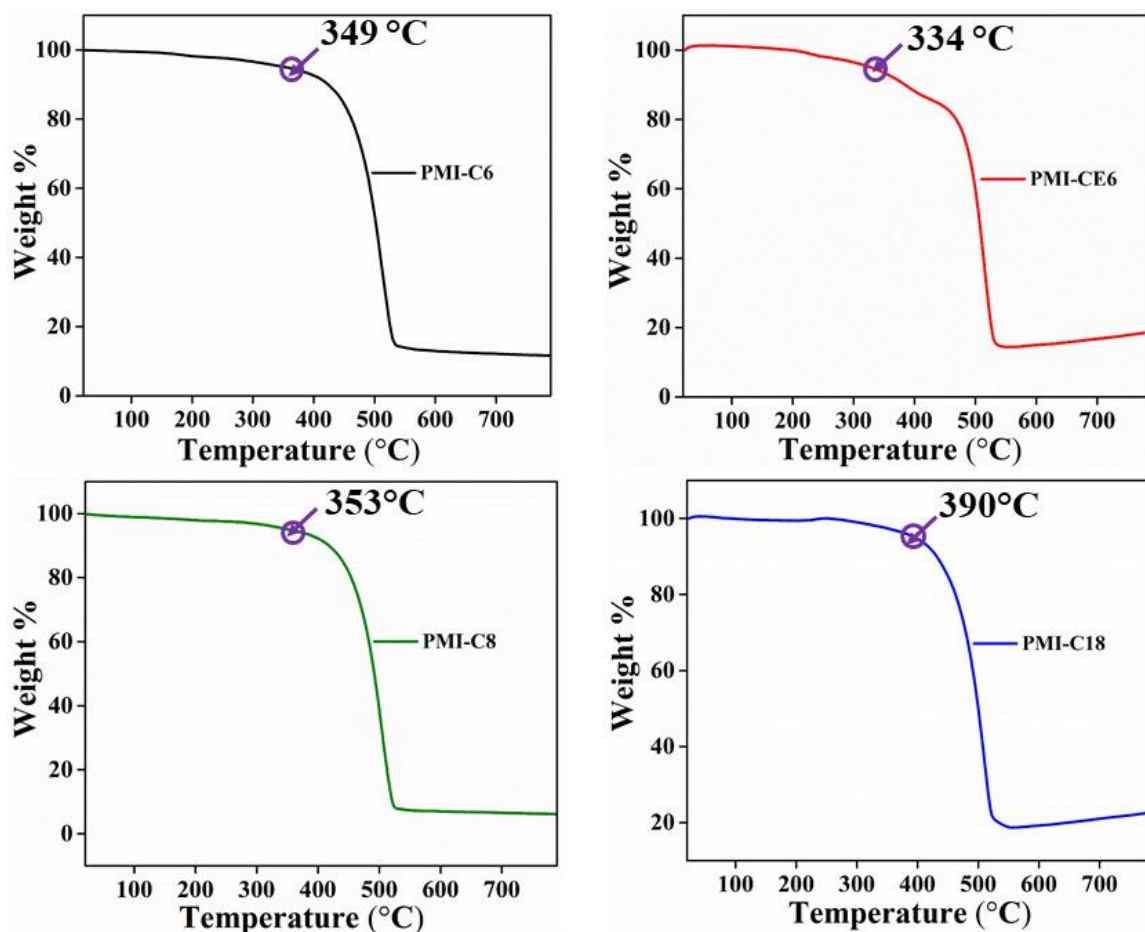


Figure 2.2. TGA thermogram of **PMI** congeners viz; **PMI-C6**, **PMI-CE6**, **PMI-C8**, and **PMI-C18** respectively at a scans rate of 10 °C min⁻¹ under the nitrogen gas atmosphere which is displaying thermal degradation of **PMI** congeners at 5% weight loss.

The UV-Vis absorption spectra and emission spectra of **PMI** congeners ($[\text{PMI}] = 3\mu\text{M}$) were performed in THF solution, and has been depicted in Figure 2.3a, 2.3b and corresponding data are represented in Table A2.1. The absorption spectra of **PMI** congeners in solution state exhibited a characteristic absorption maxima approximately at 477 nm, which can be ascribed to π - π^* transition with an identical shoulder peak at 499 nm. This implies that there is noteworthy variation in the vibronic distribution of the π - π^* electronic transitions, which subsequently represents the o-1 and o-o electronic vibronic transitions, respectively (Figure

2.3a).^{35,37,54-56} It has been observed in Figure 2.3b that the corresponding emission maxima of **PMI** congeners in solution state were centred at 534 nm with a shoulder peak at 570 nm, respectively ($\lambda_{\text{ex, max}} = 477$ nm). The optical band gaps in the solution state of **PMI** congeners have been calculated from the onset absorption spectral data that were found to be 2.33 eV (Table 2.1, A2.1, and Equation A2.1).^{32,42,53} The above observations imply that the variation in the alkyl chain length does not influence the optical behaviors of the congeners in their solution state, where the molecules remain in their molecularly dispersed form. However, the absorption spectra of **PMI** congeners in their thin film-state on glass displayed reasonable difference in their absorption maxima that suggest the possible influence of alkyl chains in their condensed state intermolecular interactions. It has been observed from the thin film-state absorption spectra of **PMI** that the 0-1 peak was approximately ~46 nm blue-shifted and the absorption maxima appeared at nearly 436 nm for all the congeners, which could be attributed to the H-type aggregation peak in their thin film-state.⁵⁷⁻⁶⁰ However, these congeners showed red-shifted absorption maxima corresponding to the 0-0 vibronic transition and the peak appeared at around 560-570 nm window that could be ascribed to the distinct molecular orientation, which could be strengthened by the presence of distinct alkyl chain at the imide position (Figure 3c, S17 and Table A2.2).^{45,53,61} Furthermore, the optical band gaps of **PMI** congeners in their thin film-state have been executed from the onset absorption peak, showed reasonable difference. The optical band gaps of **PMI-C6**, **PMI-CE6**, **PMI-C8**, and **PMI-C18** in their thin film-state were calculated to be 2.17, 2.16, 2.14 and 2.12 eV respectively (Table 2.1, A2.2 and Equation A2.2). These reasonably tuned red-shifted absorption band and optical band gaps of the **PMIs** in their thin film-state suggests the presence of distinct molecular orientation, which could be energized by the distinct pendant chain substituted at the imide position.^{45,53,61} Besides, **PMI-C6**, **PMI-CE6** and **PMI-C8** showed additional characteristics peaks at 525, 525 and 530 nm respectively compared to solution state absorption, which could be assigned to their molecular orientation that was influenced by the distinct intermolecular π - π stacking interactions of the congeners in their thin film-state (Figure 2.3c, A2.17 and Table A2.2). However, **PMI-C18** does not exhibit such characteristics peak due to its unique intermolecular π - π stacking interaction compared to other **PMI** congeners due to the presence of long alkyl chain at its imide position, which consequently confirmed the prominent role of long pendant alkyl chain at its imide position, which is discussed in the XRD and the thin film morphology analysis sections below.⁵³

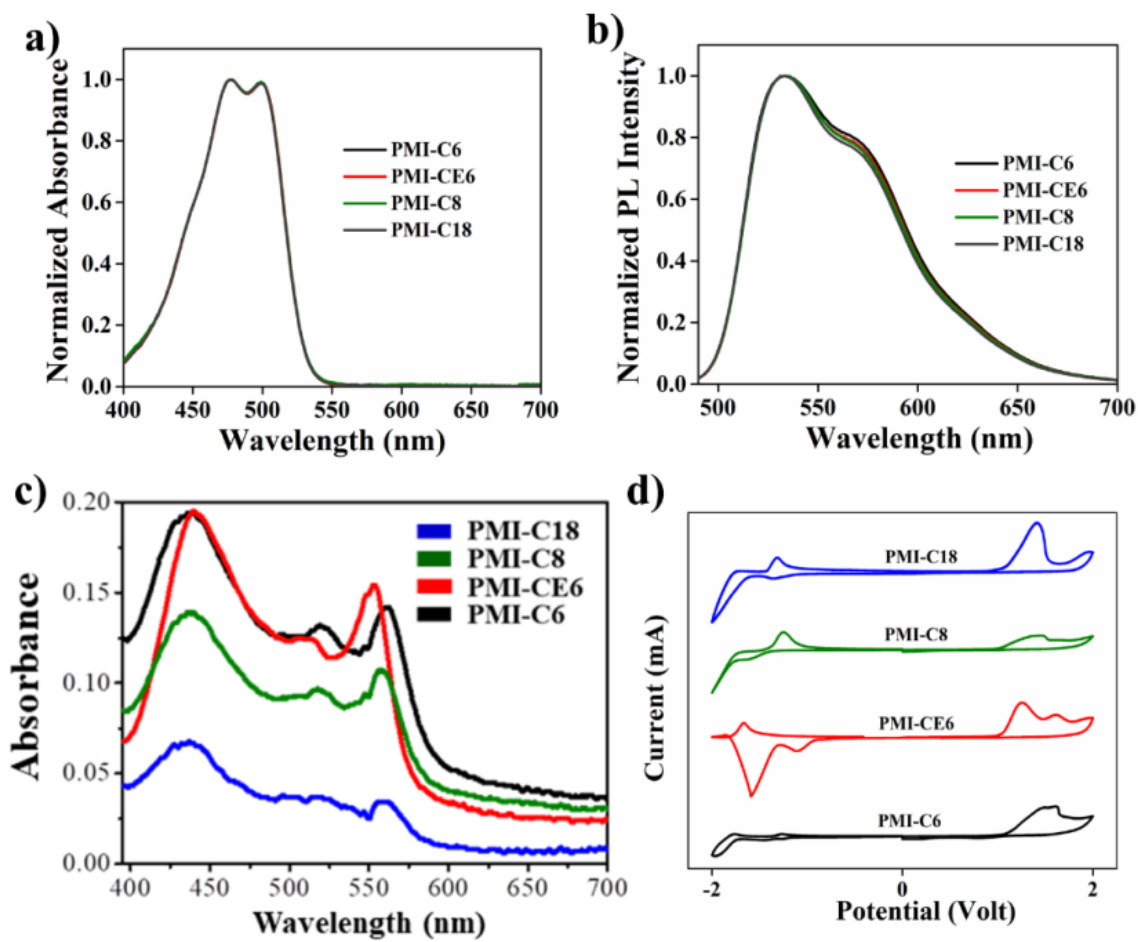


Figure 2.3. **a)** Normalized absorbance spectra in THF ($[PMI] = 3 \mu M$) **b)** Normalized photoluminescence spectra in THF ($\lambda_{ex, max} = 477 \text{ nm}$, $[PMI] = 3 \mu M$) and **c)** Absorbance spectra in thin film phase of **PMI** congeners **d)** Cyclic voltammograms (CV) plots of the drop casted thin films of **PMI** congeners on glassy carbon working electrode at a scan rate of 50 mV/s in 0.1 M tetrabutylammonium perchlorate (TBAP) in acetonitrile under the argon gas atmosphere.

The electrochemical properties of **PMI** congeners were estimated in acetonitrile solution with 0.1 M tetrabutylammonium perchlorate (TBAP) under argon gas environment at a scan rate of 50 mV/s dictated by CV measurements are presented in Figure 2.3d and the corresponding data are accumulated in Table A2.3. The standard redox couple of ferrocene/ferrocenium (Fc/Fc^+ , absolute energy level -4.8 eV) has been taken to calibrate the ($Ag/AgNO_3$) reference electrode. The electrochemical potential viz; highest occupied molecular orbital (HOMO) and lowest unoccupied molecular orbital (LUMO) energy levels were executed from the onset oxidation and onset reduction potential peaks respectively using the equation below:

$$E_{HOMO} = - (E_{onset}^{ox} + 4.80) \text{ eV} \quad (1)$$

$$E_{LUMO} = - (E_{onset}^{red} + 4.80) \text{ eV} \quad (2)$$

The electrochemical energy gap in **PMI-C6**, **PMI-CE6**, **PMI-C8**, and **PMI-C18** were calculated to be 2.26, 2.33, 2.21, and 1.96 eV respectively (Table 2.1, A2.3 and see the above equation 2.1, 2.2). Moreover, the LUMO energy levels of the **PMI-C6**, **PMI-CE6**, **PMI-C8**, and **PMI-C18** congeners were found to be -3.452, -3.392, -3.432, and -3.732 eV respectively, which indicated the high electron affinity to facilitate the electron injection, and therefore, promising for low threshold voltage n-channel OFETs characteristics (Table A2.3).^{32,42,47} Furthermore, the LUMO energy level of **PMI-C18** was significantly different and lower compared to other **PMI** congeners. This result suggests that more planar backbone and better stacking interaction leads to a better regular arrangement in **PMI-C18**, which could be strengthened by the long alkyl chain substituted at the imide position.³⁹ Thus, despite the similar band gaps of **PMIs** in their solution state, the electrochemical and optical band gaps in **PMIs** in their thin film-state showed a drastic difference, which suggests the prominent influence of alkyl chain on their condensed state HOMO/LUMO energy level. Such difference in their optical, as well as electrochemical band energies of the **PMI** congeners with similar aromatic core, clearly demonstrated the influence of the alkyl chain length to manipulate the molecular packing orientations of the congeners in their condensed state by creating distinct magnitude of bulkiness around the aromatic core, which will be discussed later.

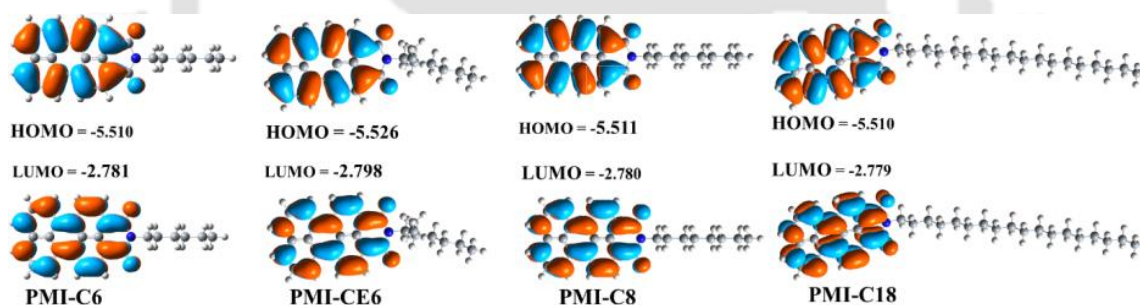


Figure 2.4. Frontier molecular orbital energy of **PMI** congeners with their corresponding HOMO and LUMO value in electron-volt (eV) executed by DFT simulation studies using B3LYP/6-31G, (+d, p) basis set in the Gaussian 09 program.

Apart from this, density functional theory (DFT) computational method has been utilized for elucidating the theoretical band gap and frontier molecular orbital geometries using the basis set B3LYP/6-31G, (+d, p) in the Gaussian 09 program (Figure 2.4, Table 2.1). From Figure 2.4, it is observed that the HOMO/LUMO energy levels of those congeners are identically distributed on the entire aromatic perylene plane and almost similar band gaps were observed for those congeners. The theoretical band gaps of **PMI-C6**, **PMI-CE6**, **PMI-C8**, and **PMI-C18** were found to be 2.730, 2.730, 2.731 and 2.731 eV respectively. These precisely similar computational results calculated in their gas phase attributed to the negligible effect of the alkyl chain length on their electronic properties, where the molecules

are considered to be in molecularly isolated form. These theoretical studies are in agreement with the experimental observations, where the optical band gaps of the congeners in their solution state demonstrated precisely similar results (Table 2.1). However, the distinct alkyl chains were supposed to strongly influence their intermolecular packing arrangements and thus control their morphology, crystallinity properties of the materials in their film-state by creating distinct magnitude of interchain interaction and steric crowding around the aromatic backbone, which will be discussed latter.

Table 2.1: Optical, electrochemical and theoretical band gap data of **PMI** congeners.

Monomer	$E_g^S \text{ opt (eV)}$	$E_g^T \text{ opt (eV)}$	$E_g^{CV} \text{ (eV)}$	$E_g^{Th} \text{ (eV)}$
PMI-C6	2.33	2.17	2.26	2.730
PMI-CE6	2.33	2.16	2.33	2.730
PMI-C8	2.33	2.14	2.21	2.731
PMI-C18	2.33	2.12	1.96	2.731

$E_g^S \text{ opt}$, $E_g^T \text{ opt}$ are Optical band gap in solution state and thin film-state, respectively. E_g^{CV} , E_g^{Th} are electrochemical and theoretical band gap, respectively.

2.3.3. XRD analysis for interpretation of molecular Packing

To further evaluate the effect of distinct pendant alkyl chain on the condensed state molecular packing orientations of the **PMI** congeners, X-ray diffraction (XRD) experiments were performed. The powder XRD (PXRD) and thin-film XRD (TXRD) of thermally deposited thin films at T_{sub} of 80 °C on the glass substrates were performed at ambient temperature (Figure 2.5). Though, several attempts to get high quality single-crystal of these congeners failed, the PXRD and TXRD were carefully analyzed to predict the nature of the intermolecular interactions and packing orientations of the congeners. The sharp diffraction observed at low-angle regions in the PXRD and TXRD could be attributed to the highly ordered and crystalline nature of the **PMI** congeners in their condensed state (Figure 2.5a, 2.5c).^{32,33} It is witnessed that crystalline grains intensely benefit the charge transport properties. The Bragg's diffraction for the **PMI-C18** at low-angle regions in powder was observed at around 2θ value of 3.5° corresponding to d-spacing of 24.93 Å, was precisely the multiple of the second diffraction peaks, which was observed at around 2θ value of 6.9° corresponding to d-spacing of 12.83 Å (Table A2.4). Similar observation was also observed in **PMI-C18** thin film. These results suggest that the **PMI-C18** congener has a layered organization in their condensed state. However, the other congeners (in PXRD and TXRD) do not exhibit such characteristics at low-angle region. The diffractions in PXRD and TXRD

were observed at low-range regions at around $2\theta = 3.5^\circ$, which corresponds to molecular length of the congeners as calculated from the computational study (Table A2.4, Figure A2.18). These observations suggest that all the congeners have highly ordered and edge-on lamellar (layered) crystalline packing arrangements.³⁴ Yet, except for **PMI-C18**, less ordered packing orientations were observed for the congeners in their condensed state, which can be witnessed from the AFM and FESEM analysis and has been elaborately described later. It was shown from the PXRD that the multiple distinct Bragg's peaks at the wide-angle region in the range of 2θ value of $37-49^\circ$ corresponding to d-spacing of 2.4-1.8 Å were observed in **PMI-C18** congeners, which could be attributed to the interchain short-contacts (Figure 2.5a, 2.5b).^{41,62} Whereas, all these interactions were almost abolished or were very weak in the **PMI** with shorter alkyl chain. The highly ordered crystalline packing orientations of the **PMI-C18** with similar aromatic core in the condensed state could be ascribed to unique molecular orientation of the long pendant alkyl chain by creating distinct magnitude of bulkiness around the aromatic backbone. Because the perylene core is prone to strong π - π interaction, multiple diffraction peaks in PXRD were observed between the 2θ values of $22-29^\circ$ corresponding to d-spacing of 3.9-3.0 Å, which entails the presence of efficient intermolecular π -stack overlap (generally H-aggregates has tendency to form co-facial stack) for the congeners (Figure 2.3a, 2.3c and A2.17). However, the long alkyl chain has strong influence in the formation of more order well-defined molecular orientations in the condensed state. Broad diffraction peaks for the congeners were observed in the deposited thin film on the glass substrate at $T_{\text{sub}} = 80^\circ\text{C}$ between the 2θ values of $10-30^\circ$, which could be ascribed to the growth nature of the thin film (Figure 2.5c).^{33,35} In addition, the tilt angle of **PMI-C6**, **PMI-CE6**, **PMI-C8**, and **PMI-C18** congeners with respect to the substrate were calculated using the equation A2.3, were found to be 31, 8, 34 and 40° respectively.^{35,42} The higher tilt angle between the substrate and the congener suggest that the more tighter molecular stacking for **PMI-C18**, which further give rise to a prominent π - π overlap between the aromatic backbone (Figure 2.5d).⁴² This observation is further evidenced by the higher onset decomposition temperature of **PMI-C18** (Figure 2.2). Thus, these above observations suggest that the long alkyl chain can efficiently increasing the π - π overlap between the aromatic core by tuning the angle between the substrate and the molecule in the thin film-state, which further strongly influence device performances.

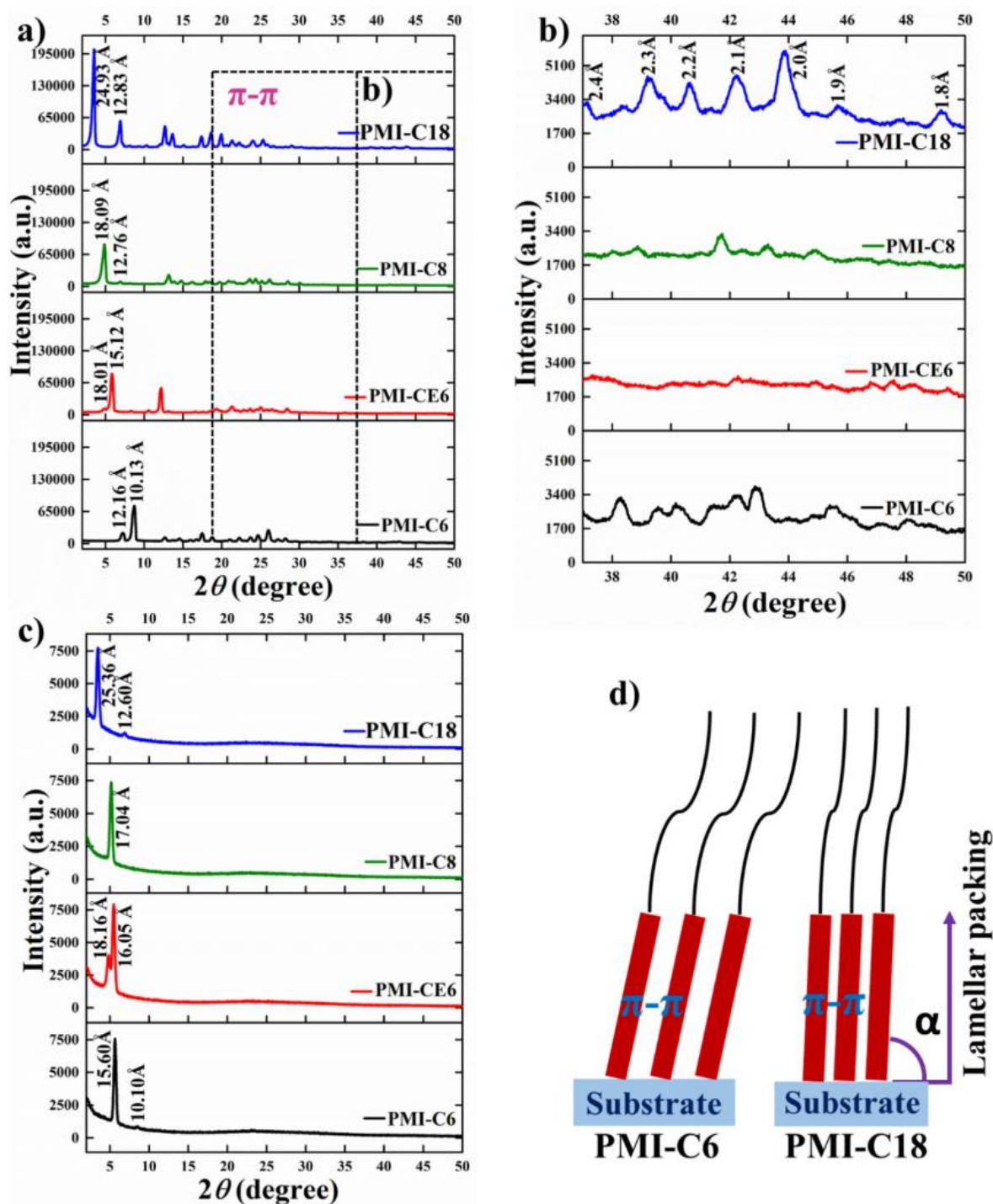


Figure 2.5. a) PXR, b) The magnified PXR pattern of a), and c) TXRD pattern of PMI congeners viz; PMI-C6, PMI-CE6, PMI-C8 and PMI-C18 respectively (with their corresponding d-spacing value) in their thin film-state, prepared by thermally evaporation technique on the glass substrates at $T_{\text{sub}} = 80$ °C. d) Schematic illustrations of molecular packing orientations of PMI-C6 and PMI-C18 congeners in their thin film-state.

2.3.4. Thin film morphology analysis in PMI congeners via AFM, FESEM and POM analysis

The thin film morphology and intermolecular packing orientations of the congeners were further investigated by AFM, FESEM and POM analysis to gain more insight into the effect of the distinct alkyl chain length on their morphology and molecular packing orientations. It is witnessed that the interfacial roughness impede the charge conduction in the OSC material due to the formation of charge trapping state.^{33-35,37-39,41,63} Surface roughness or irregular orientations of active layer in the thin film-state prominently effects the device performance. XRD data showed that the congeners are in crystalline in nature. AFM images combined with the XRD data, clearly demonstrated that growth of the microstructure of **PMI** congeners was observed along the π - π stacking direction (Figure 2.5d, see the figure 2.1a lamellar packing).⁶³ It is well established that charge transport for organic molecules is highly favorable through conjugated backbone of neighboring molecules which either efficiently overlap or are perpendicularly oriented to each other. Moreover, the ordered crystalline alignment in the large-scale of OSC on the substrate comforts efficient interconnected charge transport trails. The AFM images of the thermally evaporated ($T_{\text{sub}} = 80\text{ }^{\circ}\text{C}$) active **PMI** OSC materials on the glass substrates were recorded at the room temperature. It has been noted that surface roughness (rms) of **PMI-C6**, **PMI-CE6**, **PMI-C8** and **PMI-C18** were found to be 69.0, 50.7, 16.6 and 9.1 nm respectively (Figure 2.6). This surface roughness results clearly demonstrated that the thin film of **PMI-C18** comprising of long alkyl chain exhibited highly smooth, order, compact planar homogenous crystalline grains, while other congeners containing shorter alkyl chain display rod-like randomly oriented crystalline grain (Figure 2.6). These observations manifest that the shorter alkyl chain incorporated in **PMI** congeners may not be good candidates for FET behavior due to the higher surface roughness and less order crystalline packing alignment, which could interrupt the smooth charge transport properties through the active layer on their thin film. On contrary, the **PMI** congeners comprising longer alkyl chain exhibited smooth surface and well-defined interconnected tighter packing between the crystalline grain covering large surface area, which could reduce the charge trapping activities at the grain boundaries in the thin film.

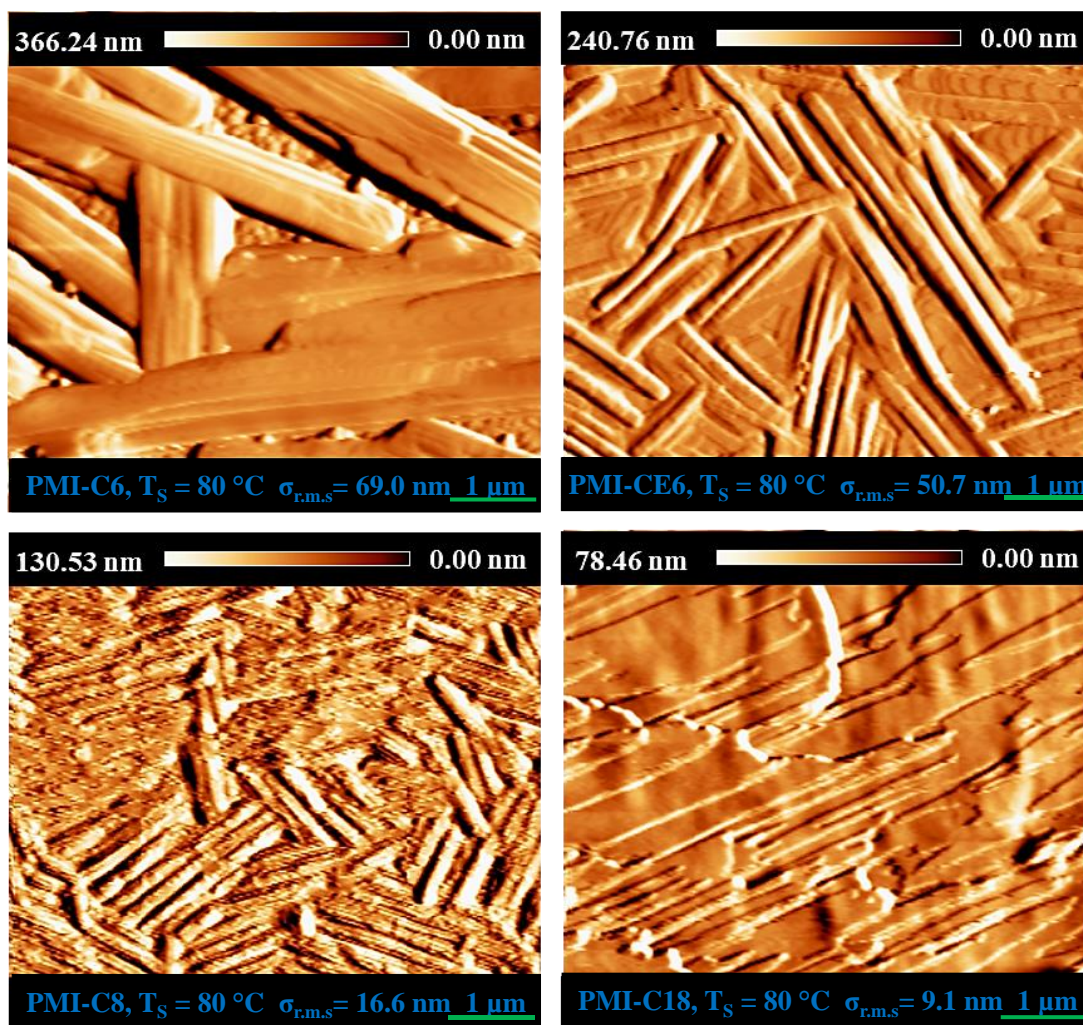


Figure 2.6. AFM topography images of thermally deposited **PMI** congeners in their thin film-state on the glass substrates at $T_{\text{sub}} = 80\text{ }^\circ\text{C}$, obtained at room temperature ($T_s = T_{\text{sub}}$: substrate temperature) to examine the roughness of the crystallites.

Furthermore, FESEM and POM studies of these congeners were also performed to analyse the morphology of **PMI** microstructure in their thin film and to support the above observations (Figure 2.7,2.8). The FESEM images of thermally deposited **PMI** congeners on the glass substrates were performed at room temperature. **PMI-C18** showed an interconnected uniform smooth film without any pores or voids. While other congeners viz; **PMI-C6** exhibited irregular crystalline grain with immense pores and voids, **PMI-CE6** comprising of branched alkyl chain displayed orderless crystallites and **PMI-C8** demonstrated randomly oriented irregular crystallites on their thin film (Figure 2.7).

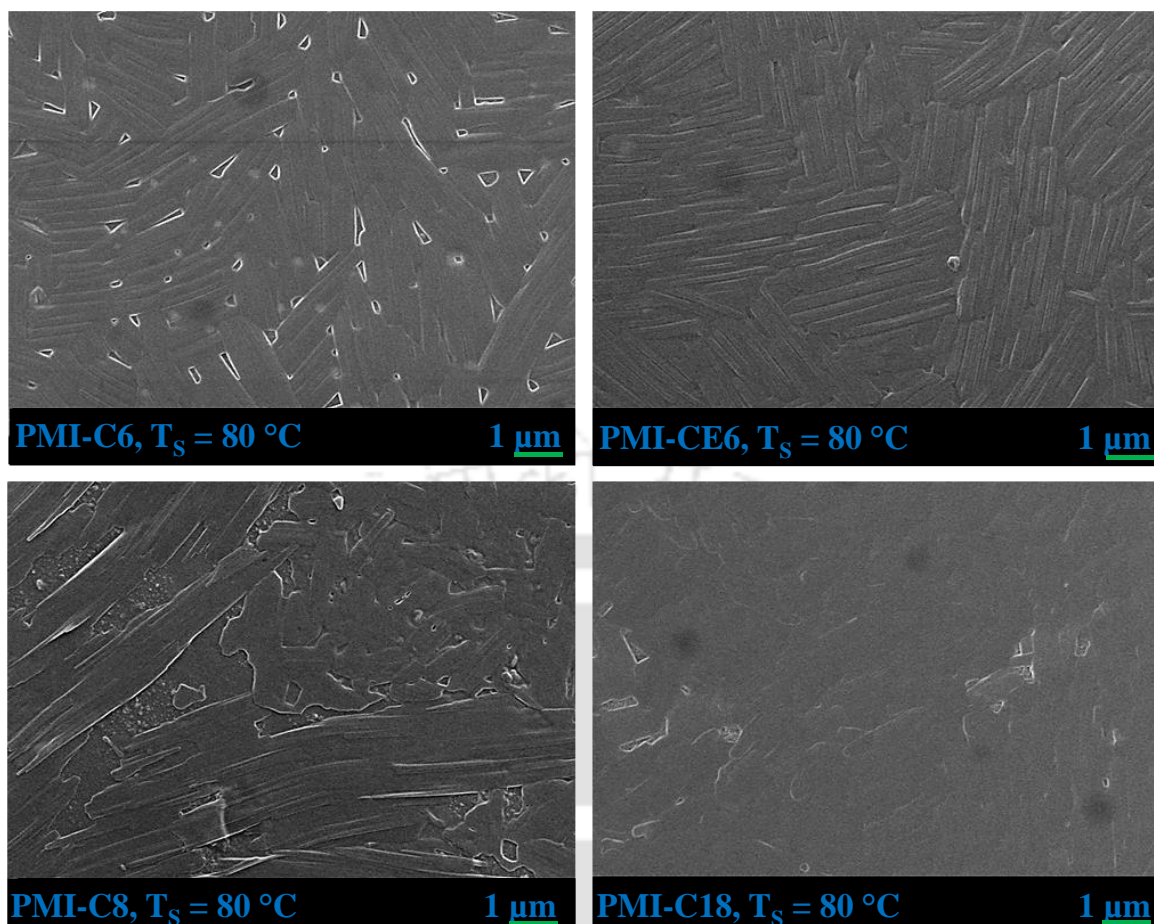


Figure 2.7. FESEM images of thermally evaporated **PMI** congeners in their thin films on the glass substrates at $T_{\text{sub}} = 80\text{ }^{\circ}\text{C}$, recorded at ambient temperature for evaluating the microstructures self-assembly behavior in their thin film-state.

POM images of thermally evaporated **PMI** congeners on the glass substrates at $T_{\text{sub}} = 80\text{ }^{\circ}\text{C}$ were performed at room temperature (Figure 2.8). These studies are further proof of the connectivity between the crystalline grains for the **PMI-C18** comprising of long alkyl chain in thin film-state. Herein, **PMI-C18** display interconnected fibrillar network with prominent microstructure crystalline domains in the thin film-state, whereas the other congeners show low quality film with enormous small black spots and no structural microstructure on their thin films. PXRD analysis of **PMI-C18** congeners revealed multiple distinct Bragg peaks in the wide-angle region ($2\theta = 37\text{--}49^{\circ}$), corresponding to d-spacings of $2.4\text{--}1.8\text{ \AA}$. These peaks indicate significant interchain short contacts, a feature less pronounced or nearly absent in **PMI** with shorter alkyl chains. The influence of the long chain is further evidenced by the higher onset decomposition temperature of $390\text{ }^{\circ}\text{C}$ for **PMI-C18**, suggesting enhanced thermal stability. This stability is attributed to the well-organized intermolecular $\pi\text{-}\pi$ stacking interactions facilitated by the longer alkyl chains. Thus these observations suggest that the alkyl chain length has a prominent role in self-assembly behaviors in thin film-state,

which subsequently tune the microstructure thin film properties, and could be attributed to the inherent structural anisotropy of the **PMI-C18** congener in the thin film-state. Thus, subsequently to demonstrate the influence of the long alkyl chain on the device characteristic of electronically similar congeners, n-type OSCs were fabricated using the **PMIs** and has been described elaborately below.

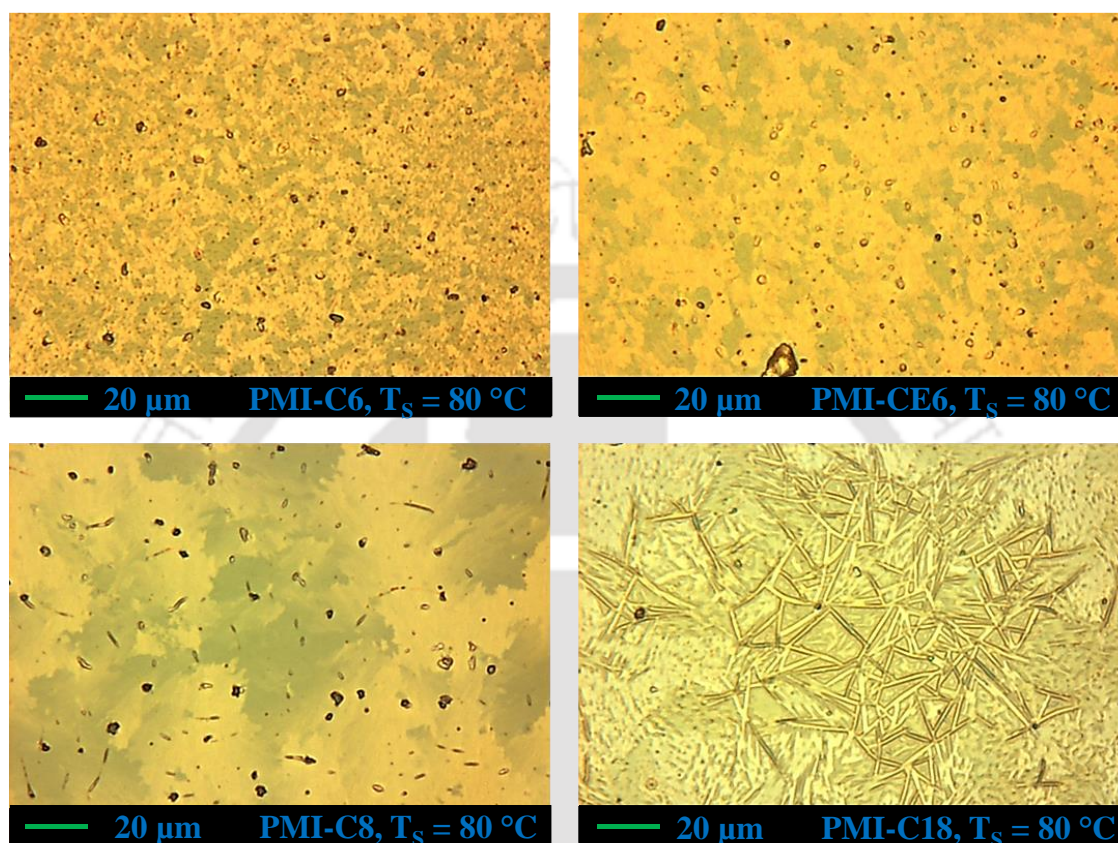


Figure 2.8. POM images of thermally deposited **PMI** congeners in their thin film-state on glass as the substrates at $T_{\text{sub}} = 80\text{ }^{\circ}\text{C}$, attained at room temperature.

2.3.5. OFET device Fabrication and Characterization

Though all the materials exhibited good solubility in most of the organic solvents, the continuity of the film obtained was very poor in the solution processed technique compared to the thermal deposition method (Figure A2.19). Hence, all the devices were fabricated by thermal deposition method in the present study. Herein, **PMI** n-type OSCs viz; **PMI-C6**, **PMI-CE6**, **PMI-C8** and **PMI-C18** were fabricated with a bottom-gate top-contact configuration by employing Al_2O_3 /PMMA double dielectric materials. Al_2O_3 , a high-k dielectric inorganic material were used to reduce the high leakage current and to afford high capacitance density. Meanwhile, PMMA a thin hydrophobic or less polar polymer dielectric interface has been employed to inhibit the charge trapping states and could be contributed to

attain the well-organized large-scale densely packed crystalline grains. Herein, glass slides were used as substrate onto which aluminum gate (~ 200 nm) was deposited by thermal evaporation method by using a shadow mask. The film was then anodized with a constant current density of 0.06 mA cm^{-2} and a voltage of 10 V in a 0.001 M citric acid monohydrate electrolyte solution at $20 \text{ }^\circ\text{C}$ using a square-shaped platinum mesh as counter electrode to form a $\sim 13 \text{ nm}$ Al_2O_3 layer over the Al film gate electrode. After anodization, to reduce the surface roughness, a 100 nm PMMA film was spin coated from a 30 mg/ml solution in anisole and dried for 1 hour at $120 \text{ }^\circ\text{C}$ under nitrogen atmosphere. Following this, the active material [PMI-C6 or PMI-CE6 or PMI-C8 or PMI-C18] was deposited by thermal deposition method under a base pressure of 10^{-6} mbar . After that aluminum source-drain electrodes were thermally evaporated, at room temperature, up to a thickness of 80 nm to calculate three terminal properties of the materials. The schematic of the fabricated device is presented in Figure 2.1a.

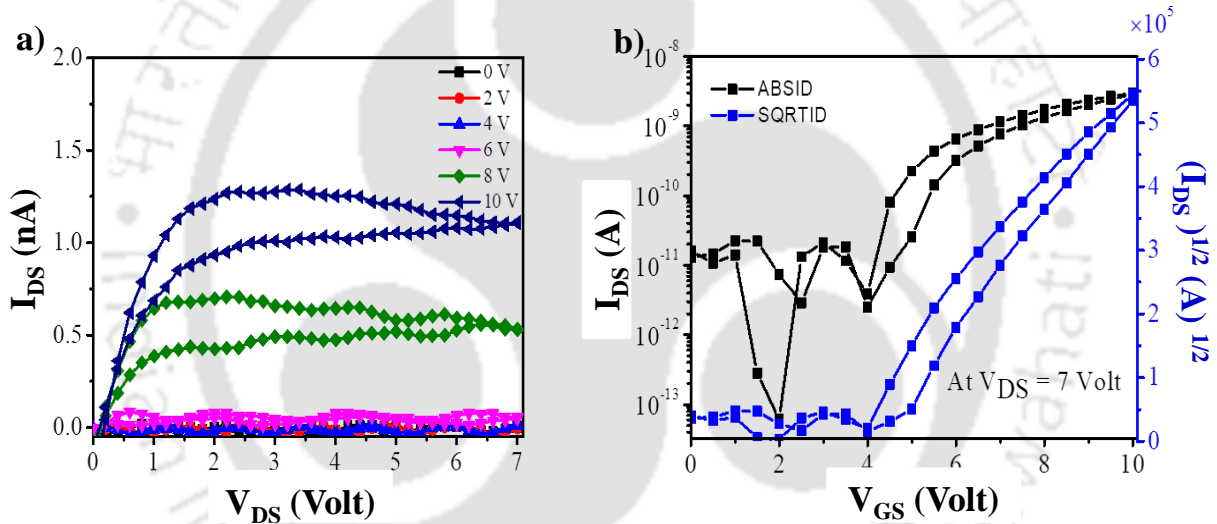


Figure 2.9. Output and transfer OFET device characteristic curves of **PMI-C18** OSC fabricated on $\text{Al}_2\text{O}_3/\text{PMMA}$ dilayer dielectric material at $T_{\text{sub}} = 80 \text{ }^\circ\text{C}$. (a) $I_{\text{DS}}-V_{\text{DS}}$ output characteristic curve (inset: different values of V_{DS}). (b) $I_{\text{DS}}-V_{\text{GS}}$ and $(I_{\text{DS}})^{1/2}$ vs V_{GS} transfer characteristics curve at $V_{\text{DS}} = 7 \text{ V}$. *ABSID: Absolute drain current; SQRTID: Square root of drain current.

The fabricated OFETs were characterized by using a Keithley 4200 semiconductor characterization system under vacuum condition. The field-effect mobility in the saturation regime was extracted using equation (2.3),

$$I_{\text{DS}} = \frac{\mu_{\text{sat}} WC_i}{2L} (V_{\text{GS}} - V_{\text{th}})^2 \quad (2.3)$$

under the condition of $V_{DS} > (V_G - V_{th})$, where I_{DS} is the source-drain current, μ is the field-effect mobility, W & L are channel width and channel length, C_i ($= 25.83 \text{ nF.cm}^{-2}$) is the capacitance per unit area of gate dielectric layer and V_G , V_{th} and V_{DS} are the gate, threshold and source-drain voltages respectively (Figure 2.9). The calculated device properties are shown in Table 2.2. Unfortunately, we have not observed any device property for those **PMI** semiconducting materials which possess short alkyl chain at the imide position viz; **PMI-C6**, **PMI-CE6** and **PMI-C8** respectively, due to the higher surface roughness and less order irregular loosely packed crystalline grains compared to **PMI-C18** comprising of longer alkyl chain. It is well known that the OFET device properties can be improved by prolonging the alkyl chain length.^{32,53} Pei et al. reported that organic materials comprising longer alkyl chains (branched or linear) exhibited higher carrier mobilities.⁶⁴ However, to the best of our knowledge, OFET characteristics in n-type **PMI** semiconductor with low threshold voltage have been achieved for the first time by simply introducing non-conjugated long alkyl chain at the imide position. It is well known that Perylene cores have been classified according to the presence of imide moiety and have been extensively studied in literature.⁴⁰ Most importantly, these **PMI** core are new in OFET device applications in comparison to other rylene and rylene diimide derivatives such as NDI and PDI core. The **PMI-C18** congener exhibited OFET characteristics with electron mobility of $1.0 \times 10^{-4} \text{ cm}^2 \text{ V}^{-1} \text{ s}^{-1}$ and current on-to-off ratio of 8.8×10^2 under vacuum condition with low threshold voltage of 4.40 V. Although few reports on OFET characteristics in n-type perylene imide and perylene imide dione derivatives that comprise different aromatic backbone (than the present **PMI** materials), exhibited comparable electron mobility, their threshold voltages were too high (references 3 of supporting information).³⁷ Whereas, this report demonstrates a comparable electron mobility and current on/off ratio for the **PMI-C18** congener with unprecedented lower threshold voltage compared to the most recently published p-type and ambipolar perylene imide derivatives, the literature reported cores are different from the **PMI** materials of this manuscript (Table A2.5 and references 4-6 of appendix). Moreover, several NDI, PDI, and polymer based semiconducting molecules have demonstrated the influence of branching alkyl chain on the OFET device performances, whereas a very few materials are reported on the effect of linear alkyl chain on the OFET characteristics.⁴⁷⁻⁵¹ Besides, this work also successfully demonstrated that the device performance of organic small molecules can be efficiently induced/improved by engineering the non-conjugated long alkyl chain in electronically similar congeners. Most importantly, along with reporting new materials for OFET application, a cost-effective Glass/ Al_2O_3 /PMMA with bottom-gate top-contact geometry device configuration has been used for the fabrication of OFET devices. The mobility and on/off ratio of this system could be improved via device engineering considering that the reduction of the NH group from the traditional disubstituted perylene

core, has led to the interruption of the core planarity and effective π -stack overlap. Such distorted core and π -stack overlap could subsequently lead to packing constraints and restrict the formation of the extended highly crystalline grains.⁶⁵⁻⁶⁷

Table 2.2: Summary of the OFET device data of **PMI-C18**, recorded and calculated under vacuum.

Active layer	V_{th} (V)	W (μm)	L (μm)	μ_e ($\text{cm}^2 \text{V}^{-1} \text{S}^{-1}$)	$I_{on/off}$
PMI-C18	4.40	800	40	1×10^{-4}	8.8×10^2

V_{th} (V), W (μm), L (μm), μ_e ($\text{cm}^2 \text{V}^{-1} \text{S}^{-1}$), $I_{on/off}$ are threshold voltage in volt, channel width in micrometer, channel length in micrometer, electron mobility in $\text{cm}^2 \text{V}^{-1} \text{S}^{-1}$ and on/off current ratio respectively.

2.4. Conclusion

In summary, four **PMI** derivatives with different alkyl chain lengths, viz; hexyl, 2-ethyl hexyl, octyl, and octadecyl have been strategically synthesized and thoroughly characterized to unveil the influence of long alkyl chains on their OFET characteristic of electronically similar small molecular systems. It was also observed that the intermolecular packing orientations, crystallinity, thermal, electrochemical and photophysical properties of small molecular systems can be efficiently controlled by manipulating the pendant alkyl chain length around the aromatic core. Though the intermolecular co-facial π - π stacking interactions are very strong in these **PMI** due to the large perylene planar core, the octadecyl chain in **PMI-C18** can efficiently control the intermolecular packing orientations that subsequently endow well-ordered interconnected crystallites microstructure among other congeners. The promising OFET characteristic such as electron mobility of $1 \times 10^{-4} \text{ cm}^2 \text{V}^{-1} \text{S}^{-1}$ and $I_{on/off}$ value of 8.8×10^2 has been achieved in **PMI-C18** derivative by incorporating simple non-conjugated alkyl chain at its imide position. All the other electronically similar **PMI** congeners with shorter alkyl chain do not possess any OFET characteristic, and thus confirmed the primary role of the long alkyl chain in the device performance of **PMI-C18**. In addition, to lower V_{th} of **4.40 V**, the effect of alkyl chain length on the OFET device

performances has also been observed in this newly designed n-type **PMI-C18** semiconductor for the first time. Thus, this simple synthetic strategy of long alkyl chains engineering could be a powerful tool in the design and development of new materials to improve OFET characteristic. Most importantly, the charge transport characteristics and charge carrier mobilities could be tuned and improved by choosing long or branched alkyl chains with appropriate substitution at the imide position of this n-type **PMI** semiconducting material. Thus, these studies of **PMI** materials in OFET could be promising for further development and application in organic electronic devices including OFETs, OLETs and organic solar cells in future.

References

- (1) Yan, H.; Chen, Z.; Zheng, Y.; Newman, C.; Quinn, J. R.; Dötz, F.; Kastler, M.; Facchetti, A. *Nature* **2009**, *457*, 679-686.
- (2) Kaltenbrunner, M.; Sekitani, T.; Reeder, J.; Yokota, T.; Kuribara, K.; Tokuhara, T.; Drack, M.; Schwodiauer, R.; Graz, I.; Bauer-Gogonea, S.; Bauer, S.; Someya, T. *Nature* **2013**, *499*, 458-463.
- (3) Sekitani, T.; Zschieschang, U.; Klauk, H.; Someya, T. *Nat. Mater.* **2010**, *9*, 1015-1022.
- (4) Sirringhaus, H.; Tessler, N.; Friend, R. H. *Science* **1998**, *280*, 1741-1744.
- (5) Janata, J.; Josowicz, M. *Nat. Mater.* **2003**, *2*, 19-24.
- (6) Sun, Z.; Li, J.; Liu, C.; Yang, S.; Yan, F. *Adv. Mater.* **2011**, *23*, 3648-3652.
- (7) Li, Y.; Fu, J.; Zhong, C.; Wu, T.; Chen, Z.; Hu, W.; Lu, J. *Adv. Energy Mater.* **2018**, *28*, 1802605.
- (8) Zhang, A.; Lieber, C. M. *Chem. Rev.* **2016**, *116*, 215-257.
- (9) Lin, P.; Yan, F. *Adv. Mater.* **2012**, *24*, 34-51.
- (10) Torsi, L.; Magliulo, M.; Manoli, K.; Palazzo, G. *Chem. Soc. Rev.* **2013**, *42*, 8612.
- (11) Gao, N.; Zhou, W.; Jiang, X.; Hong, G.; Fu, T.-M.; Lieber, C. M. *Nano Lett.* **2015**, *15*, 2143-2148.
- (12) Khim, D.; Ryu, G.-S.; Park, W.-T.; Kim, H.; Lee, M.; Noh, Y.-Y. *Adv. Mater.* **2016**, *28*, 2752-2759.
- (13) Yuvaraja, S.; Nawaz, A.; Liu, Q.; Dubal, D.; Surya, S. G.; Salama, K. N.; Sonar, P. *Chem. Soc. Rev.* **2020**, *49*, 3423-3460.
- (14) Steudel, S.; Myny, K.; Arkhipov, V.; Deibel, C.; Vusser, D. S.; Genoe, J.; Heremans, P. *Nat. Mater.* **2005**, *4*, 597-600.
- (15) Li, H.; Tee, B. C.-K.; Giri, G.; Chung, J. W.; Lee, S. Y.; Bao, Z. *Adv. Mater.* **2012**, *24*, 2588-2591.
- (16) Vasimalla, S.; Senanayak, S.; Sharma, M.; Narayan, K. S.; Iyer, P. K. *Chem. Mater.* **2014**, *26*, 4030-4037.
- (17) Liu, Q.; Wang, Y.; Kohara, A.; Matsumoto, H.; Manzhos, S.; Feron, K.; Bottle, S. E.; Bell, J.; Michinobu, T.; Sonar, P. *Adv. Funct. Mater.* **2020**, *30*, 1907452.

- (18) Liu, Q.; Kumagai, S.; Manzhos, S.; Chen, Y.; Angunawela, I.; Nahid, M. M.; Feron, K.; Bottle, S. E.; Bell, J.; Ade, H.; Takeya, J.; Sonar, P. *Adv. Funct. Mater.* **2020**, *30*, 2000489.
- (19) Liu, Q.; Bottle, S. E.; Sonar, P. *Adv. Mater.* **2020**, *32*, 1903882.
- (20) Glowatzki, H.; Sonar, P.; Singh, S. P.; Mak, A. M.; Sullivan, M. B.; Chen, W.; Wee, A. T. S.; *J. Phys. Chem. C.* **2013**, *117*, 11530-11539.
- (21) Zhao, G.; Dong, H.; Zhao, H.; Jiang, L.; Zhang, X.; Tan, J.; Meng, Q.; Hu, W. *J. Mater. Chem.* **2012**, *22*, 4409-4417.
- (22) Naab, B. D.; Himmelberger, S.; Diao, Y.; Vandewal, K.; Wei, P.; Lussem, B.; Salleo, A.; Bao, Z. *Adv. Mater.* **2013**, *25*, 4663-4667.
- (23) Jones, B. A.; Facchetti, A.; Wasielewski, M. R.; Marks, T. J. *J. Am. Chem. Soc.* **2007**, *129*, 15259-15278.
- (24) Balakrishnan, K.; Datar, A.; Oitker, R.; Chen, H.; Zuo, J.; Zang, L. *J. Am. Chem. Soc.* **2005**, *127*, 10496-10497.
- (25) Meher, N.; Iyer, P. K. *Nanoscale* **2019**, *11*, 13233-13242.
- (26) Arunagirinathan, R. N.; Meher, N.; Iyer, P. K. *ACS Appl. Electron. Mater.* **2019**, *1*, 2437-2444.
- (27) Adil, L. R.; Iyer, P. K. *Chem. Commun.* **2020**, *56*, 7633-7636.
- (28) Khatun, M. N.; Tanwar, A. S.; Meher, N.; Iyer, P. K. *Chem. Asian J.* **2019**, *14*, 4725-4731.
- (29) Briseno, A. L.; Mannsfeld, S. C. B.; Reese, C.; Hancock, J. M.; Xiong, Y.; Jenekhe, S. A.; Bao, Z.; Xia, Y. *Nano Lett.* **2007**, *7*, 2847-2853.
- (30) Balakrishnan, K.; Datar, A.; Naddo, T.; Huang, J.; Oitker, R.; Yen, M.; Zhao, J.; Zang, L. *J. Am. Chem. Soc.* **2006**, *128*, 7390-7398.
- (31) Meher, N.; Iyer, P. K. *Nanoscale* **2017**, *9*, 7674-7685.
- (32) Do, T.-T.; Takeda, Y.; Manzhos, S.; Bell, J.; Tokito, S.; Sonar, P. *J. Mater. Chem. C.* **2018**, *6*, 3774-3786.
- (33) Dey, A.; Kalita, A.; Iyer, P. K. *ACS Appl. Mater. Interfaces.* **2014**, *6*, 12295-12301.
- (34) Li, J.; Chang, J.-J.; Tan, H. S.; Jiang, H.; Chen, X.; Chen, Z.; Zhan, J.; Wu, J. *Chem. Sci.* **2012**, *3*, 846-850.
- (35) Kalita, A.; Subbarao, N. V. V.; Iyer, P. K. *J. Phys. Chem. C.* **2015**, *119*, 12772-12779.
- (36) Dao, T. T.; Matsushima, T.; Friedlein, R.; Murata, H. *Org. Electron.* **2013**, *14*, 2007-2013.
- (37) Echegaray, D. P.; Mancheño, M. J.; Arrechea-Marcos, I.; Juárez, R.; López-Espejo, G.; Navarrete, L. J. T.; Ramos, M. M.; Seoane, C.; Ortiz, R. P.; Segura, J. L. *J. Org. Chem.* **2016**, *81*, 11256-11267.
- (38) Li, L.; Tang, Q.; Li, H.; Yang, X.; Hu, W.; Song, Y.; Shuai, Z.; Xu, W.; Liu, Y.; Zhu, D. *Adv. Mater.* **2007**, *19*, 2613-2617.
- (39) Lei, T.; Dou, J. H.; Pei, J. *Adv. Mater.* **2012**, *24*, 6457-6461.
- (40) Li, C.; Wonneberger, H. *Adv. Mater.* **2012**, *24*, 613-636.
- (41) Yang, G.; Di, C.; Zhang, G.; Zhang, J.; Xiang, J.; Zhang, D.; Zhu, D. *Adv. Funct. Mater.* **2013**, *23*, 1671-1676.

- (42) Xiao, C.; Jiang, W.; Li, X.; Hao, L.; Liu, C.; Wang, Z. *ACS Appl. Mater. Interfaces*. **2014**, *6*, 18098-18103.
- (43) Ding, L.; Li, H.-B.; Lei, T.; Ying, H.-Z.; Wang, R.-B.; Zhou, Y.; Su, Z.-M.; Pei, J. *Mater.* **2012**, *24*, 1944-1949.
- (44) Zhang, F.; Hu, Y.; Schuettfort, T.; Di, C.-a.; Gao, X.; McNeill, C. R.; Thomsen, L.; Mannsfeld, S. C. B.; Yuan, W.; Sirringhaus, H.; Zhu, D. *J. Am. Chem. Soc.* **2013**, *135*, 2338-2349.
- (45) Wang, C.; Qin, Y.; Sun, Y.; Guan, Y.-S.; Xu, W.; Zhu, D. *ACS Appl. Mater. Interfaces*. **2015**, *7*, 15978-15987.
- (46) Ma, Z.; Geng, H.; Wang, D.; Shuaiab, Z. *J. Mater. Chem. C*. **2016**, *4*, 4546-4555.
- (47) Li, X.; Xiao, C.; Jiang, W.; Wang, Z. *J. Mater. Chem. C*. **2013**, *1*, 7513-7518.
- (48) Mumyatov, A. V.; Leshanskaya, L. I.; Anokhin, D. V.; Dremova, N. N.; Troshin, P. A. *Mendeleev Commun.* **2014**, *24*, 306-307.
- (49) Zhang, J.; Tan, L.; Jiang, W.; Hua, W.; Wang, Z. *J. Mater. Chem. C*. **2013**, *1*, 3200-3206.
- (50) Osaka, I.; Zhang, R.; Sauve, G.; Smilgies, D.-M.; Kowalewski, T.; McCullough, R. D. *J. Am. Chem. Soc.* **2009**, *131*, 2521-2529.
- (51) Chesterfield, R. J.; McKeen, J. C.; Newman, C. R.; Ewbank, P. C.; Filho, D. A. d. S; Bre´ das, J.-L.; Miller, L. L.; Mann, K. R. Frisbie, C. D. *J. Phys. Chem. B*. **2004**, *108*, 19281-19292.
- (52) Lefler, K. M.; Co, D. T.; Wasielewski, M. R. *J. Phys. Chem. Lett.* **2012**, *3*, 3798-3805.
- (53) Shao, J.; Zhang, X.; Tian, H.; Geng, Y.; Wang, F. *J. Mater. Chem. C*. **2015**, *3*, 7567-7574.
- (54) Cremer, J.; Mena-Osteritz, E.; Pschierer, N. G.; Müllen, K.; Bäuerle, P. *Org. Biomol. Chem.* **2005**, *3*, 985-995.
- (55) Sharma, V.; Chandra, F.; Sahoo, D.; Koner, A. L. *Eur. J. Org. Chem.* **2017**, 6901-6905.
- (56) Wang, X.; Zeng, T.; Nourrein, M.; Lai, B.-H.; Shen, K.; Wang, C.-L.; Sun, B.; Zhu, M. *RSC Adv.* **2017**, *7*, 26074-26081.
- (57) Avinash, M. B.; Govindaraju, T. A. *Nanoscale* **2011**, *3*, 2536-2543.
- (58) A. Davydov, New York, **1971**. ISBN 978-1-4899-5169-4, Springer.
- (59) Würthner, F.; Kaiser, T. E.; Saha-Möller, C. R. *Angew. Chem. Int. Ed.* **2011**, *50*, 3376-3410.
- (60) Kasha, M.; Rawls, H. R.; El-Bayoumi, M. A. *Pure Appl. Chem.* **1965**, *11*, 371.
- (61) Brown, P. J.; Thomas, D. S.; Köhler, A.; Wilson, J. S.; Kim, J.-S.; Ramsdale, C. M.; Sirringhaus, H.; Friend, R. H. *Phys. Rev. B*. **2003**, *67*, 064203.
- (62) Meher, N.; Iyer, P. K. *Angew. Chem. Int. Ed.* **2018**, *57*, 8488-8492.
- (63) Liu, C.; Xiao, C.; Li, Y.; Hu, W.; Li, Z.; Wang, Z. *Chem. Commun.* **2014**, *50*, 12462-12464.
- (64) Lei, T.; Wang, J. Y.; Pei, J. *Chem. Mater.* **2014**, *26*, 594-603.
- (65) Gsänger, M.; Oh, J. H.; Könemann, M.; Höffken, H. W.; Krause, A.-M.; Bao, Z.; Würthner, F. A. *Angew. Chem. Int. Ed.* **2010**, *49*, 740-743.

- (66) Schmidt, R.; Oh, J. H.; Sun, Y.-S.; Deppisch, M.; Krause, A.-M.; Radacki, K.; Braunschweig, H.; Könemann, M.; Erk, P.; Bao, Z.; Würthner, F. *J. Am. Chem. Soc.* **2009**, *131*, 6215-6228.
- (67) Zhan, X.; Facchetti, A.; Barlow, S.; Marks, T. J.; Ratner, M. A.; Wasielewski, M. R.; Marder, S. R. *Adv. Mater.* **2011**, *23*, 268-284.



Appendix (AI)

Characterization spectra (^1H NMR, ^{13}C NMR, IR and Mass Spectra)

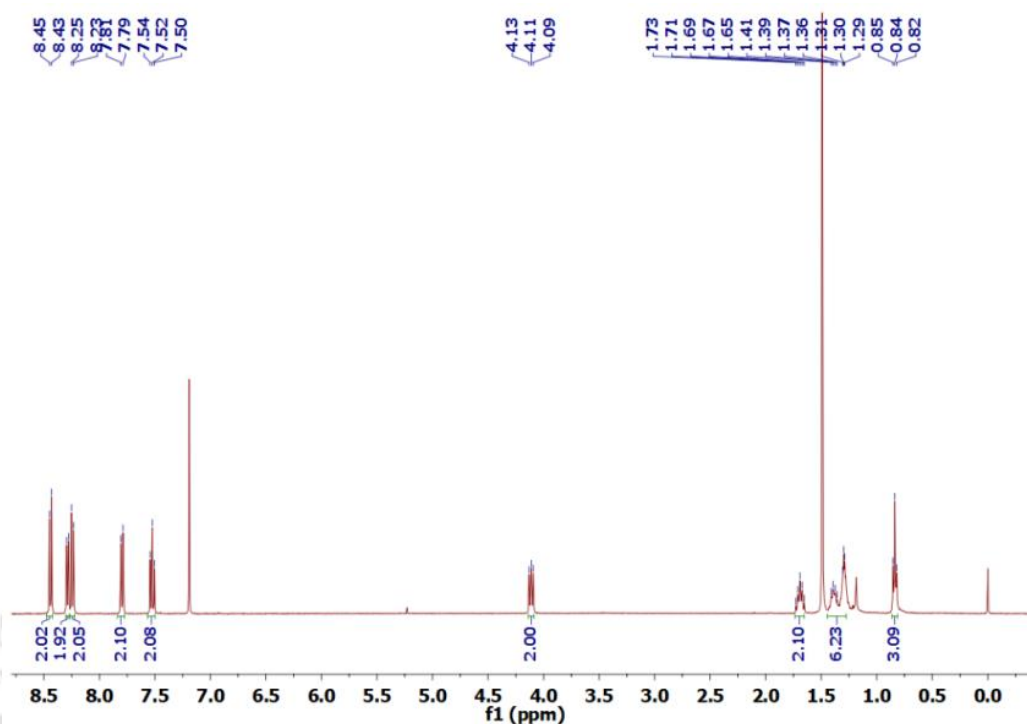


Figure A2.1. ^1H NMR spectra of PMI-C6.

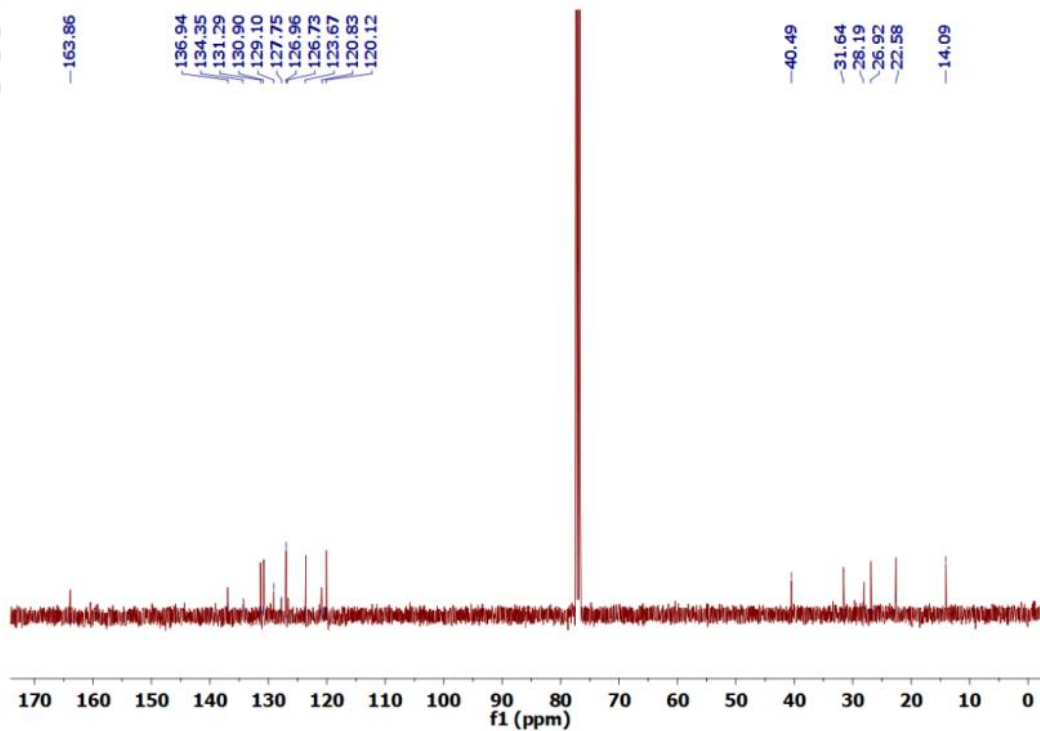


Figure A2.2. ^{13}C NMR spectra of PMI-C6.

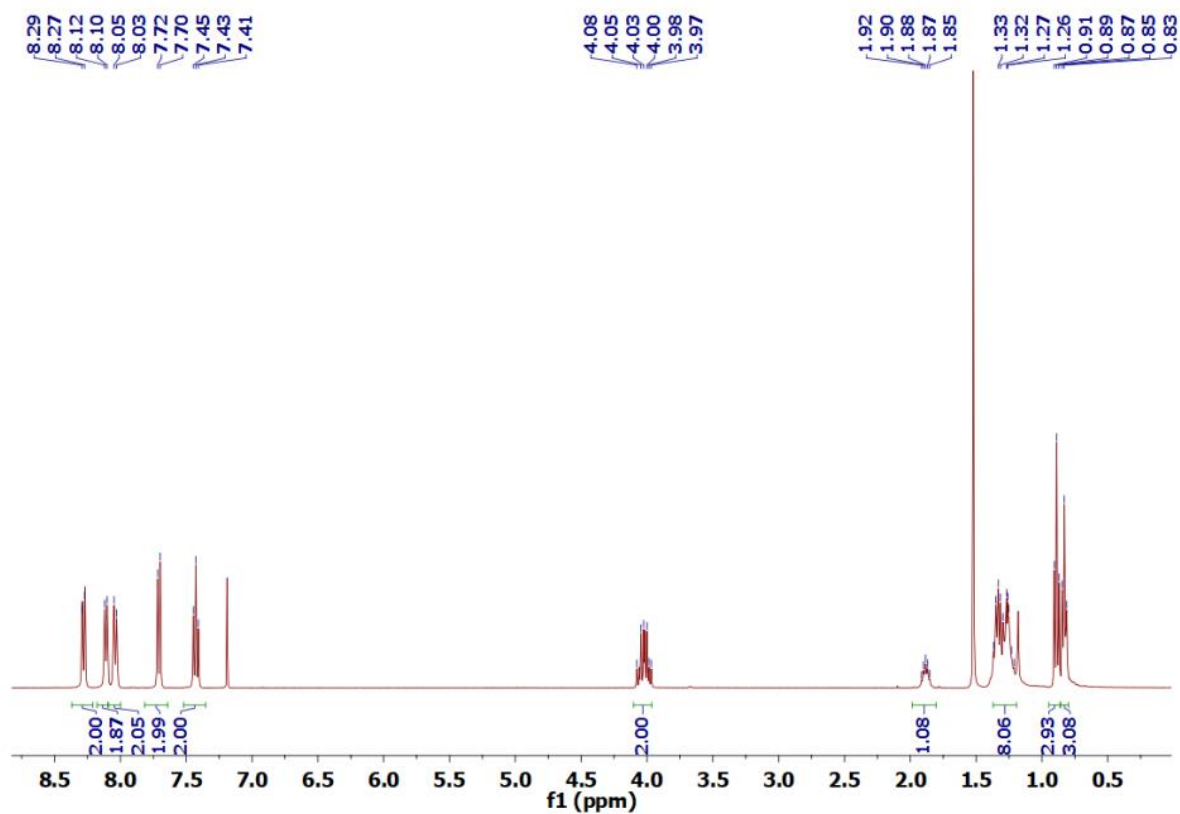


Figure A2.3. ^1H NMR spectra of PMI-CE6.

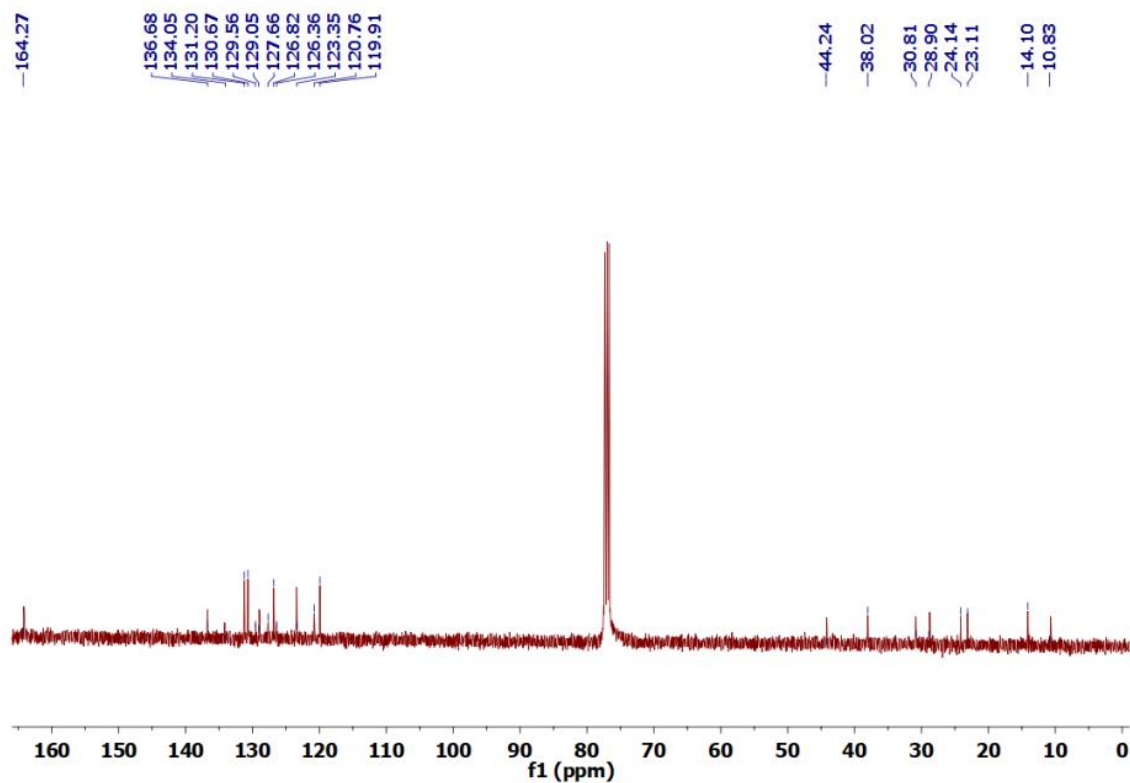


Figure A2.4. ^{13}C NMR spectra of PMI-CE6.

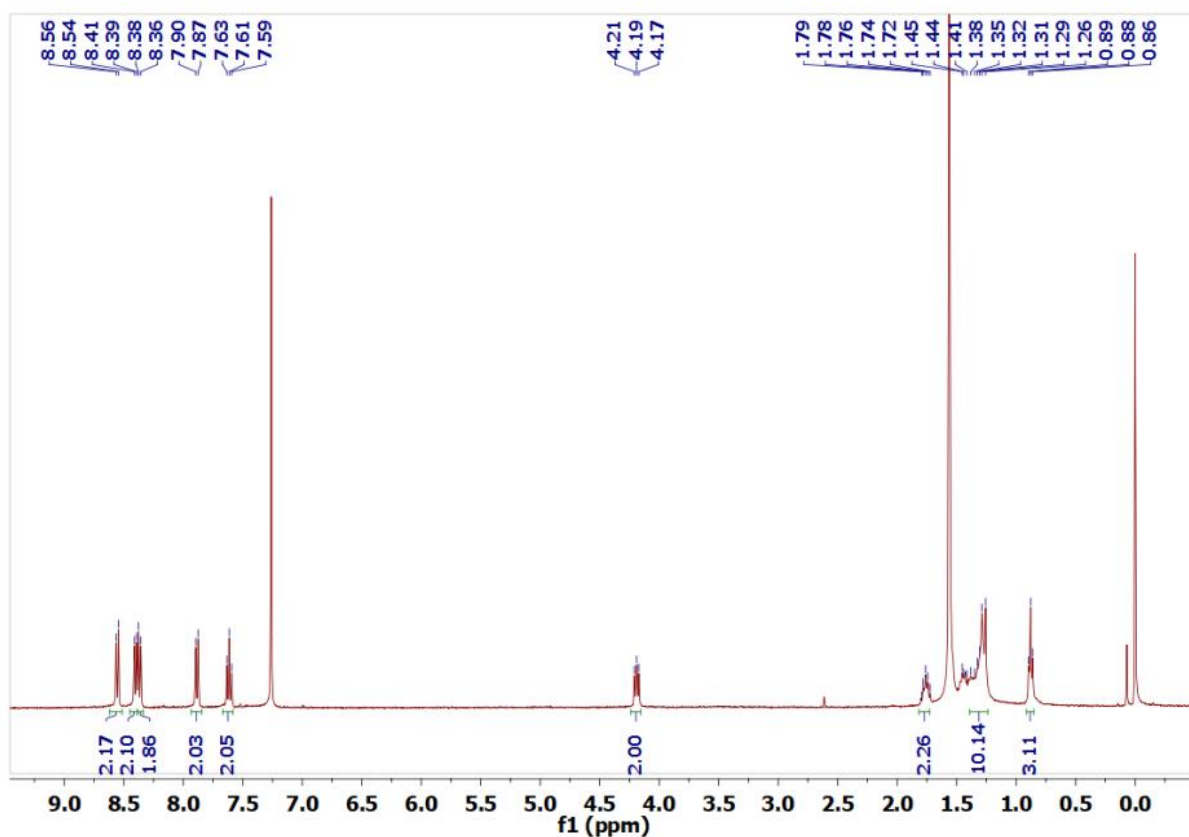


Figure A2.5. ^1H NMR spectra of PMI-C8.

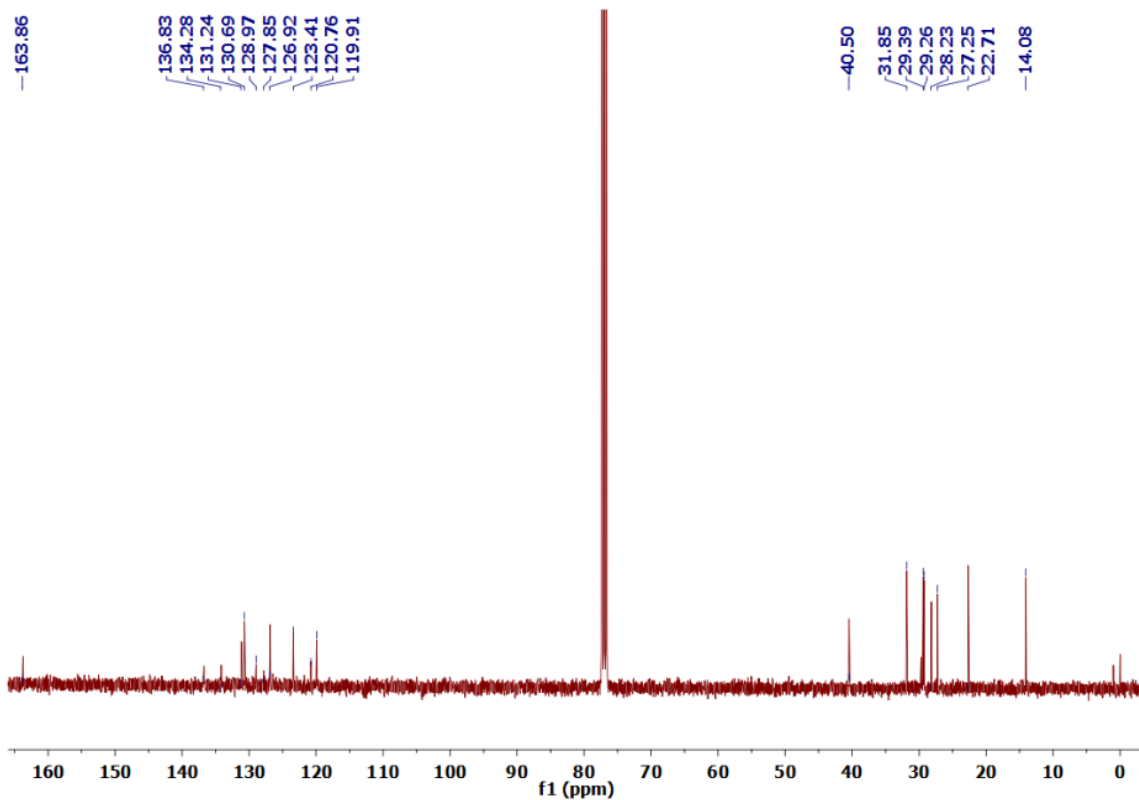


Figure A2.6. ^{13}C NMR spectra of PMI-C8.

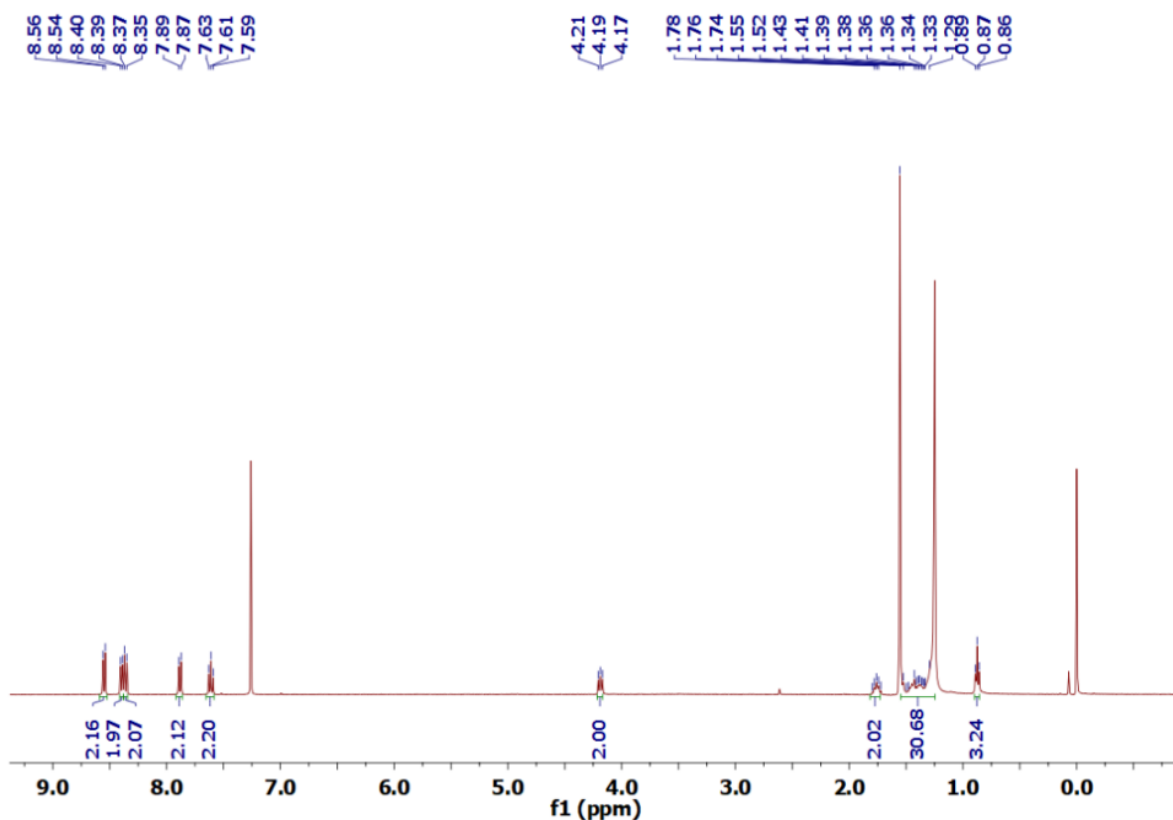


Figure A2.7. ^1H NMR spectra of PMI-C18.

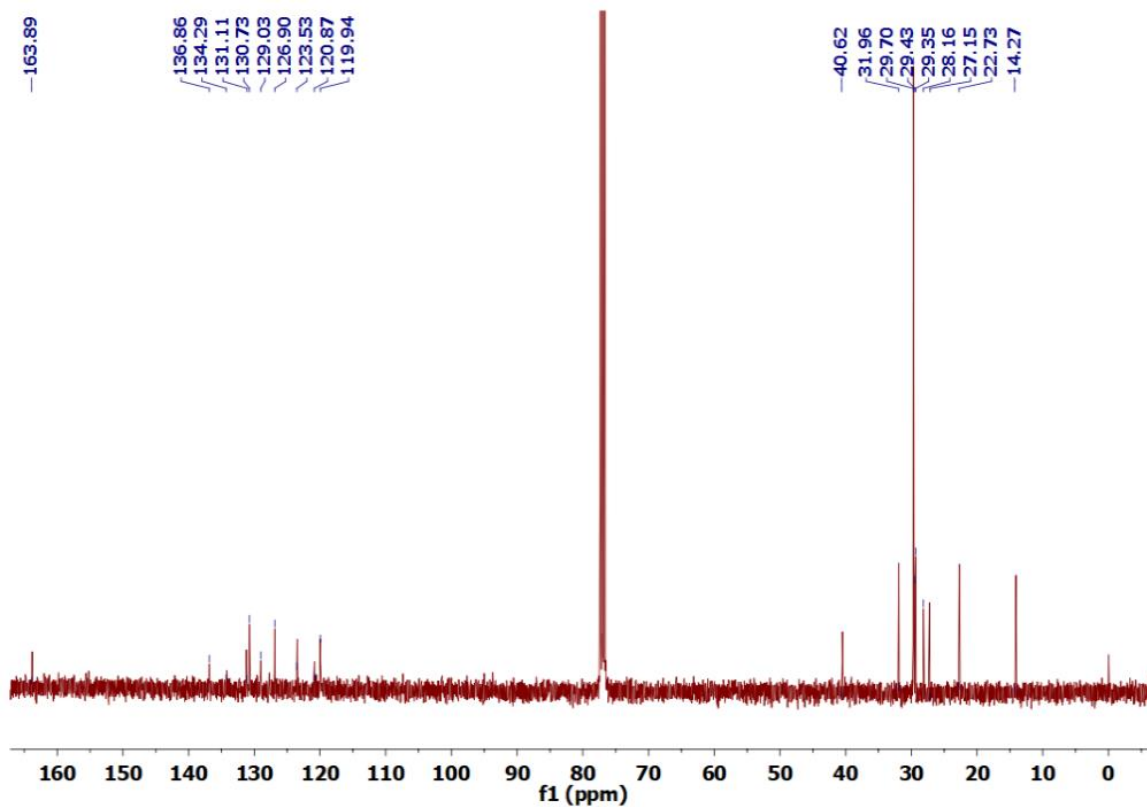


Figure A2.8. ¹³C NMR spectra of PMI-C18.

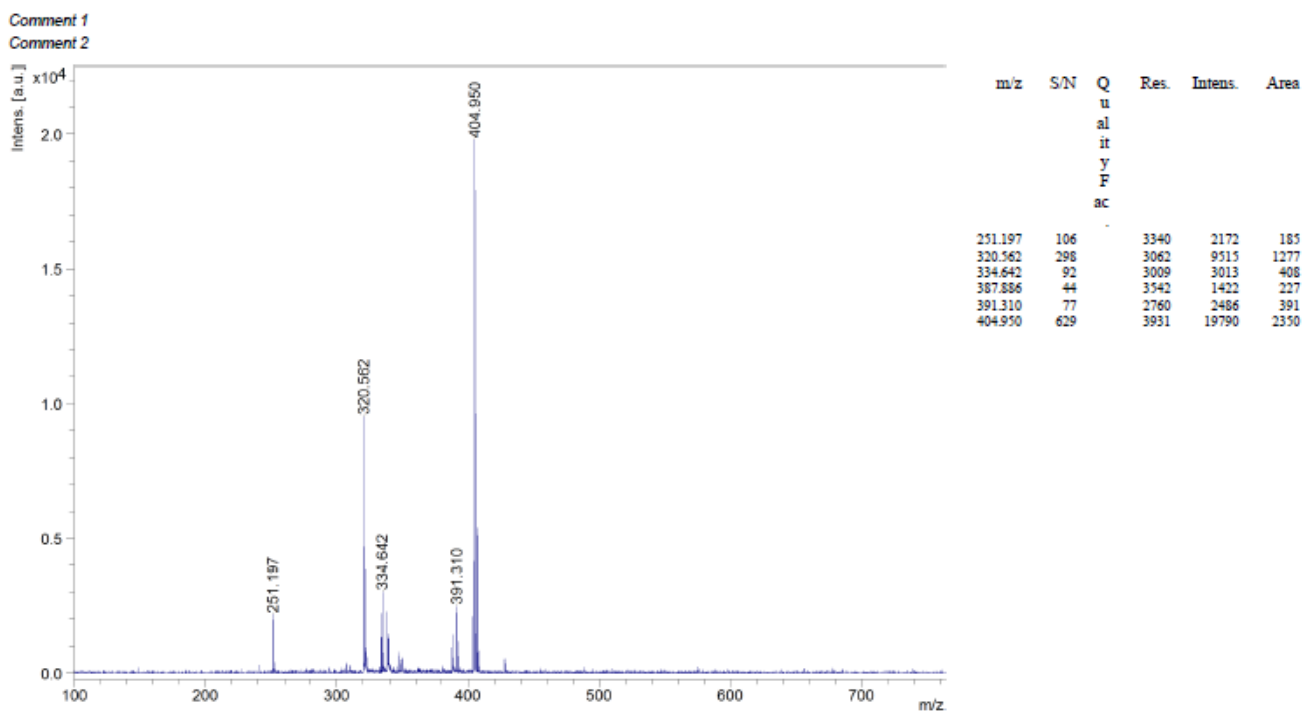


Figure A2.9. Mass spectra of PMI-C6.

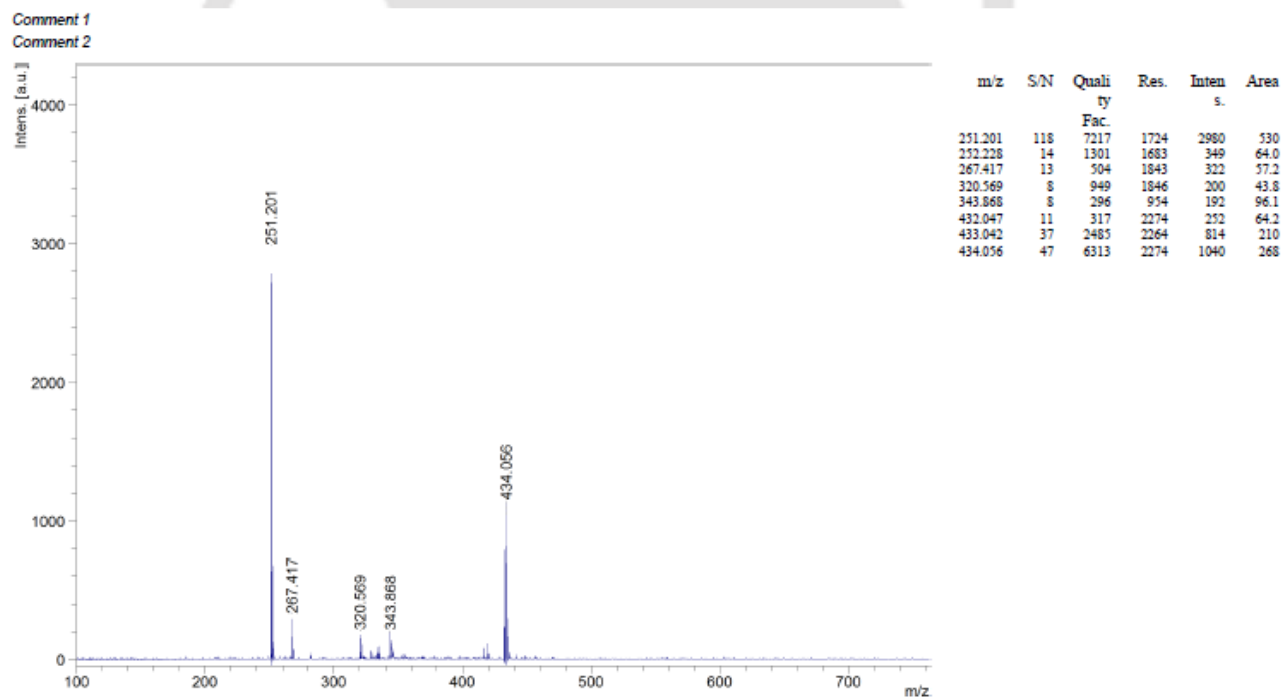


Figure A2.10. Mass spectra of PMI-CE6.

Comment 1
 Comment 2

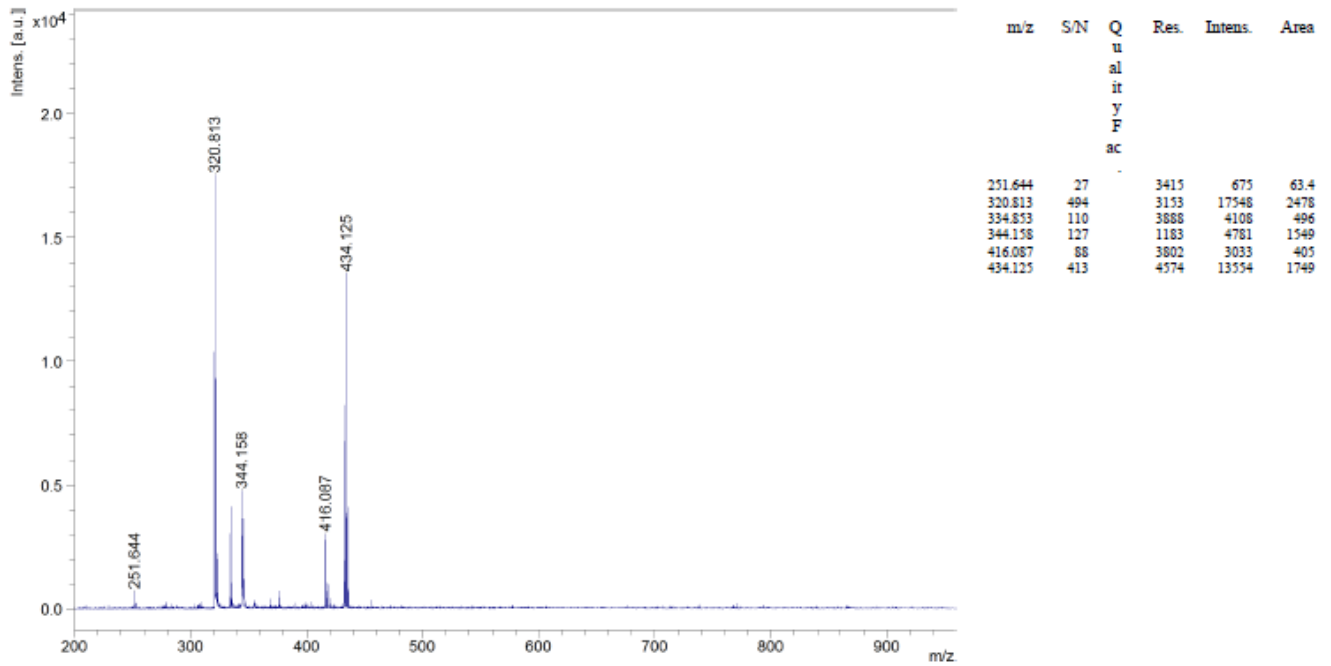


Figure A2.11. Mass spectra of PMI-C8.

Comment 1
 Comment 2

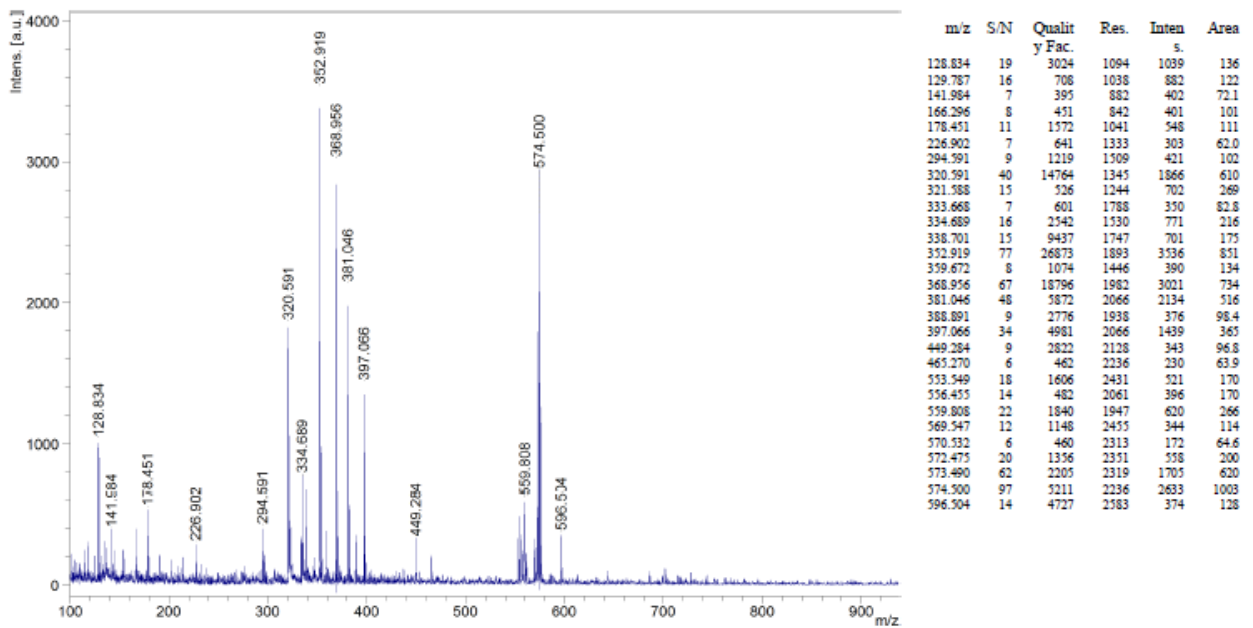


Figure A2.12. Mass spectra of PMI-C18.

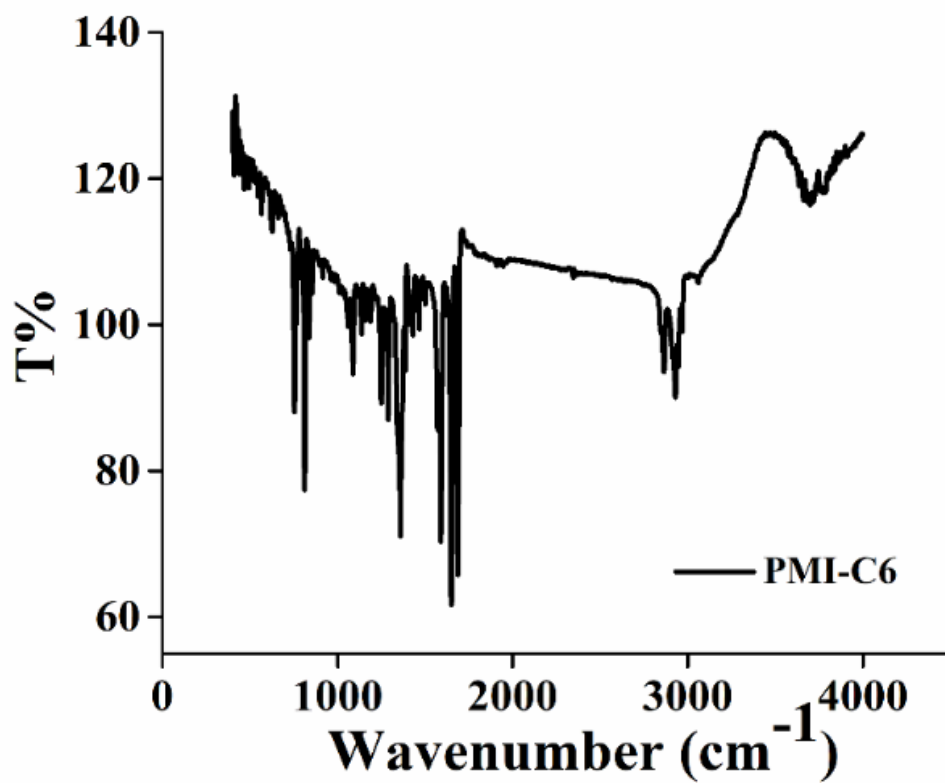


Figure A2.13. FT-IR spectra of PMI-C6.

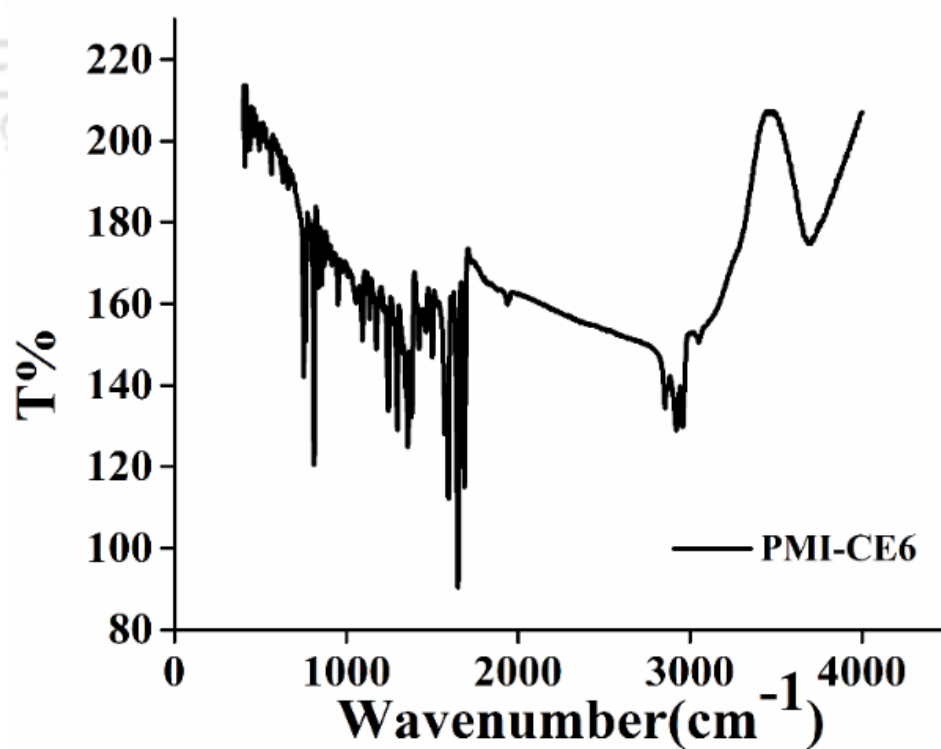


Figure A2.14. FT-IR spectra of PMI-CE6.

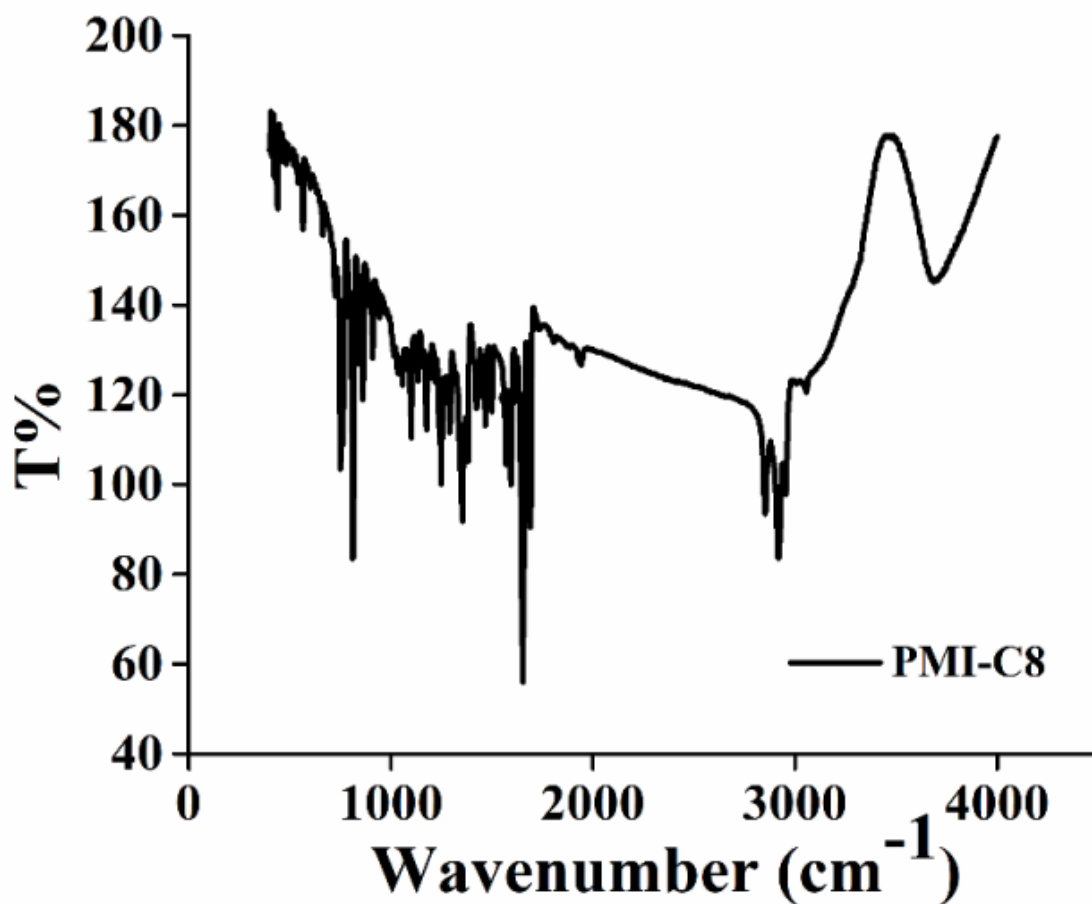


Figure A2.15. FT-IR spectra of PMI-C8.

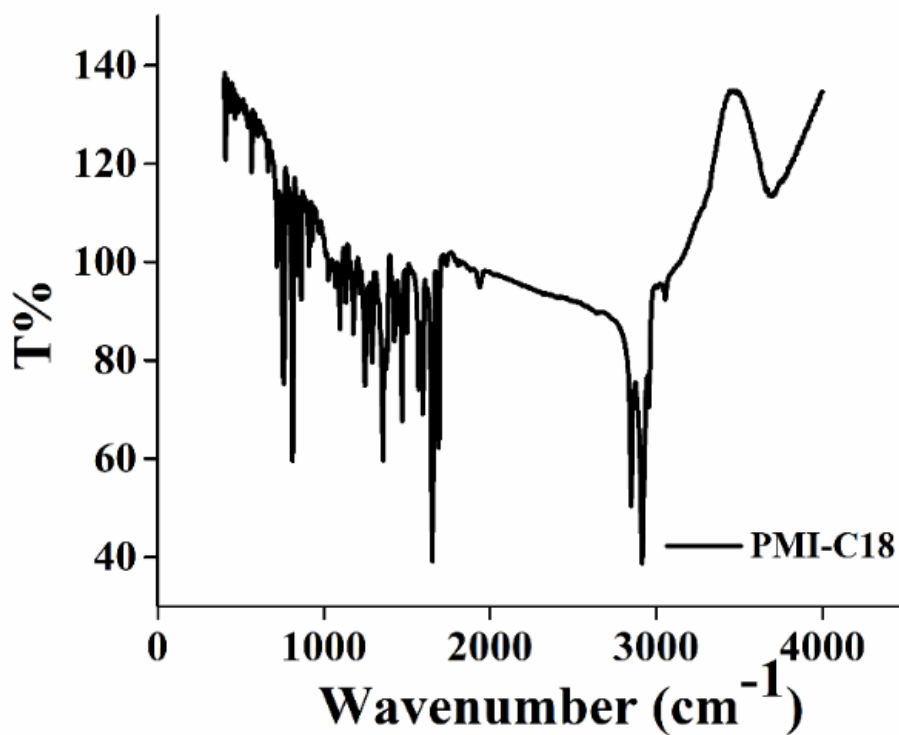


Figure A2.16. FT-IR spectra of PMI-C18.

Photophysical properties studies

Solution state optical properties investigation

Table A2.1: Absorbance and emission spectral data with their corresponding optical band gap of **PMI** congeners in solution state.

Monomer	$\lambda_{\text{abs max}}$ (solution) (nm)	λ_{onset} (solution) (nm)	$\lambda_{\text{em max}}$ (solution) (nm)	$E_{\text{g}}^{\text{S opt}}$ (eV)
PMI-C6	478, 499	530	536, 570	2.33
PMI-CE6	477, 499	530	535, 570	2.33
PMI-C8	477, 499	530	535, 570	2.33
PMI-C18	477, 499	530	534, 570	2.33

$E_{\text{g}}^{\text{S opt}}$ is Optical band gap in solution state.

Equation A2.1: Solution state optical band gap estimations

$$E_{\text{g}}^{\text{S opt}} = 1240/\lambda_{\text{onset}} = 1240/530 = \mathbf{2.33 \text{ eV}}.$$

Thin film-state optical properties estimation

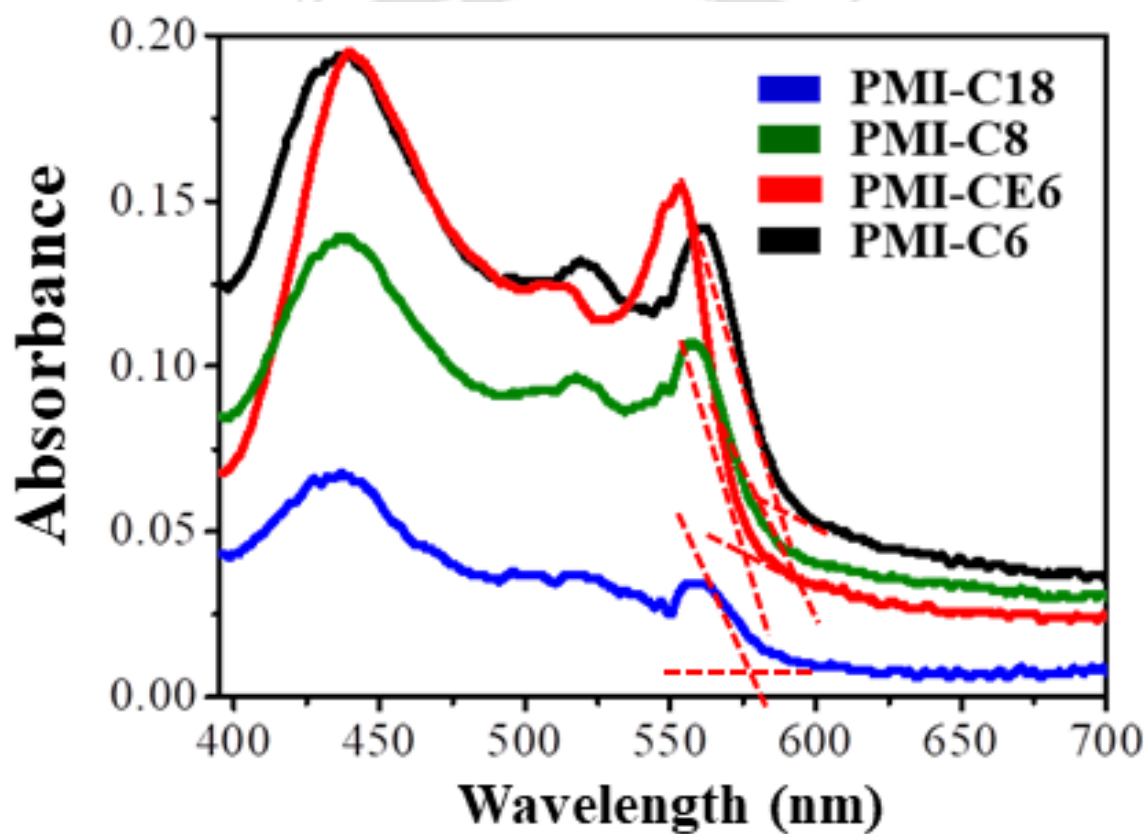


Figure A2.17. Absorbance spectra of PMI congeners in their thin film-state.

Table A2.2: Absorbance spectral and corresponding optical band gap data of PMI congeners in thin film-state.

Monomer	$\lambda_{\text{abs max}}$ (Thin film) (nm)	λ_{onset} (Thin film) (nm)	$E_{\text{g}}^{\text{T opt}}$ (eV)
PMI-C6	435, 525, 570	570	2.17

PMI-CE6	437, 525, 560	572	2.16
PMI-C8	435, 530, 560	578	2.14
PMI-C18	431, 560	583	2.12

E_g^T (opt) is Optical band gap in thin film-state.

Equation A2.2: Optical band gap estimations from absorption spectra in thin film phase.

$$E_g^T(\text{opt}) = 1240/\lambda_{\text{onset}} = 1240/583 = \mathbf{2.12 \text{ eV}}.$$

Electrochemical characteristics of the congeners

Table A2.3: Electrochemical band gap estimation of PMI congeners.

Monomer	$E_{\text{HOMO}}^{\text{CV}}$ (eV)	$E_{\text{LUMO}}^{\text{CV}}$ (eV)	E_g^{CV} (eV)
PMI-C6	-5.712	-3.452	2.26
PMI-CE6	-5.722	-3.392	2.33
PMI-C8	-5.642	-3.432	2.21
PMI-C18	-5.692	-3.732	1.96

E_g^{CV} (eV): Electrochemical band gap = $|E_{\text{HOMO}}^{\text{CV}} - E_{\text{LUMO}}^{\text{CV}}|$ eV.

Where, $E_{\text{HOMO}} = -(E_{\text{onset}}^{\text{ox}} + 4.80)$ eV and $E_{\text{LUMO}} = -(E_{\text{onset}}^{\text{red}} + 4.80)$ eV

XRD data for estimation of molecular Packing

Table A2.4: The layer d-spacing and molecular length obtained in PMI congeners

Monomer	d_1, d_2 (Å) in PXRD	d_1, d_2 (Å) in TXRD	L (Å) in DFT	Tilt angle (°)
PMI-C6	12.16, 10.13	15.60, 10.10	18.36	31
PMI-CE6	18.01, 15.12	18.16, 16.05	18.34	8
PMI-C8	18.09, 12.76	17.04	20.73	34
PMI-C18	24.93, 12.83	25.36, 12.60	33.23	40

d_1 , d_2 are interplanar spacing at low-angle and wide-angle Bragg's diffraction, L (Å) is molecular length calculated from DFT simulation study.

Equation A2.3: Tilt angle (α) = $\cos^{-1}(d/L)$, where L is molecular length calculated from DFT and d is the first diffraction peak obtained from the TXRD.

DFT computational simulation:

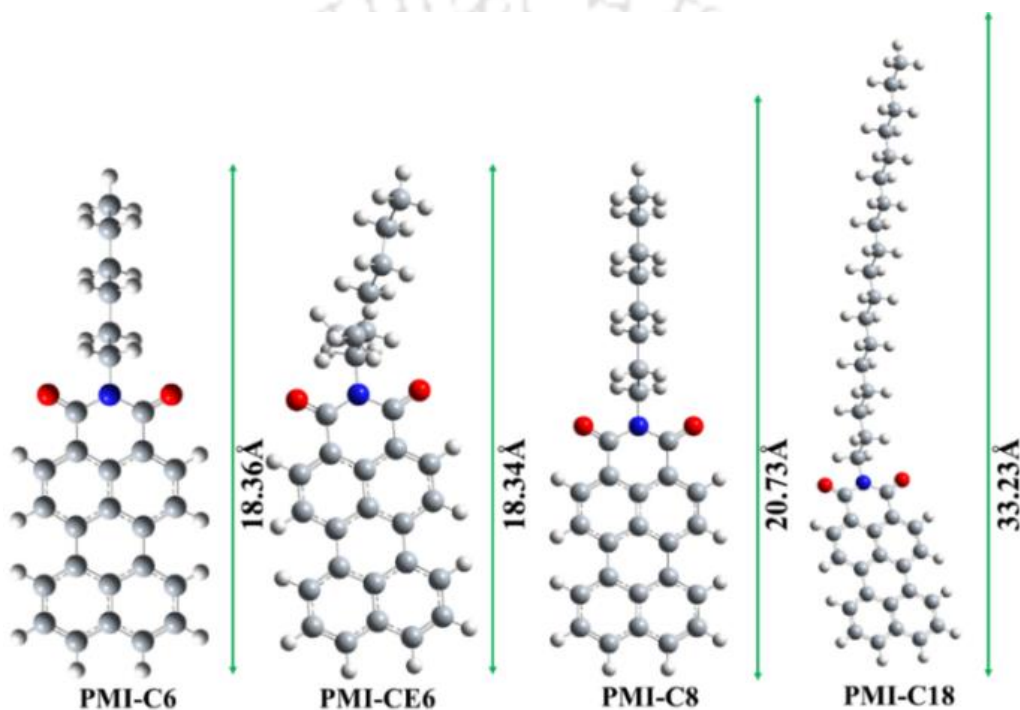


Figure A2.18. Optimized structure of PMI congeners with their corresponding molecular length evaluated from DFT using B3LYP/6-31G, (+d, p) basis set in the Gaussian 09 program.

Solution processed thin film morphology

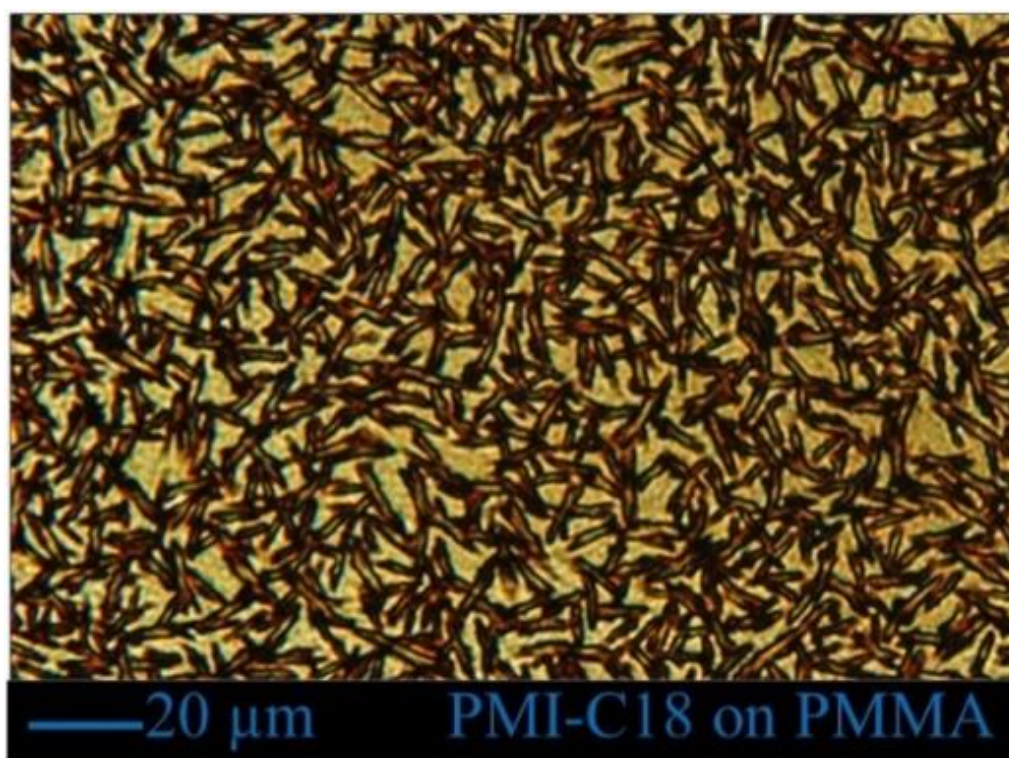


Figure A2.19. Optical image of PMI-C18 on PMMA coated glass substrate.

Table A2.5: A comparative study of OFET device parameter along with the material used, type of material as well as the deposition method and device configuration.

Ref. in SI	Publication	Material Used (Deposition Method)	Material type	$V_{th,h}/V_{th,e}$ (V)	μ_e/μ_h ($\text{cm}^2\text{v}^{-1}\text{s}^{-1}$)	$I_{on/off}$	Device configuration
	Present work	Perylene monoimide (PMI-C18) (Thermal deposition)	n-type	$V_{th,e} = 4.40$	$\mu_e = 1 \times 10^{-4}$	8.8×10^2	Bottom-gate top-contact
(3)	<i>Chem. Sci.</i> 2019 , <i>10</i> , 4951-4958.	Triperyleno[3,3]propellane triimides (Organic nanowire mask technique)	n-type	$V_{th,e} = -5.2$	$\mu_e = 4.51 \times 10^{-3}$	5.7×10^6	Organic nanowire mask technique with four electrode
(4)	<i>Mater. Chem. Front.</i> 2020 , <i>4</i> , 3539-3545.	PMI-annulated [3,3,3]propellanes	p-type	$V_{th,h} = -21.7$ to -6.6	$\mu_h = 10^{-5}$ to 10^{-4} order	10^5 to 10^4 order	Bottom-gate bottom-contact

		(Spin-coated)					
(5)	<i>Adv. Funct. Mater.</i> 2009 , <i>19</i> , 2486-2494.	Hexaperi-Hexabenzocoronene-PMI (HBC-PMI) donor acceptor dyads (Spin-coated)	Ambipolar	$V_{th,h}$ and $V_{th,e} = 20$ To 10	$\mu_e = 3 \times 10^{-6}$ $\mu_h = 3 \times 10^{-6}$	NA	bottom gold contact, bottom gate
(6)	<i>Nanoscale</i> , 2012 , <i>4</i> , 1677-1681	HBC-PMI donor acceptor dyads (Spin-coated)	p-type	NA	$\mu_h = 1 \times 10^{-6}$	NA	bottom-contact

$V_{th,h}/V_{th,e}$ are threshold voltage for hole and electron transport respectively, μ_e/μ_h are electron and hole mobility respectively, whereas NA and SI represents not available and the supporting information.

References:

- (1) Becke, A. D. *J. Chem. Phys.* **1993**, *98*, 5648.
- (2) Frisch, M. J.; Trucks, G. W.; Schlegel, H. B.; Scuseria, G. E.; Robb, M. A.; Cheeseman, J. R.; Scalmani, G.; Barone, V.; Mennucci, B.; Petersson, G. A.; Nakatsuji, H.; Caricato, M.; Li, X.; Hratchian, H. P.; Izmaylov, A. F.; Bloino, J.; Zheng, G.; Sonnenberg, J. L.; Hada, M.; Ehara, M.; Toyota, K.; Fukuda, R.; Hasegawa, J.; Ishida, M.; Nakajima, T.; Honda, Y.; Kitao, O.; Nakai, H.; Vreven, T.; Montgomery, J. A.; Peralta, J. E.; Ogliaro, F.; Bearpark, M.; Heyd, J. J.; Brothers, E.; Kudin, K. N.; Staroverov, V. N.; Kobayashi, R.; Normand, J.; Raghavachari, K.; Rendell, A.; Burant, J. C.; Iyengar, S. S.; Tomasi, J.; Cossi, M.; Rega, N.; Millam, J. M.; Klene, M.; Knox, J. E.; Cross, J. B.; Bakken, V.; Adamo, C.; Jaramillo, J.; Gomperts, R.; Stratmann, R. E.; Yazyev, O.; Austin, A. J.; Cammi, R.; Pomelli, C.; Ochterski, J. W.; Martin, R. L.; Morokuma, K.; Zakrzewski, V. G.; Voth, G. A.; Salvador, P.; Dannenberg, J. J.; Dapprich, S.; Daniels, A. D.; Farkas, O.; Foresman, J. B.; Ortiz, J. V.; Cioslowski, J.; Fox, D. J. *Gaussian 09, Revision A.02, Gaussian, Inc., Wallingford CT.* **2009**.
- (3) Lv, L.; Roberts, J.; Xiao, C.; Jia, Z.; Jiang, W.; Zhang, G.; Risko, C.; Zhang, L. *Chem. Sci.* **2019**, *10*, 4951-4958.
- (4) Lv, L., Sun, W.; Jia, Z.; Zhang, G.; Wang, F.; Tan, Z.; Zhang, L. *Mater. Chem. Front.* **2020**, *4*, 3539-3545.
- (5) Mativetsky, B. J. M.; Kastler, M.; Savage, R. C.; Gentilini, D.; Palma, M.; Pisula, W.; Müllen, K.; Samorì, P. *Adv. Funct. Mater.* **2009**, *19*, 2486-2494.
- (6) Treier, M.; Liscio, A.; Mativetsky, J. M.; Kastler, M.; Müllen, K.; Palermo, V.; Samorì, P. *Nanoscale* **2012**, *4*, 1677-1681.

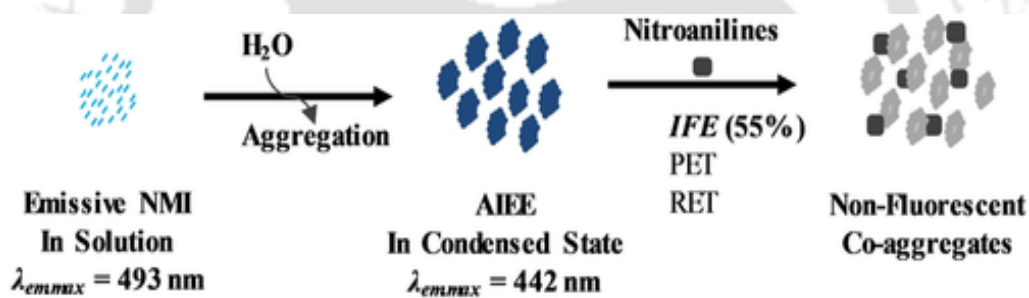
An Unprecedented Blueshifted
Naphthalimide AIEEgen for Ultrasensitive
Detection of 4-Nitroaniline in Water via
“Receptor-Free” IFE Mechanism

Khatun, M N.; Tanwar, A. S.; Meher, N.; Iyer. P. K.; *Chem.AsianJ.***2019**,*14*,4725–4731

Abstract

The development of a new naphthalene appended naphthalimide derivative (**NMI**) with aggregation-induced enhanced emission (AIEE) property for the sensitive detection of 4-nitroaniline (4-NA) in aqueous media is presented here. The newly designed naphthalimide AIEEgen has an exceptional blue-shifted condensed state emission that is devoid of any receptor site, accomplished ultrasensitive detection of 4-NA, which is one of the broad-spectrum pesticides that belong to the class III toxic chemical, at parts per billion level (LOD/36 ppb, $K_{sv}=4.1 \times 10^4 \text{ m}^{-1}$) in water with excellent selectivity even in the presence of potentially competing aliphatic and aromatic amines. The reported probe is the first of its kind, demonstrating major advantages of receptor-free inner filter effect (IFE) mechanism for the sensitive detection of 4-NA using an AIEEgenic probe. Excellent sensitivity for 4-NA is also achieved on paper-based test strip for low-cost on-site detection.

Keywords: aggregation-induced emission, IFE, sensing, 4-nitroaniline.



3.1. Introduction

Highly toxic environmental pollutants such as aromatic amines are heavily released in leather, textile, and other chemical production units along with the degradation of azo dyes (Figure A3.1). Nitroanilines are the essential precursors in many chemical syntheses of pharmaceuticals, pesticides, azo dyes, photo stabilizers, antioxidants, and many more,¹ and thus can heavily pollute the soil and groundwater leading to severe health problems like cancer, diarrhea, skin eczema, and anemia.²⁻⁴ Hence, the recognition of these kinds of toxic amines is highly essential for the control of pollution, human and aquatic health issues and security reasons.⁵ Till date, various techniques have been developed for the detection of aromatic amines based on electrophoretic methods, chromatography, ion mobility spectrometry, X-ray dispersion, cyclic voltammetry, mass spectrometry (GC-MS).⁶⁻⁸ Although these analytical techniques operated well for the detection of aromatic amines, many of them suffer from multiple disadvantages, such as complicated instrument use, high expenses, and time taking processes, that make them incompatible for quick and on-site application.⁹ As compared to other available techniques, the fluorescence-based detection technique is one of the most preferred method owing to its excellent sensitivity, portability, low cost, and quick response time.¹⁰ Thus, a wide variety of fluorescent probes have been used for sensing applications, including both organic and inorganic dyes and polymers, which can be applied only in varying fraction of organic solvent to avoid the aggregation caused quenching effect (ACQ).¹¹ Besides, the classical probes are also inefficient to be used in their solid or thin-film state that can be applied for on-site detection. Thus, considering the role of nitroanilines as a serious environmental pollutant, the sensitive detection of nitroanilines both in aqueous media and on the solid support is essential. Intending to develop an efficient fluorescent probe for nitroanilines, which can effectively work in aqueous media as well as on solid support, we designed and synthesized a simple AIEEgenic naphthalimide probe appended with naphthalene core. The concept of AIE/AIEE was first coined in 2001, where propeller-shaped molecules can go through aggregation in water and can effectively form highly fluorescent nanoparticles due to the restriction of intramolecular rotation (RIR).¹² Naphthalimide derivatives have been established as a flexible class of luminogens due to their various applications in optoelectronics, semiconductor and chemical sensors, self-assemble reproducibly and spontaneously into multifunctional nanostructures and microstructures.¹³ However, the planar aromatic core of the naphthalimide often undergo strong intermolecular π - π stacking interactions and can quench the fluorescent properties in them. Thus, a naphthalene moiety was incorporated at the fourth carbon of the naphthalimide moiety

strategically, that can potentially weaken the intermolecular π - π stacking interactions in **NMI** and transform it into an AIEEgenic probe. Herein, we demonstrate a naphthalimide based AIEEgenic luminogen for the sensitive detection of 4-nitroaniline in both water and solid support through receptor-free Inner Filter Effect (IFE) mechanism.¹⁴ Although, different types of mechanisms such as resonance energy transfer (RET), ground state complexation, photoinduced electron transfer (PET), and electrostatic interaction were reported where a specific type of interaction between the probe and the nitroanilines is required,¹⁵ the detection of the nitroaniline derivatives using AIEEgenic small molecule based on IFE mechanism has never been reported yet.

3.2. Experimental Sections

3.2.1. Materials and Methods.

Nitroaromatic compounds namely, 4-nitroaniline (4-NA), 2-nitroaniline (2-NA), 3-nitroaniline (3-NA), Nitrobenzene (NB), Aniline, 4-BromoAniline (4-Br-A), 1,3-Dinitrobenzene (1,3-DNB), 4-nitrophenol (4-NP), 2-nitrophenol (2-NP), phenol, p-aminophenol (p-AP) 2,4,6-Trifluoroaniline (TFA), 2,3,4,5,6-pentafluoroaniline (PFA), 2,6-DifluoroAniline (DFA), 2-Aminopyridine (2-AP), Triethylamine (TEA), 4-nitrotoluene (4-NT), were obtained from Merck-Sigma-Aldrich. All starting materials, reagents deuterated solvents, Naphthalene boronic ester, 4-Bromo-1,8-naphthalic anhydride, were obtained from Sigma Aldrich (INDIA). HPLC grade solvents and potassium carbonate (K_2CO_3) were obtained from Northeast Chemicals and Zenith India. The chemicals purchased were of high standard purity and used without any additional purification. Stock solutions of analytes and probe were prepared using DMF. Sensing experiment was performed using MilliQ water in 3mL quartz cuvettes. Perkin Elmer Lambda-25 and Horiba Fluoromax-4 spectrofluorometer spectrophotometer were utilized to obtain absorbance spectra, and fluorescence spectra using quartz cuvettes keeping 3 nm of slit width at room temperature (298 K) 1H NMR (400 MHz) and ^{13}C NMR (100 MHz) spectra were recorded on Varian-AS400 NMR spectrometer. Time-resolved photoluminescence (TRPL) studies executed from Edinburg Life Spec II instrument. Surface area and pore size of the material without and with analyte was analyzed using a High-pressure Adsorption Measurement unit (Model: Autosorb-IQ MP).

3.2.2. Synthesis and characterization of Naphthalenemonoimide (NMI)

The Naphthalenemonoimide (**NMI**) was prepared in two steps, starting from commercially available 4-Bromo 1,8-naphthalic anhydride (Scheme 3.1). The alkylation steps were first performed before functionalization at the 4th position of the 4-Bromo 1,8-naphthalic

anhydride core in consideration of solubility issues by a condensation reaction. All the congeners (**BNO** and **NMI**) were well characterized by different sophisticated techniques, such as ^1H and ^{13}C NMR spectroscopy, IR spectroscopy, and HRMS; these are found in this supporting information.

Synthesis of 4-Bromo-N-octylnaphthalimide (**BNO**):

To a suspension of 4-Bromo-1,8-naphthalic anhydride (554.2 mg, 2 mmol) in ethanol, octylamine (258.48 mg, 2 mmol) was added dropwise in 100 mL round bottom flask at room temperature. Then this reaction mixture was refluxed for 8 hours at 85 °C. The mixture was cooled, and the solvent was evaporated by rotary evaporator. The solid residue was poured into chloroform and washed thoroughly with water thrice. The separated organic layer was concentrated after drying over anhydrous sodium sulfate. Finally, column purification in chloroform was performed to obtain pure product **BNO**. Light brown solid (620 mg, 79.8% yield); M.P. 85-86 °C; HRMS (m/z): calcd for $\text{C}_{20}\text{H}_{22}\text{BrNO}_2$ 387.083; found 388.078 [M+H]⁺; ^1H NMR (400 MHz, CDCl_3) δ 8.65 (d, 1H), 8.56 (d, 1H), 8.40 (d, 1H), 8.03 (d, 1H), 7.84 (t, 1H), 4.16 (t, 2H), 1.76-1.69 (m, 2H), 1.44- 1.26 (m, 10H), 0.85 (t, 3H); ^{13}C NMR (100 MHz, CDCl_3) δ 163.63, 163.60, 133.17, 132.00, 131.19, 131.09, 130.58, 130.05, 129.07, 128.14, 123.19, 122.39, 40.77, 31.78, 29.31, 29.19, 28.09, 27.08, 22.68, 14.11.

Synthesis of Naphthalenemonoimide (**NMI**)

Herein, we have synthesized a new luminogen, Naphthalenemonoimide (**NMI**) in good yields via Suzuki cross-coupling. **BNO** (100 mg, 0.26 mmol), Naphthalene boronic ester and $\text{Pd}(\text{PPh}_3)_4$ were taken in a 100 mL RB flask. The complete system was degassed three times and then THF/ H_2O (3:1) was poured into the reaction mixture followed by addition of K_2CO_3 (10 equivalent). The whole reaction mixture was stirred for 18 hours at 85 °C, cooled at room temperature and filtered to remove residual solid K_2CO_3 . The filtrate was dissolved into chloroform and washed thoroughly with dilute HCl, water and brine solution. The separated organic layer was concentrated after drying over anhydrous sodium sulfate to obtain the **NMI**. Light brown powder (73 mg, 65% yield). M.P. 150-154 °C; HRMS (m/z): calculated for $\text{C}_{30}\text{H}_{29}\text{NO}_2$ 435.2198; found 436.2275 [M+H]⁺ ^1H NMR (400 MHz, CDCl_3) δ 8.74 (d, 1H), 8.54 (d, 1H), 7.92 (dd, 2H), 7.70 (d, 2H), , 7.54 (t, 2H), 7.49-7.41(m, 3H), 7.28-7.22 (m, 2H), 4.16 (t, 2H), 1.75-1.67 (m, 2H), 1.39- 1.18 (m, 10H), 0.83 (t, 3H); ^{13}C NMR (101 MHz, CDCl_3) δ 164.43, 163.97, 145.43, 136.35, 133.56, 132.89, 132.26, 131.32, 131.26, 130.71, 128.95, 128.87, 128.42, 127.84, 126.86, 126.60, 126.24, 125.94, 125.26, 122.99, 122.38, 40.68, 31.89, 29.39, 29.26, 28.28, 27.24, 22.66,14.10.

3.2.3. Preparation of Stock Solutions for Sensing.

Stock solution of the **NMI** was prepared in DMF solvent at a concentration of 1×10^{-3} M. Stock solution of various nitroaromatic compounds, namely, 4-NA, 2-NA, 3-NA, A, 4-Br-A, 4-NT, TFA, NB, PFA, 2,6-DFA, 2-AP, TEA, 1,3-DNB, 4-NP, 2-NP, phenol, and p-AP were prepared at concentrations of 1×10^{-2} M in DMF solvent system. The 9 μ L of stock solution was taken into 3 mL water in a 3 mL quartz cuvette for each titration. The 100 μ M stock solutions of analytes were added in portions, and the changes of photoluminescence spectra were recorded at room temperature ($\lambda_{ex} = 350$ nm).

3.2.4. Time-resolved photoluminescence (TRPL) studies.

Lifetime decay measurements of **NMI** (3 μ M) in the presence and absence of 100 μ M stock solution of 4-NA, 2-NA, and 3-NA were obtained using pulse excitation of 375 nm and emission at 442 nm in water. The plots were fitted bi-exponentially and average lifetime was calculated by consideration of consistency in results.

3.2.5. Preparation of Test Strips.

Whatman filter paper (80 mm diameter) was dipped into the stock solution of **NMI** and dried for getting a fluorescent paper strip. Then **NMI** coated filter paper was cut into size (1 cm \times 1 cm) and the desired number of pieces used for a portable device for sensing purposes.

3.2.6. Preparation of FESEM sample.

In 3mL water, 9 μ L stock solution of **NMI** in DMF was added, and the solution was shaken well. After that, 100 μ M 4-NA was added to it and mixed properly. From this mixture, 2 μ L is drop-casted over the aluminium foil wrapped over the glass slide.

3.2.7. Preparation of surface area analyzer (BET) sample.

In 20 mg **NMI** powder, 10 μ L stock solution of 4-NA of 10 mM concentration was added and dried properly before mounting it into the surface area analyzer. The data were compared to the surface area of **NMI** powder without 4-NA.

3.2.8. Quantum Yield Calculations

PL quantum yields (Φ_s) of **NMI** were calculated by taking quinine sulfate ($\Phi_s = 0.57$ in 0.1 M H_2SO_4) as standard and using the equation shown below:

$$\Phi_s = \Phi_r (A_r F_s / A_s F_r) (\eta_s^2 / \eta_r^2)$$

Where, s and r represent sample and reference, Φ signifies the quantum yield, A denotes absorbance, F signifies relative integrated fluorescence intensity, and η represents the refractive index of the medium.

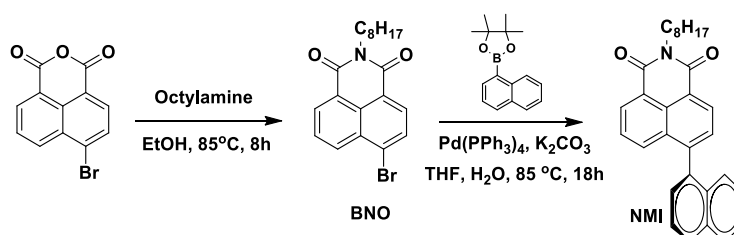
3.2.9. Method for Limit of Detection (LOD) calculation

The fluorescence spectra of **NMI** ($3 \mu\text{M}$) were recorded seven times. Then 4-NA ($0.33 \mu\text{M}$, $0.66 \mu\text{M}$, $1.0 \mu\text{M}$, $1.33 \mu\text{M}$, $1.66 \mu\text{M}$, $2.0 \mu\text{M}$, $2.33 \mu\text{M}$ and $2.66 \mu\text{M}$) were added separately to record spectra keeping the same excitation wavelength, i.e., 350 nm. A regression equation was executed from the calibration plot between emission maxima and concentration of 4-NA. Detection Limit was then calculated from the calibration curve using the equation $3\sigma/k$, where σ represent standard deviation (SD) for the emission intensity of **NMI** solution in the absence of 4-NA and K represents the slope of the calibration curve.

3.3. Results and Discussion

3.3.1. Design, Synthesis, and Characterization of NMI

Intending to generate an AIEEgenic naphthalimide probe, naphthalene moiety functionalized **NMI** was synthesized via a two steps synthetic process. Intentionally, the naphthalene moiety was substituted at the fourth carbon of the naphthalimide moiety that will effectively break its planarity and subsequently generate the AIEEgenic properties via restriction in intramolecular rotation (RIR) process. Commercially available 4-bromo-1,8-naphthalic anhydride was selected as the precursor molecule, and the alkylated **BNO** was prepared by a simple condensation reaction with octylamine (Scheme 3.1). The next step involves a Suzuki coupling of **BNO** with naphthalene boronic ester to get the naphthalene appended **NMI** in good yield (Scheme 3.1). The alkylation at the anhydride function was preferred before the functionalization of 4-Bromo-1,8-naphthalic anhydride core at the fourth carbon to take care of solubility issues during purification and characterization processes. The synthesis and purification of both **BNO** and **NMI** were established by HRMS, FTIR, and multinuclear (^1H , ^{13}C) NMR spectroscopy (Figure A3.2- A3.9). All the details of the synthesis and purification process and the characterization data have been placed in the supporting information.



Scheme 3.1. Synthetic scheme for the preparation of naphthalene-monoimide (**NMI**) from commercially available 4-bromo-1,8-naphthalic anhydride.

3.3.2. AIEE in **NMI** with Exceptional Blue-shifted Emission

To evaluate the condensed state photophysical properties in **NMI**, its emission property was recorded in DMF solution and gradually increasing the water fraction (f_w) of the medium, where most of the organic solvents including DMF acts as a good solvent for **NMI** (Figure 3.1, Table A3.1). However, the complete insolubility of **NMI** in water triggers the formation of aggregates with increasing f_w . **NMI** displayed absorption maxima at 344 nm, whereas the emission maxima of **NMI** centered at 493 nm ($\lambda_{ex} = 350$ nm) in DMF. Whereas, on increasing the f_w up to 60%, the emission intensity drastically decreased 7-fold with a red-shifted λ_{max} (543 nm) (Figure A3.1a). With increasing f_w from 60-99.8%, the aggregation in **NMI** became prominent, and surprisingly a blue-shifted emission spectrum centered at 442 nm appeared with a nearly 7-fold increase in its emission intensity (Figure A3.1a). Although the insignificant shift in the absorption maxima of **NMI** in its condensed state and solution state ruled out the presence of simple J or H-type aggregation, the strong blue-shifted emission spectra of **NMI** in its condensed state to that of its solution state suggested the presence of unique intermolecular packing interactions in **NMI** (Figure A3.1a- A3.1b).^{13f} This exceptional hypsochromic shift of the emission behavior in **NMI** was further demonstrated by capturing the digital photographs (Figure 3.2) of **NMI** during solvent evaporation under 365 nm UV irradiation, which clearly showed the transition of emission color from yellowish-green (solution state) to deep-blue (solid-state) and is identical with the powder emission of **NMI** as well (Figure 3.1g and Figure A3.10). There is a strong reduction in the red-shifted emission intensity in **NMI** with increasing f_w up to 60%, where the molecules remain in its molecularly dispersed form. This could be due to the presence of twisted intramolecular charge transfer (TICT) process and has been confirmed by theoretical calculations and recording the emission spectra of **NMI** in different solvents with varying polarity (Figure 3.1d-3.1f, and Figure 3.3).

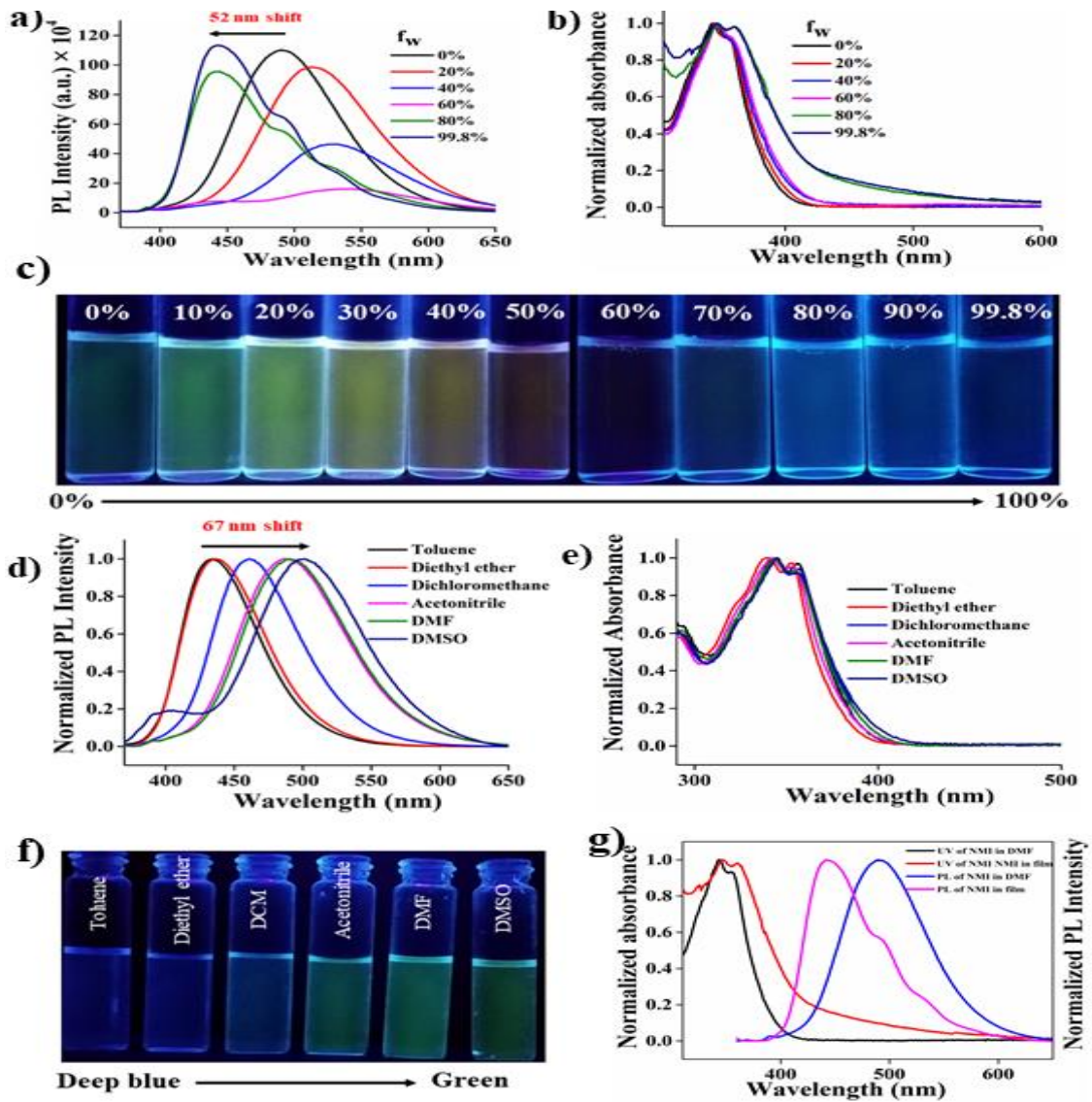


Figure 3.1. a) Fluorescence spectra of NMI at different f_w in DMF. b) Normalized absorption of NMI at different f_w in DMF. c) The digital image of NMI at different f_w in DMF under 365 nm UV irradiation. d) The normalized fluorescence spectra of NMI in different solvents from toluene to DMSO. e) Normalized absorbance spectra of NMI in different solvents from toluene to DMSO. f) The fluorescence color change of NMI under the excitation of 365 nm UV irradiation in different solvents from toluene to DMSO. g) Normalized absorption and PL spectra of NMI in solution (DMF) and in solid films. [room temperature, $\lambda_{ex}=350$ nm, $[NMI]=3 \mu M$].

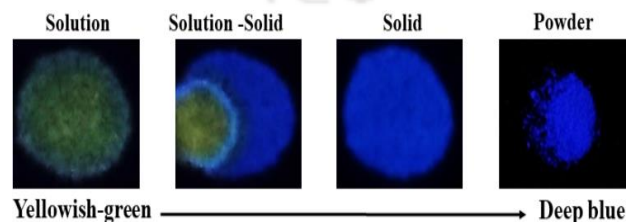


Figure 3.2. The fluorescence color change of NMI from solution to solid state which is identical with powder under the excitation of 365 nm UV light.

The computational studies were done with the help of time-dependent density functional theory (TD-DFT), in which almost complete separation of electron density over HOMO and LUMO were observed in **NMI** indicating the strong probability of intramolecular charge transfer (Figure 3.3). However, the dihedral angles of 71° between naphthalic anhydride and naphthalene moieties in its excited state indicate the feasibility of TICT phenomenon in **NMI**. To further confirm the above speculations, the emission spectra of **NMI** were recorded in different solvents with varying polarity (Figure 3.1d, Table A3.2). While considering the emission spectra from toluene to DMSO, a significant red-shift of nearly 67 nm was observed, which strongly suggested the presence of TICT phenomenon in **NMI** molecule that could be the primary reason for the decrease in the red-shifted fluorescence intensity with increasing f_w in DMF. However, with increasing f_w from 60-99.8%, the molecules start aggregating with blue-shifted emission spectra to that of its solution state, which could be attributed to being directed by their nature of intermolecular interactions. Though the crystal structure of **NMI** could not be solved due to the poor quality of single-crystal, our previous report on naphthalimide small molecules has successfully explored that the condensed state photophysical properties are exclusively dictated by the distinct intermolecular π - π stacking interaction among the planar naphthalimide aromatic core.^[13f] In other words, the condensed state photophysical properties remain unaffected by the donor-acceptor combination within the molecule. Thus, the blue-shifted emission of **NMI** in its condensed state could be assumed to be controlled by the unique intermolecular π - π stacking orientations of the naphthalimide core.

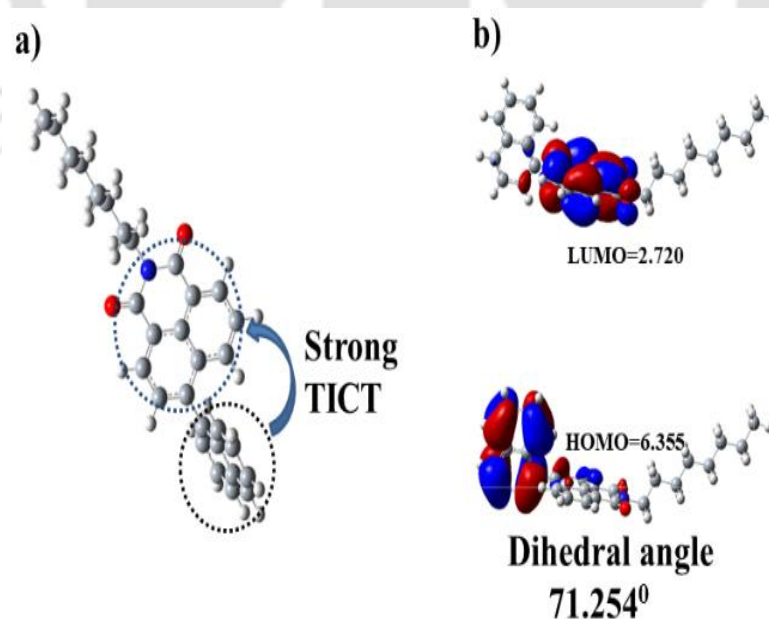


Figure 3.3. a) Optimized structure of **NMI** in its excited state. b) The frontier orbitals of **NMI** in its excited state (TD-DFT, B3LYP/6-31G,+d,p)¹⁷ and the dihedral angles between the donor naphthalene and the acceptor naphthalimide core.

3.3.3. 4-NA Detection in Aqueous Medium

The fluorescence quenching titrations were done by the systematic addition of DMF solutions of various aliphatic and aromatic amines (100 μM) to **NMI** (3 μM) dispersed in water (Figure 3.4a-4d). The intense blue emission of the monomer **NMI** ($\lambda_{em,max} = 442 \text{ nm}$) at 99.8% water fraction in DMF was evaluated for the detection of nitroaniline derivatives. 4-NA was added in parts to the dilute dispersed solution of **NMI** (3 μM), where $\sim 13\%$ of the fluorescence quenching of the AIEEgen was observed by the addition of just 6.6 μM of the analyte (Figure 3.4a). However, a strong fluorescence quenching of $\sim 91\%$ was witnessed after the addition of 100 μM of the analyte, whereas 69% and 40% of the fluorescence quenching in **NMI** emission was observed after the addition of 100 μM of 2-NA and 3-NA respectively, which clearly confirms the relatively lower sensitivity of **NMI** towards these nitroaniline derivatives (Figure A3.11-A3.12). Stern-Volmer (S-V) plot was generated for 4-NA by using S-V equation ($I_0/I = 1 + K_{sv}[Q]$), where I_0 and I are the emission maxima before and after addition of quencher [Q]; (4-NA) and K_{sv} is the S-V quenching constant, which signifies the efficiency of quenching. S-V plot shows a linear nature of curve at a lower concentration of [4-NA] and deviates from linearity at higher concentration of [4-NA] (Figure 3.4b and Figure A.13). The value of K_{sv} was calculated

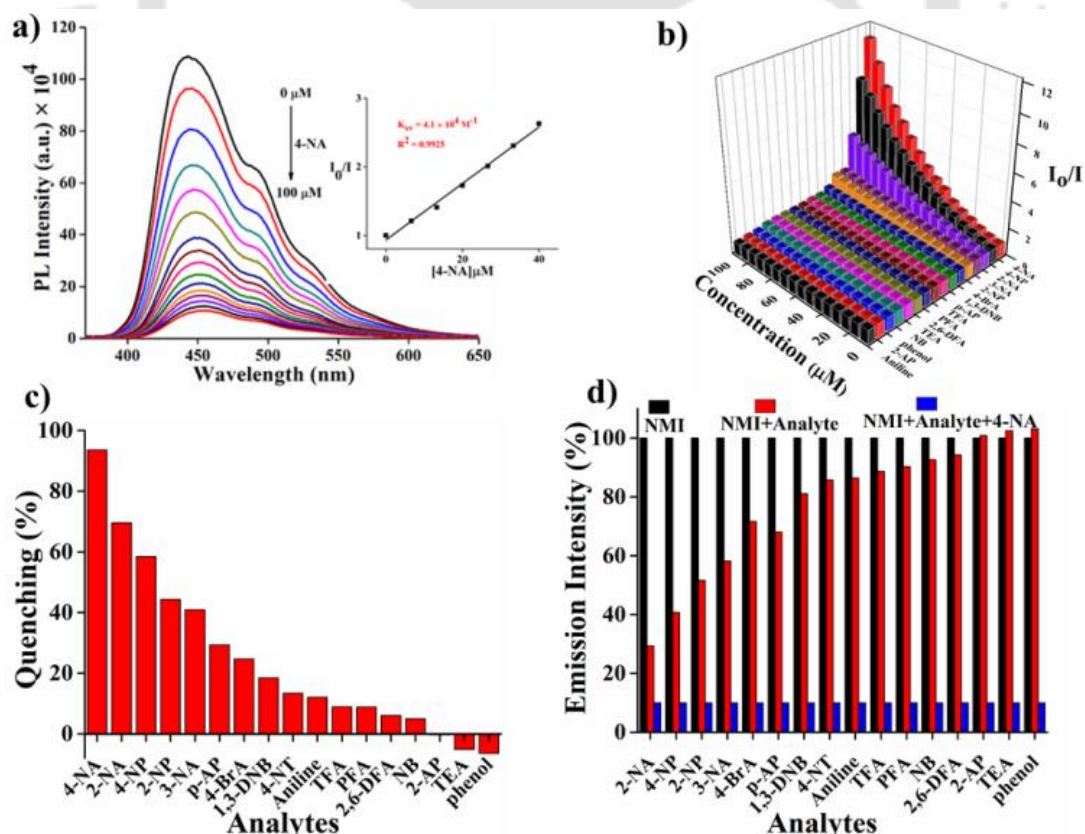


Figure 3.4. a) Fluorescence titration of **NMI** with increasing concentration of 4-NA. The inset is the respective Stern–Volmer plots. b) 3D Stern–Volmer plots for various amines. c) Fluorescence quenching in percentage calculated for various amines. d) Percentage of fluorescence quenching in **NMI** before and after the addition of different amines (100 μM) followed by 4-NA (100 μM). ($[\text{NMI}] = 3 \mu\text{M}$, at room temperature).

from the linear curve and found to be $4.1 \times 10^4 \text{ M}^{-1}$ (Inset of Figure 3.4a) while the K_{sv} value calculated for 2-NA and 3-NA was $2.5 \times 10^4 \text{ M}^{-1}$ (Figure S11b) and $1.0 \times 10^4 \text{ M}^{-1}$ (Figure A3.12b) respectively. This confirms a higher sensitivity of **NMI** AIEEgen towards 4-NA. The limit of detection (LOD) was calculated for 4-NA using the equation $(3\sigma/k)$ and found to be 36 ppb (0.235 μM) (Figure A3.14) which is superior to most of the reported 4-NA sensors in the literature (Table A3.3).^[15,16] Interestingly, there are very few research reports available for the detection of 4-NA in water and bear poor sensing parameters like LOD when compared to **NMI** AIEEgen. Furthermore, **NMI** AIEEgen is the first report for the 4-NA detection based on the AIEE phenomenon (Table A3.3).

3.3.4. Selectivity Studies

Fluorescence titrations were further carried out with various moderately dissimilar analytes such as 2-NA, 3-NA, 4-NT, 4-BrA, 1,3-DNB, Aniline, TFA, PFA, 2,6-DFA, NB, 2-AP, and TEA keeping the same experimental titration conditions. PL intensity of **NMI** was almost fully quenched by 4-NA, while 2-NA and 3-NA partially quenched the PL intensity. Percentage of quenching obtained for all the analytes has been shown in Figure 3.4c. Thus, **NMI** has significant selectivity towards 4-NA in water as compared to other analytes. This high selectivity of **NMI** probe towards 4-NA can also be observed under UV lamp (excitation wavelength = 365 nm) irradiation (Figure 3.5a).

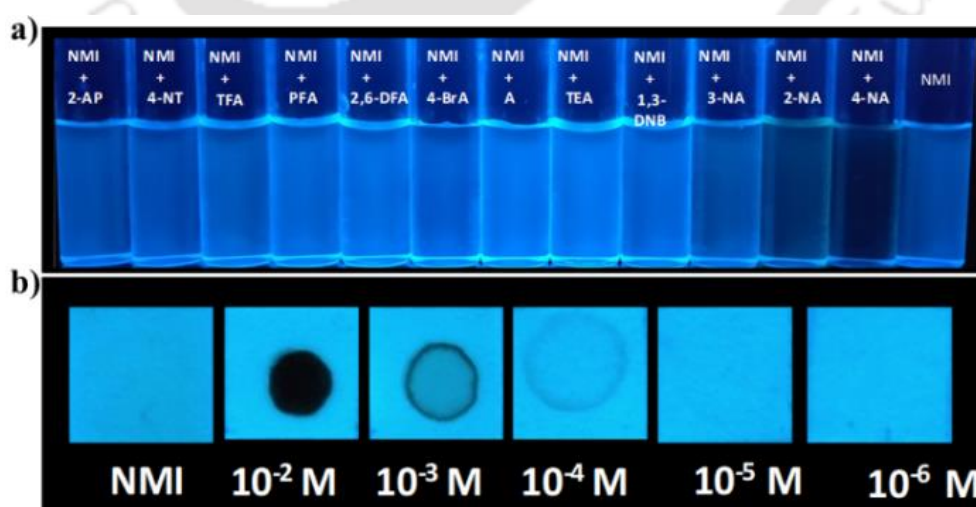


Figure 3.5 (a) Solution images of **NMI** (3 μM) in the absence and presence of 100 μM concentration of different analytes under UV illumination (365 nm). (b) Photos of fluorescent test strips after the addition of 10 μL of 4-NA solution of different concentrations under 365 nm UV irradiation.

3.3.5. Sensing Studies in Competitive Environment

To study the interference of other analytes, PL spectrum of **NMI** AIEEgen was recorded in aqueous media, and then various other analytes were added followed by the addition of 4-NA. It was found that the emission intensity of **NMI** gets fully quenched in all the solutions containing the mixture of **NMI** and various analytes only after addition of 4-NA (Figure 3.4d and A3.15-A3.14). This experiment suggests that **NMI** can also detect 4-NA in the presence of other possibly interfering chemicals.

3.3.6. Portable Test strips for Onsite Detection

Additionally, after observing these astonishing results of AIEE-active **NMI** probe for 4-NA in the aqueous media, portable test strips were prepared to explore its extended utility for on-site detection of 4-NA using Whatman filter paper as a solid platform. These strips are economical, easy to prepare in various sizes and shapes, and undergo fast fabrication of sensory **NMI** probe. For practical purposes, 1 cm × 1 cm size test strips were dip-coated with **NMI** solution (1mM) in DMF and dried before further use to get deep blue fluorescent test strips under UV lamp (365 nm) (Figure 3.5b). Subsequently, 10 μ L of various concentration of 4-NA (10^{-6} to 10^{-2} M) were dropped over these test strips, and a dark spot developed after drying, due to traces of 4-NA. These portable test strips can detect a minimum of 10^{-4} M of 4-NA. These are the best values reported in the literature for 4-NA detection in aqueous media based on IFE mechanism (Table A3.3).

3.3.7. The sensing mechanism of 4-NA detection

There are several processes which can be responsible for the quenching of fluorescence. However, based on the current experimental studies in the case of 4-NA and other nitroanilines, there could be dynamic quenching, i.e. resonance energy transfer (RET), inner filter effect (IFE), static quenching (i.e., ground state complexation), and/or photo-induced electron transfer (Figure 3.6a-3.6f and Figures A3.15-A3.18). Also, from the non-linear nature of S-V plot, it is clear that detection of 4-NA involves multiple mechanisms of sensing (Figure 3.4b and Figure A3.13). For this purpose, initially, lifetime decay profile (TRPL plot) of **NMI** AIEEgen solution in DMF was recorded at various concentrations of nitroanilines (Tables A3.4-A3.6). It was observed, that there is a small change in the lifetime before (1.50 ns) and after (1.26 ns) addition of 100 μ M 4-NA (Figure 3.6a and Table A3.4).

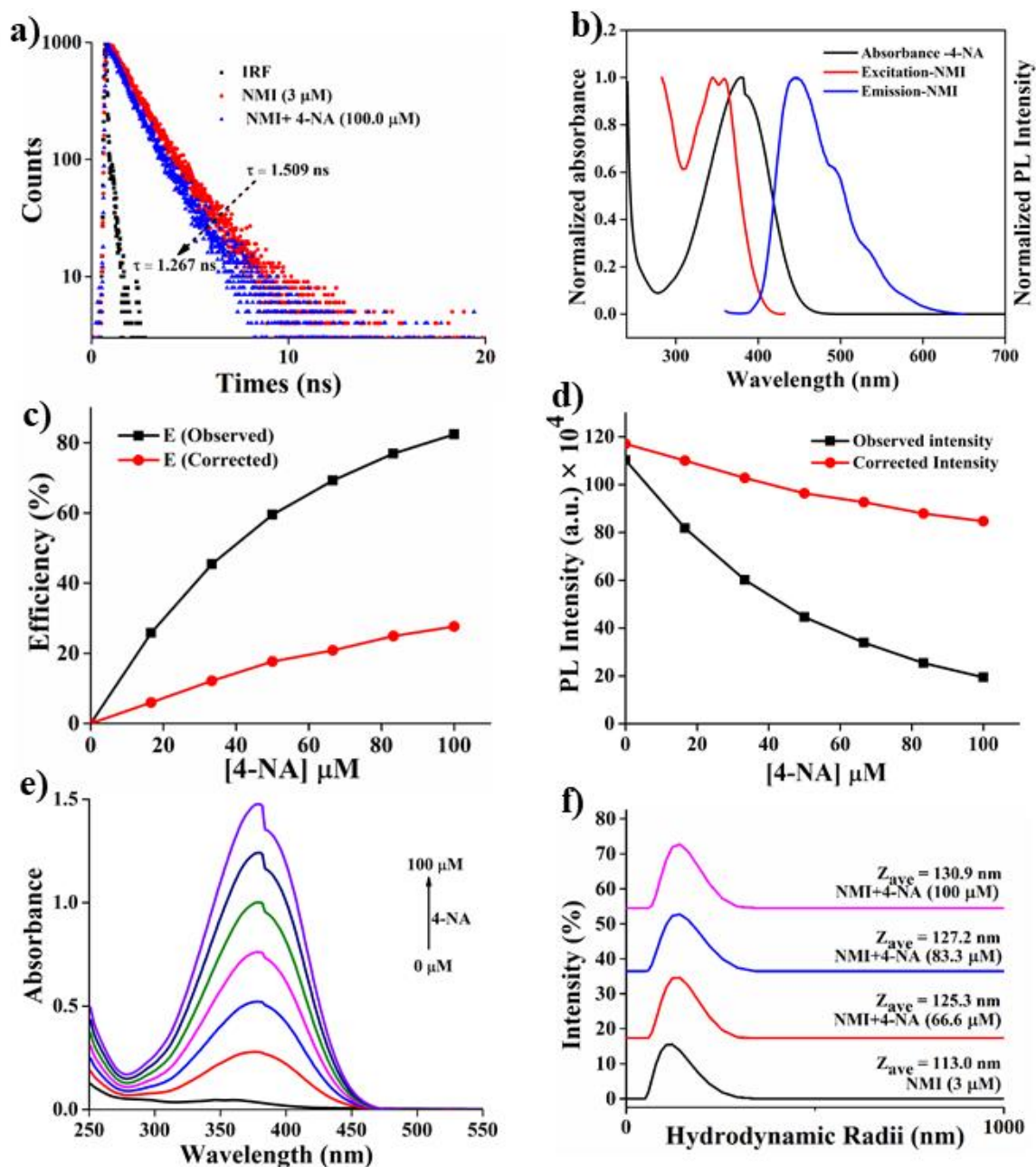


Figure 3.6 a) Fluorescence Lifetime decay study of **NMI** ($3 \mu\text{M}$) in the absence and presence of $100 \mu\text{M}$ of 4-NA. b) Spectral overlap between the emission spectrum of **NMI** and the absorption spectrum of 4-NA. c) Suppression efficiency (E, %) of the corrected (red line) and observed (black line) fluorescence intensity for **NMI** AIEEgen under the effect of 4-NA concentration. d) Observed (black line, I_{obs}) and corrected (red line, I_{corr}) fluorescence intensity of the **NMI** AIEEgen under the influence of 4-NA concentration. e) Absorption spectra of **NMI** ($3 \mu\text{M}$) with increasing concentration of 4-NA. f) Hydrodynamic Radii distribution of **NMI** by DLS with increasing concentration of 4-NA in aqueous media.

This confirms the involvement of dynamic quenching, i.e. RET in sensing mechanism and rules out the possibility of static quenching. Furthermore, UV-vis spectra of **NMI** at various concentration of 4-NA does not show the formation of any new peak in absorption spectra and

clearly excludes the formation of any ground state complexation i.e. static quenching (Figure 3.6e). However, it can also be seen from Figure 3.6b that there is a huge spectral overlap between emission and excitation spectra of **NMI** with the absorption spectrum of 4-NA in water. This indicates the presence of IFE in the existing sensing system, which was later confirmed via IFE correction ($I_{corr}/I_{obs}=10^{(A_{exc}+A_{em}/2)}$) in the observed emission intensity of **NMI** in the presence of 4-NA (Figure 3.6c-3.6d), where I_{corr} and I_{obs} are the corrected and observed PL intensity respectively, A_{exc} and A_{em} are the absorptions of the solution at excitation and emission wavelengths, respectively. There is a huge percentage of suppression efficiency (~55 %) that was observed after the IFE correction (Figure 3.6c) suggesting that IFE plays a significant role in the sensing mechanism, which is rarely observed previously. Molecular size distributions of **NMI** in water medium were studied via dynamic light scattering (DLS) where average

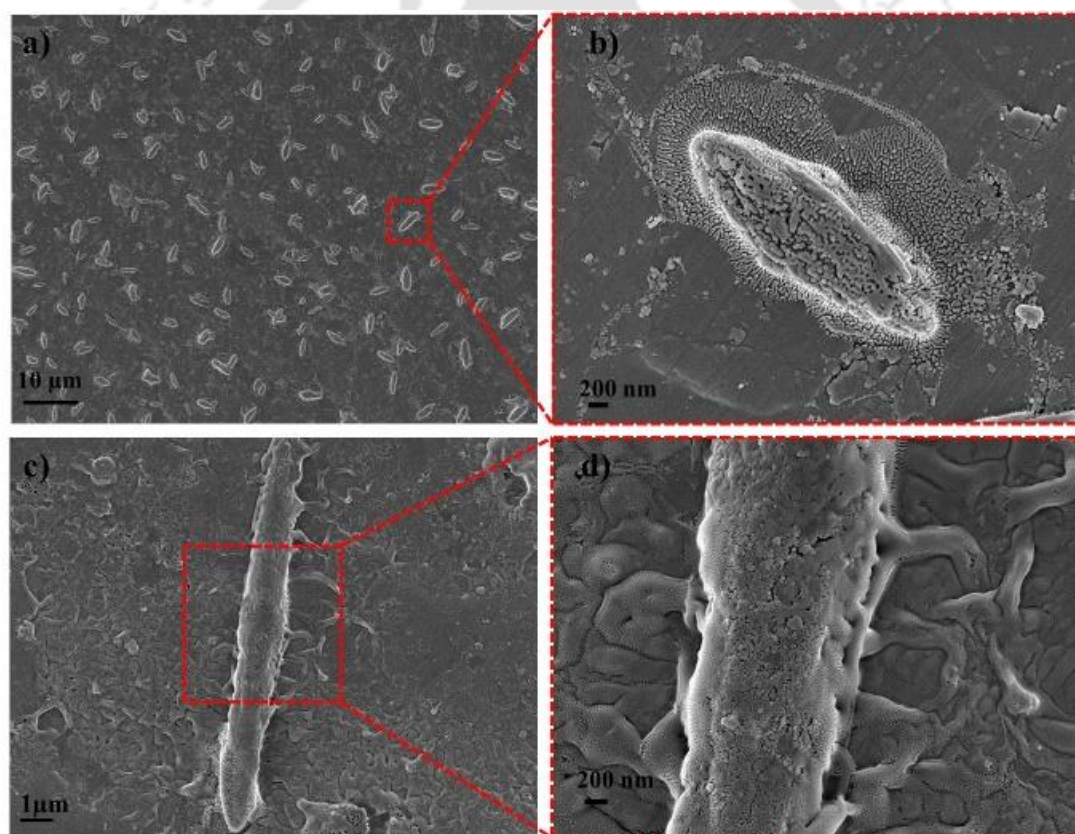


Figure 3.7. a) FESEM images of the nanostructure of the **NMI** ($3 \mu\text{M}$) luminogens formed in 99.9% f_w by a simple drop-casting technique. b) The corresponding magnified image of 'a' at the designated area. c) FESEM images of **NMI** ($3 \mu\text{M}$) showing morphological changes upon the addition of 4-NA in water. (d) The corresponding magnified image of 'c' at the designated area.

hydrodynamic radii (Z_{avg}) of **NMI** AIEEgen (113.0 nm) in water gradually increases after addition of $100 \mu\text{M}$ of 4-NA (130.9 nm), indicating surface interaction of **NMI** AIEEgen with

4-NA (Figure 3.6f). To further confirm surface interaction of **NMI** with 4-NA, molecular morphology studies were done via FESEM images where it was found that 4-NA effectively interacted with **NMI** and filled its surface voids (Figure 3.7). This was further confirmed by surface area analyzer (BET) studies, where the surface area for **NMI** AIEEgen ($10.405 \text{ m}^2/\text{g}$) decreased after addition of $100 \mu\text{M}$ 4-NA ($3.391 \text{ m}^2/\text{g}$) (Figure 3.8, Table A3.7). As shown in Table A3.7, during the adsorption and desorption, there were no changes in pore diameter in the presence and absence of 4-NA, whereas, during adsorption and desorption, the surface area and pore volume of **NMI** AIEEgen was changed.

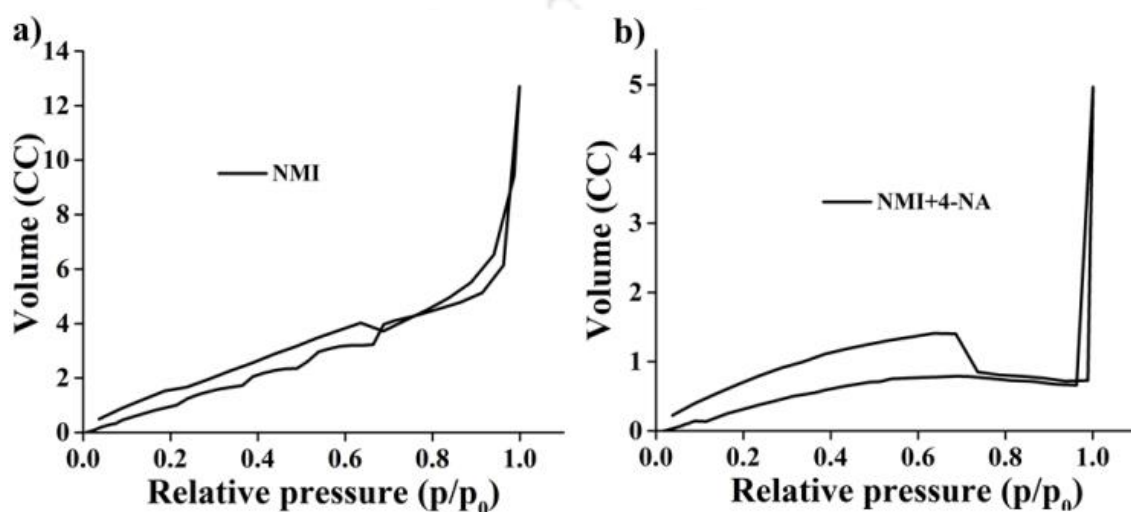


Figure 3.8. a) Adsorption and desorption curve of **NMI** luminogen b) Adsorption & desorption curve of **NMI** luminogen after addition of 4-NA.

Thus, by analyzing all the possible sensing mechanisms, it was found that IFE plays a crucial dominating role in the quenching of the fluorescence of **NMI** AIEEgen by 4-NA. This was the main reason, which is assigned to be responsible for the higher selectivity of **NMI** probe towards 4-NA, as most of the other analytes do not have effective absorption overlap with the excitation and emission spectra of **NMI** (Figure A3.15). However, positional isomers of 4-NA, i.e., 2-NA and 3-NA bring similar changes in the life-time, UV-vis spectra, and molecular size distribution to that of the 4-NA (Figure A3.16-A3.18), except IFE contribution (Figure A3.19). Similarly, IFE corrections were performed for these positional isomers of 4-NA as well. It was observed that the percentage of suppression efficiency follow a particular trend, viz. 4-NA ($\sim 60\%$) > 2-NA ($\sim 21\%$) > 3-NA ($\sim 11\%$), (Table A3.8- A3.10), which matches with their extent of absorption spectral overlap with the excitation and emission spectra of **NMI** (Figure A3.15).

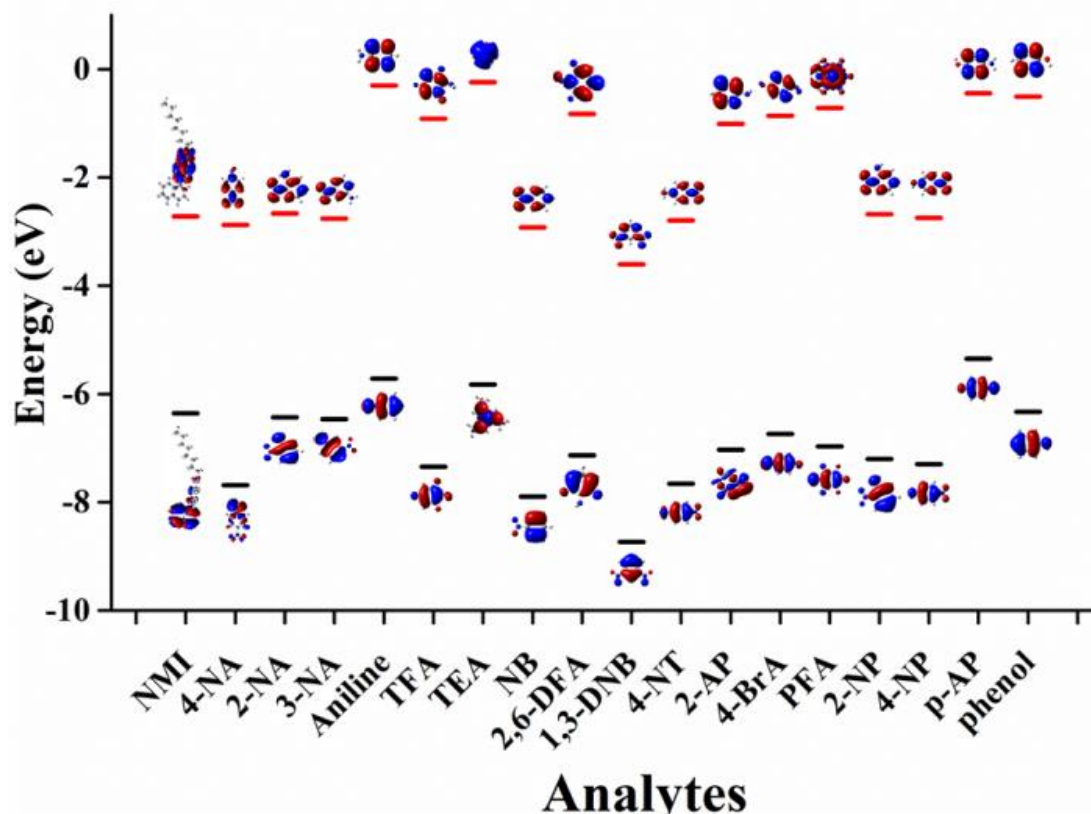


Figure 3.9. HOMO and LUMO energy of **NMI**, 4-NA, and different chemical analytes computed by DFT, B3LYP/6-31G+(d,p) run in a Gaussian 09 program.

Moreover, the highest-occupied molecular orbital (HOMO) and lowest-unoccupied molecular orbital (LUMO) of **NMI** AIEEgen and different amines were calculated to substantiate the possibility of PET (photo-induced electron transfer) using DFT with the basis set B3LYP/6-31G +(d, p) incorporated in a Gaussian 09 program (Figure 3.9 and Table A3.11) [17]. In principle, there is a strong possibility of charge transfer to the LUMO of the electron-deficit analyte, when the LUMO energy of the electron-rich **NMI** is higher as compared to that of the analytes, which could result in the quenching of the fluorophore.[18] As shown in Figure 3.9, PET occurs between **NMI** AIEEgen and 4-NA, 2-NA and 3-NA in the following order: 4-NA > 2-NA > 3-NA. It was observed that the propensity of PET was very low as IFE was more than 55%. Thus, based on the above experimental observations, it can be resolved that IFE is the most appropriate mechanism for the excellent selectivity and sensitivity of **NMI** AIEEgen towards 4-NA. However, this simple yet rare method involving an AIEEgen provided an exclusive platform for the highly sensitive and discriminative sensing of 4-NA in water.

3.4. Conclusion

In summary, a “receptor-free” neutral naphthalene appended deep blue-emitting naphthalimide derivative (**NMI**) was synthesized and thoroughly characterized. **NMI** displayed unusual AIEE behavior in water fractions with a high quantum yield. **NMI** AIEEgen was found to be an excellent fluorescent sensor for 4-NA in water as well as on portable test strips. The LOD of **NMI** was calculated to be LOD/36 ppb in solution and 104m on the test strips. The extraordinary selectivity, as well as sensitivity of the probe towards **NMI**, was achieved via receptorfree IFE mechanism. This makes **NMI** the first example of an AIEEgenic probe for the detection of 4-NA in water via IFE mechanism.

References

- (1) a) Yuan, H.; Li, D. Y.; Liu, Xu, X.; Xiong, C. *Analyst* **2015**, *140*, 1428–1431; b) Agudelo-Morales, C. E.; Silva, O. F.; Galian, R. E.; rez-Prieto, J. P. *Chem-PhysChem* **2012**, *13*, 4195–4201.
- (2) Pinheiro, H. M.; Touraud, E.; Thomas, O.; *Dyes Pigm.* **2004**, *61*, 121–139.
- (3) a) Scott, T. S.; Elsevier, Amsterdam, **1962**; b) Games, L. M.; Hites, R. A.; *Anal. Chem.* **1977**, *49*, 1433–1440; c) Wang, J. L.; Wang, G. D.; G. Ansari, A. S.; Khan, M. F.; *Toxicol. Appl. Pharmacol.* **2008**, *230*, 227–234.
- (4) a) Benigni, Passerini, R. L. *Mutat. Res.* **2002**, *511*, 191–206; b) New Jersey Department of Health and Senior Services. Hazardous Substance Fact Sheet, **2004**.
- (5) a) Tong, C. Y.; W. Liu, Guo. *Chemosphere* **2010**, *81*, 430–435; b) C. S. Rondstvedt Jr, *Ind. Eng. Chem. Prod. Res. Dev.* **1977**, *16*, 177–179.
- (6) Kappenstein, J. O.; Luch, A.; Schulz, T. G. J. *Chromatogr. A* **2011**, *1218*, 5628–5637.
- (7) Dossi, N.; Toniolo, R.; Pizzariello, A.; Susmel, S.; Bontempelli, G. *Electrophoresis* **2011**, *32*, 906–912.
- (8) Garcia-Lavandeira, J.; Salgado-Petinal, C.; Blanco, E.; Cela, R. *Anal. Bioanal. Chem.* **2010**, *397*, 751–763.
- (9) Li, R. N.; Wang, L. L.; Gao, X. T.; Dua, G. F.; Zhai, H. L.; Wang, X. Y.; Guo, G. S.; Pu, Q. S. *J. Hazard. Mater.* **2013**, *248–249*, 268–275.
- (10) a) Zhao, X. E.; Zhao, Y.; Suo, R.; *J. Sep. Sci.* **2008**, *31*, 646–658; b) Garcia-Lavandeira, J.; Salgado-Petinal, C.; Blanco, E.; Cela, R. *Anal. Bioanal. Chem.* **2010**, *397*, 751–763
- (11) a) Lee, M. H.; Han, J. H.; Lee, J.-H.; H. Choi, G. C. Kang, Kim, J. S. *J. Am. Chem. Soc.* **2012**, *134*, 17314–17319; b) Banerjee, S. E.; Veale, B.; Veale, C. M.; Phelan, S. A.; Murphy, G. M.; Tocci, Gillespie, L. J.; Frimannsson, D. O.; Kelly, J. M.; Gunnlaugsson, T. *Chem. Soc. Rev.* **2013**, *42*, 1601–1618; c) Duke, R. M.; Veale, E. B.; Pfeffer, F. M.; Kruger, P. E.; Gunnlaugsson, T. *Chem. Soc. Rev.* **2010**, *39*, 3936–3953.
- (12) a) Luo, J. D.; Xie, Z. L.; Lam, J. W.; Cheng, L.; Chen, H. Y.; Qiu, C. F.; Kwok, H. S.; Zhan, X. W.; Liu, Y. Q.; Zhu, D. B.; Tang, B. Z. *Chem. Commun.* **2001**, 1740–1741; b) An, B. K.; Kwon, S. K.; Jung, S. D.; Park, S. Y. *J. Am. Chem. Soc.* **2002**, *124*, 14410–14415; c) Mei, Hong, J. Y.; Lam, J. W. Y.; Qin, A.; Tang, Y.; Tang, B. Z. *Adv. Mater.* **2014**, *26*, 5429–5479; d) Mei, J.; Leung, N. L. C.; Kwok, R. T. K.; Lam, J. W. Y.; Tang, B. Z. *Chem. Rev.* **2015**, *115*, 11718–11940.
- (13) a) Gopikrishna, P.; Meher, N.; Iyer, P. K. *ACS Appl. Mater. Interfaces* **2018**, *10*, 12081–12111; b) Meher, N.; Chowdhury, S. R.; Iyer, P. K. *J. Mater. Chem. B* **2016**, *4*, 6023–6031; c) Meher, N.; Iyer, P. K. *Nanoscale* **2017**, *9*, 7674–7685; d) Meher, N.; Panda, S.; Kumar, S.; Iyer, P. K. *Chem. Sci.* **2018**, *9*, 3978–3985; e) Meher, N.; Iyer, P. K. *Angew. Chem. Int. Ed.* **2018**, *57*, 8488–8492; f) Meher, N.; Iyer, P. K. *Nanoscale* **2019**, *11*, 13233–13242.

- (14) a) Tanwar, A. S.; Malik, A. S. H. M.; Afroz, A.; Iyer, P. K. *ACS Sens.* **2016**, *1*, 1070–1077; b) Tanwar, A. S.; Iyer, P. K. *ACS Omega* **2017**, *2*, 4424–4430;
 c) Tanwar, A. S.; Patidar, S.; Ahirwar, S.; Dehingia, S.; Iyer, P. K. *Analyst* **2019**, *144*, 669–676.
- (15) a) Chakraborty, G.; Das, P.; Mandal, S. K. *ACS Appl. Mater. Interfaces* **2018**, *10*, 42406–42416; b) Wei, F.; Cai, X.; Nie, J.; Wang, F.; Lu, C.; Yang, G.; Chen, Z. Maa, C.; Zhang, Y. *Polym. Chem.* **2018**, *9*, 3832–3839; c) Zhan, J.; Zhu, X.; Fang, F.; Miao, F.; Tian, D.; Li, H. *Tetrahedron* **2012**, *68*, 5579–5582;
 d) Kumar, N.; Khullarab, S.; Mandal, S. K. *RSC Adv.* **2014**, *4*, 47249–47253;
 e) Li, H.; Li, Y. *Nanoscale* **2009**, *1*, 128–132.
- (16) a) Yang, Y. J.; Wang, M. J.; Zhang, K. L. *J. Mater. Chem. C* **2016**, *4*, 11404–11418; b) Deshmukh, A.; Bandyopadhyay, S.; Jamesa, A.; Patra, A.; *J. Mater. Chem. C* **2016**, *4*, 4427–4433; c) Wan, X. Y.; Jiang, F. L.; C. Liu, P.; Zhou, K. L. Chen, Y. L. Gai, Y. Yangab, M. C. Hong, *J. Mater. Chem. A* **2015**, *3*, 22369–22376; d) Shu, T.; Wang, N.; Li, Y.; Fu, D.; Fan, H.; Luo, M.; Yue, S.; *ChemistrySelect* **2017**, *2*, 12046–12050; e) Bagheri, M.; Masoomi, M. Y.; Morsali, A.; *Sensors and Actuators B* **2017**, *243*, 353–360; f) Wu, P.; Liu, Y.; Li, Y.; Jiang, M.; Li, X.-l.; Shia, Y.; Wang, J. *J. Mater. Chem. A* **2016**, *4*, 16349–16355.
- (17) Gaussian 09, M. J. Frisch, G. W. Trucks, H. B. Schlegel, G. E. Scuseria, M. A. Robb, J. R. Cheeseman, G. Scalmani, V. Barone, P. Mennucci, A. F. Izmaylov, J. Bloino, G. Zheng, J. L. Sonnenberg, M. Hada, M. Ehara, K. Toyota, R. Fukuda, J. Hasegawa, M. Ishida, T. Nakajima, Y. Honda, O. Kitao, H. Nakai, T. Vreven, J. A., Jr., Montgomery, J. E. Peralta, F. Ogliaro, M. Bearpark, J. J. Heyd, E. Brothers, K. N. Kudin, V. N. Staroverov, T. Keith, R. Kobayashi, J. Normand, K. Raghavachari, A. Rendell, J. C. Burant, S. S. Iyengar, J. Tomasi, M. Cossi, N. Rega, J. M. Millam, M. Klene, J. E. Knox, J. B. Cross, V. Bakken, C. Adamo, J. Jaramillo, R. Gomperts, R. E. Stratmann, O. Yazyev, A. J. Austin, R. Cammi, C. Pomelli, J. W. Ochterski, R. L. Martin, K. Morokuma, V. G. Zakrzewski, G. A. Voth, P. Salvador, J. J. Dannenberg, S. Dapprich, A. D. Daniels, O. Farkas, J. B. Foresman, J. V. Ortiz, J. Cioslowski, D. J. Fox, Gaussian, Inc: Wallingford, CT, 2013.
- (18) a) Lakowicz, J. R. Principles of Fluorescence Spectroscopy, 3rd Ed., *Springer*, New York, **2006**; b) Williams, D. E.; Shustova, N. B. *Chem. Eur. J.* **2015**, *21*, 15474–15479.

Appendix (AI)

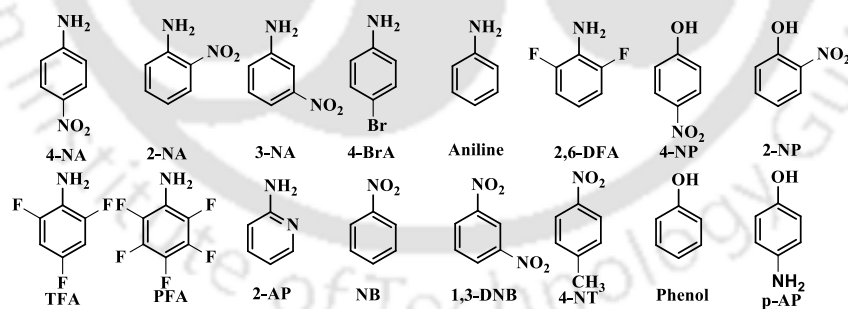


Figure A3.1. Structures of various nitro explosives and electron-deficient compounds used in the experiments.

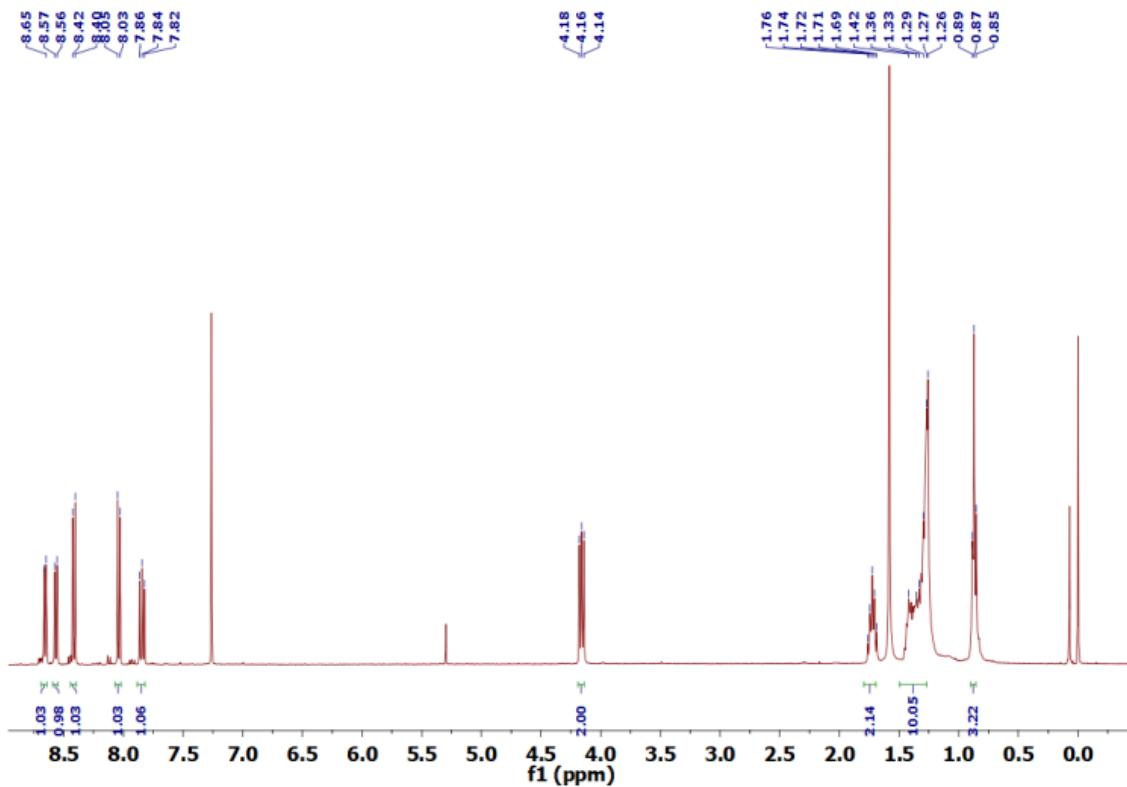


Figure A3.2. ^1H NMR spectra of BNO.

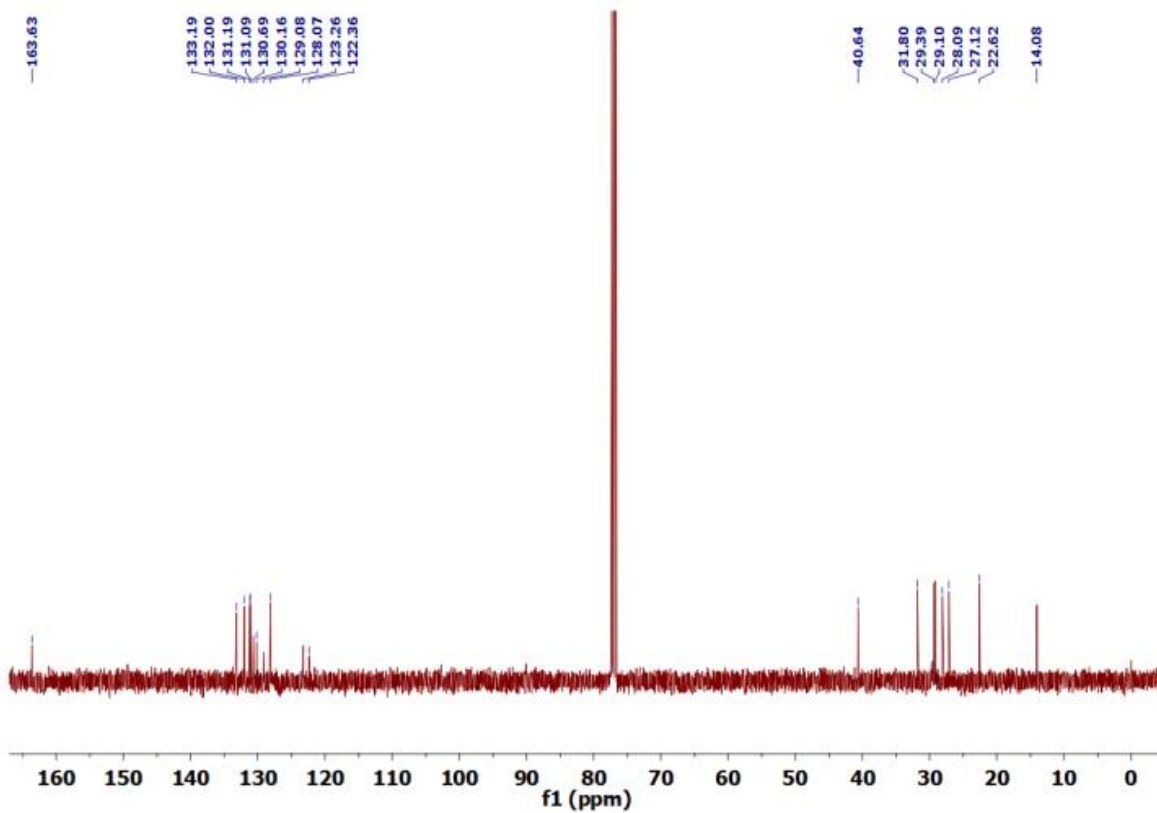


Figure A3.3. ^{13}C NMR spectra of BNO.

Sample Name	BR-MNI-8	Position	P1-A3	Instrument Name	Instrument 1
User Name		Inj Vol	20	InjPosition	
Sample Type	Sample	IRM Calibration Status	Success	Data Filename	BR-MNI-8.d
ACQ Method	EST ALS 100-500.m	Comment		Acquired Time	16-04-2019 15:58:36 (UTC+05:30)

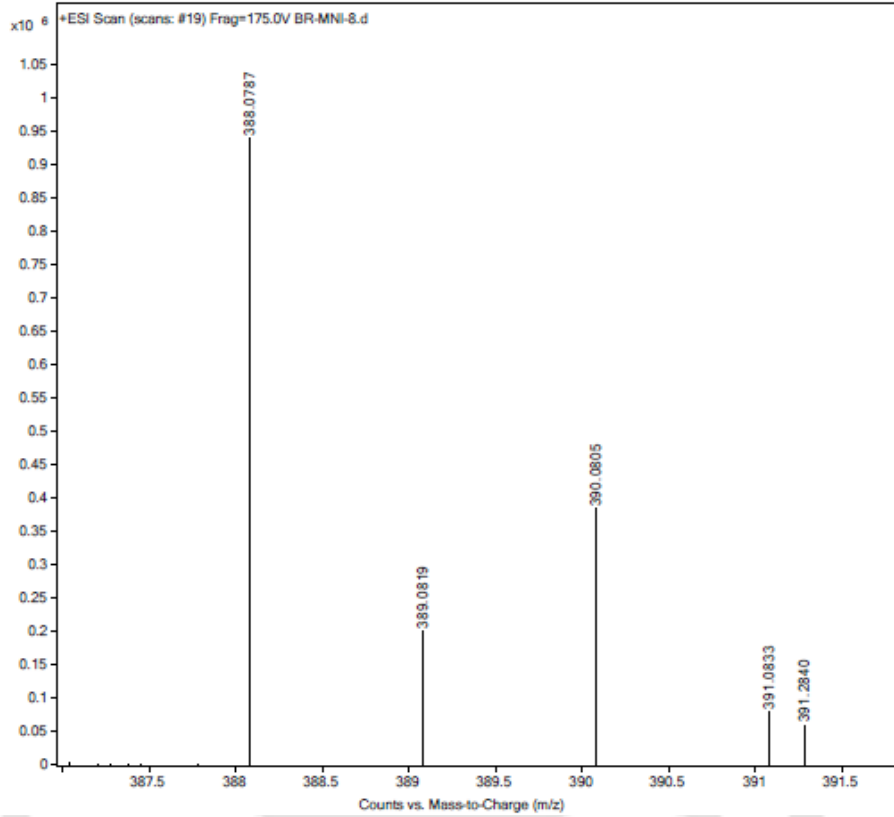


Figure A3.4. Mass spectra BNO.

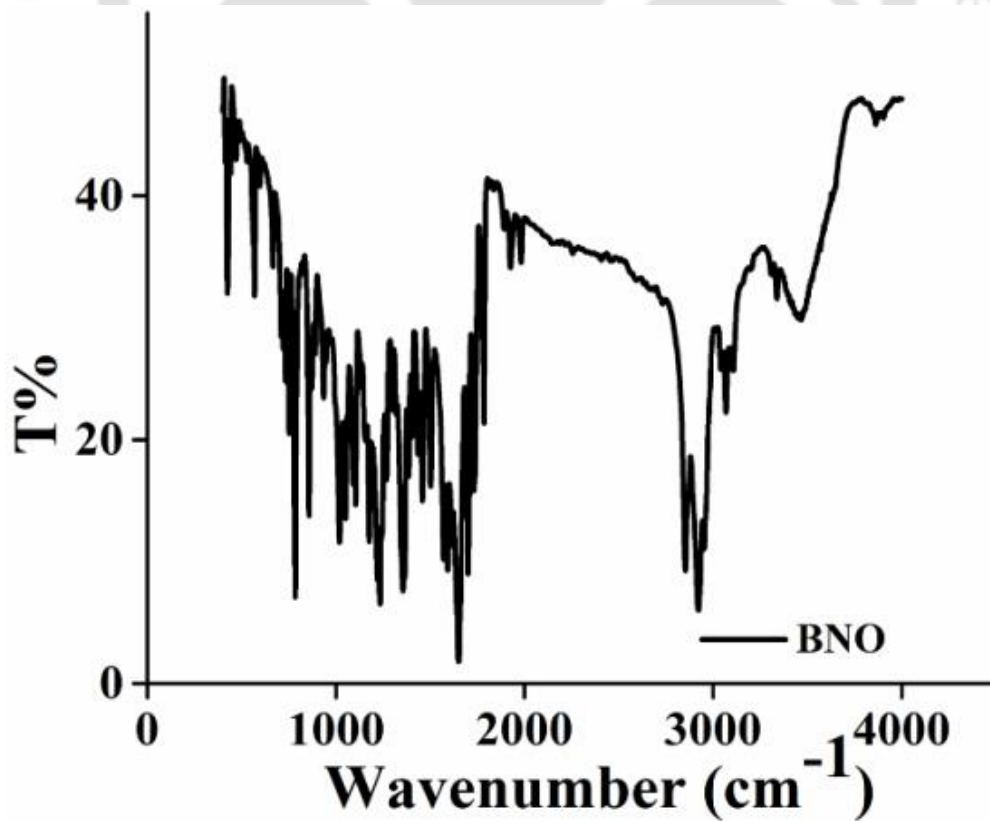


Figure A3.5. IR spectra of BNO.

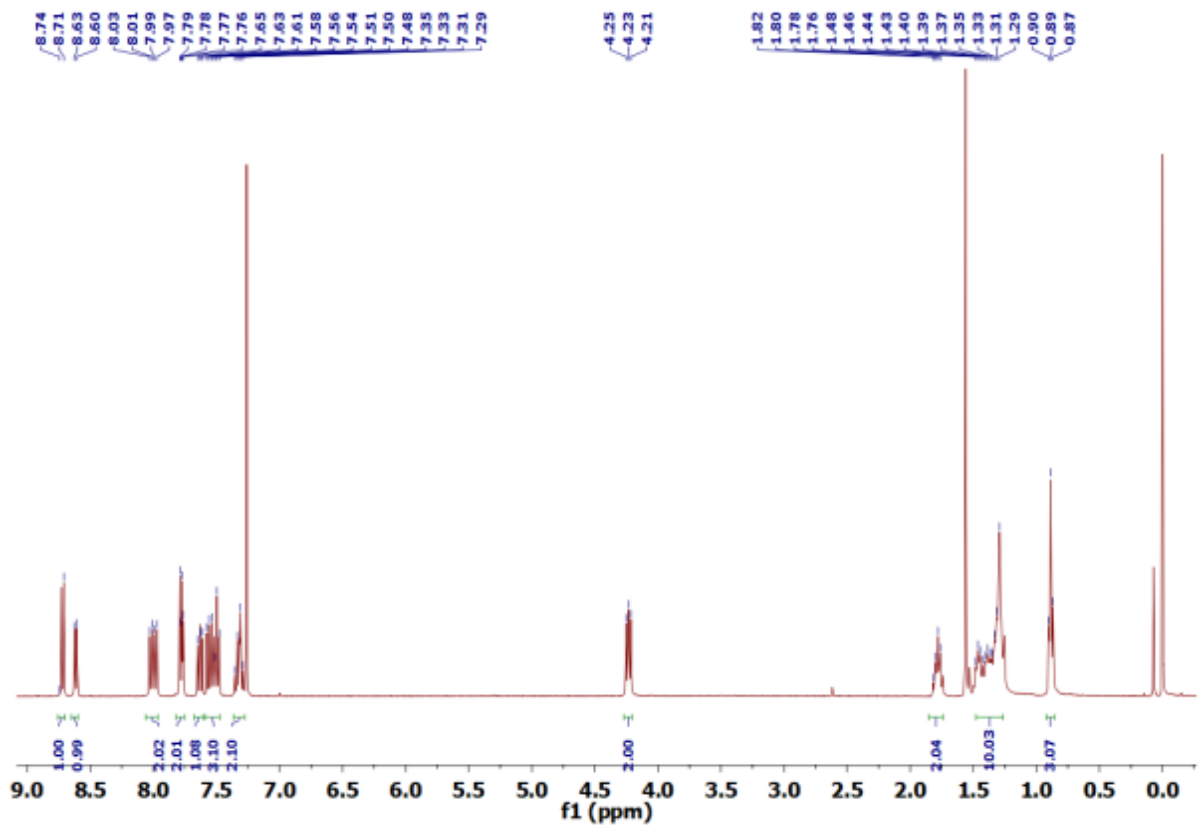


Figure A3.6. ^1H NMR spectra of NMI.

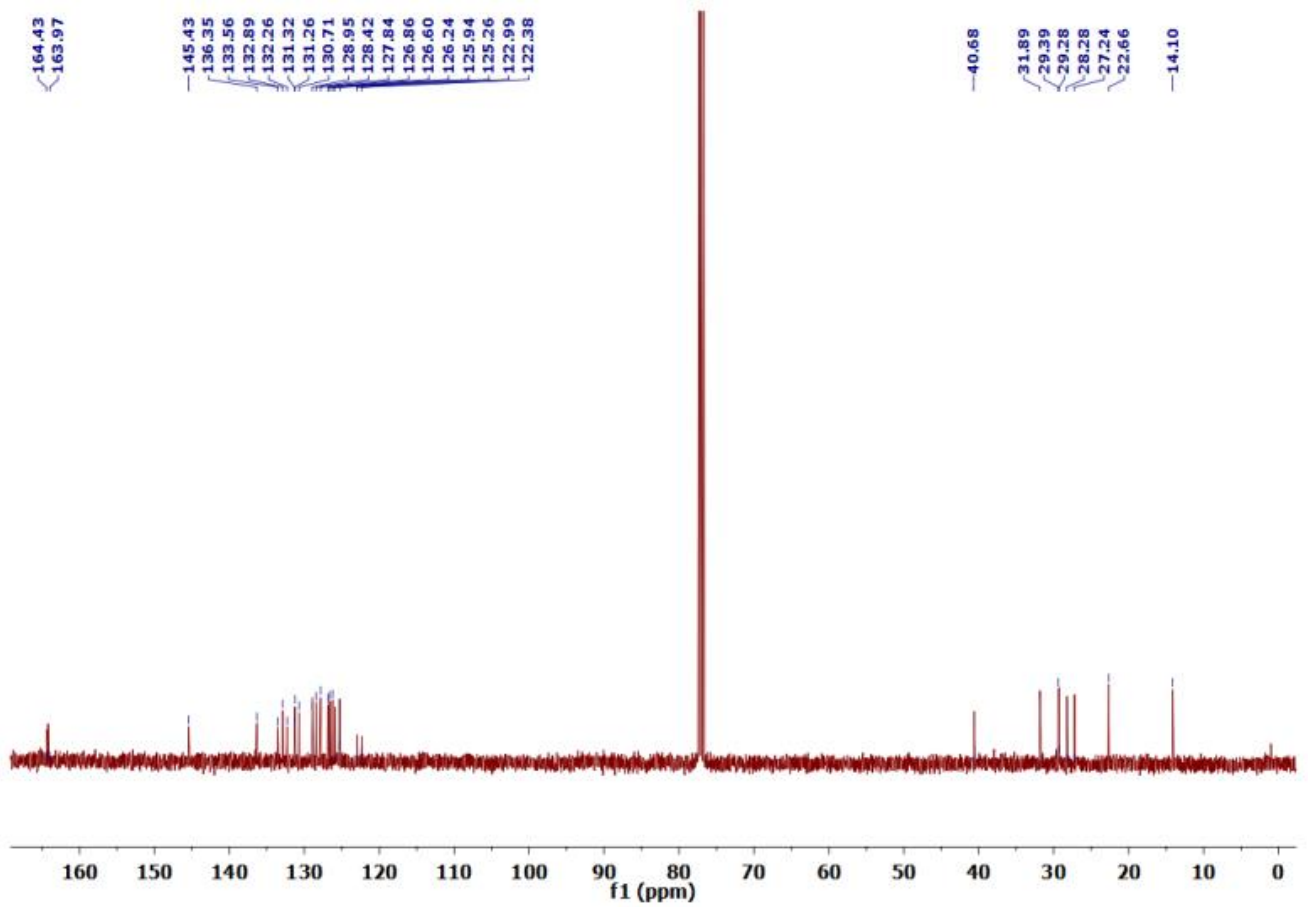


Figure A3.7. ^{13}C NMR spectra of NMI.

Sample Name	MNI-8	Position	P1-A4	Instrument Name	Instrument 1
User Name		Inj Vol	20	InjPosition	
Sample Type	Sample	IRM Calibration Status	Success	Data Filename	MNI-8.d
ACQ Method	ESI ALS 100-600.m	Comment		Acquired Time	16-04-2019 16:04:31 (UTC+05:30)

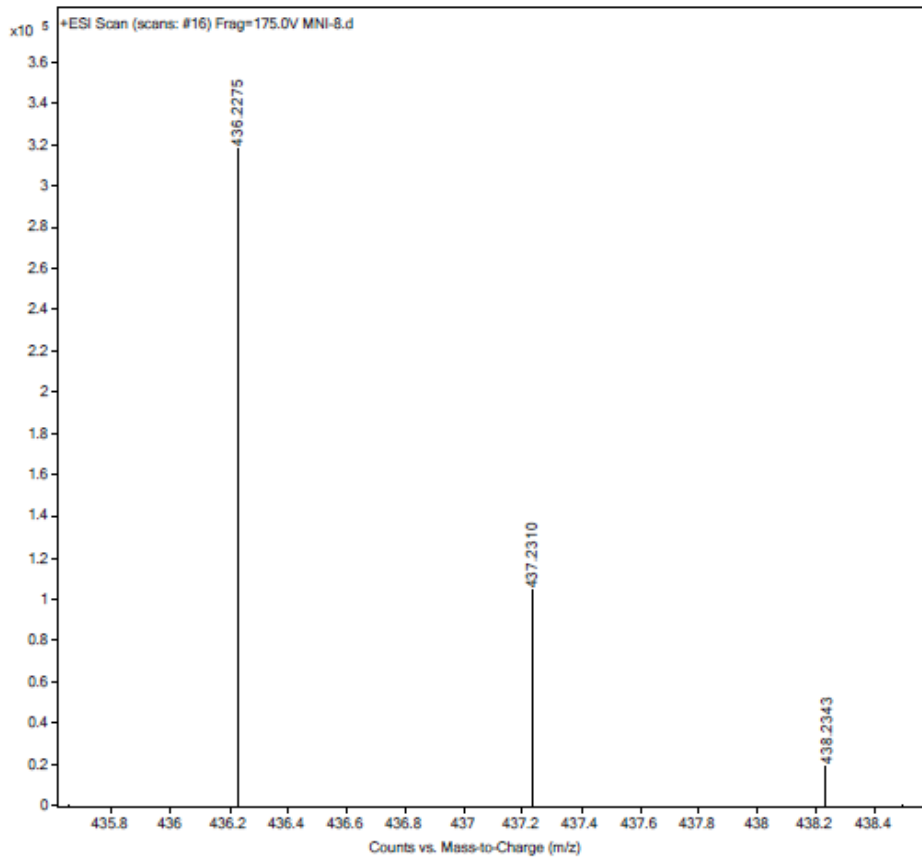


Figure A3.8. Mass spectra of NMI.



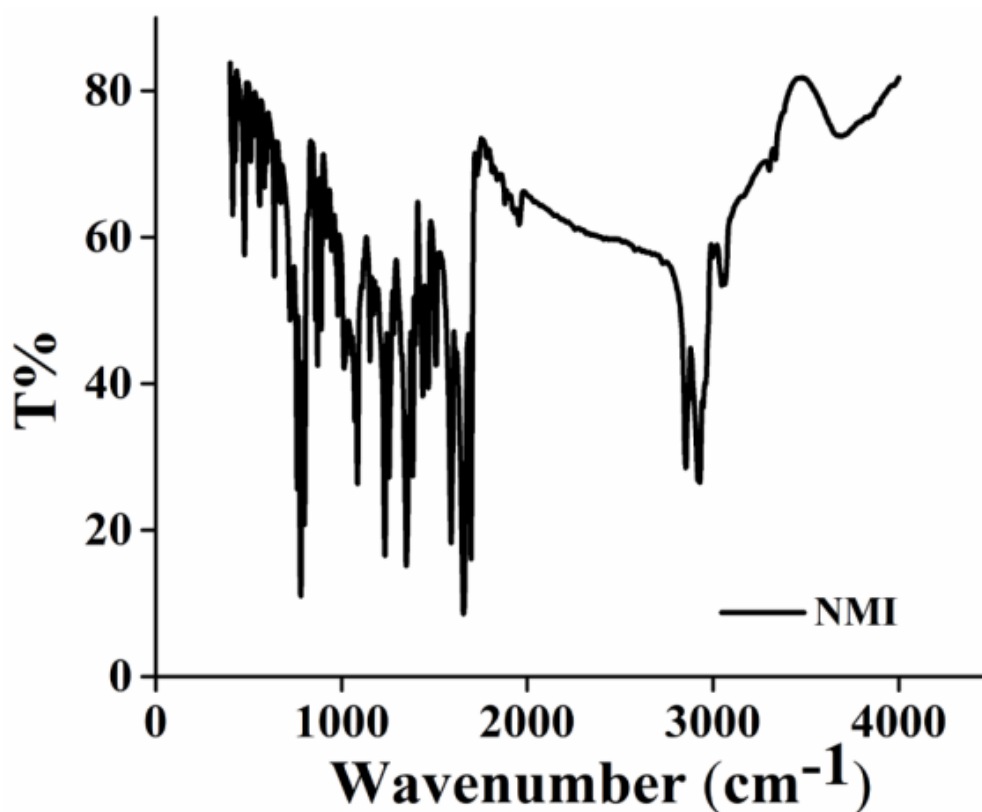


Figure A3.9. IR spectra of NMI.

Table A3.1. Photophysical properties of Naphthalimide AIEEgen with various fw in DMF at 3 μM concentration.

Compound	f_w in DMF	$\lambda_{\text{abs. max}}$ [nm]	ϵ^a [$\text{M}^{-1}\text{cm}^{-1}$]	$\lambda_{\text{em. max}}^b$ [nm]	Stokes Shift $\Delta\lambda/\text{nm}$	Φ_{FL} [%] ^c
NMI	0%	344	1165.475	493	149	23.21
	20%	344	1093.975	513	169	25.78
	40%	347	1118.075	530	183	13.10
	60%	346	1071.9	543	200	6.16
	80%	348	1066.15	442	94	23.20
	99.8%	347	1266	442	95	22.16

^aMeasured at each absorption maximum. ^bExcited at 360 nm for all compounds. ^cQuantum yields were calculated by using quinine sulfate (0.1 M H_2SO_4 , $\lambda_{\text{ex}}=350$ nm, $\Phi_{\text{FL}} = 57.7\%$) solution as reference together with the following formula: $\Phi_{\text{FL}} = \Phi_{\text{FL}}(\text{I/IR})(\text{AR/A})(\eta^2/\eta\text{R}^2)$, where Φ = quantum yield, I = Intensity of emission, A = absorbance at λ_{ex} , η = refractive index of solvent, R = reference.

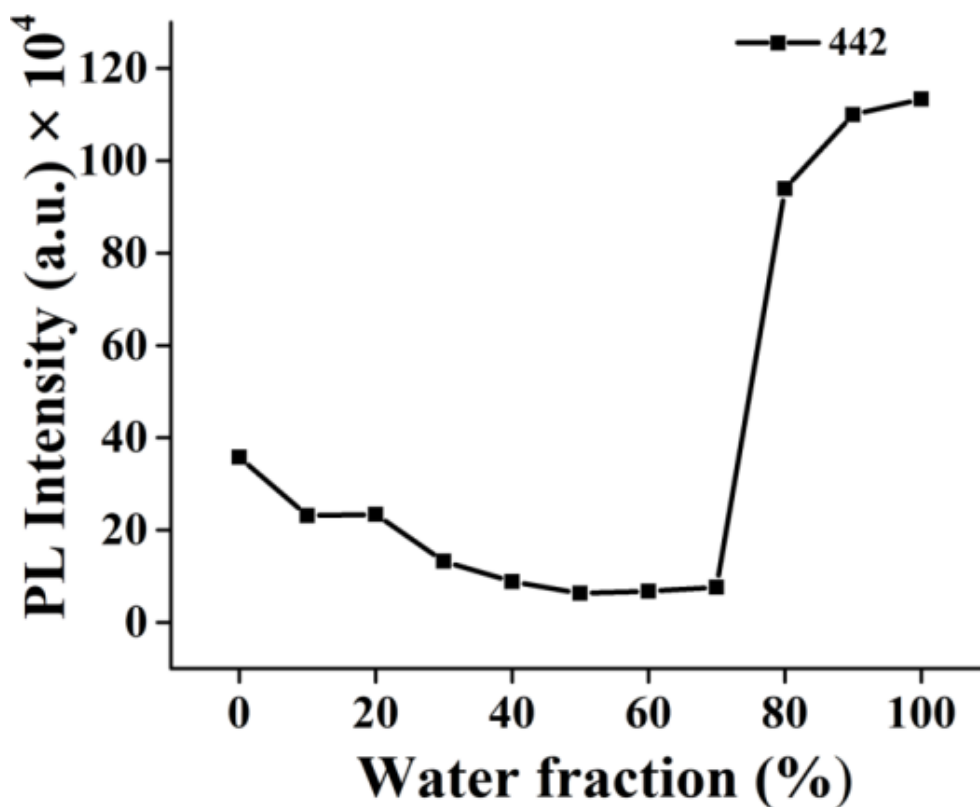


Figure A3.10. Photoluminescence intensity of NMI ($3 \mu\text{M}$) at 442 nm under different water fraction (f_w).

Table A3.2. Steady-state absorption (λ_a) and emission (λ_e) peak positions in different solvents and relative parameters (polarity, the dielectric constant of ϵ , and the refractive index of n) of the solvents.

Solvent	Polarity	λ_a of NMI	λ_e of NMI
Toluene	2.4	344	434
Diethyl ether	2.8	340	439
Dichloromethane	3.1	344	460
Acetonitrile	5.8	343	492
DMF	6.4	344	501
DMSO	7.2	345	501

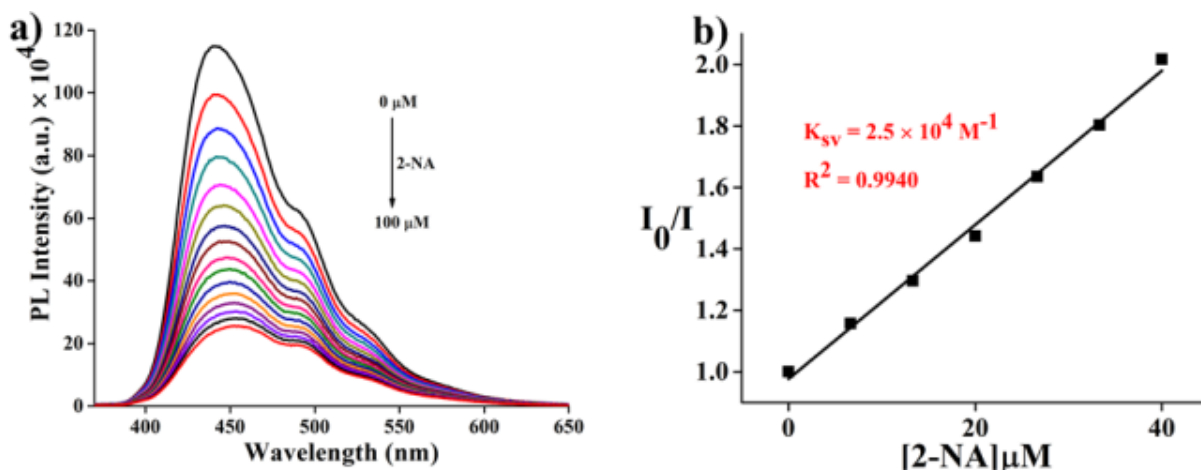


Figure A3.11. a) Fluorescence quenching of NMI (3 μM) at room temperature with increasing concentration of 2-NA (100 μM). b) Stern–Volmer (SV) plots for the fluorescence quenching of NMI by 2-NA (100 μM).

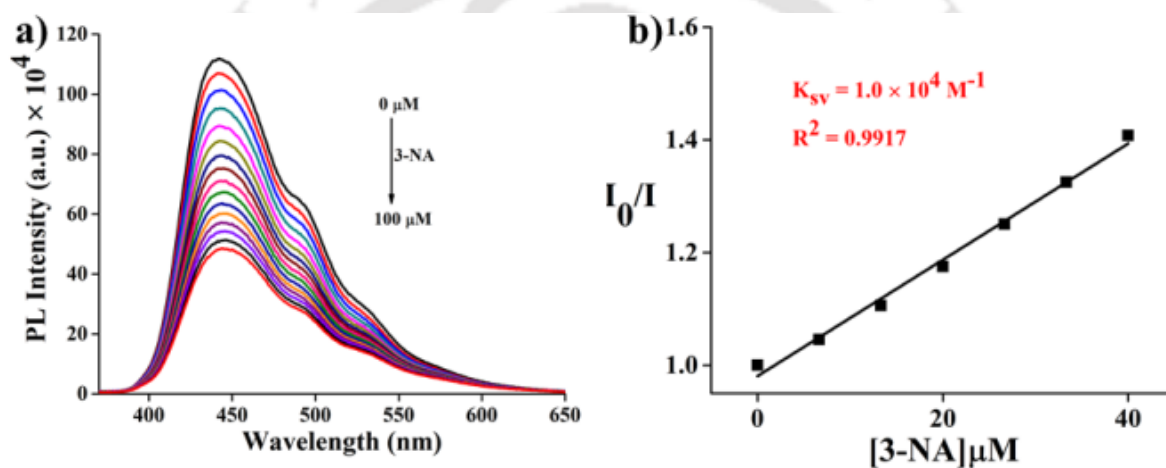


Figure A3.12. a) Fluorescence quenching of NMI (3 μM) at room temperature with increasing concentration of 3-NA (100 μM). b) Stern–Volmer (SV) plots for the fluorescence quenching of NMI by 3-NA. (100 μM).

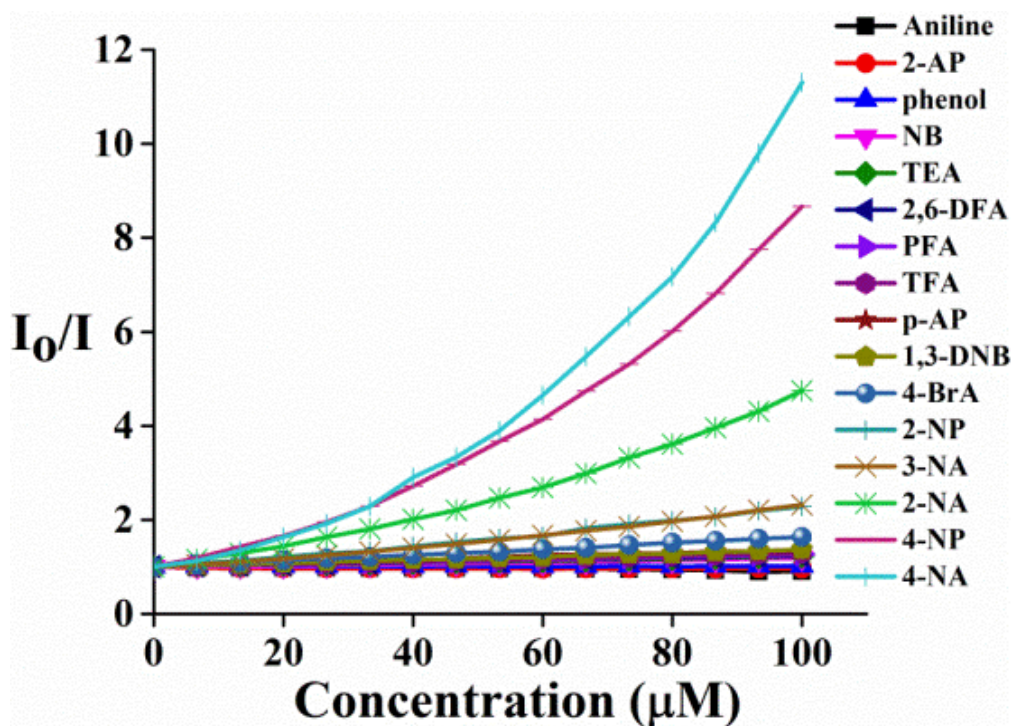


Figure A3.13. Stern-Volmer plots obtained for various interfering analytes in aqueous media.

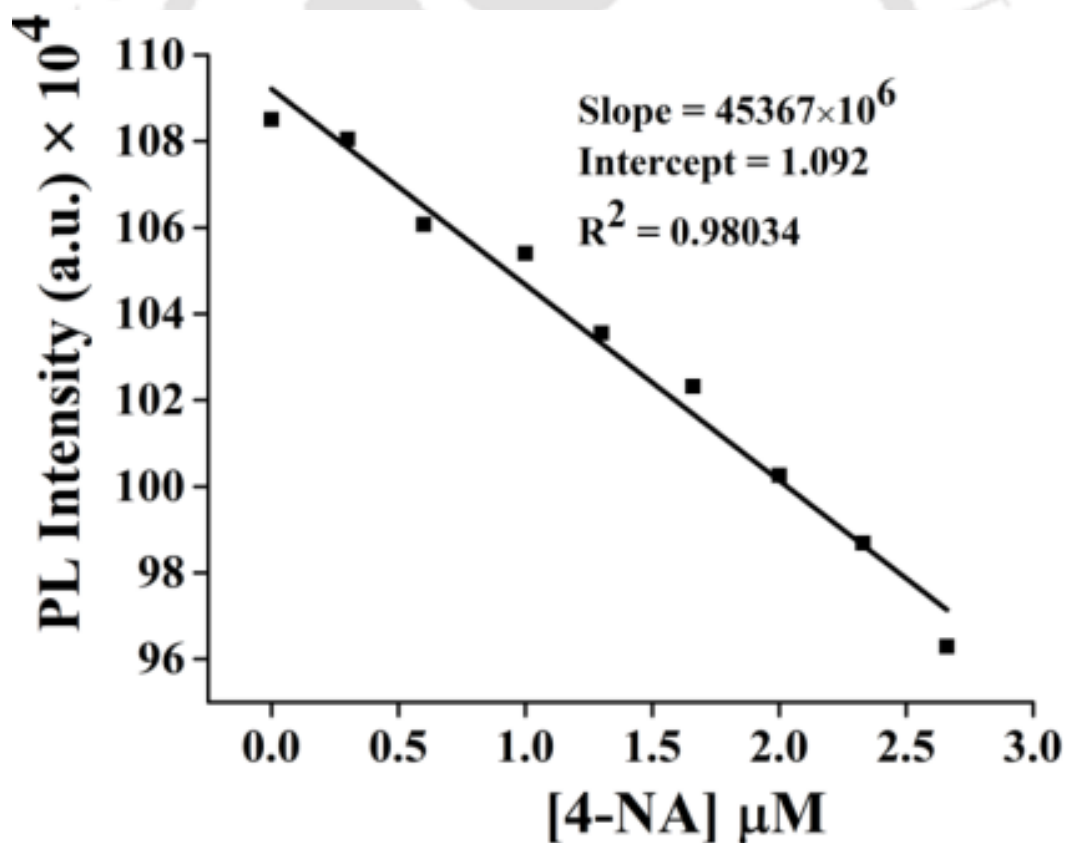


Figure A3.14. Detection limit calculated through the linear fitting of fluorescence intensity of NMI upon incremental addition of 4-NA to it at $\lambda_{em} = 442$ nm (upon $\lambda_{ex} = 350$ nm).

$$LOD = 3\sigma/k$$

$$LOD \text{ for } 4\text{-NA} = 3 \times 3557 / 45367 \times 10^6$$

= $.235 \times 10^{-6}$ M (36 ppb).

Where σ = standard deviation of five measurements of emission intensity of NMI luminogen and k is the slope from the linear fitting curve of emission intensity versus concentration of the analyte.

Table A3.3. A comparative study of some fluorescence-based 4-Nitroaniline detection.

Publication	Material Used	K_{sv} (M^{-1})	Detection Limit	Sensing Mechanism	Medium Used	Portable Test Strips
Present Manuscript	Naphthalimide AIEEgen	4.1×10^4	36 ppb ($0.235 \mu M$)	IFE	Aqueous	Prepared LOD=10^{-4} M
<i>ACS Appl. Mater. Interfaces</i> , 2018 , <i>10</i> , 42406–42416.	Zinc Based Inorganic Complex	7.87×10^4	88 ppb 0.28 ppm	PET & RET	Aqueous	Prepared 10^{-4} M
<i>J. Mater. Chem. C</i> , 2016 , <i>4</i> , 11404–11418.	Cadmium Based Inorganic Complex	9.8×10^4	0.52 ppm	Electrostatic Interactions and Energy Transfer	Water / MeOH	NA
<i>J. Mater. Chem. C</i> , 2016 , <i>4</i> , 4427–4433.	TPDC-DB	1.7×10^4	455 ppb	Static Quenching Model Based on Sphere of Action	THF	NA
<i>J. Mater. Chem. A</i> , 2015 , <i>3</i> , 22369–22376.	Zinc Based Inorganic Complex	NA	4 ppm	Both Dynamic and Static Quenching	DMF	NA
<i>ChemistrySelect</i> , 2017 , <i>2</i> , 12046–12050.	Cadmium Based Inorganic Complex	8.79×10^4	0.68 ppm	Energy Transfer (ET)	Aqueous	NA
<i>Sensors and Actuators B</i> , 2017 , <i>243</i> , 353–360.	Zinc Based Inorganic Complex	2.95×10^4	5×10^{-5} M (6.9 ppm)	0.68 ppm Water Electrostatic Interactions	Acetonitrile	<i>ChemistrySelect</i> 2017 , <i>2</i> , 12046 – 12050
<i>J. Solid State Chemistry</i> , 2015 , <i>232</i> , 96–101.	Zinc Based Inorganic Complex	5.99×10^4 2.18×10^4	NA NA	Electron Transfer	Acetonitrile	NA

<i>Dalton Trans.</i> , 2018 , 47, 7222–7228.	Zinc Based Inorganic Complex	2.28×10^4	0.1 ppm	Resonance Energy Transfer	DMF	NA
<i>Nanoscale</i> , 2009 , 1, 128–132.	Cobalt Based Inorganic Nanosheets	1.034×10^4	6.8×10^{-7} M (93.92 ppb)	Chelation and Electron Transfer	Water-Soluble Nanosheets	NA
<i>Polym. Chem.</i> , 2018 , 9, 3832–3839.	Conjugated Microporous Polymer	7.08×10^4	4.2×10^{-6} M (580.14 ppb)	PET and Hydrogen Bonding Interactions	DMF	NA
<i>J. Mater. Chem. A</i> , 2016 , 4, 16349–16355.	Luminescent Metal–Organic Framework (MOF)	4.07×10^4	3.5 ppb	Synergistic Effects of Electron Transfer and Hydrogen-Bonding Interactions	EtOH	NA
<i>Inorg. Chim. Acta.</i> , 2018 , 473, 70–74.	Cadmium Based Inorganic Complex	6.26×10^3	0.1026 ppm	Energy Transfer (ET)	DMF	NA
<i>Anal. Chem.</i> , 2012 , 84, 8083–8087.	Pyrene-QD Nanohybrids	2.1×10^4	NA	Dynamic Mechanism	Toluene	NA
<i>RSC Adv.</i> , 2015 , 5, 70086–70093.	Zinc Based Inorganic Complex	5.8×10^1	NA	Photoinduced Electron Transfer	DMA	NA
<i>Tetrahedron</i> , 2012 , 68, 5579–5582.	Calix[4]arene	2.06×10^4	NA	Host-guest Complex Driven by H-Bonding and Hydrophobic Interactions	Acetonitrile	NA

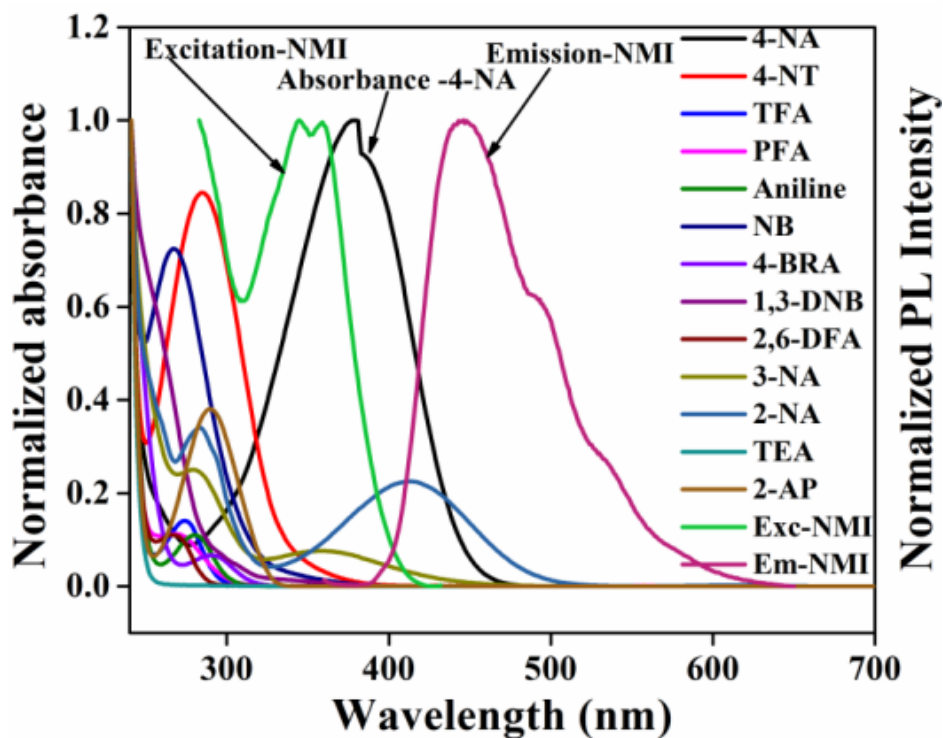


Figure A3.15. Normalized absorbance of NMI ($3 \mu\text{M}$) with different analytes in aqueous media.

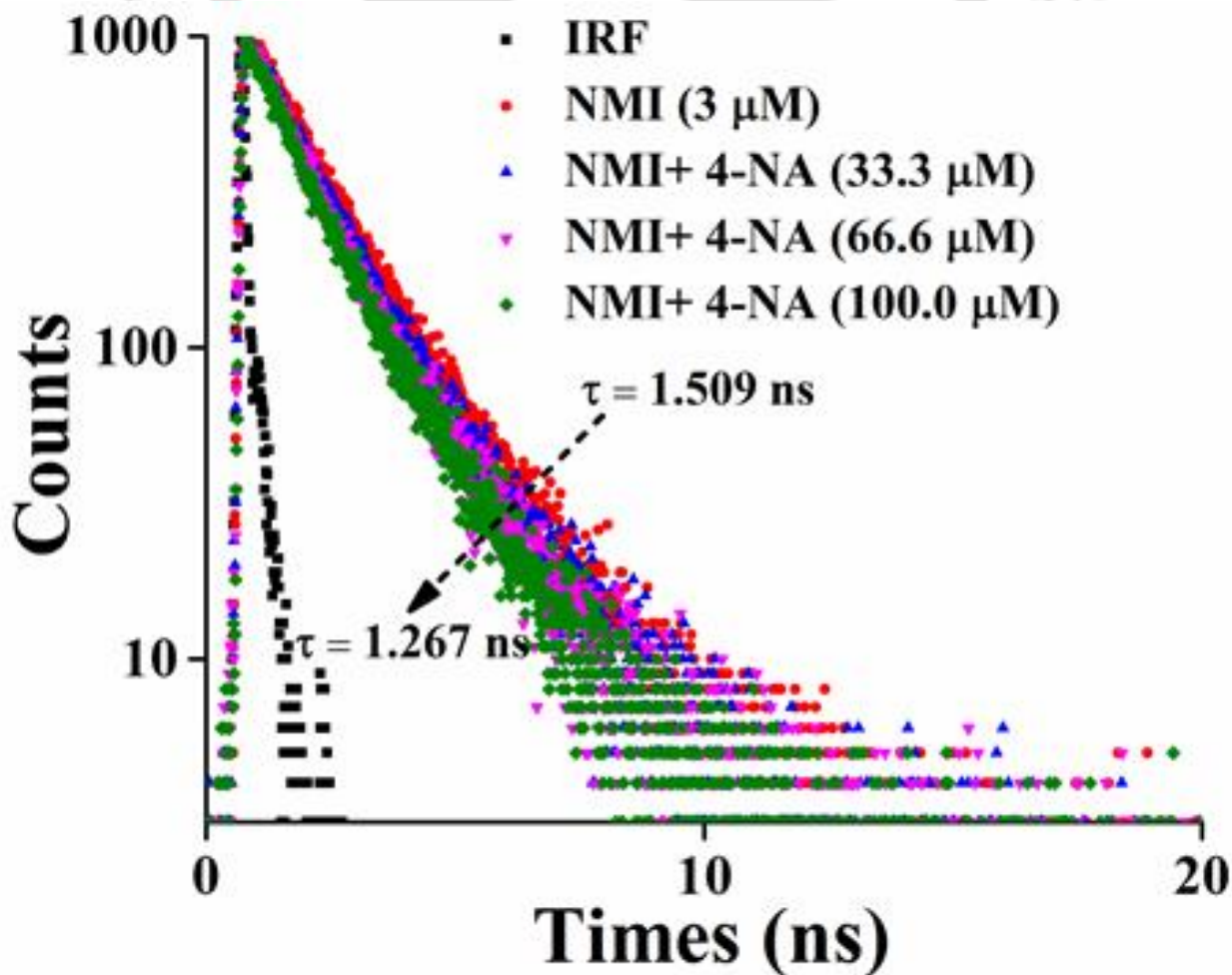


Figure A3.16. Fluorescence Lifetime decay study of NMI ($3 \mu\text{M}$) with increasing concentration of 4-NA up to $100 \mu\text{M}$.

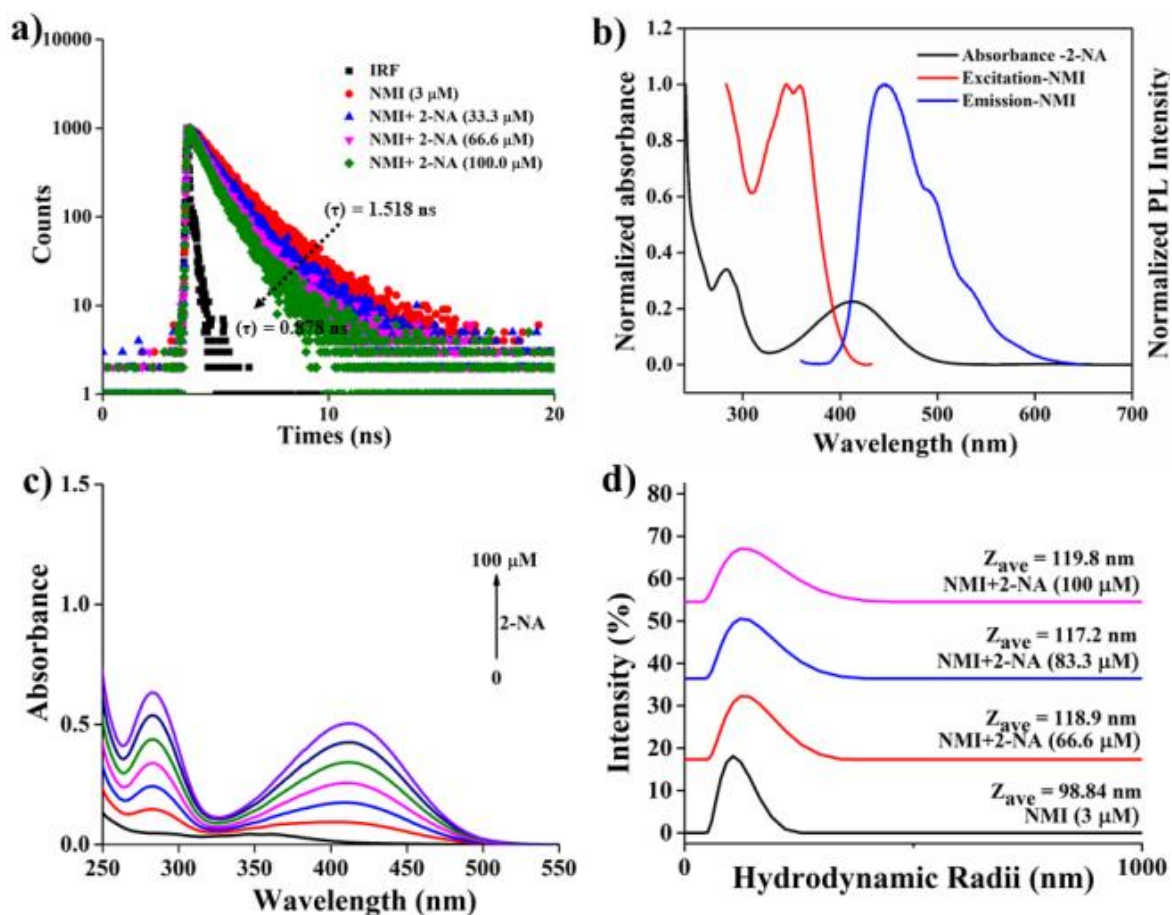


Figure A3.17. a) Fluorescence lifetime decay study of NMI (3 μM) with increasing concentration of 2-NA. b) The spectral overlap between the absorbance spectra of 2-NA and emission spectrum of NMI. c) Absorbance spectra of NMI (3 μM) with increasing concentration of 2-NA. d) Hydrodynamic Radii distribution of NMI by DLS with increasing concentration of 2-NA in aqueous media.

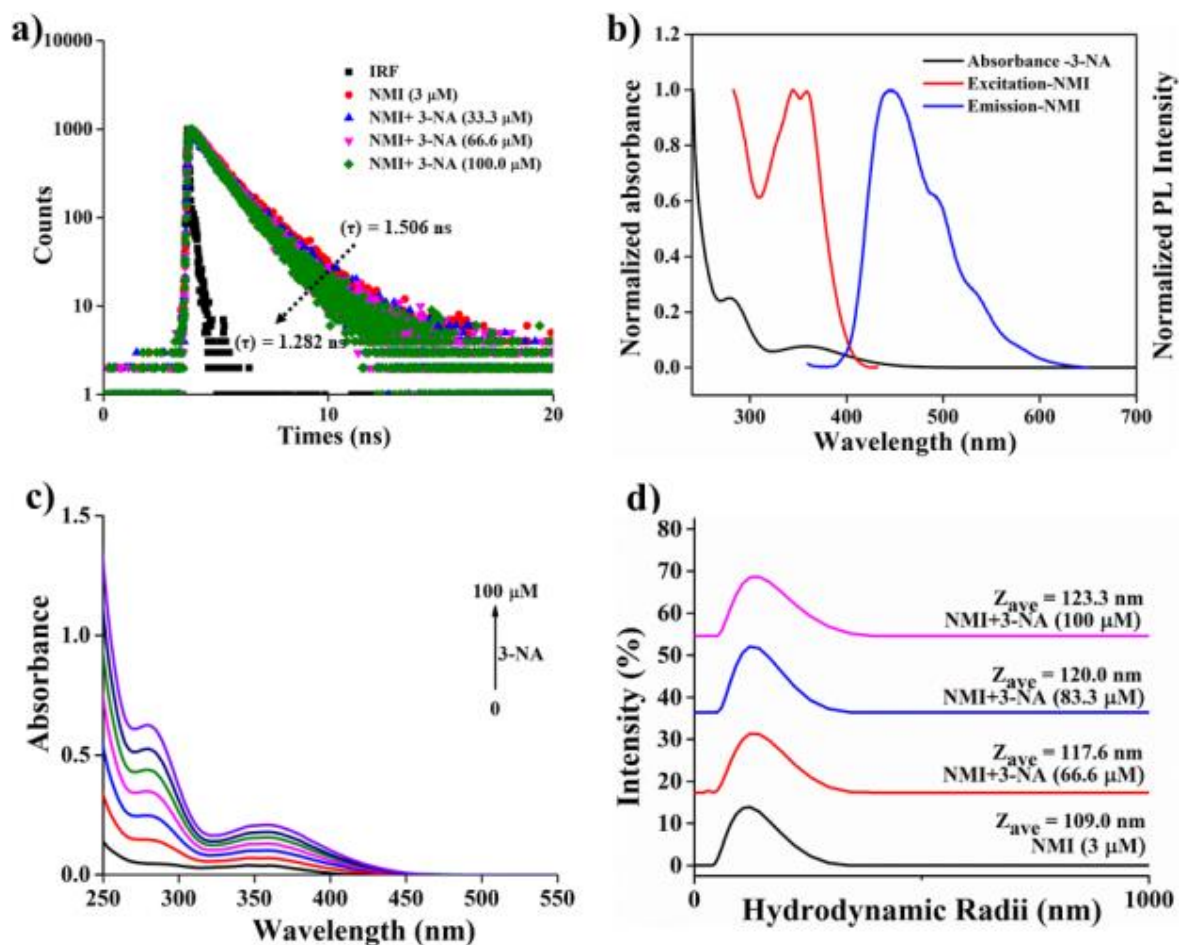


Figure A3.18. a) Fluorescence Lifetime decay of NMI (3 μM) with increasing concentration of 3-NA b) Spectral overlap between the absorbance spectra of 3-NA and emission spectrum of NMI. c) Absorbance spectra of NMI (3 μM) with increasing concentration of 3-NA. d) Hydrodynamic Radii distribution of NMI by DLS with increasing concentration of 3-NA in aqueous media.

Table A3.4 Average Lifetimes of NMI with increasing concentration of 4-NA in aqueous media.

Sample	τ_1 (ns)	%	τ_2 (ns)	%	χ^2	τ_{avg} (ns)
NMI (3μM)	0.743	29.486	1.830	70.514	0.998	1.509
NMI+66.6 μM 4-NA	0.733	32.670	1.737	67.330	1.060	1.409
NMI+83.3 μM 4-NA	0.938	58.203	1.979	41.797	0.996	1.373
NMI+100 μM 4-NA	0.507	27.009	1.549	72.991	0.995	1.267

Table A3.5. Average Lifetimes of **NMI** with increasing concentration of 2-NA in aqueous media.

Sample	τ_1 (ns)	%	τ_2 (ns)	%	χ^2	τ_{avg} (ns)
NMI (3 μ M)	0.907	39.327	1.915	60.673	1.004	1.518
NMI +66.6 μ M 2-NA	0.831	56.079	1.782	43.921	0.998	1.249
NMI +83.3 μ M 2-NA	0.729	61.656	1.619	38.344	1.004	1.070
NMI +100 μ M 2-NA	0.625	68.796	1.435	31.204	1.007	0.878

Table A3.6. Average lifetimes of **NMI** with increasing concentration of 3-NA in aqueous media.

Sample	τ_1 (ns)	%	τ_2 (ns)	%	χ^2	τ_{avg} (ns)
NMI (3 μ M)	1.213	75.040	2.387	24.960	0.998	1.506
NMI +66.6 μ M 3-NA	1.099	70.430	2.128	29.570	0.998	1.360
NMI +83.3 μ M 3-NA	0.962	60.312	2.007	39.688	1.001	1.377
NMI +100 μ M 3-NA	0.931	60.309	1.815	39.691	0.997	1.282

Table A3.7. Analysis data of Surface Area Analyzer.

	NMI	NMI+4-NA
Total pore volume	0.0197 cc/g	0.007697 cc/g
BET surface area	10.405 m ² /g	3.391 m ² /g
BJH desorption		
Surface area	5.463 m ² /g	0.882 m ² /g
Pore volume	0.019 cc/g	0.001 cc/g
Pore diameter	3.317 nm	3.316 nm
BJH adsorption		
Surface area	6.399 m ² /g	0.782 m ² /g

Pore volume	0.02 cc/g	0.001cc/g
Pore diameter	3.066 nm	3.062 nm

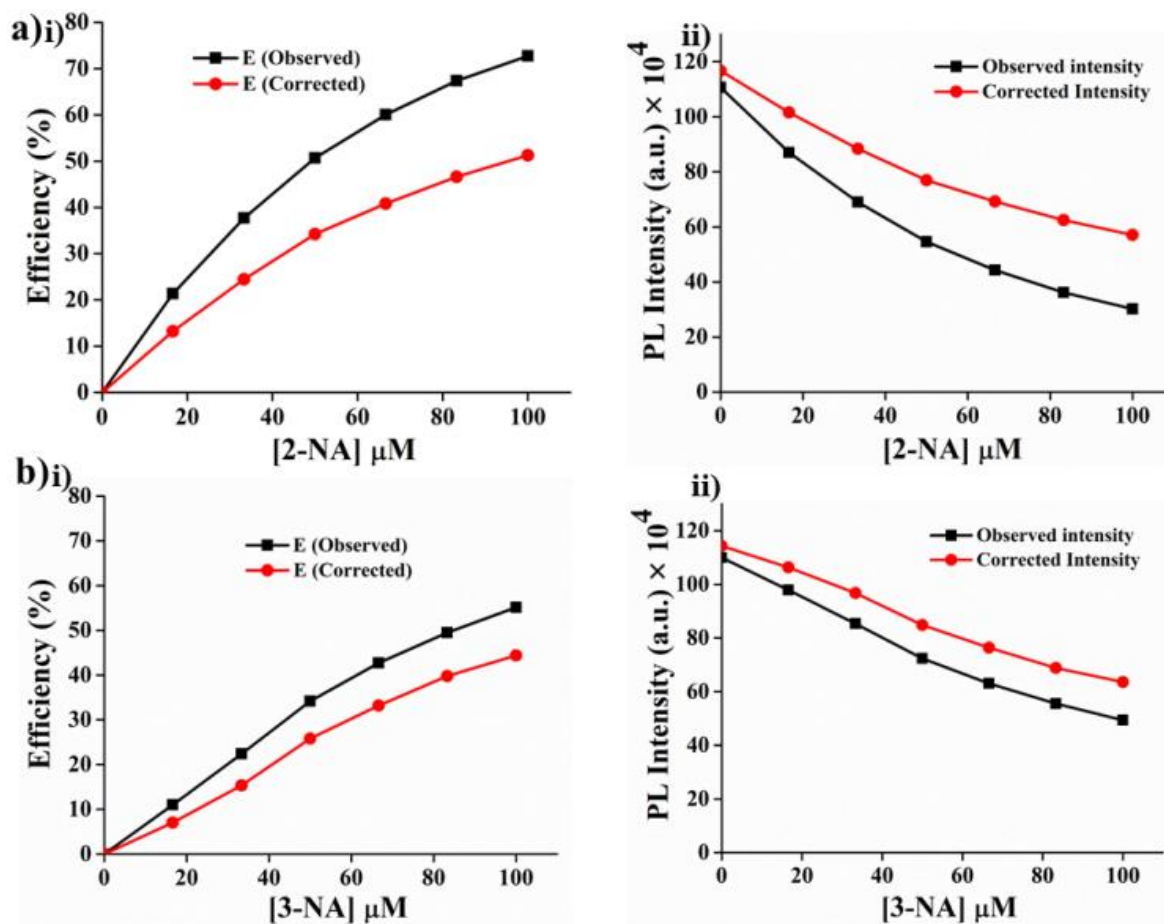


Figure A3.19. a-i) Suppression efficiency (E, %) of the corrected (red line) and observed (black line) fluorescence intensity for **NMI AIEEgen** under the influence of 2-NA concentration. aii) Observed (black line, I_{obs}) and corrected (red line, I_{corr}) fluorescence intensity of the **NMI AIEEgen** under the influence of 2-NA concentration. b-i) Suppression efficiency (E, %) of the corrected (red line) and observed (black line) fluorescence intensity for **NMI AIEEgen** under the influence of 3-NA concentration. b-ii) Observed (black line, I_{obs}) and corrected (red line, I_{corr}) fluorescence intensity of the **NMI AIEEgen** under the influence of 3-NA concentration.

Table A3.8. IFE of 4-NA on the fluorescence response of **NMI**.

[4-NA] μM	A_{ex}	A_{em}	I_{obs}	I_{corr}	I_{corr}/I_{obs} correction factor (CF)	$I_{corr}/I_{corr,0}$	E_{obs} (%)	E_{corr} (%)
0	0.045278	0.006719	1102020	1170006	1.061692	1	0	0

16.6	0.223324	0.03438	817712.1	1100151	1.345402	0.742012	25.79879	5.970427
33.33	0.401387	0.063951	601670.2	1028081	1.708713	0.54597	45.40297	12.13022
50	0.575999	0.092734	446013.1	963194.8	2.159566	0.404723	59.52768	17.67606
66.6	0.751127	0.122254	338912.4	926356	2.73332	0.307537	69.24626	20.82466
83.3	0.925859	0.152823	253799.5	878682.2	3.462111	0.230304	76.96961	24.89933
100	1.098038	0.182689	193820.4	846765.3	4.368813	0.175877	82.41226	27.62725

Table A3.9. IFE of 2-NA on the fluorescence response of NMI.

[2-NA] μM	A_{ex}	A_{em}	I_{obs}	I_{corr}	$I_{\text{corr}}/I_{\text{obs}}$ correction factor (CF)	$I_{\text{corr}}/$ $I_{\text{corr},0}$	E_{obs} (%)	E_{corr} (%)
0	0.042486	0.00405 8	1106440	1167347	1.055047	1	0	0
16.6	0.068958	0.064891	870443.3	1015465	1.166607	0.786706	21.32937	13.24041
33.33	0.091347	0.124016	689465.5	883474.5	1.281391	0.623139	37.68614	24.51745
50	0.114273	0.183828	545878.7	769390.2	1.409453	0.493365	50.66351	34.26462
66.6	0.141046	0.248388	442345.5	692593.9	1.56573	0.399792	60.0208 3	40.82597
83.3	0.166821	0.30915	361249.4	624874.3	1.729759	0.326497	67.35029	46.61181

100	0.186249	0.365921	302016.1	570315.4	1.888361	0.272962	72.7038	51.27323
-----	----------	----------	----------	----------	----------	----------	---------	----------

Table A3.10. IFE of 3-NA on the fluorescence response of NMI.

[3-NA] μM	A_{ex}	A_{em}	I_{obs}	I_{corr}	$I_{\text{corr}}/I_{\text{obs}}$ correction factor (CF)	$I_{\text{corr}}/$ $I_{\text{corr},0}$	E_{obs} (%)	E_{corr} (%)
0	0.038054	-0.00411	1099450	1143265	1.039852	1	0	0
16.6	0.069212	0.002463	978750.8	1062942	1.086019	0.890219	10.97814	7.025754
33.33	0.100718	0.00865	853107.7	967582.2	1.134185	0.77594	22.40596	15.36678
50	0.12803	0.00993 8	723491.2	848041.8	1.172152	0.658048	34.19517	25.82282
66.6	0.154046	0.012843	630148.5	763637.8	1.211838	0.573149	42.68511	33.20554
83.3	0.175995	0.010894	555127.2	688393.8	1.240065	0.504914	49.50865	39.78704
100	0.205153	0.01549	493341	636017	1.289204	0.448716	55.12838	44.36838

Table A3.11. HOMO and LUMO energies calculated for NMI and the sensing analytes using DFT with basis set B3LYP/6-31G +(d,p) in a Gaussian 09 program.

Compounds	HOMO (eV)	LUMO (eV)	Band Gap (eV)
NMI	-6.355	-2.720	3.635
4-NA	-7.686	-2.873	4.813

2-NA	-6.431	-2.661	3.770
3-NA	-6.462	-2.757	3.705
Aniline	-5.716	-0.302	5.414
TFA	-7.343	-0.914	6.429
TEA	-5.827	-0.240	5.587
NB	-7.897	-2.922	4.975
2,6-DFA	-7.132	-0.824	6.308
1,3-DNB	-8.734	-3.601	5.133
4-NT	-7.654	-2.793	4.861
2-AP	-7.028	-1.007	6.021
4-BrA	-6.739	-0.859	5.880
PFA	-6.966	-0.718	6.248

Solid-State White Light Emission, Excimer-Directed Photosensitization, and Type 1 Mitochondrion-Targeted Image-Guided Cancer Theranostics

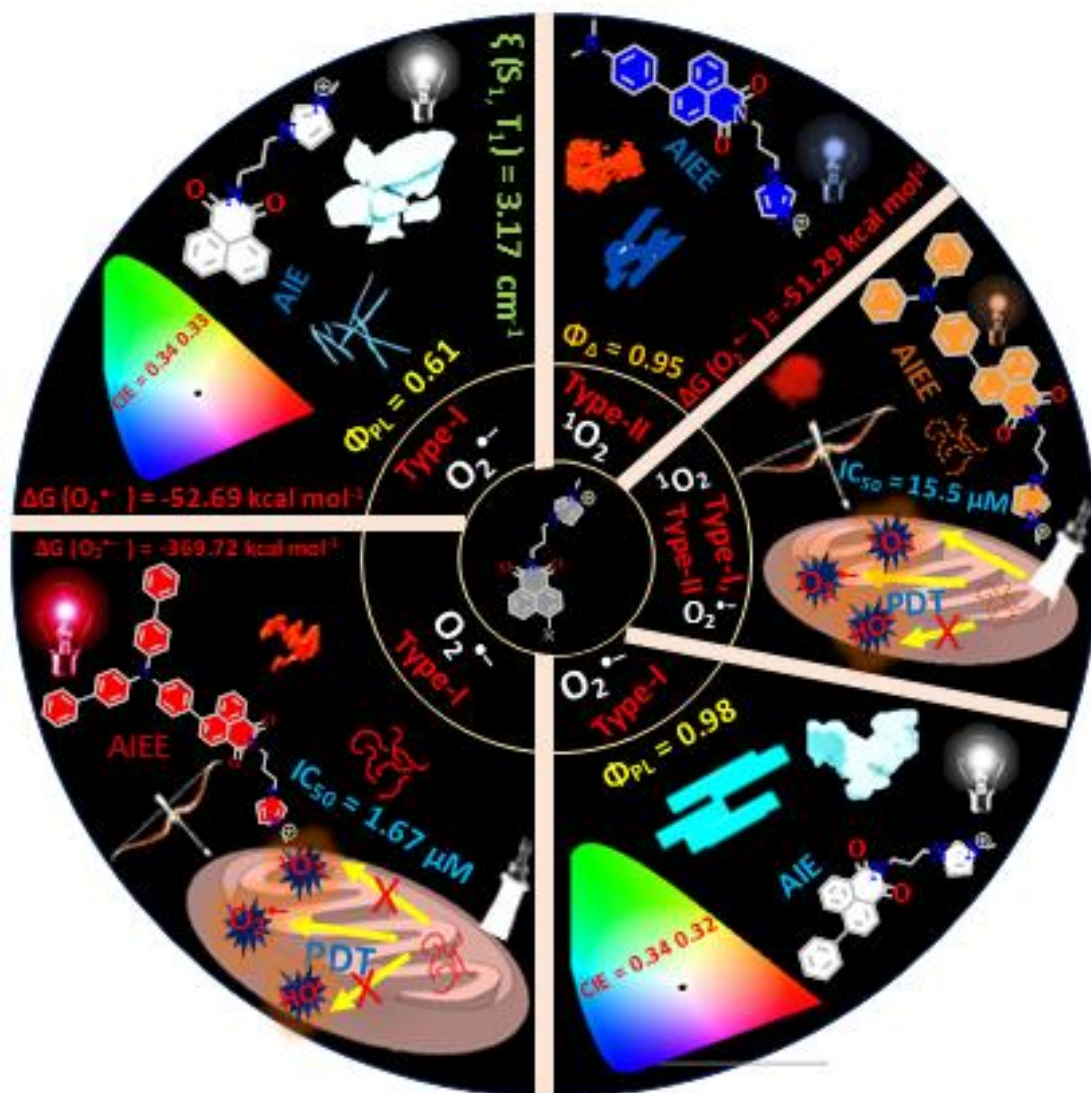
M. N. Khatun, S. Nandy, S. Kumar, P. K. Iyer. (Revision Submitted)

Indian patent submitted (TEMP/E-1/103941/2023-KOL)

Abstract

An innovative design strategy manipulated donor functional units within the ionic naphthalimide (**NIC**) core, achieving exceptional photophysical, supramolecular assembly and photosensitization. 1-(3-(1,3-dioxo-1H-benzo[de]isoquinolin-2(3H)-yl)propyl)-3-methyl-1H-imidazol-3-ium (**HNIC**) and 1-(3-(1,3-dioxo-6-phenyl-1H-benzo[de]isoquinolin-2(3H)-yl)propyl)-3-methyl-1H-imidazol-3-ium (**PNIC**) exhibited solid-state white light-emissive properties. Moreover, high photoluminescence (Φ_{PL}) of 0.99 and singlet oxygen quantum yields (Φ_{Δ}) of 0.95 were exhibited by **PNIC** and **NNIC** in aqueous environments. This study showed specific type-I ROS production (superoxide, $O_2^{\bullet-}$) efficacy. A novel AIE mechanism in rigid aromatic systems and an excimer-based ROS production approach were also introduced, diverging from traditional donor-acceptor principles. **BNIC** exhibited highly specific mitochondrion-targeted photodynamic therapy, achieving a low IC_{50} of 1.67 μM without the need for an additional targeting ligand. This research showed various photosensitizers (type-I PSs: **HNIC**, **PNIC**, 1-(3-(6-(4-aminophenyl)-1,3-dioxo-1H-benzo[de]isoquinolin-2(3H)-yl)propyl)-3-methyl-1H-imidazol-3-ium (**ANIC**), and 1-(3-(6-(4-(di([1,1'-biphenyl]-4-yl)amino)phenyl)-1,3-dioxo-1H-benzo[de]isoquinolin-2(3H)-yl)propyl)-3-methyl-1H-imidazol-3-ium (**BNIC**), type-II PS: 1-(3-(6-(4-(dimethylamino)phenyl)-1,3-dioxo-1H-benzo[de]isoquinolin-2(3H)-yl)propyl)-3-methyl-1H-imidazol-3-ium (**NNIC**), and both type-I and type-II characteristics PS: 1-(3-(6-(4-(diphenylamino)phenyl)-1,3-dioxo-1H-benzo[de]isoquinolin-2(3H)-yl)propyl)-3-methyl-1H-imidazol-3-ium (**TNIC**), respectively). This design principle holds the potential to establish a novel platform for creating advanced and versatile materials for a wide range of practical applications.

Keywords: aggregation-induced emission, solid state white light emission, distinct condensed state emitters, excimer-based PS, efficient ROS, mitochondrion-targeted image-guided type-I PDT.



4.1. Introduction

In recent decades, conventional cancer treatments like chemotherapy and radiotherapy have drawbacks: toxicity, poor clearance, limited tumor targeting, and efficacy monitoring challenges.^[1-3] Photodynamic therapy (PDT) is an emerging, precise, and noninvasive cancer treatment using light-activated photosensitizers (PSs) to generate ROS or singlet oxygen ($^1\text{O}_2$), ultimately destroying tumor cells.^[4-8] PDT involves two main mechanistic aspects: type-I and type-II processes. The type-I involves electron transfer from triplet PSs to oxygen, creating radicals ($\text{O}_2^{\cdot-}$, peroxide or hydroxyl radical) via superoxide disproportionation and Franck-Condon transition.^[4,8-10] Negative ΔG ($\Delta G < 0$) needed for allowed electron transfer.^[11] In comparison, type-II PDT involves the transfer of energy from PS triplet excitons to molecular oxygen ($^3\text{O}_2$), resulting in the formation of $^1\text{O}_2$.^[4,8] For this, PS's lowest triplet excited state (T_1) energy must exceed the 0.98 eV oxygen sensitization threshold.^[12]

The type-I processes are more favored for treating low-oxygen solid tumors, including hypoxic microenvironments, which is very rare.^[13-17] It is widely explored that fluorescent PSs offer both diagnostic and therapeutic advantages, ideally featuring strong, long-wavelength absorption, organelle-specific targeting, high ROS generation, condensed-state emission, deep tissue penetration, minimal toxicity, and stability. ^[13] However, classical PSs like BODIPY, ^[18] metal complexes, ^[19] and chlorin ^[20] derivatives have been extensively studied but suffer from aggregation-caused quenching (ACQ) effects, limiting their concentration and condensed ¹O₂ production. Existing PSs, including metal complexes, antennae-fullerene conjugates, TiO₂, ZnO, and PIO, require UV light activation and can cause notable side effects. ^[21-25] Triarylmethanes and benzophenothiazine analogs exhibit adverse ACQ effects in aqueous environments. ^[21,23,24] Strategies for enhancing ¹O₂ production involve structural manipulation, optimizing donor-acceptor (D-A) design, and controlling conjugation length to achieve effective PDT through concentrated tumor site accumulation. Enhancing photosensitization often involves increasing intersystem crossing (ISC) between singlet (S) and triplet (T) states, achieved by elevating spin-orbit coupling (SOC) and minimizing the S-T energy gap (ΔE_{ST}).^[26,27] In this context, the introduction of heavy atoms to improve SOC often results in dark toxicity.^[18,28] Another approach is to separate the distributions of the highest occupied molecular orbital (HOMO) and lowest unoccupied molecular orbital (LUMO) to enhance ISC.^[29] This strategy, combined with a D-A design, can result in red-shifted emission and increased HOMO-LUMO separation, but strong charge transfer may suppress emission at higher concentrations, affecting ¹O₂ generation efficiency.^[30] Designing D-A AIE PSs for efficient ¹O₂ production in condensed states remains a challenge. Along with, developing organelle-targeting cationic D-A AIE PSs with efficient type-I process is still a hurdle. While some type-I mitochondrion-targeted PSs exist, their specificity is limited and often require higher concentrations for effectiveness. Some of these PSs target lysosomes and mitochondria, relying on external stimuli for activation, and may not have ideal photophysical properties such as stokes shift and Φ_{PL} for the promising biological application. Unfortunately, researchers have primarily relied on experimental analysis, and have not provided theoretical data on triplet formation (Table A4.1).

This study illustrates that **BNIC** AIEgen displays significant type-I PDT effectiveness at a low concentration of 2 μ M, along with efficient mitochondrion targeting, all achieved without the need for additional targeting ligands. It attains a low IC₅₀ value of 1.67 μ M, surpassing the performance of other recently examined substances in both type-I and type-II PDT materials. **BNIC** showed higher stokes shift and 0.99 Φ_{PL} at 60% water fraction (f_w) compared to previously reported PDT materials. It displays excellent specificity and efficiently generates O₂^{•-}, as supported by various experimental and theoretical studies, including DCFDA, ABDA, TA, ESR, theoretical data (ΔG , SOC), and band energy in relation

to the normal hydrogen electrode (NHE). Despite the numerous reported type-II materials for in vitro and in vivo applications, their mechanistic understanding is still lacking, primarily relying on experimental techniques like ABDA and DCFDA. Concerns persist regarding their specificity and their Φ_{Δ} values, which are lower than the **NNIC** material with an impressive Φ_{Δ} efficiency of 0.95 at 99% f_w . Further research on the application of **NNIC** material for PDT is currently in progress (Table A4.1, A4.2). This innovative design strategy opens the door to advanced smart materials with unique photophysical properties, including condensed-state luminescence and single-molecule solid-state white light emission. It achieves this through straightforward manipulation of the D-A design strategy and anion- π^+ interactions of imidazole part. This research contributes to the ongoing effort to understand the relationships between structure and properties in condensed states, which is relevant across various fields. [31-34] Notably, this study represents the rarest single-molecule solid-state white light emissive ionic AIE PSs. While there are reports of AIE phosphorescence materials exhibiting white light emission in the solid state, the realization of single-molecule white light emissive AIE PSs in both solid and solution state is unprecedented. Furthermore, this research explored distinct PSs. **PNIC** exhibits solid-state white light emissive AIE PS characteristics while following the conventional D-A design strategy. In contrast, **HNIC** stands out by demonstrating an excimer-based solid-state white light emissive AIE PS, breaking away from the traditional D-A design principle. This study provides novel insights into the AIE and ROS generation mechanisms in organic molecules, offering a comprehensive platform that distinguishes it from previous reports (Table A4.1-A4.4).

4.2. Experimental Section

4.2.1. Materials and Instrumentations: All reagents and starting materials, including 1,8-naphthalic anhydride, 4-bromo-1,8-naphthalic anhydride, 3-aminopropyl imidazole and various boronic acid derivatives such as phenyl boronic acid, (4-aminophenyl)boronic acid, (4-(dimethylamino)phenyl)boronic acid, (4-(diphenylamino)phenyl)boronic acid, and (4-(di([1,1'-biphenyl]-4-yl)amino)phenyl)boronic acid, along with reactive oxygen species detectors like 2',7'-Dichlorodihydrofluorescein diacetate (DCFDA), 2,2,6,6-Tetramethylpiperidine (TEMP), 9,10-Anthracenediyl-bis(methylene)dimalonic acid (ABDA), and Terephthalic acid (TA), were procured from Sigma Aldrich (INDIA) in reagent-grade quality. HPLC-grade solvents were obtained from Fisher Scientific Ltd. and RANKEM. Nuclear magnetic resonance (NMR) spectra, including ^1H and ^{13}C , were recorded using a Bruker Avance 400 MHz spectrometer. The residual solvent signal served as an internal reference for all NMR experiments. Mass spectra were acquired using MALDI-TOF spectrometry. UV/visible (UV/vis) and photoluminescence (PL) spectra were obtained using

a Perkin-Elmer Model Lambda-750 spectrophotometer and a Horiba Fluoromax-4 spectrofluorometer, respectively. All measurements were performed at 298 K using 4 mm quartz cuvettes. A laser diode at 375 nm (DeltaDiode-375) was used as the excitation source for both UV/vis and PL experiments. The hydrodynamic diameter and Zeta potential of the compounds were measured using a Malvern Zetasizer instrument. Field emission scanning electron microscopy (FESEM) images were obtained using a Sigma Carl ZEISS field emission scanning electron microscope. Single crystal data were collected using a Bruker SMART APEX diffractometer equipped with a CCD area detector. For photodynamic therapy studies, a white light source with an intensity of 50 mW cm⁻² was utilized, specifically the "Pick Ur Needs 120W Plastic Lithium Battery Search Light Long 1 Km Range with Multi-Functional + Blinker Rechargeable Handheld Torch" in black. DMEM, Propidium iodide (PI), and Calcein-AM (AM) were purchased from High Media, and the Hela cell line was acquired from Sigma Aldrich (INDIA).

4.2.2. Preparation of the Test Solution: Stock solutions of **RNIC** materials, namely **HNIC**, **PNIC**, **ANIC**, **NNIC**, **TNIC**, and **BNIC**, were prepared in dimethyl sulfoxide (DMSO) at a concentration of 20 mM. For investigating the aggregation behavior, test solutions of the materials were prepared at a concentration of 100 μM. These test solutions were obtained by adjusting the water fraction in DMSO. Before recording the spectra, the prepared solutions were thoroughly shaken at room temperature to ensure effective mixing and dispersion of the compounds. This step was taken to maintain uniformity and consistency in the measurements.

4.2.3. Preparation of FESEM samples:

For the morphological analysis of supramolecular self-assembly using field emission scanning electron microscopy (FESEM), a straightforward sample preparation method was utilized, as shown in Figure A4.9. A dilute suspension of the **RNIC** derivatives at a concentration of 100 μM was prepared using a mixture of 99.9% water and -0.1% DMSO. This suspension was then drop-casted onto a glass surface coated with aluminum foil. The samples were left to air dry overnight at room temperature before conducting the analysis.

4.2.4. Theoretical Studies: Electronic properties of **RNIC** derivatives were evaluated using density functional theory (DFT) calculations. The Gaussian 16 package, utilizing the B3LYP hybrid functional, was employed for these calculations. For each derivative, ground state optimized geometries were obtained, and the electron density and energy levels of the highest occupied molecular orbital (HOMO) and lowest unoccupied molecular orbital (LUMO) were determined. The calculations utilized the 6-31G basis set, known for delivering accurate results within a reasonable computational time (ref. 1, 2 in AI).

4.2.5. Photoluminescence quantum Yield Calculations: The fluorescence quantum yields (Φ_{PL}) of **RNIC** derivatives were determined by comparing their fluorescence to that of Quinine sulphate ($\Phi_r = 0.57$ in 0.1 M H_2SO_4) as standard and using a specific equation. The equation employed for this determination is as follows:

$$\Phi_{PL} = \Phi_r (A_r F_s / A_s F_r) (\eta_s^2 / \eta_r^2) \quad (A4.1)$$

In the provided equation, the variables s and r correspond to the sample and reference, respectively. The term Φ represents the quantum yield, A indicates the absorbance, F denotes the relative integrated fluorescence intensity, and η signifies the refractive index.

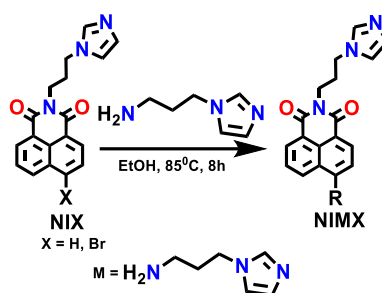
4.2.6. Synthesis of RNIC derivatives

Synthetic procedures for HNIM and NIMBr: In this experiment, 1,8-naphthalic anhydride (5 mmol) was dissolved in 20 mL of ethanol, and then 3-aminopropylimidazole (5.2 mmol) was added dropwise at room temperature. The resulting suspension was vigorously stirred and heated at 85°C for 18 hours. After the heating period, the mixture was allowed to cool to room temperature, and further cooling to 5°C for 1 hour promoted the recrystallization of imidazole naphthalimide (**HNIM**). Following recrystallization, the solvent was separated by filtration, leaving behind the purified **HNIM** as a light white crystalline solid with an impressive yield of 85%. A similar synthetic procedure was carried out to synthesize **NIMBr**, where 1,8-naphthalic anhydride was replaced with 4-bromo-1,8-naphthalic anhydride. This reaction resulted in the formation of **NIMBr** as a light brown solid with a yield of 84%.

Characterization data for 2-(3-(1H-imidazol-1-yl)propyl)-1H-benzo[de]isoquinoline-1,3(2H)-dione (HNIM): 1H NMR (400 MHz, $CDCl_3$) 3.60 (t, 2H), 4.16 (t, 2H), 4.47 (t, 2H), 7.42 (s, 1H), 7.67 (s, 1H), 7.82 (t, 2H), 8.27 (t, 2H), 8.63 (t, 2H), 10.05 (s, 1H). ^{13}C NMR (101 MHz, $CDCl_3$) δ 8.11, 28.30, 39.71, 46.03, 111.90, 120.32, 123.04, 124.00, 127.04, 129.68, 132.10, 134.44, 137.78, 138.47, 165.02. MALDI-TOF: calculated for $C_{28}H_{23}NO_2$: 305.33 [M] $^+$, Found: 306.39 [M+H] $^+$

Characterization data for 2-(3-(1H-imidazol-1-yl)propyl)-6-bromo-1H-benzo[de]isoquinoline-1,3(2H)-dione (NIMBr): 1H NMR (400 MHz, $CDCl_3$) 3.58 (t, 2H), 4.28 (t, 2H), 4.45 (t, 2H), 7.42 (s, 1H), 7.80 (s, 1H), 8.26 (t, 2H), 8.28 (t, 2H), 8.62 (s, 1H), 10.06 (s, 1H). ^{13}C NMR (101 MHz, $CDCl_3$) δ 8.11, 28.30, 30.28, 39.71, 46.03, 48.73, 110.90, 121.12, 122.14, 125.40, 126.04, 129.78, 131.17, 135.46, 138.68, 139.47, 166.22. MALDI-TOF: calculated for $C_{28}H_{23}NO_2$: 384.23 [M] $^+$, Found: 385.25 [M+H] $^+$

Synthetic Route



Scheme A4.1. The synthetic approach used for the preparation of **HNIM** and **NIMBr**.

Synthetic procedures for peri-functionalized naphthalimide (RNIM)

derivatives: In a 50 mL round-bottom flask, a mixture of compound **NIMBr** (0.5 mmol) and the corresponding boronic acid (1 mmol) was prepared along with 5 mg of Pd (PPh₃)₄ catalyst. To ensure an oxygen-free environment, the mixture was purged with nitrogen gas for 30 minutes. Subsequently, 6 mL of THF (tetrahydrofuran) was added, followed by the addition of 2 mL of a 2.0 M potassium carbonate solution. The resulting mixture was stirred at 85 °C under a nitrogen atmosphere, and the progress of the reactions was monitored using thin-layer chromatography (TLC). After 24 hours, the reactions were considered complete. The solutions were then cooled, and the organic layers were extracted using CHCl₃ (chloroform). To remove any residual moisture, the organic layers were dried with anhydrous sodium sulfate. Afterward, the solvent was evaporated, leaving behind the reaction products. The products were further purified using column chromatography, resulting in a 60% yield of the desired light brown for **PNIM**, deep brown for **ANIM**, and yellowish solid for **NNIM**, **TNIM**, and **BNIM** compounds.

Characterization data for 2-(3-(1H-imidazol-1-yl)propyl)-6-phenyl-1H-benzo[de]isoquinoline-1,3(2H)-dione (PNIM):

¹H NMR (400 MHz, CDCl₃) δ 2.50 (t, 2H), 4.30 (2, 3H), 4.50 (t, 2H), 7.50 (s, 1H), 7.52 (s, 1H), 7.72 (t, 3H), 7.73 (s, 1H), 7.73 (t, 2H), 8.31 (t, 1H), 8.67 (t, 2H), 9.57 (s, 1H). ¹³C NMR (101 MHz, CDCl₃) δ 8.70, 26.75, 29.94, 44.86, 55.95, 122.62, 123.96, 125.62, 129.33, 131.35, 141.40, 146.38, 153.10, 157.48, 158.47, 161.18, 161.85, 162.17 MALDI-TOF: calculated for C₃₆H₂₇NO₂S₂: 381.14 [M]⁺, Found:382.15 [M+H]⁺

Characterization data for 2-(3-(1H-imidazol-1-yl)propyl)-6-(4-aminophenyl)-1H-benzo[de]isoquinoline-1,3(2H)-dione (ANIM):

¹H NMR (400 MHz, CDCl₃) δ 3.61 (t, 2H), 4.29 (t, 3H), 4.47 (t, 2H), 6.90 (s, 1H), 7.45 (t, 2H), 7.72 (s, 1H), 7.73 (t, 2H), 7.74 (d, 1H), 8.43 (t, 3H). 8.49 (d, 1H), 8.65 (d, 2H). 10.26 (s, 1H) ¹³C NMR (101 MHz, CDCl₃) δ 8.11, 28.30, 30, 28, 46.08, 48.73, 111.90, 120.31, 123.04, 124.04, 127.04, 129.68, 132.14, 134.44,

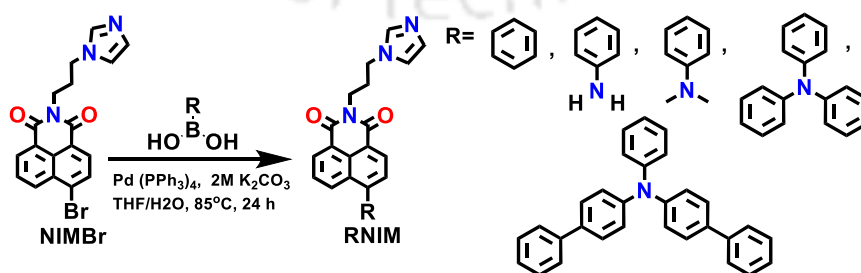
137.78, 138.47, 165.02. MALDI-TOF: calculated for $C_{40}H_{29}NO_2S_2$: 396.15 $[M]^+$, Found: 397.23 $[M+H]^+$

Characterization data for 2-(3-(1H-imidazol-1-yl)propyl)-6-(4-(dimethylamino)phenyl)-1H-benzo[de]isoquinoline-1,3(2H)-dione (NNIM): 1H NMR (400 MHz, $CDCl_3$) δ 3.11 (s, 6H), 3.18 (t, 3H), 4.25 (t, 2H), 4.27 (t, 2H), 6.86 (t, 2H), 7.33 (s, 1H), 7.44 (t, 2H), 7.45 (d, 1H), 7.77 (t, 2H), 8.45 (t, 1H), 8.65 (t, 2H), 10.26 (s, 1H). ^{13}C NMR (101 MHz, $CDCl_3$) δ 8.11, 28.09, 40, 71, 48.73, 112.89, 121.96, 123.34, 126.05, 128.01, 130.75, 131.75, 133.39, 138.47, 147.85, 150.58, 164.65. MALDI-TOF: calculated for $C_{40}H_{29}NO_2S_2$: 425.18 $[M]^+$, Found: 426.26 $[M+H]^+$

Characterization data for 2-(3-(1H-imidazol-1-yl)propyl)-6-(4-(diphenylamino)phenyl)-1H-benzo[de]isoquinoline-1,3(2H)-dione (TNIM): 1H NMR (400 MHz, $CDCl_3$) δ 2.50 (t, 3H), 4.27 (t, 3H), 4.47 (t, 2H), 7.35 (t, 3H), 7.60 (m, 5H), 7.63 (m, 6H), 7.73 (t, 2H), 7.80 (dd, 2H), 8.39 (t, 1H), 8.66 (t, 1H), 9.90 (s, 1H). ^{13}C NMR (101 MHz, $CDCl_3$) δ 8.70, 26.75, 44.86, 55.95, 122.61, 123.96, 125.62, 127.84, 128.67, 129.33, 131.35, 141.40, 146.38, 153.30, 157.48, 158.47, 161.17, 161.85, 162.17. MALDI-TOF: calculated for $C_{40}H_{29}NO_2S_2$: 548.22 $[M]^+$, Found: 549.43 $[M+H]^+$

Characterization data for 2-(3-(1H-imidazol-1-yl)propyl)-6-(4-(di([1,1'-biphenyl]-4-yl)amino)phenyl)-1H-benzo[de]isoquinoline-1,3(2H)-dione (BNIM): 1H NMR (400 MHz, $CDCl_3$) δ 3.11 (t, 3H), 4.16 (t, 3H), 4.43 (t, 3H), 7.73 (m, 10H), 7.49 (m, 9H), 7.60 (m, 6H), 7.64 (t, 3H), 7.87 (t, 1H), 8.65 (t, 1H), 10.20 (s, 1H). ^{13}C NMR (101 MHz, $CDCl_3$) δ 9.47, 23.54, 28, 29.28, 46.39, 58.49, 123.34, 126.05, 127.72, 130.06, 130.74, 136.80, 141.11, 146.18. MALDI-TOF: calculated for $C_{40}H_{29}NO_2S_2$: 700.28 $[M]^+$, Found: 701.65 $[M+H]^+$

Synthetic Route



Scheme A4.2. The synthetic approach used for the preparation of RNIM derivatives.

Synthetic procedures for perfunctionalized ionic naphthalimide (RNIC) derivatives: In a 20 mL flask, RNIM (0.5 mmol) and iodomethane (10 mmol) were dissolved in dimethylformamide (DMF). The resulting solution was then refluxed at 85 °C for 4 hours. Once the reaction was completed, the mixture was allowed to cool to room temperature, and the solvent was removed under reduced pressure (vacuum evaporation). This process resulted in a residue. The obtained residue was subjected to purification using column chromatography on silica gel. This purification step led to an 80% yield of the desired white solid for HNIC, light brown for PNIC, deep brown for ANIC, and reddish-yellow solid for NNIC, TNIC, and BNIC compounds.

Characterization data for 1-(3-(1,3-dioxo-1H-benzo[de]isoquinolin-2(3H)-yl)propyl)-3-methyl-1H-imidazol-3-ium (HNIC): ¹H NMR (400 MHz, CDCl₃) δ 3.62 (t, 3H), 4.16 (s, 3H), 4.27 (t, 2H), 4.45 (t, 2H), 7.42 (s, 1H), 7.80 (s, 1H), 7.82 (t, 2H), 8.27 (t, 2H), 8.63 (t, 2H), 10.05 (s, 1H). ¹³C NMR (101 MHz, CDCl₃) δ 8.1, 28.30, 30.28, 36.03, 39.72, 46.02, 48.73, 112.90, 122.32, 123.04, 125.30, 128.04, 129.78, 131.10, 134.74, 137.68, 139.47, 164.02. MALDI-TOF: calculated for C₃₄H₂₉NO₂: 320.13 [M]⁺, Found: 321.35 [M+H]⁺

Characterization data for 1-(3-(1,3-dioxo-6-phenyl-1H-benzo[de]isoquinolin-2(3H)-yl)propyl)-3-methyl-1H-imidazol-3-ium (PNIC): ¹H NMR (400 MHz, CDCl₃) δ 2.50 (t, 3 H), 4.30 (t, 3H), 4.50 (t, 3H), 7.50 (s, 1H), 7.58 (t, 2H), 7.69 (m, 3H), 7.74 (s, 1H), 7.74 (t, 2H), 8.30 (t, 1H), 8.66 (t, 2H), 9.73 (s, 1H). ¹³C NMR (101 MHz, CDCl₃) δ 8.44, 13.43, 29.94, 30.92, 46.13, 60.48, 122.71, 125.10, 126.36, 127.65, 128.18, 128.95, 128.52, 131.07, 131.83, 136.30, 142.01, 146.55. MALDI-TOF: calculated for C₃₆H₂₇NO₂S₂: 396.17 [M]⁺, Found: 397.23 [M]⁺

Characterization data for 1-(3-(6-(4-aminophenyl)-1,3-dioxo-1H-benzo[de]isoquinolin-2(3H)-yl)propyl)-3-methyl-1H-imidazol-3-ium (ANIC): ¹H NMR (400 MHz, CDCl₃) δ 3.60 (t, 3H), 4.39 (s, 6H), 4.29 (t, 2H), 4.42 (t, 2H), 6.90 (s, 2H), 7.44 (t, 2H), 7.72 (s, 1H), 7.73 (t, 3H), 8.43 (m, 3H). 8.62 (t, 1H), 8.64 (t, 2H), 10.26 (s, 1H). ¹³C NMR (101 MHz, CDCl₃) δ 8.11, 28.30, 30, 28, 36.03, 39.71, 48.73, 111.90, 112.32, 125.04, 125.30, 128.04, 129.78, 131.10, 136.74, 137.68, 138.47, 165.12. MALDI-TOF: calculated for C₄₀H₂₉NO₂S₂: 441.47 [M]⁺, Found: 412.45 [M+H]⁺

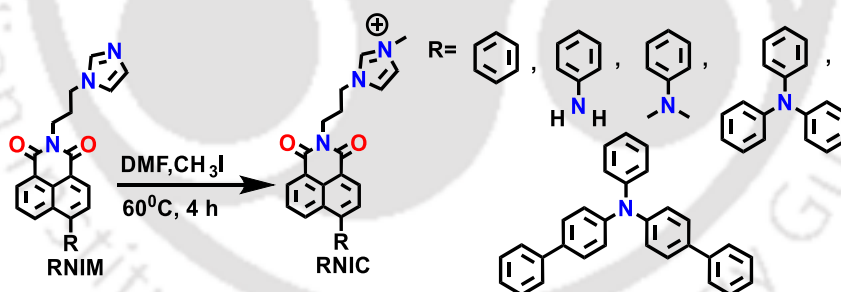
Characterization data for 1-(3-(6-(4-(dimethylamino)phenyl)-1,3-dioxo-1H-benzo[de]isoquinolin-2(3H)-yl)propyl)-3-methyl-1H-imidazol-3-ium (NNIC): ¹H NMR (400 MHz, CDCl₃) δ 3.17 (s, 6H), 3.20 (t, 3H), 4.17 (s, 3H), 4.30 (t, 2H), 4.46 (t, 2H), 6.90 (t, 2H), 7.33 (s, 1H), 7.44 (t, 2H), 7.66 (t, 2H). 8.48 (t, 1H), 8.64 (t, 2H), 10.24 (s, 1H). ¹³C NMR (101 MHz, CDCl₃) δ 8.11, 28.09, 28.30, 31.28, 35.02, 38.62, 45.12, 47.63, 111.90,

123.32, 124.04, 126.30, 129.14, 129.68, 132.10, 132.74, 136.68, 139.47, 165.06. MALDI-TOF: calculated for $C_{40}H_{29}NO_2S_2$: 431.2129 $[M]^+$, Found: 431.213 $[M]^+$

Characterization data for 1-(3-(6-(4-(diphenylamino)phenyl)-1,3-dioxo-1H-benzo[de]isoquinolin-2(3H)-yl)propyl)-3-methyl-1H-imidazol-3-ium (TNIC): 1H NMR (400 MHz, $CDCl_3$) δ 2.49 (t, 3H), 4.19 (s, 1H), 4.31 (t, 2H), 4.47 (t, 2H), 7.11 (t, 3H), 7.24 (m, 5H), 7.25 (m, 5H), 7.37 (t, 3H), 7.39 (m, 6H), 7.79 (t, 2H), 8.49 (t, 2H), 10.18 (s, 1H). ^{13}C NMR (101 MHz, $CDCl_3$) δ 8.03, 9.69, 45.85, 59, 57.91, 122.61, 124.28, 125.62, 130.67, 139.12, 142.40, 147.44, 152.97, 154.29, 157.26, 158.26, 162.79. MALDI-TOF: calculated for $C_{40}H_{29}NO_2S_2$: 563.24 $[M]^+$, Found: 563.29 $[M]^+$

Characterization data for 1-(3-(6-(4-(di([1,1'-biphenyl]-4-yl)amino)phenyl)-1,3-dioxo-1H-benzo[de]isoquinolin-2(3H)-yl)propyl)-3-methyl-1H-imidazol-3-ium (BNIC): 1H NMR (400 MHz, $CDCl_3$) δ 2.52 (t, 3H), 4.16 (s, 1H), 4.25 (t, 2H), 4.43 (t, 2H), 7.33 (m, 9H), 7.49 (m, 7H), 7.40 (t, 3H), 7.64 (m, 9H), 7.78 (m, 3H), 8.50 (t, 1H), 8.64 (t, 2H), 10.47 (s, 1H). ^{13}C NMR (101 MHz, $CDCl_3$) δ 8.44, 13.43, 29.94, 30.92, 46.13, 60.48, 122.71, 125.10, 126.36, 127.65, 128.17, 129.12, 131.07, 136.44, 140.73, 147.20. MALDI-TOF: calculated for $C_{40}H_{29}NO_2S_2$: 715.30 $[M]^+$, Found: 715.45 $[M]^+$

Synthetic Route



Scheme A4.3. The synthetic approach used for the preparation of RNIC derivatives.

4.2.7. Computational studies

The study involved optimizing and calculating the frequencies of triplet excited states, excitation energies, and transition properties of **RNIC** derivatives. These calculations were conducted using the time-dependent B3LYP/6-31G (d, p) method with the Tamm-Dancoff approximation (TDA). For the computations, the Gaussian 16 package was used, and the ORCA 5.0 module was employed at the B3LYP DEF2-SVP level. Additionally, spin-orbit coupling (SOC) constants for **HNIC**, **PNIC**, **ANIC**, **NNIC**, **TNIC**, and **BNIC** were

computed at the same level of theory mentioned above, utilizing the ORCA 5.0 software (ref. 3, 4 in AI).

4.2.8. $^1\text{O}_2$ generation quantum yield Estimation: In this study, Rose Bengal dilute solutions were used as a reference ($\Phi_{\Delta} = 0.76$ in ethanol). To mitigate the inner-filter effect, the absorbance maxima of Rose Bengal and the Photosensitizer were maintained at 0.2. Different solutions of **RNIC** derivatives were prepared at a concentration of 100 μM , and 100 μM ABDA was added to these solutions. The absorbance of ABDA at 378 nm was measured at various irradiation times using white light (400-700 nm, 50 mW cm^{-2}). This measurement allowed for the determination of the decay rate of the photosensitizing process. Subsequently, the $^1\text{O}_2$ generation quantum yield (Φ_{Δ}) of **RNIC** derivatives in 99% PBS in DMSO was calculated using specific equations, which has been given below.

$$\Phi_{\text{AIEgen}} = \Phi_{\text{RB}} (K_{\text{AIEgen}} A_{\text{RB}} / K_{\text{RB}} A_{\text{AIEgen}}) \dots \dots \dots \text{(A4.2)}$$

Where, Φ_{AIE} is the $^1\text{O}_2$ generation quantum yield of AIEgen in 99% PBS in DMSO. A_{RB} and A_{AIEgen} represent the light absorbed by Rose Begal and AIEgen, respectively, at an absorbance of 0.2. The absorption bands were integrated in the wavelength range of 400-700 nm to determine these values. K_{RB} and K_{AIEgen} are the decomposition rate constants of ABDA by Rose Begal and AIEgen, respectively. These constants were determined by plotting $\text{Ln}(A_0/A)$ against time, where A_0 and A are the absorbance of ABDA at 378 nm by photosensitizers under white light irradiation at different time points (ref. 5, 6 in AI).

4.2.9. Reactive oxygen species (ROS) Generation/Mesurament

Free Radical ($\text{O}_2^{\cdot-}$ and HO^{\cdot}) Test: Electron Paramagnetic Resonance (EPR) analysis was performed to monitor the generation of type-I Reactive Oxygen Species (ROS). For this purpose, 2,2,6,6-Tetramethylpiperidine (TEMP) was utilized as a spin-trap agent to detect the free radicals $\text{O}_2^{\cdot-}$ and HO^{\cdot} . In the experiment, 100 μM of TEMP and various solutions of **RNIC** derivatives were prepared in 99% PBS in DMSO. The solutions were then subjected to white light irradiation at a power density of 50 mW cm^{-2} for 10 minutes. Subsequently, EPR spectra of the spin-trapped radicals were recorded in the range of 3000-3600 G after irradiation. To ensure accuracy, background interference was corrected using a sample taken before irradiation ref. 7 in AI. Singlet Oxygen ($^1\text{O}_2$) Test: The objective of this test was to measure the generation of singlet oxygen ($^1\text{O}_2$). A mixed solution containing 100 μM ABDA (a singlet oxygen sensor) and various solutions of RNIC derivatives compounds was prepared in 99% PBS in DMSO. The solution was then exposed to white light irradiation at a power density of 50 mW cm^{-2} for different durations: 0, 2, 4, 6, 8, and 10 minutes. For NNIC compounds, the light irradiation time varied from 0s to 60s, with a 5s interval. After each

time interval, the degradation of ABDA's absorbance at 378 nm was promptly measured. This measurement allowed for the evaluation of singlet oxygen generation as a function of the light irradiation duration for the different **RNIC** derivatives compounds. Total ROS Test: The purpose of the total ROS test was to quantify the overall ROS levels. For this analysis, DCFDA, a chemically reduced form of fluorescein, was employed as a fluorescent indicator for ROS. A solution containing 1 μM DCFDA and various solutions of **RNIC** derivatives compounds at a concentration of 100 μM was prepared in 99% PBS in DMSO. The solution was then subjected to white light irradiation at a power density of 50 mW cm^{-2} for different durations: 0, 1, 2, 3, 4, 5, 6, 7, 8, 9, and 10 minutes. The fluorescence spectra of the mixed solution were promptly measured. This measurement allowed for the assessment of the changes in fluorescence, indicating the levels of ROS generated in response to the different **RNIC** derivatives compounds under varying durations of light irradiation. Superoxide Anion Radical ($\text{O}_2^{\cdot-}$) Test: The feasibility of the reaction producing $\text{O}_2^{\cdot-}$ was assessed through theoretical calculations conducted using the ORCA 5.0 software. Hydroxyl Radical ($\text{HO}\cdot$) Test: The objective of this test was to quantify the generation of hydroxyl radicals ($\text{HO}\cdot$). A mixed solution consisting of 100 μM TA and various solutions of **RNIC** derivatives compounds at a concentration of 100 μM was prepared in 99% PBS in DMSO. The subsequent testing process was similar to the determination of total ROS using DCFDA as the probe. However, in this case, upon trapping with $\text{HO}\cdot$, TA was converted to hydroxyl terephthalic acid, resulting in an enhanced fluorescent intensity with an λ_{ex} of 315 nm. This method allowed for the detection and measurement of the levels of hydroxyl radicals generated in response to the different **RNIC** derivatives compounds under investigation. ($\lambda_{\text{ex}} = 315 \text{ nm}$).

4.2.10. The Point of Zero Zeta Potential Evaluation

According to the literature (ref. 8 in AI), The points of zero zeta potential (PZZP) for **RNIC** derivatives were determined through calculations. Initially, the aqueous solutions of these Perylenimide materials were maintained at a neutral pH of approximately 7. However, by introducing either a dilute solution of sodium hydroxide or dilute hydrochloric acid, the pH of the solutions could be adjusted to alkaline or acidic conditions. A systematic variation of pH values within the range of 9, 7.4, 5.6, to 3 and 1 was performed, and the corresponding zeta potential of the **RNIC** materials was measured. Remarkably, as the pH values were altered from alkaline to acidic, a noticeable shift in the zeta potential was observed. In general, the zeta potential of **RNIC** derivatives showed a trend of becoming more positive as the pH values changed from alkaline to acidic conditions. However, there were exceptions for **HNIC**, **PNIC**, and **BNIC**, where the zeta potential shifted from negative to positive as

the pH values were altered from alkaline to acidic conditions. This behaviour could be due to the different amount of positive charge present in the surface of the system.

4.2.11. The Energy of the Valence Band and Conduction Band Calculations

The valence band energy (E_V) was determined using X-ray photoelectron spectroscopy (XPS) data by calculating the energy of the valence band. To calculate the conduction band energy (E_C), the energy gap was first estimated from the onset absorption data obtained from UV-visible spectroscopy. Subsequently, E_C was calculated with respect to the normal hydrogen electrode (NHE) using Equations A4.3 and A4.4 as shown below:

$$E_V = -E_{\text{HOMO}} - 4.5 \quad (\text{A4.3})$$

$$E_C = -E_{\text{LUMO}} - 4.5 \quad (\text{A4.4})$$

The calculated values of E_V and E_C for the **RNIC** derivatives were documented in Table A4.15. Furthermore, the values of E_C and E_V at the point of zero zeta potential (PZZP) with a pH of 5.6 were computed using Equations A4.5 and A4.6, respectively, based on literature data.

$$E_{C,\text{pH}} = E_C + 0.059 \times (\text{PZZP} - \text{pH}) \quad (\text{A4.5})$$

$$E_{V,\text{pH}} = E_V + 0.059 \times (\text{PZZP} - \text{pH}) \quad (\text{A4.6})$$

Where, PZZP represents the points of zero zeta potential for the **RNIC** materials at pH 5.6. The estimated E_C and E_V values at a pH of 5.6 for **HNIC**, **PNIC**, **ANIC**, **NNIC**, **TNIC** and **BNIC** were also included in Table A4.15.

4.2.12. Cell studies

4.2.12.1. Cell culture: HeLa cells, originating from human cervix adenocarcinoma, were obtained from the Cell Line Bank Sigma Aldrich in India. These cells were cultured in Dulbecco's Modified Eagle Medium (DMEM), supplemented with 10% fetal bovine serum and 100 U/ml each of penicillin and streptomycin. The cell cultures were incubated in a controlled environment with 5% CO₂ at a constant temperature of 37 °C.

4.2.12.2. Cell Imaging: Initially, 5000 cells were placed into separate wells of a 96-well plate and cultured for 24 hours in a 37°C, 5% CO₂ humidified incubator using DMEM media. The medium was then replaced with fresh medium containing 30 μM **NNIC**, 10 μM **TNIC**, and **BNIC** individually. After a 4-hr incubation, cells were observed using time series

fluorescence microscopy. **NNIC**, **TNIC**, and **BNIC** were excited at 370 nm, and emissions were collected within the 450-660 nm range.

4.2.12.3. Dark & Light Cytotoxicity Evaluated by MTT assay: In the cell viability assay conducted on HeLa cancer cell lines, the 3-(4,5-dimethylthiazol-2-yl)-2,5-diphenyltetrazolium bromide (MTT) method was employed. Initially, 5000 cells were seeded into individual wells of a 96-well plate and allowed to incubate in DMEM media inside a 5% CO₂ humidified incubator at 37 °C for 24 hours. Subsequently, the cells were treated with various concentrations of **NNIC**, **TNIC** and **BNIC** compounds for 4 hours. After the 4-hour treatment, specific cell samples were exposed to white light using a handheld torch at 50 mW cm⁻² for 20 minutes. Following the light irradiation, the cells were further incubated with other treatment groups for an additional 24 hours at 37 °C in the same 5% CO₂ humidified incubator. Upon completion of the incubation period, the MTT assay was performed. This assay measures cell viability by evaluating the reduction of MTT by mitochondrial enzymes in viable cells, leading to the formation of a formazan product. The resulting formazan product's absorbance was measured spectrophotometrically at 570 nm, with a reference filter set at 655 nm. The absorbance of the formazan product was directly proportional to the number of viable cells present in the samples, allowing for the assessment of cell viability after treatment.

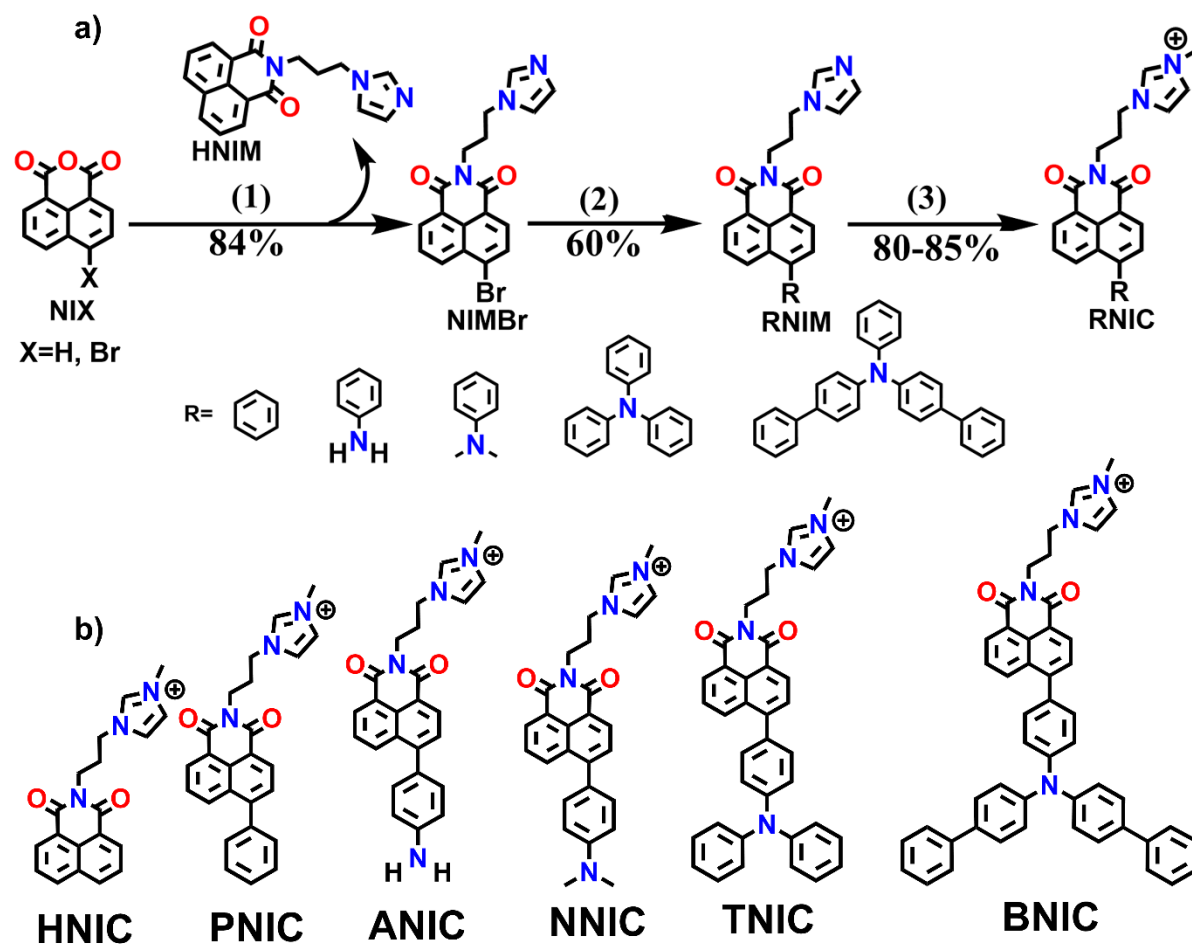
4.2.12.4. Live/dead cell co-staining assay: In the study, HeLa cells were initially seeded in 35-mm glass-bottomed dishes at a density of 3 x 10⁵ cells per dish and cultured overnight in standard culture media. Subsequently, the cells were treated with **RNIC** derivatives, such as **NNIC**, **TNIC** and **BNIC**, at a concentration of 50 μM for a duration of 4 hours. After the 4-hour treatment, the cells were subjected to white light irradiation using a handheld torch with a specific wavelength (50 mW cm⁻²) for 20 min. Following this, the cells were co-stained with 2 μM Calcein AM and 4 μM propidium iodide (PI) for 1h. After washing with DPBS (Dulbecco's Phosphate-Buffered Saline), fluorescence images of the cells were acquired using a fluorescence microscope. Additionally, another set of HeLa cells was treated with the same **RNIC** derivatives at a concentration of 50 μM for 4 hours. These cells were then treated with 2',7'-dichlorodihydrofluorescein diacetate (DCFDA) at 10 μM for 1 h. After washing with DPBS, the cells were irradiated with the same handheld torch (50 mW cm⁻²) for 30 minutes, and their fluorescence images were acquired. Moreover, HeLa cells were cultured in a normoxia environment for 24 hrs.

4.3. Result and Discussions

4.3.1. Design, synthesis and characterization of RNIC derivatives

With the aim of investigating supramolecular-assembly, condensed state photophysical properties and photosensitizing characteristics influenced by functional groups, ionic naphthalimide (**RNIC**) derivatives, namely **HNIC**, **PNIC**, **ANIC**, **NNIC**, **TNIC** and **BNIC** have been strategically designed and facilely synthesized. To influence the diverse range of applications such as sensing, therapeutics, optoelectronics, bioimaging with high fluorescence quantum yields and extraordinary thermal and chemical stability as well as excellent aggregation properties exhibited by naphthalimide cores, 4-bromo-1,8-naphthalic anhydride, a versatile precursor material, was carefully selected and subjected to a condensation reaction with 1-(3-amino propyl)-imidazole unit.^[31-34] This substitution step yielded a satisfactory yield of 81-84%. The entire process was documented in Scheme 4.1, A4.1. By employing Suzuki coupling, **NIMBr** was coupled with different boronic acid derivatives individually, resulting in the synthesis of different donor unit comprising of **RNIM** derivatives, namely **PNIM**, **ANIM**, **NNIM**, **TNIM**, and **BNIM** with satisfactory yields (Scheme 4.1, A4.2). Furthermore, effective methylation of the imidazole in **RNIM** was achieved using iodomethane, with a sequential process resulting in a satisfactory yield of 80% for the synthesis of **RNIC** derivatives such as **HNIC**, **PNIC**, **ANIC**, **NNIC**, **TNIC**, and **BNIC** (Scheme 4.1, A4.3). A rational approach for designing PSs with strong absorption in the long-wavelength range and enhanced production of ROS is to create a D-A structure. However, the strong intramolecular charge transfer in D-A structured PSs often leads to emission quenching in their aggregated-state. To overcome this ACQ effect, various donor functional groups were incorporated into the **NIC** core as molecular rotors and electron donors. The aim was to construct PSs with AIE, resulting in enhanced fluorescence and photosensitization in their aggregate-state. In this study, the incorporation of a phenyl ring at the fourth position of the **NIC** core was chosen to introduce the concept of AIE by RIR and providing a platform for hosting different functional groups.^[31,32] In addition **HNIC** to serving as controls, derivatives without donor functionality utilized to conduct a comprehensive analysis of the role played by different donor functional groups in their condensed state photophysical properties, solid state white light emission, and photosensitizing behavior. Moreover, the inclusion of imidazole ions is not only known for their notable electronic effects but also renowned for their targeting capabilities. The synthesized materials underwent comprehensive characterization using multinuclear NMR spectroscopy (¹H, ¹³C) and Matrix-Assisted Laser Desorption/Ionization (MALDI)

techniques. The detailed characterization data can be found in the Supporting Information (SI).



Scheme 4.1. (a) Synthetic route for the preparation of **RNIC** derivatives by substituting different donor functional groups at the peri-position of the ionic **NIC** core. (b) Chemical structure of the synthesized **RNIC** derivatives: **HNIC**, **PNIC**, **ANIC**, **NNIC**, **TNIC** and **BNIC**, respectively. [(1): 3-amino propyl imidazole, EtOH, 85°C, 8 h, (2): Pd(0), THF, H₂O, (3): Methyl iodide, DMF, 60°C, 4 h and Below arrow represent the yield of the corresponding product]. {Iodide ion (I⁻) has been omitted due to better clarity}.

4.3.2. Photophysical Properties

UV-vis absorption and fluorescence spectroscopy (PL) were used to explore the optical characteristics of **RNIC** derivatives (Figure 4.1, A4.1 and Table 4.1, A4.5). The structural architectures of strategically designed **RNIC** derivatives suggest that **PNIC** with a phenyl group can form a favorable extended delocalization to the **NIC** core in the solution state, resulting in 73 nm red-shifted absorbance maxima ($\lambda_{\text{abs.max}}$) compared to other **RNIC** derivatives (Figure 4.1a, and Table 4.1). Conversely, **BNIC**, which had the strongest donor group, displayed an unusual blue shifted $\lambda_{\text{abs.max}}$ of 22 nm ($\lambda_{\text{abs.max}} = 338$ nm) compared to **PNIC**. This unique behavior of **BNIC** could be attributed to less electronic communication

between the biphenyl donor and the acceptor **NIC** core. This could potentially due to the strong separation between HOMO and LUMO across the conjugation region of the molecule. Detailed insights into this phenomenon will be elucidated through subsequent theoretical investigations. Meanwhile, the remaining derivatives (**ANIC**, **NNIC**, and **TNIC**) showed closely aligned $\lambda_{\text{abs.max}}$ (287-310 nm) in the solution state. These derivatives exhibited a consistent blue shift of around 50-73 nm in $\lambda_{\text{abs.max}}$ compared to **PNIC**. This blue shifted $\lambda_{\text{abs.max}}$ was attributed to less π -conjugation, a consequence of increased donor functionality. The control derivative, **HNIC**, exhibited $\lambda_{\text{abs.max}}$ at 336 nm. Furthermore, in the solution state, a substantial adjustment of emission maxima ($\lambda_{\text{em.max}}$) was noted in accordance with their $\lambda_{\text{abs.max}}$, aligning well with the international commission on illumination (CIE) chromaticity diagram (Figure 4.1b, b' and Table 4.1, A4.5). Among these, **ANIC**, **NNIC**, and **TNIC** exhibited nearly identical $\lambda_{\text{em.max}}$ (505-534 nm), with a remarkable red shift of almost 123 nm compared to the control **HNIC** derivative. In contrast, both **PNIC** and **BNIC** demonstrated an identical $\lambda_{\text{em.max}}$ at 435 and 436 nm. The trend reveals that as the donor unit's strength increases, there is a corresponding red shift in $\lambda_{\text{em.max}}$. However, intriguingly, **BNIC**, which includes a potent donor unit, exhibited less $\lambda_{\text{em.max}}$ tuning due to reduced electronic communication in the solution state. Notably, the comparison of **HNIC** and **PNIC**'s solution state fluorescence implies a significant role played by the pendant phenyl ring. It extends conjugation to the **NIC** core, restraining excimer formation (Figure A4.1). In the aggregate and solid state, an extensive modulation of the $\lambda_{\text{em.max}}$ (~ 205 nm) occurred as donor functionality increased (Figure 4.1c, c', d, d' and Table 4.1, A4.5). Interestingly, this trend in emission spectra was unaffected by the electronic impact of functional groups. Notably, **ANIC** and **NNIC**, despite having the most red-shifted $\lambda_{\text{em.max}}$ in solution, displayed significant blue shifted $\lambda_{\text{em.max}}$ of 69 and 103 nm, respectively, in their aggregated-state compared to solution state. Conversely, **TNIC** and **BNIC** exhibited red shifted $\lambda_{\text{em.max}}$ of ~ 100 and 170 nm, respectively, in their aggregated-state relative to their solution state. The pronounced distinctions in these shifts find further elucidation through theoretical density functional theory (DFT) studies, encompassing both solution and aggregated-state. Distinctively, **HNIC** and **PNIC** exhibited nearly identical $\lambda_{\text{em.max}}$ in both their aggregated and solution state. Crucially, the wide spectrum of emission colors in the solution state, ranging from blue to green, was vividly displayed on the CIE chromaticity diagram. In the aggregated-state, the CIE plot showed colors in the blue to red region (Figure 4.1b', c', Table 4.1, A4.5). Whereas, comparing aggregated and solid-state emission spectra, **ANIC** and **NNIC** displayed significant red shifts in $\lambda_{\text{em.max}}$ of 170 and 154 nm in their solid state, respectively (Figure 4.1e, h and Table 4.1). Meanwhile, the remaining **RNIC** derivatives exhibited nearly identical emission profiles in both aggregated and solid states, attributed to a uniform degree of conjugation in their solid state akin to their aggregated-state-an aspect

elucidated later through excitation-emission matrix (EEM) matrices. Moreover, a distinct disparity in powder color became evident when subjected to white light and 365 nm UV irradiation, aligning precisely with the CIE chromaticity diagram. **HNIC** and **PNIC** emit white light in the solid state, while other **RNIC** derivatives emit distinctive red-orange light when powdered (Figure 4.1f, g and Table 4.1, A4.5). This highlights AIE properties controlled by functional groups, indicating condensed state photophysical properties' autonomy from electronic impacts.^[33-36] The functional group and anion- π^+ interaction between negatively charged iodine and positively charged **NIC** core play pivotal roles, influencing ionic naphthalimides' condensed state attributes through steric constraints. Unlike the prior focus on functional groups in neutral naphthalimide cores, this study exhibits the combination of functional groups and anion- π^+ interactions of imidazole unit for the development of distinctive condensed state properties.^[31] Although previous research mainly focused on either anion- π^+ ^[37-40] or D-A^[41,42] or counter ion effect^[43] effect design strategy to achieve distinct luminescence properties. Further, the functional groups and anion- π^+ interaction's role in perturbing intermolecular packing is explored via single crystal, SCXRD, Field emission scanning electron microscopy (FESEM), and EEM plot studies. Notably, the **NIC** materials incorporating distinct donor functionalities exhibited an exceptional stokes shift within the range of 113-245 nm, highlighting their remarkable performance. The isoquinoline-based materials **IQ-TPA** and **TPE-IQ-TPA** exhibited stokes shifts of 173 and 212, respectively (Table A4.3). This research presents the highest reported stokes shifted material to date.

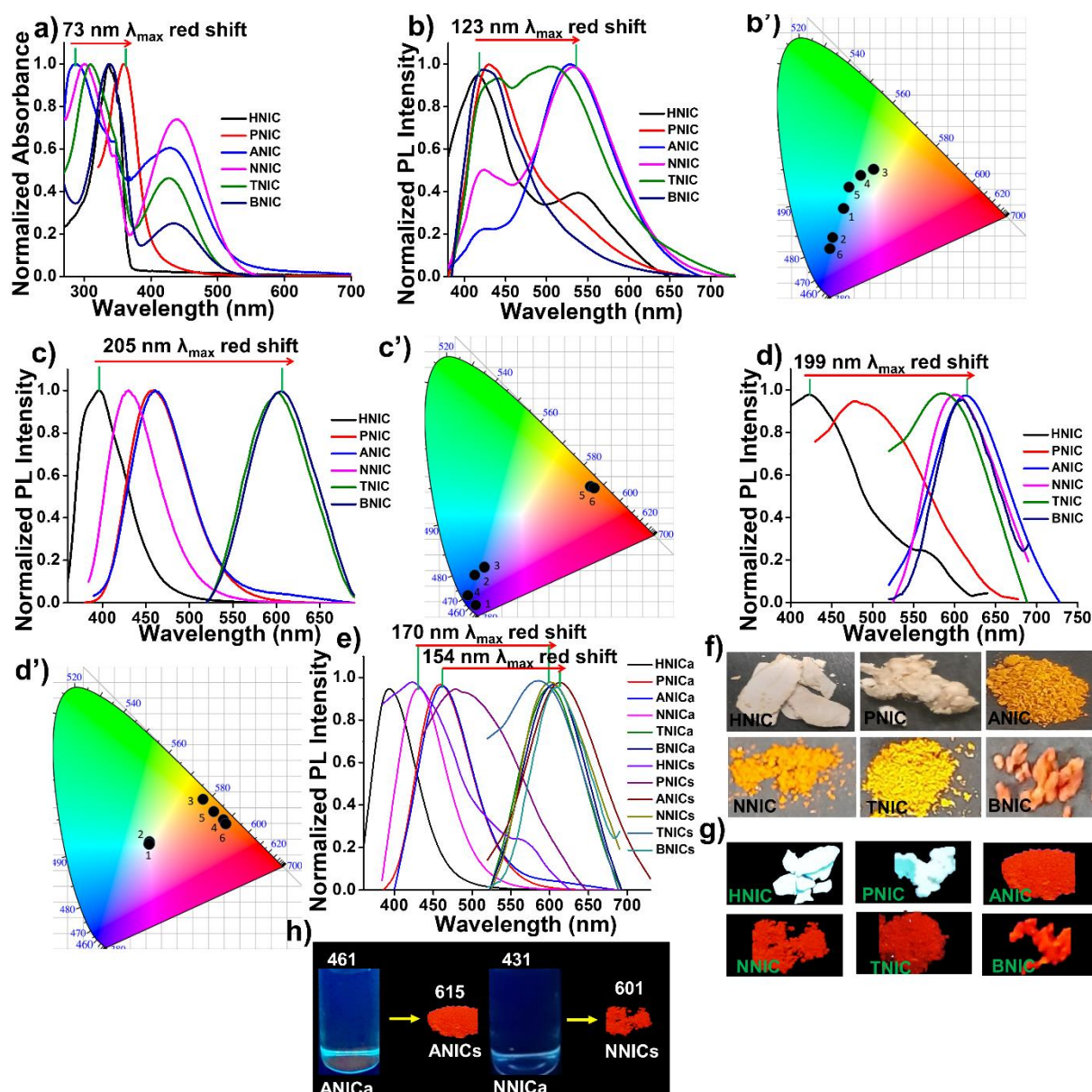


Figure 4.1. Photophysical properties of the **RNIC** derivatives (**HNIC**, **PNIC**, **ANIC**, **NNIC**, **TNIC** and **BNIC**). (a) Normalized UV-vis absorbance spectra in their solution state (in DMSO, 100 μ M). (b) The PL spectra. (b') The CIE chromaticity diagram represents solution state fluorescent color. (c) Normalized PL spectra at 99% f_w in DMSO. (c') Plot of CIE coordinate in their aggregated-state. (d) Solid state normalized PL spectra. (d') CIE chromaticity diagram plotted against solid state emission color. (e) Comparison of the PL spectra in their aggregated-state and solid state of the **RNIC** derivatives. (f and g) Digital photographs of solid **RNIC** derivatives in the powder form under day light and under UV excitation ($\lambda_{ex} = 365$ nm), respectively. (h) Digital photographs of **ANIC** and **NNIC** comparing aggregated and solid state photophysical behavior. [a, s represents the aggregated, and solid state, respectively. $\lambda_{ex} = 370$ nm, and $\lambda_{ex} = 350$ nm for **HNIC**, Inset in CIE: 1, 2, 3, 4, 5, 6 = **HNIC**, **PNIC**, **ANIC**, **NNIC**, **TNIC** and **BNIC**, respectively].

4.3.3. ACQ to AIE transformation

To assess the influence of aggregate formation on the fluorescence emission of **RNIC** derivatives, UV-vis and fluorescence spectra were acquired at varying f_w in DMSO (Figure

4.2, A4.2-A4.7, and Table 4.1, A4.6-A4.8). Across all **RNIC** derivatives **HNIC**, **PNIC**, **ANIC**, **NNIC**, **TNIC**, and **BNIC**-the $\lambda_{\text{abs.max}}$ were consistently observed within the 287-360 nm range (Figure A4.2 and Table A4.6). These peaks were attributed to the characteristic π - π^* transitions of the substituted **NIC** core. Additionally, a long-wavelength absorption peak at 450 nm emerged, a manifestation of intramolecular charge transfer (ICT) from the AIE donor to the acceptor **NIC** core. However, this peak was notably absent in **HNIC** and **PNIC**. To substantiate this ICT phenomenon, we focused on **NNIC**, **TNIC**, and **BNIC**, which encompass strong D-A components (Figure A4.3 and Table A4.7, A4.8). As solvent polarity increased, red shifts in both $\lambda_{\text{abs.max}}$ and $\lambda_{\text{em.max}}$ were evident. **NNIC** exhibited a 21 nm shift in $\lambda_{\text{abs.max}}$ and a 52 nm shift in $\lambda_{\text{em.max}}$. Likewise, **TNIC** displayed 15 nm and 49 nm shifts, and **BNIC** demonstrated 6 nm and 47 nm shifts in their long-wavelength $\lambda_{\text{abs.max}}$ and $\lambda_{\text{em.max}}$, respectively. The peculiar behavior of the ICT effect within **BNIC**, accompanied by an expanding donor group, can be attributed to the robust D-A conjugation. This interaction induces a reduction in electronic communication between the **NIC** core and the donor unit when in their diluted state. With an increase in the f_w , **ANIC**, **TNIC**, and **BNIC** exhibited nearly indistinguishable absorption spectra. A minor red shift of just 1 nm in the $\lambda_{\text{abs.max}}$ was observed at 99% f_w in contrast to 0% f_w . Conversely, **PNIC** displayed a 2 nm red shift in $\lambda_{\text{abs.max}}$, while **HNIC** exhibited a substantial 9 nm red shift, indicating the most pronounced j-aggregation among the **RNIC** derivatives (Figure A4.2 and Table A4.6). Intriguingly, while all the nitrogen (-N) comprising donor functionality consistently emitted red-orange light in the solid state, their response to AIE varied based on their functional groups as the f_w increased. Specifically, **HNIC** and **PNIC** displayed typical AIE characteristics, wherein their emission progressively intensified upon aggregation (Figure 4.2a-a", b-b", A4.4 and Table 4.1). **HNIC** comprising of single rigid aromatic core displayed AIEgenic behavior. These intriguing experimental findings, consistent across related compounds, disrupted the widely accepted RIM mechanism, thereby underscoring the dominant influence of intermolecular packing orientations among the aromatic cores. [33-36] It's worth noting that previous research revealed that neutral **HNI** and **PNI** cores exhibited AIE and ACQ traits, respectively. This highlights the significant influence of anion- π^+ interactions of imidazolium unit in tuning this emission behavior. These aspects will be further addressed in later discussions, specifically in the context of single-crystal X-ray diffraction (SCXRD) analysis. The role of anion- π^+ interactions in shaping the condensed state emission has been extensively investigated by various research groups. [37-40] The introduction of distinctive N-based donor functional groups, including aniline, dimethyl aniline, triphenylamine, or biphenyl amine, as seen in **ANIC**, **NNIC**, **TNIC**, and **BNIC**, renders the molecule an AIEE active compound. Notably, despite all the N-containing donor functionalities exhibiting peculiar AIEE behavior, they demonstrate diverse aggregation patterns. For instance, **ANIC** and **NNIC**

display a blue-shifted $\lambda_{em,max}$ at 461 nm and 431 nm, respectively at 99.9% f_w compared to 0% f_w (Figure 4.2c-c", d-d", A4.4 and Table 4.1). In contrast, **TNIC** and **BNIC** exhibit red-shifted $\lambda_{em,max}$ values at 603 nm and 604 nm, respectively, at 99.9% f_w compared to 0% f_w (Figure 4.2e-e", f-f", A4.4 and Table 4.1). At 0% f_w , **ANIC**, **NNIC**, **TNIC**, and **BNIC** exhibited $\lambda_{em,max}$ at 530 nm, 534 nm, 505 nm, and 436 nm, respectively. As f_w increased, emission intensity gradually decreased up to 20% f_w for **ANIC**, **NNIC**, and **TNIC**, and up to 40% f_w for **BNIC**. This decline can be attributed to the presence of twisted ICT characteristics. However, as f_w further increased in the solvent mixture, aggregation commenced in the **RNIC** derivatives, leading to a progressive elevation in fluorescence intensity. This pattern reflects the characteristic behavior of AIEE in **ANIC** and **NNIC**. Conversely, **TNIC** and **BNIC** demonstrated a progressive rise in emission intensity up to 60% f_w , coinciding with the onset of aggregation. Nevertheless, as more water was introduced into the solvent mixture beyond this point, the emission intensity diminished due to the occurrence of agglomeration. The distinctive emission behavior in N-based donor functionalized **RNIC** derivatives is attributed to specific intermolecular non-covalent interactions across varying solvents. Electronic contributions of functional groups appear insignificant in shaping the condensed state of these derivatives. The distinct emission wavelengths in each derivative suggest that structural arrangement or intermolecular interactions, rather than electronic effects, primarily shape their condensed state properties. An exceptional quantum yield of 0.98 at 99% f_w was exhibited by **PNIC**, marking a noteworthy instance of such a high Φ_{PL} in an aqueous environment. (Figure A4.6, A4.7, Table 4.1, A4.3, Equation A4.1). More importantly, a previously reported neutral **PNI** material showed negligible Φ_{PL} , highlighting the unique role of anion- π^+ interactions of imidazoiium moiety in achieving the highest Φ_{PL} observed in the current study. It's important to highlight that the existing literature has reported the highest Φ_{PL} values of 0.99 and 0.92, respectively. However, these measurements were conducted in the solution state using organic solvents such as toluene and dichloromethane. [44,45] Meanwhile, the **HNIC** derivative also exhibited a commendable Φ_{PL} of 0.61 at 99% f_w , standing as a comparable achievement at 99% f_w due to its excimeric emission and notable anion- π^+ interaction, which differs from the characteristics observed in previously reported **HNI** material. [31,46] In contrast, the remaining **RNIC** derivatives showed significantly lower Φ_{PL} values. However, **TNIC** and **BNIC** demonstrated 0.33 and an 0.99, respectively. In summary, the study anticipates that in the absence of substantial electronic influence, the distinct nature of functional motifs and varying strengths of anion- π^+ interactions of imidazolium unit among the derivatives yield differing degrees of steric constraints around the aromatic core. These steric constraints are pivotal in effectively modulating the intermolecular π - π stacking orientations within the **NIC** core, thereby profoundly impacting their condensed state photophysical properties.

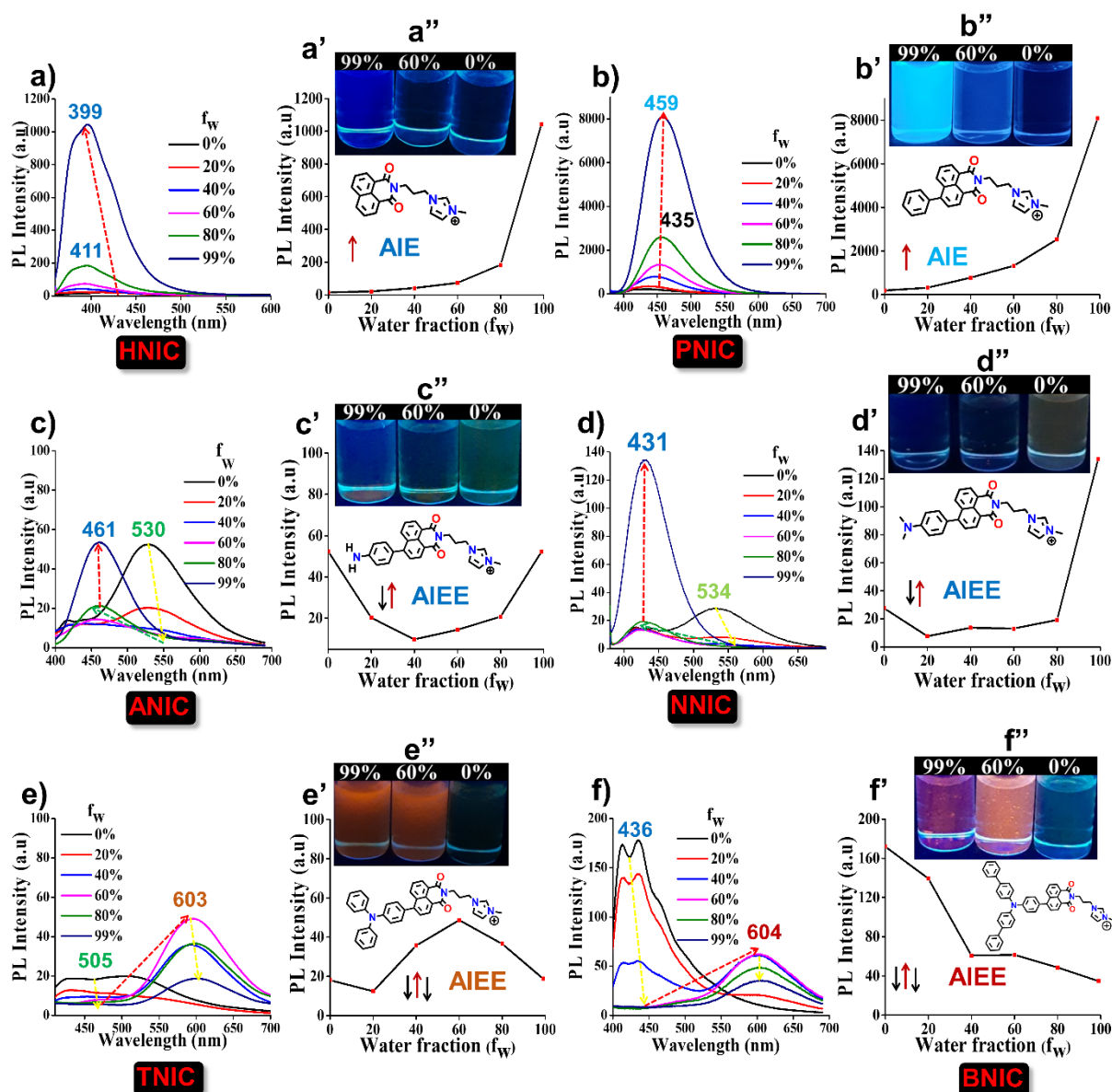


Figure 4.2. PL spectra of (a) **HNIC**, (b) **PNIC**, (c) **ANIC**, (d) **NNIC**, (e) **TNIC**, and (f) **BNIC**, respectively at various f_w in DMSO (100 μM , $\lambda_{\text{ex}} = 370$ nm, and 350 nm for **HNIC**). (a'-f') plots of $\lambda_{\text{em,max}}$ at different f_w along with Insets: (a''-f'') digital photographs under 365 nm UV illumination of the corresponding luminogens at 0%, 60% and 99% f_w in DMSO and their corresponding chemical structure. [Day light photograph of all the derivatives have been placed in Figure S5 in S1. {I- has been omitted due to better clarity}.

4.3.4. EEM spectra

Comparative EEM spectra were obtained for **RNIC** derivatives at various concentrations (100 μM to 1 mM) (Figure 4.3, A4.8). EEM spectroscopy offers insights into photophysical properties influenced by functional groups. Each EEM spectrum provides information about mixture constituents and a valuable technique for the comprehensive spectroscopic analysis of multifluorophoric. [47] Concentration-driven aggregation impacts these spectra. 2D EEM measurements spanned 390 to 650 nm, with excitation wavelength scanned from 300 to 500

nm in 10 nm increments. At 100 μM concentration, **PNIC** showed three asymmetric peaks in EEM spectra, while other derivatives had two peaks around molecular $\lambda_{\text{abs.max}}$. In dilution, **ANIC**, **NNIC**, and **TNIC** showed fluorophoric system with red-shifted λ_{ex} , while **BNIC** showed comparatively blue-shifted λ_{ex} contour profile. Higher concentrations (300 and 500 μM) led to broader contour profiles, indicating multifluorophoric components absorbing a diverse range of light. An important observation pertains to the behavior of various N-containing donor functional derivatives: **ANIC**, **NNIC**, and **TNIC** exhibited consistent red-shifted λ_{ex} contour profiles at 1 mM concentration. **BNIC** had more pronounced red-shifted λ_{ex} contour profile at higher concentration. In contrast, the behavior of **HNIC** and **PNIC** remained uniform across both diluted and concentrated states, suggesting a stable and unchanging fluorescence profile. The emergence of distinct emissive species at various λ_{ex} points within the EEM spectra corresponds directly to the level of conjugation. [47,48] Specifically, red-shifted contour profiles are indicative of new emissive species characterized by higher degree of conjugation, whereas blue-shifted profiles signify a decrease in conjugation. Therefore, the photophysical characteristics of **RNIC** in its condensed state, notably at elevated concentrations, are predominantly shaped by intermolecular interactions. These interactions are likely reinforced by distinct steric constraints imposed by the diverse functional components present in the derivatives.

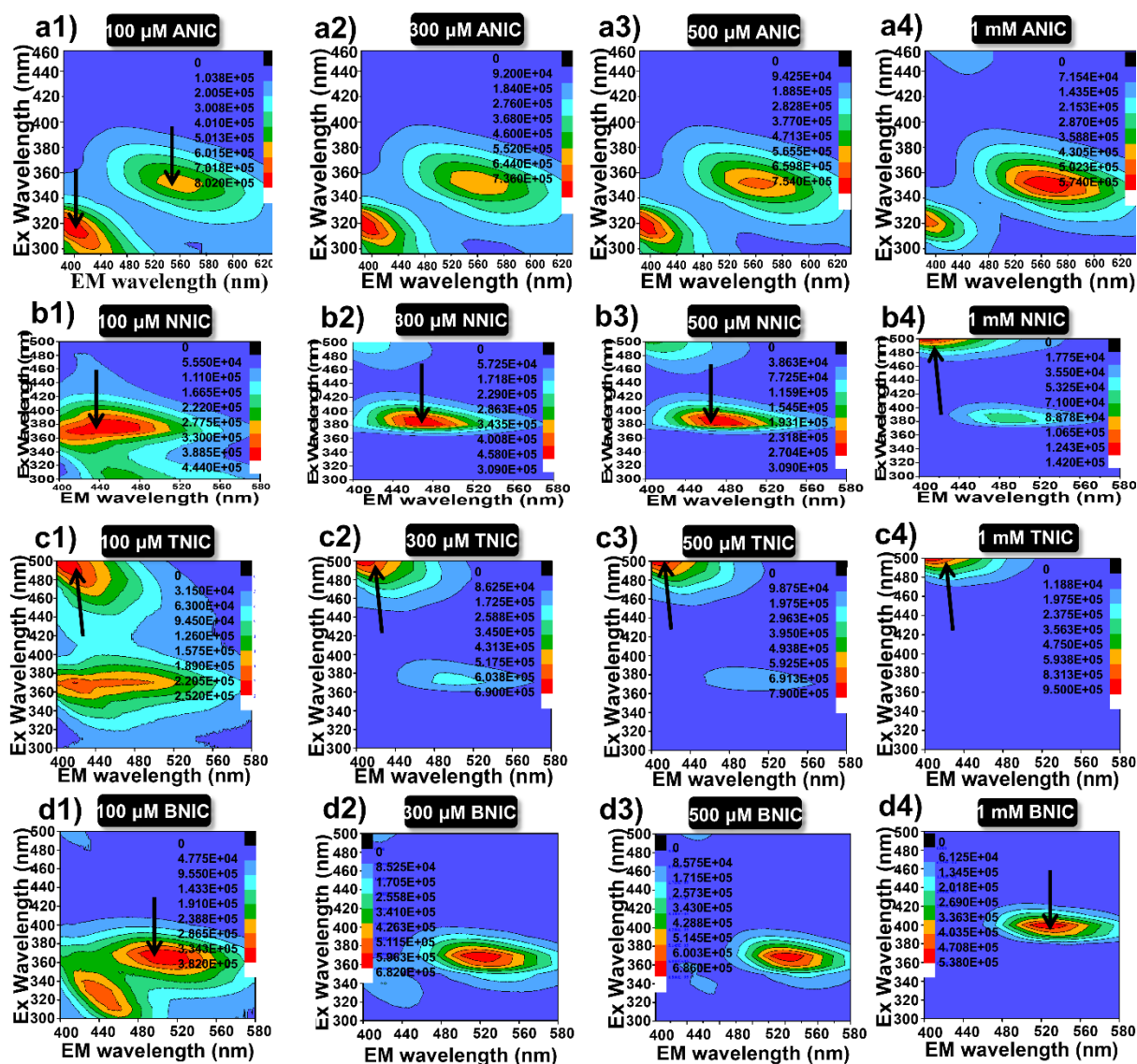


Figure 4.3. (a1-d4) Excitation-emission (EEM) 2D contour plot of the **RNIC** luminogens from lower to higher concentrations (left: 100 μM ; middle: 300 μM and 500 μM ; right: 1 mM) in DMSO.

4.3.5. Supramolecular assembly modulate condensed state luminescence

The luminescence characteristics of **RNIC** derivatives were examined using FESEM depicted (Figure 4.4 and A4.9-A4.11). These FESEM images captured the spontaneously formed self-assemblies of **RNIC** derivatives, employing a straightforward and cost-effective drop-casting technique followed by air-drying at room temperature. Morphological analysis of supramolecular assemblies at 99% f_w was conducted to examine photophysical behavior. Notably, the morphological transformations exhibited remarkable diversity, underscoring the exceptional adaptability of these **RNIC** derivatives, which offer an expansive array of potential structural outcomes. **HNIC** and **BNIC** yielded nano-ribbons (150 nm and 130 nm)

confirmed by dynamic light scattering (DLS) studies (Figure 4.4a, a', and f, f', A4.11). **TNIC** displayed non-spontaneous nano-ribbons (105 nm), while **PNIC** and **ANIC** formed nano-rods and honey-comb type nano-porous structures, respectively (Figure 4.4b, b', c, c', e, e', and A4.10). **NNIC** adopted a micro-rod configuration (Figure 4.4d, d'). **PNIC's** high Φ_{PL} resulted from its nano-rod assembly, possibly due to donor phenyl units and strong anion- π^+ interactions of imidazolium moiety. Structural order in self-assemblies correlated with emission intensity. [49-51] Literature suggests emission decline at higher f_w due to agglomerate formation from stronger stacking interactions. [52] Energy-dependent endocytosis plays a crucial role in micro-sized particle uptake. Particle morphology's impact on selective intracellular accumulation has been extensively studied through existing literature. [53,54]

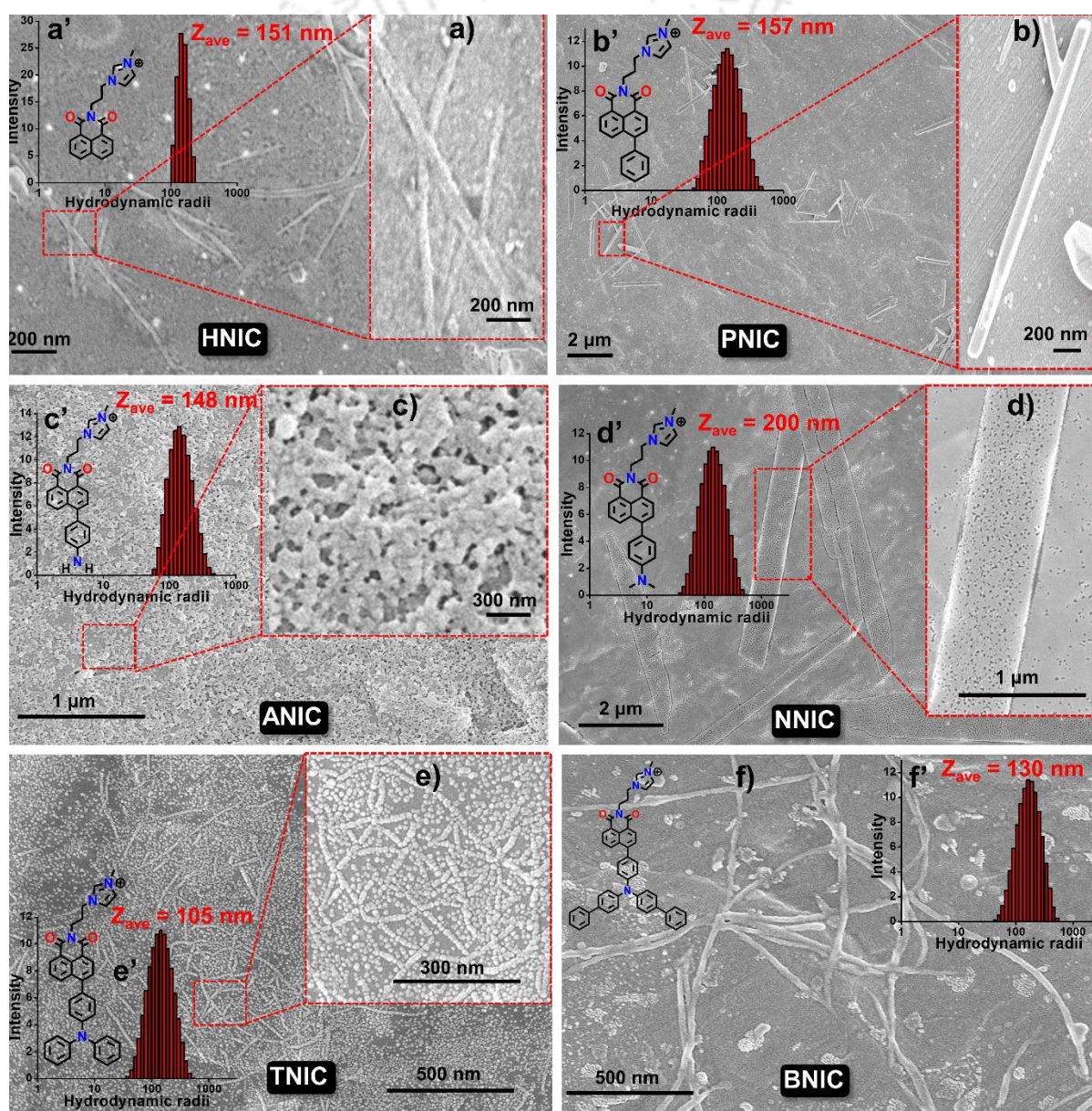


Figure 4.4. FESEM images of the nano and micro assembly of the **RNIC** derivatives spontaneously formed at 99.9% f_w in DMSO (100 μ M). Insets: The chemical structure of the **RNIC** (left) and the magnified images at the

selected area (right), (a'-f) Hydrodynamic radius vs intensity plot of all the **RNIC** luminogens at 99.9% f_w in DMSO (100 μ M).

4.3.6. SCXRD analysis

To gain deeper insights into the modulation potential of distinct donor functional groups and anion- π^+ interactions of imidazole unit on intermolecular interactions and packing configurations of **RNIC** derivatives, detailed examinations were conducted using single-crystal analysis. (Figure 4.5, A4.12 and Table A4.9). **HNIC** yielded successful single crystals from DMF. However, despite persistent attempts, the single crystals obtained for other derivatives proved inadequate for analysis through SCXRD. **HNIC** undergoes J-aggregation in its aggregated-state, confirmed by a 9 nm red-shifted $\lambda_{\text{abs,max}}$ in UV-vis spectroscopy (Figure A4.2 and Table A4.6). However, an antiparallel dimer arrangement arises from close intermolecular π - π -stacking interactions, compactly spaced at 3.4 Å. This diverges from previous **HNI** findings, where this phenomenon was absent. These distances are shorter than the typical π - π stacking of 3.5 Å. Along with, the angle between two dimer is 57.70°, which is larger than the typical value of 54.7°. This stacking prompts excimer formation, observing low-energy band intensity in **HNIC**'s PL spectra. Each dimer is further arranged within a distinct dimeric plane through multiple anion- π^+ interactions of imidazole unit (3.308-3.507 Å). These interactions involve negatively charged iodine and the positively charged **NIC** core. Moreover, additional intermolecular C=O \cdots H bonds (2.261 - 2.717 Å) and C-H \cdots π interactions (3.384 Å) occur between the imidazole section of pendant alkyl chains and **NIC** core. These interactions curtail π - π stacking, averts emission quenching by fortifying lattice rigidity. Varied interactions, including proximity-based π - π stacking, yield a brickwork configuration within the crystal plane, inducing AIE characteristics in **HNIC**. The anion- π^+ of imidazole component critically influences this altered intermolecular packing in the condensed state, distinguishing it from prior **HNI** observations. [31,55]

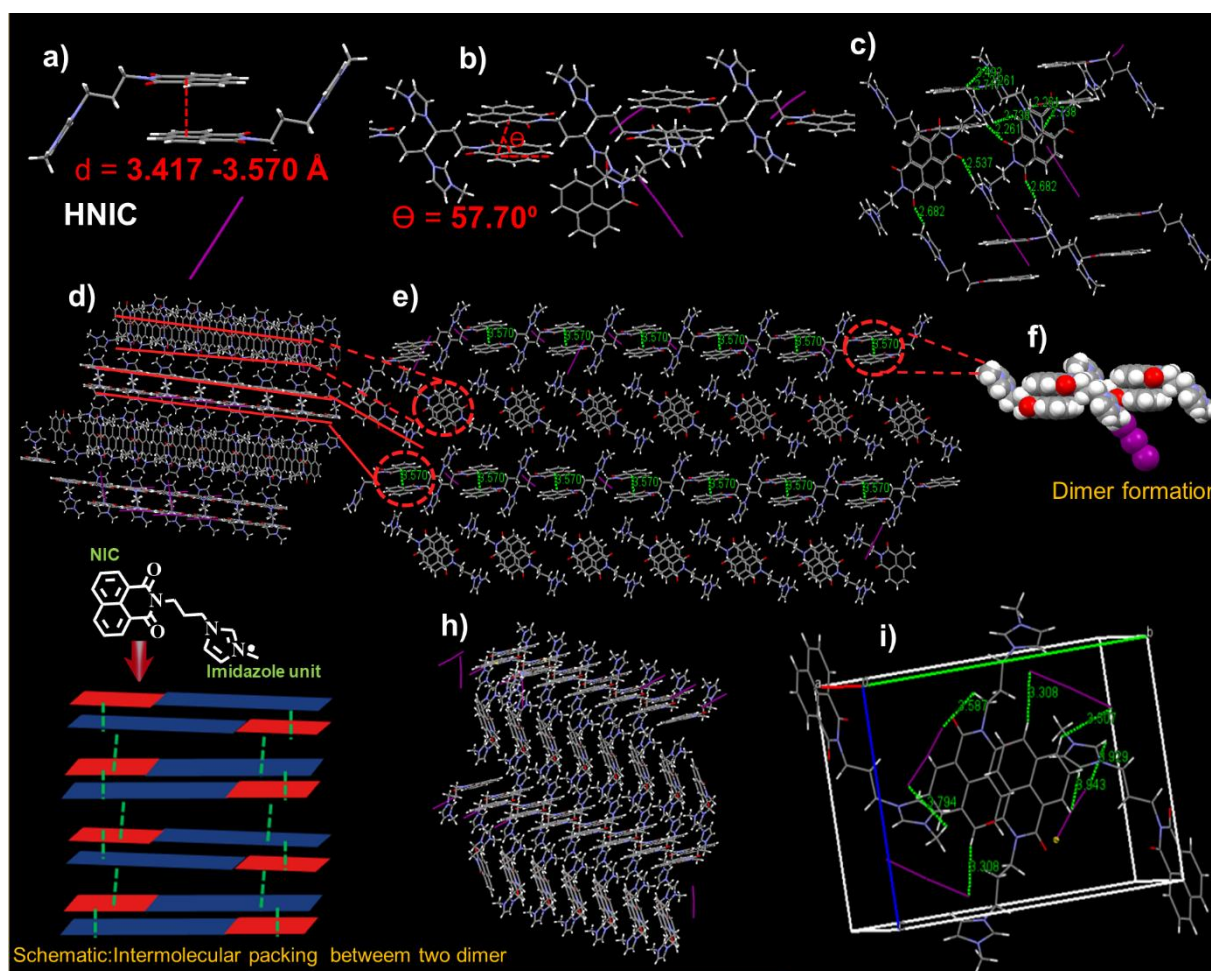


Figure 4.5. Single crystal structure of **HNIC** lumonogen via SCXRD. (a) The intermolecular plane distance. (b) The slip angle between transition dipoles and the interconnected axis is indicated by θ . (c) Different intermolecular interaction (C=O...H) between dimer in **HNIC** crystal lattice. (d, e) Insight of molecular packing arrangement showing two distinct dimeric plane. (f) Dimer formation in **HNIC** crystal lattice. (g) Anti parallel packing mode of the dimer in **HNIC**, as well as exhibiting interaction between two distinct dimeric plane. (h) Brickwork configuration in **HNIC** crystal lattice. (i) Single crystal unit cell of **HNIC** showing anion- π^+ interaction.

4.3.7. Electronic properties controlled the photophysical properties

A thorough DFT analysis (B3LYP/6-31G (d, p) method) substantiated the impact of **RNIC** derivatives' electronic attributes on their photophysical behavior (Figure 4.6a, A4.13 and Table 4.1). A noticeable trend emerged in the gaseous phase, revealing decreasing HOMO/LUMO band gaps with stronger donor functional units: 3.76 eV (**HNIC**), 3.36 eV (**PNIC**), 2.48 eV (**ANIC**), 2.14 eV (**NNIC**), and 1.87 eV (**BNIC**). LUMOs localized in the imidazolium cationic part due to its electron-withdrawing nature, while HOMOs exhibited distinct arrangements. **HNIC** and **PNIC** displayed extensive HOMO coverage over the **NIC**

core, promoting π -electron delocalization and red-shifted $\lambda_{\text{abs,max}}$ in UV-vis spectroscopy. **TNIC** and **BNIC** exhibited pronounced CT, with electron clouds transferring to potent donor regions (triphenyl and biphenyl segments), leading to substantial Stokes shifts. However, increased donor functionality reduced π -electron delocalization throughout the entire molecule, indicating decreased electronic communication, corresponding to shorter-wavelength absorption and emission. HOMOs for all the **RNIC** derivatives mainly localized within well-defined regions like phenyl, aniline, triphenylamine, or biphenyl amine. The pronounced push-pull electronic nature, along with extended π conjugation, contributed to red-orange emissive traits in **TNIC** and **BNIC**. DFT studies clarified blue-shifted emission in aggregated **ANIC** and **NNIC** versus solution. Destabilized LUMOs in **ANIC** and **NNIC** caused this distinct property. In contrast, higher HOMO destabilization in **TNIC** and **BNIC** led to their red-shifted emission at aggregated-state compared to solution state. [56-58]

4.3.8. Solid state white light emission

Advancing white-light-emitting materials is pivotal for upcoming solid-state lighting technologies. Two strategies are employed: multiple cooperating emitters and a single multifunctional emitter. Both generate at least two emissions (e.g., bluish-green and reddish-orange) to form white light. Single emitter strategy excels due to reduced phase separation issues. [59] Designing single molecules with AIE for consistent emission across visible spectrum remains challenging. The conventional benzothiophene molecule (CIBDBT) material showed white dual phosphorescence from T_1 and T_2 states in a solid state. [60] Some compounds exhibit two or three bands, suggesting multiple processes at play. By involving radiative decay from both the individual excited-state molecule and the appropriate-colored excimer/excimer, the attainment of white light is feasible. The emissions observed are most likely best explained by excimeric emission or fluorescence emission from S_1 in a distorted geometry. [55,60] Here, **HNIC** and **PNIC** AIEgens emit white light under 365 nm UV excitation (CIE 0.34,0.33 for **HNIC**, 0.34,0.32 for **PNIC**) (Figure 4.1d', g). Notably, previously reported neutral naphthalimide derivatives **HNI** and **PNI**, respectively lack these traits. **HNIC**'s white light emission likely involves AIE and excimer formation in solid state, evidenced by dimeric packing and excimeric emissions in their solution and solid state (Figure 4.5, and A4.1a, a'). This interaction spans the spectrum from blue to yellowish-orange, producing white light. **PNIC**'s white light emission results from energy transfer and charge transfer processes, covering bluish-green to yellowish-orange (Figure A4.1b, b'). The charge transfer process is supported by DFT studies, evident in notable HOMO-LUMO separation (Figure 4.6a). HOMO localizes in the donor phenyl segment, while LUMO resides in the imidazolium component. The previously reported conventional **HNI** and **PNI** materials share similar core with **HNIC** and **PNIC**, differing only in minor variations in

pendant alkyl chains. Notably, these (**HNI** and **PNI**) materials do not possess the mentioned characteristics. However, **HNI** does show excimeric emission, whereas **PNI** exhibits $\Phi_{\text{PL}} \approx 0.00$. Thus, this unique property results from the additional anion- π^+ interaction of the imidazolium component, which contributes a distinct magnitude of steric strength to the intermolecular packing arrangement in the solid state. Counter-anion profoundly impacts emission properties, offering avenues for future tuning. [43] This work presents the rarest single-component solid-state white light emissive AIE material integrating anion- π^+ interaction with AIE, employing AIE-excimer-anion- π^+ or AIE-ET-CT-anion- π^+ pathways. Notably, the reported pyrillium ionic fluorescent dye and the ionic BODIPY AIEgen has been achieved for single-component solid-state white light emission (Table A4.4). [61,62] However, it's essential to highlight that their materials primarily exhibited white light emission in the solution state. Notably, a novel mechanism for white light emission in the solid state has been introduced by this unique and very facile design principle.

4.3.9. Theoretical Calculation

As the electron-donating ability of the donor increased, D-A interaction intensified, reducing HOMO-LUMO gap. **TNIC** and **BNIC** had low energy gaps (1.87 and 1.79 eV), aligned with their optical properties (Figure 4.6a, b, and Table 4.1, A4.10-A4.12). [41,63,64] **HNIC** without a donor unit showed a higher gap (3.76 eV). Effective HOMO-LUMO separation led to small ΔE_{ST} values. **BNIC** had lowest $\Delta E_{\text{S}_1\text{T}_1}$ (0.00 eV). Significant SOC (3.17 cm^{-1}) and low $\Delta E_{\text{S}_2\text{T}_5}$ (0.056) in **HNIC** arose from $\text{S}_2\text{-T}_5$ transition due to distinctive excimer formation, supported by SCXRD and photophysical analyses. **HNIC** showed notable SOC values ($2.45, 1.930, 0.32, 0.30 \text{ cm}^{-1}$), unique to its design. This unveils an innovative mechanism for efficient AIE PSs, rather than relying solely on the conventional D-A design strategy. While numerous research groups have showed achievements in excimer-based phosphorescence, [55,65] solid-state white light emissive materials, [60,61,66] delayed fluorescence or Φ_{PL} , [46] the concept of utilizing excimer-based PSs remains unexplored until now. While a heavy atom-free thiobased naphthalimide PS (**NI-S PS**) has been reported, it's noteworthy that their approach adeptly incorporates the D-A design strategy to achieve highly efficient triplet formation. [45] Consequently, this study marks the novel phenomenon of an excimer-based PS, setting a new approach in the field. Notably, **PNIC** exhibited a significant SOC of 1.265 cm^{-1} for the S_2 to T_3 transition, accompanied by a $\Delta E_{\text{S}_2\text{T}_3}$ value of 0.045 eV. In contrast, the remaining derivatives including **ANIC**, **NNIC**, **TNIC**, and **BNIC** demonstrated moderate SOC values of 0.45, 0.33, 0.10, and 0.22 cm^{-1} , correspondingly, coupled with ΔE_{ST} values of 0.498, 0.436, 0.309, and 0.201 eV. The observed outcome exceeded the initial expectations, particularly considering **BNIC**'s highly enhanced electron D-A nature. Consequently, **HNIC** and **PNIC** excel as solid-state white light-emitting AIE PSs, while **ANIC**, **NNIC**, **TNIC**, and

BNIC are effective solid-state red-orange emission AIEE PSs. This innovative design approach emphasizes excimer-based and D-A design principles, demonstrating their importance for advancing materials in practical applications.

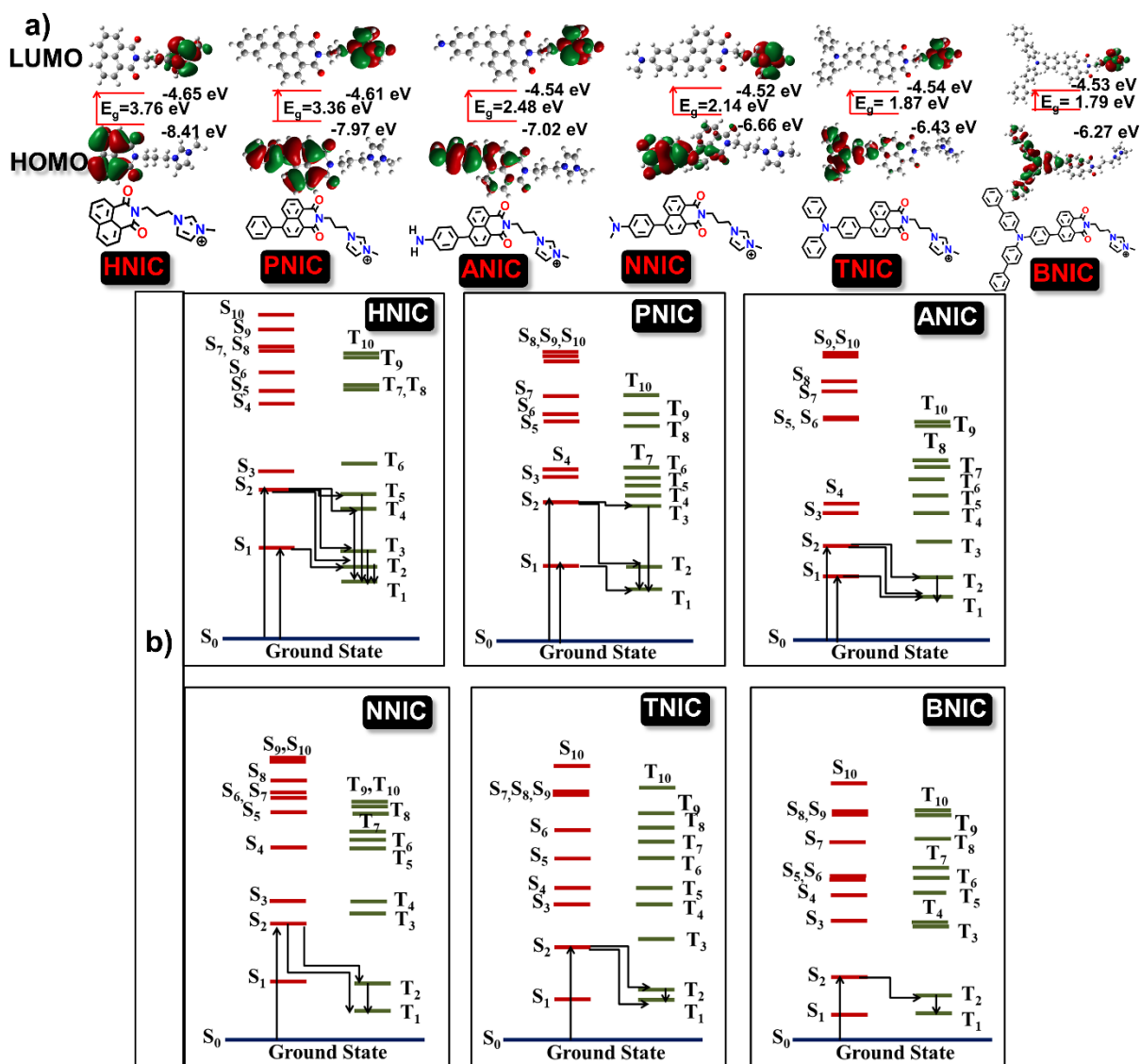


Figure 4.6. (a) Frontier molecular orbitals (HOMO and LUMO) with energies in eV calculated from the DFT/B3LYP method using the 6-31G (d, p) basis set by Gaussian 16 software in their ground state. Below the chemical structure of the respective luminogens. {I⁻ has been omitted due to better clarity}. (b) SOC Calculated by SOC-TDDFT method Using ORCA 5.0 Software for all the derivatives. **HNIC**, **PNIC**, **ANIC**, **NNIC**, **TNIC** and **BNIC**, respectively. [**HNIC**: $\Delta E_{S_1T_1} = 0.935$, $\Delta E_{S_1T_2} = 0.064$, $\Delta E_{S_2T_2} = 0.517$, $\Delta E_{S_2T_3} = 0.456$, $\Delta E_{S_2T_4} = 0.266$, $\Delta E_{S_2T_5} = 0.056$, $\zeta(S_1, T_1) = 0.00 \text{ cm}^{-1}$, $\zeta(S_1, T_2) = 0.32 \text{ cm}^{-1}$, $\zeta(S_2, T_2) = 2.45 \text{ cm}^{-1}$, $\xi(S, T_3) = 0.30 \text{ cm}^{-1}$, $\xi(S_2, T_4) = 1.930 \text{ cm}^{-1}$, $\xi(S_2, T_5) = 3.170 \text{ cm}^{-1}$. **PNIC**: $\Delta E_{S_1T_1} = 0.674 \text{ eV}$, $\Delta E_{S_2T_2} = 0.358 \text{ eV}$, $\Delta E_{S_2T_3} = 0.045 \text{ eV}$, $\xi(S_1, T_1) = 0.20 \text{ cm}^{-1}$, $\xi(S_2, T_2) = 0.30 \text{ cm}^{-1}$, $\xi(S_2, T_3) = 1.265 \text{ cm}^{-1}$. **ANIC**: $\Delta E_{S_1T_1} = 0.205 \text{ eV}$, $\Delta E_{S_2T_1} = 0.498 \text{ eV}$, $\Delta E_{S_2T_2} = 0.293 \text{ eV}$, $\xi(S_1, T_1) = 0.22 \text{ cm}^{-1}$, $\xi(S_2, T_1) = 0.45 \text{ cm}^{-1}$, $\xi(S_2, T_2) = 0.14 \text{ cm}^{-1}$. **NNIC**: $\Delta E_{S_1T_1} = 0.003 \text{ eV}$, $\Delta E_{S_2T_1} = 0.436 \text{ eV}$, $\Delta E_{S_2T_2} = 0.429 \text{ eV}$, $\xi(S_1, T_1) = 0.173 \text{ cm}^{-1}$, $\xi(S_2, T_1) = 0.33 \text{ cm}^{-1}$, $\xi(S_2, T_2) = 0.28 \text{ cm}^{-1}$. **TNIC**: $\Delta E_{S_1T_1} = 0.001 \text{ eV}$, $\Delta E_{S_2T_1} = 0.309 \text{ eV}$, $\Delta E_{S_2T_2} = 0.294 \text{ eV}$, $\xi(S_1, T_1) = 0.10 \text{ cm}^{-1}$, $\xi(S_2, T_1) = 0.10 \text{ cm}^{-1}$, $\xi(S_2, T_2) = 0.10 \text{ cm}^{-1}$. **BNIC**: $\Delta E_{S_1T_1} = 0.00 \text{ eV}$, $\Delta E_{S_2T_1} = 0.319 \text{ eV}$, $\Delta E_{S_2T_2} = 0.201 \text{ eV}$, $\xi(S_2, T_1) = 0.00 \text{ cm}^{-1}$, $\xi(S_2, T_1) = 0.00 \text{ cm}^{-1}$, $\xi(S_2, T_2) = 0.22 \text{ cm}^{-1}$].

4.3.10. Singlet Oxygen (Type 2 ROS) Detection

Motivated by the substantial SOC and abundant population of excited state triplets in **RNIC** materials, we embarked on an investigation into their Φ_{Δ} using ABDA as a commercially available probe for quantifying $^1\text{O}_2$ (Figure 4.7a, A4.14, A4.15, Table 4.1 and Equation A4.2). Clearly, **NNIC** stands out with the highest Φ_{Δ} value of 0.95 at 99% f_w . In contrast, **TNIC** and **BNIC** showed moderate Φ_{Δ} values of 0.017, whereas the signal indicating $^1\text{O}_2$ generation was non-existent for all the **RNIC** derivatives tested under identical conditions. In summary, the higher Φ_{Δ} values observed for **NNIC** signify the efficient type-II processes, while **TNIC** and **BNIC** display moderate type-II processes. On the other hand, **HNIC** and **PNIC** display no detectable generation of $^1\text{O}_2$. Notably, **NNIC** showed the highest Φ_{Δ} value reported thus far within an aqueous medium (Table A4.2, A4.3). It's important to acknowledge that recently reported materials such **TPA** containing AIEgen (**MeTTPy**), thio-based non-fluorescent naphthalimide (**NI-PSs**) and triphenyl amine (**TPA**) comprising ionic another ionic luminogens (**LOCK**), respectively have been exhibited even higher Φ_{Δ} values, such as 0.91, 1.0, and 1.1 (Table A4.3). However, it's noteworthy that these elevated values were attained in solvent systems like toluene or THF.

4.3.11. Total ROS generation evaluation

To address lower Φ_{Δ} values, the collective potential for ROS generation by **RNIC** derivatives was assessed. Increased PL intensity was observed in the aggregated-state (99% PBS fraction in DMSO, f_{PBS}) under white light, using 2,7-dichlorodihydrofluorescein (DCFDA), which is sensitive to ROS (Figure 4.7b, A4.16). Enhanced donor functionality correlated with higher ROS generation efficiency. After 10 minutes of light, **BNIC**, **TNIC**, **NNIC** showed 160-fold, 160-fold, and 120-fold PL intensity increases with DCFDA. **HNIC**, **PNIC**, **ANIC** exhibited 45-fold, 10-fold, 25-fold enhancements. These results collectively indicate both type-I and type-II processes contributed to ROS generation. Notably, within 3 minutes, using minimal 1 μM DCFDA, **BNIC**, **TNIC**, **NNIC** displayed 2×10^6 , 1×10^6 , 1×10^6 enhancements, while **HNIC**, **PNIC**, **ANIC** showed 5×10^5 , 1×10^4 , 2×10^5 enhancements. **HNIC**'s PL increase, despite lacking donor group, highlights unconventional D-A strategy's ROS generation. **BNIC**'s efficient ROS production owes to donor biphenyl amine group, reducing ΔE_{ST} due to strong HOMO/LUMO separation, thus facilitating efficient triplet population. **BNIC** AIEE PS shows prominent total ROS generation compared to recent PSs (Table A4.1). **TNIC** and **NNIC** are second-tier efficient AIEE PSs.

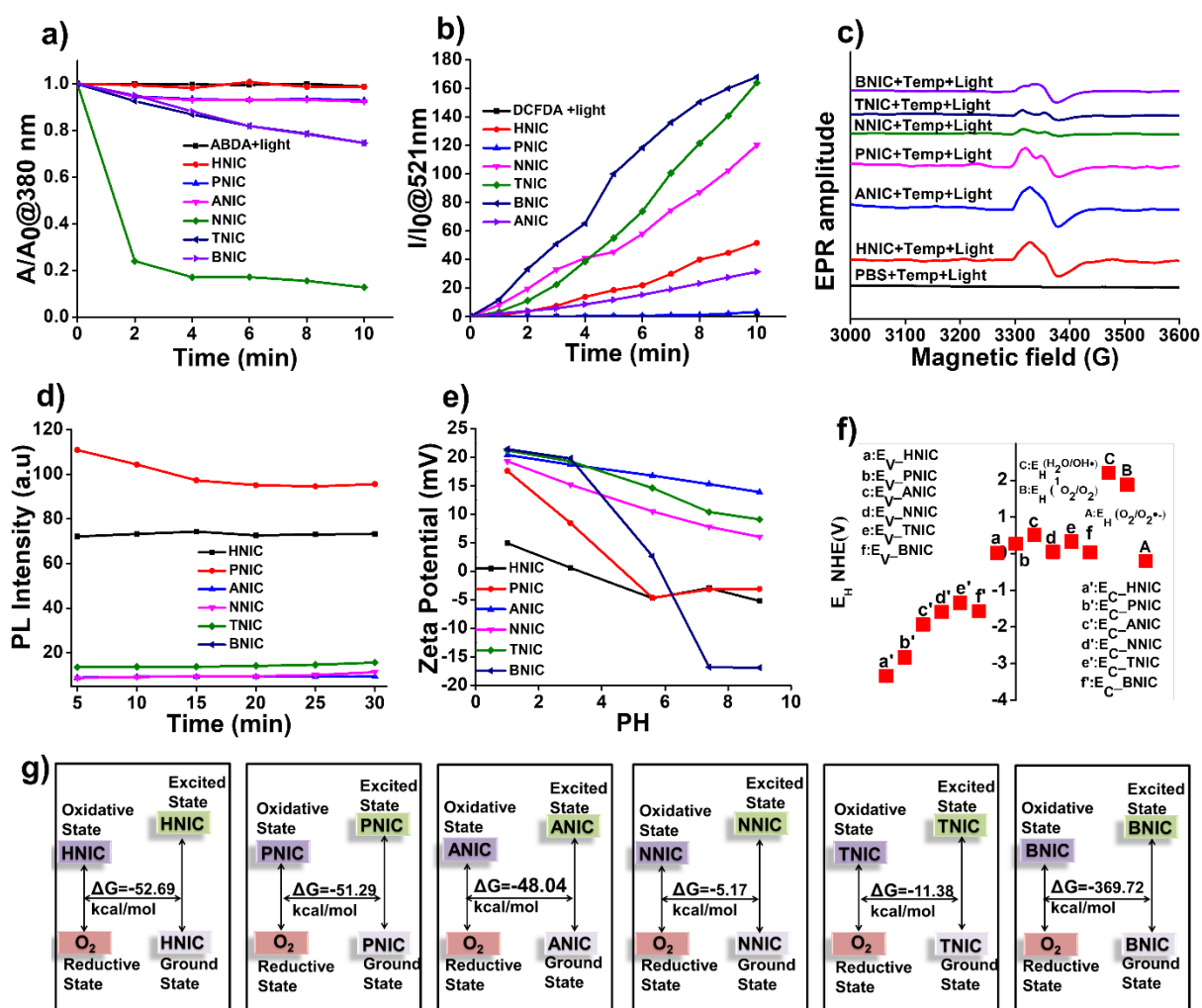


Figure 4.7. (a) Plots of ABDA (100 μM) decomposition rates at $\lambda_{\text{abs,max}}$ of 380 nm by the various PSs (100 μM). (b) Plot of PL intensities of DCFDA indicator in the presence of **RNIC** derivatives. A_0 and A are ABDA absorbance at $\lambda_{\text{abs,max}}$ of 380 nm, where, I_0 and I are the PL intensities of the indicator at $\lambda_{\text{em,max}}$ of 521 nm before and after irradiation of the white light, respectively. (c) EPR signals at their aggregated-state. (d) PL spectra of TA in the presence of **RNIC** derivatives at 528 nm. (e) Zeta potential versus pH values of **RNIC** derivatives. (f) E_c and E_v of **RNIC** derivatives at pH 5.6. The energy scale is expressed in relation to NHE. (g) Gibbs free energy changes of **HNIC**, **PNIC**, **ANIC**, **NNIC**, **TNIC** and **BNIC**, respectively, via ORCA 5.0 SOCME module at the B₃LYP DEF2-SVP level. [Aggregated-state: 99% PBS fraction in DMSO, f_{PBS}].

4.3.12. Radical (Type 1 ROS) detection

The study aimed to evaluate the capacity of **RNIC** derivatives to generate free radicals through electron spin resonance (ESR) to effectively captured $O_2^{\cdot-}$ and hydroxyl (HO^{\cdot}) (Figure 4.7c). The experiments were conducted using 2,2,6,6-tetramethyl-4-piperidinol (TEMP) as a free radical trapper. The **RNIC** derivatives were examined under white light irradiation in a condensed state (99% f_{PBS}). Remarkably, the **RNIC** derivatives exhibited ESR signals within a short span of 10 min under white light irradiation. To further investigate the ROS generation capabilities, terephthalic acid (TA) was utilized as a probe to detect HO^{\cdot} .

(Figure 4.7d).^[64] The fluorescence intensity of the **RNIC** probes remained relatively unchanged when subjected to white light irradiation for 30 min, implying that the production of HO· radicals by the **RNIC** derivatives was not significant. These observations were in harmony with the electrochemical characteristics exhibited by the **RNIC** derivatives. These properties provided corroborating evidence for a type-I photosensitization mechanism, involving the generation of O₂^{·-} through electron transfer from triplet excited states to ³O₂. The energy levels of the **RNIC** derivatives were estimated using E_{HOMO} and E_{LUMO} (Figure 4.7e, A4.17, A4.18, Table A4.13-A4.15, Equation A4.3-A4.6).^[64] The points of zero zeta potential for **HNIC**, **PNIC**, **ANIC**, **TNIC** and **BNIC** were calculated to be 0.627, 8.46, 13.9, 6.02, 9.1 and 2.63, respectively (Figure 4.7e and Table A4.15). Valence band energy (E_V) was obtained from X-ray photoelectron spectroscopy (XPS) data, while conduction band energy (E_C) was estimated from the energy gap derived from the onset absorption data acquired through UV-visible spectroscopy (Figure A4.17, A4.18 and Table A4.14, A4.15). As a result, the E_C values of **HNIC**, **PNIC**, **ANIC**, **NNIC**, **TNIC** and **BNIC** derivatives were calculated to be -3.3344, -2.83126, -1.9373, -1.59022, -1.3435 and -1.57523 eV at a pH of 5.6, respectively (Figure 4.7f and Table A4.15). These values are lower than the redox potential (E_H) of O₂/O₂^{·-} (-0.2 eV). Consequently, all the **RNIC** derivatives possess the ability to effectively transferring electrons to oxygen and generating O₂^{·-}, specifically tailored them for type-I PDT. However, the E_V values of the **RNIC** derivatives (0.0166 for **HNIC**, 0.2684 for **PNIC**, 0.5127 for **ANIC**, 0.04978 for **NNIC**, 0.3265 for **TNIC** and 0.03477 eV for **BNIC**, respectively) are smaller than the E_H values of H₂O/ HO· (2.20 eV) and ¹O₂/O₂ (1.88 eV) at a pH of 5.6, suggesting that HO· and ¹O₂ generation is not feasible (Figure 4.7f and Table A4.15). Despite this, the study explored the possibility of a type-II photosensitization process in **NNIC** most promisingly. This consideration was rooted in the fact that the first excited triplet states of the **NNIC** PS exceeded the energy threshold necessary for the effective sensitization of molecular oxygen (0.98 eV).^[12] To delve deeper into the viability of type-I PDT via intermolecular electron transfer (IET), an in-depth investigation was conducted. This involved calculating the ΔG values employing the ORCA 5.0 quantum mechanical package at the B3LYP/DEF2-SVP level. Figure 4.7g provides a visual representation of the computed ΔG values in the context of reactions involving the **RNIC** derivatives O₂. Specifically, for **HNIC**, the ΔG value with respect to O₂ was determined to be -52.69 kcal mol⁻¹. This value was comparatively lower than the ΔG values of other derivatives like **PNIC**, **ANIC**, **NNIC**, and **TNIC** (-51.29, -48.04, -5.17, and -11.38 kcal mol⁻¹), respectively (Figure 4.7g and Table A4.16-A4.29). Such differences suggest a higher likelihood of IET reactions for **HNIC**, **PNIC**, **ANIC**, and **TNIC**. Consequently, this implies that **HNIC** and **PNIC** are more predisposed to efficiently generate O₂^{·-}. In contrast, the relatively highest ΔG value for **NNIC** suggests a less favorable reaction with O₂^{·-}.

Furthermore, it is significant to note that **BNIC** (-369.72 kcal mol⁻¹) exhibited the smallest ΔG values when compared to other **RNIC** derivatives. This is the first documented case of an exceptionally low ΔG value compared to previously reported PDT materials. [64] Theoretical calculations strongly suggest that **BNIC** is the most promising candidate among the **RNIC** derivatives for type-I PDT applications. **BNIC** is highly capable of generating O₂^{•-} and to a lesser extent, ¹O₂. **HNIC**, **PNIC**, and **ANIC** are promising for type-I PDT, producing O₂^{•-} effectively. **NNIC** shows potential for type-II PDT, producing ¹O₂ more efficiently. **TNIC** is a strong contender for both type-I and type-II strategies, with moderate ¹O₂ generation and efficient O₂^{•-} production. Overall, these findings illustrate the strategic manipulation of ROS through targeted design, informing diverse PDT applications.

Table 4.1. Summary of the Photophysical and Photosensitizing data of the **RNIC** luminogens.

Materials	^a λ _{abs} (nm)	^b λ _{ex} (nm)	^c λ _{em} (nm)	^d λ _{em} (nm)	^e λ _{em} (nm)	fStokes-shift (nm)		^g Φ _{PL}	^h E _g (eV)	ⁱ Φ _Δ	^j ΔE _{ST} (eV)	^k SOC (cm ⁻¹)
						A-E	S-E					
HNIC	336	350	411	399	416	49	66	0.61	3.76	0.0008	0.935	3.17
PNIC	360	370	435	459	483	89	113	0.98	3.36	0.004	0.674	1.265
ANIC	287	370	530	461	615	91	245	0.026	2.48	0.006	0.205	0.45
NNIC	303	370	534	431	601	61	231	0.007	2.14	0.95	0.003	0.33
TNIC	310	370	505	603	589	233	219	0.006,0.33 ^p	1.87	0.017	0.001	0.10
BNIC	338	370	436	604	605	234	235	0.011,0.99 ^p	1.79	0.0168	0.000	0.22

^aλ_{ab,max}, ^bλ_{ex} and ^cλ_{em,max} are absorption, excitation and emission wavelength maxima in Solution state. ^{d,e}Aggregated and solid state λ_{em,max}, ^fstokes-shift calculated between aggregated λ_{em,max} and λ_{ex,max} (A-E), (S-E) solid λ_{em,max} and λ_{ex,max} (S-E) . ^gΦ_{PL} Quantum yield in aggregated-state. ^hE_g gaseous-state band-energies, ⁱΦ_ΔSinglet-oxygen quantum yield, ^jΔE_{ST} is first singlet and triplet state energy gap. ^kSpin-orbit coupling between singlet and triplet-state. [Concentration: 100 μM **RNIC** derivatives in DMSO solution (solution-state), 99% f_w in DMSO (Aggregated-state)] ^p p = Φ_{PL} at 60 % f_w.

4.3.13. Mitochondria targeting cell imaging and white light induced PDT performances

The exceptional ability of **NNIC**, **TNIC**, and **BNIC** AIEE gens to produce ROS and display red-orange luminescence with a large stokes shift has driven their application in vitro cell

imaging and PDT (Figure 4.8). Precisely, HeLa cells were subjected to 4 hrs incubation, exposed to 30 μM **NNIC** and 10 μM each of **TNIC** and **BNIC**, as illustrated in the figure 4.8a. This resulted in distinct visualization of reticulum-like mitochondria, sharply contrasting against the cellular background. To assess the mitochondria specificity of these **RNIC** AIEE gens, a colocalization experiment employed MitoTracker Green, a commercially designed bioprobe for mitochondria staining. Colocalization results demonstrated perfect overlap between cell imaging of **NNIC**, **TNIC**, and **BNIC** AIEE gens and MitoTracker Green, substantiated by high Pearson's correlation coefficients: 0.93, 0.94, and 0.96 respectively (Figure 4.8a). This confirms strong specificity of AIEE gens for mitochondrial staining, further validating their targeted imaging capability. Notably, **BNIC** outperforms other **RNIC** AIEE gens, demonstrating enhanced mitochondrial targeting and higher cellular accumulation at a lower concentration for cell imaging. This advantage originates from **BNIC**'s nano-ribbon supramolecular assembly, supported by established literature. [53,54] Mitochondrial staining behavior is attributed to electrostatic interaction between the positively charged imidazole unit and the negatively charged mitochondrial transmembrane potential, driving specific accumulation and targeting. This strategy eliminates the need for additional targeting agents to improve biological incorporation.

The anticancer effect of **NNIC**, **TNIC**, and **BNIC** AIEE PSs in Hela cells was studied using an MTT assay (Figure 4.8b). At a higher concentration (20 μM), **BNIC** exhibited elevated dark toxicity compared to **NNIC** and **TNIC**. Interestingly, under a 20-min light exposure, **BNIC** and **TNIC** significantly impeded cell proliferation in Hela cells with IC_{50} values of about 1.67 μM and 15.5 μM respectively. Notably, at 2 μM and 20 μM , **BNIC** and **TNIC** induced approximately 80% and 65% cell inhibition upon light irradiation. Controlled morphology in aqueous media likely contributes to this limited toxicity. [53,54] Fluorescence microscopy validated **BNIC** and **TNIC**'s robust photocytotoxicity in Hela cells, showing their potential as exceptional PSs. With an exceptionally low IC_{50} value, **BNIC** demonstrates a PDT effect that surpasses the efficacy of recently investigated materials for both type-I and type-II PDT applications. This places **BNIC** at the forefront of contenders in this field due to its unparalleled performance (Table A4.1, A4.2).

In summary, **BNIC** emerges as a promising PS due to its potent phototoxicity, precise mitochondrion targeting, and potential for synergistic image-guided photodynamic therapy. The overall studies suggest that the **BNIC** is the most specific mitochondrion targeting image-guided type-I AIEE PS (particularly $\text{O}_2^{\cdot-}$ production) compared to most recently reported materials (Table A4.1).

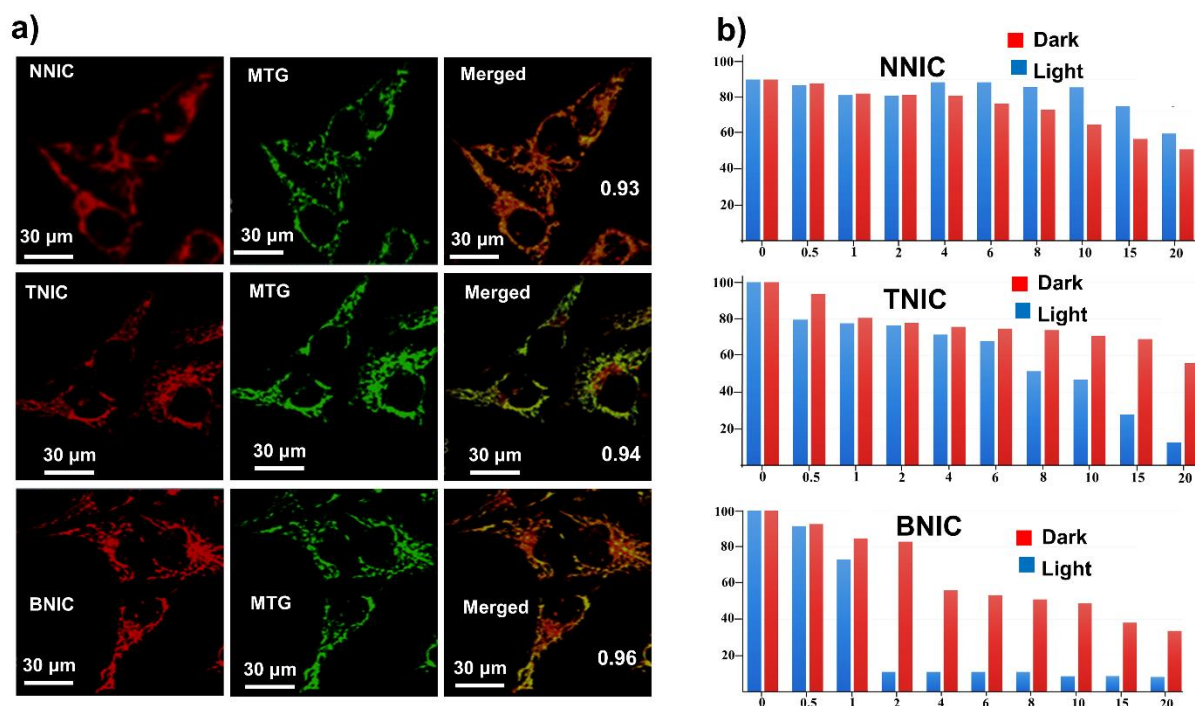


Figure 4.8. (a) Mitochondrion-targeting cell imaging of the **NNIC**, **TNIC** and **BNIC** luminognes. [Concentration: **NNIC** (50 μM), **TNIC/BNIC** (10 μM)]. (b) Cell viability of HeLa cells after treatment with different concentrations of **NNIC**, **TNIC** and **BNIC**, respectively, along with 20 min white light irradiation. [MTG represents the mitotracker green].

4.3.14. Live cell/ dead cell co-staining and intracellular ROS generation

The viability assay, utilizing calcein-AM/propidium iodide, vividly showed the impact of **TNIC** and **BNIC** on Hela cells (Figure 4.9, A4.19-A4.21). Concurrently, DCFDA with green signal indicated intracellular ROS production, aligning with previous findings. Treated cells exhibited evident morphological alterations, including reduced size, shrinkage, and cellular collapse. These shifts reinforced the idea of **BNIC**-induced photodynamic action fostering organelle destruction. This impact is likely amplified by **BNIC**'s proficient accumulation within cancer cells, which possess higher cell permeability relative to other **RNIC** derivatives. **BNIC**'s selective accumulation is facilitated by its precisely controlled morphology in aqueous environments. [53,54] Thus, **BNIC** exhibited pronounced photodynamic activity, driving type-I ROS production and cancer cell organelle destruction. Hence, **BNIC** emerges as a promising PS for PDT applications. In summary, the results highlight the capacity of readily accessible **RNIC** derivatives to serve as a versatile foundation for multifunctional AIEgens. This adaptable simplest framework carries great promise for the advancement of distinct luminescent materials, thereby promoting both scientific exploration and technological advancement.

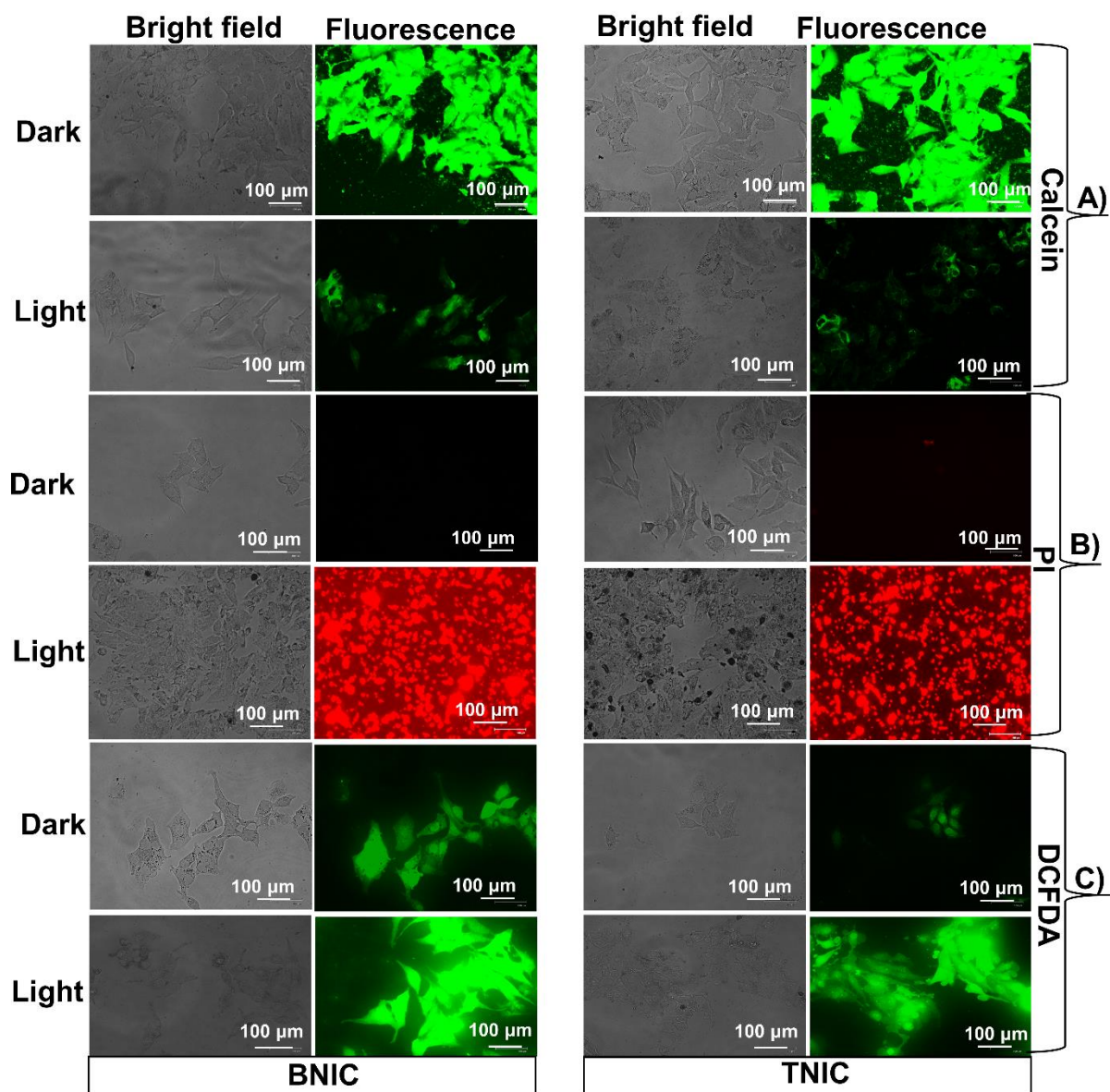


Figure 4.9. Fluorescence microscope images of HeLa cells after treatment with **BNIC** (10 μ M) and **TNIC** (20 μ M) PSs under normoxia loaded with (A) calcein-AM (2 μ M, live cell marker), (B) PI (4 μ M, dead cell marker), (C) DCFDA (10 μ M). [Concentration: **BNIC** (10 μ M), **TNIC** (20 μ M), Scale bar:100 μ m].

4.4. Conclusion

The utilization of donor functional units and anion- π^+ interactions of imidazole component resulted in distinct varieties of condensed-state emitters with a large stokes shift (245 nm), unique supramolecular behavior, and potent photosensitizing properties. This study introduced single-molecule solid-state white light-emissive AIE PSs, **HNIC** (CIE: 0.34, 0.33), and **PNIC** (CIE: 0.34, 0.32), as well as an excimer-based AIE PS, **HNIC**, and a mitochondrion-targeted image-guided AIE PS for PDT in cancer cells. **PNIC** and **NINC** exhibited remarkably high Φ_{PL} and Φ_{Δ} values of 0.98 and 0.95, respectively, in aqueous

media. The study revealed distinct types of PSSs (type-I: **HNIC**, **PNIC**, **ANIC** and **BNIC**; type-II: **NNIC**, and both type-I and type-II characteristics: **TNIC**). These PSSs specifically and predominantly generated type-I ROS, particularly $O_2^{\cdot-}$, along with exceptionally low ΔG values (ΔG for **HNIC** -52.69, **PNIC** -51.29, **ANIC** -48.04, **TNIC** -11.38, **BNIC** -369.72 kcal mol⁻¹). Efficient ROS production in the acceptor core **HNIC** suggested that the excimer played a crucial role in efficient ROS production, with a substantial SOC of 3.17 cm⁻¹. Furthermore, **BNIC** emerged as a highly promising photodynamic therapy material, boasting an extremely low IC₅₀ of 1.67 μ M without the need for extra targeting ligands.

References

- [1] Z. Yuan, D. Zhao, X. Yi, R. Zhuo, F. Li, *Adv. Funct. Mater.* **2014**, *24*, 1799.
- [2] H. Lin, Y. Chen, J. Shi, *Chem. Soc. Rev.* **2018**, *47*, 193.
- [3] M. Huo, L. Wang, Y. Chen, J. Shi, *Nat. Commun.* **2017**, *8*, 357.
- [4] Y. Shen, A. J. Shuhendler, D. Ye, J.-J. Xu, H.-Y. Chen, *Chem. Soc. Rev.* **2016**, *45*, 6725.
- [5] J. Li, K. Pu, *Chem. Soc. Rev.* **2019**, *48*, 38.
- [6] H. Zuo, J. Tao, H. Shi, J. He, Z. Zhou, C. Zhang, *Acta Biomaterialia* **2018**, *80*, 296.
- [7] H. Wang, X. Z. Yang, W. Shao, S. C. Chen, J. F. Xie, X. D. Zhang, J. Wang, Y. Xie, *J. Am. Chem. Soc.* **2015**, *137*, 11376.
- [8] D. Cui, J. G. Huang, X. Zhen, J. C. Li, Y. Y. Jiang, K. Y. Pu, *Angew. Chem., Int. Ed.* **2019**, *58*, 5920.
- [9] J. Li, Z. Zhuang, Z. Zhao, B. Z. Tang, *VIEW* **2022**, *3*, 20200121.
- [10] M. Li, J. Xia, R. Tian, J. Wang, J. Fan, J. Du, S. Long, X. Song, J. W. Foley, X. Peng, *J. Am. Chem. Soc.* **2018**, *140*, 14851.
- [11] G. J. Kavarnos, N. J. Turro, *Chem. Rev.* **1986**, *86*, 401.
- [12] H. Bian, D. Ma, X. Zhang, K. Xin, Y. Yang, X. Peng, Y. Xiao, *Small* **2021**, *17*, 2100398.
- [13] R. Bonnett, *Chem. Soc. Rev.* **1995**, *24*, 19.
- [14] J. Ge, M. Lan, B. Zhou, W. Liu, L. Guo, H. Wang, Q. Jia, G. Niu, X. Huang, H. Zhou, X. Meng, P. Wang, C. S. Lee, W. Zhang, X. Han, *Nat. Commun.* **2014**, *5*, 4596.
- [15] L. Shi, F. Hu, Y. Duan, W. Wu, J. Dong, X. Meng, X. Zhu, B. Liu, *ACS Nano* **2020**, *14*, 2183.
- [16] Z. Zhou, J. Song, L. Nie, X. Chen, *Chem. Soc. Rev.* **2016**, *45*, 6597.
- [17] J. M. Brown, W. R. Wilson, *Nat. Rev. Cancer* **2004**, *4*, 437.
- [18] J. Zhao, K. Xu, W. Yang, Z. Wang, F. Zhong, *Chem. Soc. Rev.* **2015**, *44*, 8904.
- [19] Y.-M. Wang, W. Liu, X.-B. Yin, *Chem. Sci.* **2017**, *8*, 3891.
- [20] M. Ethirajan, Y. Chen, P. Joshi, R. K. Pandey, *Chem. Soc. Rev.* **2011**, *40*, 340.
- [21] Z. Zhuang, J. Dai, M. Yu, J. Li, P. Shen, R. Hu, X. Lou, Z. Zhao, B. Z. Tang, *Chem. Sci.* **2020**, *11*, 3405.
- [22] Q. Li, C. Huang, L. Liu, R. Hu, J. Qu, *Cytometry Part A* **2018**, *93*, 997.
- [23] K. Reszka, F. S. Cruz, R. Docampo, *Chem. Biol. Interact.* **1986**, *58*, 161.
- [24] R. Docampo, S. N. Moreno, R. P. Muniz, F. S. Cruz, R. P. Mason, *Science* **1983**, *220*, 1292.
- [25] M. Li, T. Xiong, J. Du, R. Tian, M. Xiao, L. Guo, S. Long, J. Fan, W. Sun, K. Shao, X. Song, J. W. Foley, X. Peng, *J. Am. Chem. Soc.* **2019**, *141*, 2695.
- [26] S. G. Awuah, J. Polreis, V. Biradar, Y. You, *Org. Lett.* **2011**, *13*, 3884.
- [27] Y. Cakmak, S. Kolemen, S. Duman, Y. Dede, Y. Dolen, B. Kilic, Z. Kostereli, L. T. Yildirim, A. L. Dogan, D. Guc, E. U. Akkaya, *Angew. Chem., Int. Ed.* **2011**, *50*, 11937.

- [28] S. Kolemen, M. Işık, G. M. Kim, D. Kim, H. Geng, M. Buyuktemiz, T. Karatas, X.-F. Zhang, Y. Dede, J. Yoon, E. U. Akkaya, *Angew. Chem., Int. Ed.* **2015**, *54*, 5340.
- [29] H. Uoyama, K. Goushi, K. Shizu, H. Nomura, C. Adachi, *Nat.* **2012**, *492*, 234.
- [30] W. Wu, G. Feng, S. Xu, B. Liu, *Macromolecules* **2016**, *49*, 5017.
- [31] N. Meher, P. K. Iyer, *Nanoscale* **2019**, *11*, 13233.
- [32] M. N. Khatun, A. S. Tanwar, N. Meher, P. K. Iyer, *Chem. Asian J.* **2019**, *14*, 4725.
- [33] J. Mei, Y. Hong, J. W. Y. Lam, A. Qin, Y. Tang, B. Z. Tang, *Adv. Mater.* **2014**, *26*, 5429.
- [34] J. Mei, N. L. C. Leung, R. T. K. Kwok, J. W. Y. Lam, B. Z. Tang, *Chem. Rev.* **2015**, *115*, 11718.
- [35] M. Kasha, H. R. Rawls, *M. Ashraf El-Bayoumi*, **1965**, *11*, 371.
- [36] A. S. Davydov, New York, **1971**, 978-1-4899-5169-4.
- [37] B. L. Schottel, H. T. Chifotides, K. R. Dunbar, *Chem. Soc. Rev.* **2008**, *37*, 68.
- [38] M. Giese, M. Albrecht, K. Rissanen, *Chem. Commun.* **2016**, *52*, 1778.
- [39] Q. Wan, R. Zhang, Z. Zhuang, Y. Li, Y. Huang, Z. Wang, W. Zhang, J. Hou, B. Z. Tang, *Adv. Funct. Mater.* **2020**, *30*, 2002057.
- [40] P. Xiao, Z. Shen, D. Wang, Y. Pan, Y. Li, J. Gong, L. Wang, D. Wang, B. Z. Tang, *Adv. Sci.* **2022**, *9*, 2104079.
- [41] W. Wu, D. Mao, F. Hu, S. Xu, C. Chen, C.-J. Zhang, X. Cheng, Y. Yuan, D. Ding, D. Kong, B. Liu, *Adv. Mater.* **2017**, *29*, 1700548.
- [42] Z. Zheng, T. Zhang, H. Liu, Y. Chen, R. T. K. Kwok, C. Ma, P. Zhang, H. H. Y. Sung, I. D. Williams, J. W. Y. Lam, K. S. Wong, B. Z. Tang, *ACS Nano* **2018**, *12*, 8957.
- [43] T. Zhang, J. Zhang, F.-B. Wang, H. Cao, D. Zhu, X. Chen, C. Xu, X. Yang, W. Huang, Z. Wang, J. Wang, Z. He, Z. Zheng, J. W. Y. Lam, B. Z. Tang, *Adv. Funct. Mater.* **2022**, *32*, 2110526.
- [44] C. Liu, C. Ji, Z. Fan, R. Ma, M. Yin, *Chem. Commun.* **2021**, *57*, 13126.
- [45] V.-N. Nguyen, S. Qi, S. Kim, N. Kwon, G. Kim, Y. Yim, S. Park, J. Yoon, *J. Am. Chem. Soc.* **2019**, *141*, 16243.
- [46] P. Pinter, H. Mangold, I. Stengel, I. Münster, T. Strassner, *Organometallics* **2016**, *35*, 673.
- [47] J. Sun, L. Guo, Q. Li, Y. Zhao, M. Gao, Z. She, C. Jin, *Environ. Sci. Pollut. Res.* **2016**, *23*, 24061
- [48] J. Dong, K. M. Solntsev, L. M. Tolbert, *J. Am. Chem. Soc.* **2009**, *131*, 662.
- [49] Y. Deng, M. Wang, Y. Zhuang, S. Liu, W. Huang, Q. Zhao, *Sci. Appl.* **2021**, *10*, 76.
- [50] P. S. Marqués, M. Krajewska, B. D. Frank, K. Prochaska, L. Zeininger, *Chem. Eur. J.* **2023**, *29*, 202203790.
- [51] J. Ye, X. Huang, Y. Gao, X. Wang, T. Zheng, Y. Lin, X. Liu, G. Ning, *CrystEngComm* **2015**, *17*, 9311.
- [52] M. Soni, S. K. Das, P. K. Sahu, U. P. Kar, A. Rahaman, M. Sarkar, *J. Phys. Chem. C* **2013**, *117*, 14338
- [53] J. J. Rennick, A. P. R. Johnston, R. G. Parton, *Nat. Nanotechnol.* **2021**, *16*, 266.
- [54] D. Zhang, L. Wei, M. Zhong, L. Xiao, H.-W. Li, J. Wang, *Chem. Sci.* **2018**, *9*, 5260.
- [55] Y. Wang, J. Yang, Y. Tian, M. Fang, Q. Liao, L. Wang, W. Hu, B. Z. Tang, Z. Li, *Chem. Sci.* **2020**, *11*, 833.
- [56] M. Yoosefian, N. Etminan, *RSC Adv.* **2016**, *6*, 64818.
- [57] M. Yoosefian, A. Mola, *J. Mol. Liq.* **2015**, *209*, 526.
- [58] M. Yoosefian, Z. Ansarinik, N. Etminan, *J. Mol. Liq.* **2016**, *213*, 115.
- [59] W.-X. Ni, M. Li, J. Zheng, S.-Z. Zhan, Y.-M. Qiu, S. W. Ng, D. Li, *Angew. Chem., Int. Ed.* **2013**, *52*, 13472.
- [60] Z. He, W. Zhao, J. W. Y. Lam, Q. Peng, H. Ma, G. Liang, Z. Shuai, B. Z. Tang, *Nat. Commun.* **2017**, *8*, 416.

- [61] I. Muñoz Resta, J. F. Miravet, M. Yamaji, F. Galindo, *J. Mater. Chem. C* **2020**, *8*, 14348.
- [62] F.-Z. Li, X.-Y. Li, W. Ni, Z.-W. Wu, C. Lin, G. G. Gurzadyan, G.-C. Kuang, *Dyes and Pigments* **2021**, *195*, 109736.
- [63] Z. Yang, Z. Zhang, Z. Lei, D. Wang, H. Ma, B. Z. Tang, *ACS Nano* **2021**, *15*, 7328.
- [64] K. Wen, H. Tan, Q. Peng, H. Chen, H. Ma, L. Wang, A. Peng, Q. Shi, X. Cai, H. Huang, *Adv. Mater.* **2022**, *34*, 2108146.
- [65] E. A. Chandross, C. J. Dempster, *J. Am. Chem. Soc.* **1970**, *92*, 704.
- [66] B. Xu, Y. Mu, Z. Mao, Z. Xie, H. Wu, Y. Zhang, C. Jin, Z. Chi, S. Liu, J. Xu, Y.-C. Wu, P.-Y. Lu, A. Lien, M. R. Bryce, *Chem. Sci.* **2016**, *7*, 2201.

Appendix (AI)

Table A4.1. Comparison table of the recently published mitochondrion targeted image-guided type-I PSs Comparing their photophysical and photosensitizing behavior as well as PDT efficacy.

References		Present work		^a ACS Nano 2023 , <i>17</i> , 8, 7145.	^b Adv. Funct. Mater. 2020 , <i>30</i> , 2002057.	^c ACS Nano 2021 , <i>15</i> , 7735.
Materials		BNIC (Red AIEEgen)	TNIC (Red AIEEgen)	Yellow AIE gen	Far Red AIEgen	Yellow AIE gen
AIE (solvent)		99% f _w	99% f _w	99% f _w	99% f _w	99% f _w
Stokes- shift (nm)		235	233	g	g	g
Φ _{PL}	99% f _w	0.011	0.006	g	g	g
	60% f _w	0.99	0.33	g	g	g
Φ _Δ (solvent)		0.017 (99%PBS)	0.017 (99%PBS)	g	g	g
Light used		White light	White light	White light	White light	White light
ROS	Types	Type-I(O ₂ ^{•-})	Type-I(O ₂ ^{•-})	Type-I (O ₂ ^{•-} ,OH [•])	Type-I (O ₂ ^{•-} , OH [•])	Type-I (O ₂ ^{•-} , OH [•])
	Specificity	Specific	Specific	Not very specific	Not very specific	Not very specific
Total ROS	DCFDA (μM)	1	1	10	10	10
	T (min)	3	3	2	2	2
	I	2x10 ⁶	1x10 ⁶	2x10 ⁶	1x10 ⁵	1x10 ⁶
ROS (mechanism)		DCFDA, ABDA,TA, ESR, Theoretical (ΔG, SOC), Band energy/NHE)	DCFDA, ABDA,TA, ESR, Theoretical (ΔG, SOC), Band energy/NHE)	DCFH,ABDA,DHR,HPF	DCFH,HPF,EPR,ABDA	DCFH,HPF,EPR,ABDA
PDT (Cancer cell)	Material Concentration (μM)	2	20	10	8	16
	In vitro	Normoxia (Hela cell)	Normoxia (Hela cell)	Normoxia (Hela cell)	Normoxia (Hela cell)	Normoxia (Hela cell)

	In vivo	g	g	g	g	g
Cell imaging (Mitochondrion targeting)		yes	yes	yes	Lyso and mitochondrion	yes
Stimuli used		g	g	ALP	yes	g

a and c represents the references 9 and 10 in AI, b represents the reference 39 in the main manuscript.

Table A4.2. Comparison table of the recently published mitochondrion targeted image-guided type-II PSS Comparing their photophysical and photosensitizing behavior as well as PDT efficacy with **RNIC** derivatives, particularly (**NNIC** derivatives).

Reference s	<i>Adv. Opt. Mater.</i> 2020 , 8 , 1901433.	<i>Adv. Opt. Mater.</i> 2020 , 8 , 2001119.	<i>Nano Lett.</i> 2020 , 20 , 7438.	<i>Adv. Funct. Mater.</i> 2020 , 30 , 2002546.	<i>J. Am. Chem. Soc.</i> 2019 , 141 , 5612.	<i>Chem. Mater.</i> 2020 , 32 , 4681.	<i>ACS Nano</i> 2019 , 13 , 11283.	<i>ACS Nano</i> 2018 , 12 , 8145.	<i>Angew. Chem. Int. Ed.</i> 2020 , 59 , 8957.	<i>Chem. Sci.</i> , 2022 , 13 , 9373.	<i>Angew. Chem. Int. Ed.</i> 2020 , 59 , 9610.	<i>Adv. Mater.</i> 2018 , 30 , 1802105.	<i>J. Am. Chem. Soc.</i> 2020 , 142 , 15966.	
Materials	Yellow AIEgen	Yellow AIE	RedAIE	NIRII AIE	RedAIE	Red AIE	Yellow AIE	AIE	Red AIE	Red AIE	Far red AIE	Far-Red/NIR AIEgen	Yellow AIE	
AIE (solvent)	Hexane	99% f _w	99% f _w	99% f _w	EtOH	99% f _w	99% f _w	99% f _w	99% f _w	THF	THF	99% f _w	THF	
Stokes-shift (nm)	g	175	g	g	g	g	g	g	g	139	200	g	g	
Φ_{PL} (Solvent)	1.7 (Hexane)	g	g	g	g	g	g	0.069	g	0.56 (THF)	g	g	0.20	
Φ_A (solvent)	g	g	g	g	g	g	g	g	g	1.1 (THF)	0.63 (99% f _w)	g	g	
Light used	White light	White light	White light	White light	White light	White light	White light	White light	White light	White light	White light	White light	White light	
ROS	Types	Type-II	Type-II	Type-II	Type-II	Type-II	Type-II	Type-II	Type-II	Type-II	Type-II	Type-II	Type-I, Type-II	
Total ROS	DCFDA (μM)	1	g	g	g	g	g	g	5	30	5	g	g	
	T (min)	30	20	g	g	g	g	g	2	3	2	g	g	
	I	g	g	g	g	g	g	g	1x10 ⁴	1x10 ³	g	g	g	
ROS (mechanism)	DCFH, ABD A	DCFH, ABD A	ABDA	DCFH, ABD A	DCFH, ABD A	ABD A	DCFH, ABD A	DCFH, ABD A	DCFH, ABD A	ABDA, EPR, DCFH	ABDA	DCFH, ABD A	DCFH	
P D	Material Concentration	10	g	20	g	5	40	40	20	10	40	5	5	20

T	n (μM)														
	In vitro	Normoxia	Normoxia	Normoxia	Normoxia	Normoxia	Normoxia	Normoxia	Normoxia	Normoxia	Normoxia	Normoxia	Normoxia	Normoxia	
	In vivo	g	g	g	g	g	g	g	g	g	g	g	yes	yes	yes
Cell imaging (Mitochondrion targeting)	yes	Lipid droplet	Lipid-mitochondrion	yes	yes	yes	yes	yes	yes	yes	yes	yes	yes	yes	yes
Stimuli used	g	H ₂ O ₂	g	g	g	g	g	g	g	g	g	g	g	g	g

a represent the references 5, 11-18, 19, 27, and 28 placed in the AI and 42 placed in the main manuscript.

Table A4.3. Comparison table of stokes shift, Φ_{PL} and Φ_{Δ} of the AIEgen materials of the recently published materials.

References	AIEgen materials	Properties
Present work	PNIC	Φ_{PL} (Solvent system)
a <i>J. Am. Chem. Soc.</i> 2019 , <i>141</i> , 16243.	Green AIE gen	
Present work	BNIC (Red AIEgen)	Stoke shift (nm)
11 <i>Adv. Opt. Mater.</i> 2020 , <i>8</i> , 1901433.	Yellow AIE gen	
20 <i>Adv. Funct. Mater.</i> 2018 , <i>28</i> , 1704589.	Green AIE gen	
Present work	NNIC	Φ_{Δ} (Solvent system)
a <i>J. Am. Chem. Soc.</i> 2019 , <i>141</i> , 16243.	Non-fluorescent	
18 <i>Chem. Sci.</i> 2022 , <i>13</i> , 9373.	Red AIE	
5 <i>Adv. Mater.</i> 2018 , <i>30</i> , 1802105.	Red AIE	

a represent the reference 45 placed in the main manuscript.

Table A4.4 Comparison table of the recently published solid state and solution state white light emissive materials with their different mechanisms.

References	Materials (CIE)	Ionic/neutral	Properties	Solution	Solid	Mechanism
Present work	HNIC (0.34,0.33)	Ionic	AIE	No	yes	AIE-Excimer-anion- π^+ interacton
	PNIC (0.34,0.32)	Ionic	AIE	No	yes	AIE-CT-ET-anion- π^+ interacton
a <i>J. Mater. Chem. C.</i> 2020 , <i>8</i> , 14348.	Pyrylium dye (0.28,0.32)	Ionic	Fluorescent dye	No	yes	Ionic ineteraction
b <i>Dyes and Pigments</i> 2021 , <i>195</i> , 109736.	BODIPY (0.33, 0.32)	Ionic	AIE	yes	No	AIE- ET - CT
21 <i>Chem. Commun.</i> 2015 , <i>51</i> , 2130.	(0.31,0.37)	neutral	AIE	yes	No	AIE-ESIPT

c	<i>Chem. Sci.</i> 2016 , 7, 2201.	(0.27,0.29)	neutral	AIE	no	Yes	AIE-ICT
22	<i>New J. Chem.</i> 2017 , 41, 1064.	(CIE:0.45,0.38)	neutral	AIE	yes	no	AIE-ESIPT- excimer
23	<i>Chem. Commun.</i> 2017 , 53, 7909.	(0.33, 0.33)	neutral	AIE	yes	no	non-covalent nano-assembly
24	<i>Chem. Commun.</i> 2019 , 55,1879.	(0.33, 0.37)	neutral	AIE	yes	no	VIE-AIE
25	<i>Chem. Commun.</i> 2020 , 56, 7407.	(0.4, 0.34)	neutral	AIE	yes	no	AIE-CT
26	<i>Mater. Chem. Front.</i> 2021 , 5, 2361.	(0.29, 0.34)	neutral	AIE	yes	no	AIE-Electronic interaction
d	<i>Nat. Commun.</i> 2017 , 8, 416.	(0.33, 0.35)	neutral	AIE	no	yes	AIE-Dual phosphorescent

a, b, c, and d represents the references 61, 62, 66 and 60, respectively placed in the main manuscript.

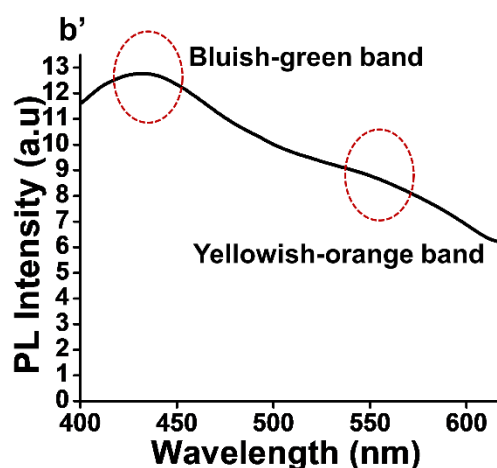
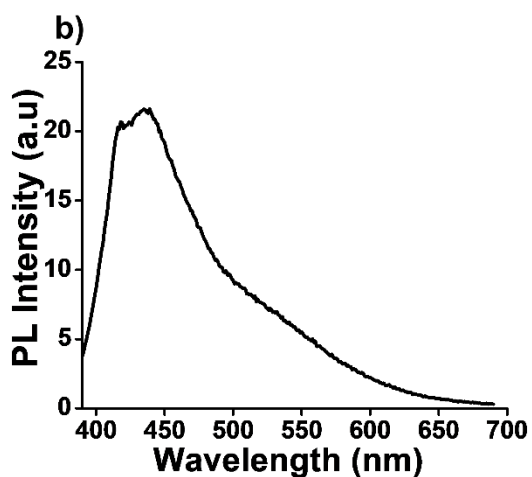
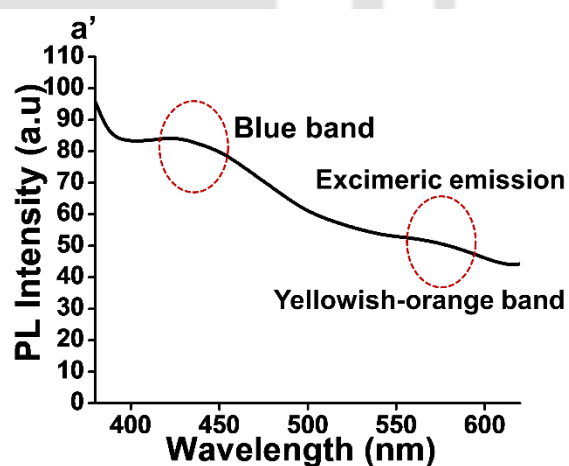
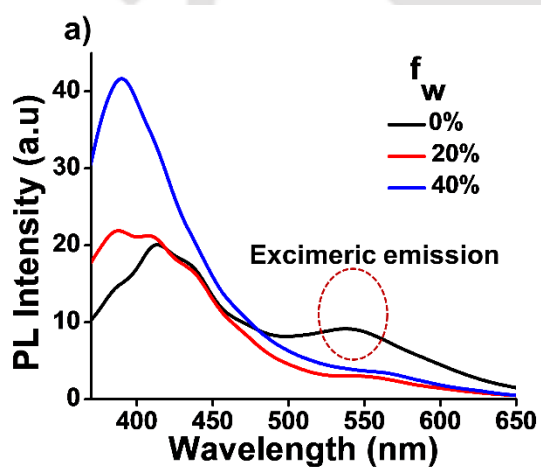


Figure A4.1. (a and a') Solution and solid state PL spectra of **HNIC** exhibiting excimer formation. (b and b') Solution and solid state PL spectra of **PNIC** exhibiting distinct emission band. [solution state (in DMSO), ($\lambda_{\text{ex}} = 370$ nm.

Table A4.5. CIE coordinates for the **RNIC** derivatives in solution, aggregate and solid state.

Materials	Solution		Aggregate		Solid	
	X	Y	X	Y	X	Y
HNIC	0.239	0.261	0.162	0.040	0.3384	0.329
PNIC	0.192	0.184	0.145	0.141	0.336	0.328
ANIC	0.301	0.461	0.166	0.165	0.535	0.457
NNIC	0.289	0.414	0.154	0.065	0.585	0.414
TNIC	0.245	0.317	0.579	0.419	0.569	0.429
BNIC	0.179	0.145	0.584	0.415	0.593	0.406

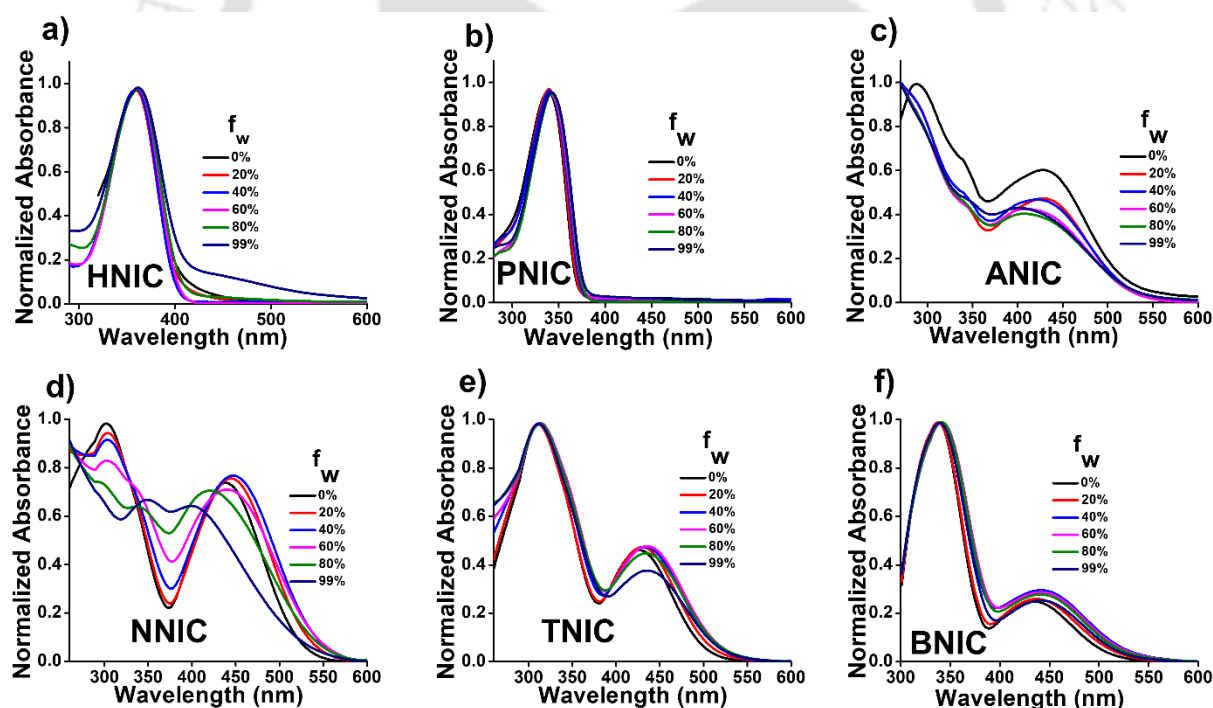


Figure A4.2. (a-f) Normalized UV-vis spectra of **RNIC** derivatives at various f_w in DMSO.

Table A4.6. UV-vis absorption data for the **RNIC** derivatives.

Materials	Water fraction (f_w)	$\lambda_{\text{abs.max}}$	A	$\Delta\lambda$
-----------	--------------------------	----------------------------	---	-----------------

HNIC	0%	336	0.276976	9
	99%	345	0.293164	
PNIC	0%	360	0.690822	2
	99%	362	0.510113	
ANIC	0%	287	0.373151	1
	99%	288	0.321992	
NNIC	0%	303	0.230986	1
	99%	304	0.134107	
TNIC	0%	310	0.554521	1
	99%	311	0.487119	
BNIC	0%	338	1.094902	1
	99%	339	0.892943	

A, $\Delta\lambda$, are the absorbance and wavelength maxima shift in their absorption.

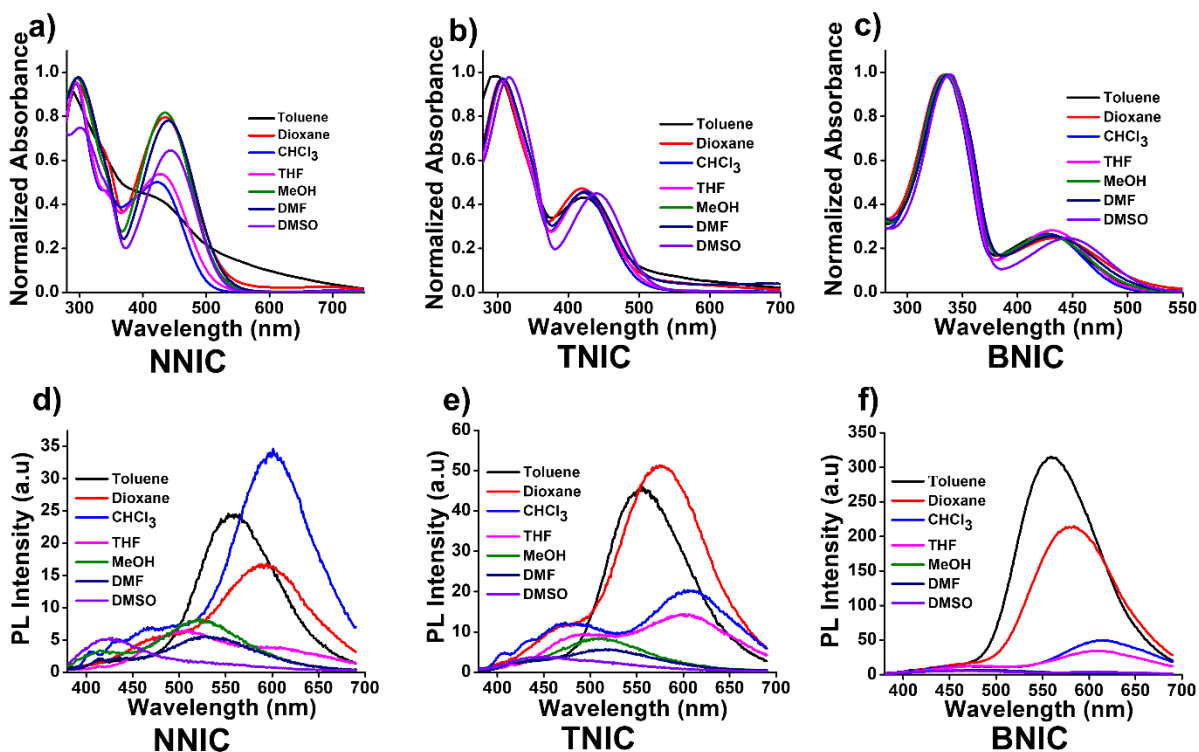


Figure A4.3. Solvatochromic effect of the NNI, TNIC and BNIC derivatives. (a-c) Normalized absorbance, (d-f) Fluorescence spectra of NNI, TNIC and BNIC derivatives in various solvents from nonpolar to polar (100 μM , $\lambda_{\text{ex}} = 370 \text{ nm}$).

Table A4.7. The solvatochromic UV-vis data for the NNI, TNIC and BNIC derivatives in various solvents from nonpolar to polar (100 μM , $\lambda_{\text{ex}} = 370 \text{ nm}$).

Materials	Solvents	$\lambda_{\text{abs.max}}$	$\Delta\lambda$
NNIC	Toluene	281	21
	Dioxane	294	
	CHCl_3	302	
	THF	295	
	MeOH	293	
	DMF	296	
	DMSO	297	
TNIC	Toluene	300	15
	Dioxane	309	
	CHCl_3	315	
	THF	305	

	MeOH	309	
	DMF	307	
	DMSO	308	
BNIC	Toluene	337	6
	Dioxane	334	
	CHCl ₃	339	
	THF	333	
	MeOH	333	
	DMF	337	
	DMSO	338	

$\Delta\lambda$ is the absorbance and wavelength maxima shift in their absorption.

Table A4.8. The solvatochromic PL data for the **NNIC**, **TNIC** and **BNIC** derivatives in various solvents from nonpolar to polar (100 μ M, λ_{ex} = 370 nm).

Materials	Solvents	$\lambda_{em,max}$	$\Delta\lambda$
NNIC	Toluene	555	52
	Dioxane	594	
	CHCl ₃	601	
	THF	602	
	MeOH	603	
	DMF	604	
	DMSO	605	
TNIC	Toluene	552	49
	Dioxane	575	
	CHCl ₃	601	
	THF	602	
	MeOH	603	
	DMF	604	
	DMSO	605	
BNIC	Toluene	563	47
	Dioxane	584	
	CHCl ₃	609	

	THF	609	
	MeOH	609	
	DMF	609	
	DMSO	610	

$\Delta\lambda$, is the wavelength maxima shift in their emission.

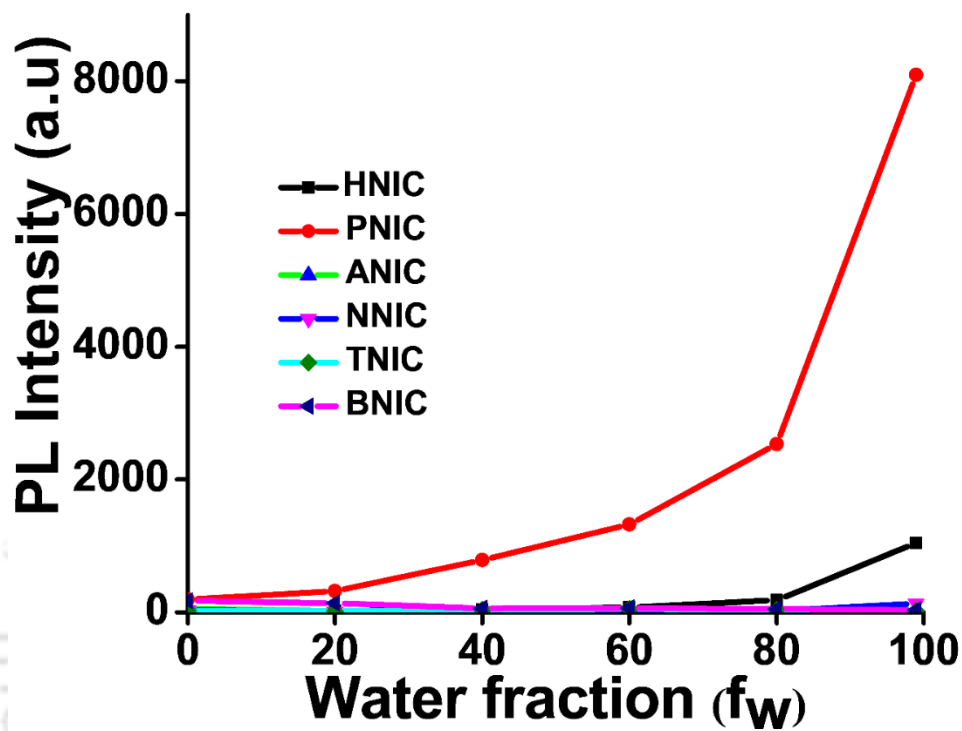


Figure A4.4. PL spectra at various f_w in DMSO at their corresponding $\lambda_{em,max}$.

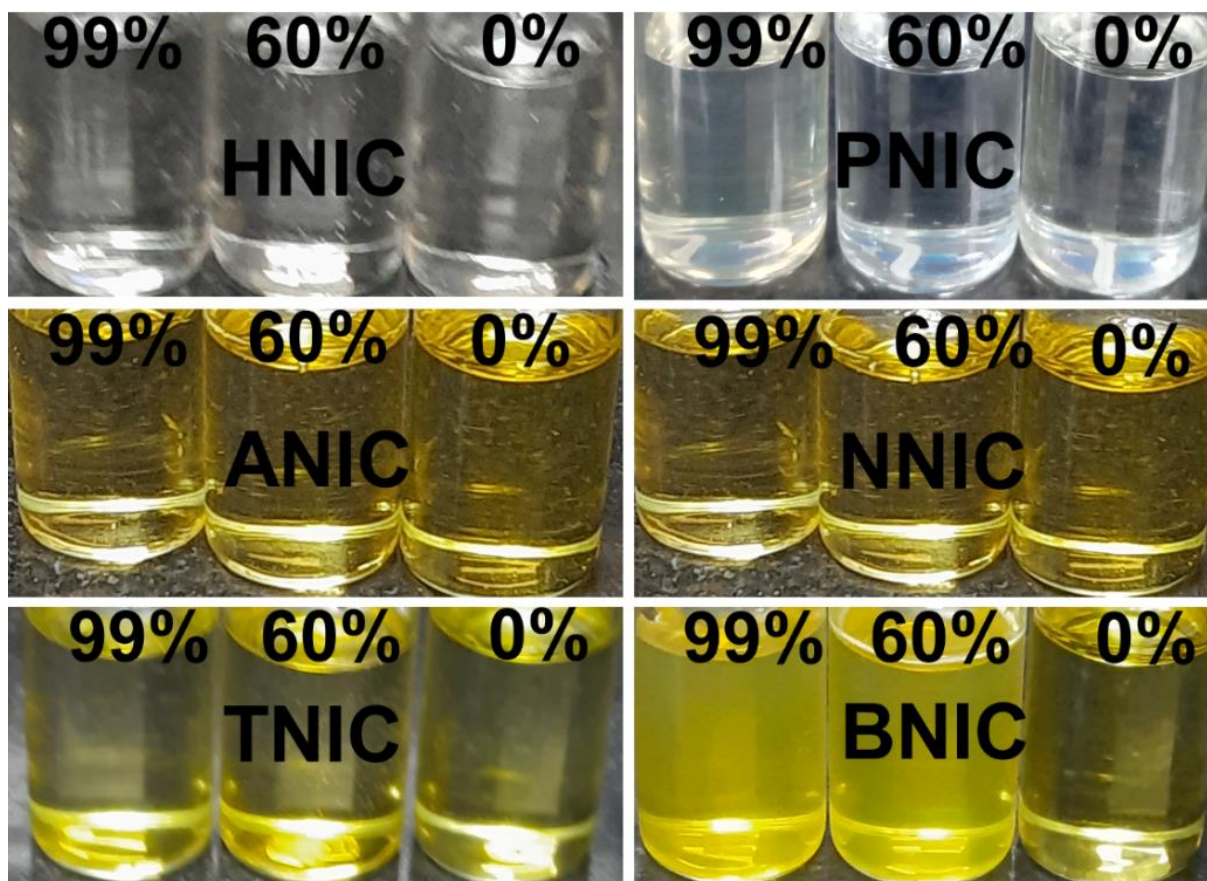


Figure A4.5. Capturing daylight photographs of **RNIC** derivatives at 0%, 60%, and 99% w_w in DMSO.

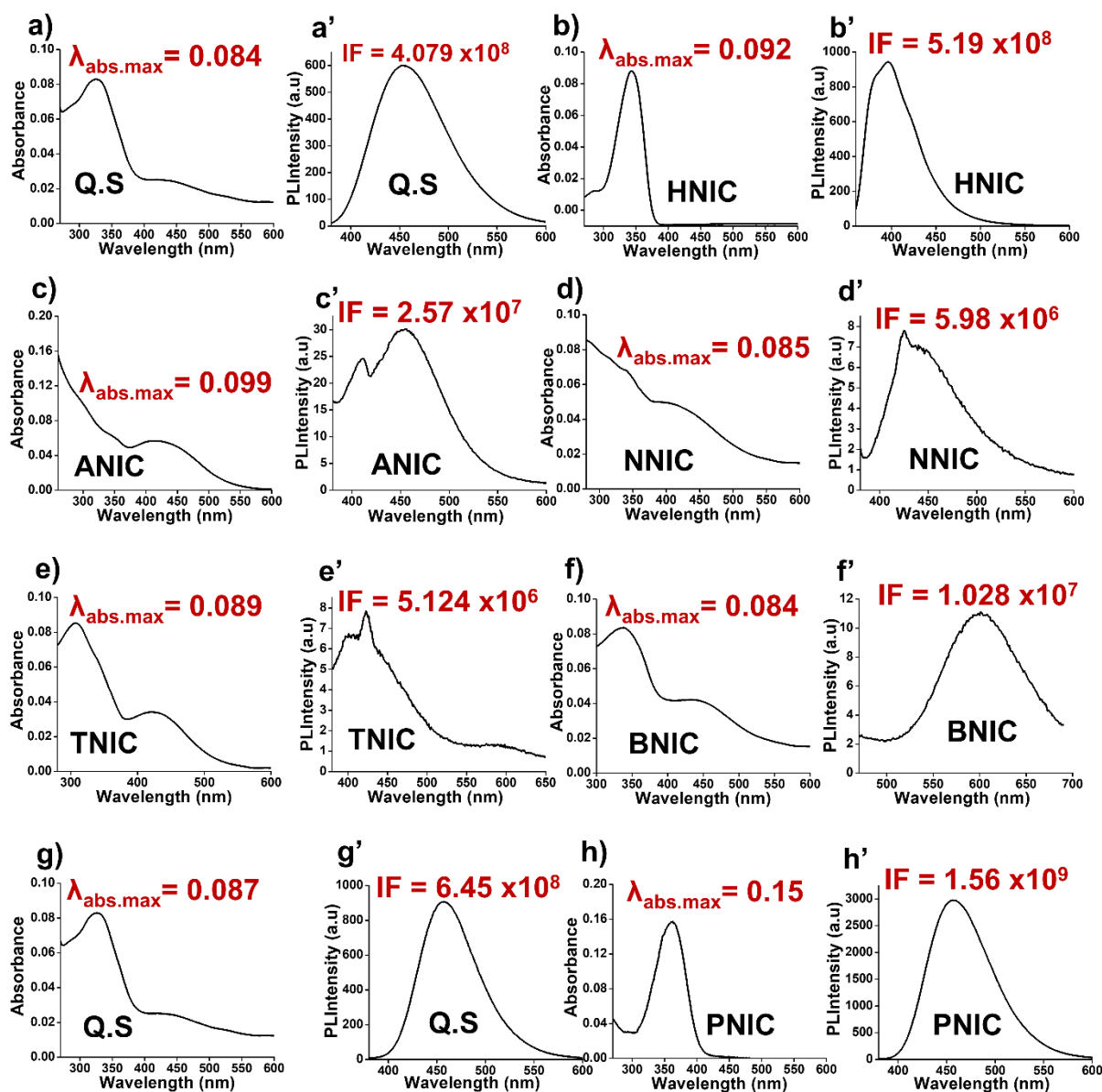


Figure A4.6. (a and a'), (b and b'), (c and c'), (d and d'), (e and e'), (f and f') are the absorbance and emission peak area of quinine sulfate (Q.S), HNIC, ANIC, NNIC, TNIC and BNIC at 99% f_w in DMSO, at their corresponding slit. (g-g') and (h-h') are the absorbance and emission peak area of Q.S, and PNIC at 99% f_w in DMSO. IF: integrated fluorescence intensity.

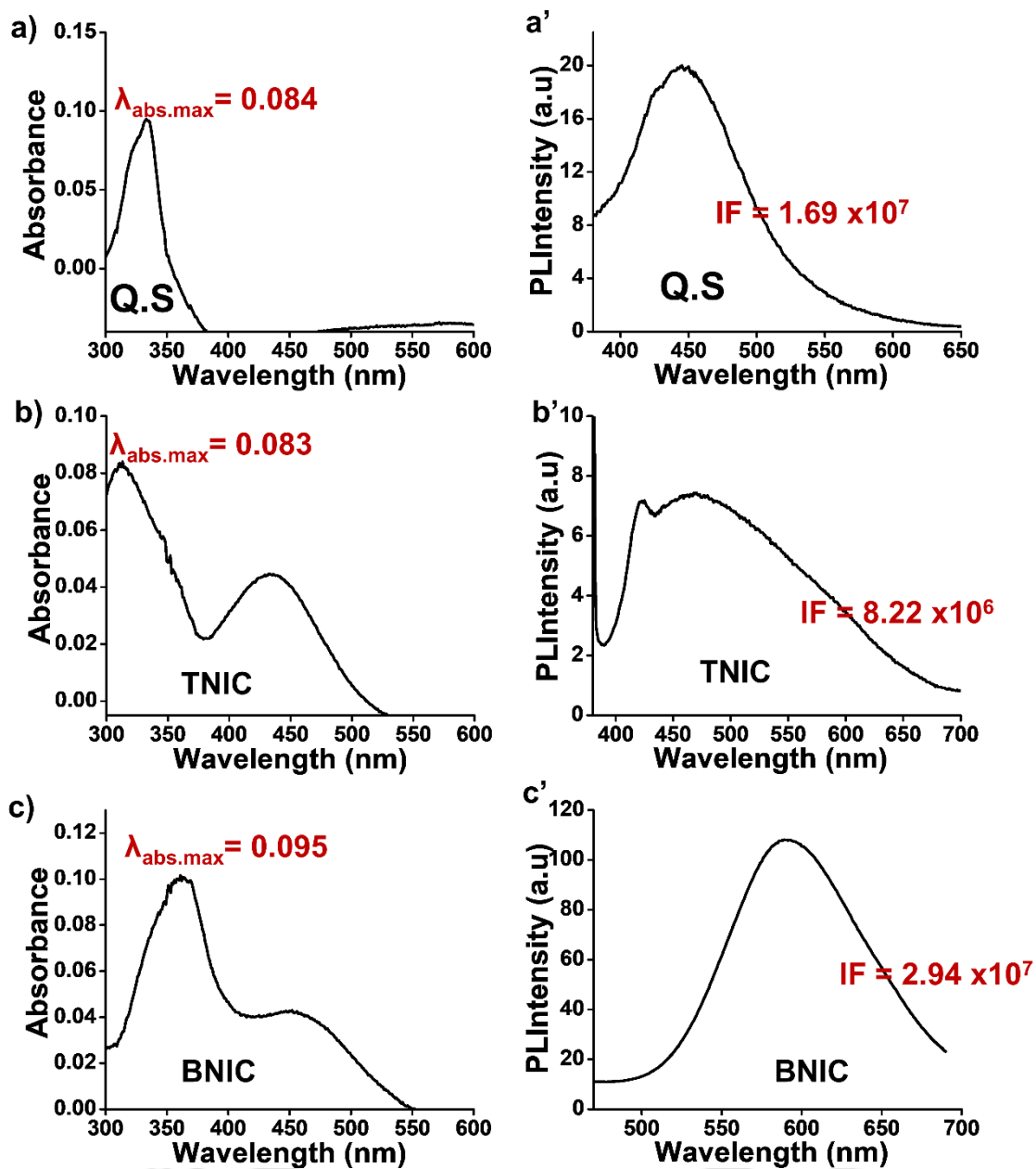


Figure A4.7. (a and a'), (b and b'), and (c-c') the absorbance and emission peak area of Q.S, TNIC and BNIC at 60% f_w in DMSO. IF: integrated fluorescence intensity.

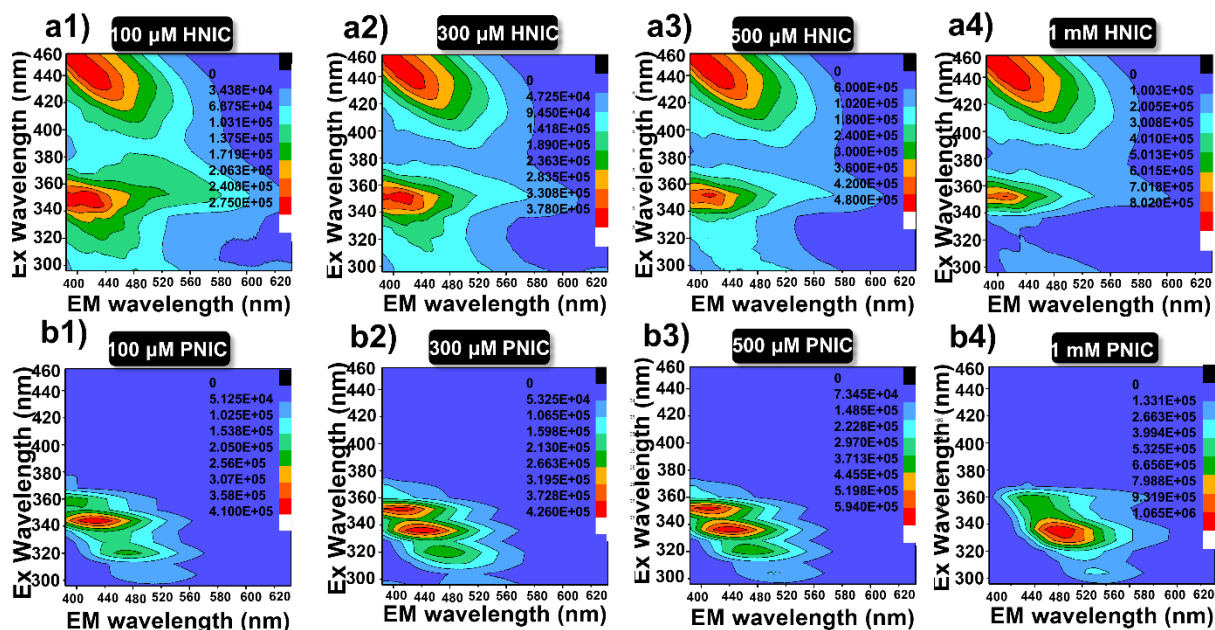


Figure A4.8. (a and b) 2D EEM contour projections of the RNIC derivatives at different concentrations (left: 100 μ M; middle: 300 μ M and 500 μ M; right: 1 mM) in DMSO.

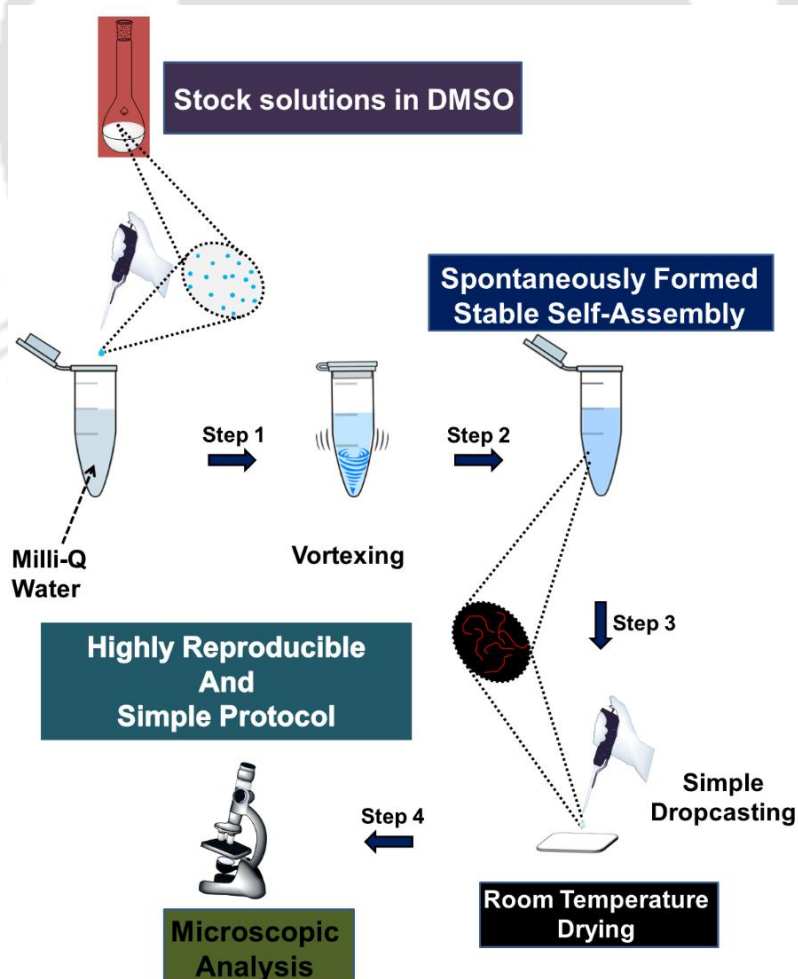


Figure A4.9. (b) Schematic illustration of the highly reproducible simple, cost-effective, and feasible strategy for the preparation of micro- and nano- supramolecular self-assembly from **RNIC** derivatives.

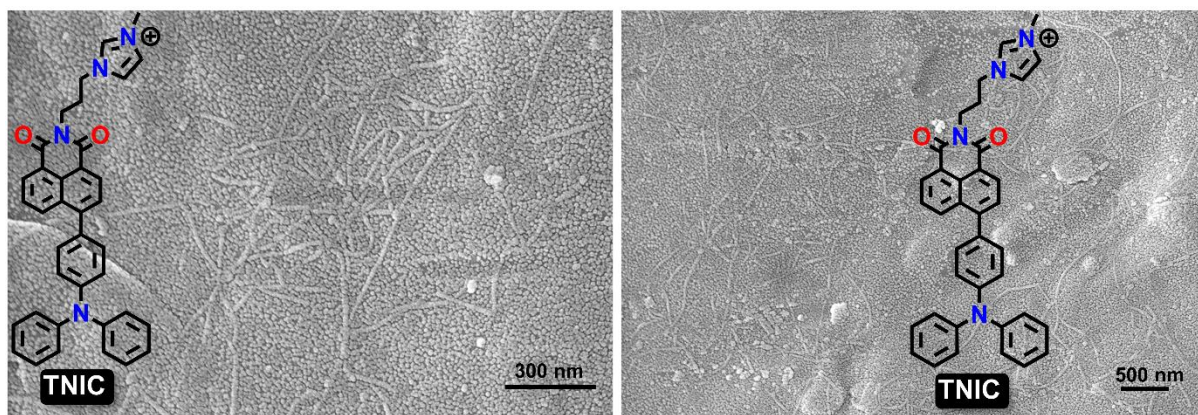


Figure A4.10. FESEM images of the nano-assembly of the **TNIC** spontaneously formed at 99.9% f_w in DMSO (100 μM) by a simple drop-casting technique on aluminum foil coated on a glass slide, followed by drying at room temperature, as graphically represented in Figure A4.9.

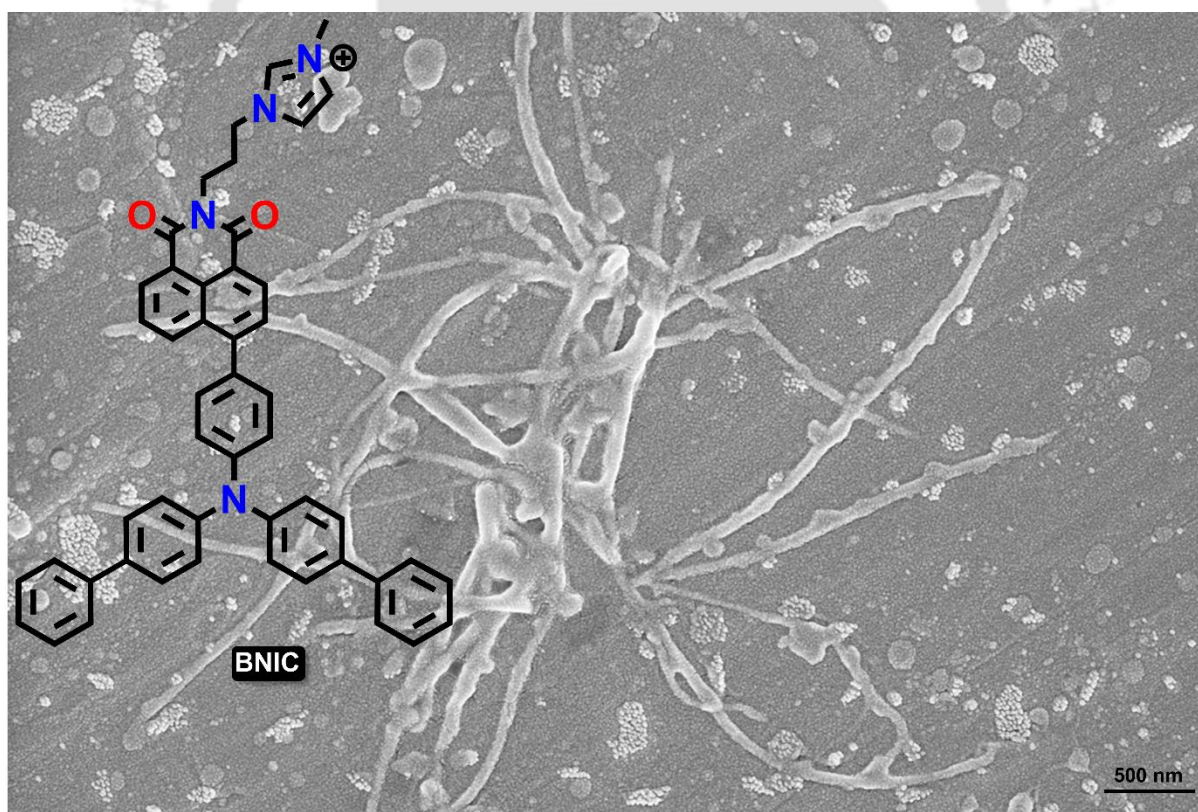


Figure A4.11. FESEM images of the nano-assembly of the **BNIC** spontaneously formed at 99.9% f_w in DMSO (100 μM) by a simple drop-casting technique on aluminum foil coated on a glass slide, followed by drying at room temperature, as graphically represented in Figure A4.9.

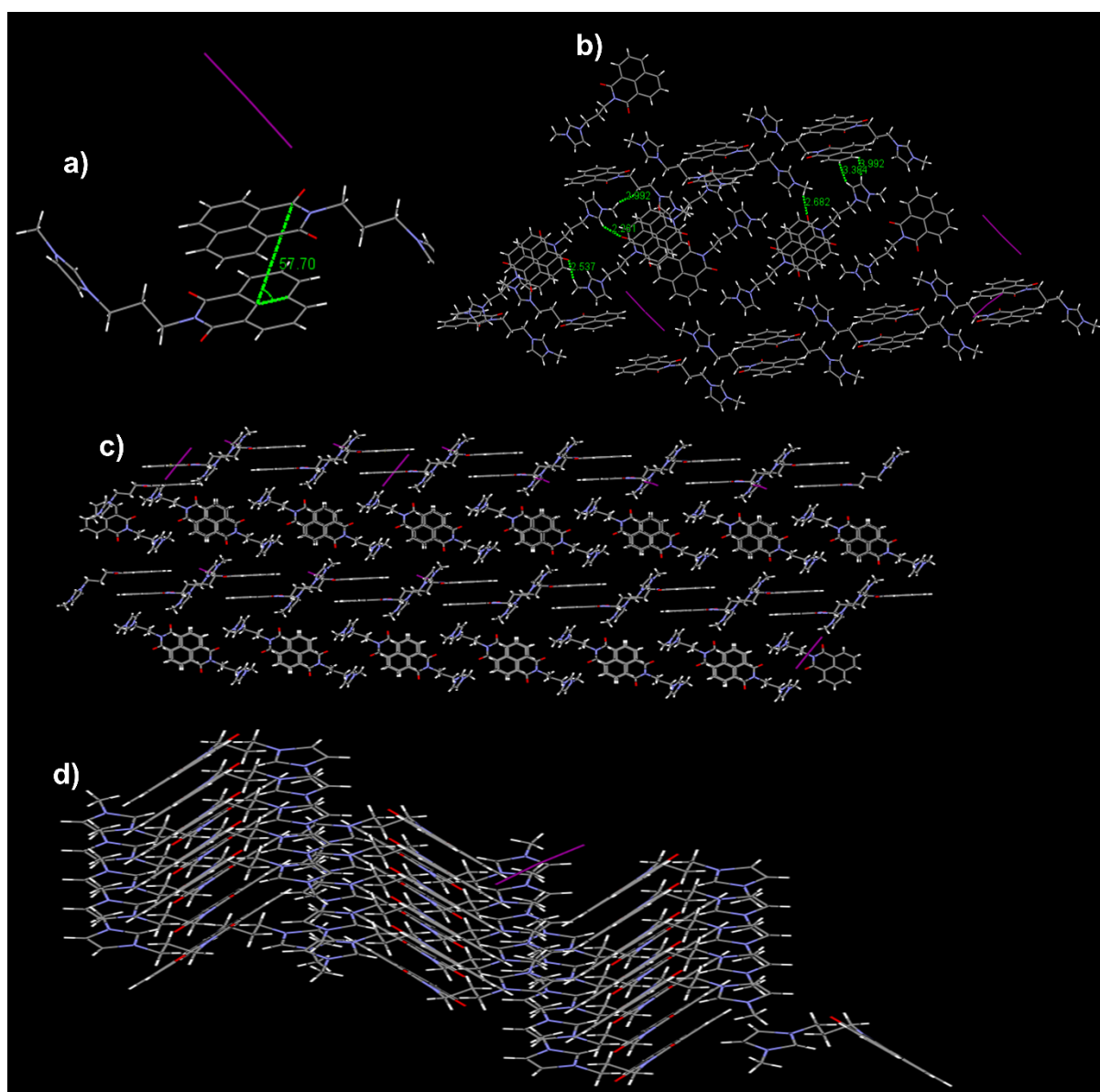


Figure A4.12. (a) The angle between two dimer. (b) Molecular arrangement in **HNIC** crystal lattice, exhibiting C-H \cdots π interaction. (c) Intermolecular packing interaction showing two distinct dimeric plane. (d) Brickwork configuration of **HNIC** in its crystal lattice.

Table A4.9. SCXRD data of the **RNIC** derivatives.

Name	HNIC
Formula	$C_{34}H_{29}NO_2$
Formula weight	71.06
Wavelength (\AA)	0.71073

Space Group	P21/n'
Crystal System	monoclinic
Temperature	298 (K)
Cell Lengths (Å)	a 9.6583(7)
	b 17.9351(13)
	c 12.7900(9)
Cell Angles (o)	α 90
	β 96.194(2)
	γ 90
Cell Volume (Å ³)	2202.6(3)
Z	4
Density (g/cm ³)	0.114
$h_{max}, k_{max}, l_{max}$	11,15,5

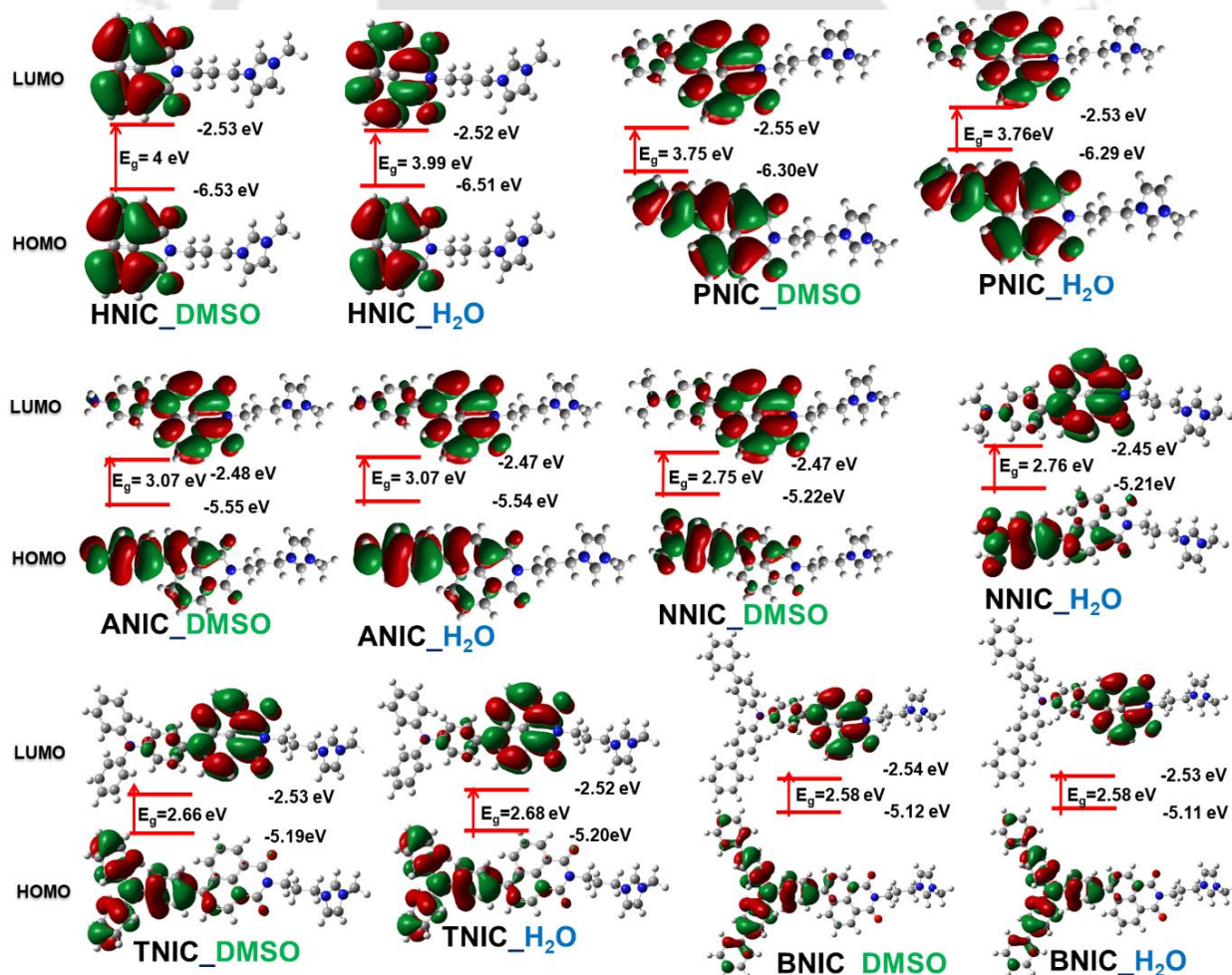


Figure A4.13. (b) Ground state band energies of optimized **RNIC** derivatives in gaseous state or with various solvation.

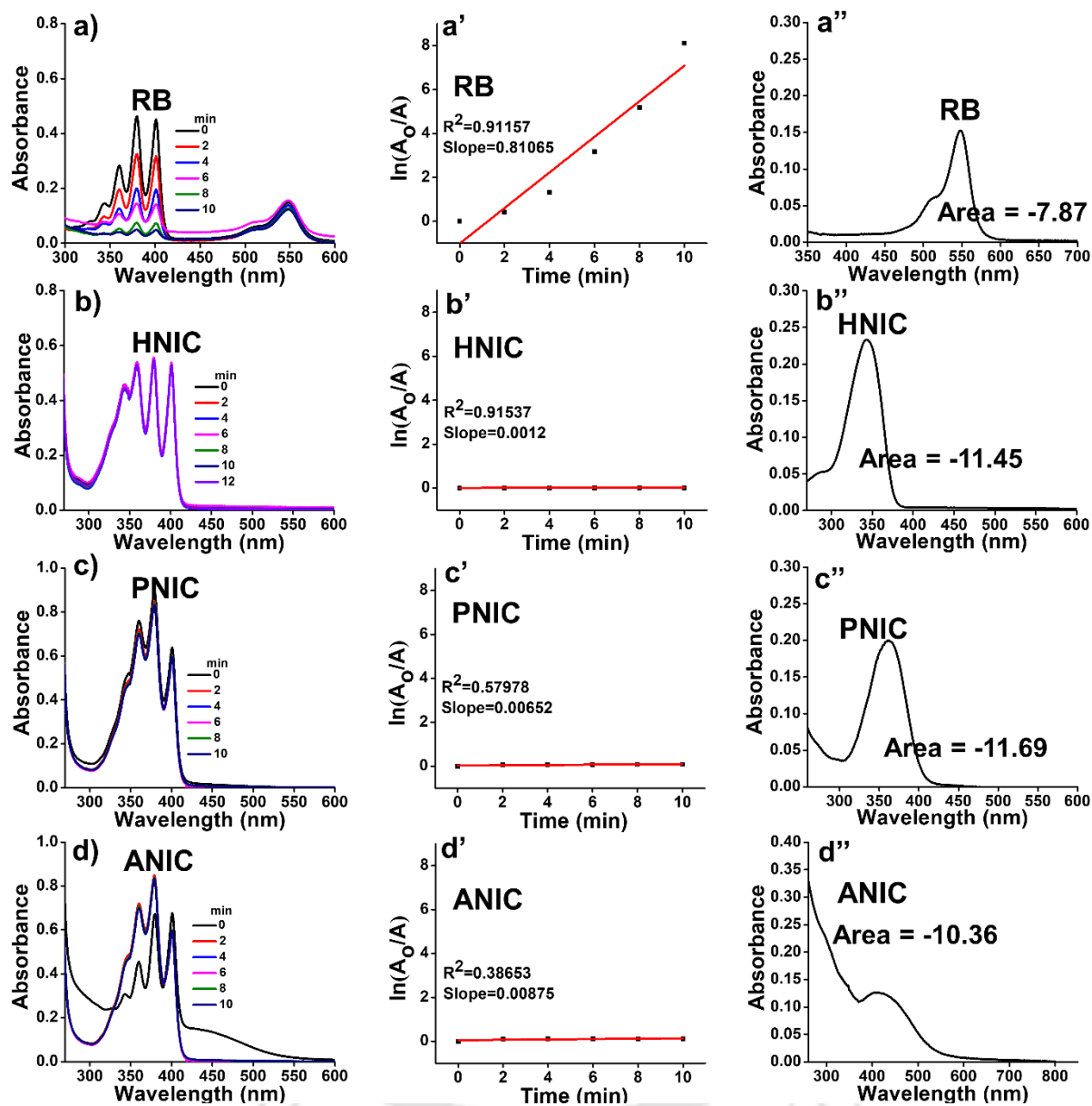


Figure A4.14. The ROS quantum yield of **RNIC** was determined using chemical trapping measurements. **ABDA** undergoing photodegradation with (a) Rose Bengal, (b) **HNIC**, (c) **PNIC**, and (d) **ANIC**, respectively under 10 min white light irradiation. Rate constants for the decomposition of **ABDA** in the presence of (a') Rose Bengal, (b') **HNIC**, (c') **PNIC**, and (d') **ANIC**, respectively, under 10 min white light irradiation. The integrated area of the absorption peak for (a'') Rose Bengal, (b'') **HNIC**, (c'') **PNIC**, and (d'') **ANIC**, respectively, after 10 min white light irradiation.

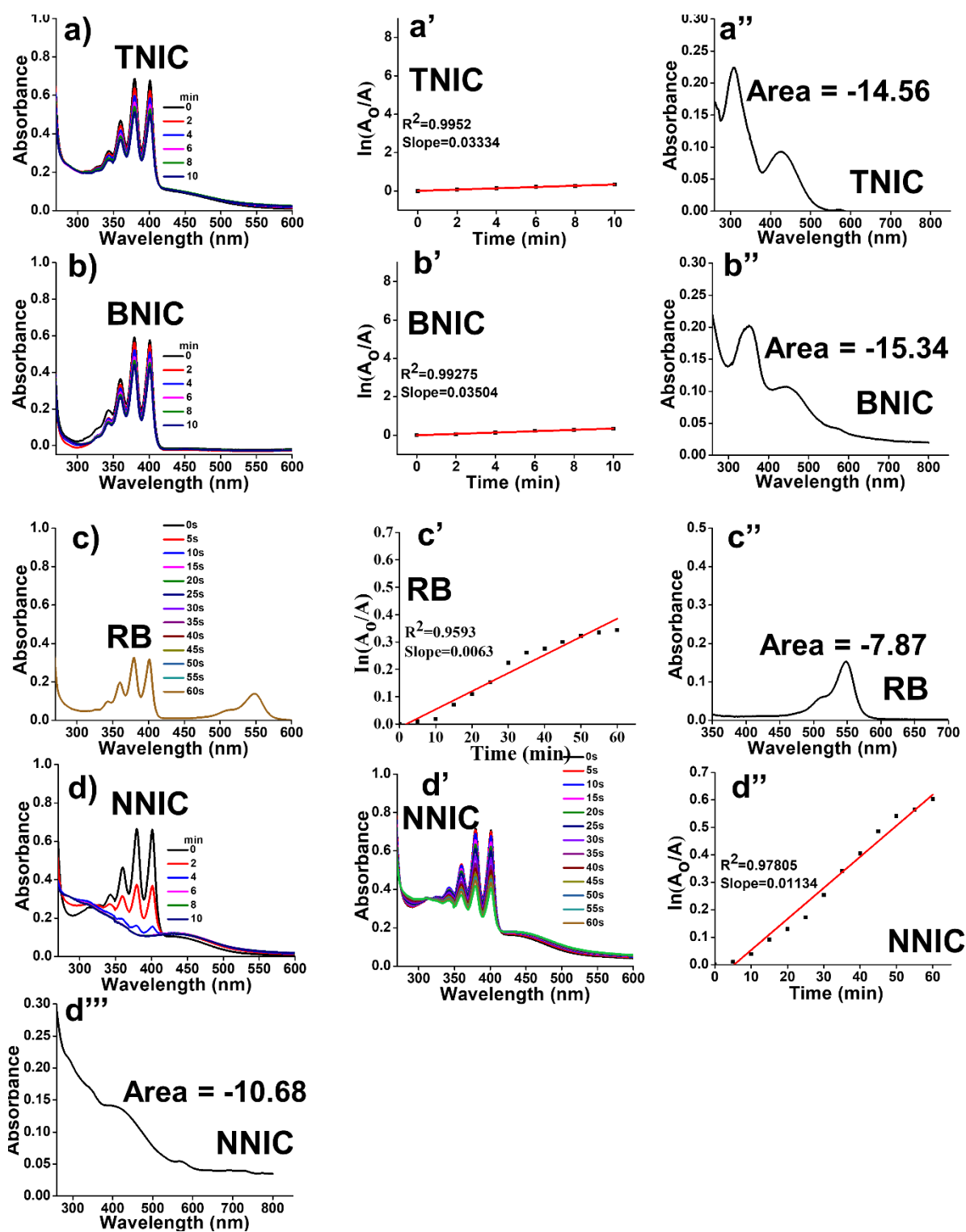


Figure A4.15. The ROS quantum yield of RNIC was determined using chemical trapping measurements. ABDA undergoing photodegradation with (a) TNIC, (b) BNIC, and (d) NNIC, respectively under 10 min white light irradiation. Rate constants for the decomposition of ABDA in the presence of (a') TNIC, and (b') BNIC, respectively under 10 min white light irradiation. The integrated area of the absorption peak for (a'') TNIC, and (b'') BNIC, and (c'') RB, respectively. ABDA undergoing photodegradation with (c) RB, and (d') NNIC, respectively under 1 min white light irradiation. Rate constants for the decomposition of ABDA in the presence of (c') RB, and (d'') NNIC, respectively under 1 min white light irradiation. (d''') The integrated area of the absorption peak for NNIC.

Table A4.10. Spin-orbit coupling matrix elements (SOCME) of **RNIC** compounds in optimized structure. $\langle S_m | H_{SO} | T_n \rangle$, cm^{-1} calculated using ORCA 5.0 at the B3LYP/6-31G (d, p) and B3LYP/DEF2SVP level.

Materials	HNIC	PNIC	ANIC	NNIC	TNIC	BNIC
$S_0 \leftrightarrow T_1$	0.678232998	0.141421356	0.83666	0.714142843	0.435889894	0.282842712
$S_1 \leftrightarrow T_1$	0	0.2	0.223607	0.173205081	0.1	0
$S_2 \leftrightarrow T_1$	3.06757233	0.591607978	0.479583	0.331662479	0.1	0
$S_3 \leftrightarrow T_1$	1.923538406	0.655743852	0	0.387298335	0.4	0.360555128
$S_4 \leftrightarrow T_1$	1.319090596	0.1	0.223607	0.556776436	0.574456265	0.4
$S_5 \leftrightarrow T_1$	0.173205081	2.949576241	0.1	0.447213595	0.565685425	0.360555128
$S_6 \leftrightarrow T_1$	1.319090596	0	0.244949	1.034408043	0.728010989	0
$S_7 \leftrightarrow T_1$	1.445683229	0.346410162	0.489898	0.916515139	0.316227766	0.3
$S_8 \leftrightarrow T_1$	2.929163703	1.090871211	2.503997	0.412310563	0.374165739	0.141421356
$S_9 \leftrightarrow T_1$	0.223606798	0.435889894	0.458258	0.316227766	0.412310563	0.244948974
$S_{10} \leftrightarrow T_1$	0.943398113	0.141421356	0.707107	0.374165739	0.223606798	0.64807407
$S_0 \leftrightarrow T_2$	0.331662479	0.447213595	0.360555	0.64807407	0.692820323	0.7
$S_1 \leftrightarrow T_2$	0.316227766	0.1	0	0.173205081	0.2	0.2
$S_2 \leftrightarrow T_2$	2.44744765	0.3	0.141421	0.282842712	0.1	0.223606798
$S_3 \leftrightarrow T_2$	1.6	0.141421356	0.538516	0.244948974	0.141421356	0
$S_4 \leftrightarrow T_2$	1.004987562	0.556776436	0.374166	0.509901951	0.244948974	0.264575131
$S_5 \leftrightarrow T_2$	0.264575131	0.9	0.774597	0.424264069	0.264575131	0.1
$S_6 \leftrightarrow T_2$	1.609347694	1.345362405	0.223607	0.754983444	0.331662479	0.331662479
$S_7 \leftrightarrow T_2$	1.044030651	0.591607978	0.282843	0.655743852	0.316227766	0
$S_8 \leftrightarrow T_2$	2.177154106	0.489897949	0.6	0.360555128	0.6	0.2
$S_9 \leftrightarrow T_2$	0.866025404	0.5	0.141421	0.529150262	0.2	0
$S_{10} \leftrightarrow T_2$	1.252996409	0.768114575	0.447214	0.387298335	0.489897949	0
$S_0 \leftrightarrow T_3$	0.282842712	1.7	1.264911	0.948683298	0.806225775	0.538516481
$S_1 \leftrightarrow T_3$	0.1	0.4	0.173205	0	0	0.1
$S_2 \leftrightarrow T_3$	0.3	1.264911064	0.663325	0.761577311	0.640312424	0.489897949

$S_3 \leftrightarrow T_3$	0.141421356	0.264575131	0.141421	0.1	0.141421356	0
$S_4 \leftrightarrow T_3$	0.360555128	0.141421356	0.1	0.141421356	0.1	0.173205081
$S_5 \leftrightarrow T_3$	0.509901951	3.006659276	0.2	0	0	0.141421356
$S_6 \leftrightarrow T_3$	3.340658618	0.1	0.824621	0.435889894	0.1	0.4
$S_7 \leftrightarrow T_3$	0.787400787	0.360555128	1.161895	0.538516481	0.374165739	0
$S_8 \leftrightarrow T_3$	1.374772708	0.938083152	2.807134	0.748331477	0.670820393	0.574456265
$S_9 \leftrightarrow T_3$	2.206807649	0.591607978	0.52915	0.793725393	0.141421356	0.141421356
$S_{10} \leftrightarrow T_3$	0.3	1.072380529	0.943398	0.374165739	0.424264069	0
$S_0 \leftrightarrow T_4$	5.328226722	1.004987562	0.3	0.141421356	0.1	0
$S_1 \leftrightarrow T_4$	0.2	0.141421356	0.547723	0.4	0.387298335	0.360555128
$S_2 \leftrightarrow T_4$	1.928730152	0.714142843	0.316228	0.360555128	0.316227766	0
$S_3 \leftrightarrow T_4$	2.898275349	0.1	0.141421	0.1	0	0
$S_4 \leftrightarrow T_4$	2.158703314	0.1	0	0.1	0.1	0
$S_5 \leftrightarrow T_4$	0.781024968	1.658312395	1.126943	0	0.1	0.244948974
$S_6 \leftrightarrow T_4$	1.349073756	0.141421356	0.2	0.4	0	0.141421356
$S_7 \leftrightarrow T_4$	1.694107435	0	0.173205	0.346410162	0.1	0
$S_8 \leftrightarrow T_4$	3.405877273	0.529150262	0.943398	0.244948974	0.223606798	0
$S_9 \leftrightarrow T_4$	0.959166305	0.1	0.316228	0.244948974	0.141421356	0.141421356
$S_{10} \leftrightarrow T_4$	2.158703314	0.360555128	0.574456	0.1	0.1	0.346410162
$S_0 \leftrightarrow T_5$	0.6	1.962141687	0.2	0.316227766	0.387298335	0.1
$S_1 \leftrightarrow T_5$	0.632455532	0.1	0.387298	0.6244998	0.574456265	0.387298335
$S_2 \leftrightarrow T_5$	3.170173497	1.187434209	0.412311	0.244948974	0.2	0.316227766
$S_3 \leftrightarrow T_5$	2.213594362	0.574456265	0.173205	0	0	0
$S_4 \leftrightarrow T_5$	1.462873884	0.223606798	0.1	0.1	0.1	0
$S_5 \leftrightarrow T_5$	0.141421356	1.034408043	0.331662	0.824621125	0.479583152	0
$S_6 \leftrightarrow T_5$	1.174734012	0.2	0.141421	0.244948974	0.360555128	0
$S_7 \leftrightarrow T_5$	1.646207763	0.2	0.223607	0.331662479	0.663324958	0
$S_8 \leftrightarrow T_5$	3.319638535	0.469041576	0.591608	0.316227766	0.412310563	0.141421356

$S_9 \leftrightarrow T_5$	0.387298335	0.547722558	0.141421	0.424264069	0.6164414	0
$S_{10} \leftrightarrow T_5$	1.676305461	1.280624847	0.173205	0.316227766	0.1	0.141421356
$S_0 \leftrightarrow T_6$	4.548626166	5.281098371	0.547723	1.024695077	0.1	0.374165739
$S_1 \leftrightarrow T_6$	0.842614977	0.412310563	0	0.663324958	0.565685425	0.346410162
$S_2 \leftrightarrow T_6$	4.240283009	2.151743479	0.6	1.183215957	0.1	0.141421356
$S_3 \leftrightarrow T_6$	0.538516481	0.68556546	0.282843	0.458257569	0	0.244948974
$S_4 \leftrightarrow T_6$	0.360555128	0.141421356	0	0.316227766	0.479583152	0
$S_5 \leftrightarrow T_6$	0.916515139	1.414213562	0.2	0.173205081	0	0
$S_6 \leftrightarrow T_6$	1.216552506	0.5	0.264575	0.728010989	0.2	0
$S_7 \leftrightarrow T_6$	1.46628783	0.331662479	0.509902	0.574456265	0.360555128	0.374165739
$S_8 \leftrightarrow T_6$	3.117691454	0.848528137	2.465766	0.331662479	0.2	0.141421356
$S_9 \leftrightarrow T_6$	1.208304597	1.034408043	0.43589	0.141421356	0.360555128	0.223606798
$S_{10} \leftrightarrow T_6$	3.382306905	2.645751311	0.787401	0	0.141421356	0.632455532
$S_0 \leftrightarrow T_7$	1.15758369	0.3	0.781025	0.583095189	0.331662479	0.282842712
$S_1 \leftrightarrow T_7$	0.469041576	0.574456265	0.556776	0.173205081	0.608276253	0.1
$S_2 \leftrightarrow T_7$	0.670820393	0.1	1.296148	0.519615242	1.135781669	0.387298335
$S_3 \leftrightarrow T_7$	0.547722558	0.244948974	0.387298	0.1	0.412310563	0.141421356
$S_4 \leftrightarrow T_7$	0.574456265	0	0.424264	0.282842712	0.331662479	0
$S_5 \leftrightarrow T_7$	0.2	0.734846923	0.141421	0.1	0	0
$S_6 \leftrightarrow T_7$	2.641968963	0.538516481	0.479583	0.244948974	0.1	0.1
$S_7 \leftrightarrow T_7$	0.3	0.141421356	0.223607	0.141421356	0.346410162	0
$S_8 \leftrightarrow T_7$	0.6	0.346410162	1.962142	0.489897949	0.574456265	0.141421356
$S_9 \leftrightarrow T_7$	1.496662955	0.244948974	0.387298	0.6164414	0.173205081	0
$S_{10} \leftrightarrow T_7$	0.412310563	0.412310563	0.244949	0.264575131	0.141421356	0
$S_0 \leftrightarrow T_8$	4.473253849	1.830300522	0.8	0.346410162	0.1	0
$S_1 \leftrightarrow T_8$	1.760681686	0.331662479	0.1	0.519615242	0.728010989	0.3
$S_2 \leftrightarrow T_8$	0.692820323	0.529150262	0.678233	0.1	0.1	0.1
$S_3 \leftrightarrow T_8$	2.04450483	0.556776436	0.316228	0.1	0	0

$S_4 \leftrightarrow T_8$	1.957038579	0.2	0.1	0.824621125	0.360555128	0
$S_5 \leftrightarrow T_8$	1.459451952	3.106444913	0.316228	0	0.2	0.374165739
$S_6 \leftrightarrow T_8$	1.539480432	0.387298335	1.00995	0.141421356	0	0
$S_7 \leftrightarrow T_8$	1.702938637	0.412310563	1.058301	0	0.244948974	0
$S_8 \leftrightarrow T_8$	3.553871129	1.1	1.135782	0.1	0.1	0
$S_9 \leftrightarrow T_8$	2.2627417	0.331662479	0.1	0.282842712	0.7	0.1
$S_{10} \leftrightarrow T_8$	2.097617696	0.556776436	0.5	0.435889894	0	0.412310563
$S_0 \leftrightarrow T_9$	2.517935662	1.509966887	5.361903	1.260952021	1.053565375	0.953939201
$S_1 \leftrightarrow T_9$	3.319638535	1.396424004	0.34641	0.1	0.2	0.469041576
$S_2 \leftrightarrow T_9$	1.513274595	0.346410162	1.438749	0.64807407	0.223606798	0.989949494
$S_3 \leftrightarrow T_9$	1.311487705	0.223606798	0.360555	0.141421356	0.141421356	0
$S_4 \leftrightarrow T_9$	1.2	0.547722558	0.2	0.244948974	0.2	0.346410162
$S_5 \leftrightarrow T_9$	2.505992817	1.6673332	0.447214	0	0.1	0.264575131
$S_6 \leftrightarrow T_9$	0.860232527	0.3	2.03224	0.4	0.1	0.2
$S_7 \leftrightarrow T_9$	0.953939201	0.264575131	2.431049	0.316227766	0.223606798	0
$S_8 \leftrightarrow T_9$	1.870828693	0.282842712	0.316228	0.5	0.4	0.768114575
$S_9 \leftrightarrow T_9$	4.047221269	0.888819442	0.519615	0.244948974	0.173205081	0.141421356
$S_{10} \leftrightarrow T_9$	1.462873884	0.244948974	1.337909	0	0.173205081	0.2
$S_0 \leftrightarrow T_{10}$	0.331662479	1.852025918	0.282843	0.948683298	0.173205081	0.223606798
$S_1 \leftrightarrow T_{10}$	0.4	0.173205081	0.774597	0	0.223606798	0.282842712
$S_2 \leftrightarrow T_{10}$	0.830662386	0.68556546	0.173205	0.244948974	0	0.244948974
$S_3 \leftrightarrow T_{10}$	0.489897949	0.360555128	1.126943	0.1	0	0.141421356
$S_4 \leftrightarrow T_{10}$	0.360555128	0.141421356	0.3	0.1	0.68556546	0
$S_5 \leftrightarrow T_{10}$	0	2.024845673	0.1	0.223606798	0.374165739	0.2
$S_6 \leftrightarrow T_{10}$	0.141421356	0.264575131	0.244949	0.883176087	0.244948974	0
$S_7 \leftrightarrow T_{10}$	0.374165739	0.173205081	0.173205	0.173205081	0	0.1
$S_8 \leftrightarrow T_{10}$	0.761577311	0.6164414	0.4	0.412310563	0.141421356	0.2
$S_9 \leftrightarrow T_{10}$	0.173205081	0.244948974	0.458258	0.734846923	0.509901951	0

$S_{10} \leftrightarrow T_{10}$	0.173205081	0.754983444	0.2	0.374165739	0	0.374165739
---------------------------------	-------------	-------------	-----	-------------	---	-------------

Table A4.11. Excited state singlet and triplet state energy difference (ΔE_{ST}) eV of **RNIC** compounds in optimized calculated using ORCA 5.0 at the B3LYP/6-31G (d, p) and B3LYP/DEF2SVP level.

	HNIC	PNIC	ANIC	NNIC	TNIC	BNIC
$S_1 \leftrightarrow T_1$	0.935	0.674	0.205	0.003	0.001	0
$S_1 \leftrightarrow T_2$	0.064	0.002	0	-0.004	-0.014	-0.118
$S_1 \leftrightarrow T_3$	0.003	-0.311	-0.394	-0.746	-0.61	-0.731
$S_1 \leftrightarrow T_4$	-0.187	-0.377	-0.857	-0.912	-0.912	-0.767
$S_1 \leftrightarrow T_5$	-0.397	-0.586	-0.913	-1.212	-1.036	-0.913
$S_1 \leftrightarrow T_6$	-0.524	-0.605	-1.032	-1.418	-1.311	-1.016
$S_1 \leftrightarrow T_7$	-0.71	-0.775	-1.138	-1.498	-1.344	-1.063
$S_1 \leftrightarrow T_8$	-0.723	-0.818	-1.25	-1.715	-1.42	-1.368
$S_1 \leftrightarrow T_9$	-0.822	-0.877	-1.284	-1.733	-1.432	-1.382
$S_1 \leftrightarrow T_{10}$	-0.924	-0.923	-1.315	-1.763	-1.484	-1.389
$S_2 \leftrightarrow T_1$	1.388	1.03	0.498	0.436	0.309	0.319
$S_2 \leftrightarrow T_2$	0.517	0.358	0.293	0.429	0.294	0.201
$S_2 \leftrightarrow T_3$	0.456	0.045	-0.101	-0.313	-0.302	-0.412
$S_2 \leftrightarrow T_4$	0.266	-0.021	-0.564	-0.479	-0.604	-0.448
$S_2 \leftrightarrow T_5$	0.056	-0.23	-0.62	-0.779	-0.728	-0.594
$S_2 \leftrightarrow T_6$	-0.071	-0.249	-0.739	-0.985	-1.003	-0.697
$S_2 \leftrightarrow T_7$	-0.257	-0.419	-0.845	-1.065	-1.036	-0.744
$S_2 \leftrightarrow T_8$	-0.27	-0.462	-0.957	-1.282	-1.112	-1.049
$S_2 \leftrightarrow T_9$	-0.369	-0.521	-0.991	-1.3	-1.124	-1.063
$S_2 \leftrightarrow T_{10}$	-0.471	-0.567	-1.022	-1.33	-1.176	-1.07
$S_3 \leftrightarrow T_1$	1.427	1.402	1.064	0.916	0.914	0.767
$S_3 \leftrightarrow T_2$	0.556	0.73	0.859	0.909	0.899	0.649
$S_3 \leftrightarrow T_3$	0.495	0.417	0.465	0.167	0.303	0.036

$S_3 \leftrightarrow T_4$	0.305	0.351	0.002	0.001	0.001	0
$S_3 \leftrightarrow T_5$	0.095	0.142	-0.054	-0.299	-0.123	-0.146
$S_3 \leftrightarrow T_6$	-0.032	0.123	-0.173	-0.505	-0.398	-0.249
$S_3 \leftrightarrow T_7$	-0.218	-0.047	-0.279	-0.585	-0.431	-0.296
$S_3 \leftrightarrow T_8$	-0.231	-0.09	-0.391	-0.802	-0.507	-0.601
$S_3 \leftrightarrow T_9$	-0.33	-0.149	-0.425	-0.82	-0.519	-0.615
$S_3 \leftrightarrow T_{10}$	-0.432	-0.195	-0.456	-0.85	-0.571	-0.622
$S_4 \leftrightarrow T_1$	1.597	1.449	1.119	1.217	1.038	0.913
$S_4 \leftrightarrow T_2$	0.726	0.777	0.914	1.21	1.023	0.795
$S_4 \leftrightarrow T_3$	0.665	0.464	0.52	0.468	0.427	0.182
$S_4 \leftrightarrow T_4$	0.475	0.398	0.057	0.302	0.125	0.146
$S_4 \leftrightarrow T_5$	0.265	0.189	0.001	0.002	0.001	0
$S_4 \leftrightarrow T_6$	0.138	0.17	-0.118	-0.204	-0.274	-0.103
$S_4 \leftrightarrow T_7$	-0.048	0	-0.224	-0.284	-0.307	-0.15
$S_4 \leftrightarrow T_8$	-0.061	-0.043	-0.336	-0.501	-0.383	-0.455
$S_4 \leftrightarrow T_9$	-0.16	-0.102	-0.37	-0.519	-0.395	-0.469
$S_4 \leftrightarrow T_{10}$	-0.262	-0.148	-0.401	-0.549	-0.447	-0.476
$S_5 \leftrightarrow T_1$	1.65	1.54	1.519	1.718	1.312	1.016
$S_5 \leftrightarrow T_2$	0.779	0.868	1.314	1.711	1.297	0.898
$S_5 \leftrightarrow T_3$	0.718	0.555	0.92	0.969	0.701	0.285
$S_5 \leftrightarrow T_4$	0.528	0.489	0.457	0.803	0.399	0.249
$S_5 \leftrightarrow T_5$	0.318	0.28	0.401	0.503	0.275	0.103
$S_5 \leftrightarrow T_6$	0.191	0.261	0.282	0.297	0	0
$S_5 \leftrightarrow T_7$	0.005	0.091	0.176	0.217	-0.033	-0.047
$S_5 \leftrightarrow T_8$	-0.008	0.048	0.064	0	-0.109	-0.352
$S_5 \leftrightarrow T_9$	-0.107	-0.011	0.03	-0.018	-0.121	-0.366
$S_5 \leftrightarrow T_{10}$	-0.209	-0.057	-0.001	-0.048	-0.173	-0.373
$S_6 \leftrightarrow T_1$	1.744	1.55	1.549	1.804	1.421	1.076

$S_6 \leftrightarrow T_2$	0.873	0.878	1.344	1.797	1.406	0.958
$S_6 \leftrightarrow T_3$	0.812	0.565	0.95	1.055	0.81	0.345
$S_6 \leftrightarrow T_4$	0.622	0.499	0.487	0.889	0.508	0.309
$S_6 \leftrightarrow T_5$	0.412	0.29	0.431	0.589	0.384	0.163
$S_6 \leftrightarrow T_6$	0.285	0.271	0.312	0.383	0.109	0.06
$S_6 \leftrightarrow T_7$	0.099	0.101	0.206	0.303	0.076	0.013
$S_6 \leftrightarrow T_8$	0.086	0.058	0.094	0.086	0	-0.292
$S_6 \leftrightarrow T_9$	-0.013	-0.001	0.06	0.068	-0.012	-0.306
$S_6 \leftrightarrow T_{10}$	-0.115	-0.047	0.029	0.038	-0.064	-0.313
$S_7 \leftrightarrow T_1$	1.858	1.593	1.613	1.873	1.485	1.368
$S_7 \leftrightarrow T_2$	0.987	0.921	1.408	1.866	1.47	1.25
$S_7 \leftrightarrow T_3$	0.926	0.608	1.014	1.124	0.874	0.637
$S_7 \leftrightarrow T_4$	0.736	0.542	0.551	0.958	0.572	0.601
$S_7 \leftrightarrow T_5$	0.526	0.333	0.495	0.658	0.448	0.455
$S_7 \leftrightarrow T_6$	0.399	0.314	0.376	0.452	0.173	0.352
$S_7 \leftrightarrow T_7$	0.213	0.144	0.27	0.372	0.14	0.305
$S_7 \leftrightarrow T_8$	0.2	0.101	0.158	0.155	0.064	0
$S_7 \leftrightarrow T_9$	0.101	0.042	0.124	0.137	0.052	-0.014
$S_7 \leftrightarrow T_{10}$	-0.001	-0.004	0.093	0.107	0	-0.021
$S_8 \leftrightarrow T_1$	1.864	1.694	1.753	1.9	1.486	1.383
$S_8 \leftrightarrow T_2$	0.993	1.022	1.548	1.893	1.471	1.265
$S_8 \leftrightarrow T_3$	0.932	0.709	1.154	1.151	0.875	0.652
$S_8 \leftrightarrow T_4$	0.742	0.643	0.691	0.985	0.573	0.616
$S_8 \leftrightarrow T_5$	0.532	0.434	0.635	0.685	0.449	0.47
$S_8 \leftrightarrow T_6$	0.405	0.415	0.516	0.479	0.174	0.367
$S_8 \leftrightarrow T_7$	0.219	0.245	0.41	0.399	0.141	0.32
$S_8 \leftrightarrow T_8$	0.206	0.202	0.298	0.182	0.065	0.015
$S_8 \leftrightarrow T_9$	0.107	0.143	0.264	0.164	0.053	0.001

$S_8 \leftrightarrow T_{10}$	0.005	0.097	0.233	0.134	0.001	-0.006
$S_9 \leftrightarrow T_1$	2.034	1.71	1.794	1.921	1.543	1.389
$S_9 \leftrightarrow T_2$	1.163	1.038	1.589	1.914	1.528	1.271
$S_9 \leftrightarrow T_3$	1.102	0.725	1.195	1.172	0.932	0.658
$S_9 \leftrightarrow T_4$	0.912	0.659	0.732	1.006	0.63	0.622
$S_9 \leftrightarrow T_5$	0.702	0.45	0.676	0.706	0.506	0.476
$S_9 \leftrightarrow T_6$	0.575	0.431	0.557	0.5	0.231	0.373
$S_9 \leftrightarrow T_7$	0.389	0.261	0.451	0.42	0.198	0.326
$S_9 \leftrightarrow T_8$	0.376	0.218	0.339	0.203	0.122	0.021
$S_9 \leftrightarrow T_9$	0.277	0.159	0.305	0.185	0.11	0.007
$S_9 \leftrightarrow T_{10}$	0.175	0.113	0.274	0.155	0.058	0
$S_{10} \leftrightarrow T_1$	2.209	1.744	1.841	1.954	1.555	1.528
$S_{10} \leftrightarrow T_2$	1.338	1.072	1.636	1.947	1.54	1.41
$S_{10} \leftrightarrow T_3$	1.277	0.759	1.242	1.205	0.944	0.797
$S_{10} \leftrightarrow T_4$	1.087	0.693	0.779	1.039	0.642	0.761
$S_{10} \leftrightarrow T_5$	0.877	0.484	0.723	0.739	0.518	0.615
$S_{10} \leftrightarrow T_6$	0.75	0.465	0.604	0.533	0.243	0.512
$S_{10} \leftrightarrow T_7$	0.564	0.295	0.498	0.453	0.21	0.465
$S_{10} \leftrightarrow T_8$	0.551	0.252	0.386	0.236	0.134	0.16
$S_{10} \leftrightarrow T_9$	0.452	0.193	0.352	0.218	0.122	0.146
$S_{10} \leftrightarrow T_{10}$	0.35	0.147	0.321	0.188	0.07	0.139

Table A4.12. Calculated different excite state singlet (S) and triplet (T) state energy of the **RNIC** derivatives via ORCA 5.0 at the B3LYP/6-31G (d, p) and B3LYP/DEF2SVP level.

Materials	S (eV)										T (eV)									
	S ₁	S ₂	S ₃	S ₄	S ₅	S ₆	S ₇	S ₈	S ₉	S ₁₀	T ₁	T ₂	T ₃	T ₄	T ₅	T ₆	T ₇	T ₈	T ₉	T ₁₀
HNIC	3.39	3.843	3.882	4.052	4.105	4.199	4.313	4.319	4.489	4.664	2.455	3.326	3.387	3.577	3.787	3.914	4.141	4.113	4.212	4.314

PNIC	2.9 96	3.3 52	3.7 24	3.7 71	3.8 62	3.8 72	3.9 15	4.0 16	4.0 32	4.0 66	2.3 22	2.9 94	3.3 07	3.3 73	3.5 82	3.6 01	3.7 71	3.8 14	3.8 73	3.9 19
ANIC	2.3 49	2.6 42	3.2 08	3.2 63	3.6 63	3.6 93	3.7 57	3.8 97	3.9 38	3.9 85	2.1 44	2.3 49	2.7 43	3.2 06	3.2 62	3.3 81	3.4 87	3.5 99	3.6 33	3.6 64
NNIC	1.9 02	2.3 35	2.8 15	3.1 16	3.6 17	3.7 03	3.7 72	3.7 99	3.8 2	3.8 53	1.8 99	1.9 06	2.6 48	2.8 14	3.1 14	3.3 2	3.4	3.6 17	3.6 35	3.6 65
TNIC	1.9 55	2.2 63	2.8 68	2.9 92	3.2 66	3.3 75	3.4 39	3.4 4	3.4 97	3.5 09	1.9 54	1.9 69	2.5 65	2.8 67	2.9 91	3.2 66	3.2 99	3.3 75	3.3 87	3.4 39
BNIC	1.7 19	2.0 38	2.4 86	2.6 32	2.7 35	2.7 95	3.0 87	3.1 02	3.1 08	3.2 47	1.7 19	1.8 37	2.4 5	2.4 86	2.6 32	2.7 35	2.7 82	3.0 87	3.1 01	3.1 08



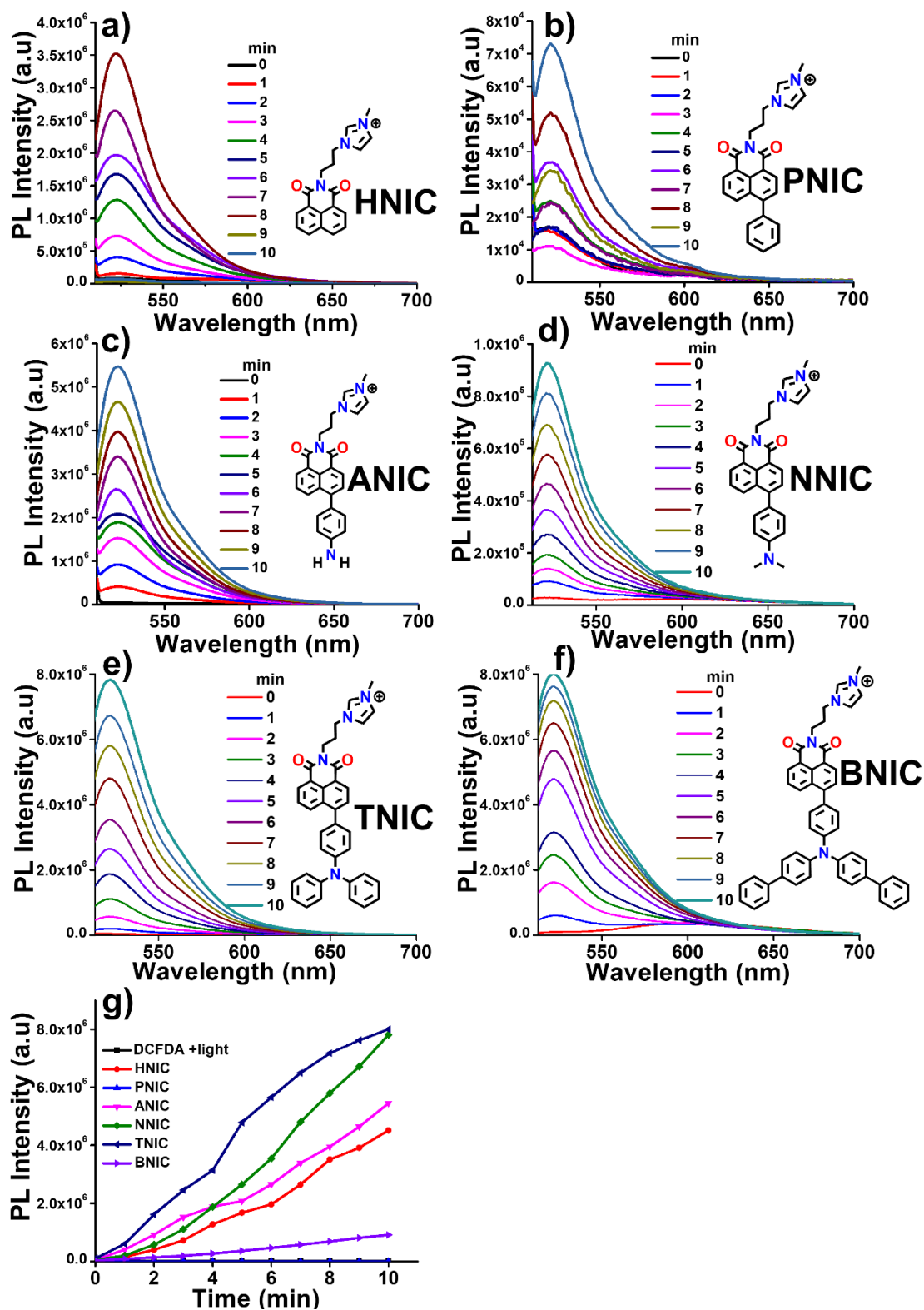


Figure A4.16. ROS generation by the RNIC derivatives. (a-f) Evaluation of the general ROS generation using DCFDA (1 μ M) indicator by PSs (100 μ M) upon white light excitation for different time periods at 99% PBS fraction in DMSO ($\lambda_{\text{ex}}=500$ nm). Inset: Chemical structure of the RNIC derivatives. (g) Plot of PL intensities of DCFDA indicator in the presence of RNIC derivatives.

Table A4.13. Zeta potential data of **RNIC** derivatives at different PH.

PH	HNIC	PNIC	ANIC	NNIC	TNIC	BNIC
1	4.93	17.6	20.4	19.3	21.2	21.4
3	0.627	8.46	18.7	15.2	19.3	19.8
5.6	-4.72	-4.65	16.8	10.5	14.6	2.63
7.4	-2.95	-3.17	15.3	7.8	10.4	-16.8
9	-5.21	-3.09	13.9	6.02	9.1	-16.9

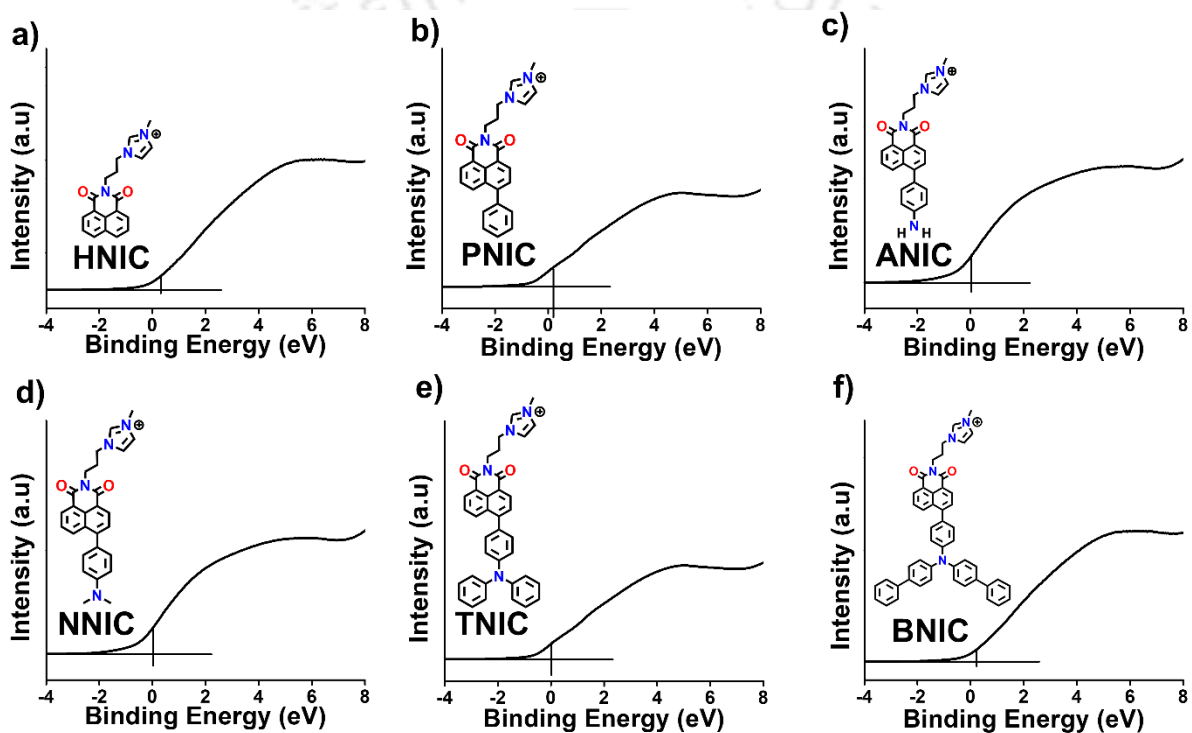


Figure A4.17. XPS spectra displaying valence band energy (E_v): (a) HNIC, (b) PNIC, (c) ANIC, (d) NNIC, (e) TNIC, and (f) BNIC, respectively.

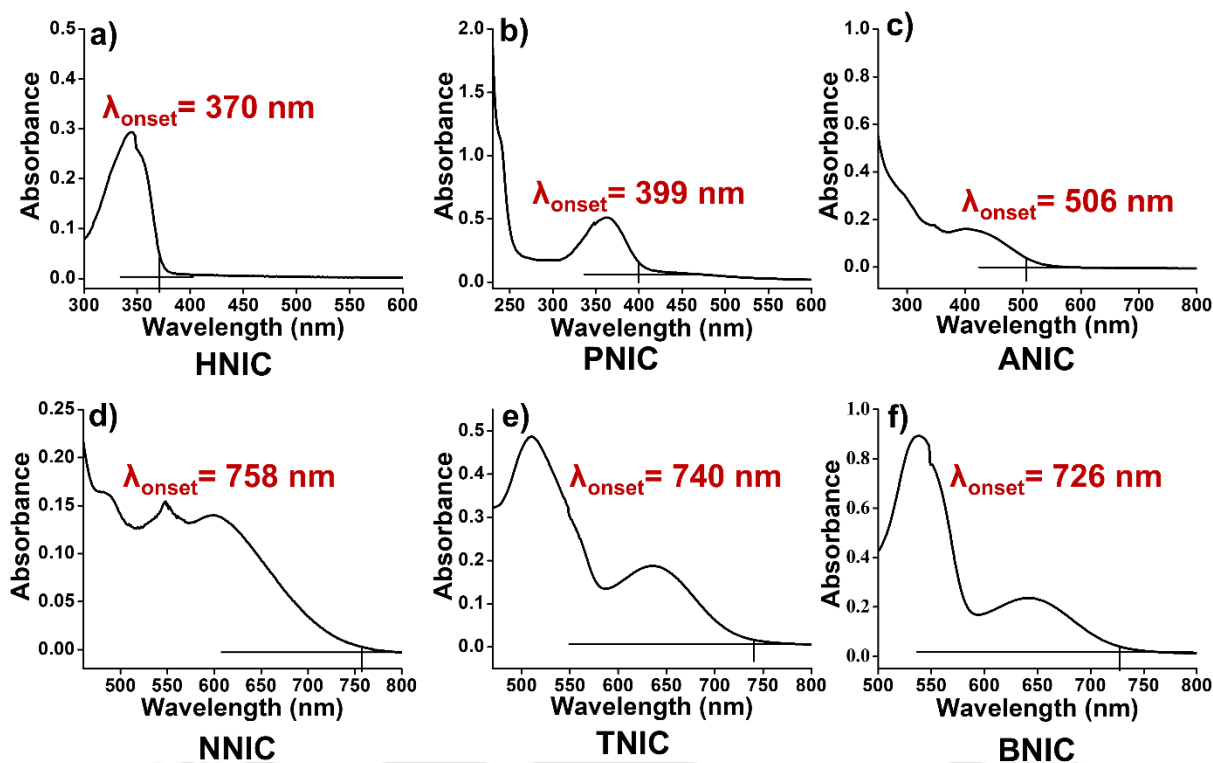


Figure A4.18. (a-f) UV-vis spectroscopy of exhibiting onset absorption (a) HNIC, (b) PNIC, (c) ANIC, (d) NNIC, (e) TNIC, and (f) BNIC, respectively.

Table A4.14. Optical band gap data RNIC derivatives calculated from the onset absorption of the UV-vis spectroscopy.

Materials	λ_{onset}	E_g (eV)
HNIC	370	3.351
PNIC	399	3.10
ANIC	506	2.45
NNIC	758	1.64
TNIC	740	1.67
BNIC	726	1.71

λ_{onset} onset UV-vis absorption.

Table A4.15. E_c and E_v at a pH of 5.6 RNIC derivatives.

Materials	E_g	E_{HOMO}	E_{LUMO}	E_v	E_c	PZZP	$E_{v,5.6}$	$E_{c,5.6}$
HNIC	3.351	-4.810	-1.459	0.31	-3.041	0.627	0.0166	-3.3344
PNIC	3.10	-4.6	-1.5	0.10	-3	8.46	0.2684	-2.83126

ANIC	2.45	-4.523	-2.073	0.023	-2.427	13.9	0.5127	-1.9373
NNIC	1.64	-4.525	-2.885	0.025	-1.615	6.02	0.04978	-1.59022
TNIC	1.67	-4.62	-2.95	0.12	-1.55	9.1	0.3265	-1.3435
BNIC	1.71	-4.710	-3.10	0.21	-1.40	2.63	0.03477	-1.57523

PZZP, the point of zero zeta potential.

Table A4.16. Calculated Gibbs free energy of **RNIC** derivatives using **ORCA 5.0** at the B3LYP/6-31G (d, p) and B3LYP/DEF2SVP level using quantum mechanism package.

Materials	G (Eh)		ΔG (Kcal mol⁻¹)
HNIC	HNIC+O ₂	-1047.73533495	-52.69
	HNIC	-1047.651374	
PNIC	PNIC+O ₂	-1278.40231082	-51.29
	PNIC	-1278.320573	
ANIC	ANIC+O ₂	-1333.66753682	-48.05
	ANIC	-1333.590971	
NNIC	O ₂	-150.09346315	-5.17
	NNIC+O ₂	-1562.22399193	
	NNIC	-1412.12221216	
TNIC	O ₂	-150.09346315	-11.38
	TNIC+O ₂	-1944.52406111	
	TNIC	-1794.44872692	
BNIC	O ₂	-150.09346315	-369.72
	BNIC+O ₂	-2405.84826613	
	BNIC	-2256.34399712	

Table A4.17. Calculated Gibbs free energy O_2 using ORCA 5.0 at the B3LYP/6-31G (d, p) and B3LYP/DEF2SVP level using a quantum mechanism package.

GIBBS FREE ENERGY

O_2

The Gibbs free energy is $G = H - T \cdot S$

Total enthalpy ... -150.07131287 Eh

Total entropy correction ... -0.02215028 Eh -13.90 kcal/mol

Final Gibbs free energy ... -150.09346315 Eh

For completeness - the Gibbs free energy minus the electronic energy

G-E(el) ... -0.01441918 Eh -9.05 kcal/mol

Timings for individual modules:

Sum of individual times ... 12.524 sec (= 0.209 min)

GTO integral calculation ... 2.186 sec (= 0.036 min) 17.5 %

SCF iterations ... 4.342 sec (= 0.072 min) 34.7 %

Analytical frequency calculation... 5.995 sec (= 0.100 min) 47.9 %



Table A4.18. Calculated Gibbs free energy of **HNIC** using ORCA 5.0 at the B3LYP/6-31G (d,p) and B3LYP/DEF2SVP level using quantum mechanism package.

```

GIBBS FREE ENERGY
-----
                                         HNIC
The Gibbs free energy is G = H - T*S
Total enthalpy ... -1047.588145 Eh
Total entropy correction ... -0.063229 Eh -39.68 kcal/mol
-----
Final Gibbs free energy ... -1047.651374 Eh
For completeness - the Gibbs free energy minus the
electronic energy
G-E(el) ... 0.29434596 Eh 184.7 kcal/mol
Timings for individual modules:
Sum of individual times ... 43967.091 sec (= 732.785 min)
GTO integral calculation ... 4.74 sec (= 0.079 min) 0 %
SCF iterations ... 165.148 sec (= 2.752 min) 0.4 %
CIS module ... 157.11 sec (= 2.618 min) 0.4 %
SCF Gradient evaluation ... 86.897 sec (= 1.448 min) 0.2 %
Numerical frequency calculation ... 43553.196 sec (=725.887 min)
99.1 %

```

Table A4.19. Calculated Gibbs free energy of **HNIC** and **O₂** using ORCA 5.0 at the B3LYP/6-31G (d,p) and B3LYP/DEF2SVP level using quantum mechanism package.

```

-----
                                         HNIC+O2
GIBBS FREE ENERGY
-----
The Gibbs free energy is G = H - T*S
Total enthalpy ... -1047.67636762 Eh
Total entropy correction ... -0.05896733 Eh -37.00 kcal/mol
-----
Final Gibbs free energy ... -1047.73533495 Eh
For completeness - the Gibbs free energy minus the electronic
energy
G-E(el) ... 0.30059463 Eh 188.63 kcal/mol
Timings for individual modules:
Sum of individual times ... 965.742 sec (= 16.096 min)
GTO integral calculation ... 7.168 sec (= 0.119 min) 0.7 %
SCF iterations ... 132.533 sec (= 2.209 min) 13.7 %
Analytical frequency calculation... 826.041 sec (= 13.767 min)
85.5 %

```

Table A4.20. Calculated Gibbs free energy of **PNIC** using ORCA 5.0 at the B3LYP/6-31G (d,p) and B3LYP/DEF2SVP level using quantum mechanism package.

```

-----
GIBBS FREE ENERGY                                     PNIC
-----
The Gibbs free energy is G = H - T*S
Total enthalpy ... -1278.251757 Eh
Total entropy correction ... -0.068816 Eh -43.18 kcal/mol
-----
Final Gibbs free energy ... -1278.320573 Eh
For completeness - the Gibbs free energy minus the
electronic energy
G-E(el) ... 0.37312194 Eh 234.14 kcal/mol
Timings for individual modules:
Sum of individual times ... 77563.872 sec (=1292.731 min)
GTO integral calculation ... 4.735 sec (= 0.079 min) 0 %
SCF iterations ... 216.553 sec (= 3.609 min) 0.3 %
CIS module ... 242.135 sec (= 4.036 min) 0.3 %
SCF Gradient evaluation ... 112.243 sec (= 1.871 min) 0.1 %
Numerical frequency calculation ... 76988.205 sec (=1283.137 min) 99.3
%

```

Table A4.21. Calculated Gibbs free energy of **PNIC** and **O₂** using ORCA 5.0 at the B3LYP/6-31G (d,p) and B3LYP/DEF2SVP level using quantum mechanism package.

```

-----
GIBBS FREE ENERGY                                     PNIC+O2
-----
The Gibbs free energy is G = H - T*S
Total enthalpy ... -1278.33351732 Eh
Total entropy correction ... -0.06879350 Eh -43.17 kcal/mol
-----
Final Gibbs free energy ... -1278.40231082 Eh
For completeness - the Gibbs free energy minus the electronic energy
G-E(el) ... 0.37673172 Eh 236.40 kcal/mol
Timings for individual modules:
Sum of individual times ... 1590.016 sec (= 26.500 min)
GTO integral calculation ... 4.322 sec (= 0.072 min) 0.3 %
SCF iterations ... 173.370 sec (= 2.890 min) 10.9 %
Analytical frequency calculation... 1412.324 sec (= 23.539 min) 88.8 %

```

Table A4.22. Calculated Gibbs free energy of **ANIC** using ORCA 5.0 at the B3LYP/6-31G (d,p) and B3LYP/DEF2SVP level using quantum mechanism pac kage.

GIBBS FREE ENERGY

ANIC

The Gibbs free energy is $G = H - T \cdot S$

Total enthalpy ... -1333.520574 Eh

Total entropy correction ... -0.0703972 Eh -44.17 kcal/mol

Final Gibbs free energy ... -1333.590971 Eh

For completeness - the Gibbs free energy minus the
electronic energy

G-E(el) ... 0.38792649 Eh 243.43 kcal/mol

Timings for individual modules:

Sum of individual times ... 106846.706 sec (=1780.778 min)

GTO integral calculation ... 5.353 sec (= 0.089 min) 0 %

SCF iterations ... 265.421 sec (= 4.424 min) 0.2 %

CIS module ... 330.526 sec (= 5.509 min) 0.3 %

SCF Gradient evaluation ... 143.862 sec (= 2.398 min) 0.1 %

Numerical frequency calculation ... 106101.544 sec (=1768.359 min)
99.3 %



Table A4.23. Calculated Gibbs free energy of ANIC and O₂ using ORCA 5.0 at the B3LYP/6-31G (d,p) and B3LYP/DEF2SVP level using quantum mechanism package.

```

-----
GIBBS FREE ENERGY                                ANIC+O2
-----
The Gibbs free energy is G = H - T*S
Total enthalpy ... -1333.59628390 Eh
Total entropy correction ... -0.07125292 Eh -44.71 kcal/mol
-----
Final Gibbs free energy ... -1333.66753682 Eh
For completeness - the Gibbs free energy minus the electronic
energy
G-E(el) ... 0.39013978 Eh 244.82 kcal/mol
Timings for individual modules:
Sum of individual times ... 1737.482 sec (= 28.958 min)
GTO integral calculation ... 3.553 sec (= 0.059 min) 0.2 %
SCF iterations ... 182.776 sec (= 3.046 min) 10.5 %
Analytical frequency calculation... 1551.153 sec (= 25.853 min)
89.3 %

```

Table A4.24. Calculated Gibbs free energy of NNIC using ORCA 5.0 at the B3LYP/6-31G (d,p) and B3LYP/DEF2SVP level using quantum mechanism package.

```

-----
GIBBS FREE ENERGY                                NNIC
-----
The Gibbs free energy is G = H - T*S
Total enthalpy ... -1412.04863803 Eh
Total entropy correction ... -0.07357413 Eh -46.17 kcal/mol
-----
Final Gibbs free energy ... -1412.12221216 Eh
For completeness - the Gibbs free energy minus the electronic
energy
G-E(el) ... 0.44655022 Eh 280.21 kcal/mol
Timings for individual modules:
Sum of individual times ... 1791.596 sec (= 29.860 min)
GTO integral calculation ... 3.631 sec (= 0.061 min) 0.2 %
SCF iterations ... 156.328 sec (= 2.605 min) 8.7 %
Analytical frequency calculation... 1631.637 sec (= 27.194
min) 91.1 %

```

Table A4.25. Calculated Gibbs free energy of **NNIC** and **O₂** using ORCA 5.0 at the B3LYP/6-31G (d,p) and B3LYP/DEF2SVP level using quantum mechanism package.

```

-----
GIBBS FREE ENERGY
-----
The Gibbs free energy is G = H - T*S
Total enthalpy ... -1562.12997398 Eh
Total entropy correction ... -0.09401795 Eh -59.00 kcal/mol
-----
Final Gibbs free energy ... -1562.22399193 Eh
For completeness - the Gibbs free energy minus the electronic
energy
G-E(el) ... 0.44011589 Eh 276.18 kcal/mol
Timings for individual modules:
Sum of individual times ... 2724.863 sec (= 45.414 min)
GTO integral calculation ... 3.706 sec (= 0.062 min) 0.1 %
SCF iterations ... 124.887 sec (= 2.081 min) 4.6 %
Analytical frequency calculation... 2596.270 sec (= 43.271 min)
95.3 %

```

Table A4.26. Calculated Gibbs free energy of **TNIC** using ORCA 5.0 at the B3LYP/6-31G (d,p) and B3LYP/DEF2SVP level using quantum mechanism package.

```

-----
GIBBS FREE ENERGY
-----
The Gibbs free energy is G = H - T*S
Total enthalpy ... -1794.36637023 Eh
Total entropy correction ... -0.08235669 Eh -51.68 kcal/mol
-----
Final Gibbs free energy ... -1794.44872692 Eh
For completeness - the Gibbs free energy minus the electronic
energy
G-E(el) ... 0.56189979 Eh 352.60 kcal/mol
Timings for individual modules:
Sum of individual times ... 3767.134 sec (= 62.786 min)
GTO integral calculation ... 10.335 sec (= 0.172 min) 0.3 %
SCF iterations ... 257.099 sec (= 4.285 min) 6.8 %
Analytical frequency calculation... 3499.700 sec (= 58.328 min)
92.9 %

```

Table A4.27. Calculated Gibbs free energy of **TNIC** and **O₂** using ORCA 5.0 at the B3LYP/6-31G (d,p) and B3LYP/DEF2SVP level using quantum mechanism package.

```

-----
GIBBS FREE ENERGY
-----
TNIC+O2

The Gibbs free energy is G = H - T*S
Total enthalpy ... -1944.44108118 Eh
Total entropy correction ... -0.08297993 Eh -52.07 kcal/mol
-----
Final Gibbs free energy ... -1944.52406111 Eh
For completeness - the Gibbs free energy minus the electronic
energy
G-E(el) ... 0.56569973 Eh 354.98 kcal/mol
Timings for individual modules:
Sum of individual times ... 3652.325 sec (= 60.872 min)
GTO integral calculation ... 2.827 sec (= 0.047 min) 0.1 %
SCF iterations ... 250.228 sec (= 4.170 min) 6.9 %
Analytical frequency calculation... 3399.270 sec (= 56.655 min)
93.1 %

```

Table A4.28. Calculated Gibbs free energy of **BNIC** using ORCA 5.0 at the B3LYP/6-31G (d,p) and B3LYP/DEF2SVP level using quantum mechanism package.

```

-----
GIBBS FREE ENERGY
-----
BNIC

The Gibbs free energy is G = H - T*S
Total enthalpy ... -2256.22544459 Eh
Total entropy correction ... -0.11855253 Eh -74.39 kcal/mol
-----
Final Gibbs free energy ... -2256.34399712 Eh
For completeness - the Gibbs free energy minus the electronic energy
G-E(el) ... 0.68961238 Eh 432.74 kcal/mol
Timings for individual modules:
Sum of individual times ... 59449.222 sec (= 990.820 min)
GTO integral calculation ... 366.590 sec (= 6.110 min) 0.6 %
SCF iterations ... 38672.424 sec (= 644.540 min) 65.1 %
SCF Gradient evaluation ... 11393.766 sec (= 189.896 min) 19.2 %
Geometry relaxation ... 87.042 sec (= 1.451 min) 0.1 %
Analytical frequency calculation... 8929.400 sec (= 148.823 min) 15.0
%

```

Table A4.29. Calculated Gibbs free energy of **BNIC** and **O₂** using ORCA 5.0 at the B3LYP/6-31G (d,p) and B3LYP/DEF2SVP level using quantum mechanism package.

GIBBS FREE ENERGY **BNIC+O₂**

The Gibbs free energy is $G = H - T*S$
Total enthalpy ... -2405.75207693 Eh
Total entropy correction ... -0.09618920 Eh -60.36 kcal/mol

Final Gibbs free energy ... -2405.84826613 Eh
For completeness - the Gibbs free energy minus the electronic
energy
G-E(el) ... 0.72094236 Eh 452.40 kcal/mol
Timings for individual modules:
Sum of individual times ... 11250.290 sec (= 187.505 min)
GTO integral calculation ... 9.931 sec (= 0.166 min) 0.1 %
SCF iterations ... 548.492 sec (= 9.142 min) 4.9 %
Analytical frequency calculation... 10691.867 sec (= 178.198
min) 95.0 %



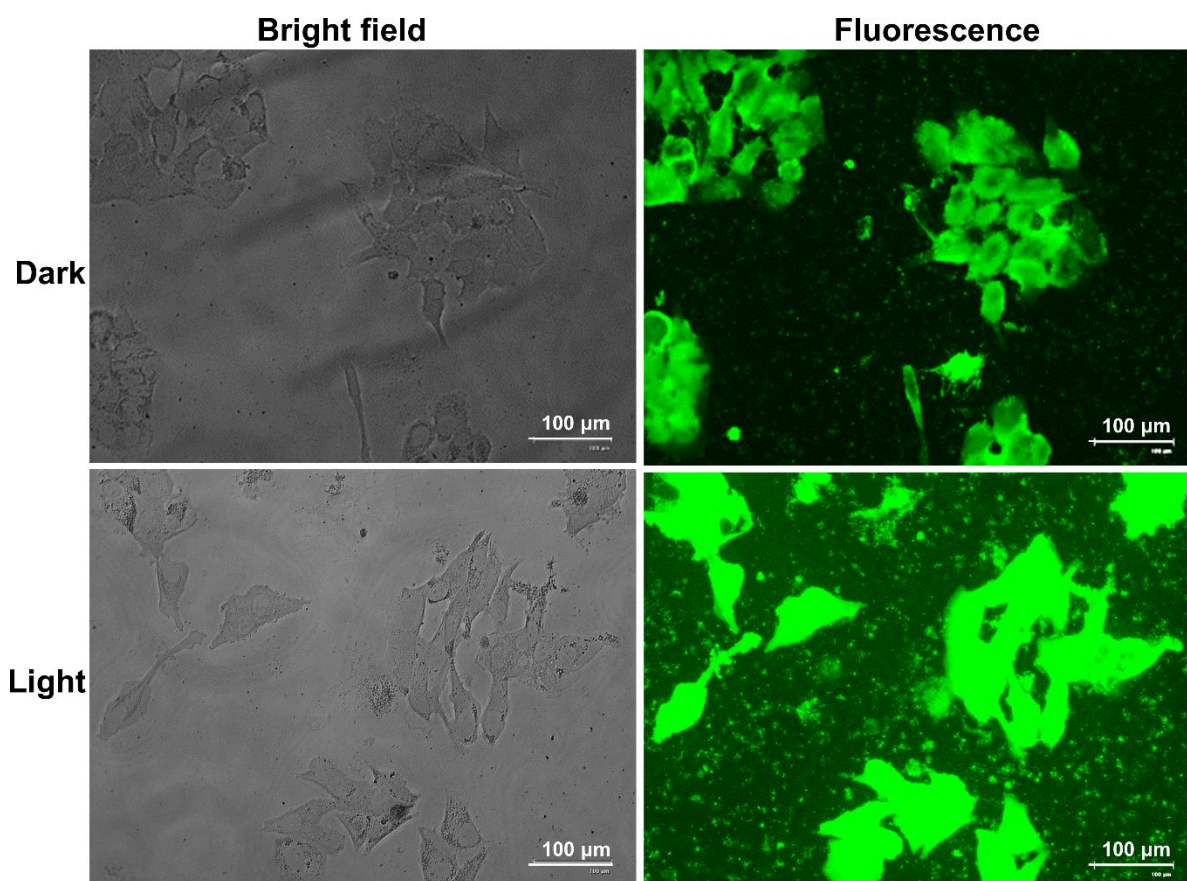


Figure A4.19. Fluorescence microscope images were captured of of HeLa cells after treatment with NNIC under normoxia and loaded with (a) calcein-AM (2 μM, live cell marker). [Scale bar:100 μm].

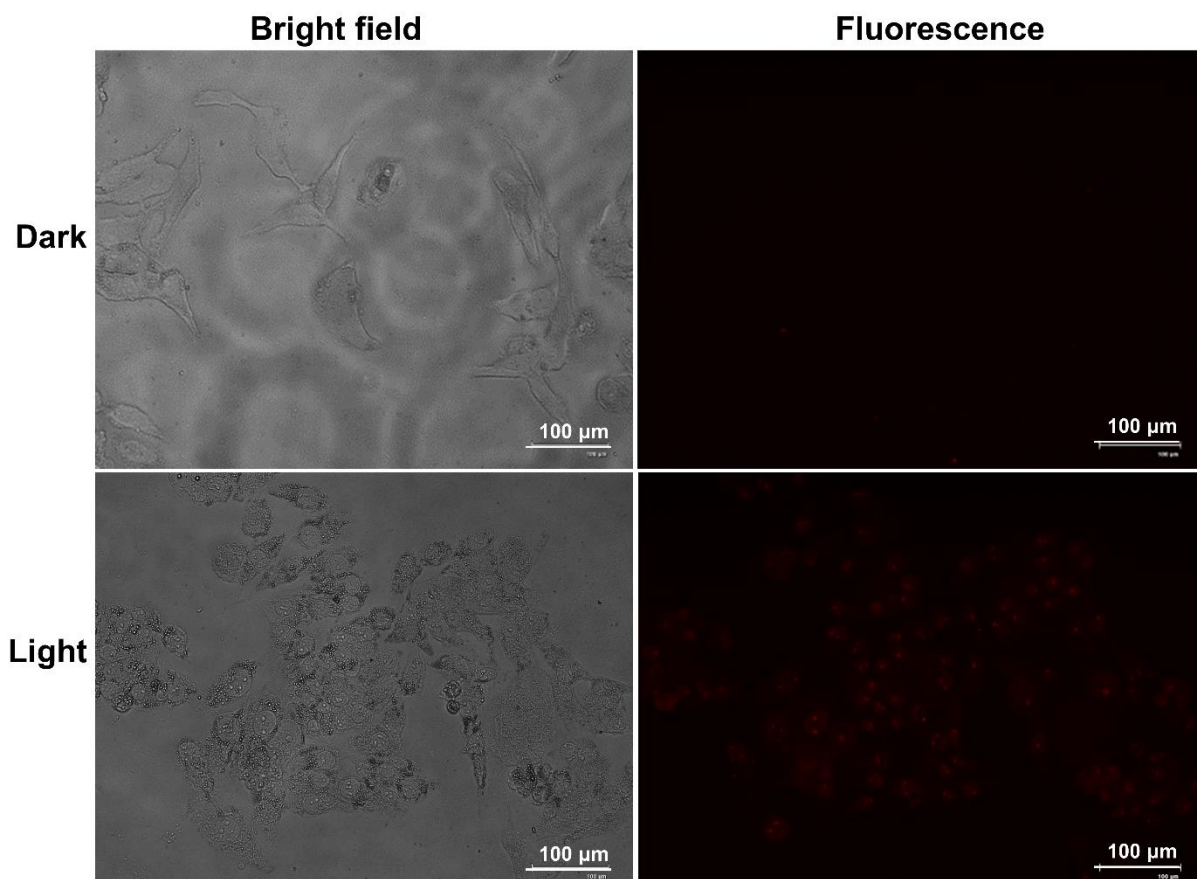


Figure A4.20. Fluorescence microscope images were captured of HeLa cells after treatment with NNIC under normoxia and loaded with (a) PI (4 μM, dead cell marker). [Scale bar:100 μm].

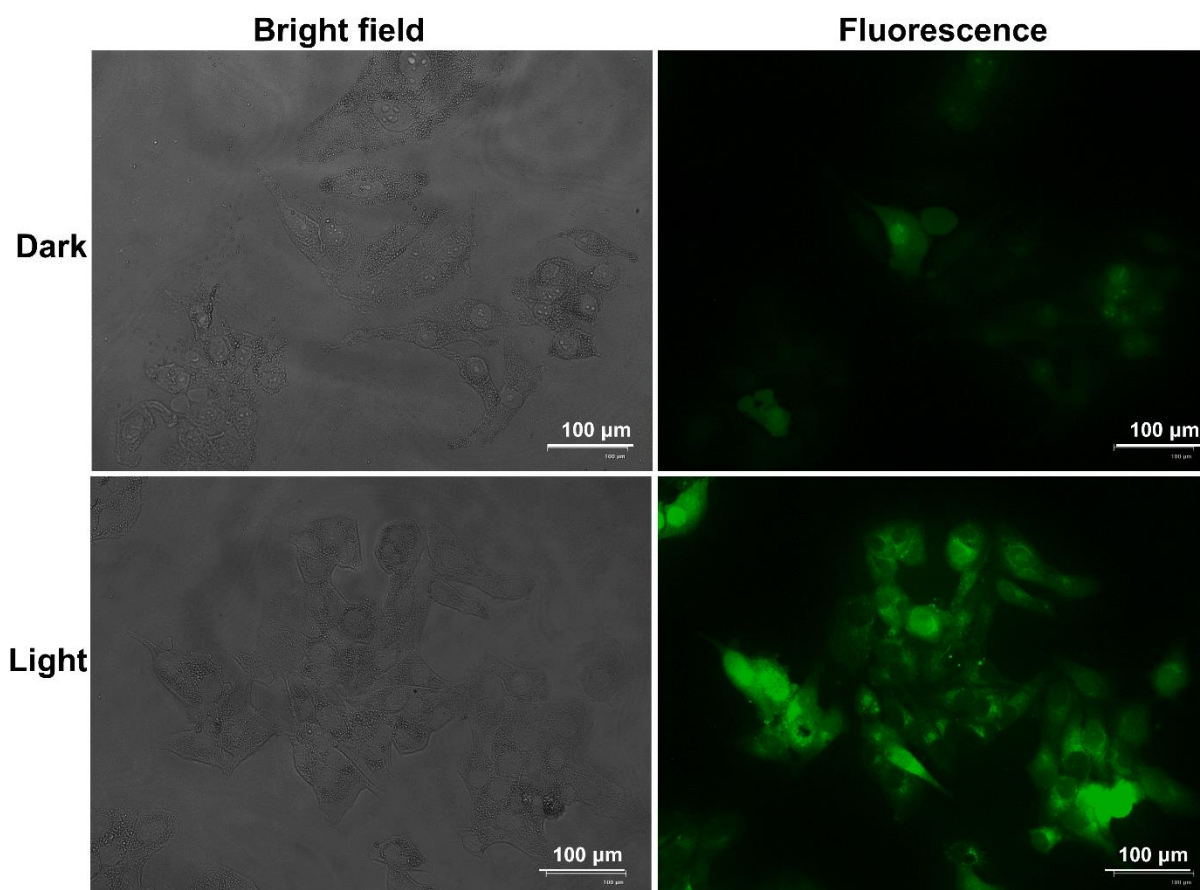


Figure A4.21. Fluorescence microscope images were captured of HeLa cells after treatment with NNIC under normoxia and loaded with (a) DCFDA (ROS detection probe). [Scale bar:100 μm].

Supporting figures

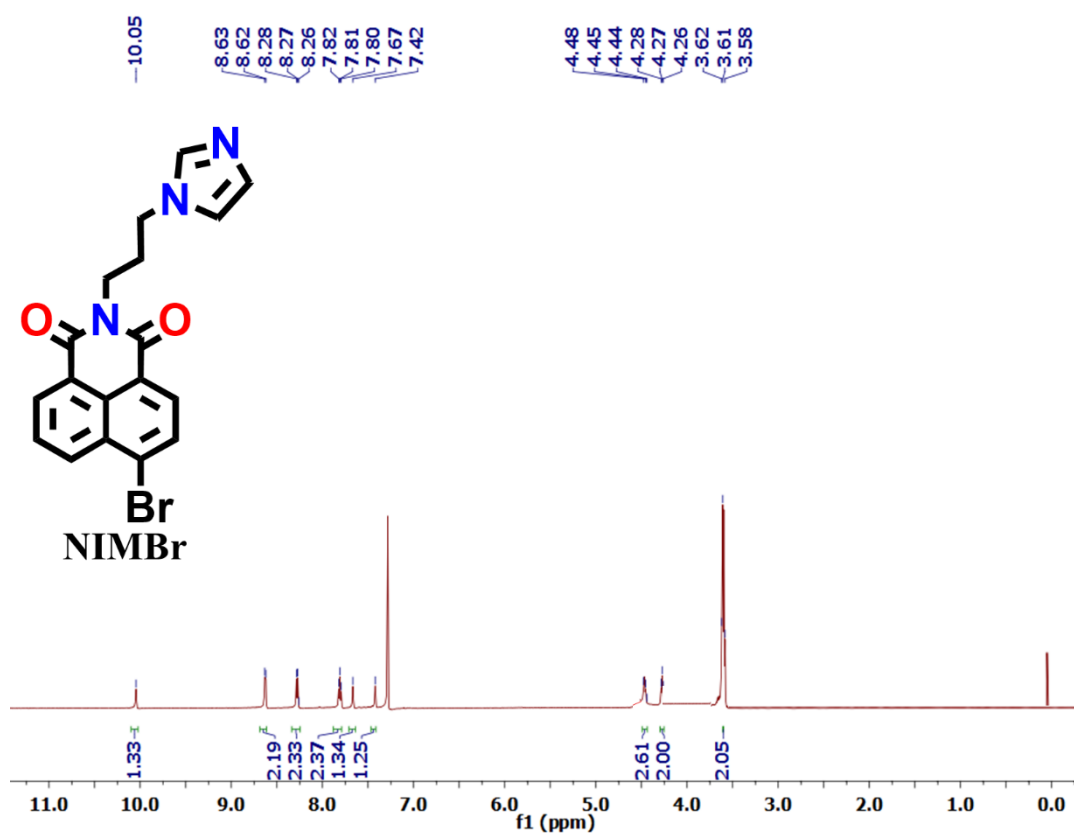


Figure A4.22. ^1H NMR spectra of NIMBr.

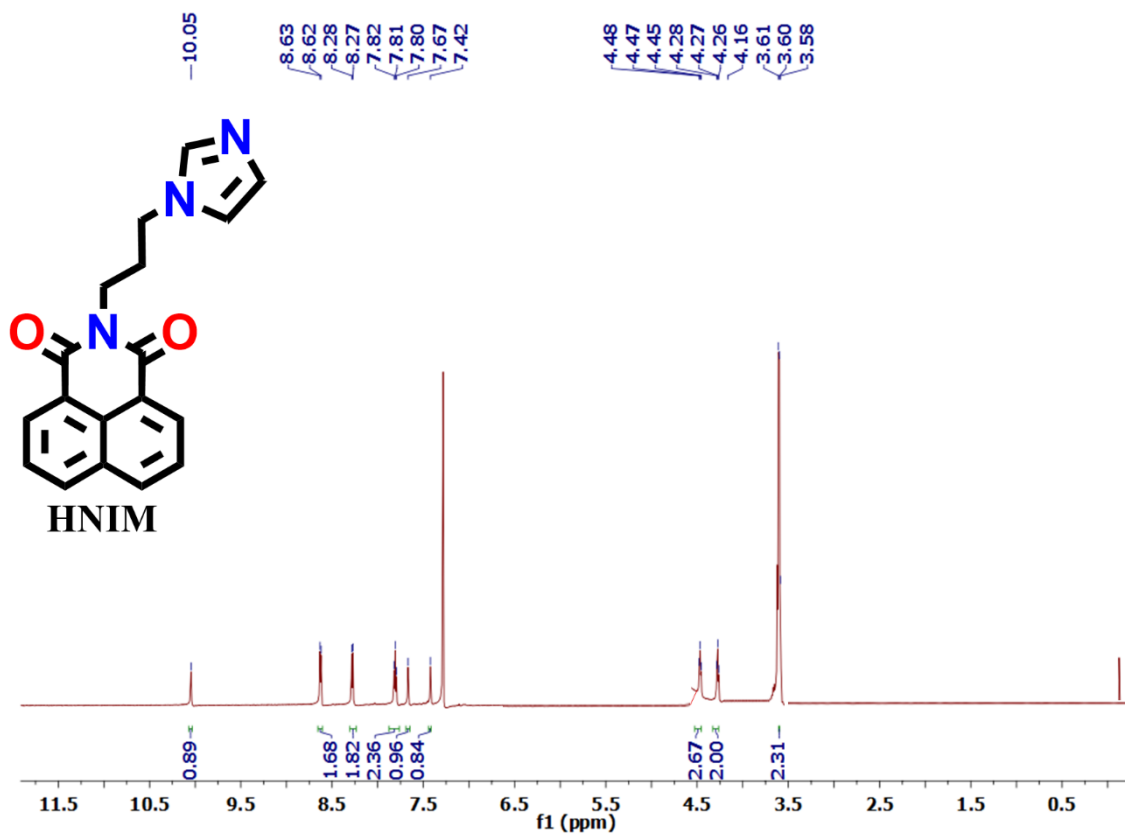


Figure A4.23. ^1H NMR spectra of HNIM.

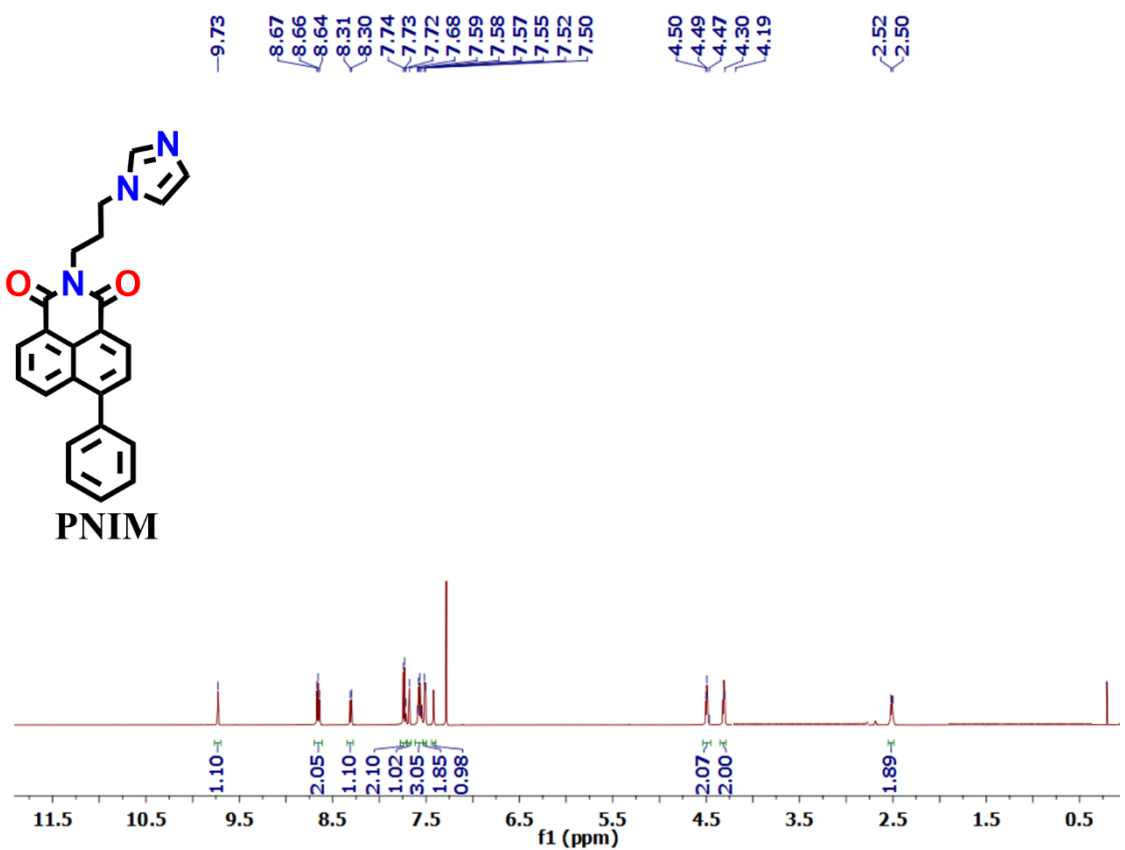


Figure A4.24. ^1H NMR spectra of PNIM.

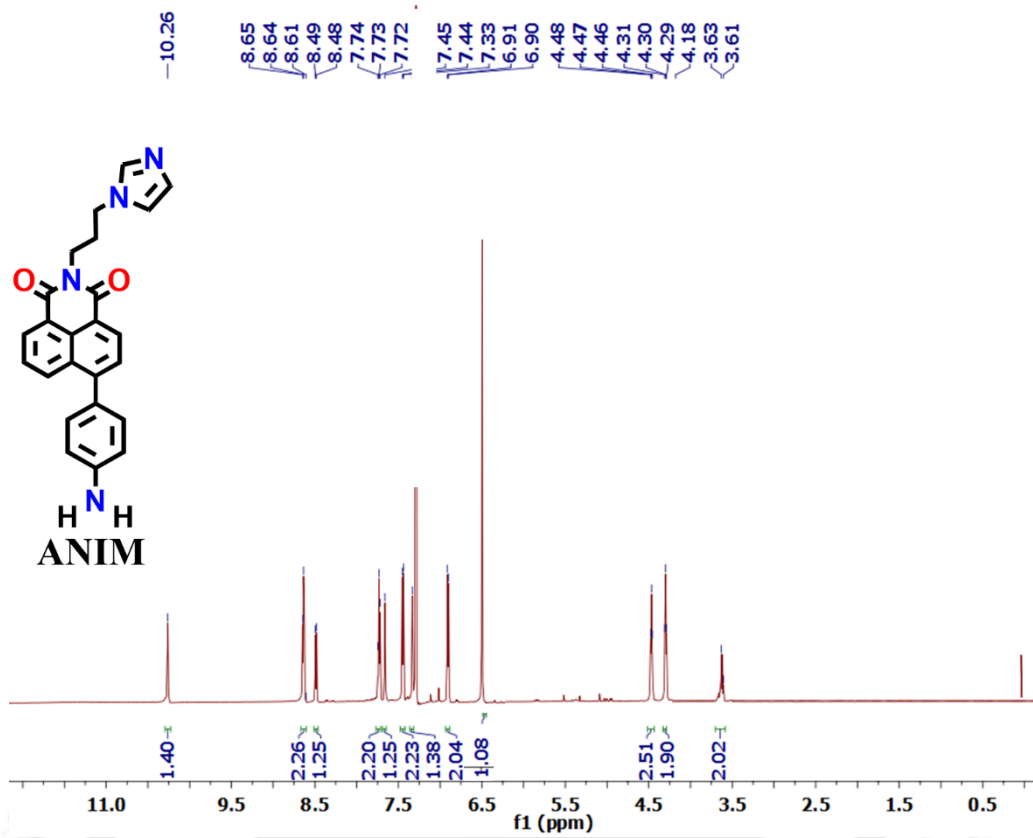


Figure A4.25. ^1H NMR spectra of ANIM.

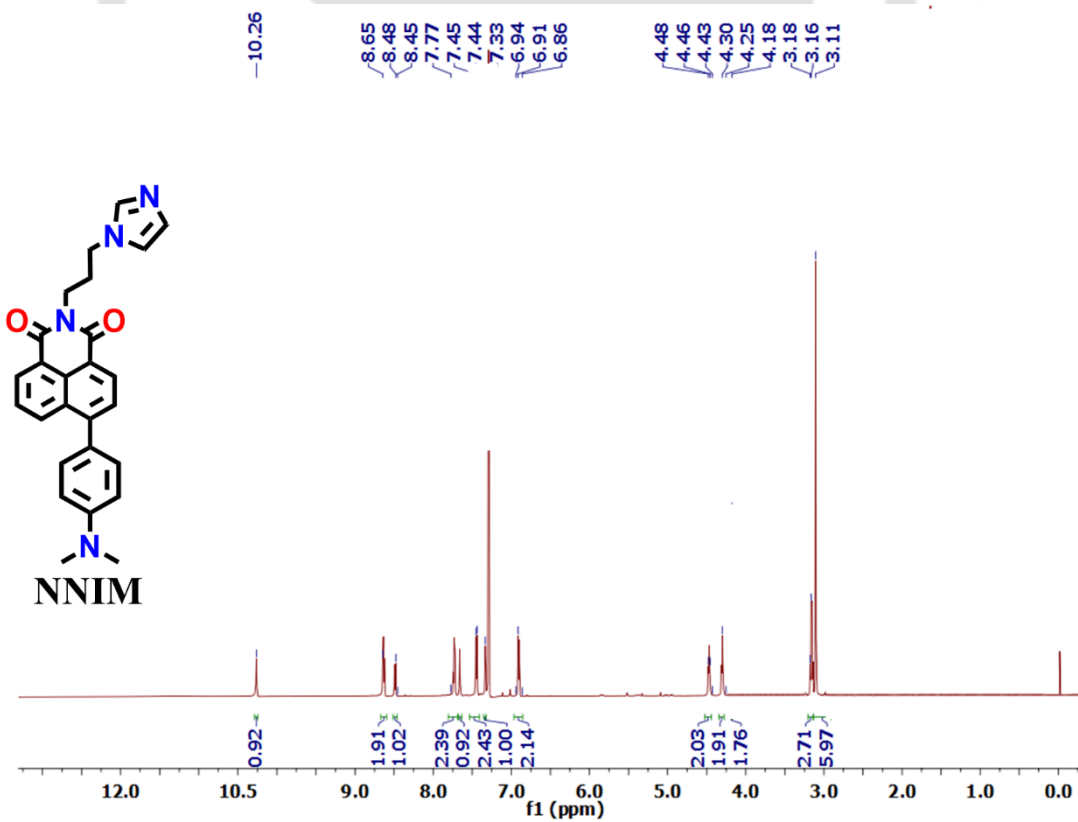


Figure A4.26. ^1H NMR spectra of NNIM.

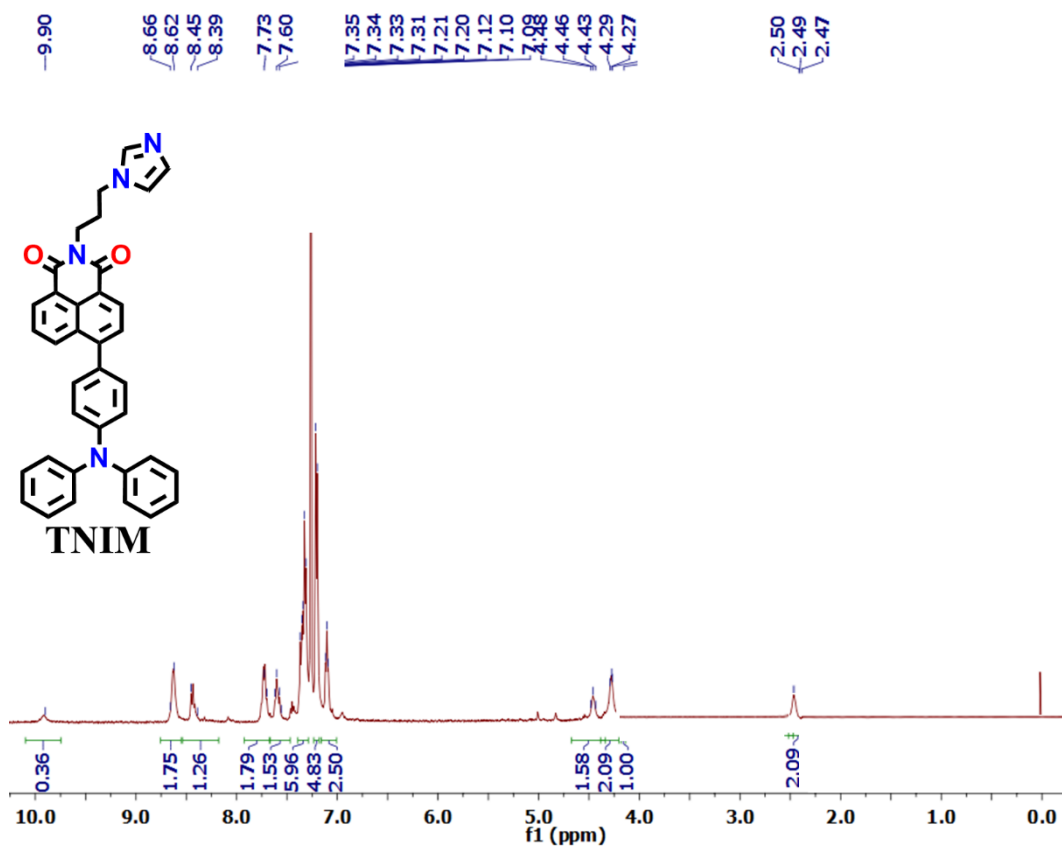


Figure A4.27. ¹H NMR spectra of TNIM.

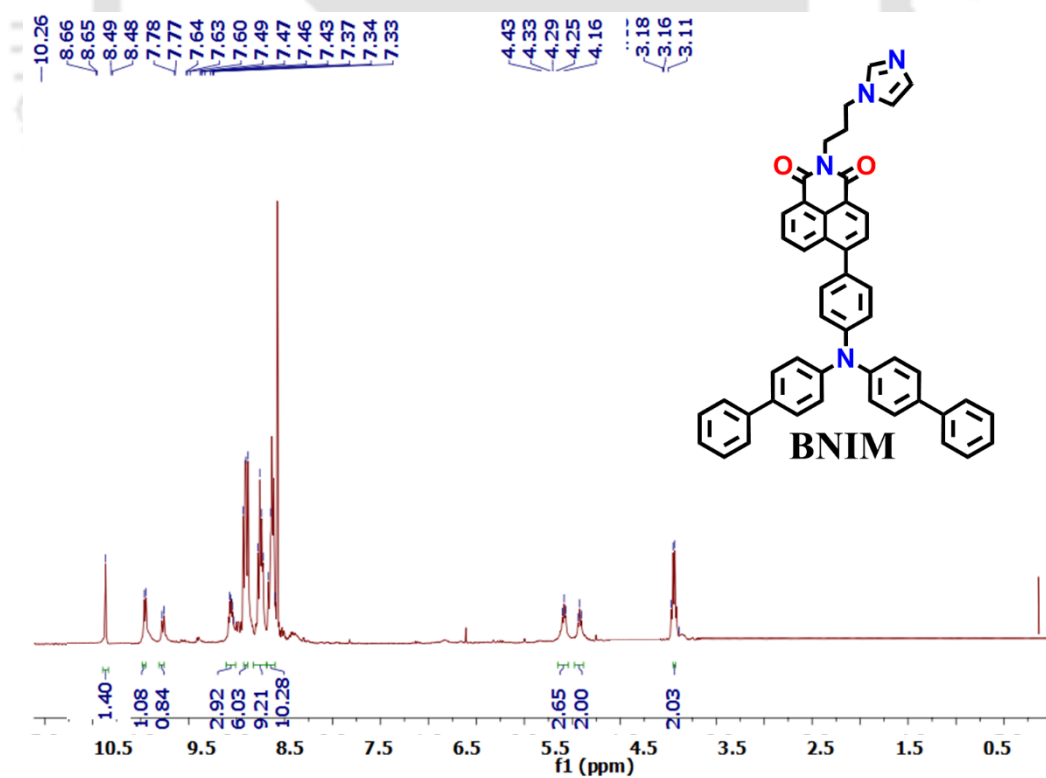


Figure A4.28. ¹H NMR spectra of BNIM.

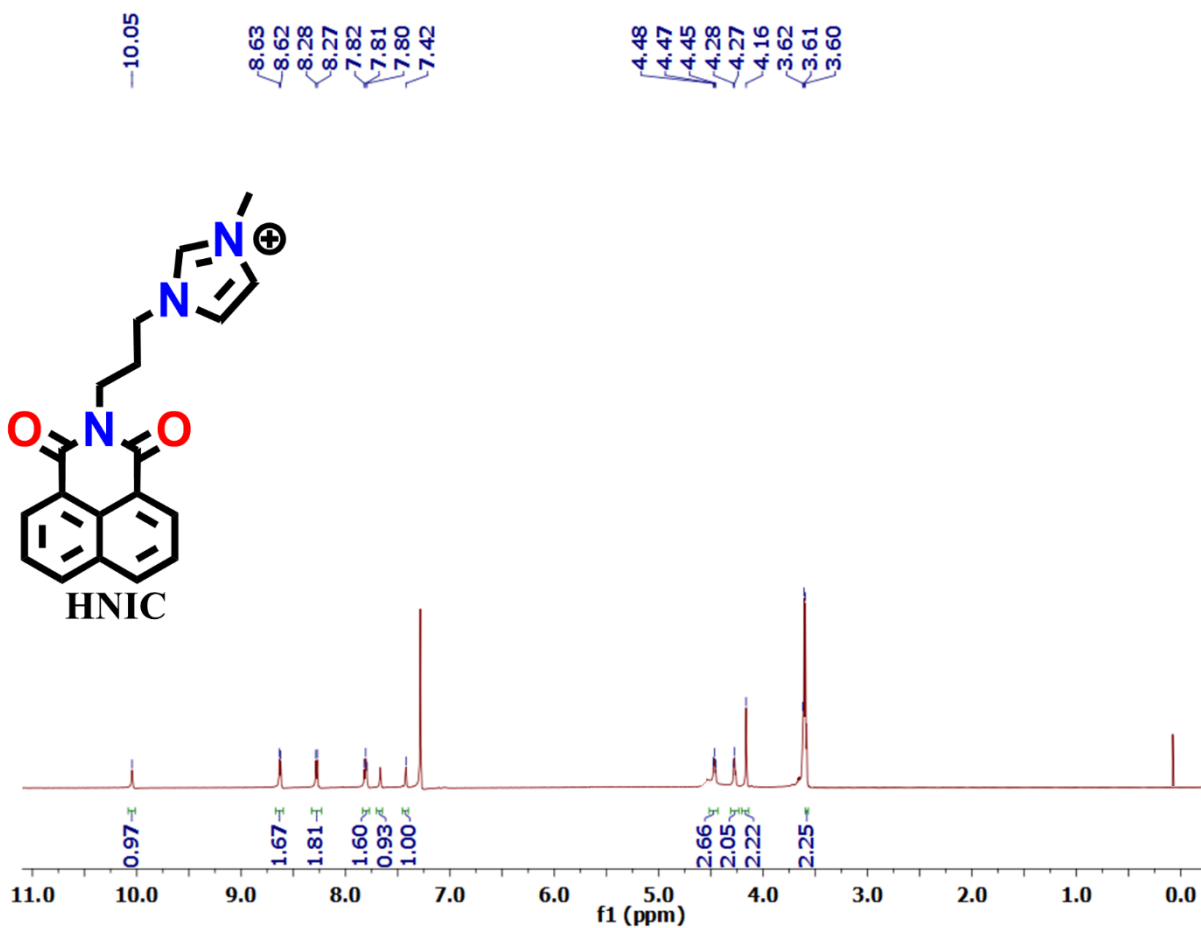


Figure A4.29. ¹H NMR spectra of HNIC.

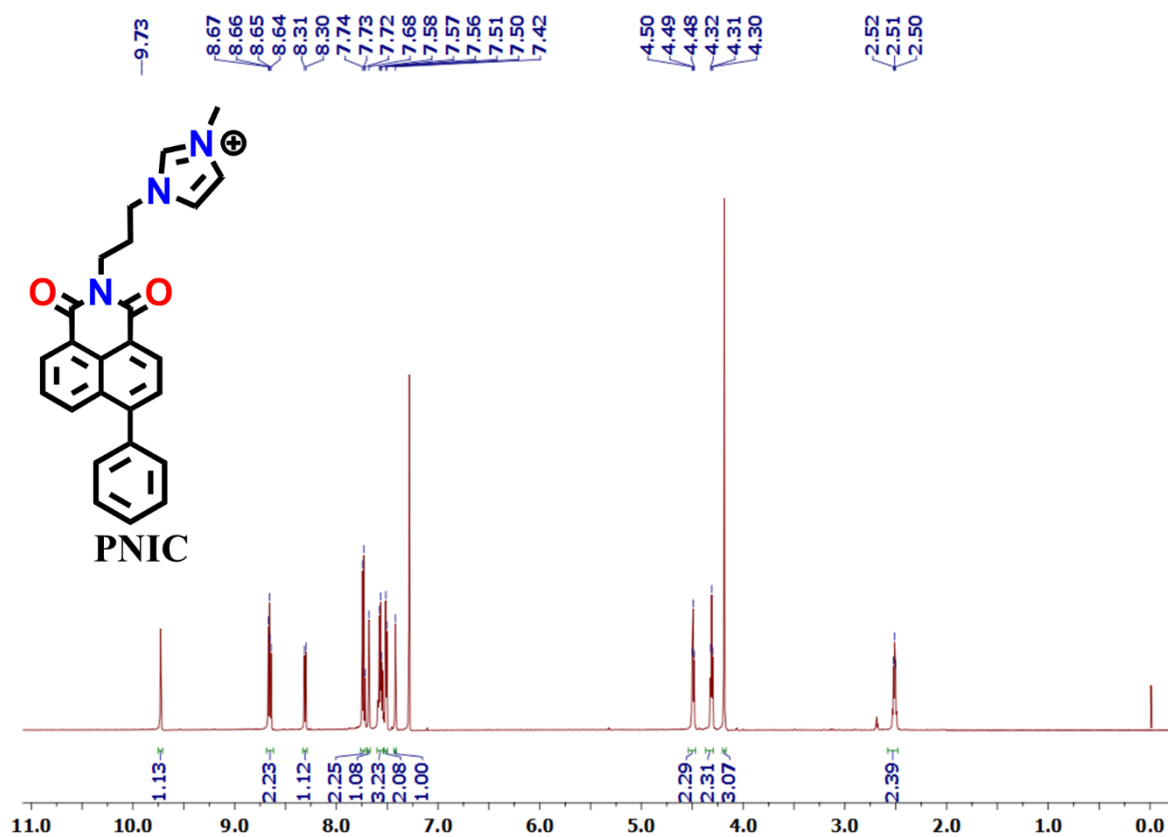


Figure A4.30. ^1H NMR spectra of PNIC.

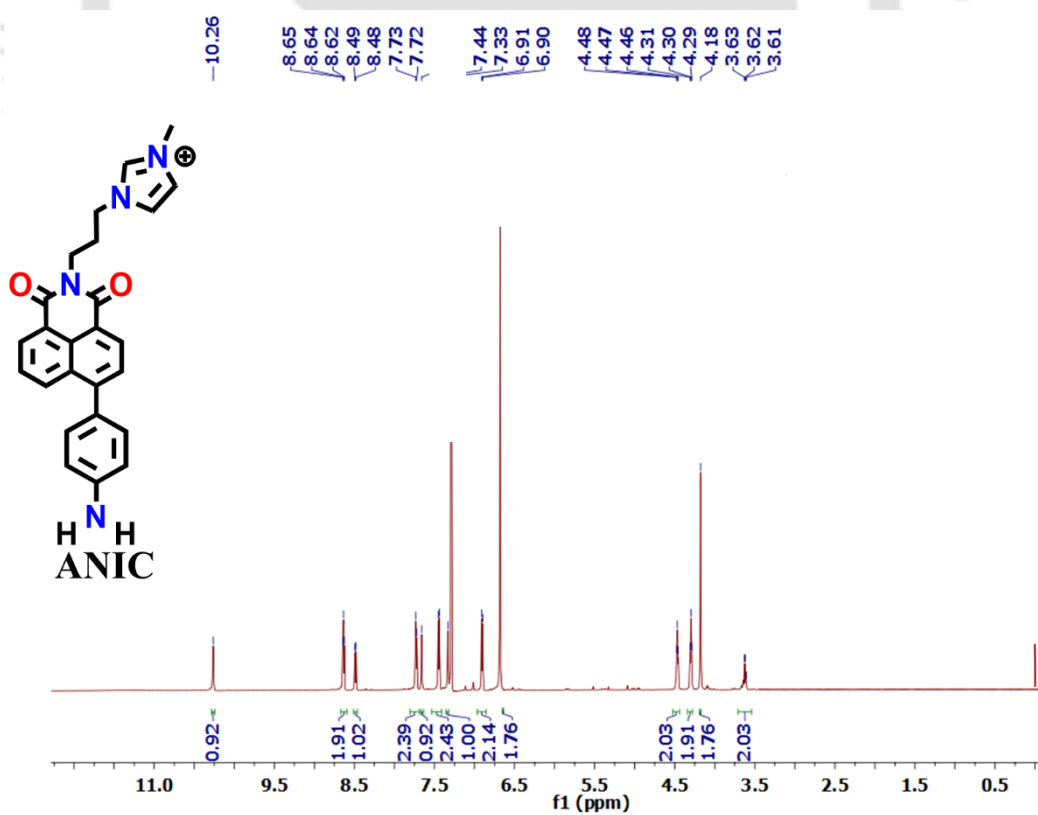


Figure A4.31. ^1H NMR spectra of ANIC.

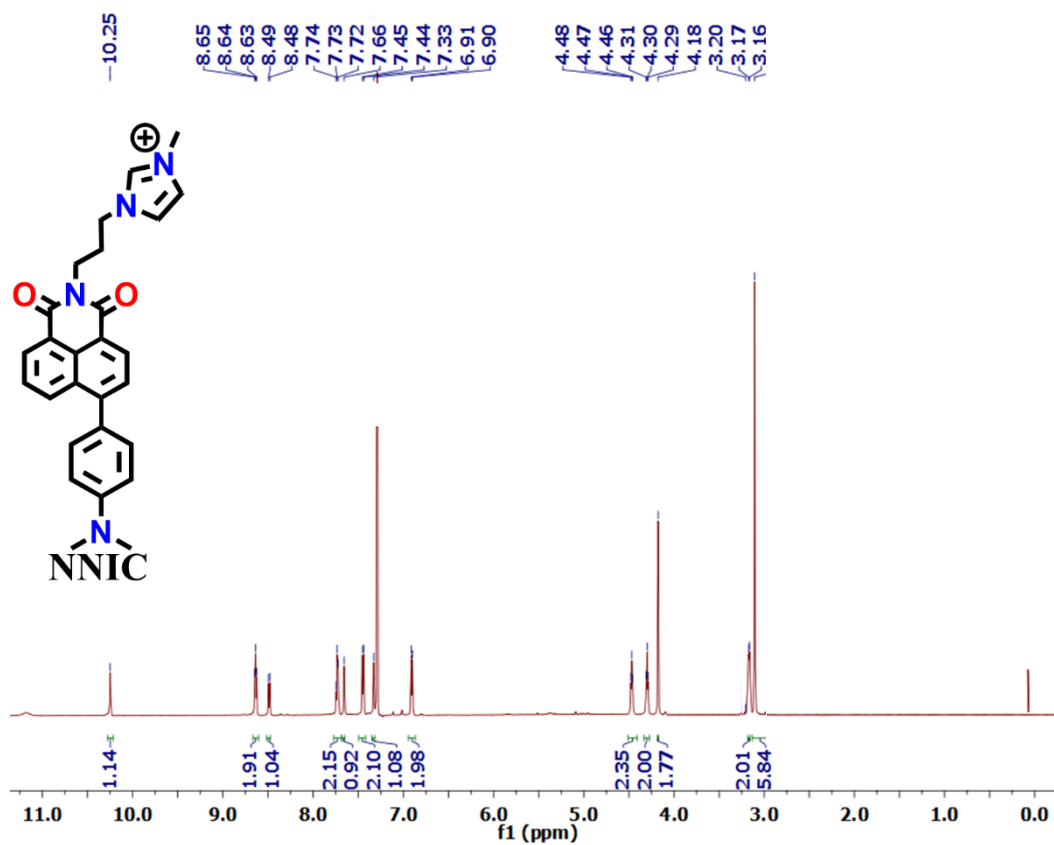


Figure A4.32. ^1H NMR spectra of NNIC.

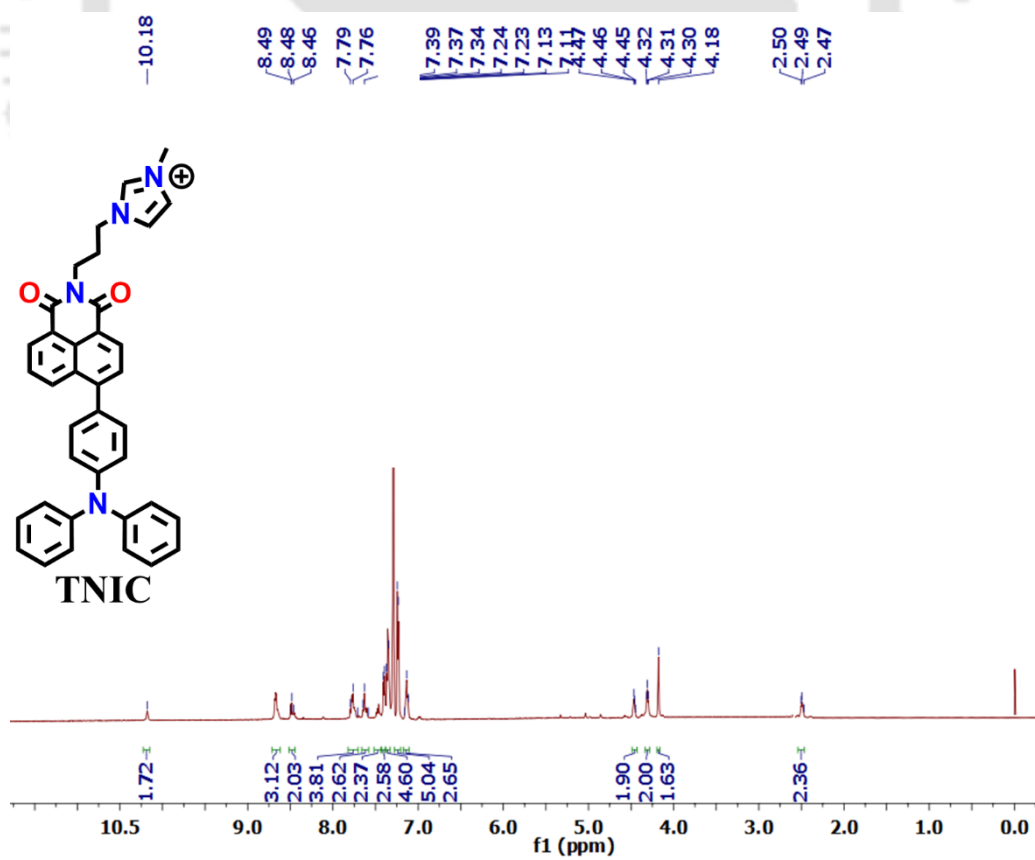


Figure A4.33. ^1H NMR spectra of TNIC.

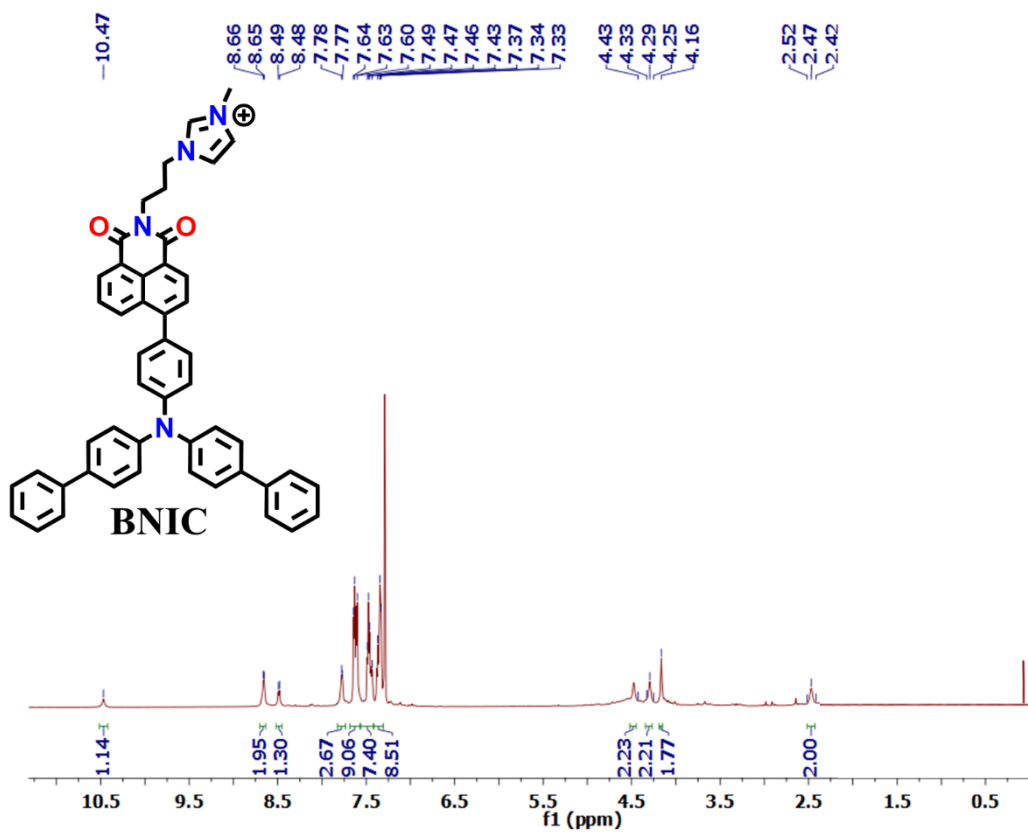


Figure A4.34. ^1H NMR spectra of BNIC.

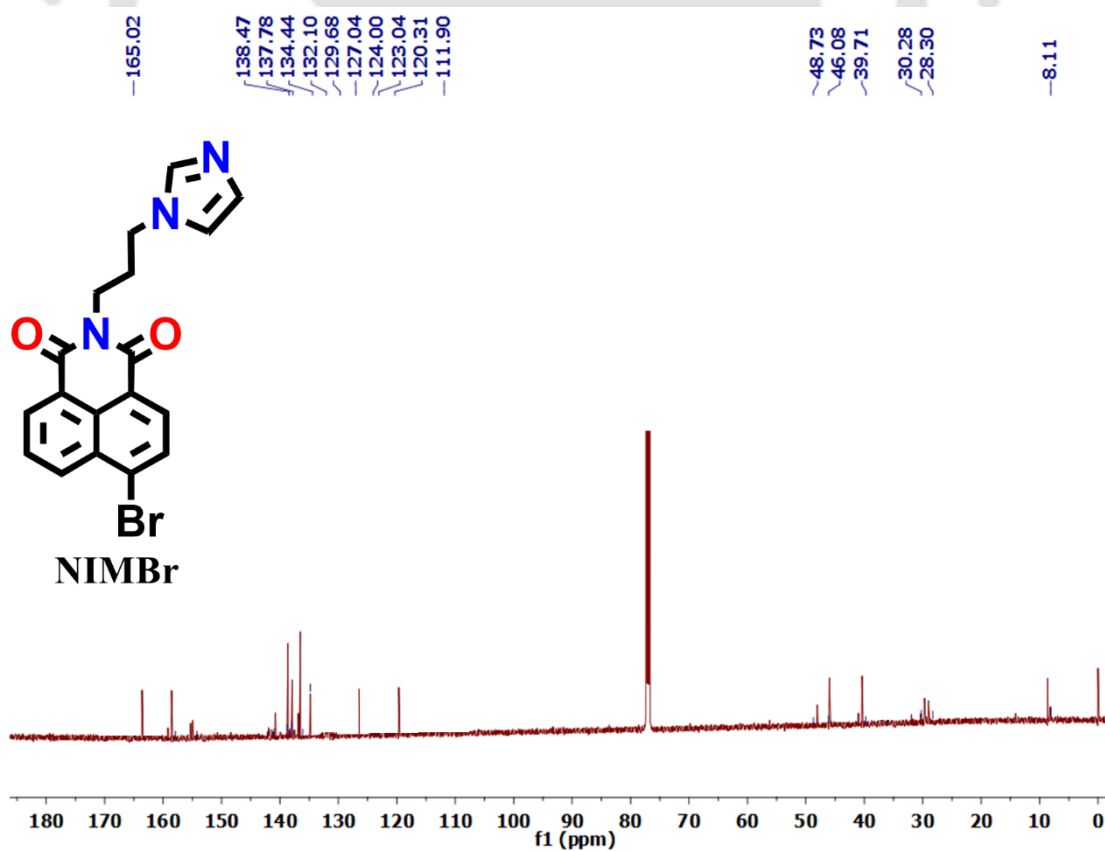


Figure A4.35. ^{13}C NMR spectra of NIMBr.

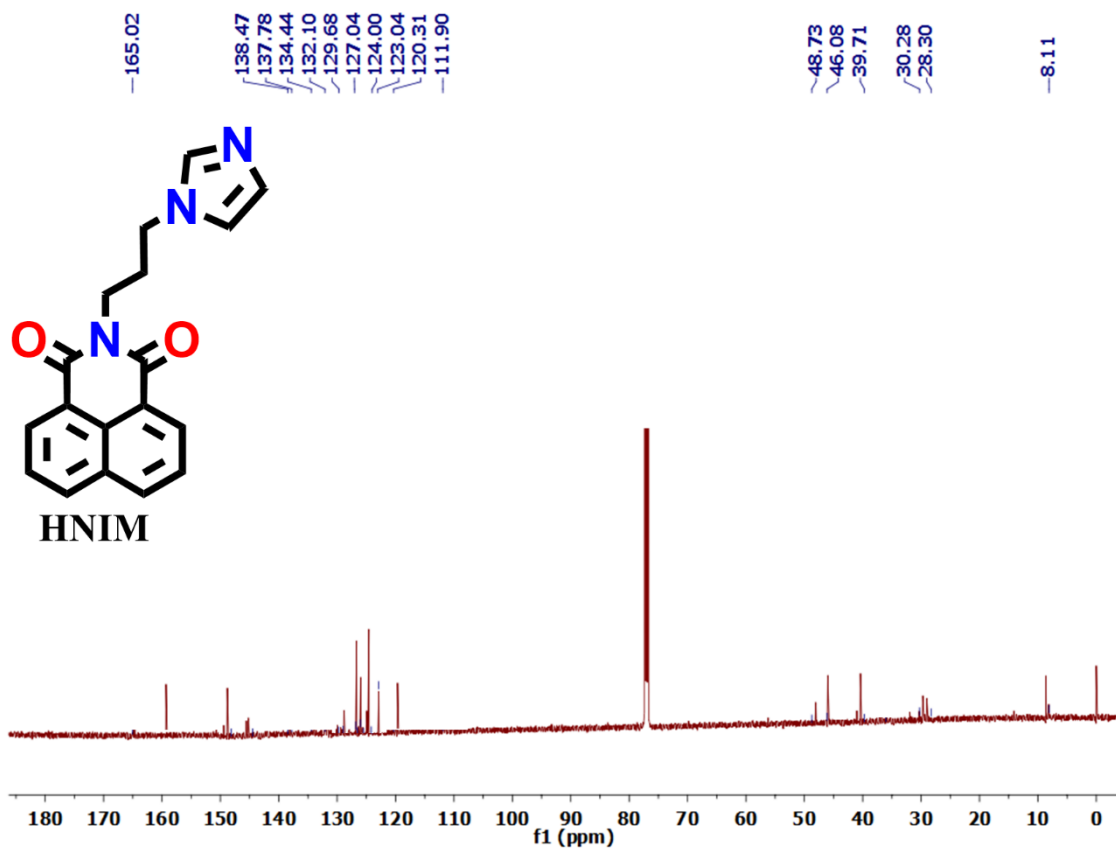


Figure A4.36. ^{13}C NMR spectra of HNIM.

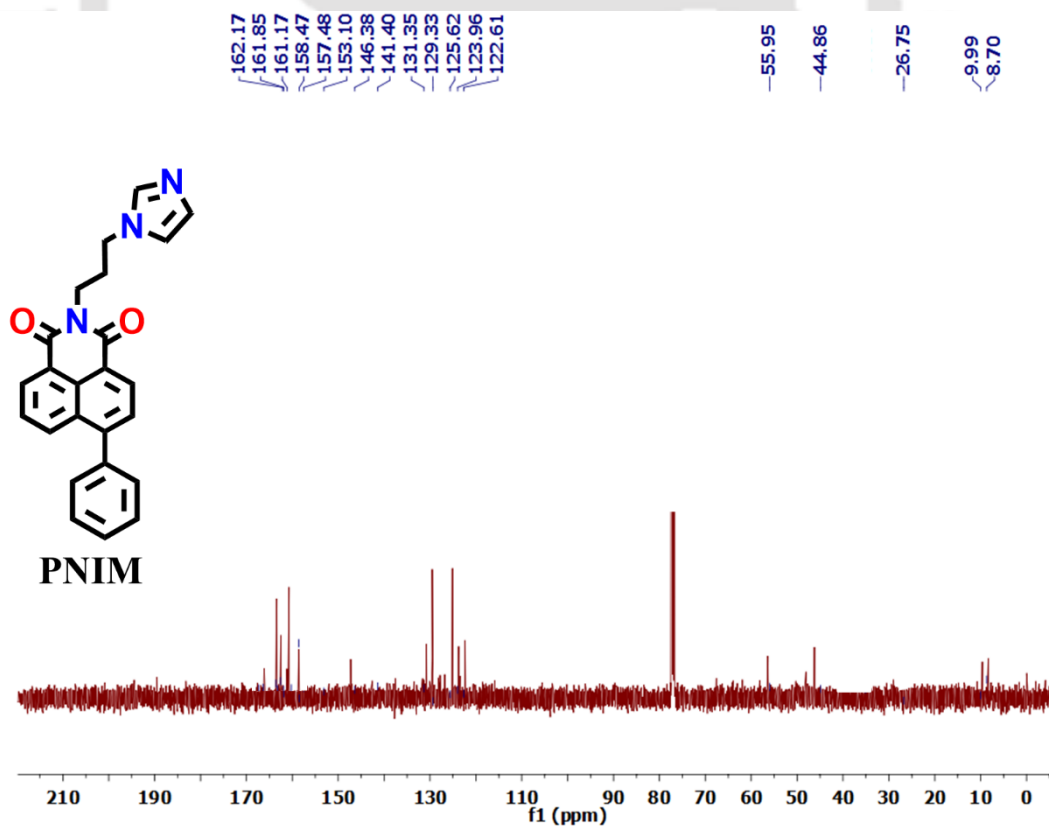


Figure A4.37. ^{13}C NMR spectra of PNIM.

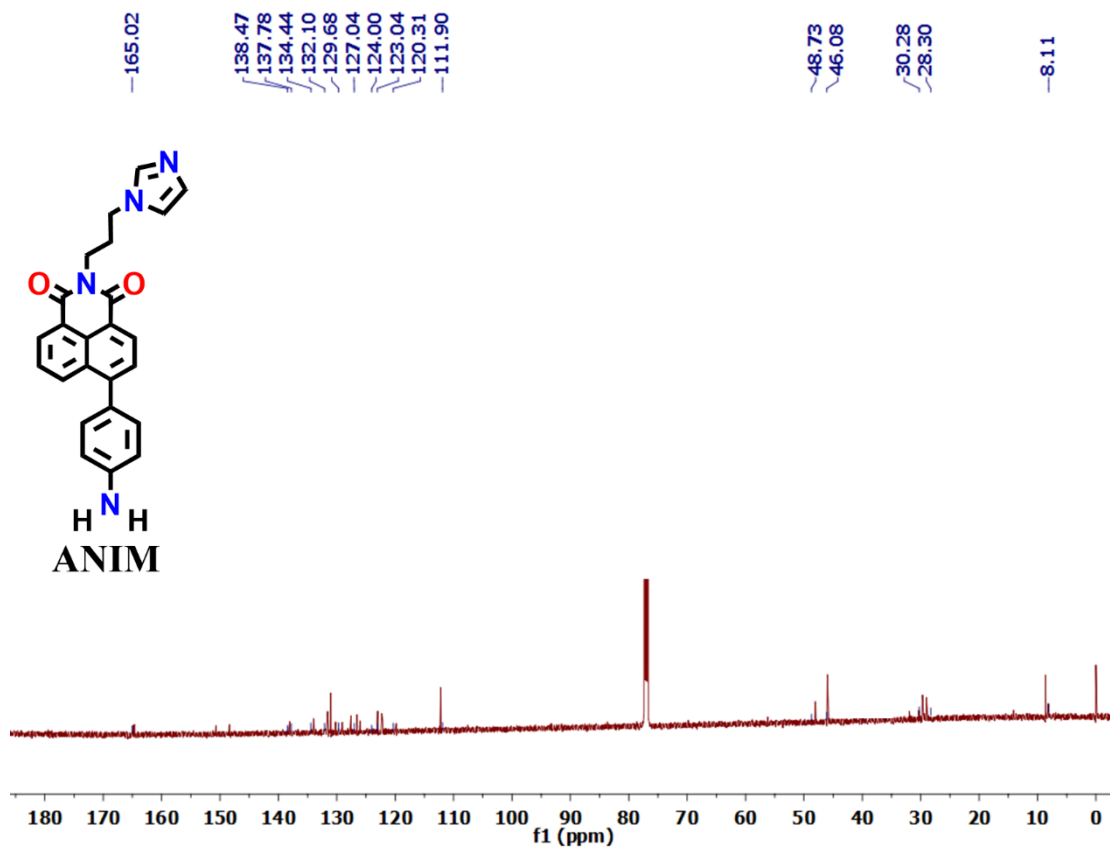


Figure A4.38. ^{13}C NMR spectra of ANIM.

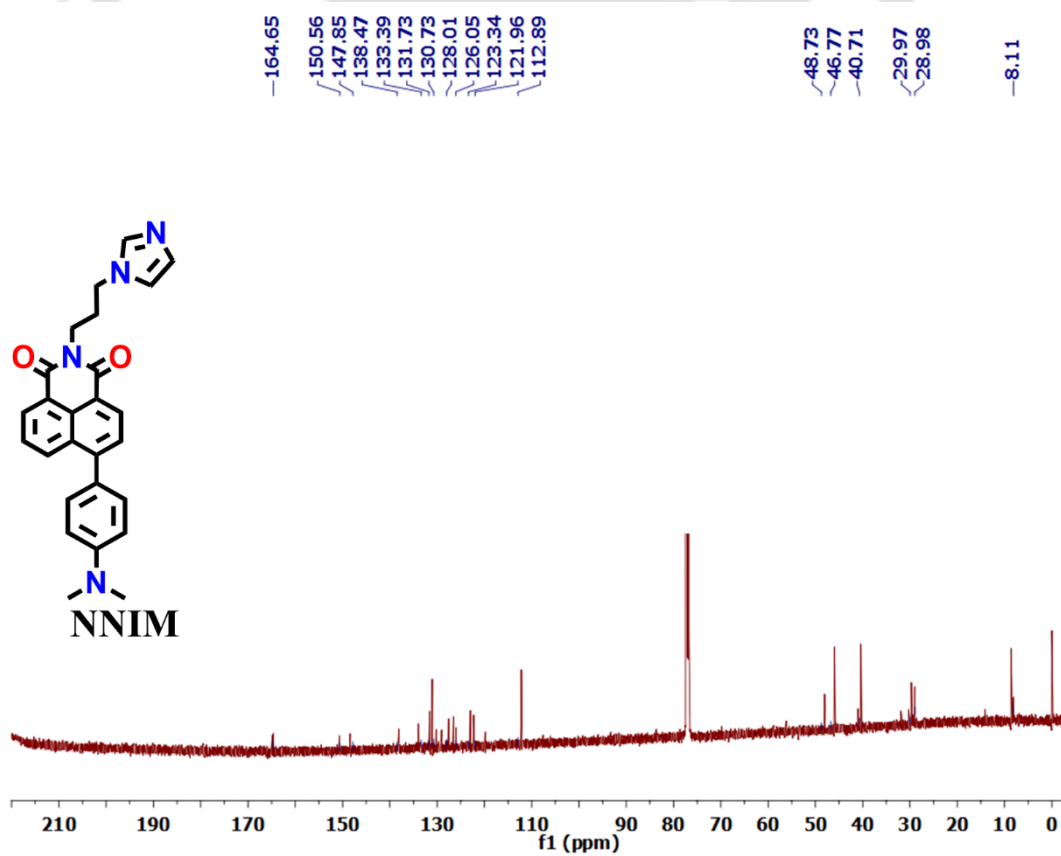


Figure A4.39. ^{13}C NMR spectra of NNIM.

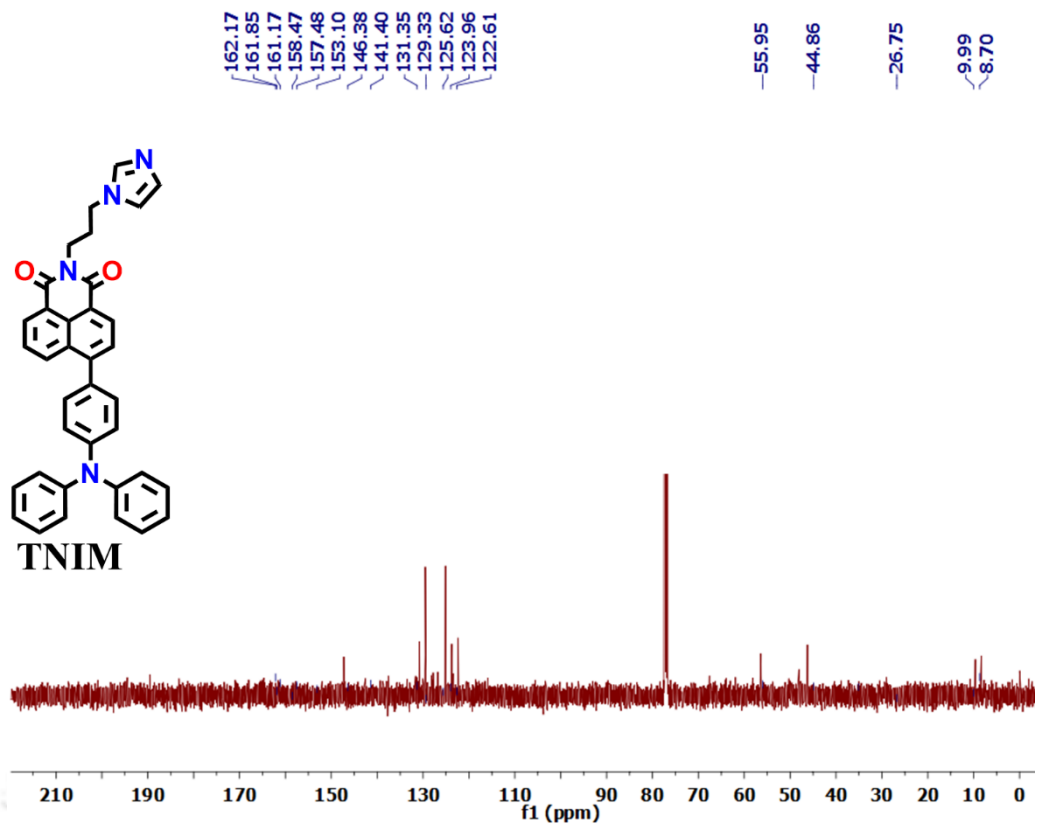


Figure A4.40. ^{13}C NMR spectra of TNIM.

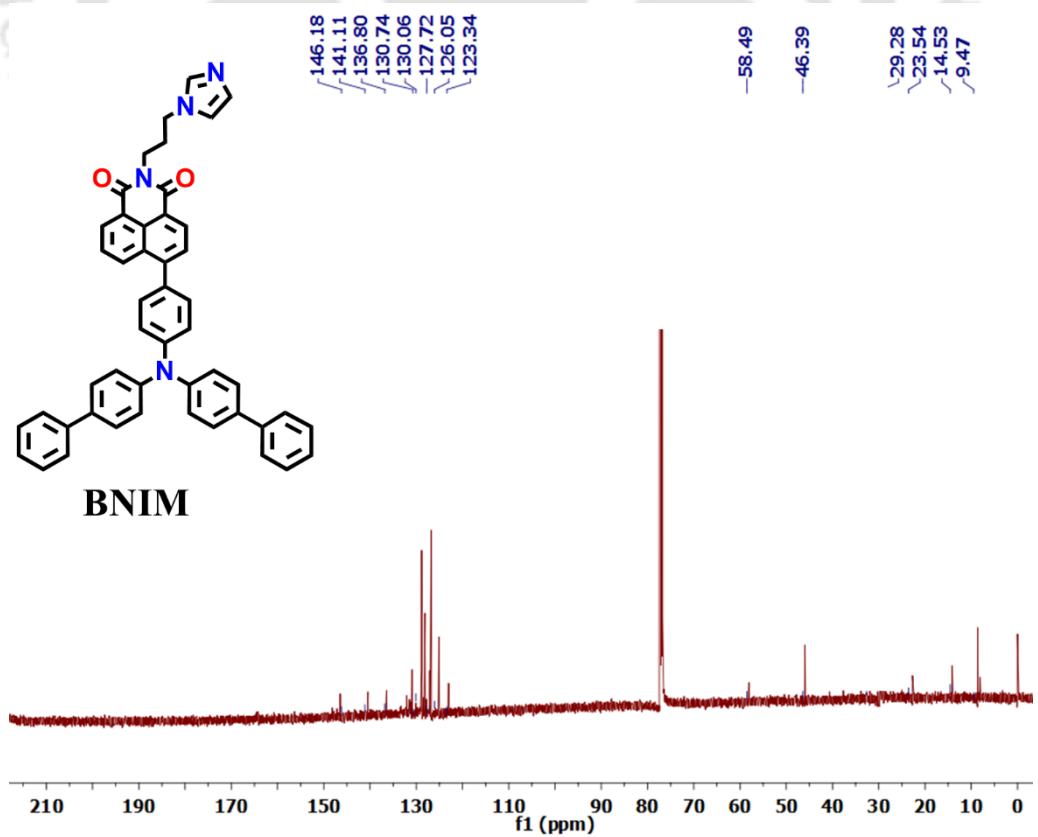


Figure A4.41. ^{13}C NMR spectra of BNIM.

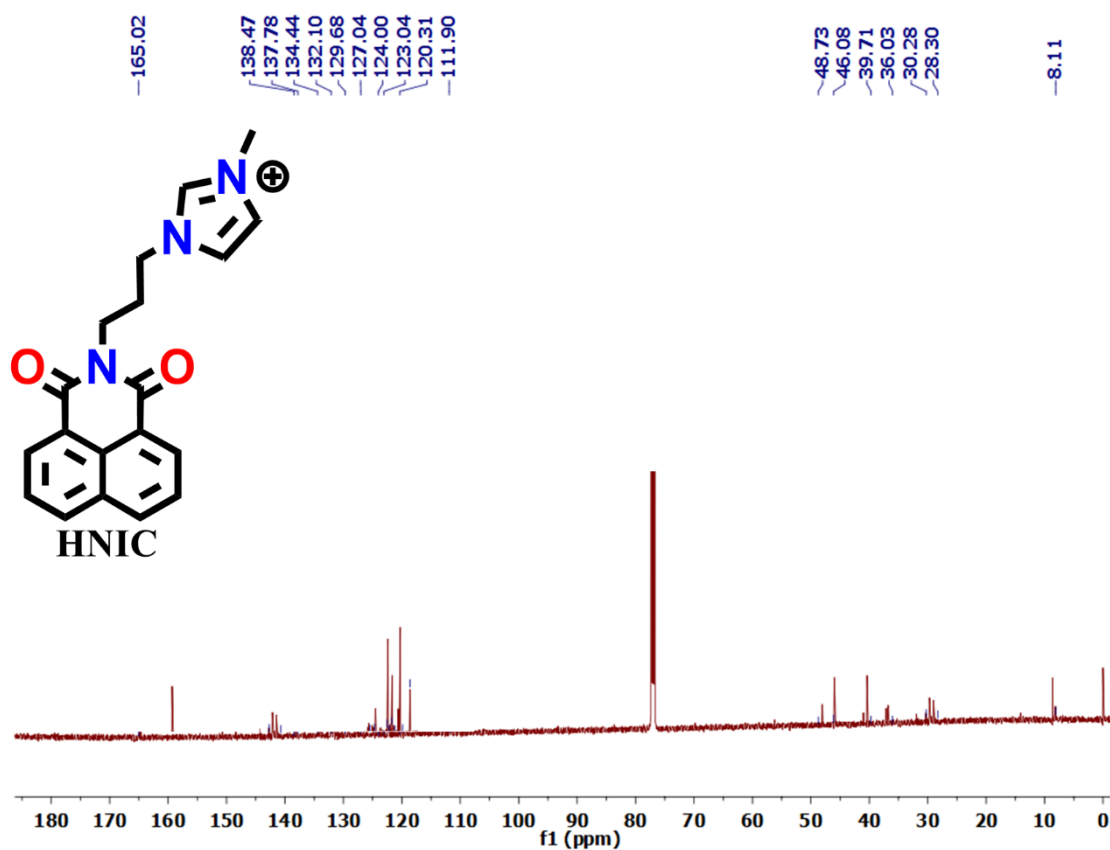


Figure A4.42. ^{13}C NMR spectra of HNIC.

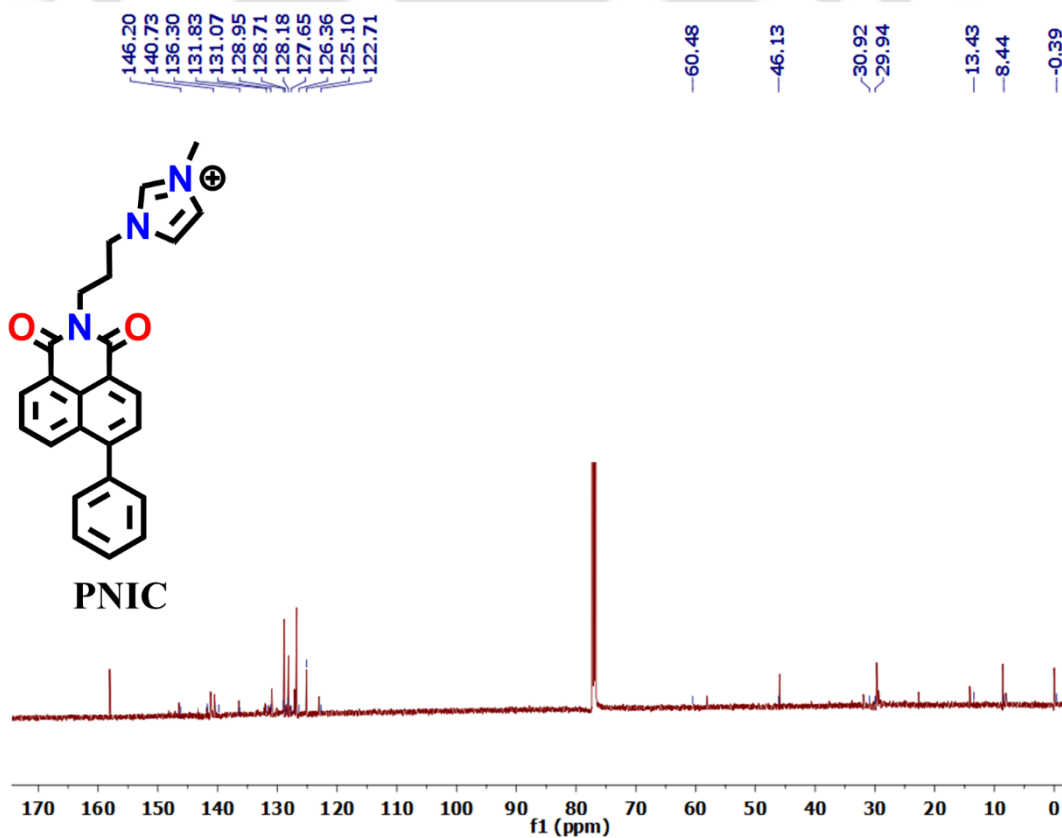


Figure A4.43. ^{13}C NMR spectra of PNIC.

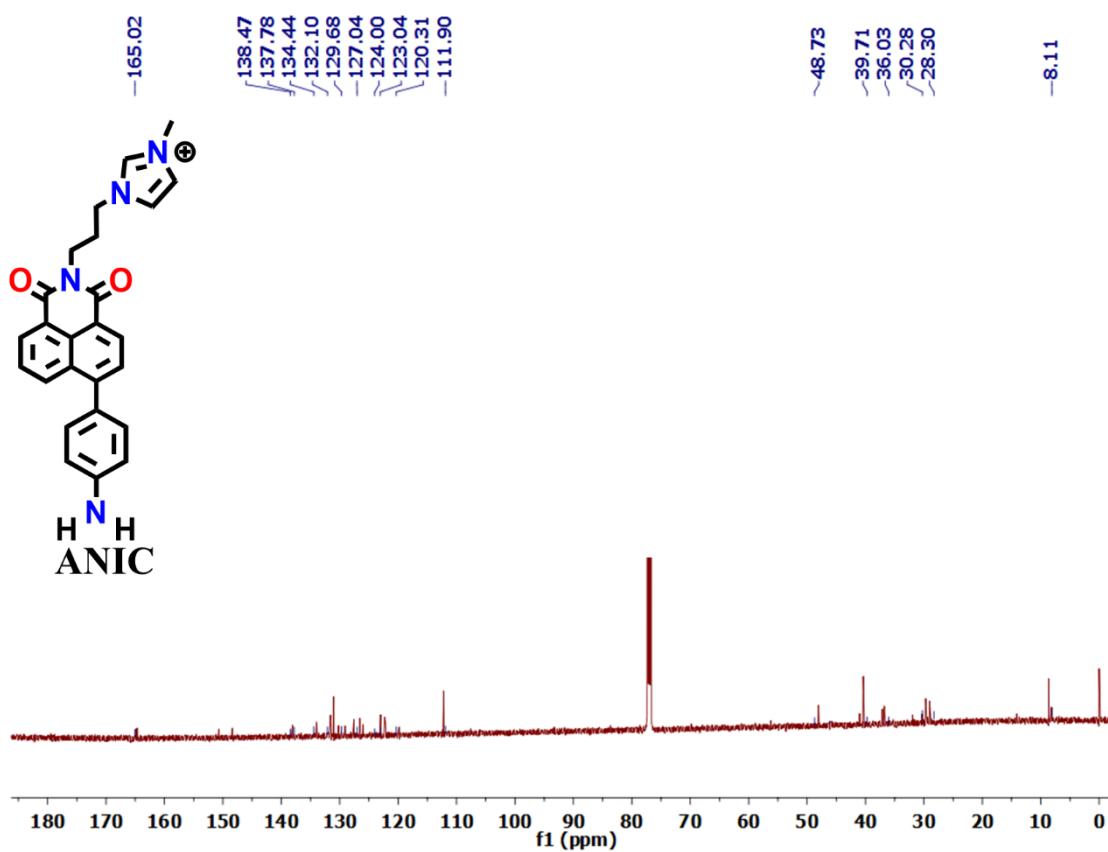


Figure A4.44. ^{13}C NMR spectra of ANIC.

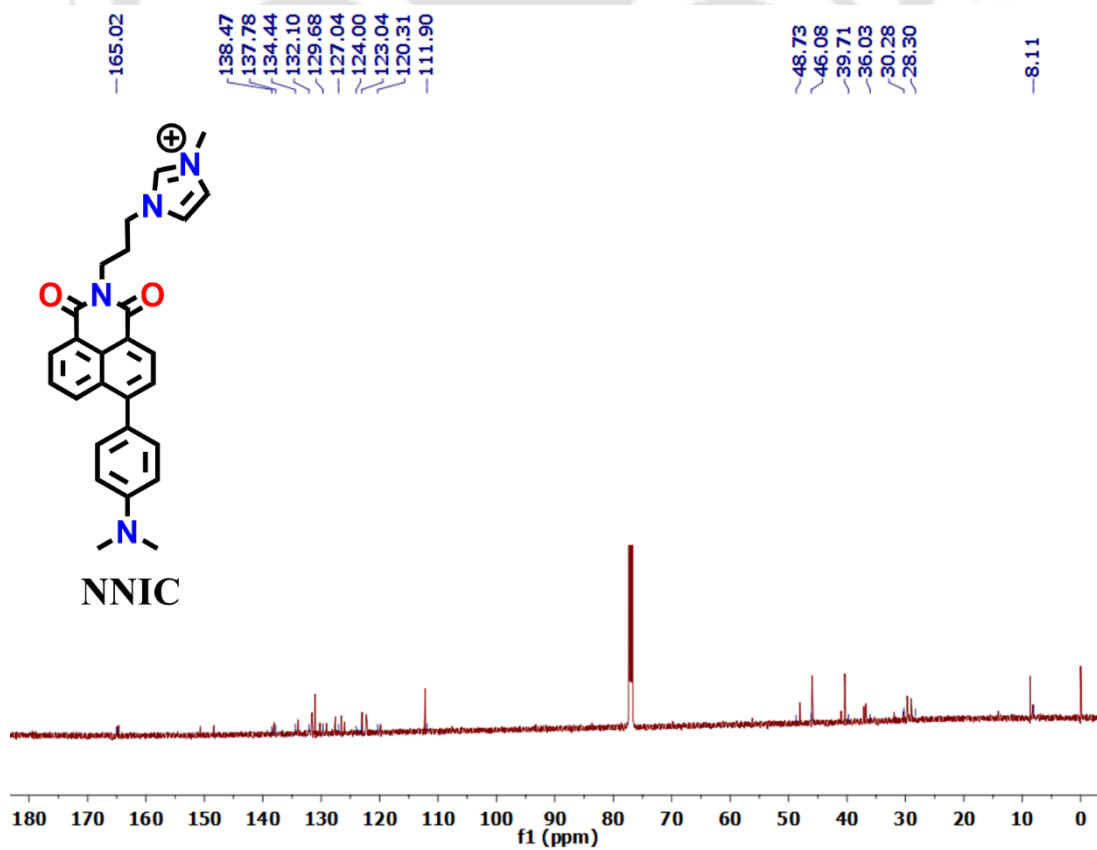


Figure A4.45. ^{13}C NMR spectra of NNIC.

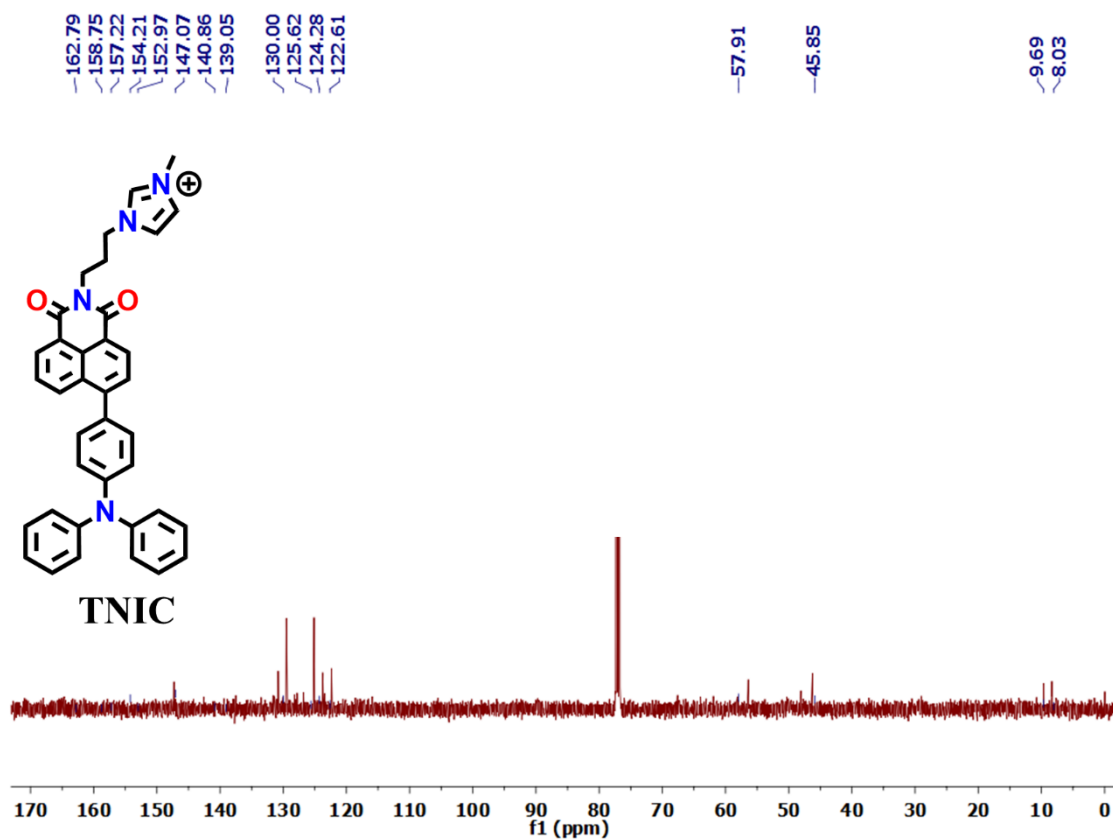


Figure A4.46. ^{13}C NMR spectra of TNIC.

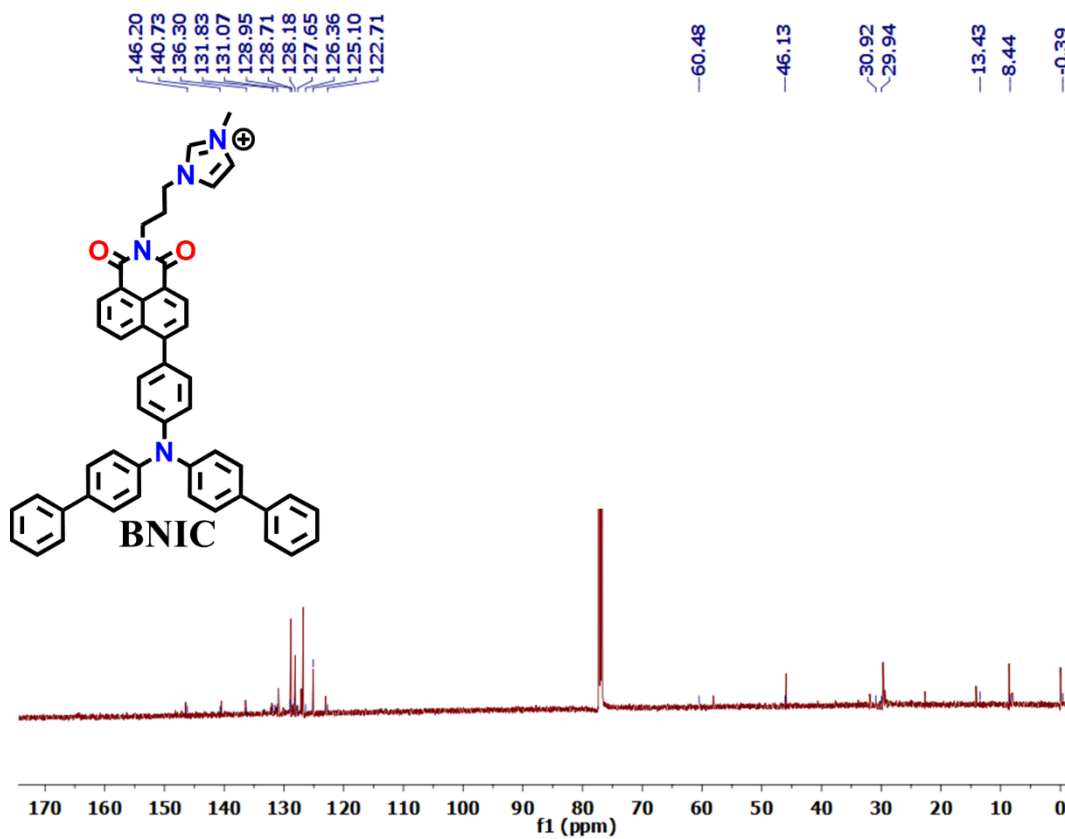


Figure A4.47. ^{13}C NMR spectra of **BNIC**.

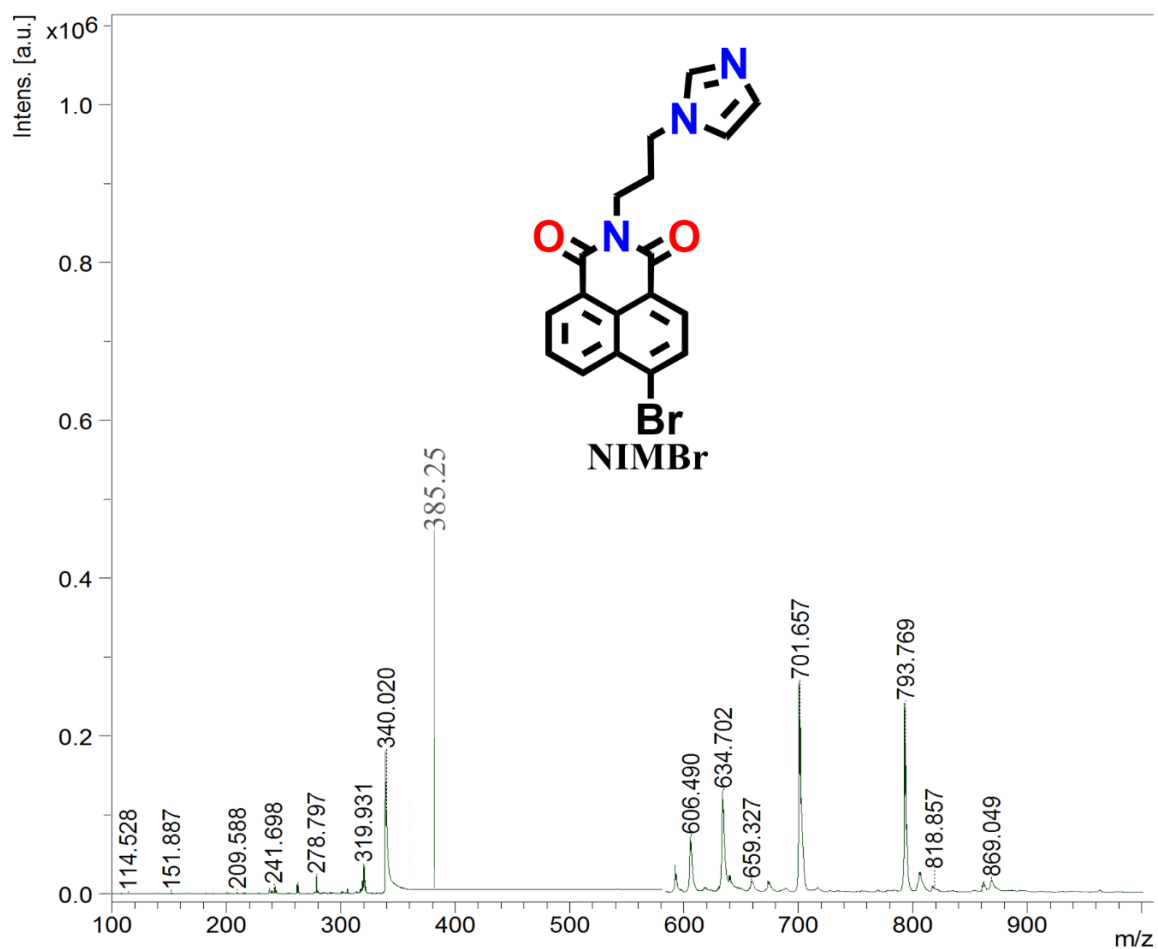


Figure A4.48. MalDI-TOF spectra of **NIMBr**.

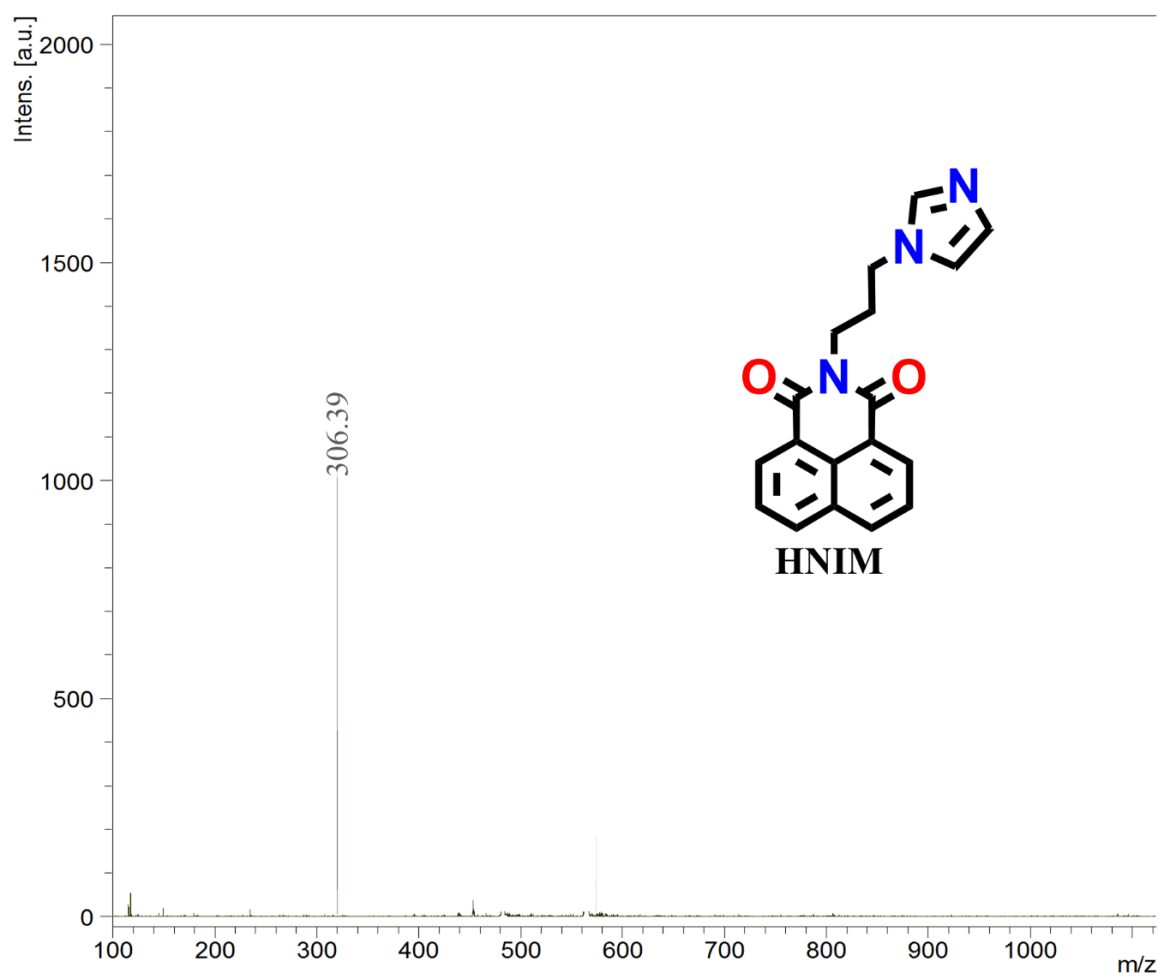


Figure A4.49. Maldi-TOF spectra of HNIM.

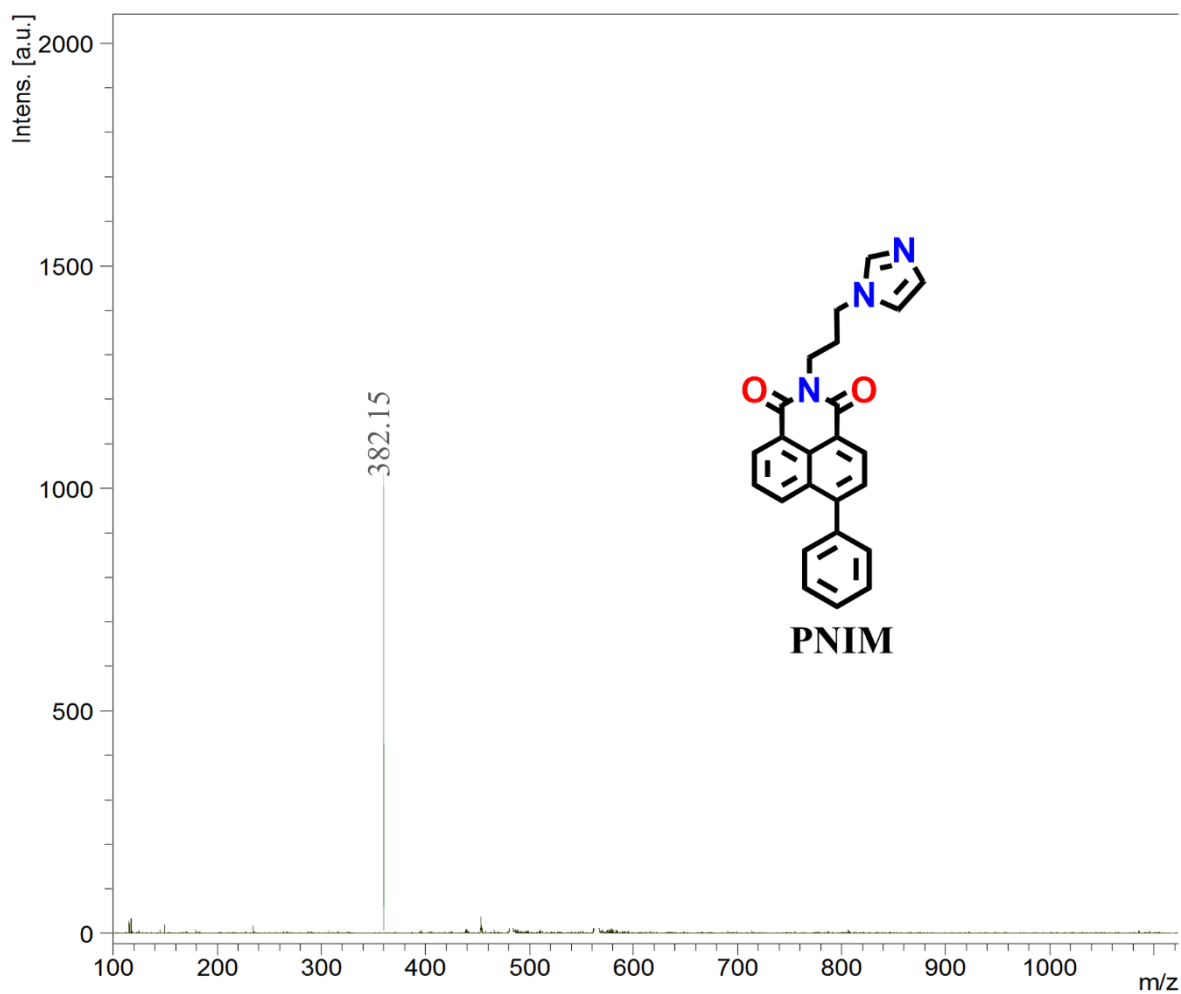


Figure A4.50. Maldi-TOF spectra of **PNIM**.

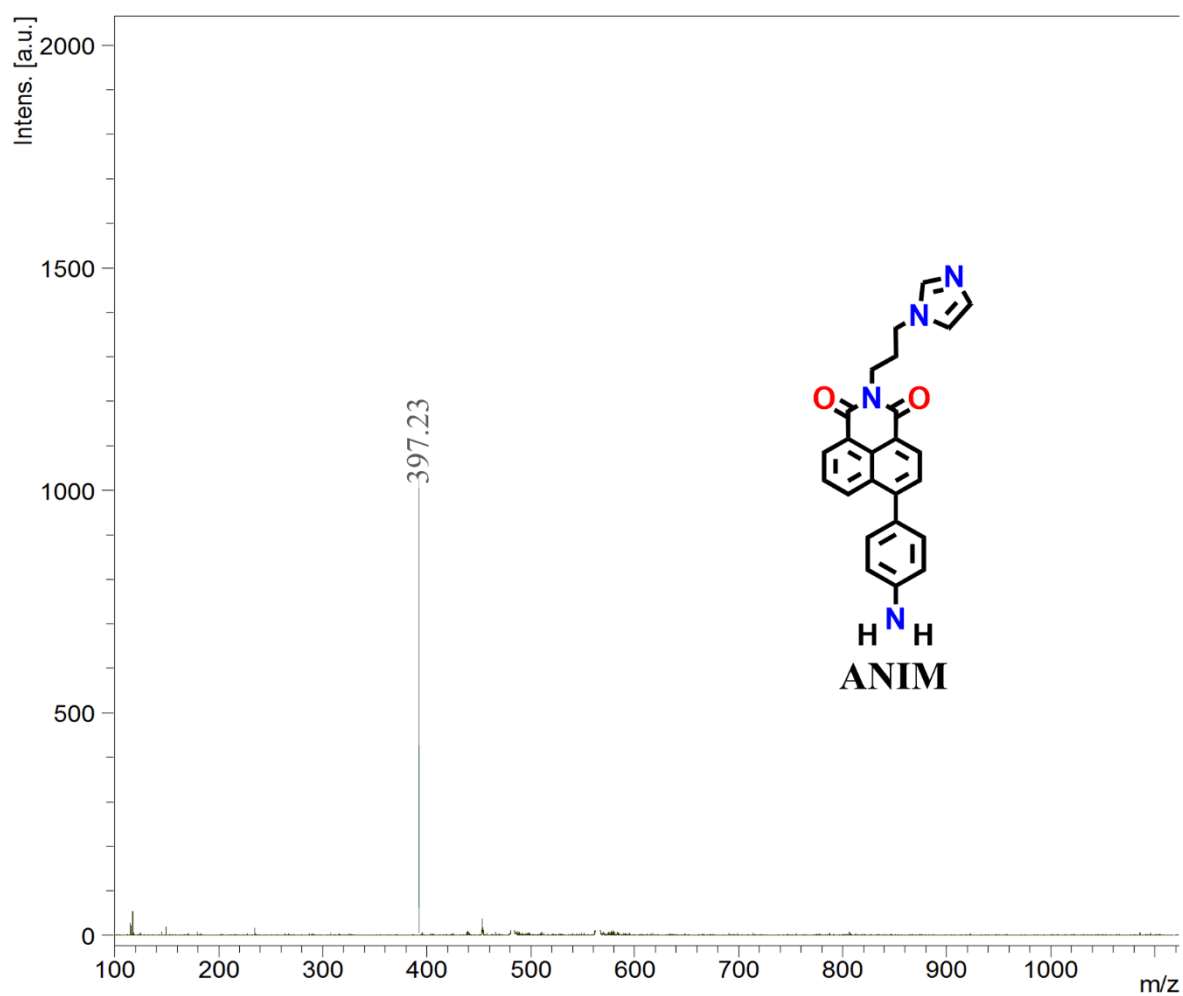


Figure A4.51. Maldi-TOF spectra of ANIM.

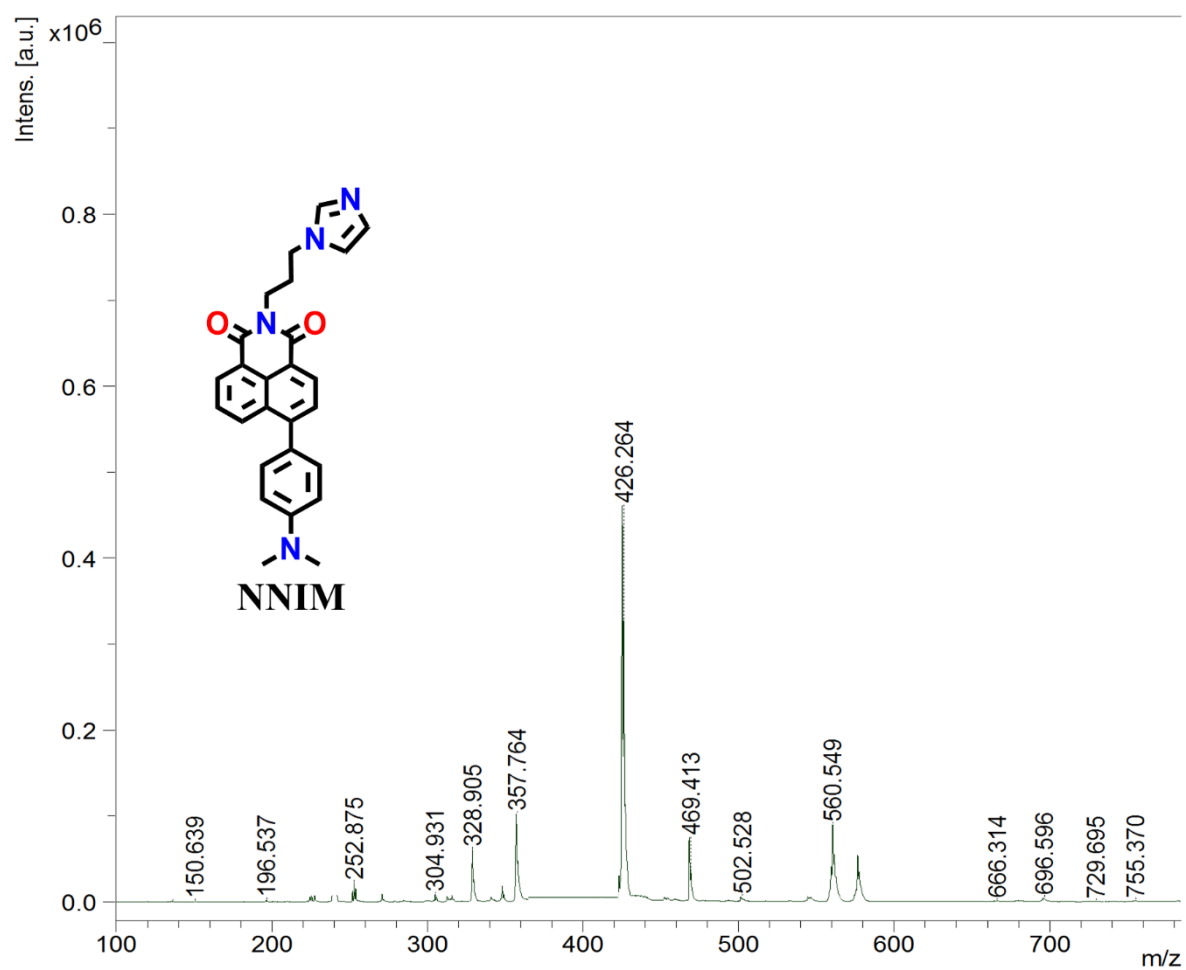


Figure A4.52. Maldi-TOF spectra of NNIM.

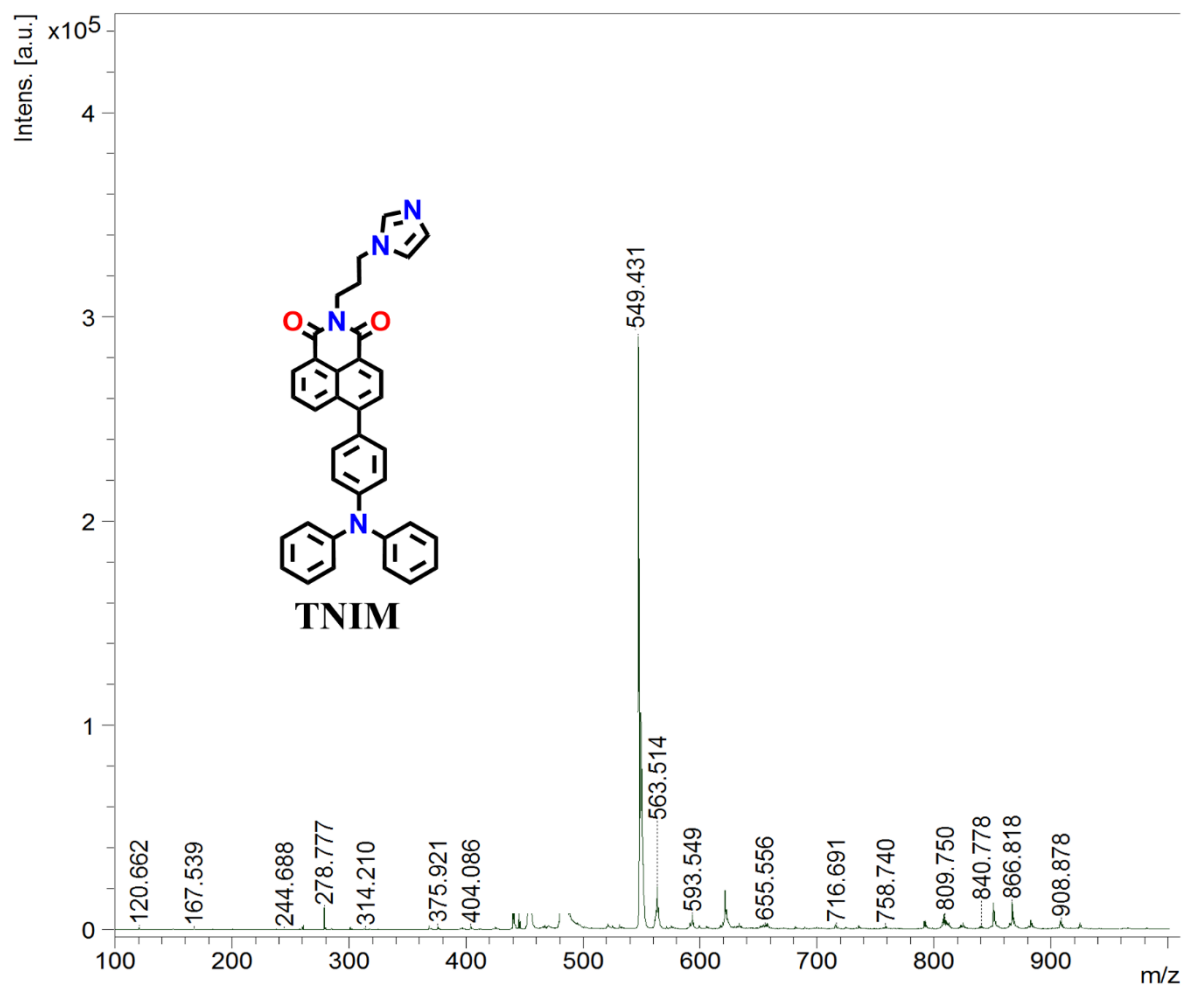


Figure A4.53. Maldi-TOF spectra of TNIM.

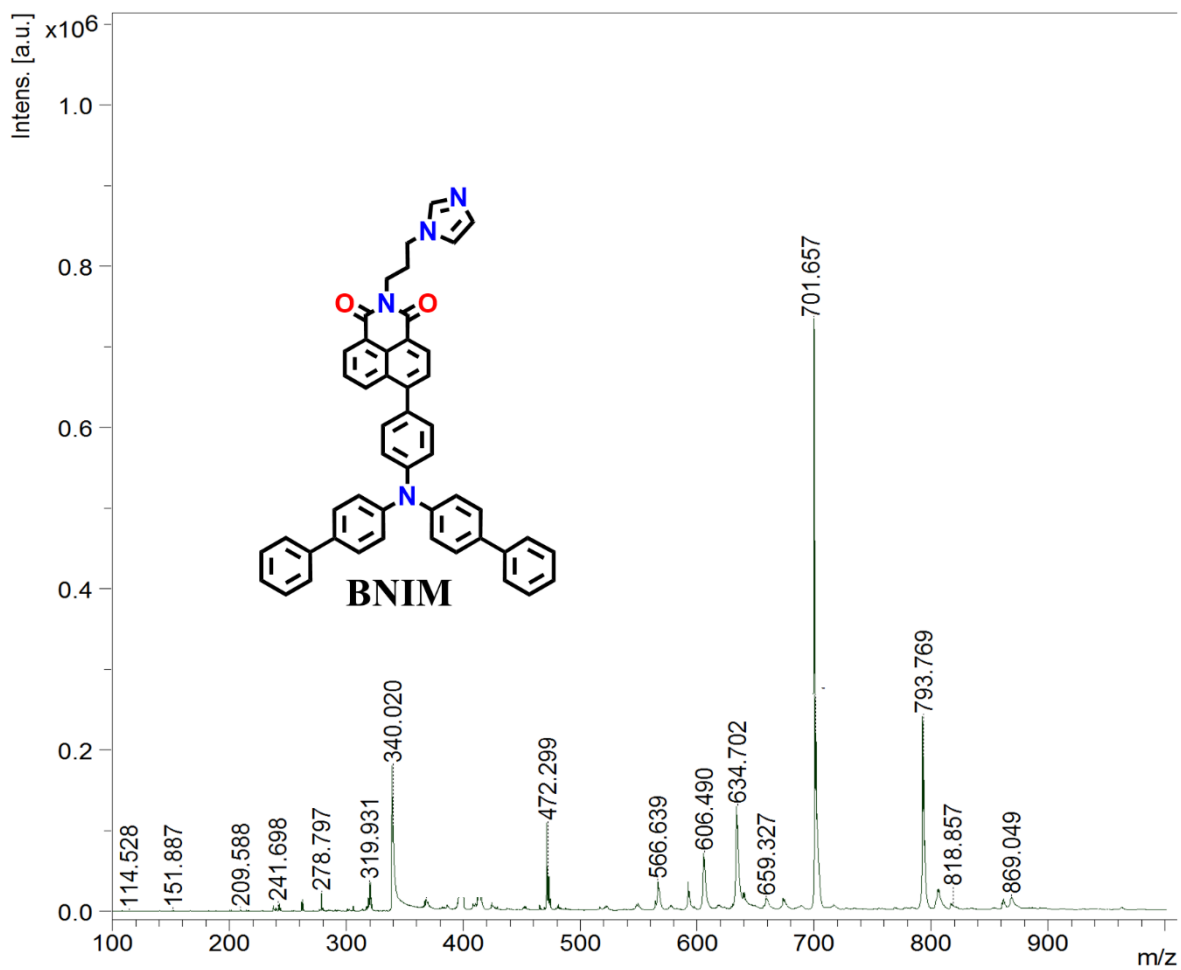


Figure A4.54. Maldi-TOF spectra of BNIM.

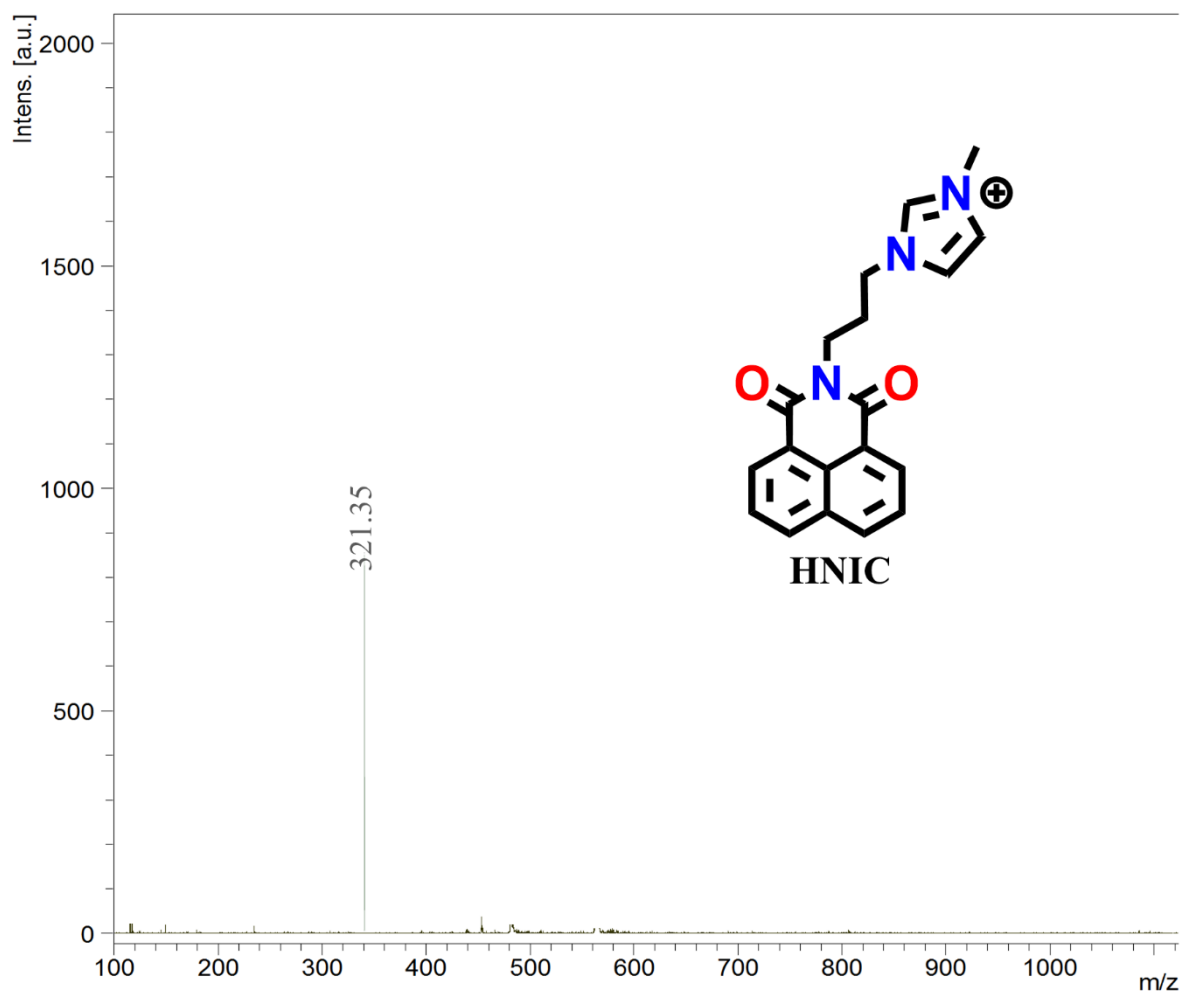


Figure A4.55 Maldi-TOF spectra of HNIC.

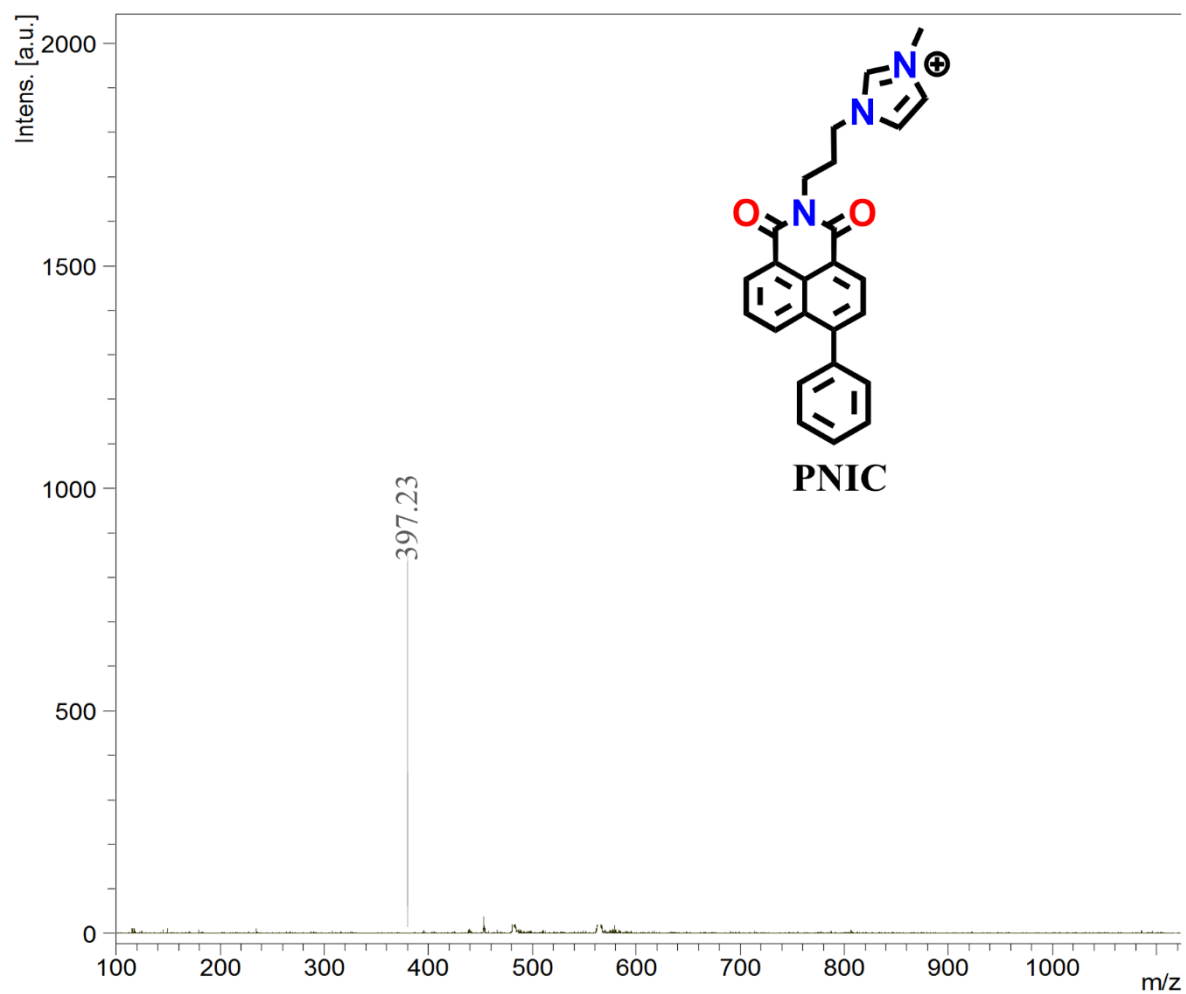


Figure A4.56. Maldi-TOF spectra of PNIC.

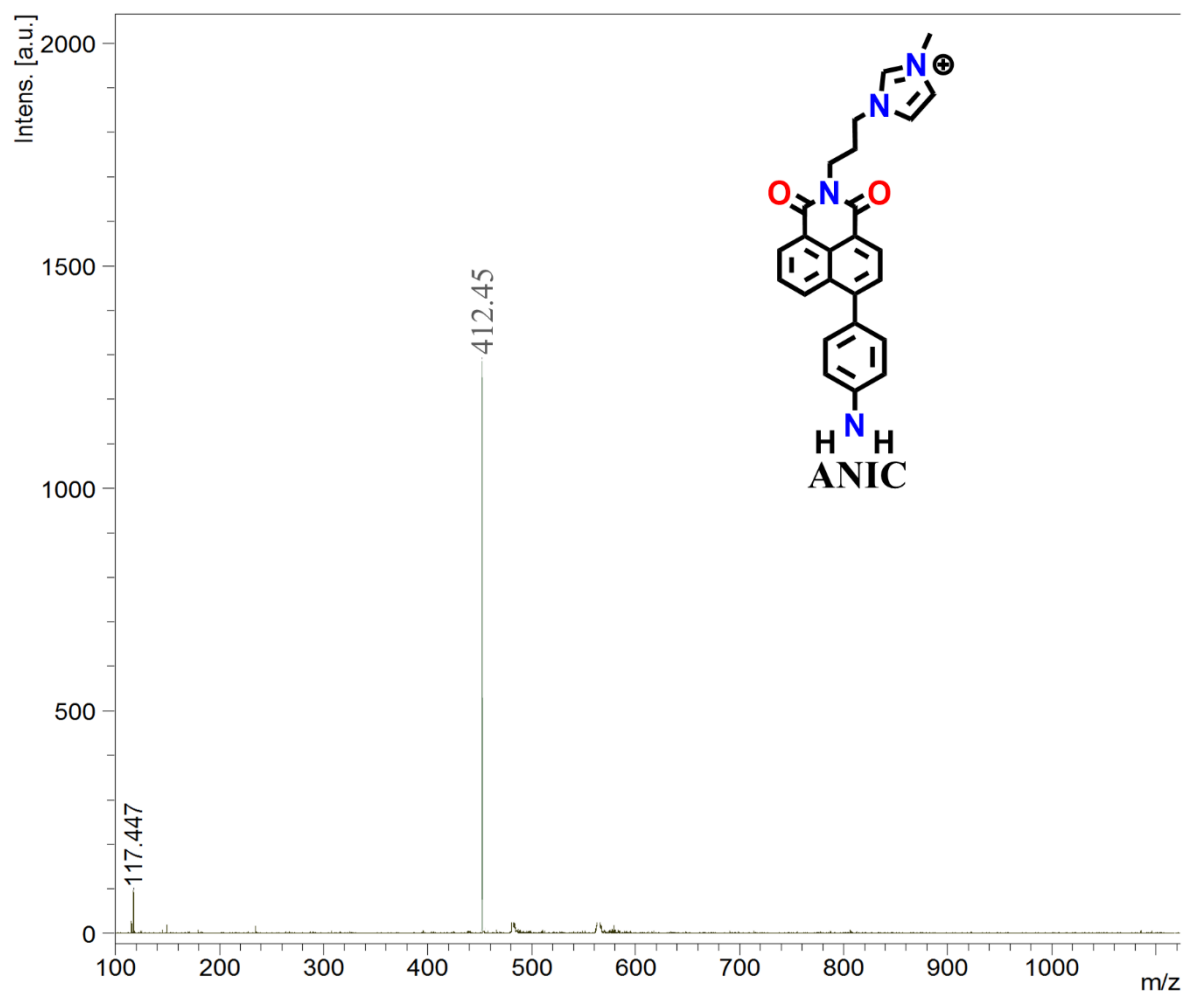


Figure A4.57. Maldi-TOF spectra of ANIC.

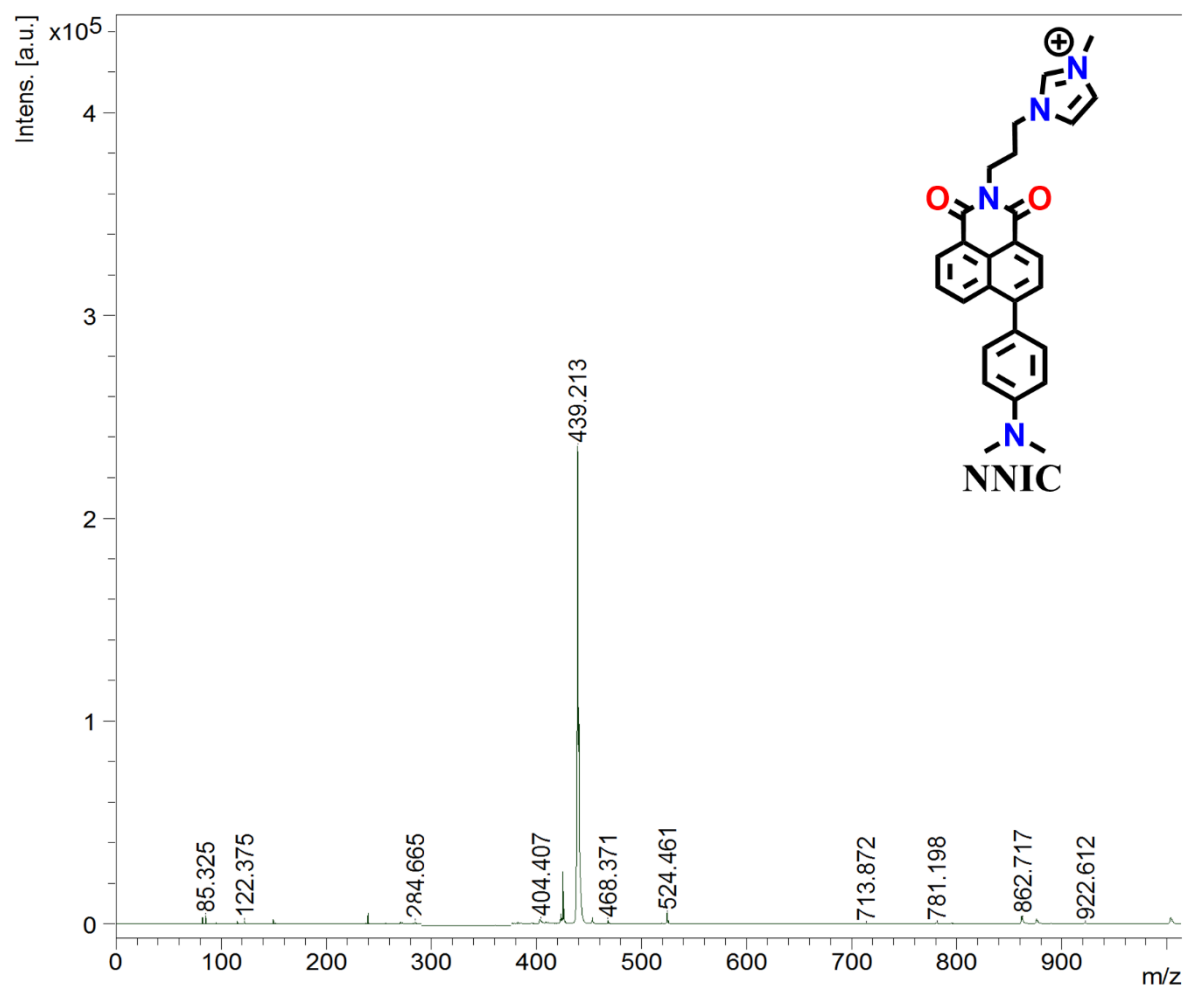


Figure A4.58. Maldi-TOF spectra of NNIC.

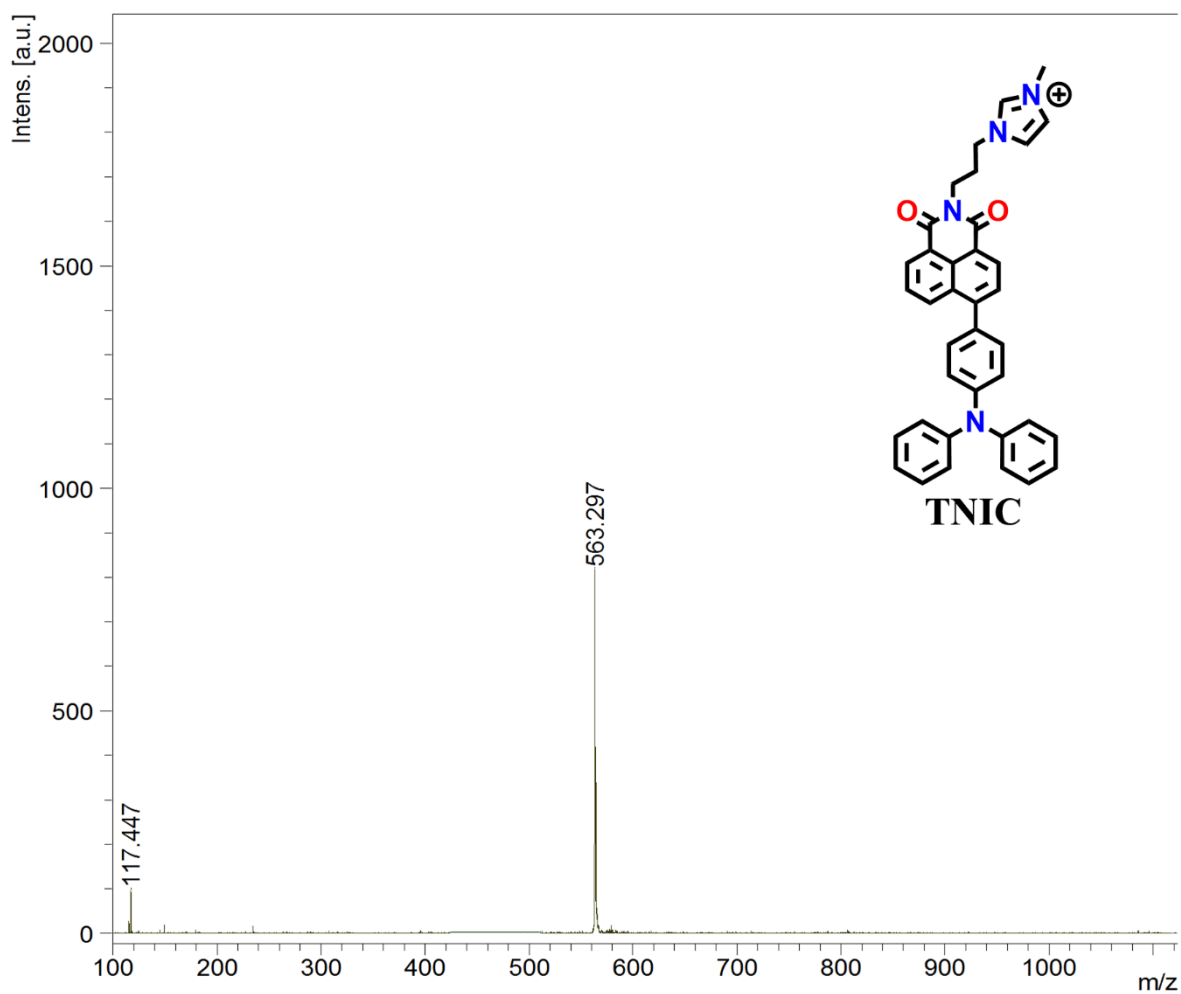


Figure A4.59. Maldi-TOF spectra of **TNIC**.

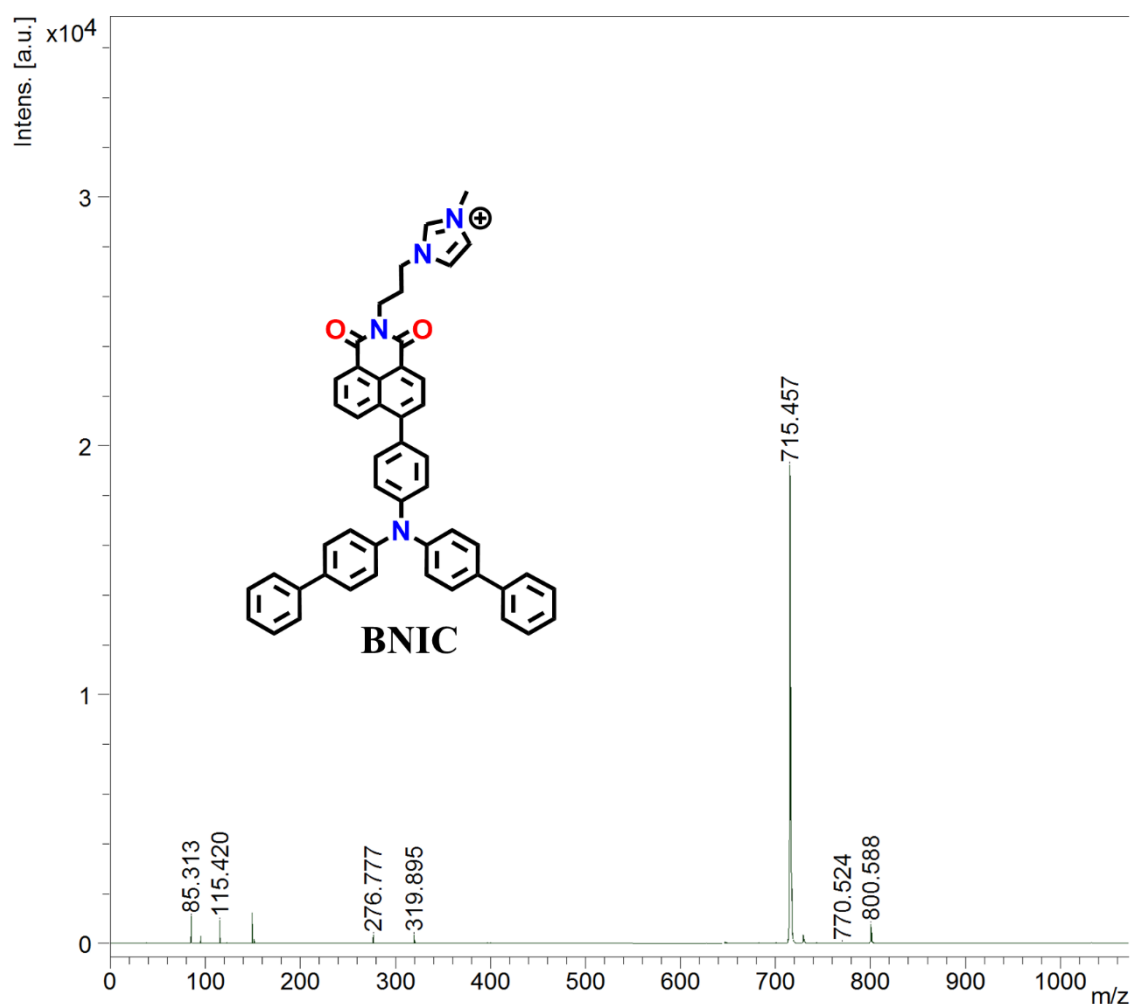


Figure A4.60. Maldi-TOF spectra of **BNIC**.

References

- [1] A. D. Becke, *J. Chem. Phys.* **1993**, *98*, 5648.
- [2] M. J. Frisch, G. W. Trucks, H. B. Schlegel, G. E. Scuseria, M. A. Robb, J. R. Cheeseman, G. Scalmani, V. Barone, B. Mennucci, G. A. Petersson, H. Nakatsuji, M. Caricato, X. Li, H. P. Hratchian, A. F. Izmaylov, J. Bloino, G. Zheng, J. L. Sonnenberg, M. Hada, M. Ehara, K. Toyota, R. Fukuda, J. Hasegawa, M. Ishida, T. Nakajima, Y. Honda, O. Kitao, H. Nakai, T. Vreven, J. A. Montgomery, J. E. Peralta, F. Ogliaro, M. Bearpark, J. J. Heyd, E. Brothers, K. N. Kudin, V. N. Staroverov, R. Kobayashi, J. Normand, K. Raghavachari, A. Rendell, J. C. Burant, S. S. Iyengar, J. Tomasi, M. Cossi, N. Rega, J. M. Millam, M. Klene, J. E. Knox, J. B. Cross, V. Bakken, C. Adamo, J. Jaramillo, R. Gomperts, R. E. Stratmann, O. Yazyev, A. J. Austin, R. Cammi, C. Pomelli, J. W. Ochterski, R. L. Martin, K. Morokuma, V. G. Zakrzewski, G. A. Voth, P. Salvador, J. J. Dannenberg, S. Dapprich, A. D. Daniels, O. Farkas, J. B. Foresman, J. V. Ortiz, J. Cioslowski, D. J. Fox. Gaussian 09, Revision A.02, Gaussian, Inc. Wallingford CT, **2009**.
- [3] F. Neese, *WIREs Comput. Mol. Sci.* **2018**, *8*, 1327.
- [4] F. Neese, *Comput. Mol. Sci.* **2012**, *2*, 73.
- [5] D. Wang, M. M. S. Lee, G. Shan, R. T. K. Kwok, J. W. Y. Lam, H. Su, Y. Cai, B. Z. Tang, *Adv. Mater.* **2018**, *30*,

1802105.

- [6] W. Wu, D. Mao, S. Xu, M. Panahandeh-Fard, Y. Duan, F. Hu, D. Kong, B. Liu, *Adv. Funct. Mater.* **2019**, *29*, 1901791.
- [7] X. Shi, S. H. P. Sung, J. H. C. Chau, Y. Li, Z. Liu, R. T. K. Kwok, J. Liu, P. Xiao, J. Zhang, B. Liu, J. W. Y. Lam, B. Z. Tang, *Small Methods* **2020**, *4*, 2000046.
- [8] Y. Li, W. Zhang, J. Niu, Y. Chen, *ACS Nano* **2012**, *6*, 5164.
- [9] K. W. K. Lam, J. H. C. Chau, E. Y. Yu, F. Sun, J. W. Y. Lam, D. Ding, R. T. K. Kwok, J. Sun, X. He, B. Z. Tang, *ACS Nano* **2023**, *17*, 7145.
- [10] K. Chen, P. He, Z. Wang, B. Z. Tang, *ACS Nano* **2021**, *15*, 7735.
- [11] K. Chen, R. Zhang, Z. Wang, W. Zhang, B. Z. Tang, *Adv. Opt. Mater.* **2020**, *8*, 1901433.
- [12] G. Jiang, C. Li, X. Liu, Q. Chen, X. Li, X. Gu, P. Zhang, Q. Lai, J. Wang, *Adv. Opt. Mater.* **2020**, *8*, 2001119.
- [13] J. Liu, X. Liu, M. Wu, G. Qi, B. Liu, *Nano Lett.* **2020**, *20*, 7438.
- [14] S. Wang, H. Chen, J. Liu, C. Chen, B. Liu, *Adv. Funct. Mater.* **2020**, *30*, 2002546.
- [15] T. Zhang, Y. Li, Z. Zheng, R. Ye, Y. Zhang, R. T. K. Kwok, J. W. Y. Lam, B. Z. Tang, *J. Am. Chem. Soc.* **2019**, *141*, 5612.
- [16] B. Guo, M. Wu, Q. Shi, T. Dai, S. Xu, J. Jiang, B. Liu, *Chem. Mater.* **2020**, *32*, 4681.
- [17] Z. Liu, H. Zou, Z. Zhao, P. Zhang, G.-G. Shan, R. T. K. Kwok, J. W. Y. Lam, L. Zheng, B. Z. Tang, *ACS Nano* **2019**, *13*, 11283.
- [18] F.-Z. Xu, L. Zhu, H.-H. Han, J.-W. Zou, Y. Zang, J. Li, T. D. James, X.-P. He, C.-Y. Wang, *Chem. Sci.* **2022**, *13*, 9373.
- [19] H.-T. Feng, Y. Li, X. Duan, X. Wang, C. Qi, W. Jacky, D. Ding, B. Tang, *J. Am. Chem. Soc.* **2020**, *142*, 15966.
- [20] M. Jiang, X. Gu, R. T. K. Kwok, Y. Li, H. H. Y. Sung, X. Zheng, Y. Zhang, J. W. Y. Lam, I. D. Williams, X. Huang, K. S. Wong, B. Z. Tang, *Adv. Funct. Mater.* **2018**, *28*, 1704589.
- [21] A. Maity, F. Ali, H. Agarwalla, B. Anothumakkool, A. Das, *Chem. Commun.* **2015**, *51*, 2130.
- [22] S. Samanta, U. Manna, G. Das, *New J. Chem.* **2017**, *41*, 1064.
- [23] K. Pal, V. Sharma, A. L. Koner, *Chem. Commun.* **2017**, *53*, 7909.
- [24] H. Wang, Y. Li, Y. Zhang, J. Mei, J. Su, *Chem. Commun.* **2019**, *55*, 1879.
- [25] M. Denißen, R. Hannen, D. Itskalov, L. Biesen, N. Nirmalananthan-Budau, K. Hoffmann, G. J. Reiss, U. Resch-Genger, T. J. J. Müller, *Chem. Commun.* **2020**, *56*, 7407.
- [26] J. Chatsirisupachai, P. Nalaoh, C. Kaiyasuan, P. Chasing, T. Sudyoasuk, V. Promarak, *Mater. Chem. Front.* **2021**, *5*, 2361.
- [27] Z. Zheng, T. Zhang, H. Liu, Y. Chen, R. T. K. Kwok, C. Ma, P. Zhang, H. H. Y. Sung, I. D. Williams, J. W. Y. Lam, K. S. Wong, B. Z. Tang, *ACS Nano* **2018**, *12*, 8145.

[28] W. Xu, M. M. S. Lee, J.-J. Nie, Z. Zhang, R. T. K. Kwok, J. W. Y. Lam, F.-J. Xu, D. Wang, B. Z. Tang, *Angew. Chem., Int. Ed.* **2020**, *59*, 9610.



Sulphur-Atom Positional Engineering in Perylenimide: Structure-Property Relationships and H-aggregation-Directed Type-I Photodynamic Therapy

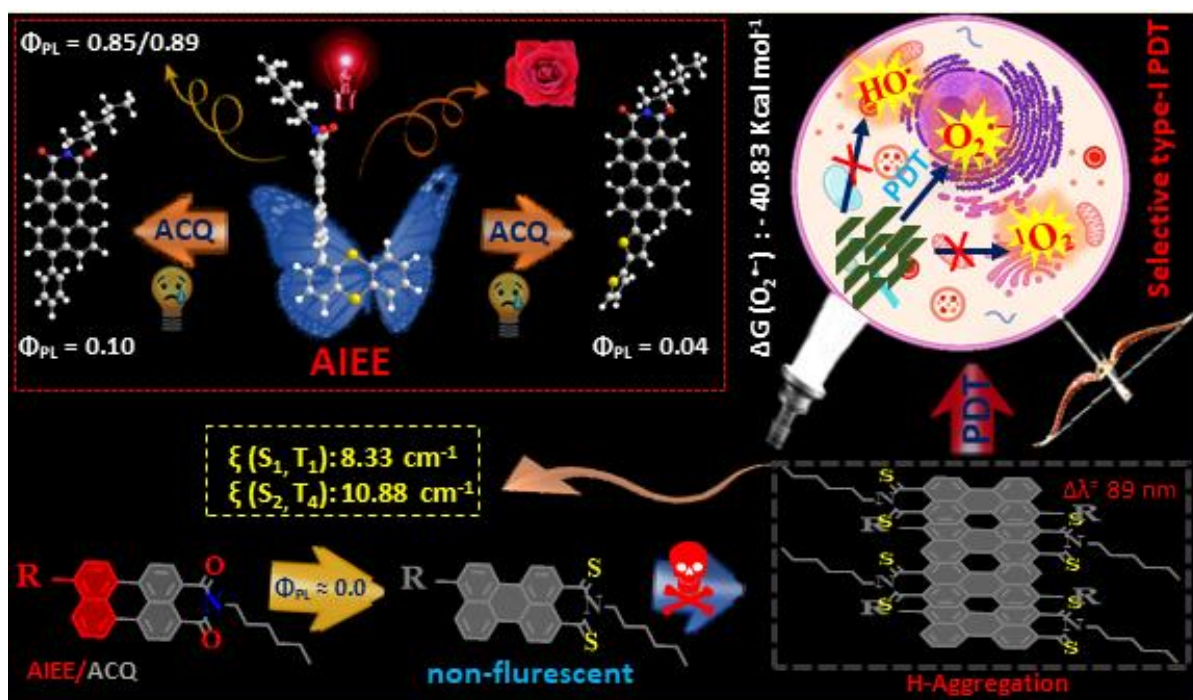
Khatun, M. N.; Nandy, S.; jyoti, H.; Ghosh, S.S.; Kumar, S.; Iyer, P. K. (Revision submitted)

DOI <https://doi.org/10.1039/D4SC01180E> (Chemical Science) (Indian patent submitted (TEMP/E-1/80303/2023-KOL))

Abstract

An innovative design strategy of placing sulfur (S)-atoms within pendant functional groups and carbonyl positions in conventional perylenimide (**PNI-O**) has been demonstrated to strategically investigate condensed state structure-property relationship and potential photodynamic therapy (PDT) application. Incorporation of simply S-atoms at the perifunctionalized perylenimide (**RPNI-O**) leads to aggregation-induced enhanced emission (AIEEgen), 2-hexyl-8-(thianthren-1-yl)-1H-benzo[5,10]anthra[2,1,9-def]isoquinoline-1,3(2H)-dione (**API**), which achieves a remarkable photoluminescence quantum yield (Φ_{PL}) of 0.85 in aqueous environments and established novel AIE mechanisms. Additionally, substitution of the S-atom at the carbonyl position in **RPNI-O** leads to thioperlylenimides (**RPNI-S**): 2-hexyl-8-phenyl-1H-benzo[5,10]anthra[2,1,9-def]isoquinoline-1,3(2H)-dithione (**PPIS**), 8-([2,2'-bithiophen]-5-yl)-2-hexyl-1H-benzo[5,10]anthra[2,1,9-def]isoquinoline-1,3(2H)-dithione (**THPIS**), and 2-hexyl-8-(thianthren-1-yl)-1H-benzo[5,10]anthra[2,1,9-def]isoquinoline-1,3(2H)-dithione (**APIS**), with distinct photophysical properties (enlarge spin-orbit coupling (SOC) and $\Phi_{PL} \approx 0.00$), and developed diverse potent photosensitizers (PSs). The present work has provided novel SOC enhancement mechanism via pronounced H-aggregation. Surprisingly, the lowest singlet oxygen quantum yield (Φ_{Δ}) and theoretical calculation suggests the very specific type-I PDT for **RPNI-S**. Interestingly, **RPNI-S** efficiently produce superoxide ($O_2^{\cdot-}$) due to its remarkable lower Gibbs free energy (ΔG) values (**THPIS**: $-40.83 \text{ kcal mol}^{-1}$). The non-toxic and heavy-atom free very specific thio-based **PPIS** and **THPIS** PSs showed selective and efficient PDT under normoxia, which is very rare.

Keywords: aggregation-induced emission; S-atom positional engineering; distinct condensed state emitters; H-aggregation; diverse type-I/type-II ROS; specific photosensitizers ($O_2^{\cdot-}$), photodynamic therapy.



5.1. Introduction

In recent years, PDT, a photochemical reaction-based treatment that utilizes light together with appropriate PSs, has been attracting great attention due to its distinct advantages over most conventional therapies in cancer treatments.^{1,2} Yet, classical PSs have low excited state triplet formation, and the introduction of heavy atoms to enlarge SOC and subsequently to enhance intersystem crossing (ISC) into their structures often raises major concerns about cost as well as high dark toxicity.^{3,4} In PDT, two distinct mechanisms, type-I and type-II, governs the reactions of PSs with ground state oxygen ($^3\text{O}_2$).⁵ Type-I PDT involves intermolecular electron transfer (IET) process which is the transfer of an electron from the triplet excitons of the PS to $^3\text{O}_2$, leading to the formation of $\text{O}_2^{\bullet-}$. This process can occur independently of any reducing intermediary, resulting in the generation of hydrogen peroxide (H_2O_2) and hydroxyl radicals (HO^\bullet) through superoxide disproportionation and Franck-Condon transition.⁶ Crucially, this type of reaction requires an allowed electron transfer, indicated by a negative Gibbs free energy change ($\Delta G < 0$).⁷ On the other hand, type-II PDT relies on the energy transfer from PS triplet excitons to $^3\text{O}_2$, resulting in the formation of $^1\text{O}_2$.⁵ Comparatively, the type-I process in PDT mechanisms is more advantageous due to its lower dependence on oxygen content, and it remains relatively rare to date.^{8,9} From several past decades, the S-substituted nucleobases anticancer drugs have received increasing interest due to their potential chemotherapeutic applications and are still being explored for their potential therapeutic abilities.¹⁰⁻¹² Additionally, the excellent excited triplet formation triggered by the thiocarbonyl group of thiobases PSs, could result in more

prospective PSs with very promising application in PDT. However, numerous drawbacks of thiobases drugs including long irradiation times, need of higher concentrations, etc. have limited their obvious practical applications.¹³⁻¹⁵ Yet, numerous S-substituted derivatives at the carbonyl group have been comprehensively designed as heavy-atom-free materials.¹⁶⁻²⁰ The development of such S-substituted carbonyl group in tumor treatment has not been extensively studied, which subsequently motivated us to reflect upon thionation approach for future exploration of PSs with clinical acceptance. While heavy-atom-free thio-based naphthalimide (**NI**) PSs were designed for hypoxic environments, lacking specificity, selectivity, and HO \cdot generation. The study did not thoroughly explore type-I mechanisms and varied PS production. It was limited to one cell line, raising questions about broader applicability. Additional targeting agents were needed for prior heavy-atom-free PSs in biological environments. The absence of an S-atom at a functional position in their design is noteworthy, as it may significantly impact PDT-mediated cancer treatment and other unique properties, rather than solely relying on PDT applications (Table A5.1).¹⁹

Considering these insights, **PNI-O** core has been chosen as the potent core due to its exceptional Φ_{PL} , chemical stability, and thermal resilience, as well as its promising potential applications in various fields, including sensors,²¹ therapeutics,²² optoelectronics,^{23,24} and bioimaging.²⁵ Then, an innovative design strategy involving the incorporation of S-atoms into both pendant functional groups and carbonyl positions within a planar **PNI-O** core, distinct from previous thio-based approach, has been demonstrated here. The aim is to explore the structure-property relationship in the condensed state, especially in the context of potential PDT applications for cancer treatment. This investigation is in line with a well-established and ongoing effort to understand condensed state structure-property relationships, driven by their significance across various fields.²⁶⁻³⁰ Incorporating S-atoms at both the functional and carbonyl positions results in entirely distinct properties within **PNI-O**. The introduction of simply S-atoms at functional positions triggers a unique transformation from aggregation-caused quenching (ACQ)-to-AIEE behavior within the extremely planar **PNI-O** core, results high Φ_{PL} of 0.85 (with unique microse supramolecular-assembly) and large stokes shift of 146 nm, which are rarely observed. This modification establishes a novel AIE mechanism. While, S-atoms at the carbonyl position leads to completely drop in the fluorescence intensity ($\Phi_{\text{PL}} \approx 0.00$) and enlarge SOC, promoting type-I PDT reactions with efficient production of O $_2^{\cdot-}$. This strategy demonstrates broad PDT applicability, targeting cancer cells (Hela and MCF7) and normal cells without the need for additional targeting agents, emphasizing its cost-effectiveness. Notably, the biocompatible heavy-atom-free thio-based PSs exhibit selective and efficient PDT efficacy, marking the first such reported instance. This work also provides SOC enhancement mechanisms through prominent H-aggregation (Table A5.2). While previous research

showed improved SOC and ISC, this research unveils the key role of pronounced H-aggregation in this enhancement, opening up new possibilities for future PSs.¹⁶⁻²⁰ This approach allows for precise control over the generation of distinct variation of type-I and type-II ROS, expanding the potential applications of these PSs.

In conclusion, this research introduces a novel concept of highly specific and selective heavy-atom-free thio-based PSs, exhibiting simple and precise method to manipulate condensed state emissions, supramolecular assembly, and unique PSs development, marking a significant breakthrough in the field.

5.2. Experimental Section

5.2.1. Materials and Instrumentations: All reagents and starting materials, including Perylene-3,4,9,10-tetracarboxylic acid anhydride (PDA), imidazole, Zinc acetate [Zn (OAc)₂], and various boronic acid derivatives such as phenyl boronic acid, thianthrenyl boronic acid, and 2,2'-bithiophene-5-boronic acid pinacol ester, and other reactive oxygen species detector such as 2',7'-Dichlorodihydrofluorescein diacetate were (DCFDA), 2,2,6,6-Tetramethylpiperidin (TEMP), 9,10-Anthracenediyl-bis(methylene)dimalonic acid (ABDA), Terephthalic acid (TA) were purchased from Sigma Aldrich (INDIA) in reagent-grade quality. HPLC-grade solvents were obtained from Fisher Scientific Ltd. and RANKEM. Nuclear magnetic resonance (NMR) spectra, including ¹H and ¹³C, were recorded using a Bruker Avance 400 MHz spectrometer. The residual solvent signal was used as an internal reference for all solutions used in the NMR experiments. Mass spectra were obtained using MALDI-TOF spectrometry. UV/visible (UV/vis) and photoluminescence (PL) spectra were recorded using a Perkin-Elmer Model Lambda-750 spectrophotometer and a Horiba Fluoromax-4 spectrofluorometer, respectively. Measurements were performed at 298 K using 4 mm quartz cuvettes. A laser diode at 375 nm (DeltaDiode-375) served as the excitation source for both UV/vis and PL experiments. The hydrodynamic diameter and Zeta potential of the compounds were measured using a Malvern Zetasizer instrument. Field emission scanning electron microscopy (FESEM) images were obtained using a Sigma Carl ZEISS field emission scanning electron microscope. Single crystal data were collected using a Bruker SMART APEX diffractometer equipped with a CCD area detector. For photodynamic therapy studies, a white light source with an intensity of 50 mW cm⁻², specifically the "Pick Ur Needs 120W Plastic Lithium Battery Search Light Long 1 Km Range with Multi-Functional + Blinker Rechargeable Handheld Torch" in black, was utilized. DMEM, Propidium iodide (PI), and Calcein-AM (AM) were purchased from High Media. The HeLa cell line was purchased from Sigma Aldrich (INDIA).

5.2.2. Preparation of the Test Solution: Stock solutions of **RPNI-O** materials, including **PPI**, **THPI**, and **API**, as well as derivatives of **RPNI-S** such as **PPIS**, **THPIS**, and **APIS**, were prepared at a concentration of 20 mM in dimethyl sulfoxide (DMSO). To study the aggregation behavior, test solutions of the materials were prepared at a concentration of 100 μM . These test solutions were prepared by varying the water fraction in DMSO. Prior to recording the spectra, the resulting solutions were thoroughly shaken at room temperature to ensure proper mixing and dispersion of the compounds.

5.2.3. Preparation of FESEM samples:

The morphological analysis of the supramolecular self-assembly was conducted using field emission scanning electron microscopy (FESEM). A simple methodology was employed to prepare the samples for imaging, as depicted in Figure A5.8. A dilute suspension of the Perylene derivatives at a concentration of 100 μM was prepared using a mixture of 99.9% water and -0.1% DMSO. Subsequently, this suspension was drop-casted onto a glass surface coated with aluminum foil. The samples were then allowed to air dry overnight at room temperature prior to analysis.

5.2.4. Theoretical Studies: Density functional theory (DFT) calculations were employed to evaluate the electronic properties of **RPNI-O** and **RPNI-S** derivatives. The Gaussian 16 package, incorporating the B3LYP hybrid functional, was utilized to perform these calculations. For each derivative, the ground state optimized geometries were obtained, and the electron density and energy of the highest occupied molecular orbital (HOMO) and lowest unoccupied molecular orbital (LUMO) were determined. The calculations employed the 6-31G basis set, which is known to provide accurate results within a reasonable computational time (ref.1, 2 in AI).

5.2.5. Photoluminescence quantum Yield Calculations: The fluorescence quantum yields (Φ_{PL}) of **RPNI-O** and **RPNI-S** derivatives were determined by comparing them to the fluorescence quantum yield of Rhodamine 6G ($\Phi_{\text{r}} = 0.95$ in ethanol) using a specific equation. The equation used is as follows:

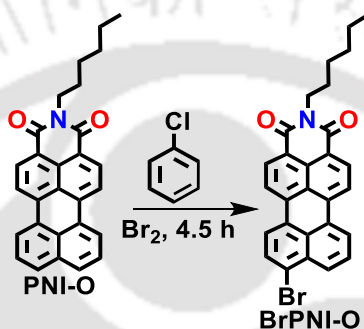
$$\Phi_{\text{PL}} = \Phi_{\text{r}} (A_{\text{r}}F_{\text{s}}/A_{\text{s}}F_{\text{r}}) (\eta_{\text{s}}^2/\eta_{\text{r}}^2) \quad (\text{A5.1})$$

In this equation, s and r refer to the sample and reference, respectively. Φ represents the quantum yield, A denotes the absorbance, F signifies the relative integrated fluorescence intensity, and η represents the refractive index.

resulting solid, which appeared red in color, was subjected to crystallization using methanol. This process yielded a 95% yield of the desired compound.

Characterization data for 8-bromo-2-hexyl-1H-benzo[5,10]anthra[2,1,9-def]isoquinoline-1,3(2H)-dione (BrPNI-O): ^1H NMR (400 MHz, CDCl_3) δ 0.93 (t, 3H), 1.3-1.6 (m, 6H), 1.88 (dd, 2H), 3.77 (t, 2H), 7.69 (t, 1H), 7.86 (d, 1H), 8.13 (d, 1H), 8.27 (d, 2H), 8.33 (d, 1H), 8.38 (d, 1), 8.55 (dd, 2H). ^{13}C NMR (101 MHz, CDCl_3) δ 14.09, 22.58, 26.92, 28.19, 31.64, 40.49, 120.12, 123.67, 126.96, 127.75, 129.15, 130.80, 131.32, 172.56 MALDI-TOF: calculated for $\text{C}_{28}\text{H}_{22}\text{BrNO}_2$: 484.38 $[\text{M}]^+$, Found: 483.39 $[\text{M}-\text{H}]^+$

Synthetic Route



Scheme A5.2. The synthetic method employed to prepare **BrPNI-O**.

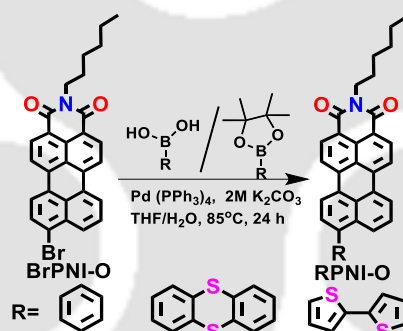
Synthetic procedures for RPNI-O: In a 50 mL round-bottom flask, Compound BrPNI-O (0.5 mmol) and the corresponding boronic acid (1 mmol) were combined with 5 mg of Pd (PPh_3)₄ catalyst. The mixture was then subjected to nitrogen gas for 30 minutes to remove any oxygen. Following this, 6 mL of THF (tetrahydrofuran) were added to the flask, followed by the addition of 2 mL of a 2.0 M potassium carbonate solution. The resulting mixture was stirred at 85 °C under a nitrogen atmosphere, and the progression of the reactions was monitored using thin-layer chromatography (TLC). After 24 hours, the solutions were cooled and extracted using CHCl_3 (chloroform). The organic layers were subsequently dried using anhydrous sodium sulfate. The solvent was evaporated, and the resulting product was purified using column chromatography, yielding a 60% yield of the desired Red solid for **PPI** and **API** and **THPI** (brownish solid) compound.

Characterization data for 2-hexyl-8-phenyl-1H-benzo[5,10]anthra[2,1,9-def]isoquinoline-1,3(2H)-dione (PPI): ^1H NMR (400 MHz, CDCl_3) δ 0.89 (t, 3H), 1.41 (m, 6H), 1.76 (dt, 2H), 4.14 (t, 2H), 7.53 (m, 7H), 7.98 (d, 1H), 8.37 (d, 2H), 8.42 (t, 2H), 8.55 (m, 2H). ^{13}C NMR (101 MHz, CDCl_3) δ 14.07, 22.62, 26.77, 28.07, 29.02, 31.56, 40.39, 114.10, 120.13, 119.69, 123.56, 126.05, 128.52, 129.20, 130.01, 131.99, 132.66, 136.66, 139.74, 143.11, 163.73. MALDI-TOF: calculated for $\text{C}_{34}\text{H}_{29}\text{NO}_2$: 481.20 $[\text{M}]^+$, Found: 482.66 $[\text{M}+\text{H}]^+$

Characterization data for 8-([2,2'-bithiophen]-5-yl)-2-hexyl-1H-benzo[5,10]anthra[2,1,9-def]isoquinoline-1,3(2H)-dione (THPI): ^1H NMR (400 MHz, CDCl_3) δ 0.88 (t, 3 H), 1.39 (m, 5H), 1.75 (dt, 3H), 4.19 (t, 2H), 7.08 (t, 1H), 7.29 (m, 4H), 7.64 (t, 1H), 7.70 (d, 1H), 8.35 (m, 3H), 8.41 (t, 2H), 8.54 (m, 2H). ^{13}C NMR (101 MHz, CDCl_3) δ 12.98, 22.92, 26.64, 27.25, 28.02, 30.90, 32.50, 39.56, 113.69, 118.96, 119.56, 122.50, 126.83, 127.54, 128.52, 131.29, 135.54, 138.75, 142.01, 162.55. MALDI-TOF: calculated for $\text{C}_{36}\text{H}_{27}\text{NO}_2\text{S}_2$: 569.14 $[\text{M}]^+$, Found: 569.43 $[\text{M}]^+$

Characterization data for 2-hexyl-8-(thianthren-1-yl)-1H-benzo[5,10]anthra[2,1,9-def]isoquinoline-1,3(2H)-dione (API): ^1H NMR (400 MHz, CDCl_3) δ 0.89 (t, 3H), 1.39 (m, 6H), 1.77 (m, 2H), 4.22 (t, 2H), 7.15 (t, 3H), 7.34 (d, 1H), 7.40 (t, 3H), 7.54 (dd, 3H), 7.65 (d, 3H), 8.50 (m, 1), 8.64 (dd, 2H). ^{13}C NMR (101 MHz, CDCl_3) δ 14.09, 27.09, 28, 59, 31.57, 40.49, 120.36, 121.25, 126.28, 127.84, 128.67, 129.12, 132.4, 135.44, 136.43, 137.39, 139.66, 164.12. MALDI-TOF: calculated for $\text{C}_{40}\text{H}_{29}\text{NO}_2\text{S}_2$: 619.79 $[\text{M}]^+$, Found: 620.79 $[\text{M}+\text{H}]^+$

Synthetic Route



Scheme A5.3. The synthetic method employed to prepare **RPNI-O**.

Synthetic procedures for RPNI-S: In a 20 mL flask, **RPNI-O** (0.5 mmol) and Lawesson's reagent (1.5 mmol) were dissolved in dry toluene. The resulting solution was refluxed under a nitrogen atmosphere for a duration of 24 hours. After completion of the reaction, the mixture was allowed to cool down to room temperature, and the solvent was evaporated under reduced pressure. The residue obtained was subjected to purification using column chromatography on silica gel, employing a hexane/dichloromethane (DCM) mixture as the eluent. Subsequent drying under vacuum conditions yielded a bluish powder (53% yield).

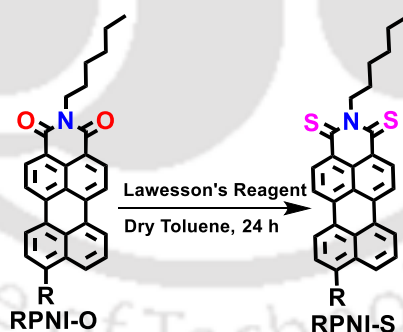
Characterization data for 2-hexyl-8-phenyl-1H-benzo[5,10]anthra[2,1,9-def]isoquinoline-1,3(2H)-dithione (PPIS): ^1H NMR (400 MHz, CDCl_3) δ 0.90 (t, 3H), 1.40 (m, 6H), 1.78 (dt, 2H), 4.21 (m, 2H), 7.16 (q, 3H), 7.34 (d, 3H), 7.41 (t, 1H), 7.53 (d, 1H),

7.56 (d, 1H), 7.65 (d, 1H), 8.48 (dd, 1H), 8.54 (d, 1H), 8.63 (dd, 2H). ¹³C NMR (101 MHz, CDCl₃) δ 13.07, 21.66, 25.87, 27.03, 28.67, 30.57, 49.54, 113.04, 118.31, 119.47, 121.45, 122.33, 125.63, 126.94, 127.56, 128.09, 129.95, 131.95, 132.25, 138.75, 142.09, 165.3. MALDI-TOF: calculated for C₃₄H₂₇NS₂: 513.15 [M]⁺, Found: 513.29 [M]⁺

Characterization data for 8-([2,2'-bithiophen]-5-yl)-2-hexyl-1H-benzo[5,10]anthra[2,1,9-def]isoquinoline-1,3(2H)-dithione (THPIS): ¹H NMR (400 MHz, CDCl₃) δ 0.89 (t, 3H), 1.41 (m, 6H), 1.76 (dt, 2H), 4.19 (t, 2H), 7.08 (t, 1H), 7.29 (m, 6H), 7.64 (t, 1H), 7.71 (d, 1H), 8.35 (m, 3H), 8.40 (dd, 1H), 8.54 (t, 2H). ¹³C NMR (101 MHz, CDCl₃) δ 13.09, 21.59, 25.67, 27.04, 28.77, 30.67, 48.54, 114.04, 117.31, 118.57, 120.55, 121.43, 123.73, 125.74, 125.56, 127.01, 128.95, 130.05, 131.25, 141.45, 142.09, 169.3. MALDI-TOF: calculated for C₃₆H₂₇NS₄: 601.10 [M]⁺, Found: 601.19 [M]⁺

Characterization data for 2-hexyl-8-(thianthren-1-yl)-1H-benzo[5,10]anthra[2,1,9-def]isoquinoline-1,3(2H)-dithione (APIS): ¹H NMR (400 MHz, CDCl₃) δ 0.91 (t, 3H), 1.42 (m, 6H), 1.78 (dt, 2H), 4.21 (t, 2H), 7.16 (t, 3H), 7.34 (t, 1H), 7.40 (t, 1H), 7.51 (d, 4H), 7.56 (m, 1H), 7.65 (d, 2H), 8.47 (m, 1H), 8.54 (d, 1H), 8.63 (dd, 2H). ¹³C NMR (101 MHz, CDCl₃) δ 14.10, 22.61, 26.89, 28.12, 31.62, 42.4, 120.36, 121.25, 123.40, 124.03, 126.89, 127.13, 128.67, 129.21, 132.43, 135.44, 136.01, 137.89, 139.66, 170.30. MALDI-TOF: calculated for C₄₀H₂₉NS₄: 651.11 [M]⁺, Found: 650.40 [M-H]⁺

Synthetic Route



Scheme A5.4. The synthetic method employed to prepare **RPNI-S**.

5.2.7. Computational studies

In this study, the optimization and frequencies of triplet excited states, excitation energies, and transition properties of these Peryleneimide materials **RPNI-O** and **RPNI-S** derivatives were carried out. These calculations were performed using the time-dependent B3LYP/6-31G(d,p) method within the Tamm-Dancoff approximation (TDA). The computational software used for these calculations was the Gaussian 16 package, with the ORCA 5.0 module

utilized at the B3LYP DEF2-SVP level. Furthermore, the spin-orbit coupling (SOC) constants for **PPI**, **THPI**, **API**, **PPIS**, **THPIS** and **APIS** were also computed at the same level mentioned above, employing the ORCA 5.0 software (ref.3, 4 in AI).

5.2.8. ¹O₂ generation quantum yield Estimation: In this study, dilute solutions of Rose Bengal were used as a reference ($\Phi_{\Delta} = 0.76$ in ethanol). To eliminate the inner-filter effect, the absorbance maxima of Rose Bengal and Photosensitizer were maintained at 0.2. Additionally, various solutions of **RPNI-O** and **RPNI-S** derivatives were prepared at a concentration of 100 μM . Then 100 μM ABDA was added to these solutions. The absorbance of ABDA at 378 nm was measured at various irradiation times using white light (400-700 nm, 50 mW cm^{-2}). This measurement allowed the determination of the decay rate of the photosensitizing process. The ¹O₂ generation quantum yield (Φ_{Δ}) of **RPNI-O** and **RPNI-S** derivatives in 99% PBS in DMSO was then calculated using the following equations:

$$\Phi_{\text{AIEgen}} = \Phi_{\text{RB}} (K_{\text{AIEgen}} A_{\text{RB}} / K_{\text{RB}} A_{\text{AIEgen}}) \dots \dots \dots \text{(A5.2)}$$

Where, Φ_{AIE} is the ¹O₂ generation quantum yield of AIEgen in 99% PBS in DMSO. A_{RB} and A_{AIEgen} represent the light absorbed by Rose Bengal and AIEgen, respectively, at an absorbance of 0.2. The absorption bands were integrated in the wavelength range of 400-700 nm to determine these values. K_{RB} and K_{AIEgen} are the decomposition rate constants of ABDA by Rose Bengal and AIEgen, respectively. These constants were determined by plotting $\text{Ln}(A_0/A)$ against time, where A_0 and A are the absorbance of ABDA at 378 nm by photosensitizers under white light irradiation at different time points (ref.5, 6 in AI).

5.2.9. Reactive oxygen species (ROS) Generation/Mesurament

Free Radical ($\text{O}_2^{\cdot-}$ and HO^{\cdot}) Test: Electron Paramagnetic Resonance (EPR) analysis was conducted to monitor the generation of type-I Reactive Oxygen Species (ROS). 2,2,6,6-Tetramethylpiperidine (TEMP) was used as a spin-trap agent to detect the free radicals $\text{O}_2^{\cdot-}$ and HO^{\cdot} . 100 μM TEMP and 100 μM of various solution of **RPNI-O** and **RPNI-S** derivatives were prepared in 99% PBS in DMSO. The solution was irradiated with white light at a power density of 50 mW cm^{-2} for 10 minutes. EPR spectra of the spin-trapped radicals were recorded in the range of 3000-3600 G after irradiation. Background interference was corrected using a sample before irradiation (ref.7 in AI). Singlet Oxygen (¹O₂) Test: This test was aimed at measuring the generation of singlet oxygen (¹O₂). A mixed solution containing 100 μM ABDA (a singlet oxygen sensor) and 100 μM of various solution of **RPNI-O** and **RPNI-S** derivatives compounds was prepared in 99% PBS in DMSO. The solution was irradiated with white light at a power density of 50 mW cm^{-2} for different durations: 0, 2, 4, 6, 8, 10, and 20 minutes. The degradation of ABDA's absorbance at 378 nm was measured

promptly after each time interval. **Total ROS Test:** The total ROS test aimed to measure the overall reactive oxygen species (ROS) levels. DCFDA, a chemically reduced form of fluorescein, was used as a fluorescent indicator for ROS. A solution of 10 μM DCFDA and 100 μM of various solutions of **RPNI-O** and **RPNI-S** derivatives compounds was prepared in 99% PBS in DMSO. The solution was irradiated with white light at a power density of 50 mW cm^{-2} for different durations: 0, 5, 10, 15, 20, 25, and 30 minutes. The fluorescence spectra of the mixed solution were rapidly measured. **Superoxide Anion Radical ($\text{O}_2^{\cdot-}$) Test:** The feasibility of the reaction producing $\text{O}_2^{\cdot-}$ was checked through theoretical calculations using the ORCA 5.0 software. **Hydroxyl Radical (HO^{\cdot}) Test:** This test aimed to measure the generation of hydroxyl radicals (HO^{\cdot}). A mixed solution containing 100 μM TA and 100 μM of various solutions of **RPNI-O** and **RPNI-S** derivatives compounds was prepared in 99% PBS in DMSO. The subsequent testing process was the same as the determination of total ROS using DCFDA as the probe. Upon trapping with HO^{\cdot} , TA was converted to hydroxyl terephthalic acid, resulting in an enhanced fluorescent intensity ($\lambda_{\text{ex}} = 315 \text{ nm}$).

5.2.10. The Point of Zero Zeta Potential Evaluation

According to the literature (ref. 8 in AI), the points of zero zeta potential (PZZP) for **RPNI-O** and **RPNI-S** derivatives, were calculated. The aqueous solutions of these Perylenimide materials were initially at a neutral pH of about 7. However, by introducing a dilute solution of sodium hydroxide or dilute hydrochloric acid, the pH of the solutions could be adjusted to either alkaline or acidic conditions. When the pH values of the **RPNI-O** and **RPNI-S** materials were altered within the range of 9, 7.4, 5.6, to 3 and 1, a noticeable change in the zeta potential was observed. Specifically, as the pH values changed from alkaline to acidic, the zeta potential underwent a transition from negative to positive.

5.2.11. The Energy of the Valence Band and Conduction Band Calculations

The valence band energy (E_V) was determined by calculating the energy of the band (E_V) from X-ray photoelectron spectroscopy (XPS) data. To calculate the conduction band energy (E_C), the energy gap was first estimated from the onset absorption data from UV-visible spectroscopy. Subsequently, E_C was calculated with respect to the normal hydrogen electrode (NHE) using Equations A5.3 and A5.4, as shown below:

$$E_V = -E_{\text{HOMO}} - 4.5 \quad (\text{A5.3})$$

$$E_C = -E_{\text{LUMO}} - 4.5 \quad (\text{A5.4})$$

The calculated E_V and E_C values for the **RPNI-O** and **RPNI-S** derivatives were recorded in Table A5.17. Additionally, E_C and E_V at a point of zero zeta potential (PZZP) with a pH of 5.6 were computed based on literature data, using Equations A5.5 and A5.6, respectively:

$$E_{C,pH} = E_C + 0.059 \times (\text{PZZP} - \text{pH}) \quad (\text{A5.5})$$

$$E_{V,pH} = E_V + 0.059 \times (\text{PZZP} - \text{pH}) \quad (\text{A5.6})$$

Where, PZZP represents the points of zero zeta potential for the **RPNI-O** and **RPNI-S** materials at pH 5.6. The estimated E_C and E_V values at a pH of 5.6 for **PPI**, **THPI**, **API**, **PPIS**, **THPIS** and **APIS** were also included in Table A5.17.

5.2.12. Cell studies

5.2.12.1. Cell culture: HeLa cells, derived from human cervix adenocarcinoma, were procured from the Cell Line Bank Sigma Aldrich in India. These cells were cultured in Dulbecco's Modified Eagle Medium (DMEM), which was supplemented with 10% fetal bovine serum and 100 U/ml each of penicillin and streptomycin. The cell cultures were maintained in a controlled environment with 5% CO₂ at a constant temperature of 37 °C.

5.2.12.2. Dark & Light Cytotoxicity Evaluated by MTT assay: In the cell viability assay conducted on cancer cells (HeLa and MCF7 cell lines), the 3-(4,5-dimethylthiazol-2-yl)-2,5-diphenyltetrazolium bromide (MTT) method was employed. Initially, 5000 cells were seeded into individual wells of a 96-well plate and allowed to incubate in DMEM media inside a 5% CO₂ humidified incubator at 37 °C for 24 hours. Subsequently, the cells were treated with different concentrations of **RPNI-O** and **RPNI-S** compounds for a duration of 4 hours. After the 4-hour treatment, specific cell samples were exposed to white light using a handheld torch 50 mW cm⁻², for 30 minutes. Following the irradiation step, the cells were further incubated with other treatment groups for an additional 24 hours at 37 °C in the same 5% CO₂ humidified incubator. Upon completion of the incubation period, the MTT assay was performed. The MTT assay measures cell viability based on the reduction of MTT by mitochondrial enzymes in viable cells, producing a formazan product. This formazan product is detected spectrophotometrically at 570 nm, with a reference filter set at 655 nm. The resulting absorbance of the formazan product is directly proportional to the number of viable cells present in the samples.

5.2.12.3. Cellular Uptake: After an overnight incubation period, HeLa cells were seeded into 96-well plates with a cell density of 1×10^4 cells per well. Twenty-four hours later, the HeLa cells were treated with varying concentrations of **RPNI-S** derivatives such as **PPIS**, **THPIS** and **APIS**, respectively, at 20 μM, while HEK 293T cells were treated with 100 μM

of the same compounds. Additionally, HeLa cells were exposed to **RPNI-O** derivative at a concentration of 20 μM and 100 μM , and HEK 293T cells were treated with 100 μM of the corresponding compound. These treatments were carried out for different time intervals under normal oxygen conditions ranging from 0, 1, 2, 3, 4, 5 to 6 hours. Subsequently, the cells were washed three times with DPBS to remove any excess **RPNI-O** and **RPNI-S** compounds. The optical density (OD) values of each well were then measured using a multifunction microplate reader (BioTek, Synergy H1). (BioTek, Synergy H1, $\lambda_{\text{abs.max}} = 500$ nm for **PPI**, **THPI** and **API**, whereas, $\lambda_{\text{abs.max}} = 590$ nm for **PPIS**, $\lambda_{\text{abs.max}} = 580$ nm for **THPIS** and 636 nm for **APIS**).

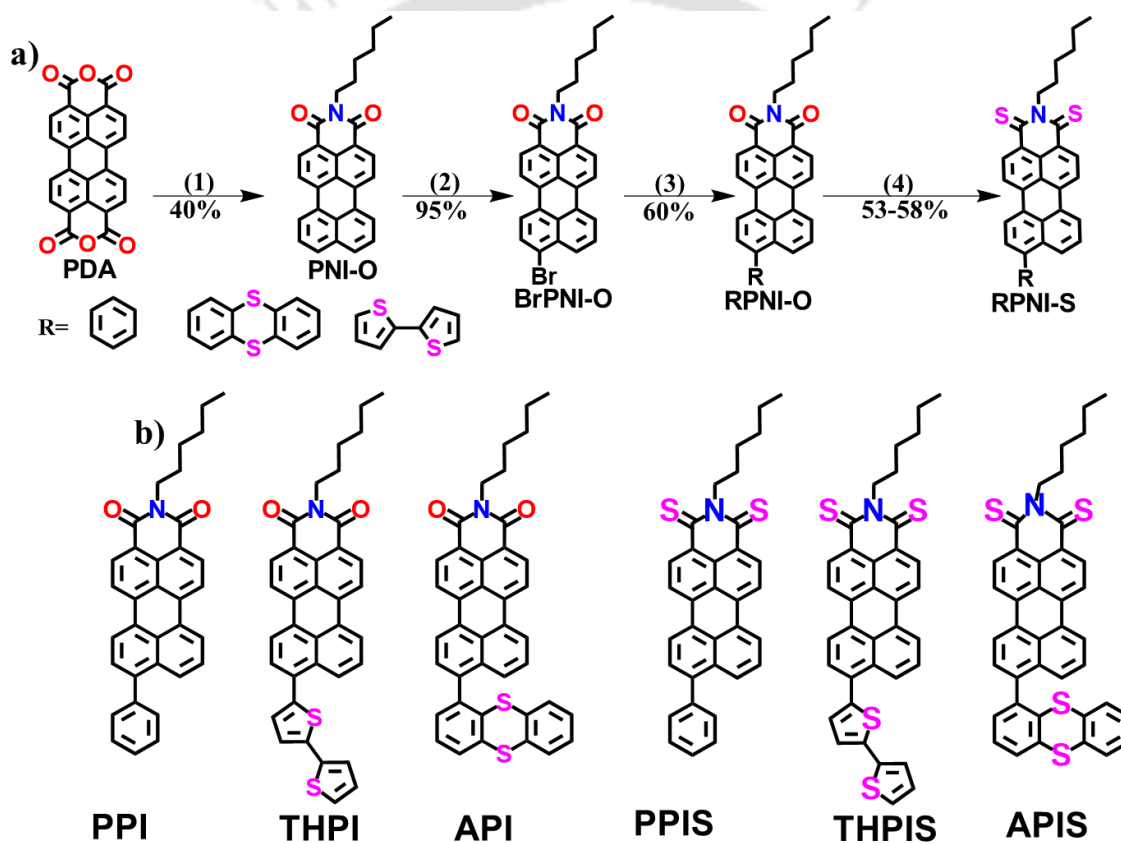
5.2.12.4. Live/dead cell co-staining assay: In the study, HeLa cells were initially seeded in 35-mm glass-bottomed dishes at a density of 3×10^5 cells per dish and cultured overnight in standard culture media. Subsequently, the cells were treated with **RPNI-S** derivatives, such as **PPIS**, **THPIS**, and **APIS**, at a concentration of 50 μM for a duration of 4 hours. After the 4-hour treatment, the cells were subjected to white light irradiation using a handheld torch with a specific wavelength (50 mW cm^{-2}) for 30 min. Following this, the cells were co-stained with 2 μM Calcein AM and 4 μM propidium iodide (PI) for 1 h. After washing with DPBS (Dulbecco's Phosphate-Buffered Saline), fluorescence images of the cells were acquired using a fluorescence microscope. Additionally, another set of HeLa cells was treated with the same **RPNI-S** derivatives at a concentration of 50 μM for 4 hours. These cells were then treated with 2',7'-dichlorodihydrofluorescein diacetate (DCFDA) at 10 μM for 1 h. After washing with DPBS, the cells were irradiated with the same handheld torch (50 mW cm^{-2}) for 30 minutes, and their fluorescence images were acquired. Moreover, HeLa cells were cultured in a normoxic environment (21% O_2) for 24 hours.

5.3. Result and Discussions

5.3.1. Design, synthesis and characterization of **RPNI-O** and **RPNI-S** derivatives

The primary objective of this research was to explore the condensed state photophysical behavior as well as the photosensitizing capabilities of newly designed heavy-atom free **RPNI-O** and **RPNI-S**. To achieve this, **RPNI-O** (**PPI**, **THPI**, and **API**) and **RPNI-S** (**PPIS**, **THPIS**, and **APIS**) has been strategically developed by introducing S-atom positional engineering at the pendant functional group and carbonyl position in **PNI-O** core (Scheme 5.1 and A5.1-A5.4). For the synthesis, very cheap perylene-3,4,9,10-tetracarboxylic acid anhydride (PDA) was selected as a versatile precursor material, which underwent a condensation reaction with hexylamine in good yields (Scheme A5.1). Subsequently, **BrPNI-**

O has been synthesized via bromination of the **PNI-O** core (yield-95%) (Scheme A5.2), which underwent Suzuki coupling with various boronic acid derivatives, including phenyl, bithiophene, and thianthrenyl, leading to the successful synthesis of **RPNI-O** derivatives (Scheme A5.3). Additionally, thioperlylenimide (**RPNI-S**) was prepared using a one-pot synthesis approach (Scheme A5.4) involving the reaction between the parent **RPNI-O** and a commercial Lawesson's reagent, resulting in the formation of **RPNI-S** compounds. The detailed synthetic procedure and reaction scheme can be found in the corresponding Scheme 5.1 and A5.1-A5.4 in the appendix (AI). The synthesized materials were extensively characterized using multinuclear NMR spectroscopy (^1H , ^{13}C) and Matrix-Assisted Laser Desorption/Ionization (MALDI) techniques. Further details of the comprehensive characterization data can be found in the supporting figures in AI file.



Scheme 5.1. (a) Synthetic route for the preparation of **RPNI-O** (**PPI**, **THPI**, and **API**) and thioperlylenimides (**RPNI-S**), viz. **PPIS**, **THPIS**, and **APIS**, lack an S-atom, and instead, the S-atom is positioned within the pendant rotor groups at the peri-position of the **PNI-O** core. (b) Chemical structure of the synthesized **RPNI-O** and **RPNI-S**. [(1): Hexyl amine, H_2O , 20 h, (2): Chlorobenzene, Br_2 , 4.5 h, (3): $\text{Pd}(0)$, THF, H_2O , (4): Lawesson's reagent, toluene, 20 h, and Below arrow represent the yield of the corresponding product].

5.3.2. Photophysical Properties

UV-vis absorption and fluorescence spectroscopy were employed to investigate the optical properties of **RPNI-O** and **RPNI-S** (Figure 5.1, A5.1-A5.3 and Table 5.1). The introduction

of S-atoms at the carbonyl position in **RPNI-O** resulted in a notable bathochromic shift in the absorption bands. This S-substitution caused a remarkable 130 nm redshift in the absorption maximum ($\lambda_{\text{abs.max}}$) (from 506 to 636 nm) and a corresponding 125 nm red-shifted emission maxima ($\lambda_{\text{em.max}}$) in their solution state (Figure 5.1a, b). This substantial shift could be attributed to the highly stabilized lowest unoccupied molecular orbital (LUMO) and destabilized highest occupied molecular orbital (HOMO) in **RPNI-S**.¹⁸⁻²⁰ The reduced energy gap between the HOMO and LUMO levels in **RPNI-S** inevitably resulted in red-shifted spectra, and discussed elaborately in later sections. In contrast, the alteration of S-atom position at the pendant functional group (-R) in **RPNI-O** led to blue-shifted absorption maxima in **API** when compared to other **RPNI-O** derivatives, namely **PPI** and **THPI**. This observed blue shift can be attributed to the reduced electronic communication in **API** in its solution state. Crucially, the international commission on illumination (CIE) chromaticity diagram vividly displayed a wide spectrum of emission colors in the solution state, ranging from yellow (580 nm) to near-infra red (NIR) at 705 nm (Figure 5.1b', Table 5.1 and Table A5.3). In this context, **RPNI-O** derivatives, such as **PPI**, showed yellow emission, while both **THPI** and **API** displayed bright red emissive color. In contrast, **RPNI-S** derivatives exhibited emission colors that remained entirely undetectable under 365 nm UV-light illumination, even though $\lambda_{\text{em.max}}$ peaks were observed at 655 nm for **PPIS**, 647 nm for **THPIS**, and 705 nm for **APIS**, respectively (Figure 5.1b', Table 5.1 and Table A5.3). Interestingly, **API** exhibited notable condensed state emissive properties in both its aggregated-state and solid state, owing to the presence of two S-atoms in one fused aromatic anthracene ring (rotor). In contrast, **PPI** and **THPI**, lacking an S-atom at the pendant R rotor, and having two S-atoms located in two different pendant aromatic rings (rotor), showed suppressed emission in their aggregated-state. This finding is in contrast to what is expected based on the RIM mechanism, which typically leads to the generation of condensed state emitters. To shed more light on this discrepancy and provide a comprehensive understanding, a detailed explanation of this mechanism is provided through single crystal X-ray diffraction (SCXRD) analysis. Furthermore, **API** exhibits remarkably high Φ_{PL} of 0.85 in its aggregated-state, likely attributed to the unique intermolecular packing arrangement influenced by self-assembly behavior in its condensed state. Additionally, **API** showed Φ_{PL} of 0.89 in its highest $\lambda_{\text{em.max}}$. In contrast, other **RPNI-O** derivatives, namely **PPI** and **THPI**, display significantly much lower Φ_{PL} of 0.10 and 0.04 respectively, in their aggregated-state. Conversely, the **RPNI-S** compounds exhibited nearly non-fluorescent behavior ($\Phi_{\text{PL}} \approx 0.00$) (Table 5.1, Figure A5.2, A5.3, and Equation A5.1). The suppression of fluorescence indicated that thionation enhanced the ISC process, causing a more efficient transition from the singlet excited state to the triplet excited state.^{16,18-20} The CIE chromaticity diagram highlights the distinct emissive colors of **RPNI-O** in their aggregated-state. Specifically, **PPI** and **THPI**

exhibited quenched emission despite having distinct $\lambda_{em,max}$ peaks, whereas **API** displayed deep red emission. In contrast, **PPIS**, **THPIS**, and **APIS** showed both an undetectable $\lambda_{em,max}$ peak and non-emissive features under 365 nm UV irradiation (Figure 5.1c' Table 5.1 and Table A5.3). In the solid state, **API** showed a slightly blue-shifted $\lambda_{em,max}$ compared to other **RPNI-O** derivatives, with a similar trend observed overall (Figure 5.1d, d'). However, when comparing the aggregated-states, **API** exhibited a significant 50 nm blue shift in its $\lambda_{em,max}$ compared to **PPI** and **THPI** (Figure 5.1c). The validity of this observation was reinforced and elaborated upon using excitation emission matrix (EEM) spectra. Moreover, **API** displayed a noteworthy 31 nm red shift in its $\lambda_{em,max}$ (646 nm) when in the solid state, compared to the aggregated-state (614 nm) (Figure 5.1e). This difference can be attributed to the unique intermolecular packing arrangement influenced by the steric constraints of the pendant S-substituted anthranyl rotor group in **RPNI-O**. In contrast, the other derivatives exhibited minimal shifts between their aggregated-state and solid state $\lambda_{em,max}$. Further, distinct variations in the powder colors were observed under white light and 365 nm UV irradiation, and this difference correlated well with the CIE chromaticity diagram. **API** emitted a strong and bright red emission, while **PPI** and **THPI** showed faint emission. Interestingly, **RPNI-S** showed complete quenching of emission in its solid state under 365 nm UV light illumination (Figure 5.1f, g, d' and Table A5.3).

The obtained results provide strong evidence that the presence and positional manipulation of the S-atom within the pendant functional unit played a crucial role in controlling its unique AIE properties.²⁶⁻³⁰ Conversely, substituting the S-atom at the carbonyl position leads to distinct characteristics in the condensed state luminescence. To gain insights into the individual effects of the S-atom at the pendant functional unit and the carbonyl position, as well as the impact of altering the S-atom position within the functional unit, a comparative study of the EEM was carried out. Furthermore, all the **RPNI-O** compounds exhibited remarkably large Stokes shifts, ranging from 146 to 170 nm (Table 5.1). This is noteworthy as it represents a rarest instance of such significant Stokes shifts reported in recent literature. These shifts are attributed to an excited-state intramolecular charge transfer (ICT) between the electron donor and acceptor within the dye molecule itself.³⁰ The substantial Stokes shifts make these materials highly suitable for bio-imaging applications, as they minimize interference between excitation and emission signals.^{31,32}

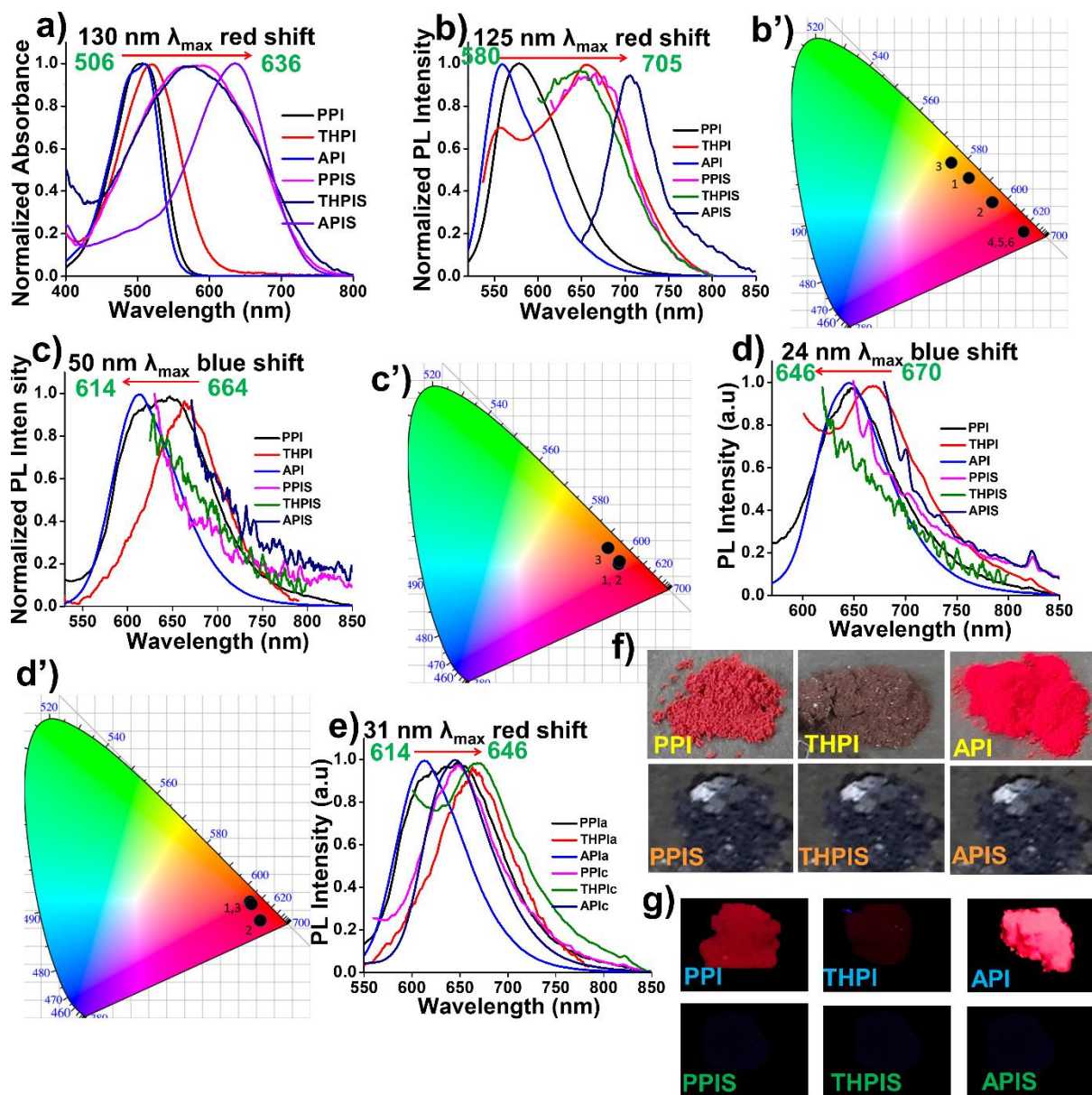


Figure 5.1. Photophysical characteristics of all the **RPNI-O** (**PPI**, **THPI** and **API**) and **RPNI-S** (**PPIS**, **THPIS** and **APIS**) derivatives. (a) Normalized absorbance spectra in their solution state (in DMSO, 100 μ M). (b) The normalized PL spectra in their solution ($\lambda_{\text{ex}} = 500$ nm). (b') The CIE diagram at their solution state. (c) Normalized PL spectra at 99% f_w in DMSO ($\lambda_{\text{ex}} = 500$ nm). (c') The CIE plot represents aggregated-state emission color. (d) Normalized solid state PL spectra ($\lambda_{\text{ex}} = 500$ nm). (d') CIE plot represents solid state emission color. (e) Comparison of aggregated-state and solid state fluorescence spectra of the **RPNI-O** and **RPNI-S** derivatives ($\lambda_{\text{ex}} = 500$ nm). Capturing of digital photographs (f) under day light and (g) under UV irradiation ($\lambda_{\text{ex}} = 365$ nm) of solid powder of **RPNI-O** derivatives (**PPI**, **THPI** and **API**) and **RPNI-S** (**PPIS**, **THPIS** and **APIS**), respectively. [a, s represents the aggregated, and solid state, respectively, Inset in CIE: 1, 2, 3, 4, 5, 6 = **PPI**, **THPI**, **API**, **PPIS**, **THPIS** and **APIS**, respectively. In Figure 5.1c' and 1d' CIE plot, the points 4,5, and 6 which represents the **PPIS**, **THPIS** and **APIS**, respectively, were absent due to its non-emissive characteristics].

5.3.3.ACQ to AIEE transformation

In this study, an investigation was conducted on how the fluorescence emission of the **RPNI-O** and **RPNI-S** derivatives is affected by aggregation. To achieve this, UV-vis and photoluminescence (PL) spectra were recorded at different f_w in DMSO (good solvent). (Figure 5.2, A5.1, A5.4, A5.5 and Table 5.1, A5.4-A5.6). The **RPNI-O** derivatives (**PPI**, **THPI**, and **API**) exhibited distinct absorption peaks, centered at 506 nm, 517 nm, and 510 nm, respectively. These peaks are characteristic of the π - π^* transition associated with the substituted **PNI-O** core. Additionally, the **API** derivative displayed an additional long-wavelength absorption peak at 510 nm, which is attributed to the ICT process from the AIE donor to the acceptor **PNI-O** core. The consistent trend of red-shifted UV and PL spectra in more polar solvents with the increase in the donor functional group across **RPNI-O** derivatives indicates a stronger ICT effect (Figure A5.4, and Table A5.5, A5.6).³³ However, this trend deviates in the case of **API**. The lesser red-shifted UV and PL spectra in **API**, compared to the other **RPNI-O** derivatives, can be attributed to a reduced influence of the donor-acceptor (D-A) interaction, leading to decreased electronic communication in **RPNI-O** core in its diluted state. This phenomenon validates the less stabilized LUMO and more stabilized HOMO in **API** compared to other **RPNI-O** derivatives. Consequently, this results in blue-shifted $\lambda_{\text{abs.max}}$ in **API**, setting it apart from the other derivatives. The distinct behavior in **API** highlights its unique electronic structure and offers insights into the effects of donor functionality on the electronic communication in **PNI-O** core under different solvent conditions. However, the increase in water content led to significant alterations in the absorption spectra of **RPNI-O** derivatives (**PPI** and **THPI**). At 99% f_w , both **PPI** and **THPI** exhibited substantial blue-shifts of 60 nm and 46 nm, respectively, indicating the presence of H-type aggregation and a strong π - π stacking planar core (Figure A5.5a, b and Table A5.4). Conversely, **API** showed a notable red-shift of 10 nm at 99% f_w , indicating the presence of J-type aggregation (Figure A5.5c and Table A5.4). In contrast to the **RPNI-O** derivatives, the **RPNI-S** derivatives exhibited red-shifted $\lambda_{\text{abs.max}}$, with wavelengths of 590 nm, 590 nm, and 636 nm for **PPIS**, **THPIS**, and **APIS**, respectively, at 0% f_w . However, with an increase in water content to 99%, these derivatives displayed remarkable blue-shifts in their $\lambda_{\text{abs.max}}$, leading to 89 nm, 76 nm and 23 nm blue-shifts, all attributed to the H-type aggregation phenomenon (Figure A5.5d-f, and Table A5.4). This marks the highest reported blue-shifted $\lambda_{\text{abs.max}}$ in the aggregated-state (Table A5.2). Literature has reported the significance of H-aggregation in effectively capturing and stabilizing triplet excited states.³⁴⁻
³⁶ This highlights the significant impact of the S-atom positional strategy at the functional unit and carbonyl position, as they drastically alter the absorption properties of the **RPNI-S** derivatives in comparison to **RPNI-O**. It is intriguing to note that even though **API** and

APIS share the same electronic structure, a simple modification involving the introduction of the S-atom at the carbonyl position led to a profound change in their aggregation behavior. This seemingly minor alteration had a significant impact on the properties of the compounds, illustrating the sensitivity of the aggregation behavior to specific structural changes.

In figure 5.2, at 0% f_w , **RPNI-O** (**PPI**, **THPI**, and **API**) exhibited distinct $\lambda_{em,max}$ peaks at 580 nm, 655 nm, and 559 nm, respectively (Figure 5.2a-c, A5.1). As the f_w increased, the emission intensity of **PPI** and **THPI** gradually decreased and eventually became completely quenched at 99% f_w , accompanied by a progressive red-shift in their $\lambda_{em,max}$, reaching 646 nm and 664 nm, respectively. This behavior is known as ACQ phenomenon. On the other hand, **API** displayed a different trend in emission behavior. Its $\lambda_{em,max}$, located at 559 nm, initially decreased from 0% to 20% f_w due to the presence of twisted intramolecular charge transfer (TICT) characteristics.³³ At 40% f_w , **API** reached its maximum emission intensity, and the $\lambda_{em,max}$ were red shifted, centered at 646 nm. This behavior signifies the typical AIEE features in **API**. However, as more water was added to the solvent mixture in **API**, the emission intensity decreased due to agglomeration, as illustrated in the supramolecular self-assembly section. Thus, the abnormal ACQ behavior of **PPI** and **THPI** has been observed in their aggregated-state, even though they possess pendant phenyl and bithiophene functional groups that allow dynamic rotation in solution. These experimental findings contradict the widely accepted mechanism of RIM for AIE systems. Instead, they emphasize the important role of the S-atom at the functional unit in **RPNI-O**, which seems to be energized by the intermolecular orientation and packing arrangement in the **RPNI-O** derivatives. This S-atom's introduction and positional manipulation influence is responsible for the observed ACQ behavior in **PPI** and **THPI**, offering a new perspective on the factors that govern emission properties in these compounds in their condensed state. In contrast, the **RPNI-S** derivatives exhibited non-emission characteristics in both their solution and aggregated-state (Figure 5.2d-f, A5.1). Notably, when in a diluted state, **RPNI-S** derivatives such as **PPIS**, **THPIS**, and **APIS** exhibited $\lambda_{em,max}$ peak at 655 nm, 647 nm, and NIR (705) nm, respectively. However, the emission colors were markedly distinct from those of **RPNI-O** derivatives, rendering them essentially undetectable. Furthermore, in the aggregated state, **RPNI-S** displayed an entirely undetectable $\lambda_{em,max}$. This lack of emission can be attributed to the increased SOC and a higher population of excited state triplets.^{16,18-20} Additionally, the S-atom manipulation influences the distinct emission properties in the condensed state, which can be further explained by the characterization of triplet states via theoretical calculation.

Thus, these findings strongly support the notion that the S-atom positional manipulation plays a prominent role in generating the AIE characteristics observed in materials with

extremely strong π - π stacking interaction. Additionally, the S-atom substitution and positional manipulation influences the distinct emission properties in the condensed state, which can be further modulated by the specific intermolecular packing arrangement and the characterization of triplet states. Thus, the presence of the S-atom and positional alteration is critical in shaping both AIE behavior and the unique emission properties in these materials, offering potential avenues for tailored optical properties through careful control of intermolecular interactions and triplet state characteristics.

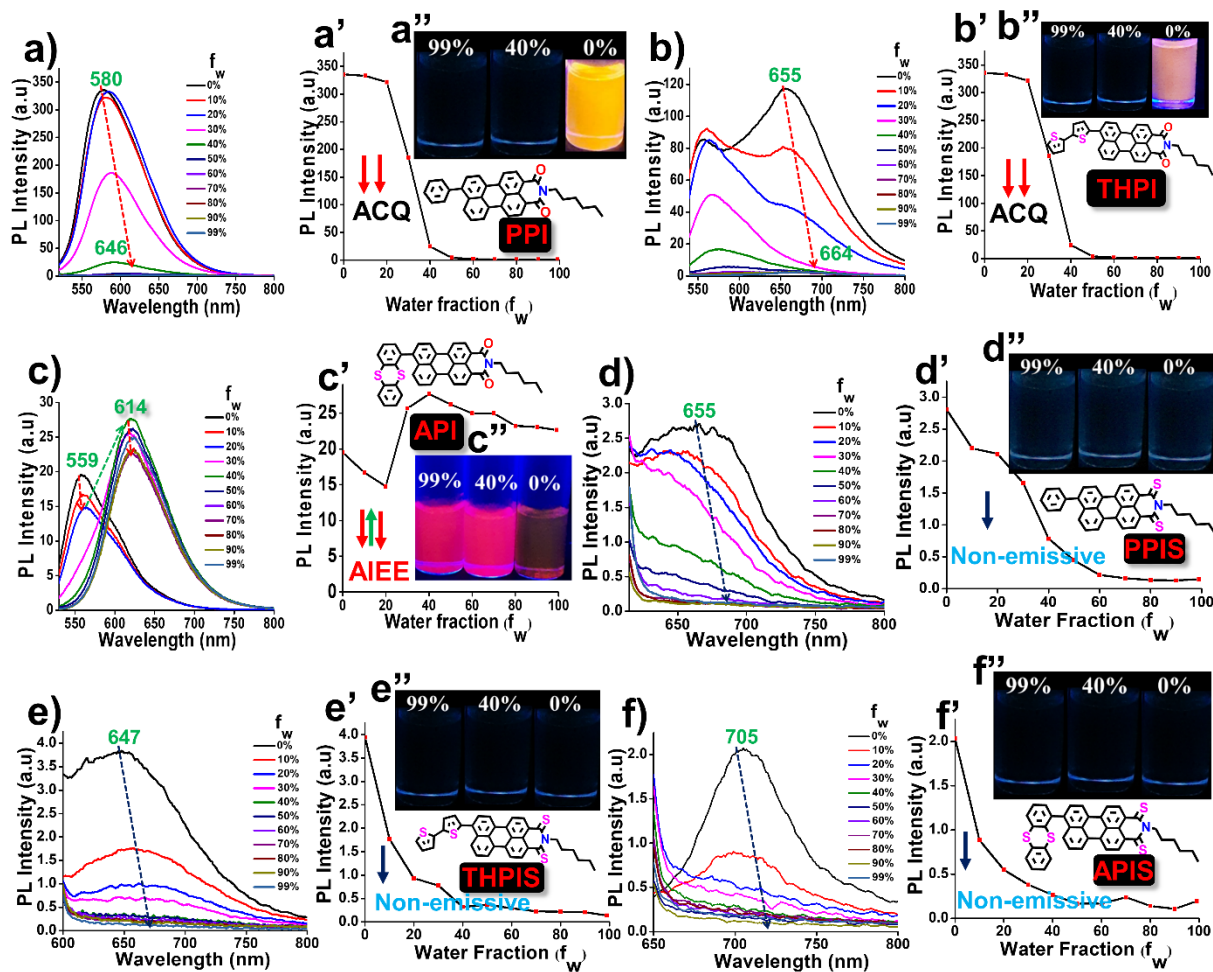


Figure 5.2. PL spectra of (a) PPI, (b) THPI, (c) API, (c) PPIS, (d) THPIS, and (e) APIS at various f_w in DMSO (100 μ M, $\lambda_{ex} = 500$ nm). (a'-f') plots of $\lambda_{em,max}$ along with Insets: (a''-f'') Digital photographs under 365 nm UV illumination of the corresponding luminogens at 0%, 40% and 99% f_w in DMSO and chemical structure of the respective RPNI-O and RPNI-S luminogens, Day light photograph of all the derivatives have been placed in Figure A5.6 of AI.

5.3.4. Excitation-emission matrix spectra

In order to enhance the photophysical characteristics of RPNI-O and RPNI-S derivatives in their condensed state, a comparative investigation of their EEM spectra was performed (Figure 5.3, A5.7). This analysis was conducted for solutions with varying concentrations,

allowing to gain deeper insights into their optical properties. EEM spectroscopy is widely recognized as a valuable method for characterizing the spectroscopic properties of systems containing multiple fluorophores.³⁷ Each EEM spectrum provides valuable spectral information about the chemical components within a mixture. To investigate the effect of concentration on aggregation, two-dimensional (2D) EEM spectra were collected for each compound at various concentrations, viz.: 100 μM (diluted), 300 μM , 500 μM , and 1 mM (concentrated). For **RPNI-O** derivatives, the excitation wavelength was systematically scanned from 400 to 600 nm in 10 nm increments and emission values ranging from 500 to 750 nm were recorded. On the other hand, for **RPNI-S**, a similar scanning process was conducted, but with the excitation wavelength range extending from 500 to 700 nm, and the emission values measured within the range of 600 to 850 nm. At lower concentrations (100 μM), **RPNI-O** derivatives (**PPI** and **API**) displayed distinct asymmetric peaks in their EEM spectra, while **THPI** exhibited partially separated peaks. As the concentration increased (300 μM and 500 μM), **PPI** and **THPI** showed broadening in their contour profiles along the Y-axis (representing λ_{ex}), indicating the presence of multiple fluorophoric components. The observed broadening in the EEM spectra at higher concentrations (300 μM and 500 μM) suggested the presence of multiple fluorophoric components within the **RPNI-O** derivatives. These components have the ability to absorb light across a wide range of wavelengths. Conversely, **API** exhibited two separate fluorophoric systems, responding differently to different λ_{ex} with one at higher λ_{ex} and the other at lower λ_{ex} . At higher concentrations, **PPI** and **THPI** displayed a fluorophoric system in red-shifted λ_{ex} , suggesting increased conjugation and enhanced electronic communication between the pendant functional units (phenyl or bithiophene) and the **PNI-O** core.^{37,38} In a concentrated solution (1 mM), **PPI** and **THPI** showed weak emission with a red-shift in λ_{ex} , while **API** exhibited a highly emissive system with a blue-shifted λ_{ex} and a non-fluorescent species at higher λ_{ex} . **API** exhibited a unique blue-shifted λ_{ex} fluorophoric system in its condensed state, different from other **RPNI-O** derivatives. This behavior is attributed to reduced molecular conjugation influenced by the twisted structure of the thianthranlyl group within the **PNI-O** core and this phenomenon was verified further by SCXRD analysis. **RPNI-S** derivatives display weak fluorescent emission at lower concentrations, which diminishes completely in a concentrated solution of 1 mM. In this study, it was found that **THPIS** exhibited non-emissive fluorophoric system with the blue-shifted λ_{ex} compared to **PPIS** and **APIS**. The emission properties are influenced by intermolecular packing interactions and are thought to be reinforced by particular steric constraints imposed by the S-atom substitution and positional manipulation at the pendant functional unit in **RPNI-O**. The introduction of the S-atom at the carbonyl position in **RPNI-O** appears to play a critical role in determining the

non-fluorescent behavior at higher concentrations, thereby differentiating the emission characteristics of **RPNI-S** from **RPNI-O** derivatives.

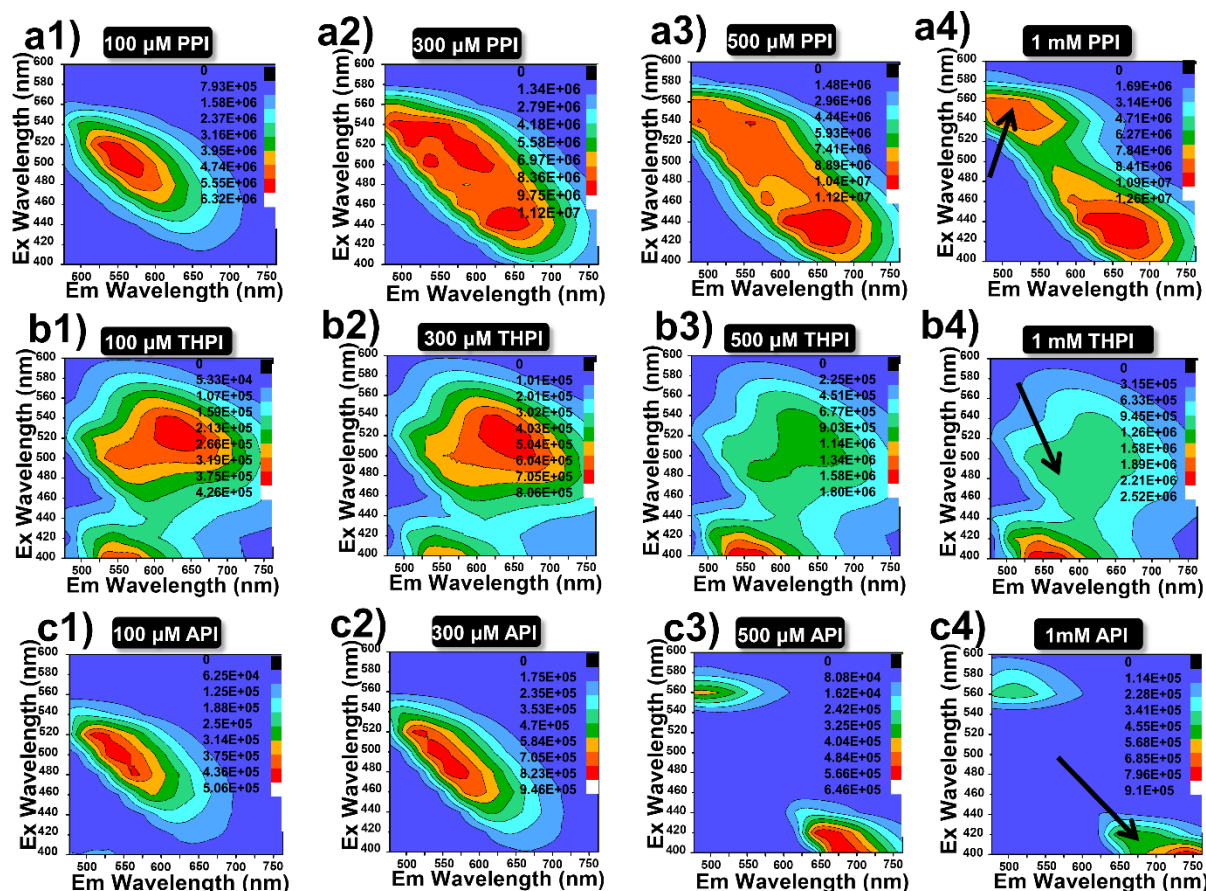


Figure 5.3. (a1-c4) 2D EEM contour projections of the **RPNI-O** luminogens at different concentrations (left: 100 μ M; middle: 300 μ M and 500 μ M; right: 1 mM) in DMSO.

5.3.5. Supramolecular self-assembly

The luminescent properties of **RPNI-O** and **RPNI-S** derivatives were investigated using Field Emission Scanning Electron Microscopy (FESEM) (Figure 5.4, A5.8). The FESEM images of the spontaneously formed self-assembled **RPNI-O** and **RPNI-S** derivatives were obtained using a simple, reliable, and cost effective drop-casting method, followed by air-drying at room temperature. The self-assembly behavior of these derivatives was investigated using strategic positional manipulation of the S-atom at the functional unit attached to the **RPNI-O** skeleton and at the carbonyl position. To gain deeper understanding of the fluorescence behavior resulting from aggregation, morphological analyses were carried out on the supramolecular assemblies formed at 99% f_w . The remarkable variation in morphological transformation emphasized the exceptional tunability of these **RPNI-O** and **RPNI-S** derivatives, allowing for a wide range of structural possibilities. **RPNI-O** derivatives like **PPI** and **THPI** formed spherical nanoparticles with

sizes of 105 nm and 100 nm, respectively, as confirmed by dynamic light scattering (DLS) measurements (Figure 5.4a, b and a', b'). **API** exhibited unique microrose self-assembly structures, leading to the highest Φ_{PL} generation of 0.85 confirming the discovery of the highest reported Φ_{PL} to date. It is worth noting that the existing literature reports the highest Φ_{PL} value of 0.99 and 0.92, respectively (measurement was conducted in the solution state using organic solvent such as toluene and dichloromethane as the solvent, respectively) unlike the present work performed in an aqueous environment (aggregated-state).^{19,20} The unique intermolecular packing arrangement in **API** was determined to be the primary factor contributing to these distinct characteristics (Figure 5.4c).³⁹ **RPNI-S** derivatives, including **PPIS** and **THPIS**, exhibited self-assembly in the form of microcrystalline rods, while **APIS** displayed a different pattern characterized by micro agglomeration (Figure 5.4d-f). The degree of order in supramolecular self-assembly was directly correlated with the intensity of their emission in the aggregated-state.⁴⁰⁻⁴² In previous literature, it was hypothesized that the decrease in fluorescence emission of AIEgenic materials at higher f_w was due to the formation of agglomerates resulting from stronger stacking interactions.⁴³ Furthermore, existing literature extensively supports the essential role of energy-dependent endocytosis in the uptake of micro-sized particles. Additionally, numerous studies have highlighted the significant influence of particle morphology on their selective uptake within the intracellular environment.^{44,45}

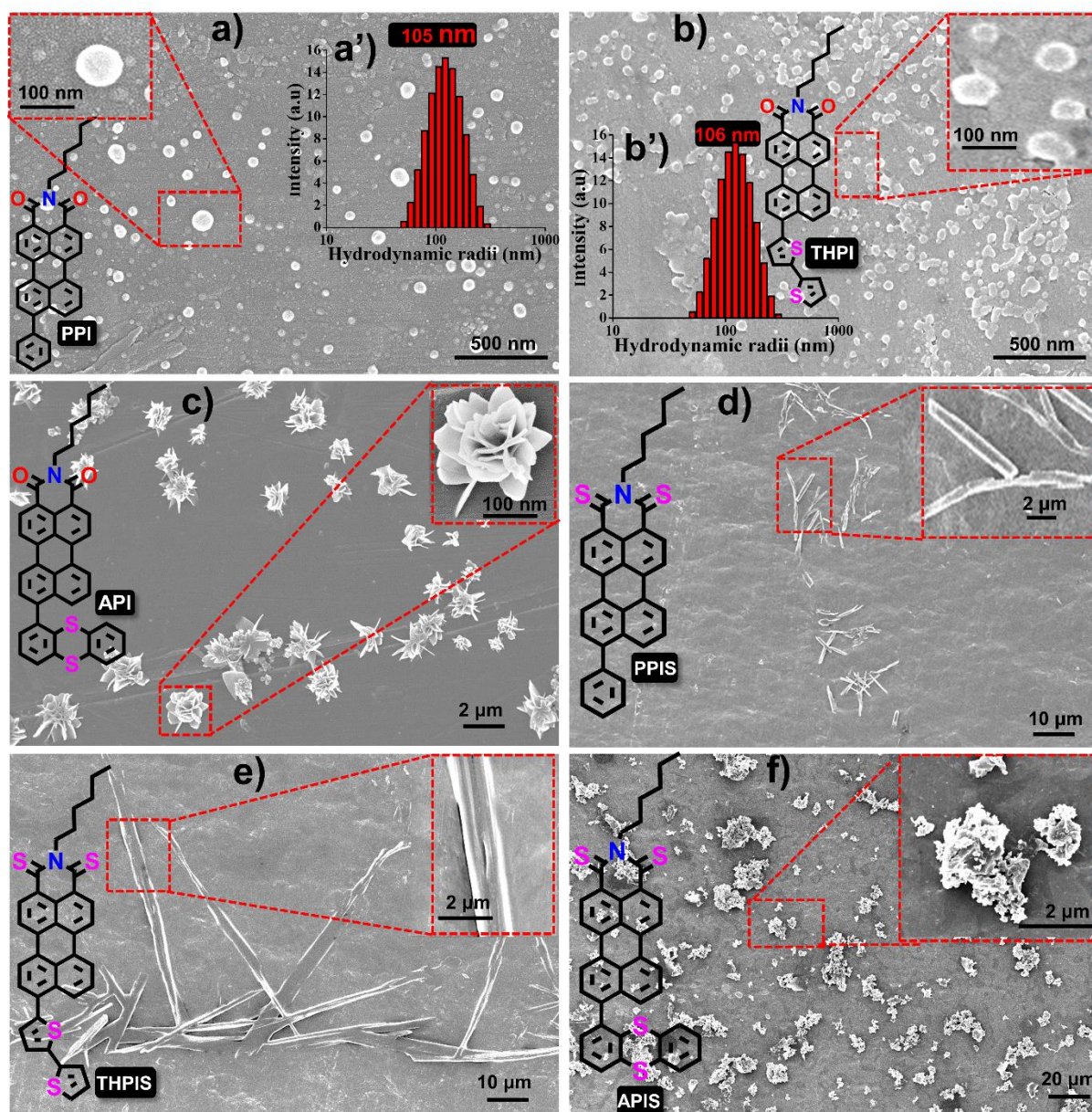


Figure 5.4. FESEM images of the micro and nano-assembly of the **RPNI-O** and **RPNI-S** derivatives spontaneously formed at 99.9% f_w in DMSO (100 μM). Insets: The chemical structure of the **RPNI-O** and **RPNI-S** (left) and the magnified image at the selected area (right) and left for **PPI**, and (a' and b') Hydrodynamic radius vs intensity plot of **PPI** and **THPI** at 99.9% f_w in DMSO (100 μM).

5.3.6. SCXRD analysis

To acquire further understanding of the tuning and triggering characteristics of **RPNI-O** derivatives in condensed state, the effects of positional S-substitution within the functional unit were investigated. This exploration involved a comprehensive analysis of intermolecular interactions and packing arrangements through the examination of single crystal (Figure 5.5, A5.9 and Table A5.7). **PPI**, **THPI**, and **API** were successfully crystallized from DMF, providing valuable single crystals for analysis. However, attempts to obtain single crystals of

other **RPNI-S** derivatives have so far been unsuccessful. The S-substituted **API**, containing two S atoms within the one fused aromatic ring, exhibits a notably increased π - π stacking distance of 4.169 Å and a larger dihedral angle of 75.01° compared to other **RPNI-O** derivatives. This phenomenon is attributed to the pendant thianthranlyl unit's highly twisted structure within the otherwise planar **PNI-O** core. Consequently, this structural twist effectively mitigates the adverse effects of π - π stacking interactions in the condensed state. In contrast, the remaining **RPNI-O** derivatives exhibited robust π - π interactions, likely attributed to their lower dihedral angles between the functional groups and the planar perylene core.³⁰ Previous research has extensively documented that electron-donating substituents weaken these detrimental π - π interactions by increasing the π -electron density of the aromatic core.^{46,47} In contrast, **THPI**, which includes a bithiophene electron-donor functional group with two S-atoms present in two distinct aromatic rings, exhibited a contrary trend. Surprisingly, despite the electron-donor nature of the functional group, **THPI** demonstrated stronger π - π interactions. Moreover, the angle (θ) between the transition dipoles and the interconnected axis was found to be 75.01° for **PPI** and 55.12° for **THPI**. These values exceed the critical threshold of 54.7°, indicating the presence of H-aggregates and lending further support to the observed blue-shifted $\lambda_{\text{abs.max}}$. Conversely, for **API**, the θ value of 42.08° aligns with the findings of a red-shifted $\lambda_{\text{abs.max}}$ (Figure A5.9).³⁵

This confirms that the strategic manipulation of S-atoms position at the functional unit plays a crucial role in generating distinct intermolecular packing orientations. The study revealed that the intermolecular π - π interactions in the perylenimide systems are predominantly governed by steric constraints rather than the electronic influence of functional groups. Consequently, the formation of unique and well-defined supramolecular assemblies is driven by finely tailored intermolecular packing orientations of the **PNI-O** cores, leading to the modulation of their condensed state emission properties.^{48,49}

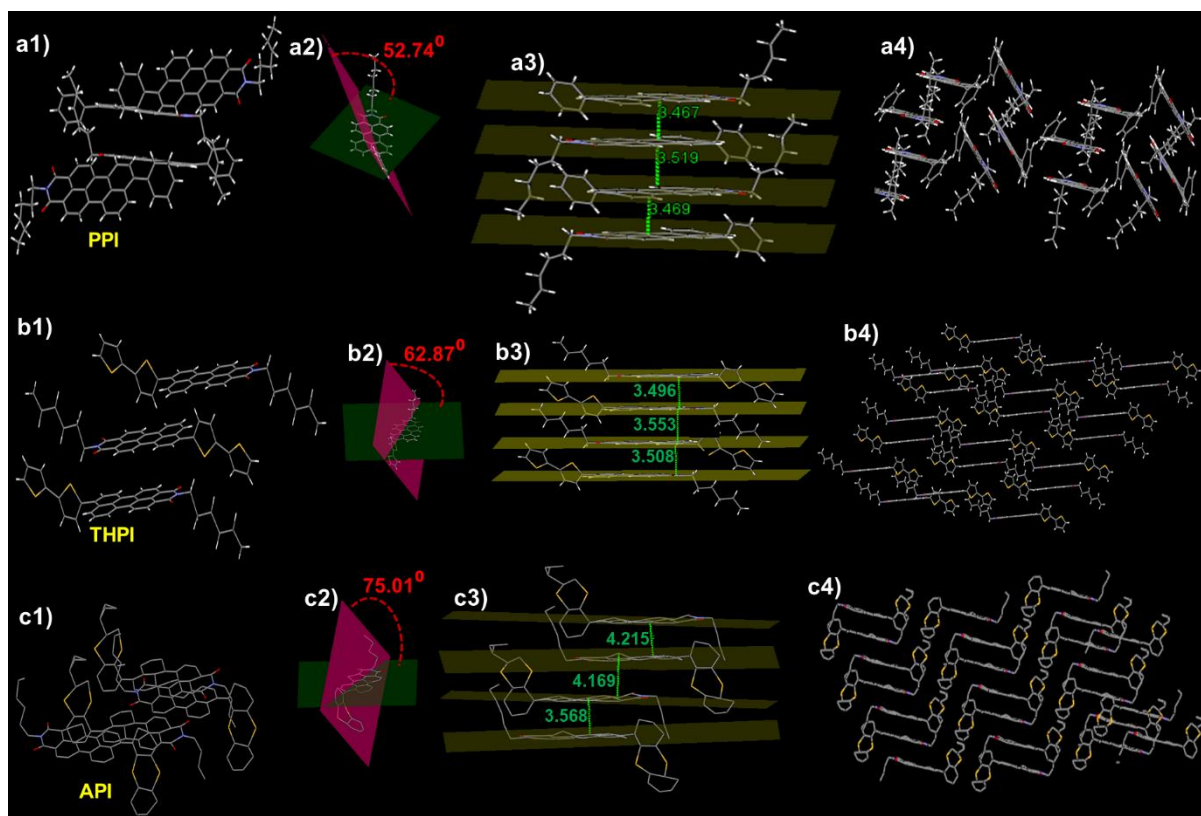


Figure 5.5. Single crystal structure of (a1) **PPI**, (b1) **THPI** and (c1) **API** confirmed via SCXRD. (a1-c1) Insight of molecular packing arrangement. (a2-c2) Dihedral angle between two plane of rotor and acceptor plane. Green plane: perylene core plane, pink plane: the plane of rotor (phenyl, bithiophene and thianthranlyl in crystals of **PPI**, **THPI** and **API** with (a3-c3) intermolecular plane distances and (a4-c4) different molecular packing organization exhibiting J- and H-aggregation pattern, respectively.

5.3.7. Electronic properties driving the photophysical behavior

To validate the hypothesis concerning the distinct electronic properties of **RPNI-O** and **RPNI-S** derivatives and their impact on photophysical behavior, a computational analysis using density functional theory (DFT) using the B3LYP/6-31G (d, p) method was conducted (Figure 5.6a) in gaseous state. This analysis aimed to gain deeper insights into the electronic structure and characteristics of these derivatives. The investigation demonstrated that **RPNI-S** derivatives exhibited a significant stabilization of the LUMO and, simultaneously, a destabilization of the HOMO compared to **RPNI-O**. Consequently, the decrease in the energy gap between the HOMO and LUMO from 2.70 to 2.09 eV provides support for the observed more pronounced red-shifted UV-vis absorption spectra.^{16,18-20} The presence of its electron-donor bithiophene group primarily contributed to **THPI-S** exhibiting the smallest energy gap among the derivatives. On the other hand, **API** exhibited higher band energy compared to other **RPNI-O** derivatives, attributed to its more stabilized HOMO and less

stabilized LUMO. This confirmation accounts for the blue-shifted absorption spectra observed in **API** when compared to **PPI** and **THPI** in diluted state. The blue-shift indicates reduced electronic communication, which is a result of **API**'s more twisted thianthranly moiety acting as a weaker donor.³⁰ These results further confirmed the significance of the S-atom positional engineering in influencing the electronic properties of the derivatives and demonstrated the importance of their distinct electronic characteristics in governing their photophysical behavior.

5.3.8. Theoretical Calculation

The conversion of **RPNI-O** to **RPNI-S** led to remarkable fluorescence quenching, motivating further theoretical calculations on the optimized structures of **RPNI-O** and **RPNI-S** to understand the triplet state formation mechanism (Figure 5.6b, c, and Table 5.1, A5.8-A5.14). The spin-orbit coupling matrix elements (SOCMEs) were calculated using ORCA 5.0 at the B3LYP/DEF2-SVP level, ensuring a reasonable TD-DFT error. Replacing oxygen with sulfur resulted in significantly increased SOC constants and decreased singlet-triplet energy gap (ΔE_{ST}) for **RPNI-S**. The SOC from the S_2 state to the T_4 state was identified as the dominant contributor to the formation of the excited triplet population. Notably, SOC increased as the electron-donating ability of the -R groups increased. The ΔE_{ST} between the S_2 and the nearest T_4 states reduced gradually from **APIS** (0.098 eV) to **PPIS** (0.096 eV), and further to **THPIS** (0.094 eV), facilitating the efficient ISC process with SOC values of 10.88 cm^{-1} , 9.20 cm^{-1} , and 5.73 cm^{-1} for **PPIS**, **THPIS**, and **APIS**, respectively. Large SOC values were also observed between the lowest state transition of S_1 to T_1 for **RPNI-S** derivatives, with values of 8.33 cm^{-1} for **PPIS**, 6.90 cm^{-1} for **THPIS**, and 4.44 cm^{-1} for **APIS** with the lowest ΔE_{ST} values of 0.4 eV. Additionally, large SOC values were also found for **PPIS** between the transition of S_7 to T_7 (9.16 cm^{-1}) and **THPIS** of S_7 to T_7 (6.19 cm^{-1}) with ΔE_{ST} values of 0.23 eV and 0.25 eV, respectively.^{36,50,51} It has been documented that H-aggregates efficiently trap and stabilize the excited state triplet through strong π - π coupling.³⁴⁻³⁶ Extensive research has been focused on enhancing triplet exciton through methods like photoinduced electron transfer or photoinduced intramolecular charge transfer.^{52,53} However, the enhancement of SOC through prominent H-aggregation represents a unique and innovative approach within this domain. Extensive research has consistently affirmed that H-aggregation significantly extends the excited electron's lifetime by suppressing the fluorescence, likely attributed to singlet wavefunction delocalization, which subsequently energized by the strong π - π coupling. This extension affords sufficient time for the electrons to effectively engage in substantial SOC, which crucially enabled the efficient ISC process.³⁴⁻³⁶ Interestingly, despite the presence of a less electron-donating phenyl group in **PPIS** compared to the bithiophene in **THPIS**, the SOC value of **PPIS** was

found to be greater. The presence of H-aggregation is corroborated by the significant blue-shifted $\lambda_{\text{abs.max}}$. This difference can be attributed to the more prominent H-aggregation in **PPIS** compared to **THPIS** (Figure A5.5, A5.9 and Table A5.2, A5.4). Unfortunately, single crystals for the **RPNI-S** derivatives could not be obtained. Nonetheless, a similar type of H-aggregation is anticipated to be observed as with **PPI** and **THPI**, with **RPNI-S** having a larger θ value, making the H-aggregation even more remarkable. **RPNI-S** is derived from **RPNI-O** through a minor modification involving the substitution of oxygen (O) atoms with S-atoms at the carbonyl position of the **RPNI-O** (Figure A5.9). Notably, Table A5.2 demonstrates that **RPNI-S** derivatives exhibited a significant blue-shifted $\lambda_{\text{abs.max}}$ in the aggregated-state compared to the previously reported materials.^{35,36,51} Herein, the traditional triazine derivative (DPhCzT) and organoboronium (OB4)₄ material demonstrate a distinct stabilization of the triplet excited state through H-aggregation, leading to the generation of ultralong phosphorescence.^{35,36} This research represents the novel findings regarding the efficient generation of SOC through pronounced H-aggregation. It is widely explored that SOC plays a pivotal role across various fields, including achieving persistent PL,⁵⁴ developing distinct light-emitting materials and devices,⁵⁵⁻⁵⁸ realizing ultralong room temperature phosphorescence,⁵⁹ and development of efficient PSs.¹⁶⁻²⁰ Extensive research has been devoted to enhancing SOC values in organic compounds, often achieved through strategies such as introducing heavy-atoms^{3,60} or by enhancing the D-A effect.⁶¹⁻⁶³ In contrast, this study represents a cost-effective and rare design strategy to enhance SOC by incorporating S-atoms at the carbonyl position, avoiding costly heavy-atom incorporation. Importantly, this marks a significant instance of an elevated SOC value compared to previously explored PSs as well as other conventional organic materials, which has been presented in table A5.14a (it is worth noting that distinct computational methods were employed for each study). In comparison, the reported dibenzo furan compound (**DPBF**) achieved a SOC value of 20.33 cm⁻¹, but it is crucial to note that this was based on theoretical studies conducted on aggregated molecules.⁵⁹ Additionally, another notable compound, selenine, demonstrated a substantial SOC value of 11.94 cm⁻¹ (Table A5.14a). On the other hand, the heavy-atom free **NI** and **PDI-4S** PSs exhibited notably high SOC values of 27.8 and 85 cm⁻¹, respectively. Importantly, these values were obtained using a distinct computational methodology, considering significantly more complex molecular systems.^{19,20} In contrast, this study unveils a precise and simple design strategy to enhance SOC through S-atoms introduction at the carbonyl position, emphasizing the rare mechanism of SOC enhancement via promising H-aggregation, which could be energized by the distinct magnitude of the excited triplet state stabilization and prolonging the excited state electron's lifetimes.

Furthermore, the excited state singlet and triplet energies were lower in **RPNI-S** compared to **RPNI-O**, and the energy levels were well distributed (Figure 5.6b, c and Table A5.14b). In

contrast, **RPNI-O** demonstrated the highest state transition comprising of lower SOC value as well, which is considered less favorable from a quantum mechanical perspective under identical condition. These observations highlight the significant influence of the S-atom at the carbonyl position in the system. Thus, the S-atom at the carbonyl position played a prominent role in **RPNI-S**, leading to enhanced SOC through prominent H-aggregation.

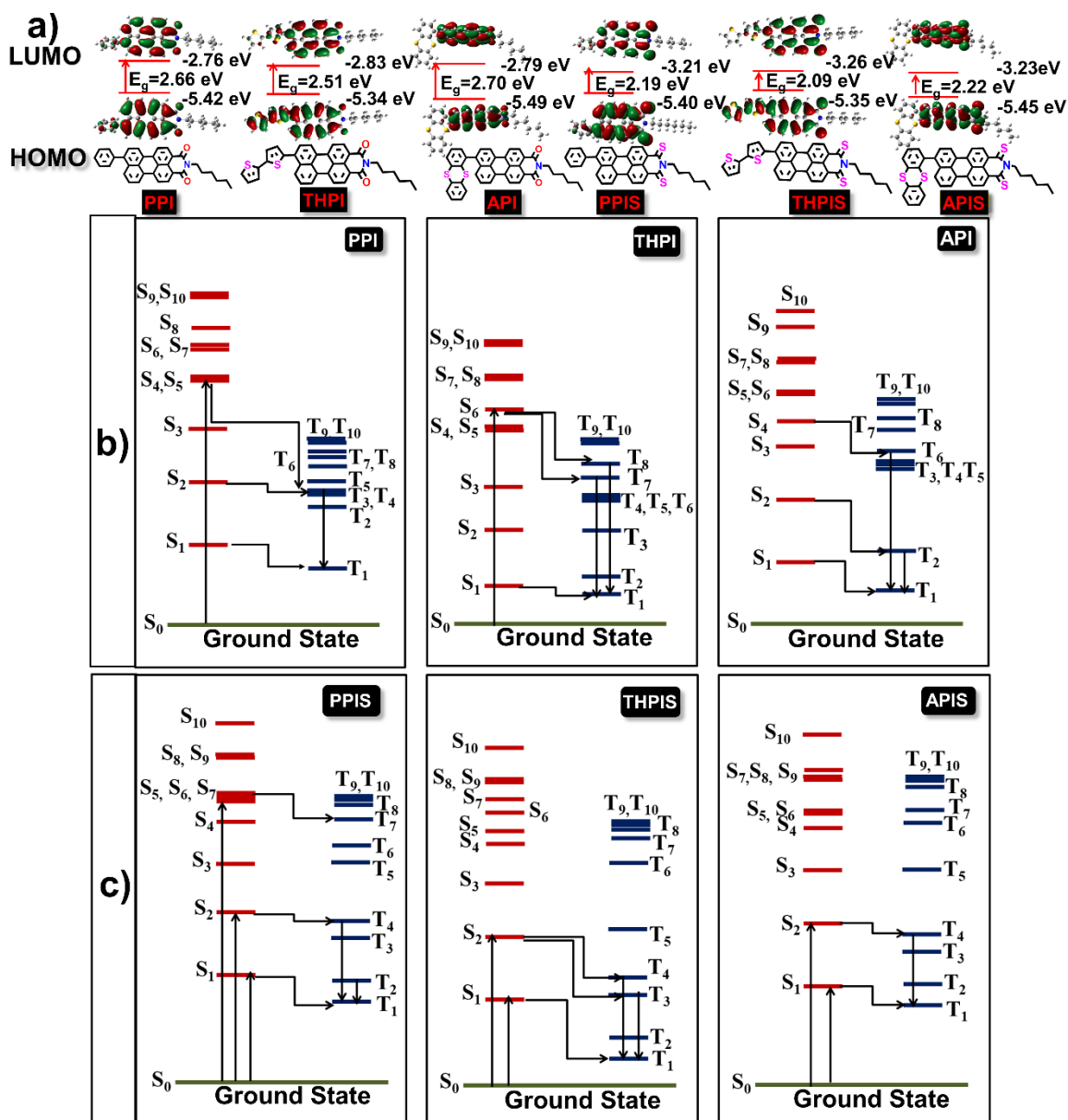


Figure 5.6. (a) Frontier molecular orbitals (HOMO and LUMO) with energies in eV calculated from the DFT/B3LYP method using the 6-31G (d, p) basis set by Gaussian 16 software in their ground state. Below the chemical structure of the respective luminogens. (b) SOCME Calculated by SOC-TDDFT method using ORCA 5.0 software for all the derivatives. **RPNI-O**: PPI, THPI, and API, respectively and **RPNI-S**: PPIS, THPIS and APIS, respectively. [PPI: $\Delta E_{S_1T_1}=1.19$ eV, $\Delta E_{S_2T_4}=0.19$ eV, $\Delta E_{S_4T_3}=0.576$ eV, $\xi(S_1,T_1)=0.3$ cm⁻¹, $\xi(S_2,T_4)=3.53$ cm⁻¹, $\xi(S_4,T_3)=3.81$ cm⁻¹. THPI: $\Delta E_{S_1T_1}=0.98$ eV, $\Delta E_{S_6T_7}=0.42$ eV, $\Delta E_{S_6T_{10}}=0.14$ eV, $\xi(S_1,T_1)=0.65$ cm⁻¹, $\xi(S_6,T_7)=3.44$ cm⁻¹, $\xi(S_6,T_{10})=3.50$ cm⁻¹. API: $\Delta E_{S_1T_1}=1.01$ eV, $\Delta E_{S_2T_2}=0.23$ eV, $\Delta E_{S_4T_6}=0.087$ eV, $\xi(S_1,T_1)=1.92$ cm⁻¹, $\xi(S_2,T_4)=2.36$ cm⁻¹, $\xi(S_4,T_3)=3.13$ cm⁻¹. PPIS: $\Delta E_{S_1T_1}=0.40$ eV, $\Delta E_{S_2T_4}=0.096$ eV, $\Delta E_{S_7T_7}=0.23$ eV, $\xi(S_1,T_1)=$

8.33 cm⁻¹, $\xi(S_2, T_4) = 10.88$ cm⁻¹, $\xi(S_7, T_7) = 9.16$ cm⁻¹. **THPIS**: $\Delta E_{S_1T_1} = 0.42$ eV, $\Delta E_{S_2T_4} = 0.094$ eV, $\Delta E_{S_2T_3} = 0.25$ eV, $\xi(S_1, T_1) = 6.90$ cm⁻¹, $\xi(S_2, T_4) = 9.20$ cm⁻¹, $\xi(S_2, T_3) = 6.19$ cm⁻¹. **APIS**: $\Delta E_{S_1T_1} = 0.39$ eV, $\Delta E_{S_2T_4} = 0.098$ eV, $\xi(S_1, T_1) = 4.44$ cm⁻¹, $\xi(S_2, T_4) = 5.73$ cm⁻¹].

5.3.9. Singlet oxygen (type 2 ROS) detection

Inspired by the remarkable SOC and abundant excited state triplet population in **RPNI-S**, an investigation into their Φ_Δ was conducted using ABDA as a commercially available probe for quantifying ¹O₂ (Figure 5.7a, A5.10, A5.11, A5.12a-c, A5.13b-d, and Equation A5.2). Table 5.1 presents the findings, demonstrating that **RPNI-S** displayed moderate Φ_Δ for **PPIS** (0.04), **THPIS** (0.34), and **APIS** (0.26), whereas the signal for ¹O₂ was virtually undetectable for all **RPNI-O** derivatives tested under the same conditions. Notably, the Φ_Δ showed a slight increase with the electron-donating ability of the -R groups. Thus, the lower Φ_Δ indicates reduced type-II processes for **THPIS** and **APIS** and a complete absence of ¹O₂ generation for **PPIS**.

5.3.10. Total ROS generation evaluation

In response to the lower Φ_Δ , an evaluation of the overall ROS generation capabilities of **RPNI-S** derivatives was conducted (Figure 5.7b, A5.12d-f, A5.13a and A5.13e-g). For this purpose, a fluorescent indicator, 2,7-dichlorodihydrofluorescein (DCFDA), known for its ability to detect various types of ROS, was utilized. Under white light irradiation for different durations, DCFDA in the presence of **RPNI-S** materials exhibited a gradual increase in PL intensity in their aggregated-state (99% PBS fraction in DMSO, f_{PBS}). Interestingly, as the donor functionality increased, the efficiency of ROS generation also increased. After 30 minutes of light irradiation, **PPIS**, **THPIS**, and **APIS** showed approximately 39-fold, 40-fold, and 29-fold increase in PL intensity, respectively, in the presence of DCFDA (Figure 5.7b). These results indicate the involvement of both type-I and type-II processes in the ROS generation of **RPNI-S** derivatives. Particularly noteworthy is the remarkable enhancement in PL intensity after just 5 minutes of white light irradiation, using just 10 μ M of DCFDA: **PPIS**, **THPIS**, and **APIS** exhibited enhancements of 2.5×10^5 , 1×10^6 , and 2×10^5 , respectively, while **RPNI-O** derivatives showed lower enhancements of PL intensity (Figure A5.13a and A5.13 e-g). These findings highlight the rapid and highly efficient production of ROS observed in **THPIS** PS. This efficiency is attributed to the presence of the promising donor bithiophene unit in **THPIS**, setting it apart from other **RPNI-O** and **RPNI-S** derivatives. Consequently, **THPIS** displays the smallest ΔE_{ST} value, facilitating a highly efficient triplet population in the aggregated-state.

5.3.11. Type 1 ROS evaluation

To assess the ability of **RPNI-S** to generate free radicals, electron spin resonance (ESR) was conducted using 2,2,6,6-tetramethyl-4-piperidinol (TEMP) as a widely used free radical trapper for $O_2^{\cdot-}$ and HO^{\cdot} (Figure 5.7c, d) The experiments were carried out on both **RPNI-S** and **RPNI-O** derivatives in their condensed state (99% f_{PBS}) under white light irradiation. Notably, the derivatives exhibited ESR signals after just 10 minutes of white light irradiation at both the 99% f_{PBS} and the solid state. In the solid state, the observation of ESR signal for **RPNI-S** even without the presence of any trapping agent indicates the effective stabilization of the triplet state. This stabilization is attributed to the notable H-aggregation phenomenon exhibited by these derivatives, which leads to the efficient energization of the triplet state, subsequently enhancing its stability.³⁴⁻³⁶ In contrast, no ESR signals were observed for **RPNI-O** derivatives under the same conditions. Building upon the type-I process observations, TA was chosen as a fluorescence probe to detect HO^{\cdot} (Figure 5.7e, A5.14a).^{6,51} The fluorescence intensity of **RPNI-S** probes showed no significant change when TA solutions were subjected to white light irradiation, indicating that **RPNI-S** did not produce HO^{\cdot} . These findings align with the electrochemical properties of the **RPNI-S** derivatives and support the mechanism of type-I PDT, wherein $O_2^{\cdot-}$ is generated through electron transfer from the triplet excited states to 3O_2 . Upon subjecting the ROS generation capabilities of these **RPNI-S** derivatives under white light irradiation, the band edge energy levels were estimated using E_{HOMO} and E_{LUMO} . (Figure 5.7f,g, A5.14b,c, A5.15, A5.16, Table A5.15-A5.17 and Equation A5.3-A5.6).⁵¹ The points of zero zeta potential for **PPIS**, **THPIS**, and **APIS** were determined to be 2.68, 2.18, and 4.35, respectively (Figure 5.7f and Table A5.15). The valence band energy (E_V) was determined from X-ray photoelectron spectroscopy (XPS) data (Figure A5.15, and Table A5.17). The conduction band energy (E_C) was estimated from the energy gap obtained from the onset absorption data from UV-visible spectroscopy and was referenced to the normal hydrogen electrode (NHE) (Figure A5.16, and Table A5.16, A5.17).⁵¹ As a result, the E_C values of **PPIS**, **THPIS**, and **APIS** were found to be -0.74228, -0.83178, and -0.96375 eV at a pH of 5.6, respectively. These values are lower than the redox potential (E_H) of $O_2/O_2^{\cdot-}$ (-0.2 eV) (Figure 5.7g and Table A5.17). Consequently, all three **RPNI-S** derivatives were capable of transferring electrons to oxygen and generating $O_2^{\cdot-}$, making them suitable PSs for type-I PDT. However, the E_V values of the **RPNI-S** derivatives (0.92772 for **PPIS**, 0.777822 for **THPIS**, and 0.656225 eV for **APIS**, respectively) are smaller than the E_H values of H_2O/HO^{\cdot} (2.20 eV) and $^1O_2/O_2$ (1.88 eV) at a pH of 5.6, suggesting that HO^{\cdot} and 1O_2 cannot be generated. Consequently, the type-II PDT process is not feasible for **RPNI-S** derivatives (Figure 5.7g and Table A5.17). On the other hand, **RPNI-O** does produce slight ROS, following the type-I process in PDT, as validated by the

experiments involving TA and band energy calculations with respect to NHE (Figure A5.14 a, c and Table A5.17). This result indicates that the driving force for generating $O_2^{\cdot-}$ continuously improves with larger atom sizes of sulfur compared to oxygen.⁵¹

Furthermore, the feasibility of type-I PDT, specifically in generating $O_2^{\cdot-}$ through IET mechanism, was further investigated by calculating the ΔG values using the ORCA 5.0 quantum mechanism package at the B3LYP/DEF2-SVP level (Figure 5.7h and Table A5.18-A5.25).^{50,51} Figure 5.7h illustrates that the ΔG value between **THPIS** and O_2 is $-40.83 \text{ kcal mol}^{-1}$, which is smaller than the ΔG values of **PPIS** and **APIS** (-0.548 and $-10.26 \text{ kcal mol}^{-1}$, respectively). This indicates a higher probability of IET reaction for **THPIS**. This signifies the exceptionally lower recorded instance of a ΔG value of **THPIS** in comparison to previously reported PSs. For instance, tetraphenylethene (TPE) based PS (TPE-PTB) showed a ΔG value of $-14.3839 \text{ kcal mol}^{-1}$, while tellurium (Te) comprising PS (PTTe) exhibited a ΔG value of $-32.16 \text{ kcal mol}^{-1}$.^{50,51} Based on the theoretical calculations, **THPIS** is theoretically predicted to be the most excellent type 1 PDT material among the three **RPNI-S** derivatives, efficiently generating $O_2^{\cdot-}$ and slight 1O_2 . On the other hand, **PPIS** is the second most promising type-I PDT material among the **RPNI-S** derivatives, efficiently generating only $O_2^{\cdot-}$.^{6,50,51}

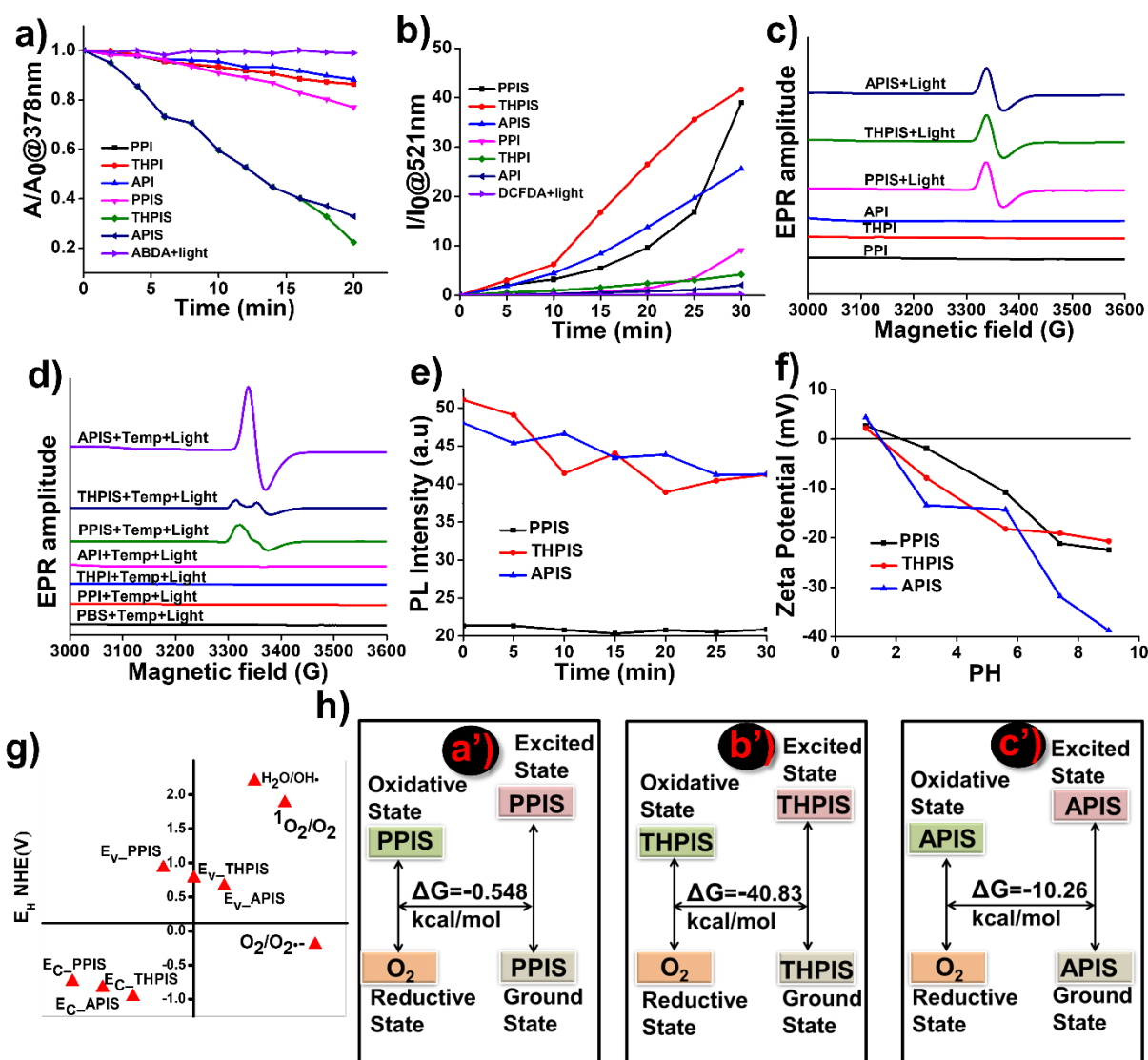


Figure 5.7. (a) Plots of ABDA (100 μM) degradation rates at $\lambda_{\text{abs,max}}$ of 378 nm by the various PSs (100 μM). (b) Plot of fluorescence intensities of DCFDA indicator in the presence of **RPNI-O** and **RPNI-S** derivatives. A_0 and A are ABDA absorbance at $\lambda_{\text{abs,max}}$ of 378 nm, where, I_0 and I are the PL intensities of the indicator at $\lambda_{\text{em,max}}$ of 521 nm before and after irradiation of the white light, respectively. (c and d) EPR signals at their solid state and aggregated-state. (e) PL spectra of TA in the presence of **RPNI-S** derivatives at 528 nm. (f) Zeta potential versus pH values of **RPNI-S** derivatives. (g) E_c and E_v of **RPNI-S** derivatives at pH 5.6. The energy scale is expressed in relation to NHE. E_H for $\text{H}_2\text{O}/\text{HO}^\bullet$, $^1\text{O}_2/\text{O}_2$, and $\text{O}_2/\text{O}_2^{\bullet-}$ are 2.2, 1.88, and -0.2 eV, respectively. (h) Gibbs free energy changes of (a') **PPIS**, (b') **THPIS** and (c') **APIS**, respectively, via ORCA 5.0 SOCME module at the B3LYP DEF2-SVP level. [Aggregated-state: 99% PBS fraction in DMSO, f_{PBS}].

Table 5.1. Photophysical and Photosensitizing characteristics of **RPNI-O** and **RPNI-S** derivatives.

Materials	^a λ_{abs} (nm)	^b λ_{ex} (nm)	^c λ_{em} (nm)	^d λ_{em} (nm)	^e λ_{em} (nm)	^f Stokes- shift (nm)	^g Φ_{PL}	^h E_{g} (eV)	ⁱ Φ_{Δ}	^j ΔE_{ST} (eV)	^k SOC (cm^{-1})
PPI	506	500	580	646	646	146	0.10	2.60	0.015	1.19	3.81
THPI	510	500	655	664	670	170	0.04	2.51	0.019	0.65	3.50
API	517	500	559	614	646	146	0.85,0.89	2.70	0.017	1.92	3.13
PPIS	590	605	655	G	G	G	G	2.19	0.04	0.40	10.88
THPIS	590	590	647	G	G	G	G	2.09	0.34	0.42	9.20
APIS	636	640	705	G	G	G	G	2.22	0.26	0.39	5.73

^a $\lambda_{\text{ab,max}}$, ^b λ_{ex} and ^c $\lambda_{\text{em,max}}$ are absorption, excitation and emission wavelength maxima in Solution state. ^{d,e}Aggregated and solid state $\lambda_{\text{em,max}}$, ^fstokes-shift calculated between solid $\lambda_{\text{em,max}}$ and $\lambda_{\text{ex,max}}$. ^g Φ_{PL} Quantum yield in aggregated-state. ^h E_{g} gaseous-state band-energies, ⁱ Φ_{Δ} Singlet-oxygen quantum yield, ^j ΔE_{ST} is first singlet and triplet state energy gap. ^kSpin-orbit coupling between singlet and triplet-state. [Concentration: 100 μM of **RPNI-O** and **RPNI-S** derivatives in DMSO solution (solution-state), 99% f_w in DMSO (Aggregated-state)], G = not observed.

5.3.12. Photodynamic therapy

The efficient ROS generation by these **RPNI-S** derivatives led to in vitro PDT studies on both Hela and MCF7 cancer cells, as well as normal cell (Figure 5.8). Cellular uptake experiments revealed that **PPIS**, **THPIS**, and **APIS** reached their maximum enrichment in Hela cells after 4 hours of post-treatment (Figure A5.17).⁵¹ **RPNI-S** derivatives demonstrated superior cellular uptake ability at 20 μM concentration specifically towards Hela cancer cells, while remaining non-toxic to normal cells even at concentrations up to 100 μM . However, **APIS** exhibited lower cellular uptake towards Hela cell, possibly due to its detrimental micro-aggregate morphology in aqueous media (Figure 5.4f, A5.17). On the other hand, **RPNI-O** showed low cellular uptake at 20 μM concentration but was easily internalized by both normal cells and Hela cancer cells at 100 μM concentration (Figure A5.18). Furthermore, the anticancer effect of **RPNI-S**, encompassing **PPIS**, **THPIS**, and **APIS**, was meticulously investigated in Hela and MCF7 cancer cells, as well as normal cells, utilizing the MTT assay under both dark and light conditions (Figure 5.8).¹⁹ This assay was selected for its wide applicability and capability to effectively measure cellular uptake efficacy. Under 20

min of white light irradiation, both **THPIS** and **PPIS** significantly inhibited cell proliferation, with an IC_{50} of approximately 4.5 μ M and 15.5 μ M in HeLa cells (Figure 5.8d-f). On the other hand, a PDT effect was observed on MCF-7 cells at higher concentrations (**PPIS**: 200 μ M, and **THPIS**: 75 μ M, respectively) (Figure 5.8a-c). This clearly indicates the pronounced selectivity of these two **RPNI-S** derivatives towards HeLa cells over MCF-7 cells. Notably, at 20 μ M and 50 μ M concentrations, **THPIS** and **PPIS** induced approximately 80% cell inhibition upon light exposure. At 100 μ M concentration, **THPIS** exhibited complete cell inhibition, although it showed slight dark toxicity. On the other hand, **APIS** exhibited negligible cytotoxicity under both dark and light treatments, despite its efficacy in producing ROS. This minimal cytotoxicity is likely attributed to its lower cellular uptake, which has been regulated by its anomalous micro-aggregate morphology (Figure 5.4f, A5.17). Crucially, these **RPNI-S** derivatives demonstrated minimal cytotoxicity towards normal cells both in the absence and presence of light (Figure 5.8g-i). This lack of toxicity can be attributed to their meticulous cellular uptake ability which has been strengthened by the precisely controlled morphology when in aqueous media (Figure 5.4d-f, A5.17).^{44,45} This optimized cellular uptake mechanism contributes to their biocompatibility and supports their potential for safe and effective use in biomedical applications. Conversely, **RPNI-O** derivatives showed minimal changes upon both dark and light treatment towards both normal cells as well as HeLa cancer cells (Figure A5.19). Moreover, as depicted in figure A5.19, **RPNI-O** derivatives predominantly demonstrate dark toxicity towards HeLa cells, as evidenced by the IC_{50} of approximately 100 μ M. Alternatively, the reduced effectiveness in PDT can be attributed to a decrease in ROS production associated with these derivatives (Figure A5.11, A5.13 and Table 5.1). The aforementioned results suggest a notable contrast in potential efficacy between **RPNI-S** and **RPNI-O** derivatives in the biological environment. These attributes underline the potential of **RPNI-S** as a more effective option for broader biological applications. In addition, fluorescence microscopic imaging further confirmed the excellent phototoxicity of **THPIS** towards HeLa cells, highlighting its potential as an outstanding PS (Figure 5.9). In conclusion, **THPIS**, distinguished by its remarkable biocompatibility, demonstrated exceptional phototoxicity and efficient cellular uptake without requiring additional targeting agents. These features strongly position **THPIS** as a highly promising PS for diverse phototherapeutic applications. Ongoing research and optimizations hold potential to further enhance its efficacy and extend its utility in cancer therapy and related fields. However, while **PPIS** is demonstrating the second most promising potential as PDT material after **THPIS**, ongoing research in our laboratory is currently exploring this approach with **APIS**, utilizing liposomes to enhance its cellular uptake in a biological environment. This enhancement is expected to correspondingly increase the efficacy of PDT of **APIS** in cancer cells.

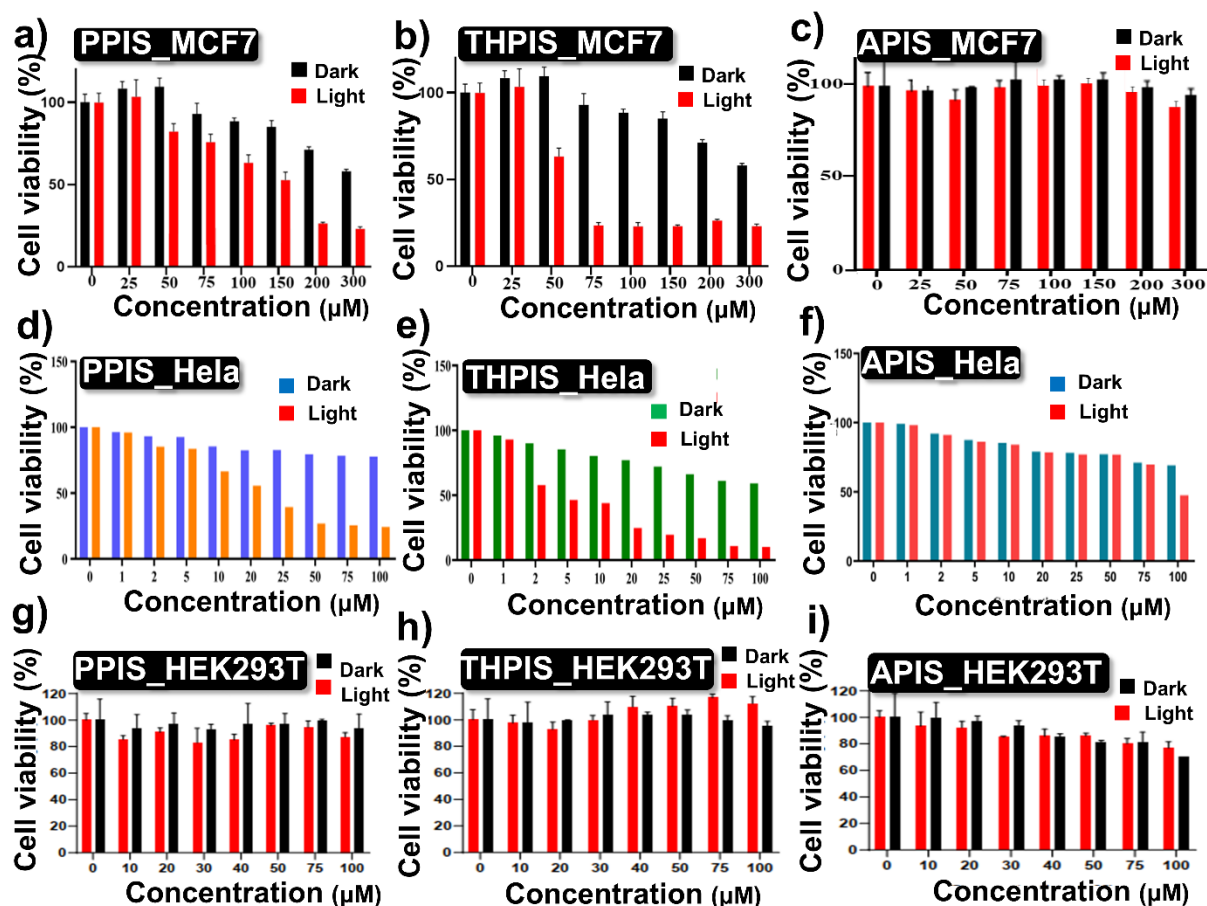
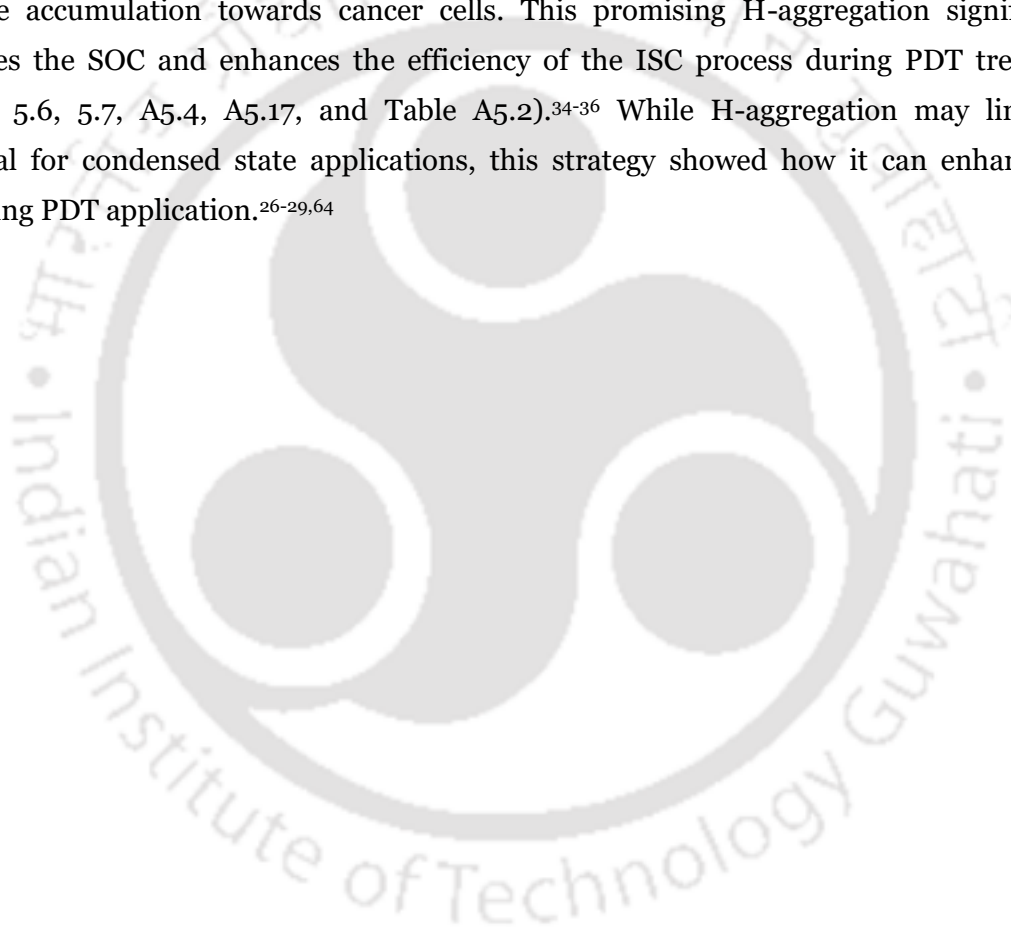


Figure 5.8. (a-c) Cell viability of MCF 7 cells after treatment with different concentrations of (a) **PPIS**, (b) **THPIS**, and (c) **APIS**, respectively, along with white light irradiation. (d-f) Cell cytotoxicity of HeLa cells after treatment with different concentrations of (d) **PPIS**, (e) **THPIS**, and (f) **APIS**, respectively, along with white light irradiation. (g-h) Cell viability of HEK293T cells after treatment with different concentrations of (g) **PPIS**, (h) **THPIS**, and (i) **APIS**, respectively, along with white light irradiation.

5.3.13. Live cell/ dead cell co-staining and intracellular ROS generation

The viability assay, visualized using calcein-AM/propidium iodide, clearly showed the impact of **THPIS**, **PPIS** and **APIS** on HeLa cells upon white light irradiation (Figure 5.9, 5.10 and A5.20-A5.22).¹⁹ Additionally, intracellular ROS production was confirmed using DCFDA, where green fluorescence served as a marker for the generation of total ROS (Figure 5.9, c and 5.10, c). These results were consistent with the findings mentioned earlier (Figure 5.7, 5.8). Furthermore, the treated cells exhibited noticeable morphological changes, including reduced size, shrinkage, and cellular collapse under the white light irradiation (Figure 5.9, a-c and 5.10, a-c). These observations further substantiate the concept that **THPIS**-induced photodynamic action enhances outcomes in photodynamic therapy for HeLa cells by inducing organelle destruction. This effect is likely amplified by the efficient

accumulation of **THPIS** within Hela cancer cells, which possess higher cell permeability compared to both normal cells and MCF-7 cancer cells (Figure A5.17). This selective accumulation is facilitated by the precisely controlled morphology of **THPIS** in aqueous media (Figure 5.4e).^{44,45} Thus, **THPIS** demonstrated significant photodynamic activity, resulting in efficient ROS and subsequent organelle destruction within cancer cells. Its enhanced therapeutic effect is attributed to its pronounced accumulation within cancer cells, and its ability to induce selective phototoxicity, making it a promising candidate for PDT applications (Figure 5.4e and A5.17). Thus, based on the theoretical and experimental studies regarding ROS generation efficacy, it is plausible to assert that the exceptional PDT efficacy observed in **PPIS** and **THPIS** can be attributed to their pronounced H-aggregation and effective accumulation towards cancer cells. This promising H-aggregation significantly amplifies the SOC and enhances the efficiency of the ISC process during PDT treatment (Figure 5.6, 5.7, A5.4, A5.17, and Table A5.2).³⁴⁻³⁶ While H-aggregation may limit the potential for condensed state applications, this strategy showed how it can enhance the promising PDT application.^{26-29,64}



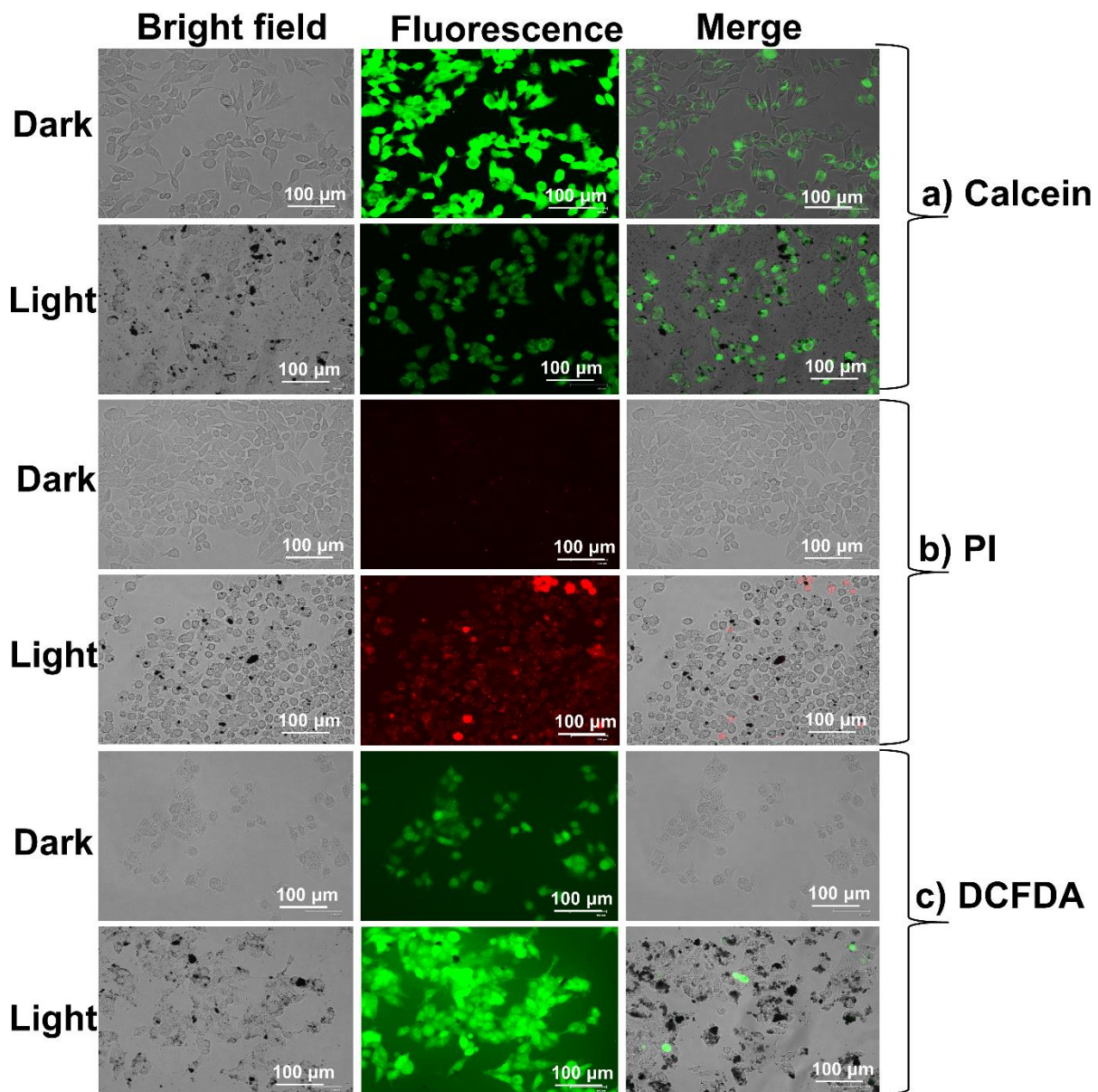


Figure 5.9. Fluorescence microscope images of HeLa cells after treatment with **PPIS** under normoxia and loaded with (a) calcein-AM (2 μ M, live cell marker), (b) PI (4 μ M, dead cell marker), (c) DCFDA (10 μ M). [Concentration of **PPIS**: (50 μ M), scale bar: 100 μ m].

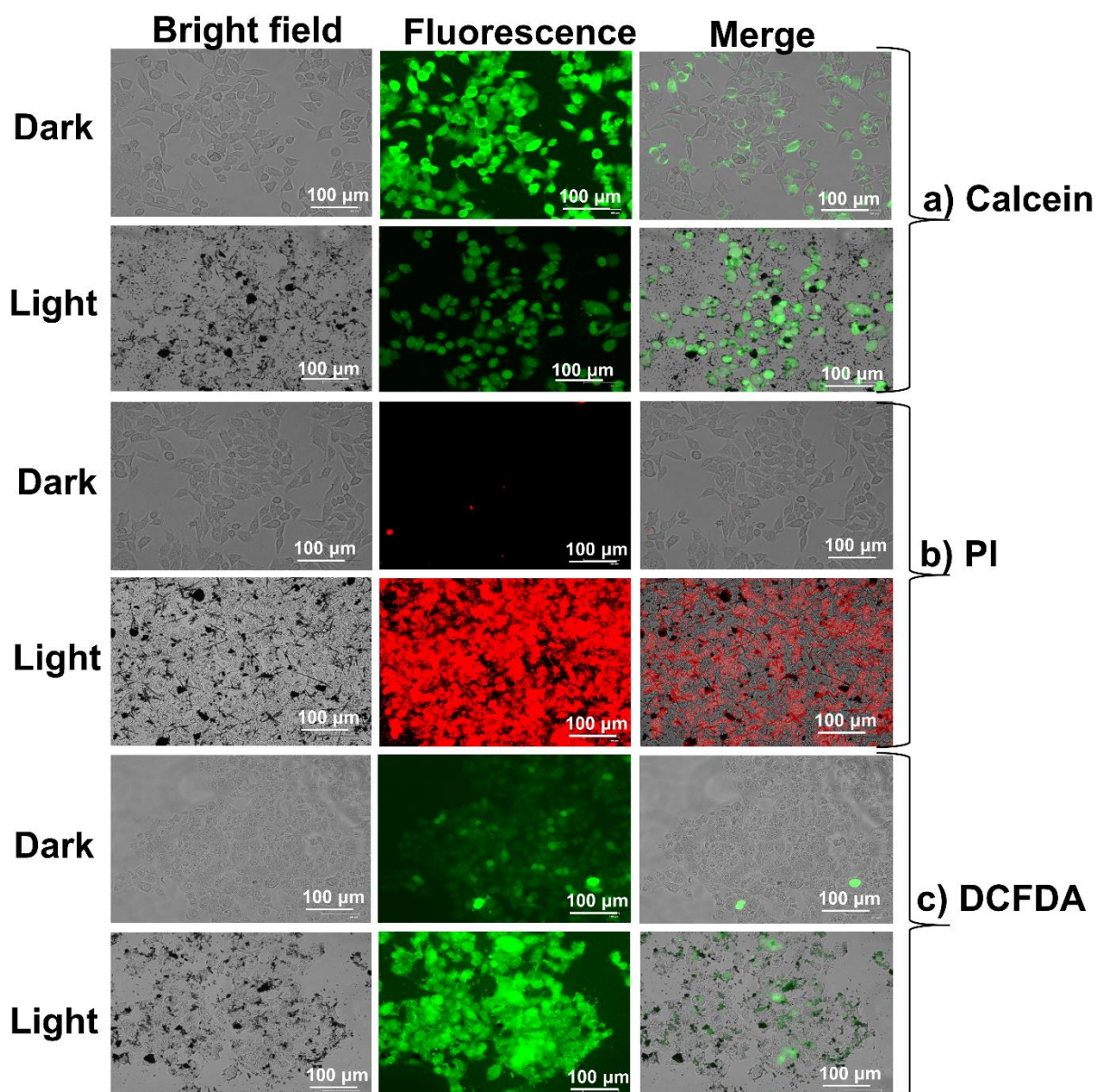


Figure 5.10. Fluorescence microscope images of HeLa cells after treatment with **THPIS** under normoxia and loaded with (a) calcein-AM (2 μM , live cell marker), (b) PI (4 μM , dead cell marker), (c) DCFDA (10 μM). [Concentration of **THPIS**: (50 μM), scale bar: 100 μm].

5.4. Conclusion

This work proposes that meticulous modulation of the S-atom conformation can lead to enhanced SOC (10.88 cm^{-1}), Φ_{PL} (0.85), and the advancement of potent PSs. Precise incorporation of S-atoms at the pendant functional group in **RPNI-O** showed drastic photophysical properties: stokes shift of 170 nm, red emitting AIEEgen, and established novel AIE mechanism. Surprisingly, introducing S-atoms at the carbonyl position in **RPNI-O** results **RPNI-S**, which exhibits unprecedented structure-property relationships (130 nm red-shifted $\lambda_{\text{ab,max}}$, a subsequent extension of $\lambda_{\text{em,max}}$ into NIR, and $\Phi_{\text{PL}} \approx 0.00$ in the

aggregated-state). Furthermore, **RPNI-S** established a novel SOC enhancement mechanism via prominent H-aggregation. Because, the strong π - π coupling intrinsic in H-aggregation efficiently traps and stabilizes the excited state triplet. **RPNI-S** exhibited efficient IET reaction for type-I PDT, evidenced by exceptionally lower ΔG value (**THPIS**:-40.83 kcal mol⁻¹). Interestingly, the lower Φ_{Δ} , ΔG and energy level suggest the efficient production of O₂⁻ and minimal type-II ROS (¹O₂) for **THPIS**. Herein, **PPIS** very specific and particularly generates O₂⁻. The biocompatible and very specific heavy-atom free **PPIS** and **THPIS** PSs selective and efficient PDT efficacy under normoxia, which is exceptionally rare. Thus, this strategy provides important perspective for the potential development of future PSs via pronounced H-aggregation and distinct condensed state emitters for diverse applications.

References

- (1) Luby, B. M.; Walsh, C. D.; Zheng, G. Advanced Photosensitizer Activation Strategies for Smarter Photodynamic Therapy Beacons. *Angew. Chem., Int. Ed.* **2019**, *58*, 2558-2569.
- (2) Castano, A. P.; Mroz, P.; Hamblin, M. R. Photodynamic Therapy and Anti-Tumour Immunity. *Nat. Rev. Cancer* **2006**, *6*, 535-545.
- (3) Kolemen, S.; Işık, M.; Kim, G. M.; Kim, D.; Geng, H.; Buyuktemiz, M.; Karatas, T.; Zhang, X.-F.; Dede, Y.; Yoon, J.; Akkaya, E. U. Intracellular Modulation of Excited-State Dynamics in a Chromophore Dyad: Differential Enhancement of Photocytotoxicity Targeting Cancer Cells. *Angew. Chem., Int. Ed.* **2015**, *54*, 5340-5344.
- (4) Cakmak, Y.; Kolemen, S.; Duman, S.; Dede, Y.; Dolen, Y.; Kilic, B.; Kostereli, Z.; Yildirim, L. T.; Dogan, A. L.; Guc, D.; Akkaya, E. U. Designing Excited States: Theory-Guided Access to Efficient Photosensitizers for Photodynamic Action. *Angew. Chem., Int. Ed.* **2011**, *50*, 11937-11941.
- (5) Baptista, M. S.; Cadet, J.; Mascio, P. D.; Ghogare, A. A.; Greer, A.; Hamblin, M. R.; Lorente, C.; Nunez, S. C.; Ribeiro, M. S.; Thomas, A. H.; Vignoni, M.; Yoshimura, T. M. Type I and Type II Photosensitized Oxidation Reactions: Guidelines and Mechanistic Pathways. *Photochem. Photobiol.* **2017**, *93*, 912-919.
- (6) Li, M.; Xia, J.; Tian, R.; Wang, J.; Fan, J.; Du, J.; Long, S.; Song, X.; Foley, J. W.; Peng, X. Near-Infrared Light-Initiated Molecular Superoxide Radical Generator: Rejuvenating Photodynamic Therapy against Hypoxic Tumors. *J. Am. Chem. Soc.* **2018**, *140*, 14851-14859.
- (7) Kavarnos, G. J.; Turro, N. J. Photosensitization by Reversible Electron Transfer: Theories, Experimental Evidence, and Examples. *Chem. Rev.* **1986**, *86*, 401-449.
- (8) Shi, L.; Hu, F.; Duan, Y.; Wu, W.; Dong, J.; Meng, X.; Zhu, X.; Liu, B. Hybrid Nanospheres to Overcome Hypoxia and Intrinsic Oxidative Resistance for Enhanced Photodynamic Therapy. *ACS Nano* **2020**, *14*, 2183-2190.
- (9) Brown, J. M.; Wilson, W. R. Exploiting Tumour Hypoxia in Cancer Treatment. *Nat. Rev. Cancer.* **2004**, *4*, 437-447.

- (10) Pollum, M.; Jockusch, S.; Crespo-Hernández, C. E. 2,4-Dithiothymine as a Potent UVA Chemotherapeutic Agent. *J. Am. Chem. Soc.* **2014**, *136*, 17930-17933.
- (11) Reelfs, O.; Xu, Y. Z.; Massey, A.; Karran, P.; Storey, A. Thiothymidine plus low-dose UVA kills hyperproliferative human skin cells independently of their human papilloma virus status. *Mol. Cancer Ther.* **2007**, *6*, 2487-2495.
- (12) Martínez-Fernández, L.; Corral, I.; Granucci, G.; Persico, M. Competing Ultrafast Intersystem Crossing and Internal Conversion: A Time Resolved Picture for the Deactivation of 6-Thioguanine. *Chem. Sci.* **2014**, *5*, 1336-1347.
- (13) Farrell, K. M.; Brister, M. M.; Pittelkow, M.; Sølling, T. I.; Crespo-Hernández, C. E. Heavy-Atom-Substituted Nucleobases in Photodynamic Applications: Substitution of Sulfur with Selenium in 6-Thioguanine Induces a Remarkable Increase in the Rate of Triplet Decay in 6-Selenoguanine. *J. Am. Chem. Soc.* **2018**, *140*, 11214-11218.
- (14) Mai, S.; Pollum, M.; Martínez-Fernández, L.; Dunn, N.; Marquetand, P.; Corral, I.; Crespo-Hernández, C. E.; González, L. The Origin of Efficient Triplet State Population in Sulfur-Substituted Nucleobases. *Nat. Commun.* **2016**, *7*, 13077.
- (15) Ashwood, B.; Pollum, M.; Crespo-Hernández, C. E. Photochemical and Photodynamical Properties of Sulfur-Substituted Nucleic Acid Bases. *Photochem. Photobiol.* **2019**, *95*, 33-58.
- (16) Tilley, A. J.; Pensack, R. D.; Lee, T. S.; Djukic, B.; Scholes, G. D.; Seferos, D. S. Ultrafast Triplet Formation in Thionated Perylene Diimides. *J. Phys. Chem. C* **2014**, *118*, 9996-10004.
- (17) Zhao, J.; Chen, K.; Hou, Y.; Che, Y.; Liu, L.; Jia, D. Recent Progress in Heavy-Atom-Free Organic Compounds Showing Unexpected Intersystem Crossing (ISC) Ability. *Org. Biomol. Chem.* **2018**, *16*, 3692-3701.
- (18) Hussain, M.; Zhao, J.; Yang, W.; Zhong, F.; Karatay, A.; Yaglioglu, H. G.; Yildiz, E. A.; Hayvali, M. Intersystem Crossing and Triplet Excited State Properties of Thionated Naphthalenediimide Derivatives. *J. Lumin.* **2017**, *192*, 211-217.
- (19) Nguyen, V.-N.; Qi, S.; Kim, S.; Kwon, N.; Kim, G.; Yim, Y.; Park, S.; Yoon, J. An Emerging Molecular Design Approach to Heavy-Atom-Free Photosensitizers for Enhanced Photodynamic Therapy under Hypoxia. *J. Am. Chem. Soc.* **2019**, *141*, 16243-16248.
- (20) Liu, C.; Ji, C.; Fan, Z.; Ma, R.; Yin, M. A Facile Design of Thio-Perylenediimides with Controllable Fluorescent, Photodynamic and Photothermal Effects towards Cancer Theranostics. *Chem. Commun.* **2021**, *57*, 13126-13129.
- (21) Pal, K.; Sharma, V.; Sahoo, D.; Kapuria, N.; Koner, A. L. Large Stokes-Shifted NIR-Emission from Nanospace-Induced Aggregation of Perylenemonoimide-Doped Polymer Nanoparticles: Imaging of Folate Receptor Expression. *Chem. Commun.* **2018**, *54*, 523-526.
- (22) Yang, N.; Song, S.; Ren, J.; Liu, C.; Li, Z.; Qi, H.; Yu, C. Controlled Aggregation of a Perylene-Derived Probe for Near-Infrared Fluorescence Imaging and Phototherapy. *ACS Appl. Bio Mater.* **2021**, *4*, 5008-5015.
- (23) Khatun, M. N.; Dey, A.; Meher, N.; Iyer, P. K. Long Alkyl Chain Induced OFET Characteristic with Low Threshold Voltage in an n-Type Perylene Monoimide Semiconductor. *ACS Appl. Electron. Mater.* **2021**, *3*, 3575-3587.

- (24) Li, C.; Wonneberger, H. Perylene Imides for Organic Photovoltaics: Yesterday, Today, and Tomorrow. *Adv. Mater.* **2012**, *24*, 613-636.
- (25) Jana, A.; Bai, L.; Li, X.; Ågren, H.; Zhao, Y. Morphology Tuning of Self-Assembled Perylene Monoimide from Nanoparticles to Colloidosomes with Enhanced Excimeric NIR Emission for Bioimaging. *ACS Appl. Mater. Interfaces* **2016**, *8*, 2336-2347.
- (26) Mei, J.; Hong, Y.; Lam, J. W. Y.; Qin, A.; Tang, Y.; Tang, B. Z. Aggregation-Induced Emission: The Whole is More Brilliant than the Parts. *Adv. Mater.* **2014**, *26*, 5429-5479.
- (27) Khatun, M. N.; Tanwar, A. S.; Meher, N.; Iyer, P. K. An Unprecedented Blueshifted Naphthalimide AIEEgen for Ultrasensitive Detection of 4-Nitroaniline in Water via "Receptor-Free" IFE Mechanism. *Chem. Asian J.* **2019**, *14*, 4725-4731.
- (28) Meher, N.; Iyer, P. K. Spontaneously Self-Assembled Naphthalimide Nanosheets: Aggregation-Induced Emission and Unveiling a-PET for Sensitive Detection of Organic Volatile Contaminants in Water. *Angew. Chem., Int. Ed.* **2018**, *57*, 8488-8492.
- (29) Meher, N.; Panda, S.; Kumar, S.; Iyer, P. K. Aldehyde Group Driven Aggregation-Induced Enhanced Emission in Naphthalimides and its Application for Ultradetection of Hydrazine on Multiple Platforms. *Chem. Sci.* **2018**, *9*, 3978-3985.
- (30) Chen, K.; Zhang, R.; Wang, Z.; Zhang, W.; Tang, B. Z. Structural Modification Orientated Multifunctional AIE Fluorescence Probes: Organelles Imaging and Effective Photosensitizer for Photodynamic Therapy. *Adv. Opt. Mater.* **2020**, *8*, 1901433.
- (31) Luo, J.; Xie, Z.; Lam, J. W. Y.; Cheng, L.; Chen, H.; Qiu, C.; Kwok, H. S.; Zhan, X.; Liu, Y.; Zhu, D.; Tang, B. Z. Aggregation-Induced Emission of 1-Methyl-1,2,3,4,5-Pentaphenylsilole. *Chem. Commun.* **2001**, *18*, 1740-1741.
- (32) An, B.-K.; Kwon, S.-K.; Jung, S.-D.; Park, S. Y. Enhanced Emission and Its Switching in Fluorescent Organic Nanoparticles. *J. Am. Chem. Soc.* **2002**, *124*, 14410-14415.
- (33) Sasaki, S.; Drummen, G. P. C.; Konishi, G.-I. Recent Advances in Twisted Intramolecular Charge Transfer (TICT) Fluorescence and Related Phenomena in Materials Chemistry. *J. Mater. Chem. C* **2016**, *4*, 2731-2743.
- (34) Yuan, J.; Chen, R.; Tang, X.; Tao, Y.; Xu, S.; Jin, L.; Chen, C.; Zhou, X.; Zheng, C.; Huang, W. Direct Population of Triplet Excited States through Singlet-Triplet Transition for Visible-Light Excitable Organic Afterglow. *Chem. Sci.* **2019**, *10*, 5031-5038.
- (35) An, Z.; Zheng, C.; Tao, Y.; Chen, R.; Shi, H.; Chen, T.; Wang, Z.; Li, H.; Deng, R.; Liu, X.; Huang, W. Stabilizing Triplet Excited States for Ultralong Organic Phosphorescence. *Nat. Mater.* **2015**, *14*, 685-690.
- (36) Yang, L.; Wang, X.; Zhang, G.; Chen, X.; Zhang, G.; Jiang, J. Aggregation-Induced Intersystem Crossing: A Novel Strategy for Efficient Molecular Phosphorescence. *Nanoscale* **2016**, *8*, 17422-17426.
- (37) Dong, J.; Solntsev, K. M.; Tolbert, L. M. Activation and Tuning of Green Fluorescent Protein Chromophore Emission by Alkyl Substituent-Mediated Crystal Packing. *J. Am. Chem. Soc.* **2009**, *131*, 662-670.

- (38) Zhen, G.; Lu, X.; Wang, B.; Zhao, Y.; Chai, X.; Niu, D.; Zhao, A.; Li, Y.; Song, Y.; Cao, X. Synergetic Pretreatment of Waste Activated Sludge by Fe(II)-Activated Persulfate Oxidation under Mild Temperature for Enhanced Dewaterability. *Bioresour. Technol.* **2012**, *124*, 29-36.
- (39) Nagai, A.; Kokado, K.; Miyake, J.; Chujo, Y. Quantum Yield and Morphology Control of BODIPY-Based Supramolecular Self-Assembly with a Chiral Polymer Inhibitor. *Polym. J.* **2010**, *42*, 37-42.
- (40) Deng, Y.; Wang, M.; Zhuang, Y.; Liu, S.; Huang, W.; Zhao, Q. Circularly Polarized Luminescence from Organic Micro-/Nano-Structures. *Light: Sci. Appl.* **2021**, *10*, 76.
- (41) Marqués, P. S.; Krajewska, M.; Frank, B. D.; Prochaska, K.; Zeininger, L. Morphology-Dependent Aggregation-Induced Emission of Janus Emulsion Surfactants. *Chem. Eur. J.* **2023**, *29*, 202203790.
- (42) Ye, J.; Huang, X.; Gao, Y.; Wang, X.; Zheng, T.; Lin, Y.; Liu, X.; Ning, G. Morphology-Controlled Assembly and Enhanced Emission of Fluorescence in Organic Nanospheres and Microrods Based on 1,2-Diphenyl-4-(4-Dibenzothienyl) Phenyl-1,3-Cyclopentadiene. *CrystEngComm* **2015**, *17*, 9311-9317.
- (43) Soni, M.; Das, S. K.; Sahu, P. K.; Kar, U. P.; Rahaman, A.; Sarkar, M. Synthesis, Photophysics, Live Cell Imaging, and Aggregation Behavior of Some Structurally Similar Alkyl Chain Containing Bromonaphthalimide Systems: Influence of Alkyl Chain Length on the Aggregation Behavior. *J. Phys. Chem. C* **2013**, *117*, 14338-14347.
- (44) Rennick, J. J.; Johnston, A. P. R.; Parton, R. G. Key Principles and Methods for Studying the Endocytosis of Biological and Nanoparticle Therapeutics. *Nat. Nanotechnol.* **2021**, *16*, 266-276.
- (45) Zhang, D.; Wei, L.; Zhong, M.; Xiao, L.; Li, H.-W.; Wang, J. The Morphology and Surface Charge-Dependent Cellular Uptake Efficiency of Upconversion Nanostructures Revealed by Single-Particle Optical Microscopy. *Chem. Sci.* **2018**, *9*, 5260-5269.
- (46) Zhang, X.; Du, L.; Zhao, W.; Zhao, Z.; Xiong, Y.; He, X.; Gao, P. F.; Alam, P.; Wang, C.; Li, Z.; Leng, J.; Liu, J.; Zhou, C.; Lam, J. W. Y.; Phillips, D. L.; Zhang, G.; Tang, B. Z. Ultralong UV/Mechano-Excited Room Temperature Phosphorescence from Purely Organic Cluster Excitons. *Nat. Commun.* **2019**, *10*, 5161.
- (47) Cozzi, F.; Cinquini, M.; Annuziata, R.; Siegel, J. S. "Through-Space Interactions between Face-to-Face, Center-to-Edge Oriented Arenes: Importance of Polar- π Effects." *J. Am. Chem. Soc.* **1993**, *115*, 5330-5331.
- (48) Davydov, A. S. "Theory of Molecular Excitons." Plenum Press: New York, **1971**.
- (49) Kasha, M.; Rawls, H.; El-Bayoumi, M. The Exciton Model in Molecular Spectroscopy. *Pure Appl. Chem.* **1965**, *11*, 371-392.
- (50) Li, Y.; Tang, R.; Liu, X.; Gong, J.; Zhao, Z.; Sheng, Z.; Zhang, J.; Li, X.; Niu, G.; Kwok, R. T. K.; Zheng, W.; Jiang, X.; Tang, B. Z. Bright Aggregation-Induced Emission Nanoparticles for Two-Photon Imaging and Localized Compound Therapy of Cancers. *ACS Nano* **2020**, *14*, 16840-16853.
- (51) Wen, K.; Tan, H.; Peng, Q.; Chen, H.; Ma, H.; Wang, L.; Peng, A.; Shi, Q.; Cai, X.; Huang, H. Achieving Efficient NIR-II Type-I Photosensitizers for Photodynamic/Photothermal Therapy upon Regulating Chalcogen Elements. *Adv. Mater.* **2022**, *34*, 2108146.
- (52) Filatov, M. A.; Karuthedath, S.; Polestshuk, P. M.; Savoie, H.; Flanagan, K. J.; Sy, C.; Sitte, E.; Telitchko, M.; Laquai, F.; Boyle, R. W.; Senge, M. O. Generation of Triplet Excited States via Photoinduced Electron Transfer in Meso-Anthra-BODIPY: Fluorogenic Response toward Singlet Oxygen in Solution and in Vitro. *J. Am. Chem. Soc.* **2017**, *139*, 6282-6285.

- (53) Dance, Z. E. X.; Mickley, S. M.; Wilson, T. M.; Ricks, A. B.; Scott, A. M.; Ratner, M. A.; Wasielewski, M. R. Intersystem Crossing Mediated by Photoinduced Intramolecular Charge Transfer: Julolidine-Anthracene Molecules with Perpendicular π Systems. *J. Phys. Chem. A* **2008**, *112*, 4194-4201.
- (54) Dou, Y.; Demangeat, C.; Wang, M.; Xu, H.; Dryzhakov, B.; Kim, E.; Le Bahers, T.; Lee, K.-S.; Attias, A.-J.; Hu, B. Spin-Orbital Coupling and Slow Phonon Effects Enabled Persistent Photoluminescence in Organic Crystal under Isomer Doping. *Nat. Commun.* **2021**, *12*, 3485.
- (55) He, Z.; Zhao, W.; Lam, J. W. Y.; Peng, Q.; Ma, H.; Liang, G.; Shuai, Z.; Tang, B. Z. White Light Emission from a Single Organic Molecule with Dual Phosphorescence at Room Temperature. *Nat. Commun.* **2017**, *8*, 416.
- (57) Li, J.; Yao, Q.; Wu, L.; Hu, Z.; Gao, B.; Wan, X.; Liu, Q. Designing Light-Element Materials with Large Effective Spin-Orbit Coupling. *Nat. Commun.* **2022**, *13*, 919.
- (58) Uoyama, H.; Goushi, K.; Shizu, K.; Nomura, H.; Adachi, C. Highly Efficient Organic Light-Emitting Diodes from Delayed Fluorescence. *Nat.* **2012**, *492*, 234-238.
- (59) Ma, H.; Peng, Q.; An, Z.; Huang, W.; Shuai, Z. Efficient and Long-Lived Room-Temperature Organic Phosphorescence: Theoretical Descriptors for Molecular Designs. *J. Am. Chem. Soc.* **2019**, *141*, 1010-1015
- (60) Rodriguez-Serrano, A.; Rai-Constapel, V.; Daza, M. C.; Doerr, M.; Marian, C. M. Internal Heavy Atom Effects in Phenothiazinium Dyes: Enhancement of Intersystem Crossing via Vibronic Spin-Orbit Coupling. *Phys. Chem. Chem. Phys.* **2015**, *17*, 11350-11358.
- (61) Wang, M.; Chatterjee, T.; Foster, C. J.; Wu, T.; Yi, C.-L.; Yu, H.; Wong, K.-T.; Hu, B. Exploring Mechanisms for Generating Spin-Orbital Coupling through Donor-Acceptor Design to Realize Spin Flipping in Thermally Activated Delayed Fluorescence. *J. Mater. Chem. C* **2020**, *8*, 3395-3401.
- (62) Yang, Z.; Zhang, Z.; Sun, Y.; Lei, Z.; Wang, D.; Ma, H.; Tang, B. Z. Incorporating Spin-Orbit Coupling Promoted Functional Group into an Enhanced Electron D-A System: A Useful Designing Concept for Fabricating Efficient Photosensitizer and Imaging-Guided Photodynamic Therapy. *Biomaterials* **2021**, *275*, 120934.
- (63) Singh, R.; Chen, D.-G.; Wang, C.-H.; Wu, C.-C.; Hsu, C.-H.; Wu, C.-H.; Lai, T.-Y.; Chou, P.-T.; Chen, C.-T. Tuning Intramolecular Charge Transfer and Spin-Orbit Coupling of AIE-Active Type-I Photosensitizers for Photodynamic Therapy. *J. Mater. Chem. B* **2022**, *10*, 6228-6236.
- (64) Yan, Z.; Xu, H.; Guang, S.; Zhao, X.; Fan, W.; Liu, X. Y. A Convenient Organic-Inorganic Hybrid Approach Toward Highly Stable Squaraine Dyes with Reduced H-Aggregation. *Adv. Funct. Mater.* **2012**, *22*, 345-352.

Appendix (AI)

Table A5.1. Below is a comparison table of recently published heavy-atom-free materials, highlighting their design strategies, structure-property relationships, and photosensitizing behaviors for PDT efficacy.

References		Present work			<i>J. Am. Chem. Soc.</i> 2019 , <i>141</i> , 16243-16248
Materials		THPIS	PPIS	API	MANI-S
AIE		Non-fluorescent (a)	Non-fluorescent (a)	Red AIEE _{gen} (a)	Non-fluorescent (b)
Stokes- shift (nm)		g	g	146	g
Φ_{PL}		g	g	0.85 (a)	g
Φ_{Δ}		0.29 (c)	0.11 (c)	g	1.00 (d)
Light used		50mWcm ⁻² (e)	50 mWcm ⁻² (e)	50 mWcm ⁻² (e)	100 mWcm ⁻² (e)
ROS	Types	Type-I, Type-II (¹ O ₂ , O ₂ ⁻)	Type-I (O ₂ ⁻)	Type-I (O ₂ ⁻)	Type-I, Type-II (¹ O ₂ , O ₂ ⁻)
	Specificity	Specific	Specific	Specific	Not very specific
Total ROS	DCFDA (μ M)	10	10	10	10

	T (min)	5	5	5	3
	I	1x10 ⁶	2.5x10 ⁵	5x10 ⁴	7.5x10 ⁴
ROS (mechanism)		DCFDA, ABDA, TA, ESR, Theoretical (ΔG , SOC), Band energy/NHE)	DCFDA, ABDA, TA, ESR, Theoretical (ΔG , SOC), Band energy/NHE)	DCFDA, ABDA, TA, ESR, Theoretical (ΔG , SOC), Band energy/NHE)	DCFDA, DPBF, DHE, Theoretical (SOC)
PDT (Cancer cell)	In vitro	Normoxia (Hela, MCF7, normal cell)	Normoxia (Hela, MCF7, normal cell)	g	Hypoxia (Hela cell)
	Selectivity	Selective	Selective	g	g
Liposome		x	x	g	Albumin
Design strategy		Structure-property relationship and application (H-aggregation unveiled PDT efficacy)			Application-based
		S-atom at the carbonyl and functional position			S-atom at the carbonyl position

a, b, c, and d, respectively, are the different solvent systems (a = 99% f_w, b = toluene, c = 99% PBS, and d = ethanol, respectively), whereas, e is the white light used for the photosensitization [g = not observed, x = not used (normal cell non-toxic)].

Table A5.2: Comparison of the blue-shifted $\lambda_{\text{abs.max}}$ with the reported data has demonstrated enhanced H-aggregation, which is crucial for PDT efficacy by boosting the SOC value.

References	Materials	Blue-shifted $\lambda_{\text{abs.max}}$ (nm)	H-aggregation
Present work	PPIS	89	Highly pronounced
	THPIS	76	Highly pronounced
	APIS	23	Moderate

a	<i>Adv. Mater.</i> 2022 , <i>34</i> , 210814	PTTe	74	Pronounced
		PTSe	71	Pronounced
		PTS	30	Moderate
b	<i>Nature Materials</i> 2015 , <i>14</i> , 685-690	DPhCzT	14	Moderate
b	<i>Nanoscale</i> 2016 , <i>8</i> , 17422-17426	(OB4) ₄	10	Moderate

a, b and c are the references 51, 35, and 36 present in the main manuscript.

Table A5.3: CIE coordinates for the **RPNI-O** and **RPNI-S** derivatives in solution, aggregated and solid state.

Materials	Solution		Aggregated		Solid	
	X	Y	X	Y	X	Y
PPI	0.562	0.437	0.638	0.36	0.689	0.31
THPI	0.635	0.364	0.644	0.355	0.725	0.274
API	0.504	0.493	0.617	0.382	0.684	0.315
PPIS	0.73	0.269	A	A	A	A
THPIS	0.724	0.275	A	A	A	A
APIS	0.734	0.265	A	A	A	A

A = not observed due to non-emissive characteristics.

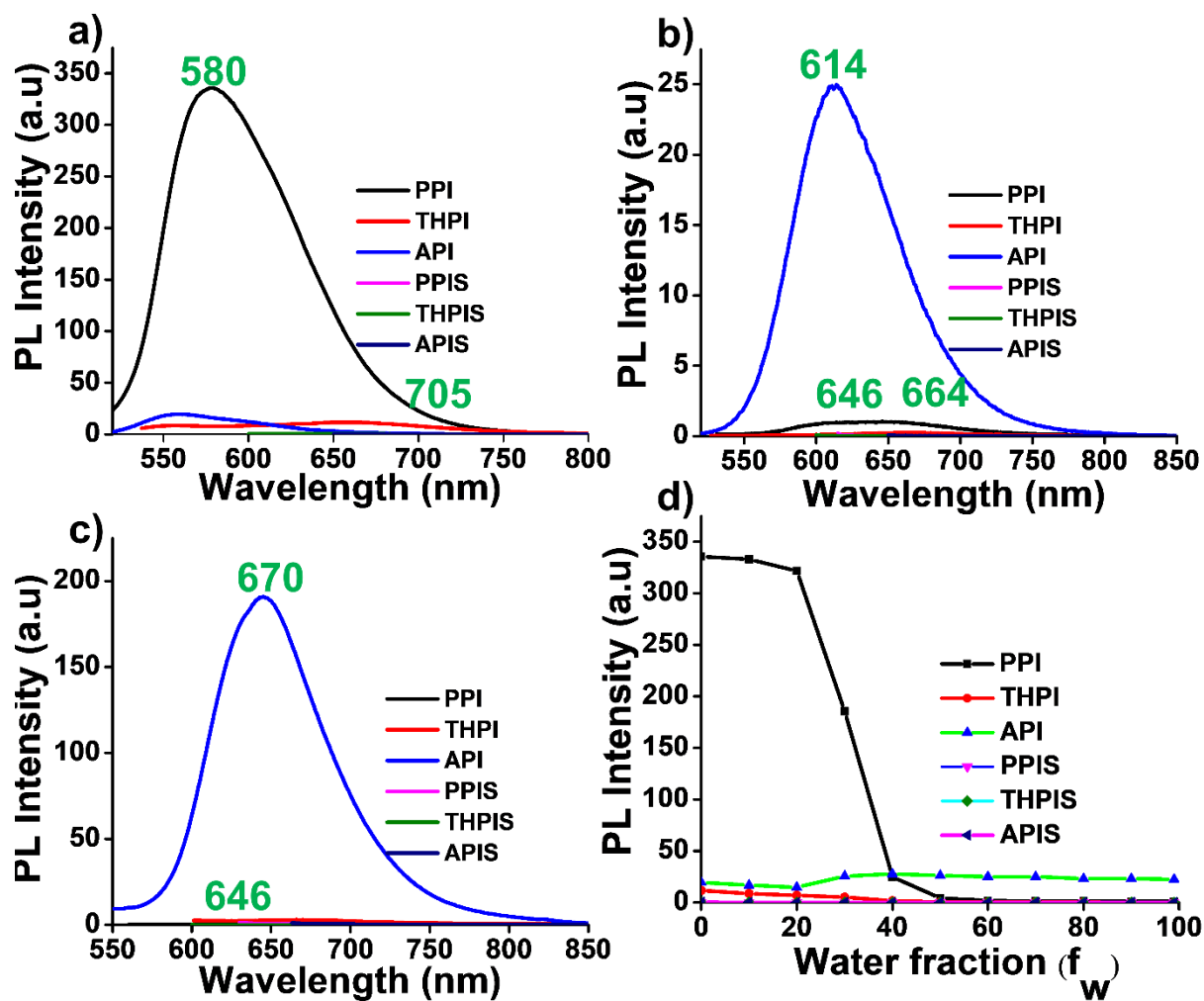


Figure A5.1. Photophysical characteristics of all the RPNI-O (PPI, THPI, and API) and RPNI-S (PPIS, THPIS, and APIS) derivatives. (a) The PL spectra in their solution state represent monomeric emission ($\lambda_{ex} = 500$ nm). (b) PL spectra in their aggregated-state (at 99% f_w in DMSO) ($\lambda_{ex} = 500$ nm). (c) Solid state PL spectra ($\lambda_{ex} = 500$ nm). (d) Fluorescence intensity plot at various f_w in DMSO at their corresponding $\lambda_{em,max}$.

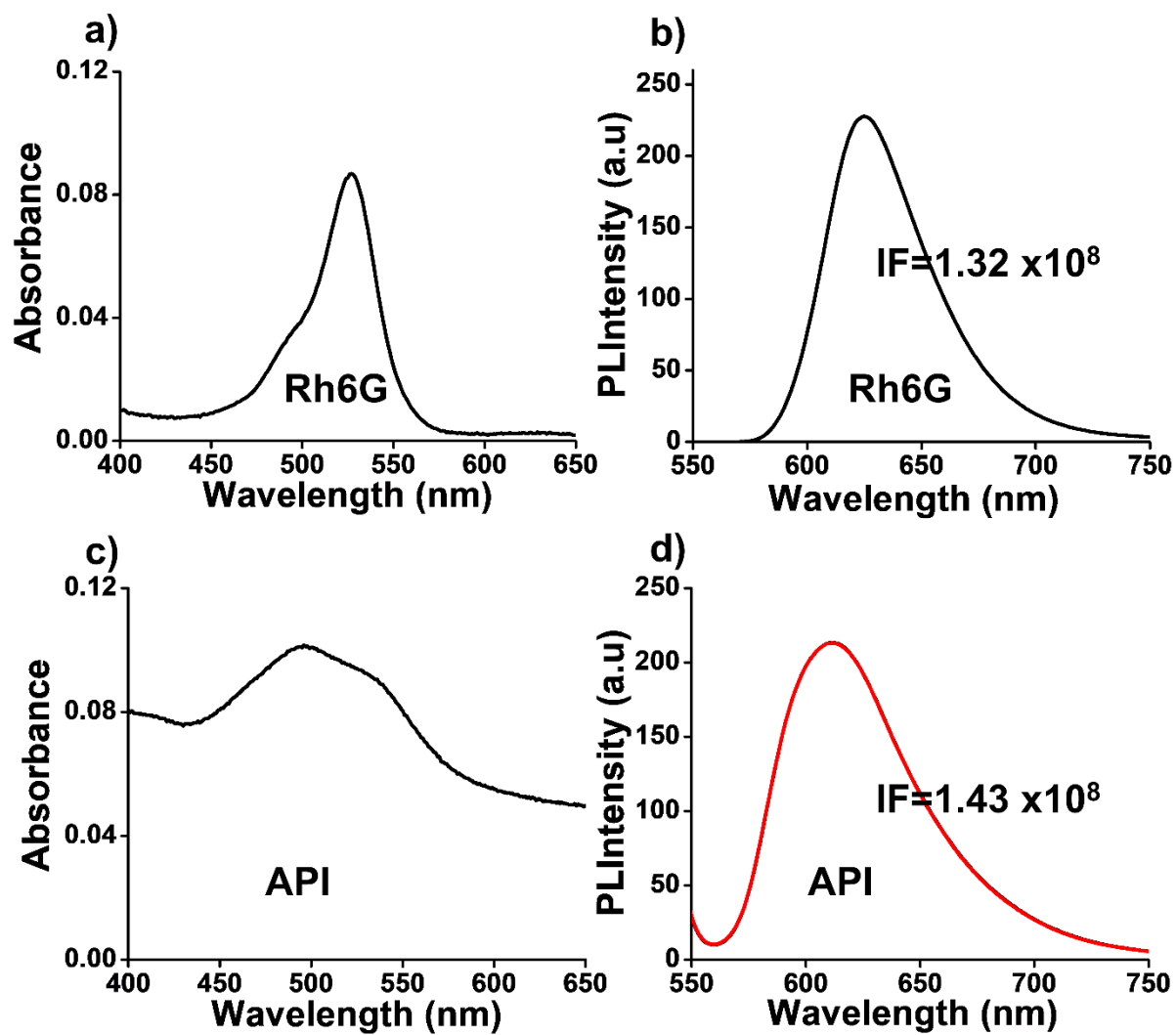


Figure A5.2. (a and b) The absorbance and emission peak area of rhodamine 6G. (c and d) The absorbance and emission peak area of API at 40% f_w in DMSO. IF: integrated fluorescence intensity.

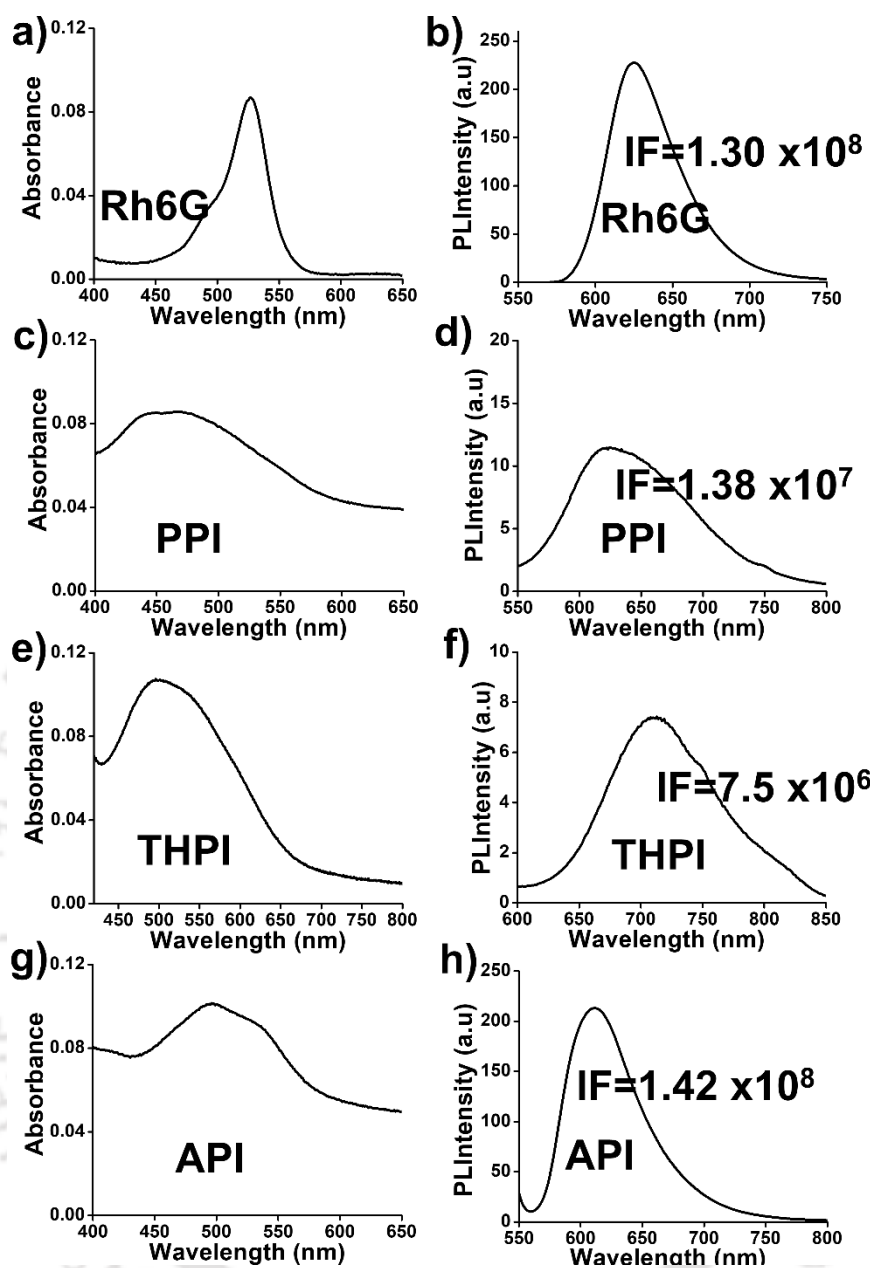


Figure A5.3. (a and b) The absorbance and emission peak area of rhodamine 6G. (c, d), (e, f) and (g, h) The absorbance and emission peak area of **PPI**, **THPI**, and **API** at 99% f_w in DMSO. IF: integrated fluorescence intensity. Rh6G represent rhodamine 6G.

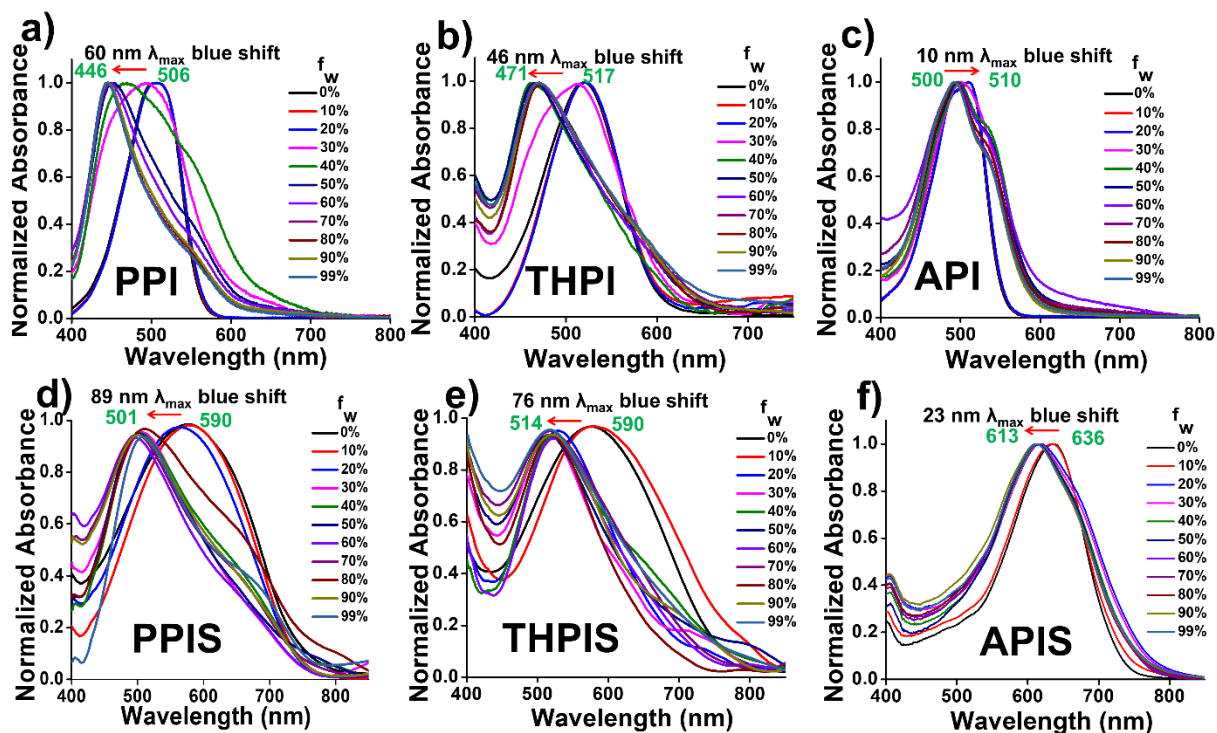


Figure A5.4. Normalized UV-vis spectra (a-c) of RPNI-O derivatives (PPI, THPI, and API), and (d-f) RPNI-S derivatives (PPIS, THPIS, and APIS) at various water fractions (f_w) in DMSO.

Table A5.4. UV-vis absorption data for the RPNI-O and RPNI-S derivatives.

Materials	Water fraction (f_w)	$\lambda_{\text{abs.max}}$ (nm)	A	$\Delta\lambda$ (nm)
PPI	0%	506	0.394105	60
	99%	446	0.159005	
THPI	0%	517	0.059899	46
	99%	471	0.021479	
API	0%	510	0.248319	10
	99%	500	0.151884	
PPIS	0%	590	0.053059	89

	99%	501	0.006136	
THPI	0%	580	0.030367	76
	99%	514	0.012369	
API	0%	636	0.37716	23
	99%	613	0.220526	

A , $\Delta\lambda$, are the absorbance and wavelength maxima shift in their absorption.

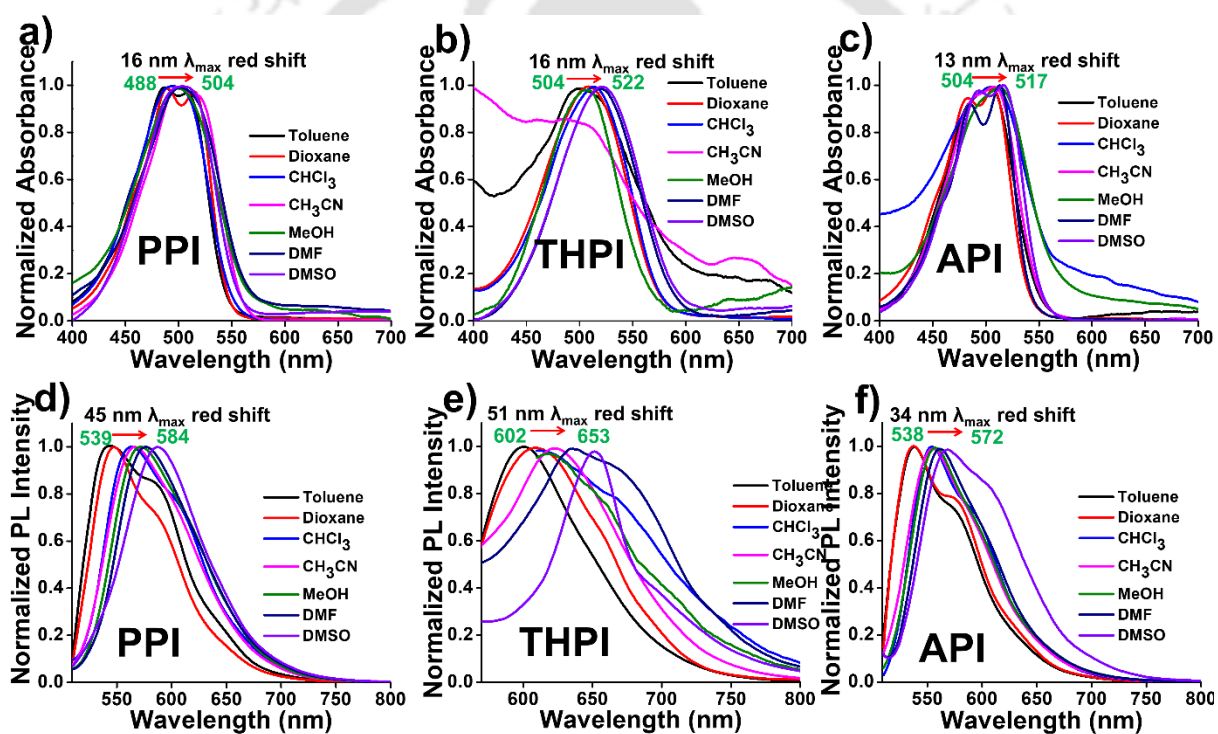


Figure A5.5. Solvatochromic effect of the **RPNI-O** derivatives. (a-c) Normalized absorbance, (d-f) Normalized fluorescence spectra of **PPI**, **THPI**, and **API** in various solvents from nonpolar to polar (100 μ M, λ_{ex} = 500 nm).

Table A5.5. The solvatochromic UV-vis data for the **RPNI-O** derivatives in various solvents from nonpolar to polar (100 μ M, λ_{ex} = 500 nm).

Materials	Solvents	$\lambda_{abs.max}$ (nm)	$\Delta\lambda$ (nm)
PPI	Toluene	488	16

	Dioxane	488	
	CHCl ₃	494	
	CH ₃ CN	497	
	MeOH	498	
	DMF	502	
	DMSO	504	
THPI	Toluene	504	16
	Dioxane	508	
	CHCl ₃	514	
	CH ₃ CN	514	
	MeOH	518	
	DMF	522	
	DMSO	522	
API	Toluene	504	13
	Dioxane	507	
	CHCl ₃	507	
	CH ₃ CN	507	
	MeOH	512	
	DMF	513	
	DMSO	517	

$\Delta\lambda$ is the wavelength maxima shift in their absorption.

Table A5.6. The solvatochromic PL data for the **RPNI-O** derivatives in various solvents from nonpolar to polar (100 μ M, $\lambda_{\text{ex}} = 500$ nm).

Materials	Solvents	$\lambda_{\text{em.max}}$ (nm)	$\Delta\lambda$ (nm)
PPI	Toluene	539	45
	Dioxane	547	
	CHCl ₃	562	
	CH ₃ CN	566	

	MeOH	573	
	DMF	578	
	DMSO	584	
THPI	Toluene	602	51
	Dioxane	609	
	CHCl ₃	611	
	CH ₃ CN	622	
	MeOH	623	
	DMF	631	
	DMSO	653	
API	Toluene	538	34
	Dioxane	539	
	CHCl ₃	554	
	CH ₃ CN	554	
	MeOH	559	
	DMF	559	
	DMSO	572	

$\Delta\lambda$, is the wavelength maxima shift in their absorption.

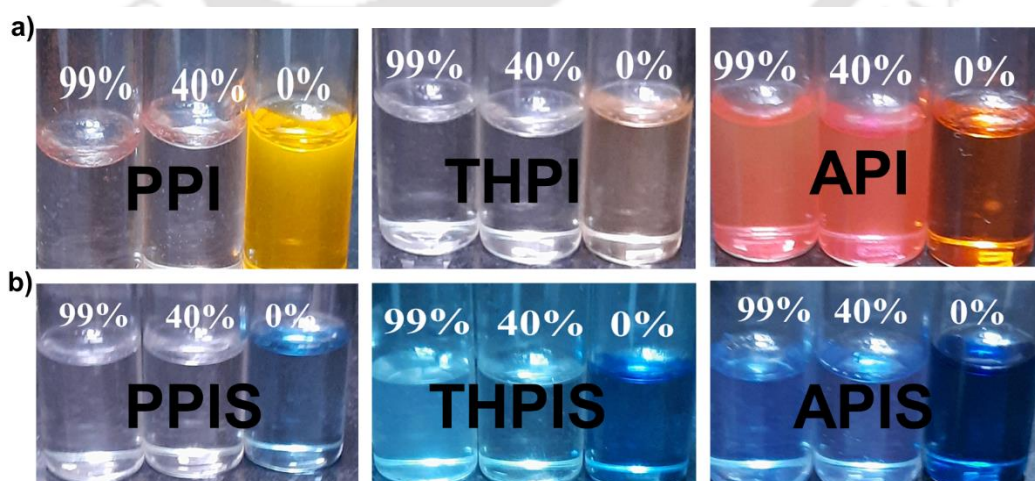


Figure A5.6. Capturing daylight photographs of **RPNI-O** derivatives (**PPI**, **THPI**, and **API**), and **RPNI-S** derivatives (**PPIS**, **THPIS**, and **APIS**), respectively at 0%, 40%, and 99% *f_w* in DMSO.

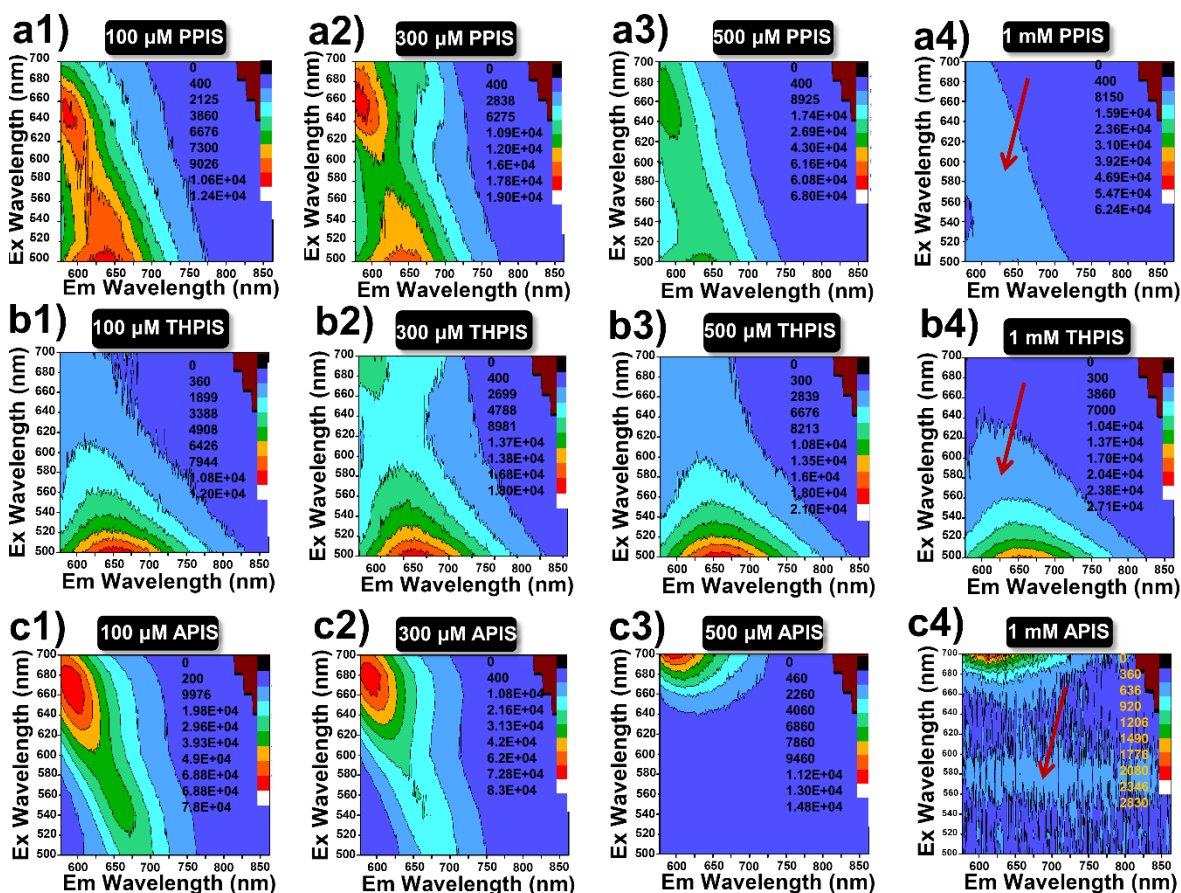


Figure A5.7. (a1-c4) 2D Excitation-emission (EEM) contour projections of the **RPNI-S** derivatives at different concentrations (left: 100 μM ; middle: 300 μM and 500 μM ; right: 1 mM) in DMSO.

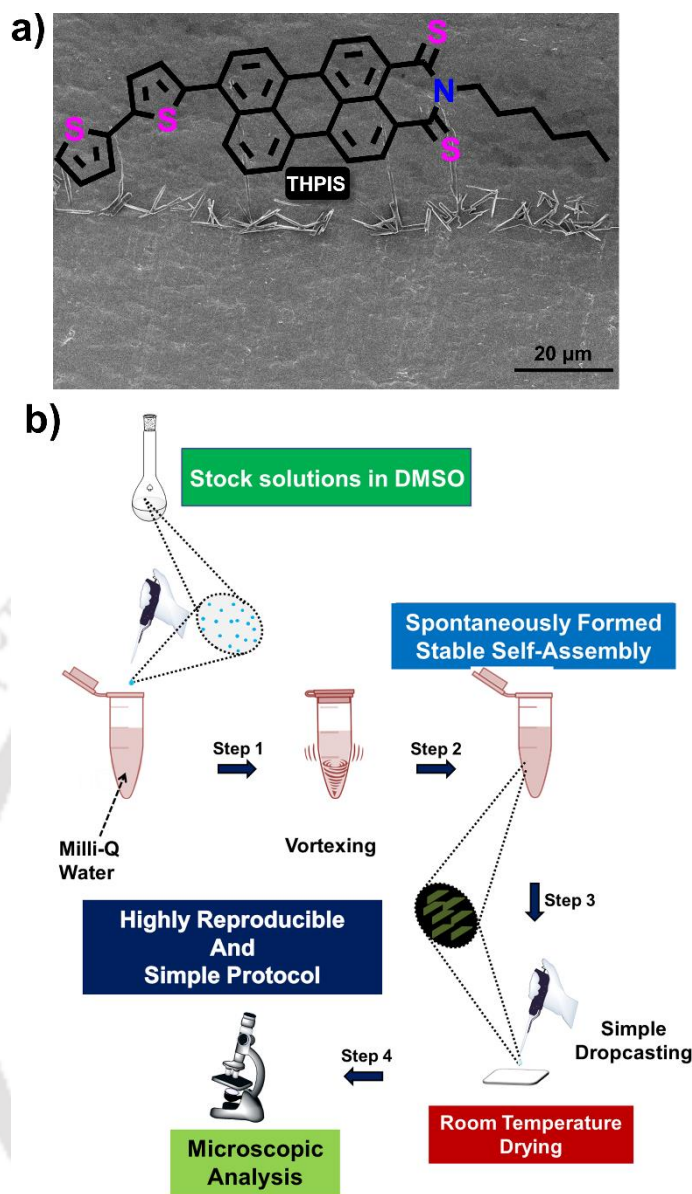


Figure A5.8. a) FESEM images of the micro-assembly of the **THPIS** spontaneously formed at 99.9% f_w in DMSO (100 μM) by a simple drop-casting technique on aluminum foil coated on a glass slide, followed by drying at room temperature, as graphically represented in b. b) Schematic illustration of the highly reproducible simple, cost-effective, and feasible strategy for the preparation of micro- and nano-supramolecular self-assembly from **RPNI-O** and **RPNI-S** derivatives.

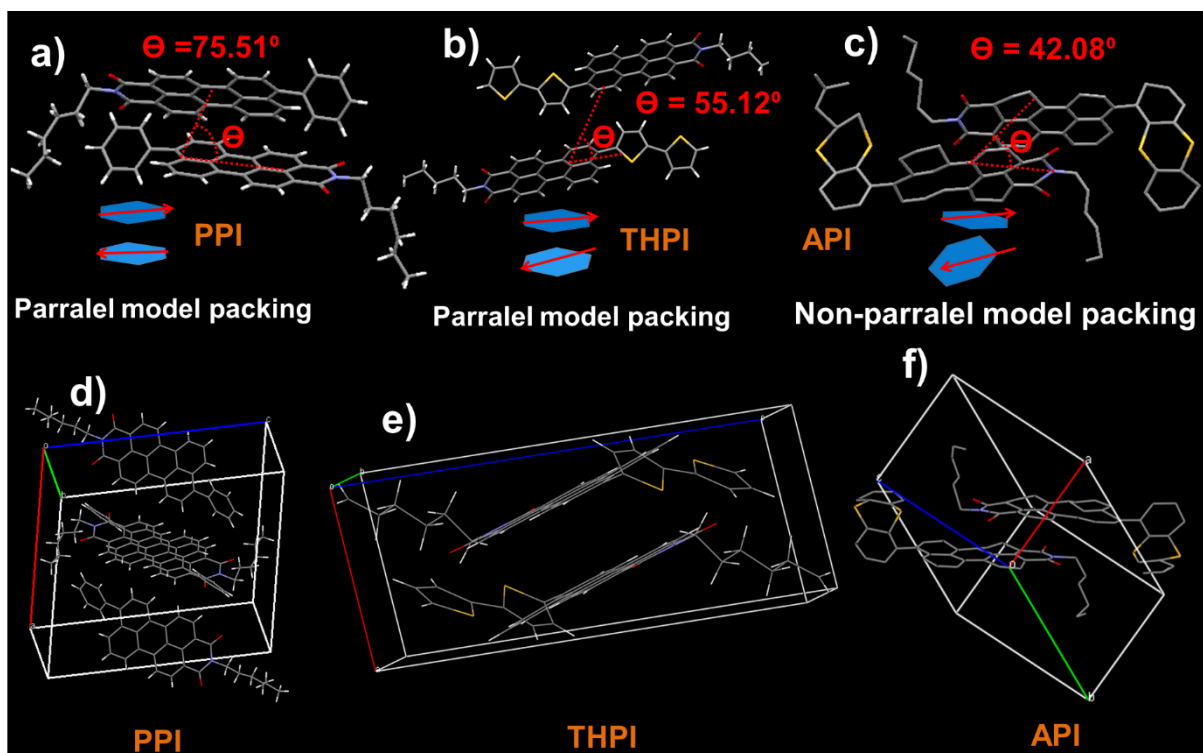


Figure A5.9. Single crystal structures of (a) **PPI**, (b) **THPI**, and (c) **API**, respectively showing evidence of H-aggregate formation in these molecules, corresponding to their schematic showing the π - π -stacking interaction among the **PNI-O** cores. The angle between the transition dipoles and the interconnected axis is indicated by θ . (d-f) single crystal unit cell of (d) **PPI**, (e) **THPI**, and (f) **API**, respectively.

Table A5.7. SCXRD data of the **RPNI-O** derivatives.

Name	PPI	THPI	API
Formula	$C_{34}H_{29}NO_2$	$C_{36}H_{27}NO_2S_2$	$C_{40}H_{29}NO_2S_2$
Formula weight	108.37	70.71	607.75
Wavelength (\AA)	0.71073	0.71073	0.71073
Space Group	P -1	P -1	P -1
Crystal System	triclinic	triclinic	triclinic

Temperature	293 (K)	293 (K)	293 (K)
Cell Lengths (Å)	a 17.6473(9)	a 7.3852(5)	a 8.766(6)
	b 7.5383(4)	b 11.7473(8)	b 11.916(8)
	c 18.6063(9)	c 16.5975(11)	c 15.464(11)
Cell Angles (°)	α 89.999(2)	α 83.044(2)	α 101.43(2)
	β 94.196(2)	β 84.880(2)	β 92.94(2)
	γ 90.014(2)	γ 77.501(2)	γ 111.20(2)
Cell Volume (Å³)	2468.6(2)	1392.51(16)	1462.8(18)
Z	1	2	2
Density (g/cm³)	0.418	0.361	1.380
F(000)	78	98	636
hmax, kmax, lmax	2,8,2	8,1,3	9,13,16

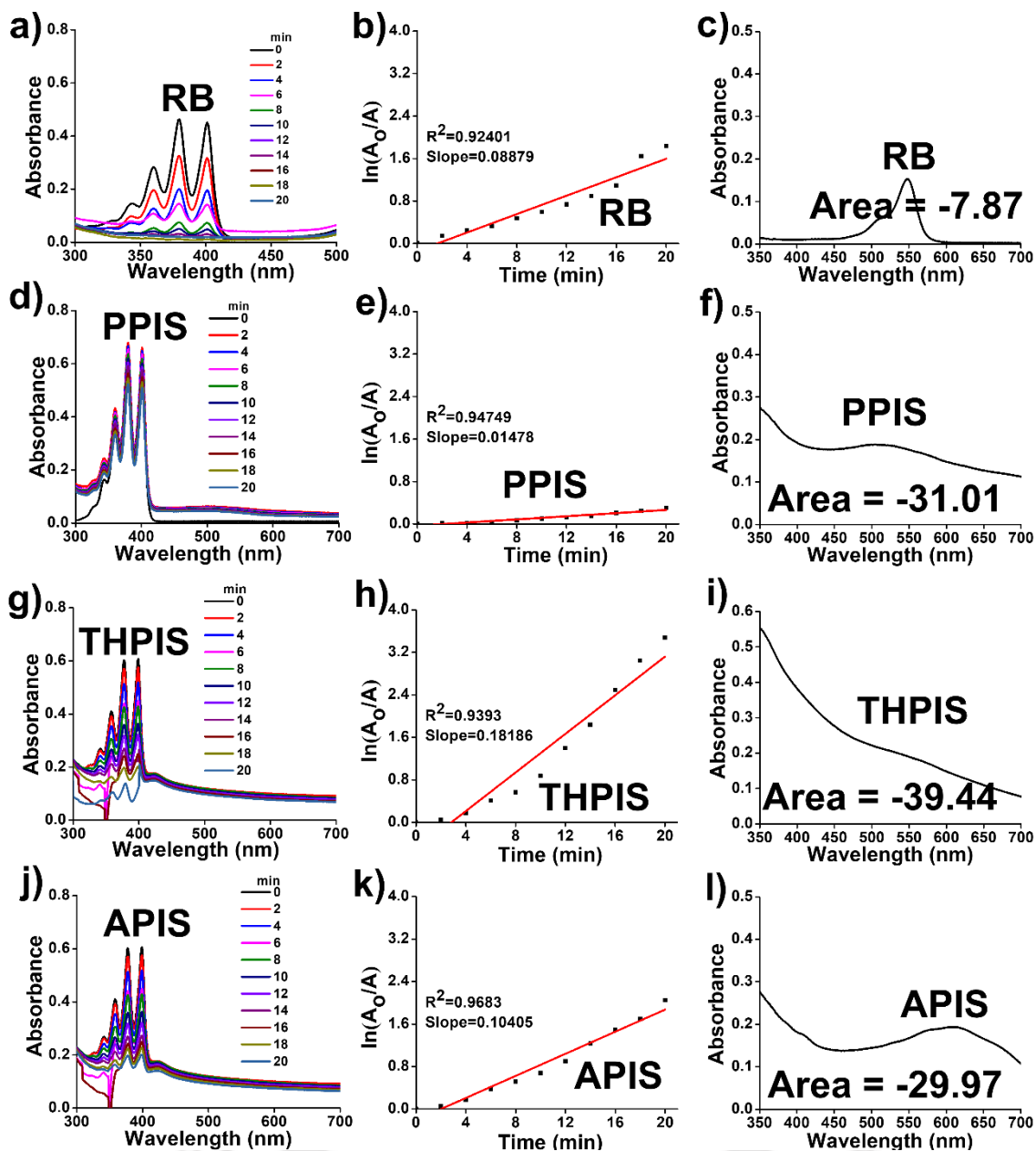


Figure A5.10. The ROS quantum yield of **RPNI-S** was determined through chemical trapping measurements. ABDA undergoing photodegradation with (a) Rose Bengal, (d) **PPIS**, (g) **THPIS**, and (j) **APIS**, respectively. Rate constants for the decomposition of ABDA in the presence of (b) Rose Bengal, (e) **PPIS**, (h) **THPIS**, and (k) **APIS**, respectively. The integrated area of the absorption peak for (c) Rose Bengal, (f) **PPIS**, (i) **THPIS**, and (l) **APIS**, respectively.

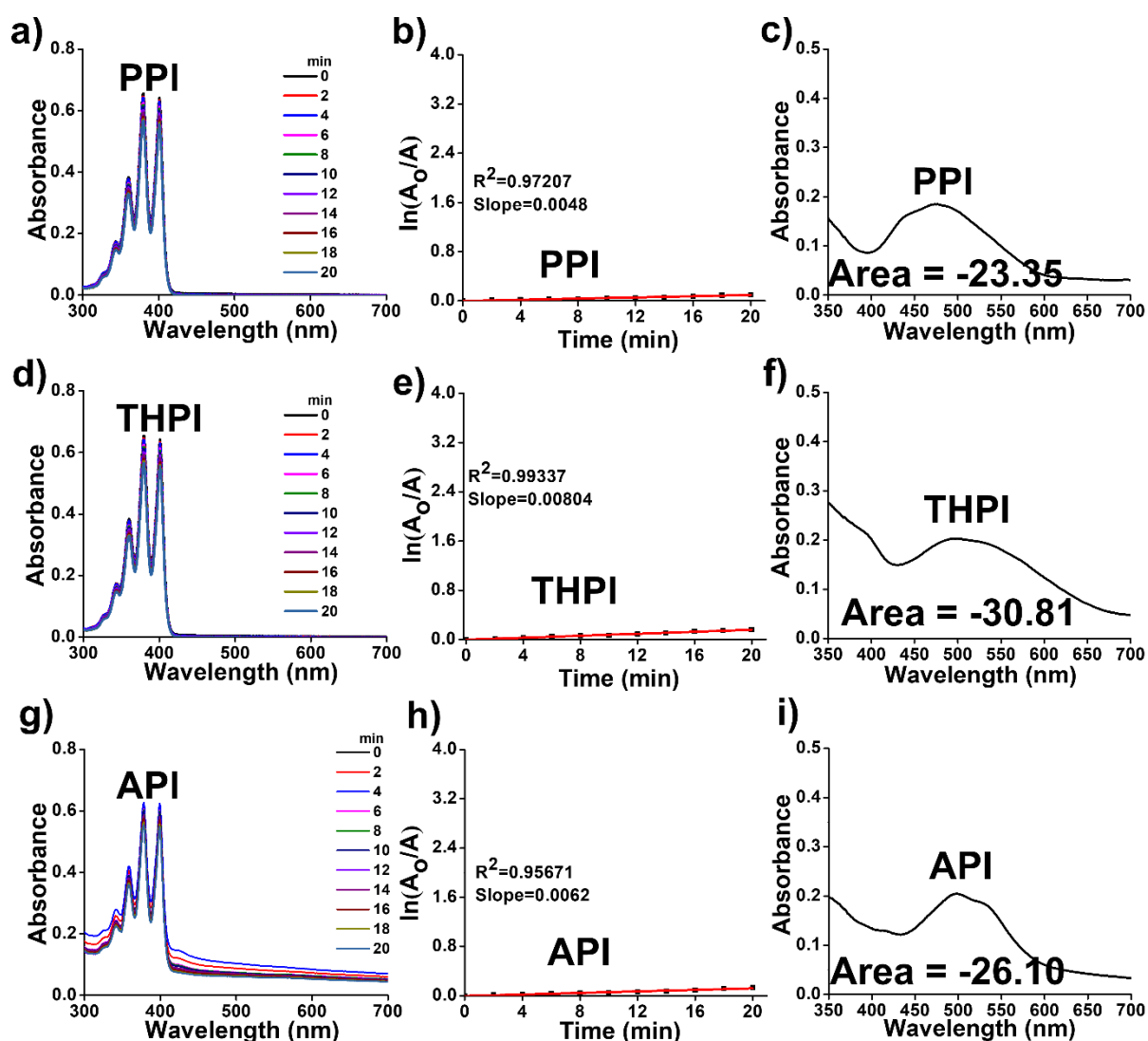


Figure A5.11. The ROS quantum yield of **RPNI-O** was determined through chemical trapping measurements. ABDA undergoing photodegradation with (a) **PPI**, (d) **THPI**, and (g) **API**, respectively. Rate constants for the decomposition of ABDA in the presence of (b) **PPI**, (e) **THPI**, and (h) **API**, respectively. The integrated area of the absorption peak for (c) **PPI**, (f) **THPI**, and (i) **API**, respectively.

Table A5.8. Spin-orbit coupling matrix elements (SOCMEs) of **PPIS** compound in optimized structure. $\langle S_m | H_{so} | T_n \rangle$, cm^{-1} and ΔE_{ST} , eV calculated using ORCA 5.0 at the B3LYP/6-31G (d, p) and B3LYP/DEF2SVP level.

Excite state electronic transition	ΔE_{ST} (eV)	SOC (cm^{-1})
S₁↔T₁	0.402	8.33
S₁↔T₂	0.205	3.00
S₂↔T₁	0.794	6.53

S₂↔T₂	0.597	4.16
S₂↔T₃	0.251	7.24
S₂↔T₄	0.096	10.80
S₃↔T₂	0.99	7.88
S₃↔T₃	0.637	5.46
S₃↔T₄	0.482	4.25
S₄↔T₄	0.99	6.00
S₄↔T₅	0.637	1.34
S₄↔T₆	0.482	0.75
S₅↔T₅	0.681	3.01
S₅↔T₆	0.36	3.69
S₅↔T₇	0.16	2.63
S₅↔T₈	0.092	1.25
S₅↔T₉	0.046	5.01
S₅↔T₁₀	0.02	6.57
S₆↔T₅	0.72	5.09
S₆↔T₆	0.3990	6.16
S₆↔T₇	0.199	5.20
S₆↔T₈	0.131	3.08
S₆↔T₉	0.085	2.43
S₆↔T₁₀	0.059	1.76
S₇↔T₅	0.754	6.54
S₇↔T₆	0.44	6.50
S₇↔T₇	0.233	9.16
S₇↔T₈	0.165	3.02
S₇↔T₉	0.119	1.32
S₇↔T₁₀	0.093	3.01
S₈↔T₅	0.864	1.18

S₈↔T₆	0.543	2.05
S₈↔T₇	0.343	2.62
S₈↔T₈	0.275	0.88
S₈↔T₉	0.229	5.74
S₈↔T₁₀	0.203	4.75
S₉↔T₅	0.905	1.38
S₉↔T₆	0.584	1.99
S₉↔T₇	0.384	1.57
S₉↔T₈	0.316	1.09
S₉↔T₉	0.27	2.65
S₉↔T₁₀	0.244	4.32
S₁₀↔T₇	0.46	2.79
S₁₀↔T₈	0.392	1.34
S₁₀↔T₉	0.346	4.79
S₁₀↔T₁₀	0.32	3.83

Table A5.9. SOCMEs of **THPIS** compound in optimized structure. $\langle S_m | H_{SO} | T_n \rangle$, cm^{-1} and ΔE_{ST} , eV calculated using ORCA 5.0 at the B3LYP/6-31G (d, p) and B3LYP/DEF2SVP level.

Excite state electronic transition	ΔE_{ST} (eV)	SOC (cm^{-1})
S₁↔T₁	0.418	6.90
S₁↔T₂	0.202	2.32
S₂↔T₁	0.81	5.49
S₂↔T₂	0.594	5.15
S₂↔T₃	0.247	6.14
S₂↔T₄	0.094	9.20
S₃↔T₂	0.798	5.47
S₃↔T₃	0.451	3.75

S₃↔T₄	0.298	2.70
S₃↔T₅	0.017	0.60
S₃↔T₃	0.857	4.90
S₄↔T₄	0.704	3.61
S₄↔T₅	0.423	0.65
S₄↔T₆	0.043	0.44
S₅↔T₄	0.892	4.91
S₅↔T₅	0.611	1.65
S₅↔T₆	0.231	0.87
S₅↔T₇	0.054	0.52
S₆↔T₅	0.921	3.56
S₆↔T₆	0.541	5.97
S₆↔T₇	0.364	4.40
S₆↔T₈	0.227	3.92
S₆↔T₉	0.075	3.02
S₆↔T₁₀	0.046	1.91
S₇↔T₅	0.98	2.14
S₇↔T₆	0.60	3.32
S₇↔T₇	0.423	3.29
S₇↔T₈	0.286	3.00
S₇↔T₉	0.134	5.45
S₇↔T₁₀	0.105	0.80
S₈↔T₆	0.649	2.74
S₈↔T₇	0.472	4.14
S₈↔T₈	0.3350	4.50
S₈↔T₉	0.183	0.57
S₈↔T₁₀	0.154	0.75
S₉↔T₆	0.724	2.13

S₉↔T₇	0.547	1.57
S₉↔T₈	0.41	2.00
S₉↔T₉	0.258	4.21
S₉↔T₁₀	0.229	1.41
S₁₀↔T₆	0.826	1.14
S₁₀↔T₇	0.649	0.80
S₁₀↔T₈	0.512	0.88
S₁₀↔T₉	0.36	2.33
S₁₀↔T₁₀	0.331	0.44

Table A5.10. SOCMs of **APIS** compound in optimized structure. $\langle S_m | H_{SO} | T_n \rangle$, cm^{-1} and ΔE_{ST} , eV calculated using ORCA 5.0 at the B3LYP/6-31G (d, p) and B3LYP/DEF2SVP level.

Excite state electronic transition	ΔE_{ST} (eV)	SOC (cm^{-1})
S₁↔T₁	0.386	4.44
S₁↔T₂	0.207	1.62
S₂↔T₁	0.778	6.37
S₂↔T₂	0.599	4.47
S₂↔T₃	0.253	3.83
S₂↔T₄	0.098	5.73
S₃↔T₂	0.907	2.36
S₃↔T₃	0.561	2.58
S₃↔T₄	0.406	2.16
S₄↔T₃	0.682	5.63
S₄↔T₄	0.527	4.34
S₄↔T₅	0.121	2.16
S₅↔T₄	0.916	3.63
S₅↔T₅	0.51	1.34

S₅↔T₆	0.311	1.46
S₅↔T₇	0.034	0.42
S₆↔T₄	0.958	1.61
S₆↔T₅	0.552	2.18
S₆↔T₆	0.353	1.00
S₆↔T₇	0.076	0.52
S₇↔T₅	0.897	1.47
S₇↔T₆	0.698	3.49
S₇↔T₇	0.421	2.96
S₇↔T₈	0.325	2.54
S₇↔T₉	0.161	1.60
S₇↔T₇	0.128	0.20
S₈↔T₅	0.911	1.11
S₈↔T₆	0.712	4.25
S₈↔T₇	0.435	3.15
S₈↔T₈	0.339	2.94
S₈↔T₉	0.175	1.71
S₈↔T₁₀	0.142	3.28
S₉↔T₅	0.956	1.89
S₉↔T₆	0.757	2.57
S₉↔T₇	0.48	1.85
S₉↔T₈	0.384	1.88
S₉↔T₉	0.22	1.36
S₉↔T₁₀	0.187	3.04
S₁₀↔T₆	0.853	1.16
S₁₀↔T₇	0.576	0.77
S₁₀↔T₈	0.48	0.97
S₁₀↔T₉	0.316	0.69

S₁₀↔T₁₀	0.283	2.04
--------------------------------------	-------	------

Table A5.11. SOCMs of **PPI** compound in optimized structure. $\langle S_m | H_{SO} | T_n \rangle$, cm^{-1} and ΔE_{ST} , eV calculated using ORCA 5.0 at the B3LYP/6-31G (d, p) and B3LYP/DEF2SVP level.

Excite state electronic transition	ΔE_{ST} (eV)	SOC (cm^{-1})
S₁↔T₁	1.196	0.3
S₁↔T₂	-0.17	0.77
S₂↔T₁	1.678	3.70
S₂↔T₂	0.305	2.14
S₂↔T₃	0.207	2.39
S₂↔T₄	0.19	3.53
S₂↔T₅	0.048	3.72
S₃↔T₂	0.609	0.39
S₃↔T₃	0.511	1.93
S₃↔T₄	0.352	0.95
S₃↔T₅	0.21	1.56
S₄↔T₃	0.576	3.81
S₄↔T₄	0.559	1.51
S₄↔T₅	0.417	3.22
S₄↔T₆	0.275	2.14
S₄↔T₇	0.143	1.89
S₄↔T₈	0.174	3.69
S₄↔T₉	0.083	3.13
S₄↔T₁₀	0.024	0.78
S₅↔T₄	0.594	2.45
S₅↔T₅	0.452	3.54
S₅↔T₆	0.31	3.00

S₅↔T₇	0.209	0.88
S₅↔T₈	0.178	2.49
S₅↔T₉	0.118	2.77
S₅↔T₁₀	0.059	0.95
S₆↔T₅	0.53	3.17
S₆↔T₆	0.388	3.12
S₆↔T₇	0.287	1.67
S₆↔T₈	0.256	1.23
S₆↔T₉	0.196	1.74
S₆↔T₁₀	0.137	0.79
S₇↔T₅	0.585	2.62
S₇↔T₆	0.443	2.64
S₇↔T₇	0.342	1.49
S₇↔T₈	0.311	1.54
S₇↔T₉	0.251	1.32
S₇↔T₁₀	0.192	0.59
S₈↔T₆	0.522	2.35
S₈↔T₇	0.421	1.92
S₈↔T₈	0.39	2.75
S₈↔T₉	0.33	1.58
S₈↔T₁₀	0.271	0.35
S₉↔T₆	0.614	2.07
S₉↔T₇	0.513	3.03
S₉↔T₈	0.482	2.49
S₉↔T₉	0.422	1.32
S₉↔T₁₀	0.363	0.26
S₁₀↔T₆	0.642	2.67
S₁₀↔T₇	0.541	2.15

S₁₀↔T₈	0.51	3.07
S₁₀↔T₉	0.45	1.58
S₁₀↔T₁₀	0.391	0.35

Table A5.12. SOCMEs of **THPI** compound in optimized structure. $\langle S_m | H_{SO} | T_n \rangle$, cm^{-1} and ΔE_{ST} , eV calculated using ORCA 5.0 at the B3LYP/6-31G (d, p) and B3LYP/DEF2SVP level.

Excite state electronic transition	ΔE_{ST} (eV)	SOC (cm^{-1})
S₁↔T₁	0.981	0.65
S₁↔T₂	0.036	0.85
S₂↔T₁	1.442	0.91
S₂↔T₂	0.497	0.74
S₃↔T₂	0.761	2.33
S₃↔T₃	0.257	1.33
S₃↔T₄	0.203	1.07
S₃↔T₅	0.176	0.3
S₃↔T₆	0.153	1.85
S₃↔T₇	0.04	3.37
S₄↔T₃	0.554	0.32
S₄↔T₄	0.50	1.47
S₄↔T₅	0.473	0.92
S₄↔T₆	0.45	0.47
S₄↔T₇	0.337	1
S₄↔T₈	0.184	0.4
S₄↔T₉	0.091	0.97
S₄↔T₁₀	0.05	1.66
S₅↔T₄	0.568	2.26
S₅↔T₅	0.541	1.55

S₅↔T₆	0.518	1.07
S₅↔T₇	0.405	1.36
S₅↔T₈	0.252	0.51
S₅↔T₉	0.159	1.63
S₅↔T₁₀	0.118	2.25
S₆↔T₅	0.56	2.67
S₆↔T₆	0.537	2.01
S₆↔T₇	0.424	3.44
S₆↔T₈	0.271	2.55
S₆↔T₉	0.178	1.81
S₆↔T₁₀	0.137	3.50
S₇↔T₅	0.683	1.90
S₇↔T₆	0.66	1.58
S₇↔T₇	0.547	2.98
S₇↔T₈	0.394	3.06
S₇↔T₉	0.301	1.54
S₇↔T₁₀	0.26	0.51
S₈↔T₆	0.687	0.37
S₈↔T₇	0.574	0.24
S₈↔T₈	0.421	0
S₈↔T₉	0.328	0.32
S₈↔T₁₀	0.287	0.2
S₉↔T₆	0.728	1.59
S₉↔T₇	0.651	1.68
S₉↔T₈	0.462	1.55
S₉↔T₉	0.369	1.82
S₉↔T₁₀	0.328	1.73
S₁₀↔T₆	0.783	0.87

S₁₀↔T₇	0.67	1.08
S₁₀↔T₈	0.517	1.84
S₁₀↔T₉	0.424	1.65
S₁₀↔T₁₀	0.383	2.07

Table A5.13. SOCMEs of API compound in optimized structure. $\langle S_m | H_{SO} | T_n \rangle$, cm^{-1} and ΔE_{ST} , eV calculated using ORCA 5.0 at the B3LYP/6-31G (d, p) and B3LYP/DEF2SVP level.

Excite state electronic transition	ΔE_{ST} (eV)	SOC (cm^{-1})
S₁↔T₁	1.015	1.920
S₁↔T₂	0.003	0.57
S₂↔T₁	1.238	0.87
S₂↔T₂	0.226	2.36
S₃↔T₂	0.551	2.18
S₃↔T₃	0.141	0.69
S₃↔T₄	0.116	0.223
S₃↔T₅	0.096	0.47
S₄↔T₃	0.234	2.04
S₄↔T₄	0.209	1.87
S₄↔T₅	0.189	2.43
S₄↔T₆	0.087	3.13
S₄↔T₇	0.041	2.97
S₅↔T₄	0.571	1.95
S₅↔T₅	0.551	0.28
S₅↔T₆	0.449	0.48
S₅↔T₇	0.403	0.77
S₅↔T₈	0.265	0.39
S₅↔T₉	0.167	0.96

S5↔T10	0.122	1.43
S6↔T5	0.571	2.87
S6↔T6	0.469	1.84
S6↔T7	0.423	1.76
S6↔T8	0.285	1.67
S6↔T9	0.187	0.97
S6↔T10	0.142	2.23
S7↔T5	0.694	2.93
S7↔T6	0.592	1.42
S7↔T7	0.546	1.61
S7↔T8	0.408	1.89
S7↔T9	0.31	1.23
S7↔T10	0.265	0.74
S8↔T6	0.619	0.93
S8↔T7	0.573	0.85
S8↔T8	0.435	1.22
S8↔T9	0.337	0.84
S8↔T10	0.292	0.81
S9↔T6	0.692	0.56
S9↔T7	0.646	0.75
S9↔T8	0.508	1.36
S9↔T9	0.41	1.47
S9↔T10	0.365	1.72
S10↔T6	0.735	0.49
S10↔T7	0.689	0.56
S10↔T8	0.551	1.09
S10↔T9	0.453	1.13
S10↔T10	0.408	1.45

Table A5.14a. Comparison of the SOCMEs with the most probable lowest excited singlet and triplet state transitions is conducted using the optimized isolated structures of previously reported PSs and conventional organic materials.

	References	Materials	SOC (cm ⁻¹)
	Present work	PPIS	10.88
		THPIS	9.20
		APIS	5.73
a	<i>Adv. Mater.</i> 2022 , 34, 2108146.	PTTe	0.28
9	<i>Angew. Chem. Int. Ed.</i> 2018 , 57, 7997-8001.	o-MCBA	0.624
10	<i>ACS Nano</i> 2019 , 13, 11283-11293.	TPAPyPF6	0.648015
b	<i>ACS Nano</i> 2020 , 14, 16840-16853.	TPE-PTB	4.53
11	<i>ACS Nano</i> 2021 , 15, 7328-7339.	MeTIN	1.242
12	<i>Chem. Sci.</i> 2020 , 11, 10921-10927.	PTP	0.04
c	<i>J. Mater. Chem. B.</i> 2022 , 10, 6228-6236.	gem-OMe-TPE-1CUM	0.340
d	<i>Nanoscale</i> 2016 , 8, 17422-17426	(OB4) ₁	0.42
13	<i>Phys. Chem. Chem. Phys.</i> 2023 , 25, 24386-24394.	BODIPY heterodimers	0.74
14	<i>J. Phys. Chem. A</i> 2007, 111, 10490-10499.	monoaza[5]helicenes	0.1-3.0

15	<i>J. Phys. Chem. C.</i> 2023 , 127, 2694-2704.	BT ₂ O ₃ Cz	0.462
e	<i>Biomaterials</i> 2021 , 275, 120934.	TPAIN	0.7250
f	<i>Phys. Chem. Chem. Phys.</i> , 2015, 17, 11350-11358.	intra-cyclic selenium (selenine)	11.94

a, b, c, d, e, and f correspond to references 51, 50, 63, 36, 62, and 60, respectively, present in the main manuscript.

Table A5.14b. Calculated different excite state singlet (S) and triplet (T) state energy of the **RPNI-O** and **RPNI-S** derivatives via ORCA 5.0 at the B₃LYP/6-31G (d, p) and B₃LYP/DEF2SVP level.

Materials	S (eV)										T (eV)									
	S ₁	S ₂	S ₃	S ₄	S ₅	S ₆	S ₇	S ₈	S ₉	S ₁₀	T ₁	T ₂	T ₃	T ₄	T ₅	T ₆	T ₇	T ₈	T ₉	T ₁₀
PPIS	1.61	2.004	2.390	2.811	3.147	3.186	3.220	3.330	3.371	3.447	1.210	1.407	1.753	1.908	2.466	2.787	2.987	3.055	3.101	3.127
THPIS	1.595	1.987	2.191	2.597	2.785	3.095	3.154	3.203	3.278	3.380	1.177	1.393	1.740	1.893	2.174	2.554	2.731	2.868	3.020	3.049
APIS	1.613	2.005	2.313	2.434	2.823	2.865	3.210	3.224	3.269	3.365	1.227	1.406	1.752	1.907	2.313	2.512	2.789	2.885	3.049	3.082
PPI	2.677	3.152	3.456	3.521	3.556	3.634	3.689	3.768	3.860	3.888	1.474	2.847	2.945	2.962	3.104	3.246	3.347	3.378	3.438	3.497
THPI	2.403	2.864	3.128	3.425	3.493	3.512	3.635	3.662	3.703	3.758	1.422	2.367	2.871	2.925	2.952	2.975	3.088	3.241	3.334	3.375
API	2.513	2.736	3.061	3.154	3.516	3.536	3.659	3.686	3.759	3.802	1.498	2.510	2.920	2.945	2.965	3.067	3.113	3.251	3.349	3.394

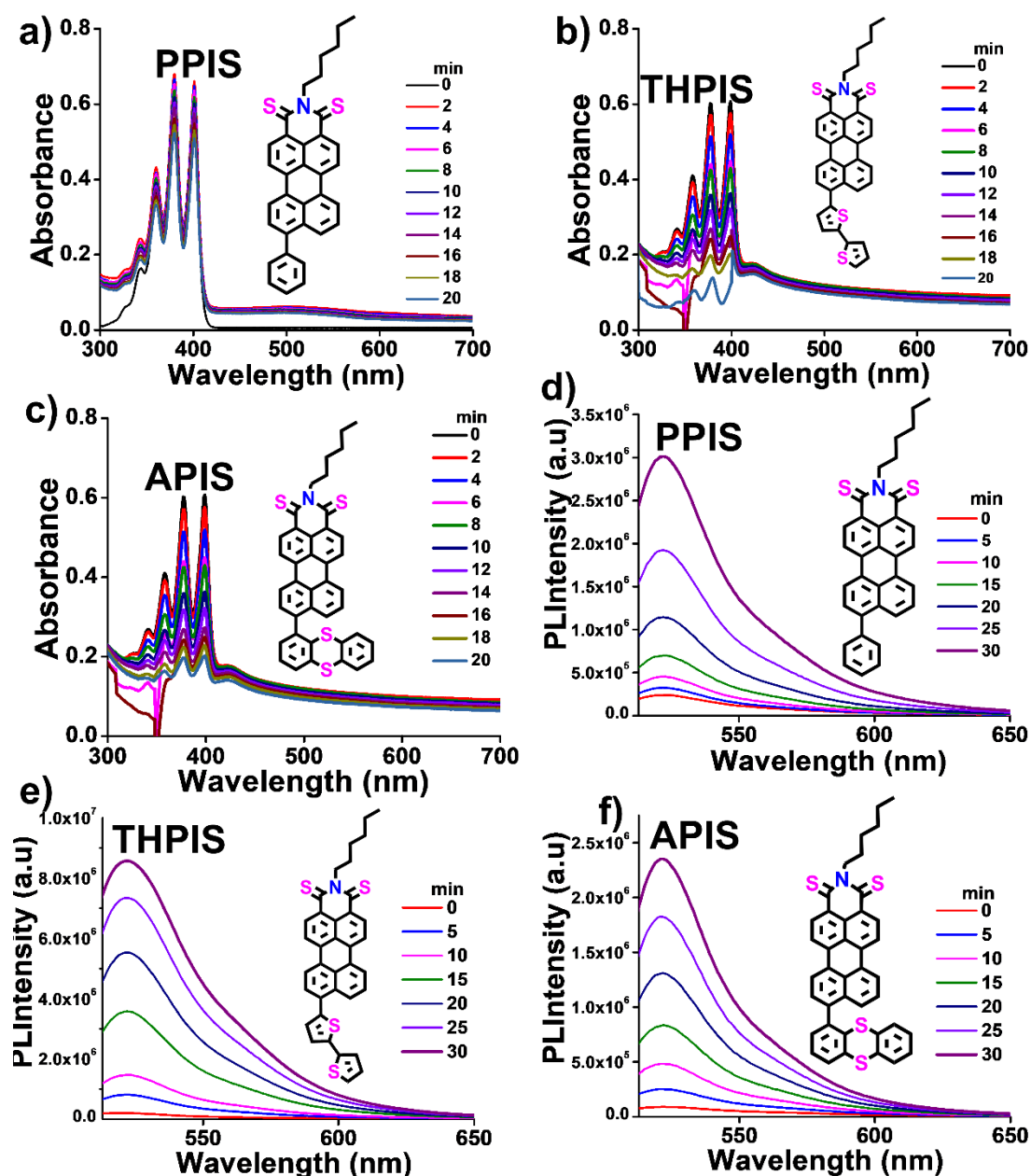


Figure A5.12. ROS generation by the **RPNI-S** derivatives. (a-c) Plots of ABDA (100 μ M) degradation rates at $\lambda_{\text{abs.max}}$ of 378 nm by the various PSs (100 μ M) (a) **PPIS**, (b) **THPIS**, and (c) **APIS**, respectively and (d-f) Evaluation of the general ROS generation using DCFDA (10 μ M) indicator by PSs (100 μ M) (d) **PPIS**, (e) **THPIS** and (f) **APIS**, respectively upon white light excitation for different time periods at 99% PBS fraction in DMSO ($\lambda_{\text{ex}}=500$ nm). Inset: Chemical structure of the **RPNI-S** derivatives.

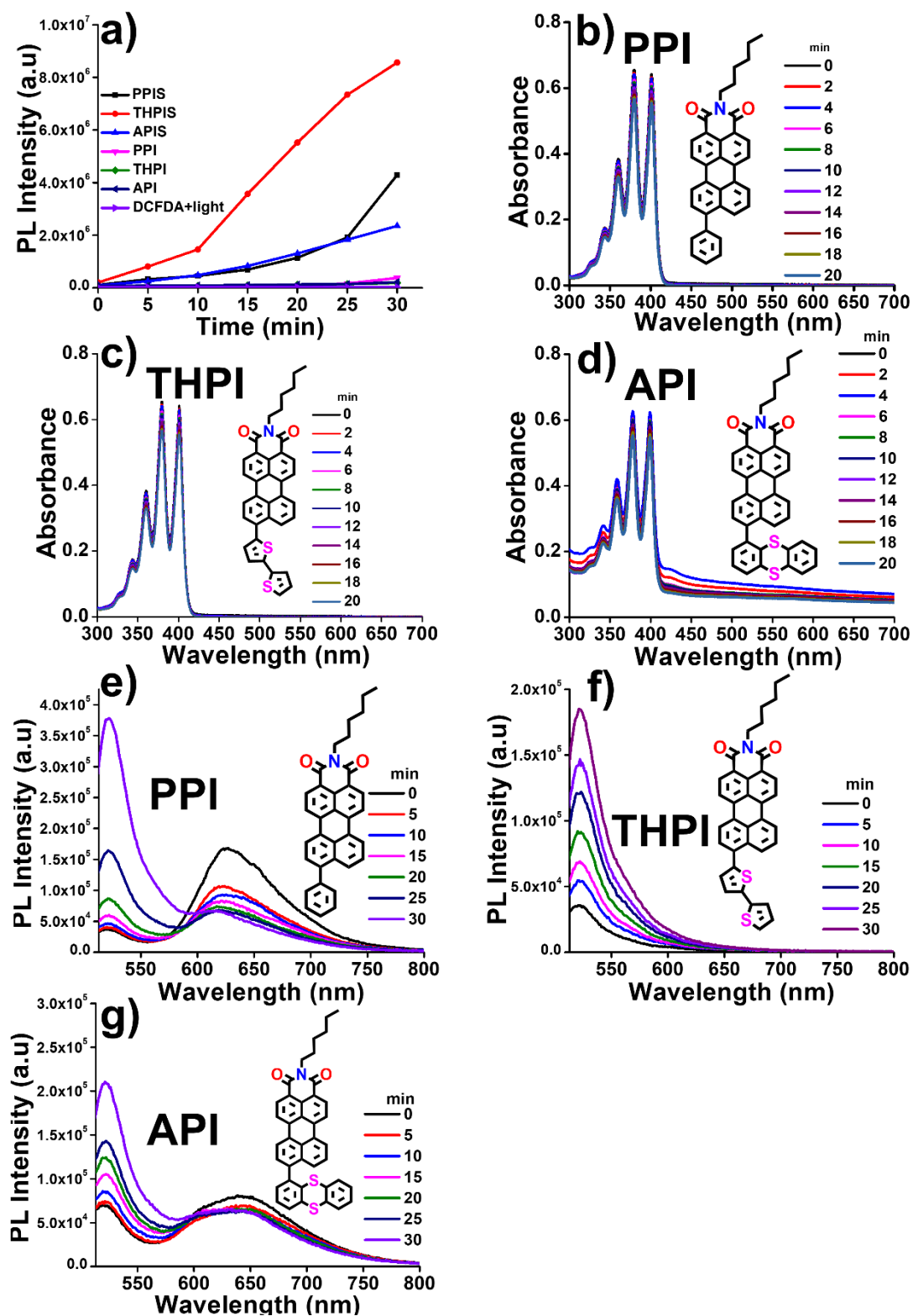


Figure A5.13. (a) Plot of fluorescence intensities of DCFDA indicator in the presence of the **RPNI-O** and **RPNI-S** derivatives, respectively. ROS generation by the **RPNI-O** derivatives. (b-d) Plots of ABDA (100 μM) degradation rates at $\lambda_{\text{abs,max}}$ of 378 nm by the various PSs (100 μM) (b) **PPI**, (c) **THPI**, and (d) **API**, respectively and (e-g) Evaluation of the general ROS generation using DCFDA (10 μM) indicator by PSs (100 μM) (e) **PPI**, (f) **THPI** and (g) **API**, respectively upon white light excitation for different time periods at 99% PBS fraction in DMSO ($\lambda_{\text{ex}}=500$ nm). Inset: Chemical structure of the **RPNI-O** derivatives.

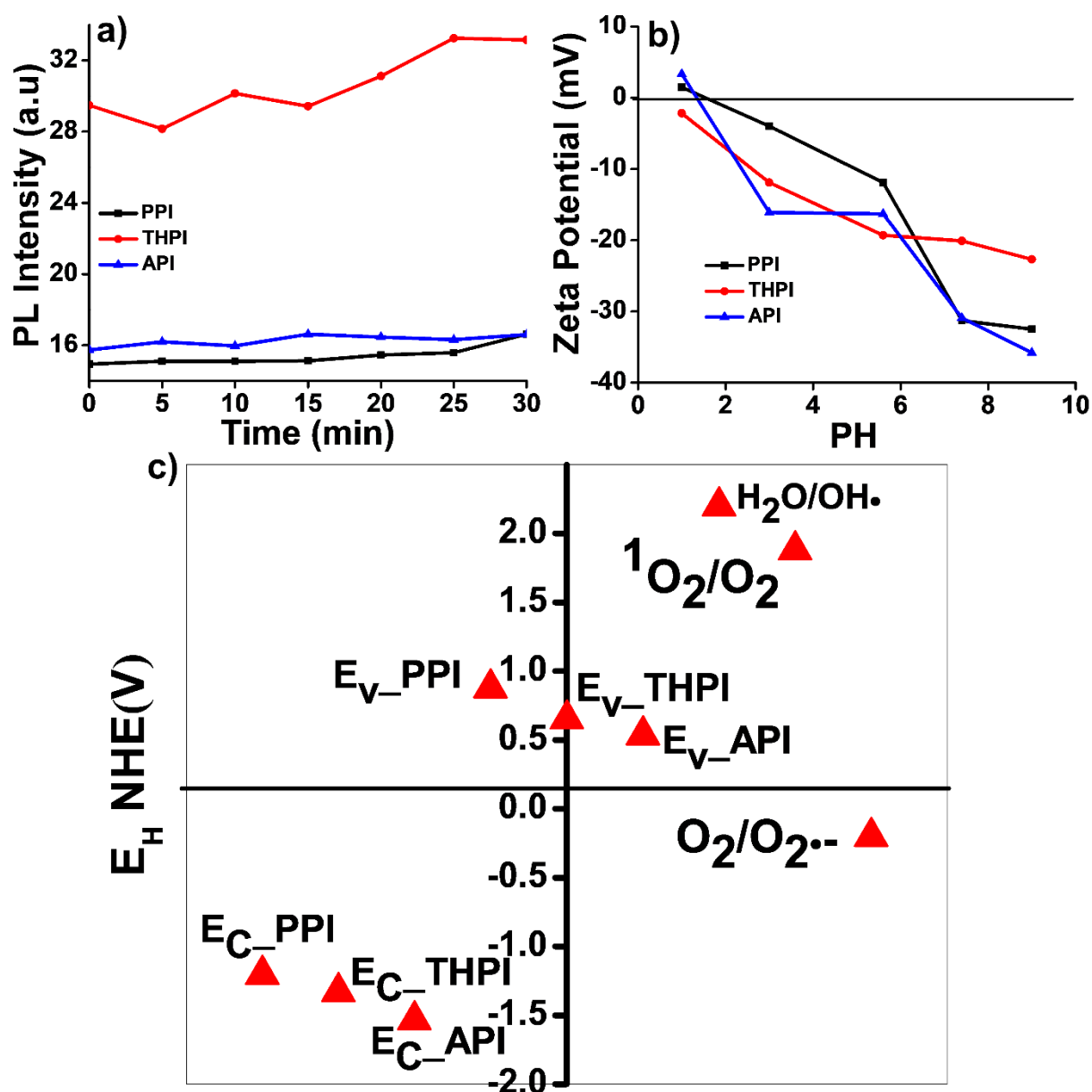


Figure A5.14. (a) PL spectra of TA at 528 nm. (b) Zeta potential versus pH values of **RPNI-O** derivatives. (c) E_c and E_v of **RPNI-S** derivatives at pH 5.6. The energy scale is expressed in relation to NHE. E_H for $H_2O/OH\cdot$, $^1O_2/O_2$, and $O_2/O_2^{\cdot-}$ are 2.2, 1.88, and -0.2 eV, respectively.

Table A5.15. Zeta potential data of **RPNI-O** and **RPNI-S** derivatives at different PH.

Materials	PH				
	1	3	5.6	7.4	9
PPI _ζ	1.49	-3.99	-11.90	-31.30	-32.50
THPI _ζ	-2.18	-11.90	-19.30	-20.10	-22.70

API_{ζ}	3.35	-16.10	-16.30	-30.90	-35.80
$PPIS_{\zeta}$	2.68	-1.89	-10.79	-21.13	-22.45
$THPIS_{\zeta}$	2.18	-7.90	-18.20	-19.10	-20.70
$APIS_{\zeta}$	4.35	-13.4	-14.30	-31.90	-38.80

ζ is the zeta potential of the respective materials.

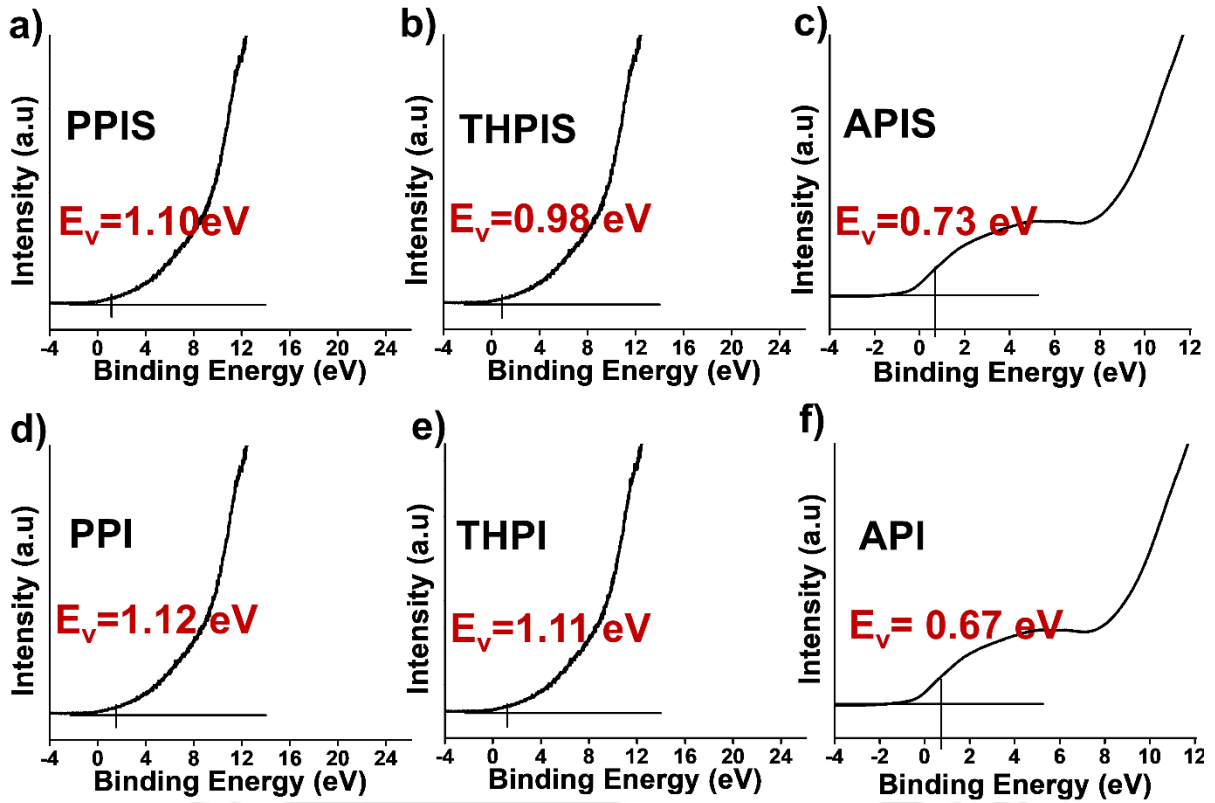


Figure A5.15: XPS spectra displaying valence band energy (E_v): (a) PPIS, (b) THPIS, (c) APIS, (d) PPI, (e) THPI, and (f) API, respectively.

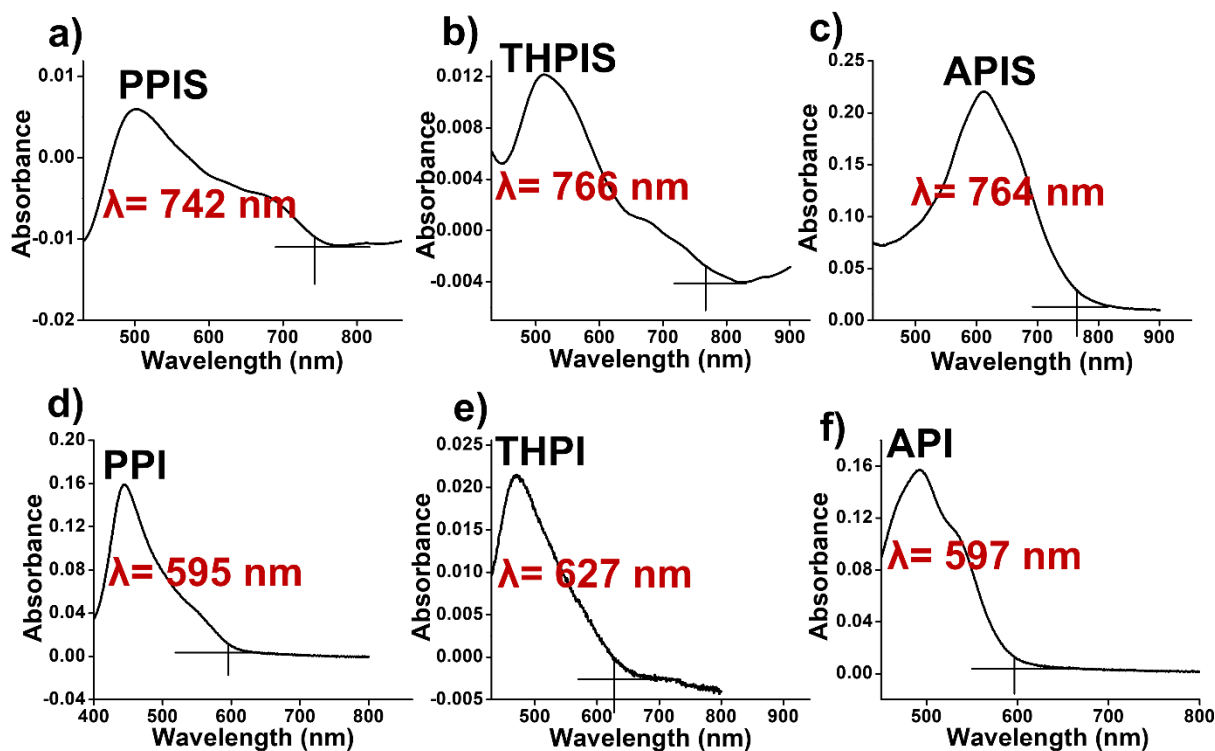


Figure A5.16: UV-vis spectroscopy of exhibiting onset absorption (a) PPIS, (b) THPIS, (c) APIS, (d) PPI, (e) THPI, and (f) API, respectively.

Table A5.16. Optical band gap data of RPNI-O and RPNI-S derivatives calculated from the onset absorption of the UV-vis spectroscopy.

Materials	λ_{onset}	E_g (eV)
PPIS	742	1.67
THPIS	766	1.61
APIS	764	1.62
PPI	595	2.08
THPI	627	1.98
API	597	2.07

λ_{onset} onset UV-vis absorption.

Table A5.17. E_c and E_v at a pH of 5.6 of RPNI-O and RPNI-S derivatives.

Materials	E_g	E_{HOMO}	E_{LUMO}	E_v	E_c	PZZP	$E_{v,5.6}$	$E_{c,5.6}$
PPIS	1.67	-5.60	-3.93	1.10	-0.57	2.68	0.92772	-0.74228

THPIS	1.61	-5.48	-3.87	0.98	-0.63	2.18	0.77822	-0.83178
APIS	1.62	-5.23	-3.61	0.73	-0.89	4.35	0.65625	-0.96375
PPI	2.08	-5.62	-3.54	1.12	-0.96	1.49	0.87751	-1.20249
THPI	1.98	-5.61	-3.63	1.11	-0.87	-2.18	0.65098	-1.32902
API	2.07	-5.17	-3.10	0.67	-1.40	3.35	0.53725	-1.53275

PZZP, the point of zero zeta potential.

Table A5.18. Calculated Gibbs free energy of O_2 using **ORCA 5.0** at the B3LYP/6-31G (d, p) and B3LYP/DEF2SVP level using quantum mechanism package.

Materials	G (Eh)		ΔG (Kcal mol ⁻¹)
PPIS	O_2	-150.09346315	-0.548
	PPIS+ O_2	-2310.53867284	
	PPIS	-2160.44608328	
THPIS	O_2	-150.09346315	-40.83
	THPIS+ O_2	-3182.63436769	
	THPIS	-3032.55916191	
APIS	O_2	-150.09346315	-10.26
	APIS+ O_2	-3336.04242916	
	APIS	-3185.96532129	

Table A5.19. Calculated Gibbs free energy of O_2 using ORCA 5.0 at the B3LYP/6-31G (d, p) and B3LYP/DEF2SVP level using a quantum mechanism package.

O_2

GIBBS FREE ENERGY

The Gibbs free energy is $G = H - T \cdot S$
Total enthalpy ... -150.07131287 Eh
Total entropy correction ... -0.02215028 Eh -13.90 kcal/mol

Final Gibbs free energy ... -150.09346315 Eh
For completeness - the Gibbs free energy minus the electronic energy
G-E(el) ... -0.01441918 Eh -9.05 kcal/mol
Timings for individual modules:
Sum of individual times ... 12.524 sec (= 0.209 min)
GTO integral calculation ... 2.186 sec (= 0.036 min) 17.5 %
SCF iterations ... 4.342 sec (= 0.072 min) 34.7 %
Analytical frequency calculation... 5.995 sec (= 0.100 min) 47.9 %



Table A5.20. Calculated Gibbs free energy of **PPIS** using ORCA 5.0 at the B3LYP/6-31G (d, p) and B3LYP/DEF2SVP level using quantum mechanism package.

```

-----
GIBBS FREE ENERGY
-----
The Gibbs free energy is G = H - T*S
Total enthalpy ... -2160.36500661 Eh
Total entropy correction ... -0.08107666 Eh -50.88 kcal/mol
-----
Final Gibbs free energy ... -2160.44608328 Eh
For completeness - the Gibbs free energy minus the
electronic energy
G-E(el) ... 0.46404158 Eh 291.19 kcal/mol
Timings for individual modules:
Sum of individual times ... 2449.244 sec (= 40.821 min)
GTO integral calculation ... 3.581 sec (= 0.060 min) 0.1 %
SCF iterations ... 217.116 sec (= 3.619 min) 8.9 %
Analytical frequency calculation... 2228.548 sec (= 37.142
min) 91.0 %

```

Table A5.21. Calculated Gibbs free energy of **PPIS** and **O₂** together using ORCA 5.0 at the B3LYP/6-31G (d,p) and B3LYP/DEF2SVP level using quantum mechanism package.

```

-----
GIBBS FREE ENERGY
-----
The Gibbs free energy is G = H - T*S
Total enthalpy ... -2310.44123598 Eh
Total entropy correction ... -0.09743686 Eh -61.14 kcal/mol
-----
Final Gibbs free energy ... -2310.53867284 Eh
For completeness - the Gibbs free energy minus the electronic energy
G-E(el) ... 0.45873772 Eh 287.86 kcal/mol
Timings for individual modules:
Sum of individual times ... 19281.091 sec (= 321.352 min)
GTO integral calculation ... 103.385 sec (= 1.723 min) 0.5 %
SCF iterations ... 12827.456 sec (= 213.791 min) 66.5 %
SCF Gradient evaluation ... 2722.936 sec (= 45.382 min) 14.1 %
Geometry relaxation ... 24.973 sec (= 0.416 min) 0.1 %
Analytical frequency calculation... 3602.340 sec (= 60.039 min) 18.7 %

```

Table A5.22. Calculated Gibbs free energy of **THPIS** using ORCA 5.0 at the B3LYP/6-31G (d,p) and B3LYP/DEF2SVP level using quantum mechanism package.

THPIS

GIBBS FREE ENERGY

The Gibbs free energy is $G = H - T \cdot S$

Total enthalpy ... -3032.47582297 Eh

Total entropy correction ... -0.08333893 Eh -52.30 kcal/mol

Final Gibbs free energy ... -3032.55916191 Eh

For completeness - the Gibbs free energy minus the electronic energy

G-E(el) ... 0.47671745 Eh 299.14 kcal/mol

Timings for individual modules:

Sum of individual times ... 3337.858 sec (= 55.631 min)

GTO integral calculation ... 4.858 sec (= 0.081 min) 0.1 %

SCF iterations ... 251.657 sec (= 4.194 min) 7.5 %

Analytical frequency calculation... 3081.344 sec (= 51.356 min) 92.3 %



Table A5.23. Calculated Gibbs free energy of **THPIS** and **O₂** together using ORCA 5.0 at the B3LYP/6-31G (d, p) and B3LYP/DEF2SVP level using quantum mechanism package.

THPIS+O₂

GIBBS FREE ENERGY

The Gibbs free energy is $G = H - T*S$
 Total enthalpy ... -3182.55043554 Eh
 Total entropy correction ... -0.08393215 Eh -52.67 kcal/mol

Final Gibbs free energy ... -3182.63436769 Eh
 For completeness - the Gibbs free energy minus the electronic energy
 G-E(el) ... 0.48055338 Eh 301.55 kcal/mol

Timings for individual modules:
 Sum of individual times ... 5309.271 sec (= 88.488 min)
 GTO integral calculation ... 3.579 sec (= 0.060 min) 0.1 %
 SCF iterations ... 2394.155 sec (= 39.903 min) 45.1 %
 Analytical frequency calculation... 2911.537 sec (= 48.526 min) 54.8 %

Table A5.24. Calculated Gibbs free energy of **APIS** using ORCA 5.0 at the B3LYP/6-31G (d,p) and B3LYP/DEF2SVP level using quantum mechanism package.

APIS

GIBBS FREE ENERGY

The Gibbs free energy is $G = H - T*S$
 Total enthalpy ... -3185.87795057 Eh
 Total entropy correction ... -0.08737072 Eh -54.83 kcal/mol

Final Gibbs free energy ... -3185.96532129 Eh
 For completeness - the Gibbs free energy minus the electronic energy
 G-E(el) ... 0.52321755 Eh 328.32 kcal/mol

Timings for individual modules:
 Sum of individual times ... 4288.483 sec (= 71.475 min)
 GTO integral calculation ... 2.835 sec (= 0.047 min) 0.1 %
 SCF iterations ... 288.080 sec (= 4.801 min) 6.7 %
 Analytical frequency calculation... 3997.568 sec (= 66.626 min) 93.2 %

Table A5.25. Calculated Gibbs free energy of **APIS** and **O₂** together using ORCA 5.0 at the B3LYP/6-31G (d, p) and B3LYP/DEF2SVP level using quantum mechanism package.

APIS+O₂

GIBBS FREE ENERGY

The Gibbs free energy is $G = H - T \cdot S$
 Total enthalpy ... -3335.95158265 Eh
 Total entropy correction ... -0.09084651 Eh -57.01 kcal/mol

Final Gibbs free energy ... -3336.04242916 Eh
 For completeness - the Gibbs free energy minus the electronic energy
 G-E(e) ... 0.52511206 Eh 329.51 kcal/mol

Timings for individual modules:
 Sum of individual times ... 7444.600 sec (= 124.077 min)
 GTO integral calculation ... 73.874 sec (= 1.231 min) 1.0 %
 SCF iterations ... 2387.693 sec (= 39.795 min) 32.1 %
 Analytical frequency calculation... 4983.033 sec (= 83.051 min)
 66.9 %

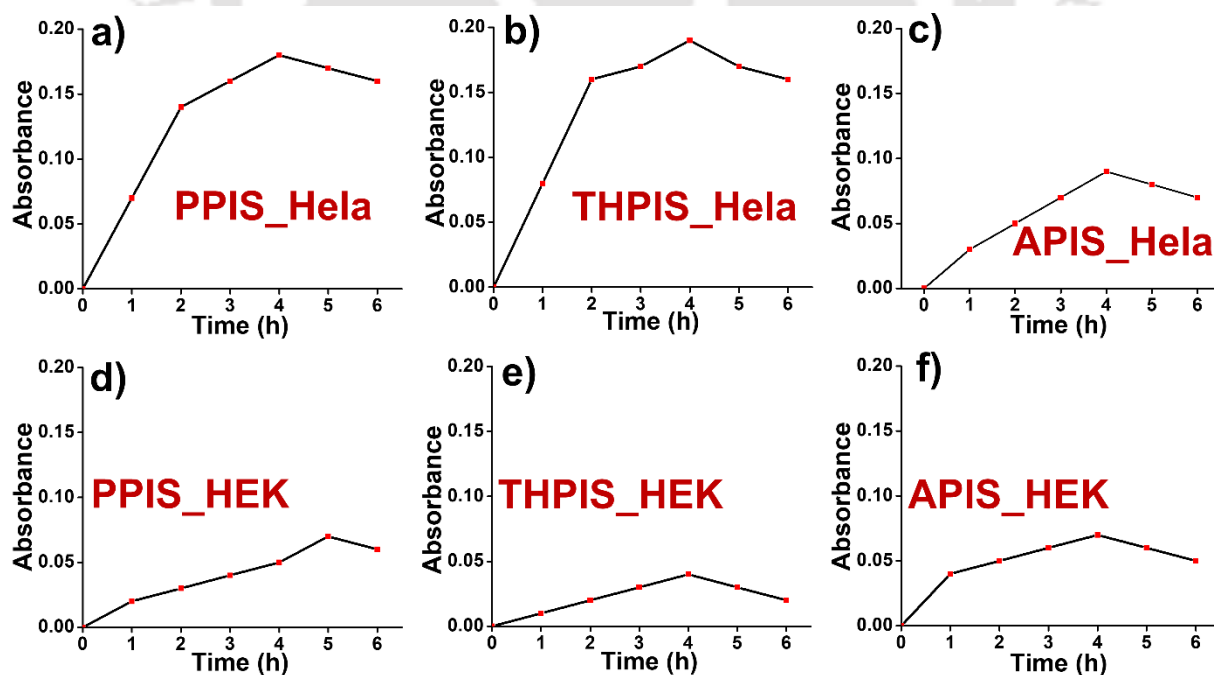


Figure A5.17. (a-c) Cellular uptake data of the (a) **PPIS**, (b) **THPIS**, and (c) **APIS** in HeLa cell. [concentration of **PPIS**, **THPIS**, and **APIS**: 20 μ M]. (d-f) Cellular uptake data of the (d) **PPIS**, (e) **THPIS**, and (f) **APIS** in HEK 293T. [concentration of **PPIS**, **THPIS**, and **APIS**: 100 μ M].

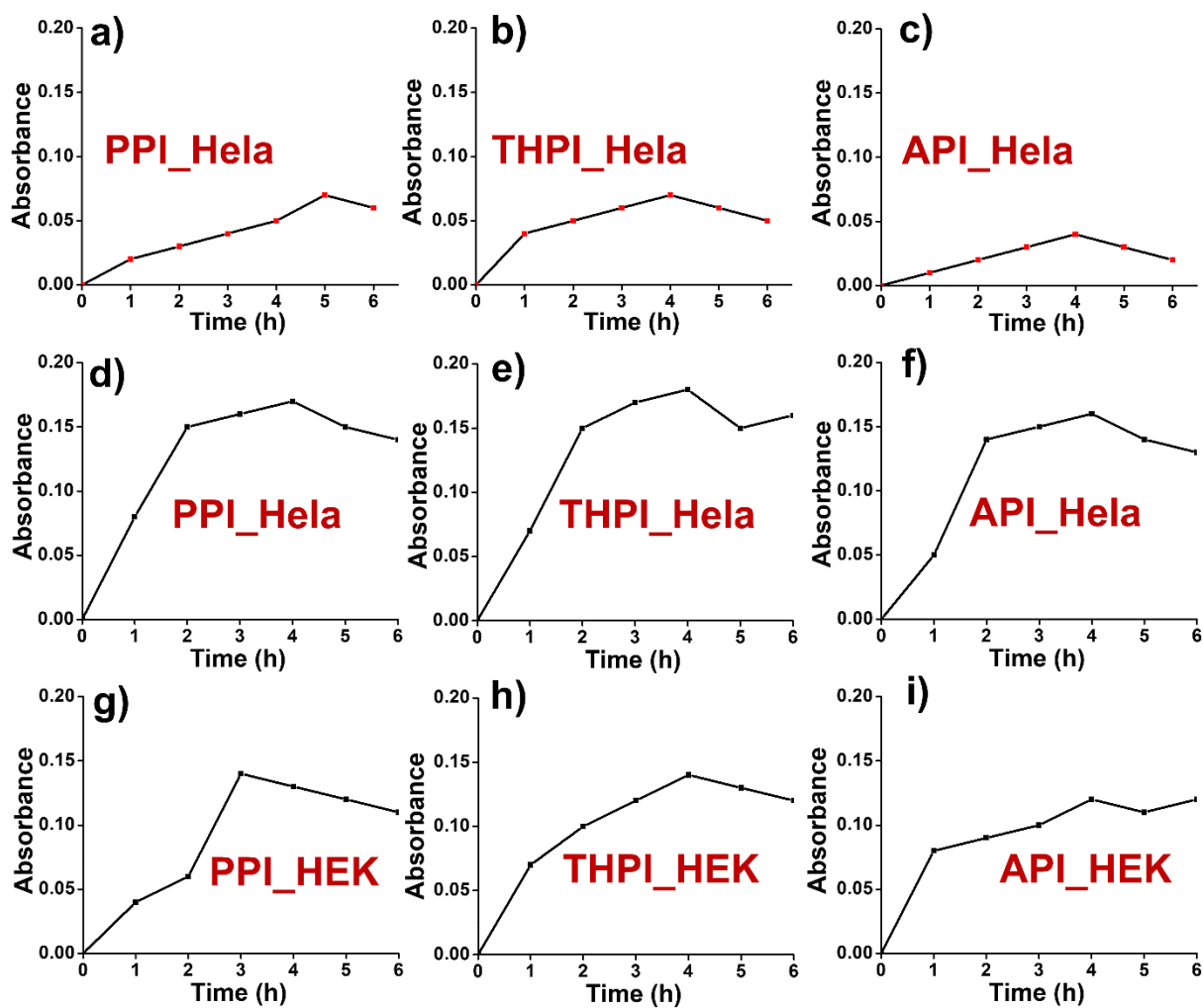


Figure A5.18. (a-c) Cellular uptake data of the (a) PPI, (b) THPI, and (c) API in HeLa cell. [concentration of PPI, THPI, and API: 20 μM]. (d-f) Cellular uptake data of the (d) PPI, (e) THPI, and (f) API in HeLa cell. [concentration of PPI, THPI, and API: 100 μM]. (d-f) Cellular uptake data of the (d) PPI, (e) THPI, and (f) API in HEK293. [concentration of PPI, THPI, and API: 100 μM].

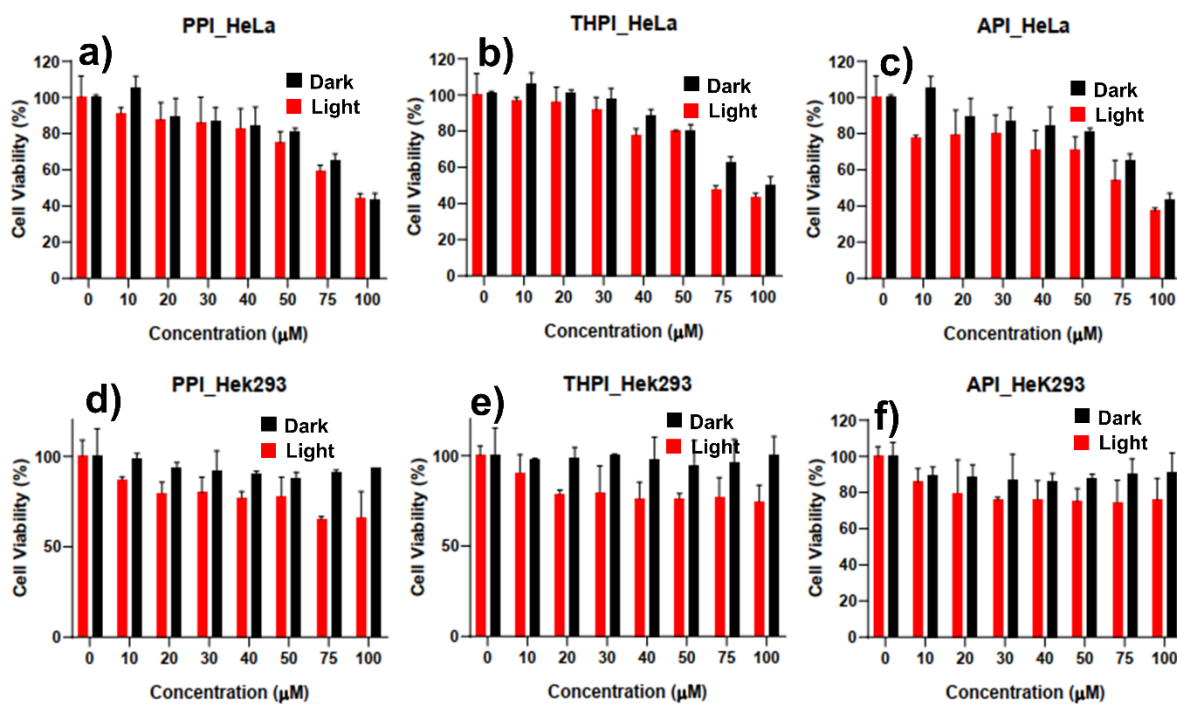


Figure A5.19. (a-c) Cell viability of HeLa cells after treatment with different concentrations of (a) **PPI** (b) **THPI**, and (c) **API**, respectively, along with white light irradiation. (g-h) Cell cytotoxicity of HEK293T cells after treatment with different concentrations of (g) **PPI** (h) **THPI**, and (i) **API**, respectively, along with white light irradiation.

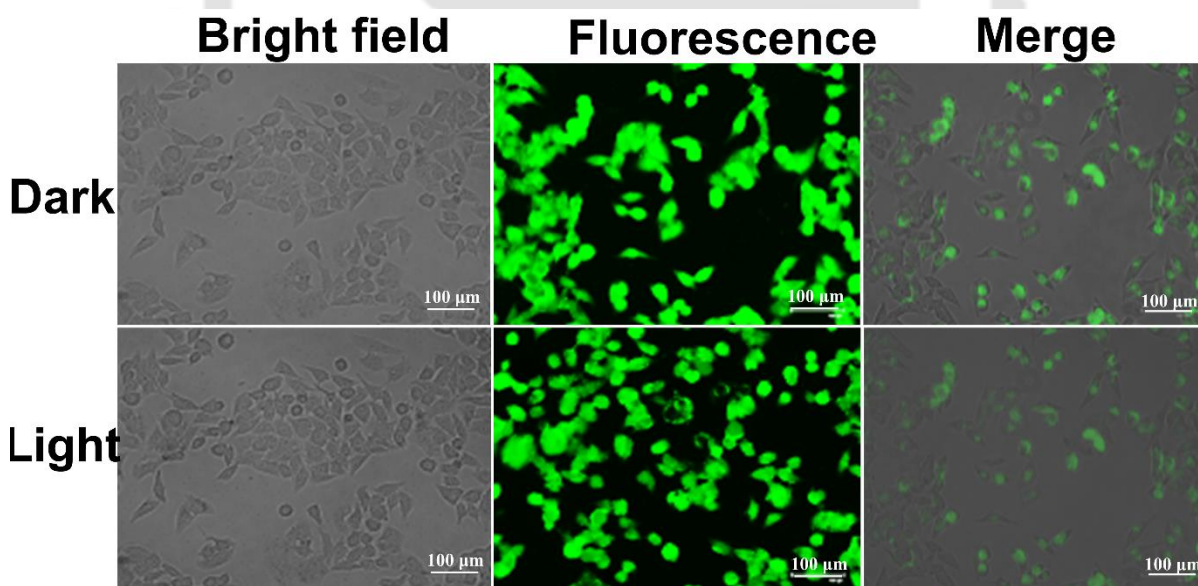


Figure A5.20. Fluorescence microscope images of HeLa cells after treatment with **APIS** under normoxia and loaded with calcein-AM (2 μM, live cell marker). [Concentration of **APIS**: (50 μM), scale bar: 100 μm].

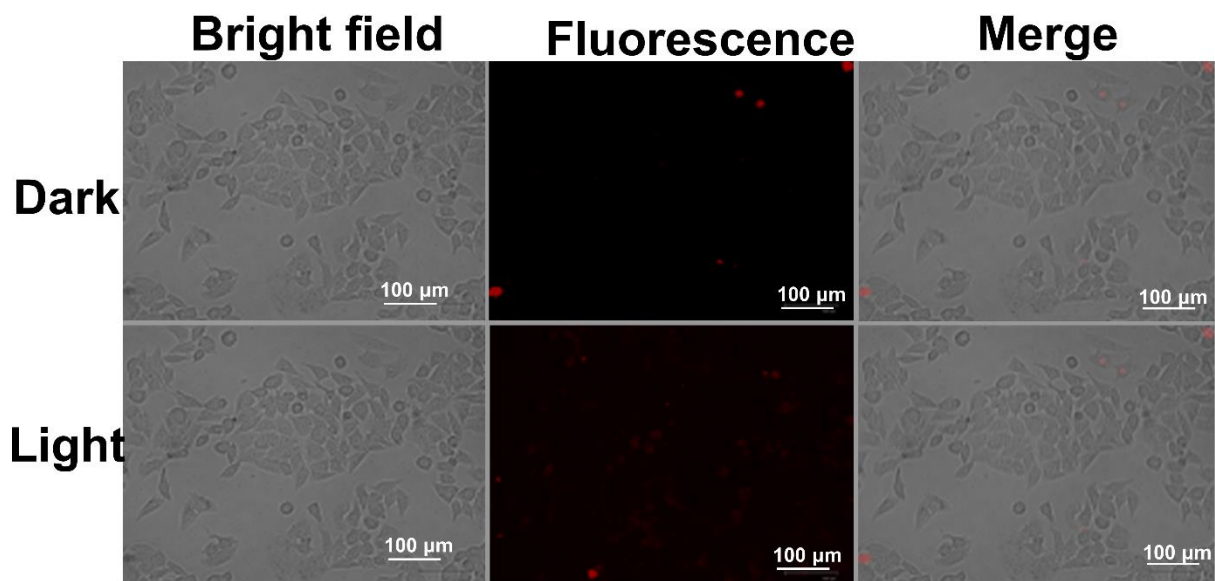


Figure A5.21. Fluorescence microscope images of HeLa cells after treatment with APIS under normoxia and loaded with PI (4 μ M, dead cell marker). [Concentration of APIS: (50 μ M), scale bar: 100 μ m].

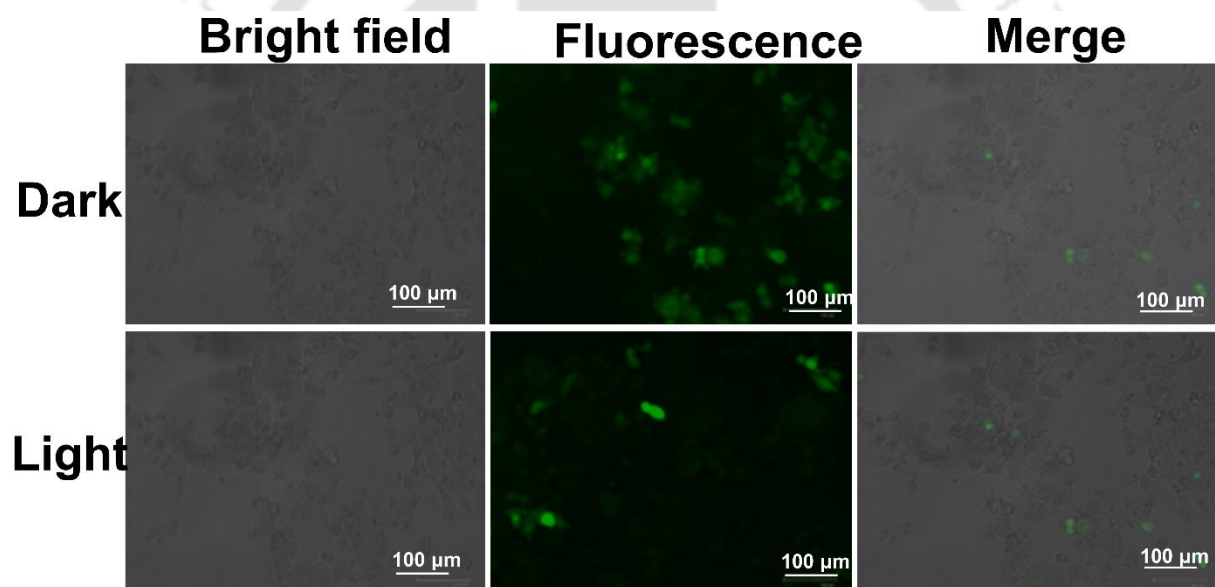


Figure A5.22. Fluorescence microscope images of HeLa cells after treatment with APIS under normoxia and loaded with DCFDA (ROS detection probe). [Concentration of APIS: (50 μ M), scale bar: 100 μ m].

Supporting figures

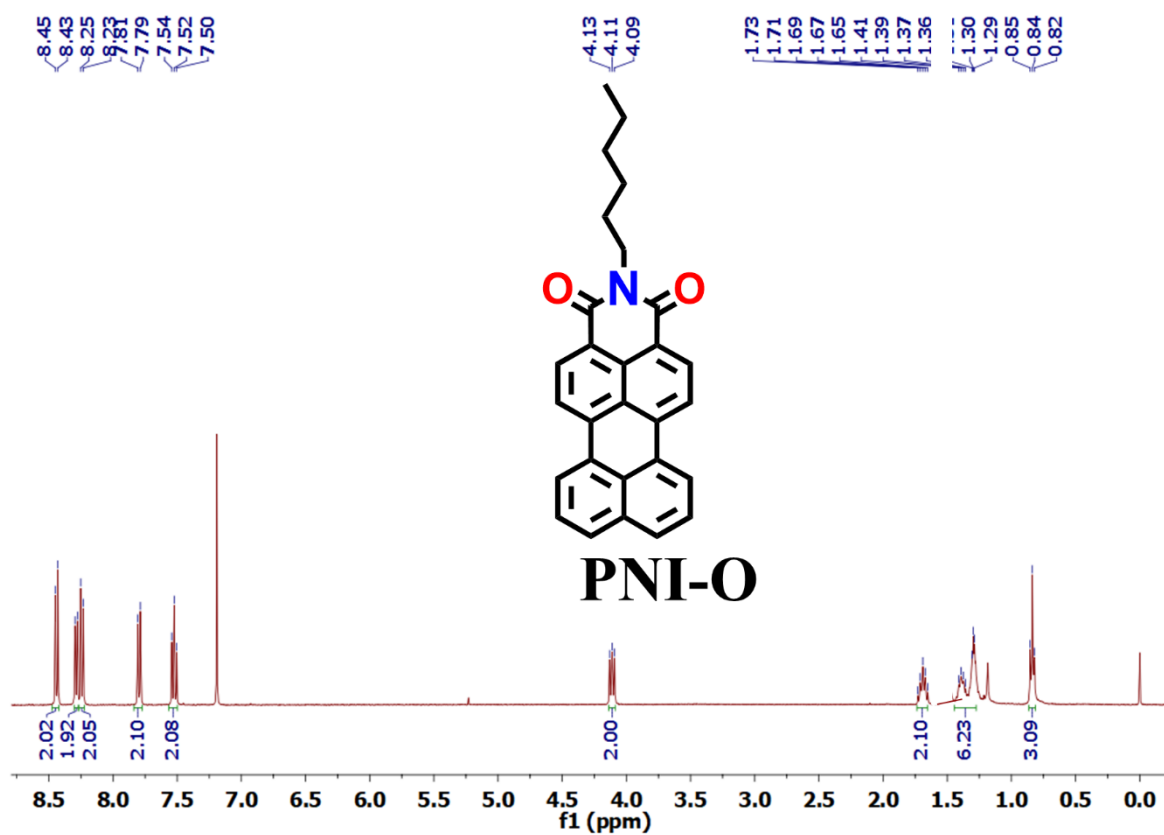


Figure A5.23. ¹H NMR spectra of PNI-O.

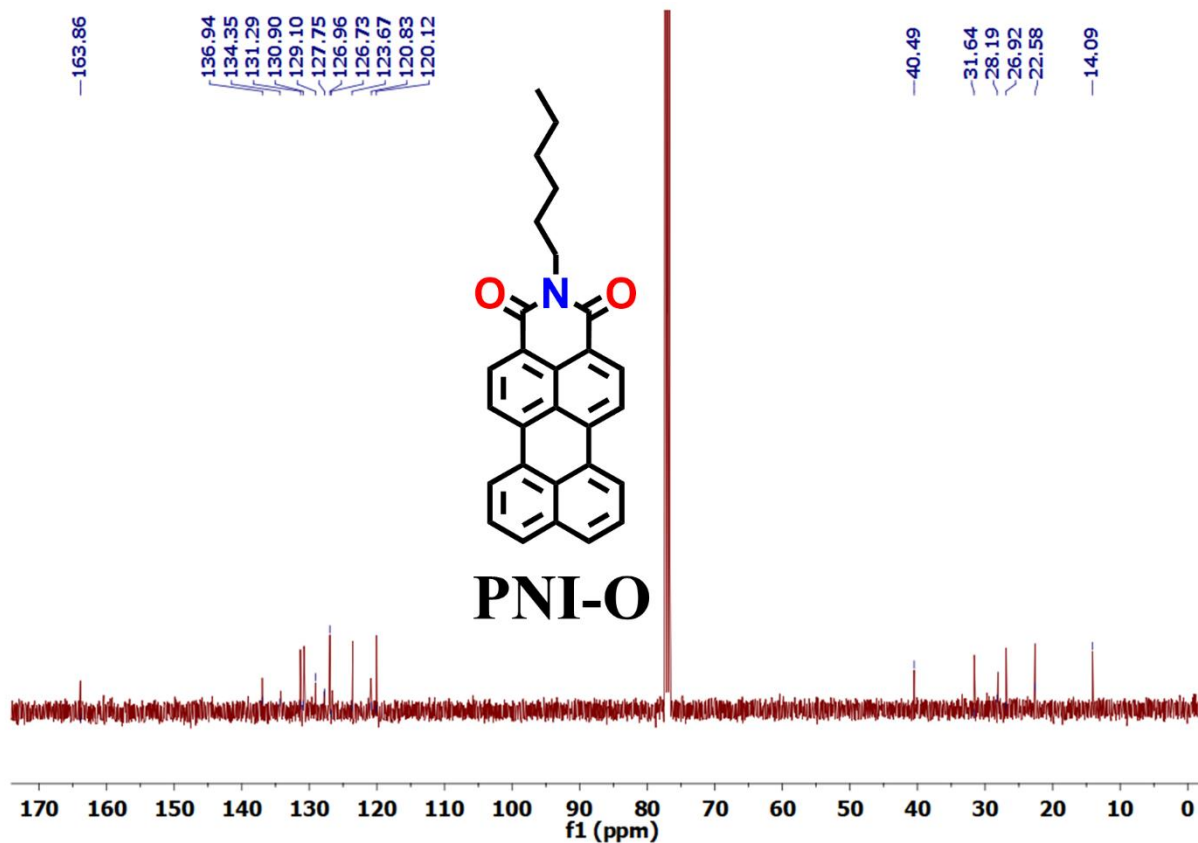


Figure A5.24. ¹³C NMR spectra of PNI-O.

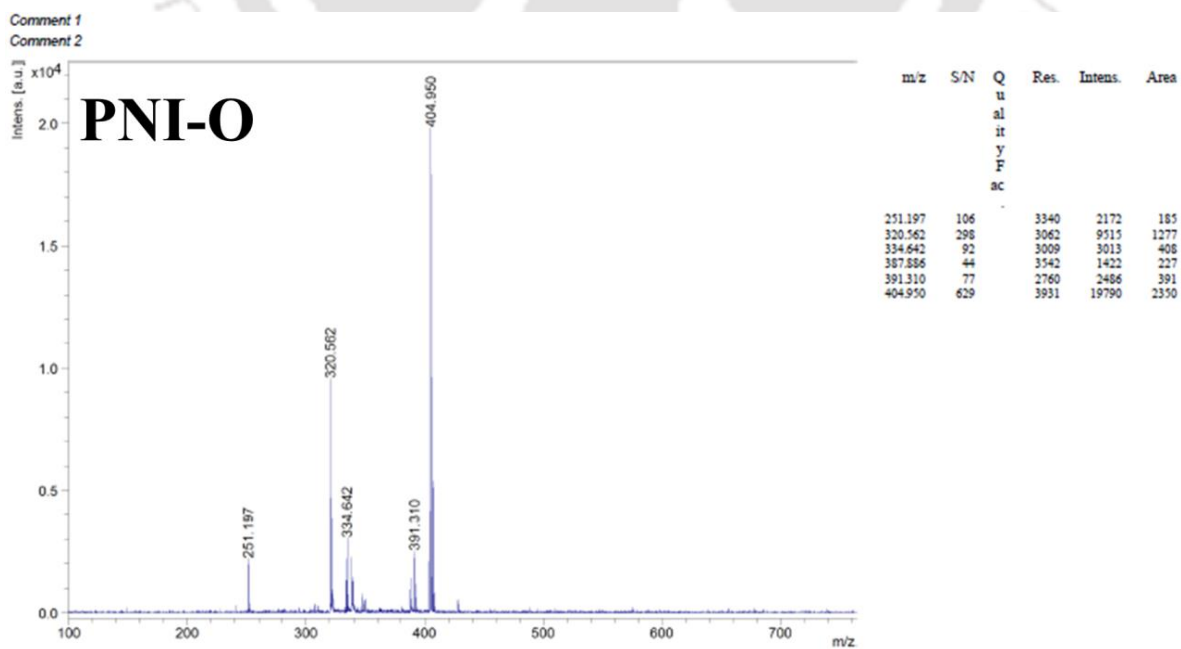


Figure A5.25. Maldi-TOF spectra of PNI-O.

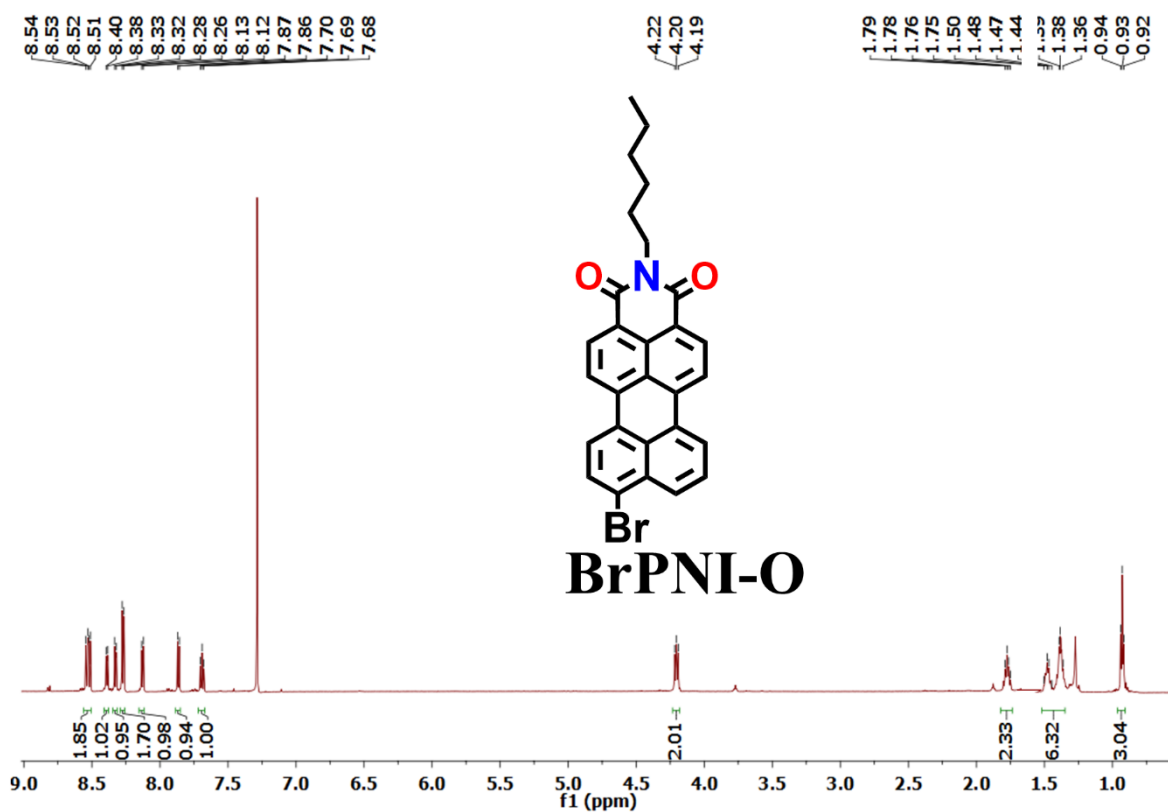


Figure A5.26. ¹H NMR spectra of BrPNI-O.

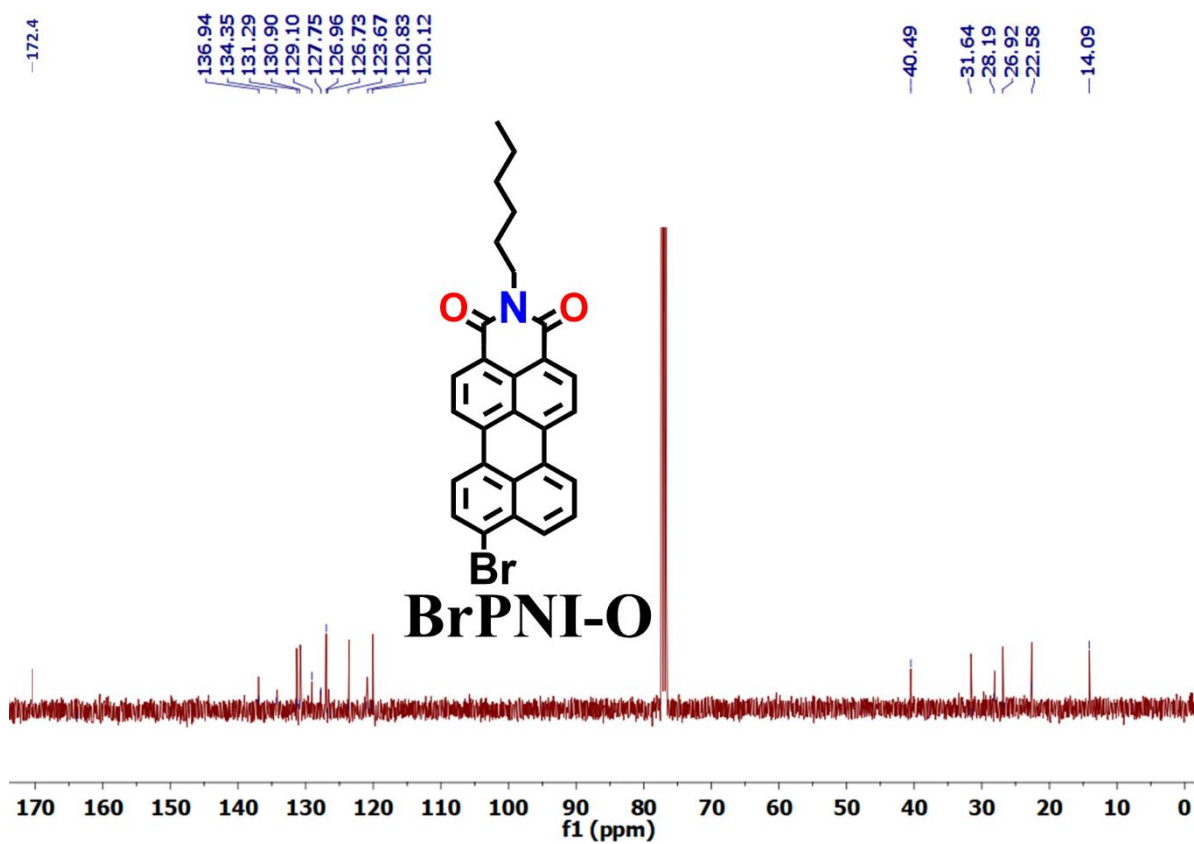


Figure A5.27. ¹³C NMR spectra of BrPNI-O.

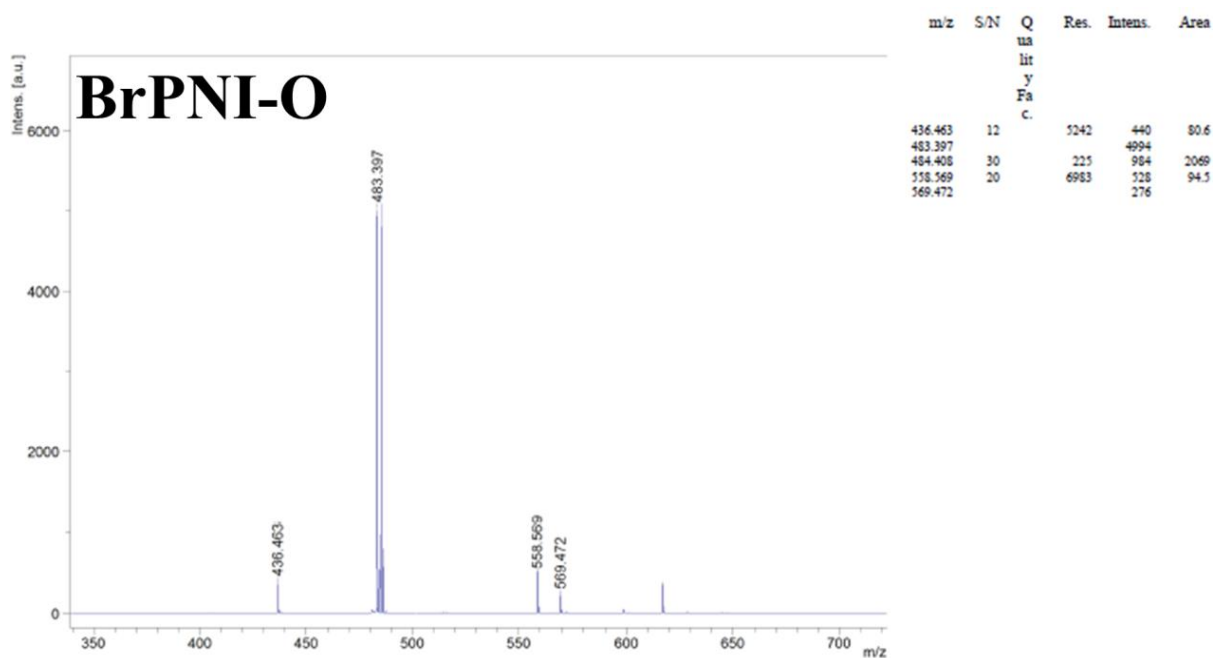


Figure A5.28. Maldi-TOF spectra of BrPNI-O.

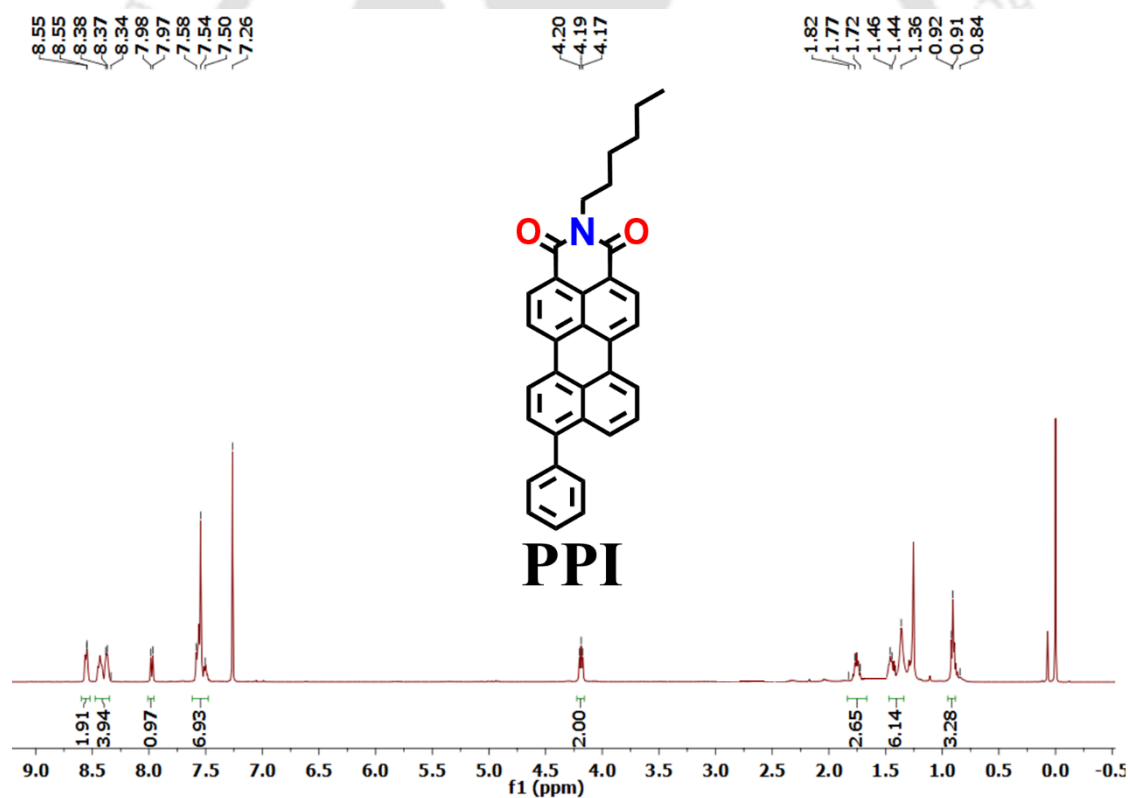


Figure A5.29. ¹H NMR spectra of PPI.

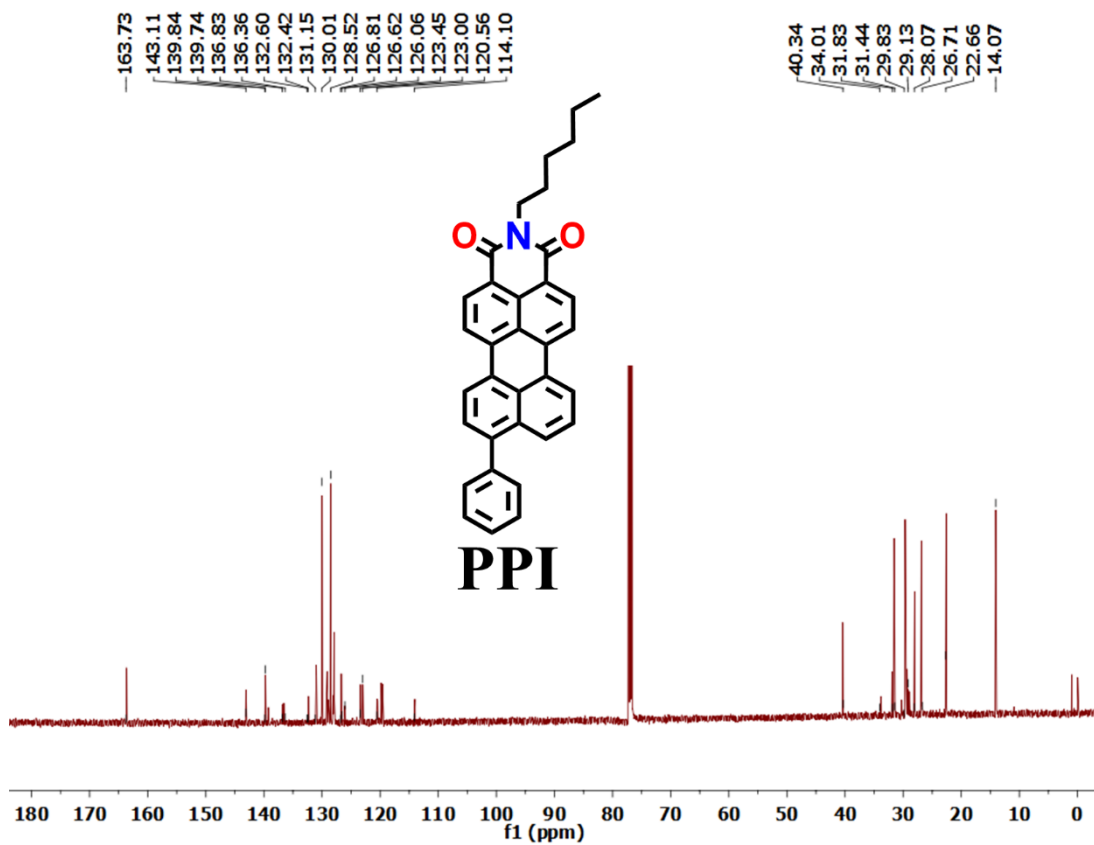


Figure A5.30. ¹³C NMR spectra of PPI.

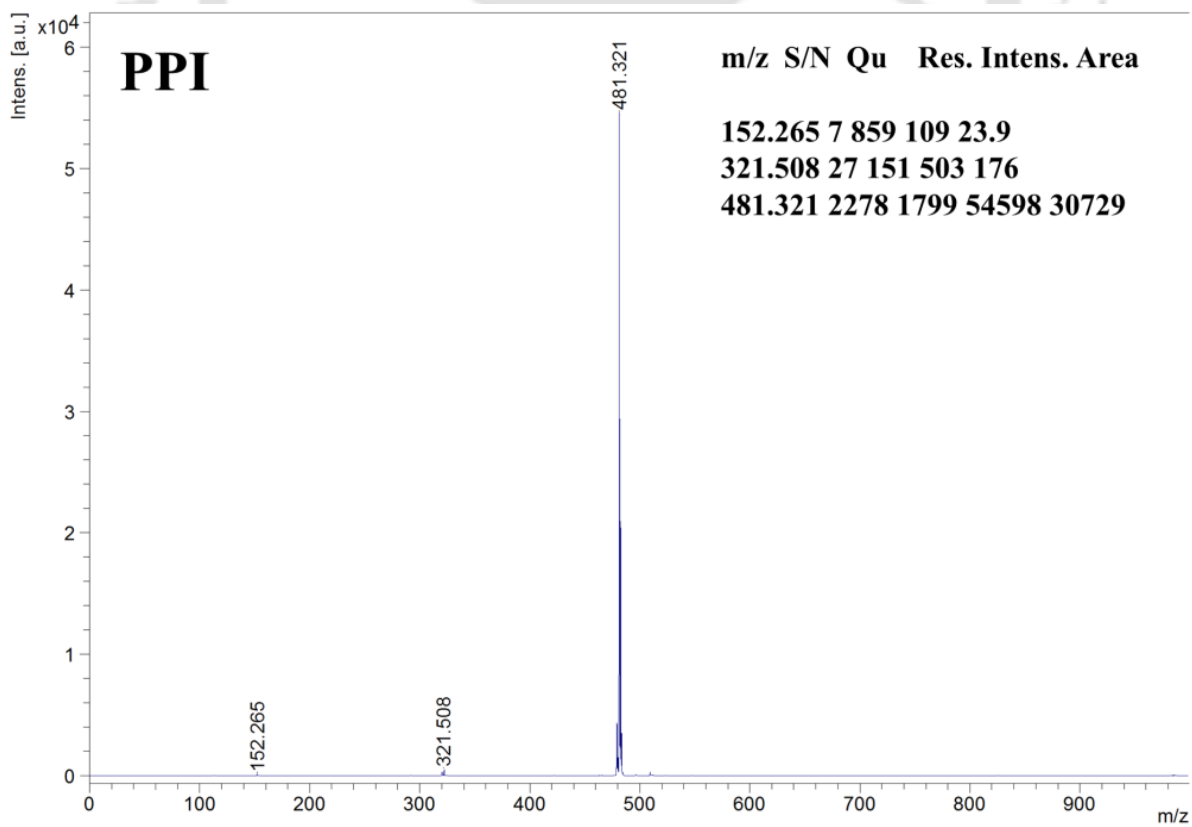


Figure A5.31. Maldi-TOF spectra of PPI.

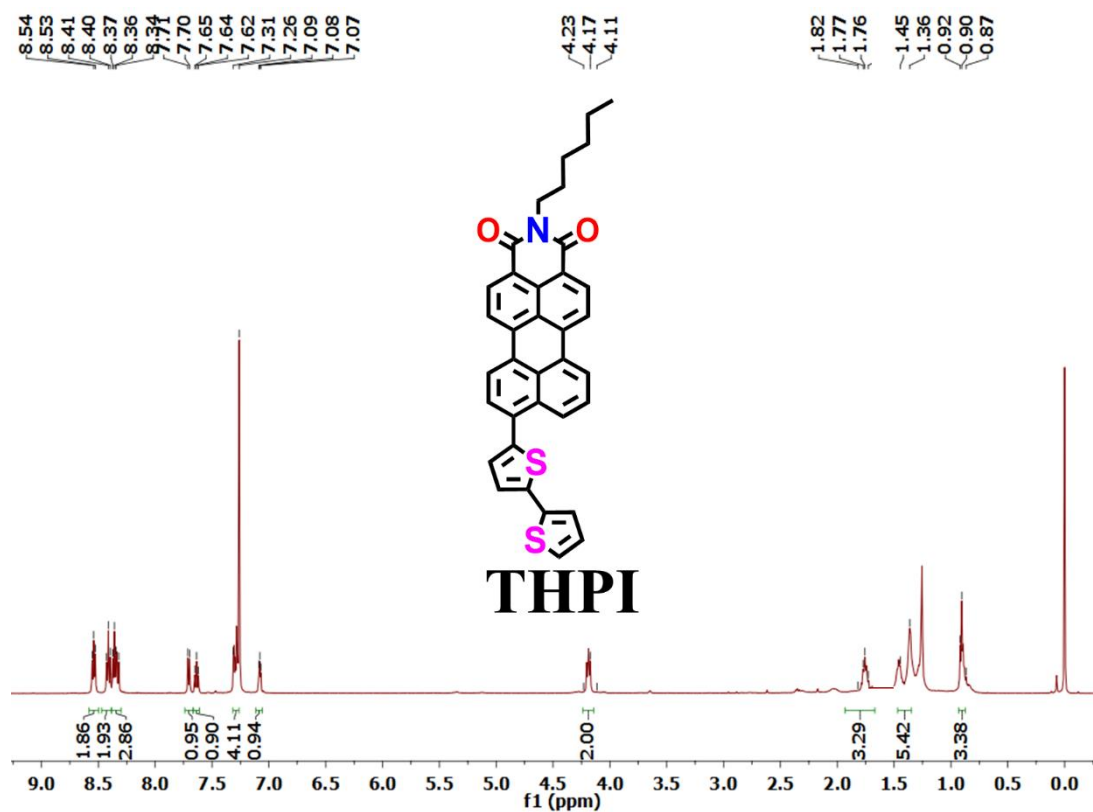


Figure A5.32. ^1H NMR spectra of THPI.

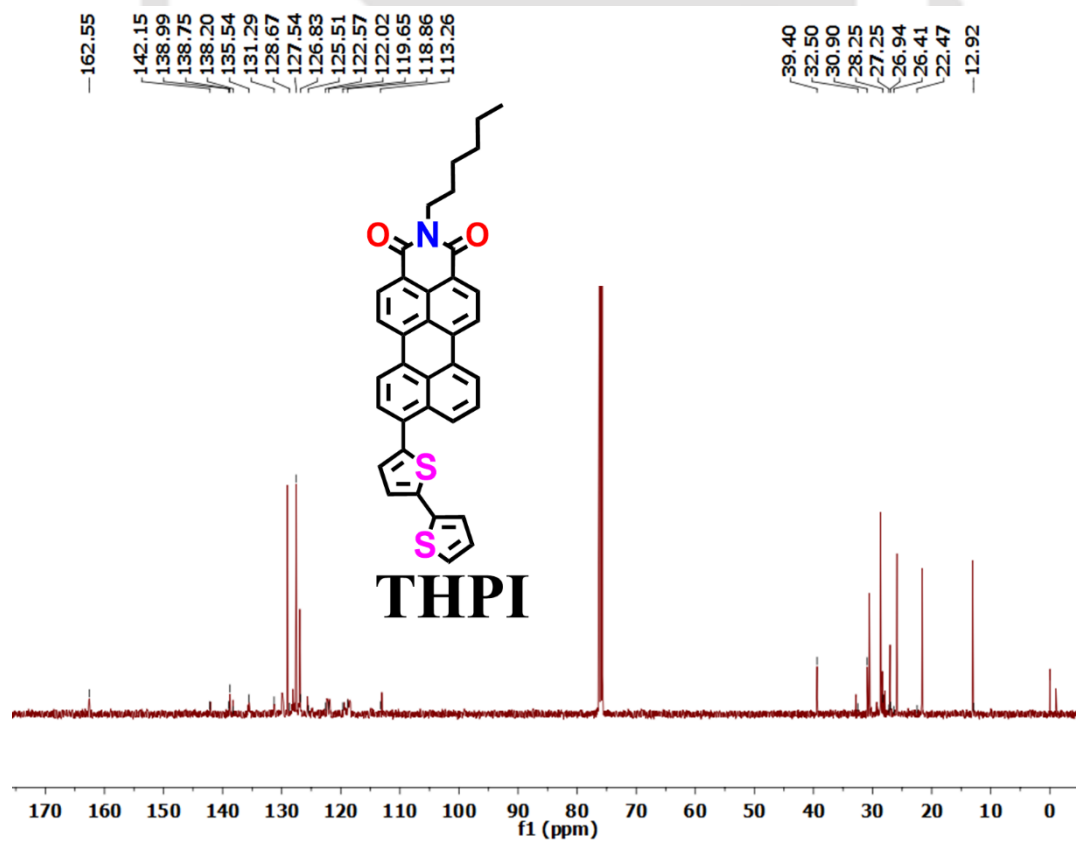


Figure A5.33. ^{13}C NMR spectra of THPI.

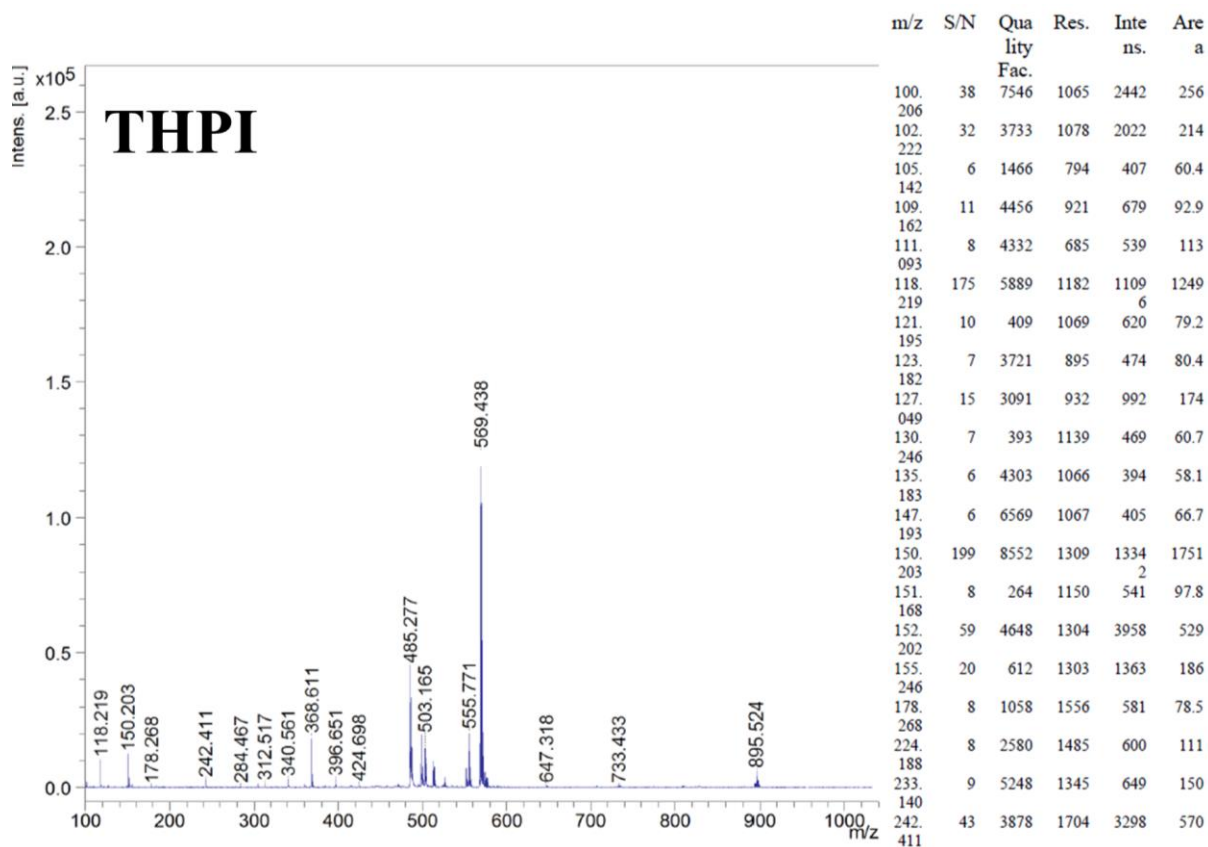


Figure A5.34. Maldi-TOF spectra of THPI.

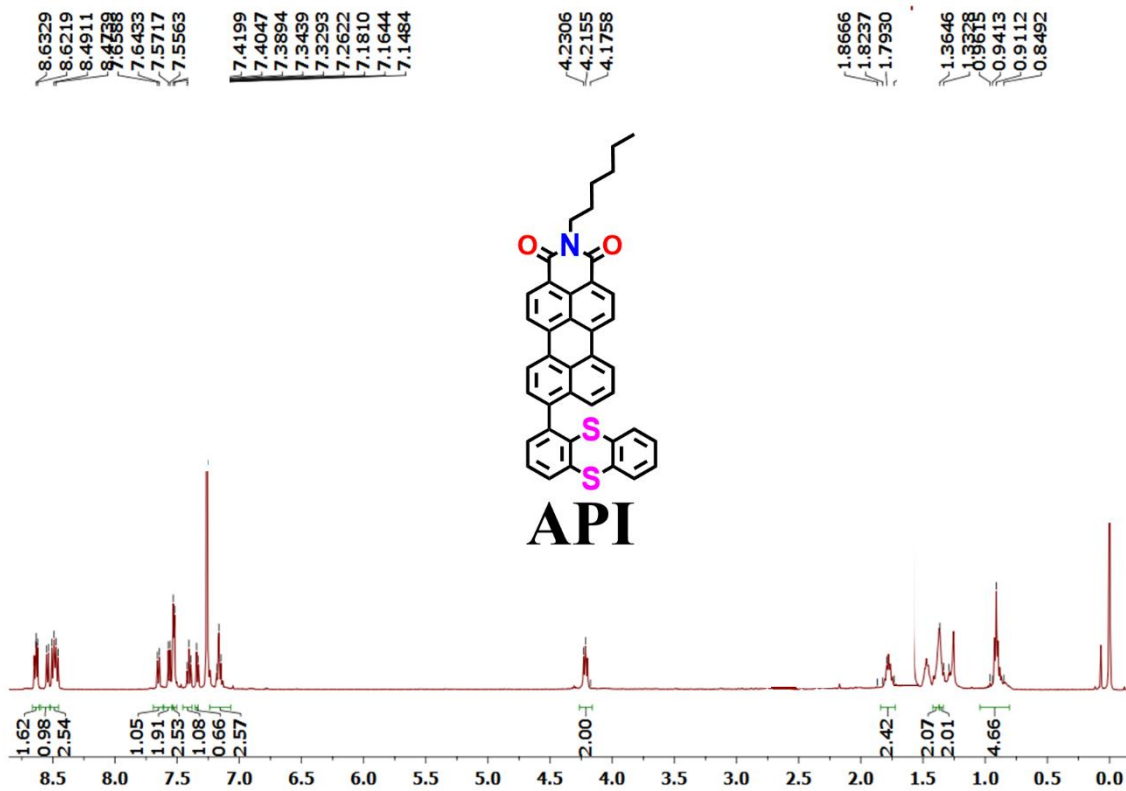


Figure A5.35. ¹H NMR spectra of API.

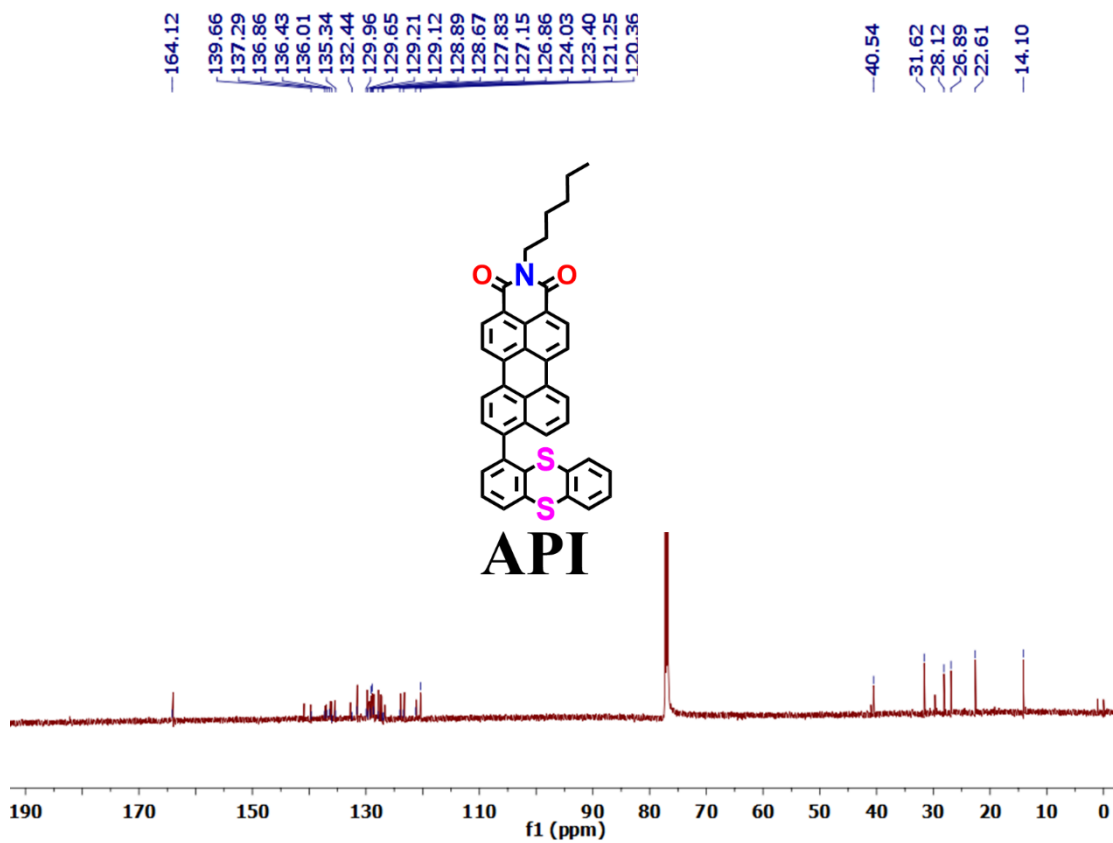


Figure A5.36. ¹³C NMR spectra of API.

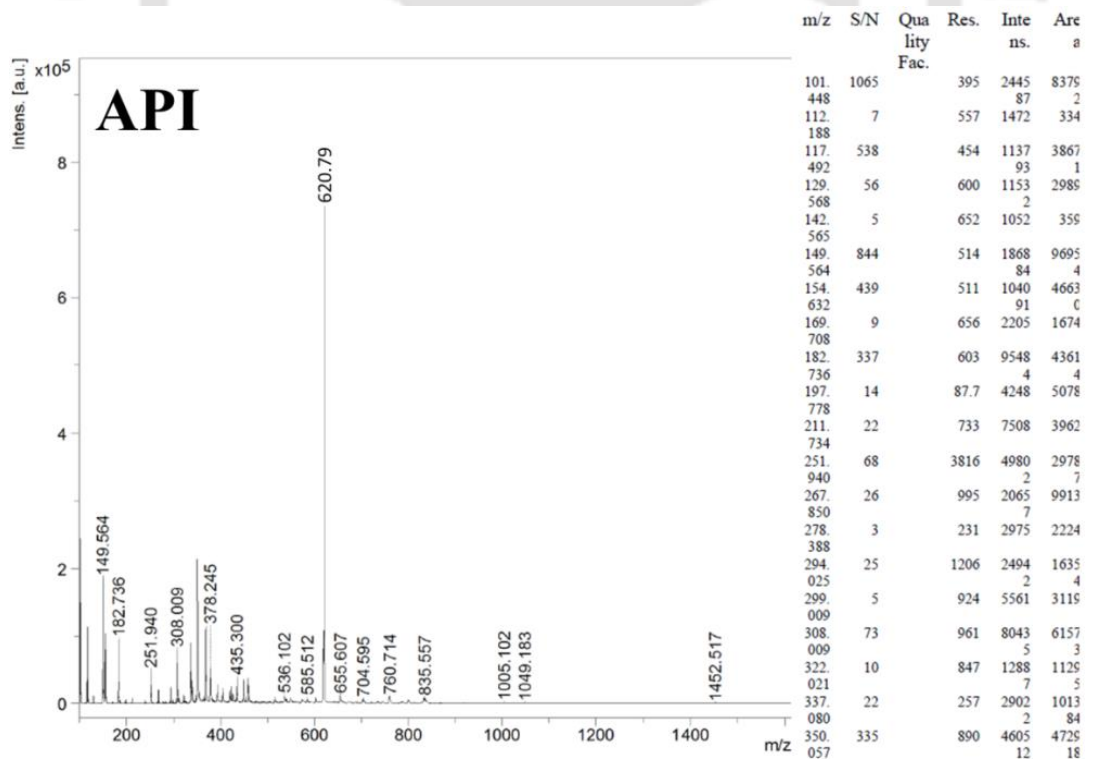


Figure A5.37. Maldi-TOF spectra of API.

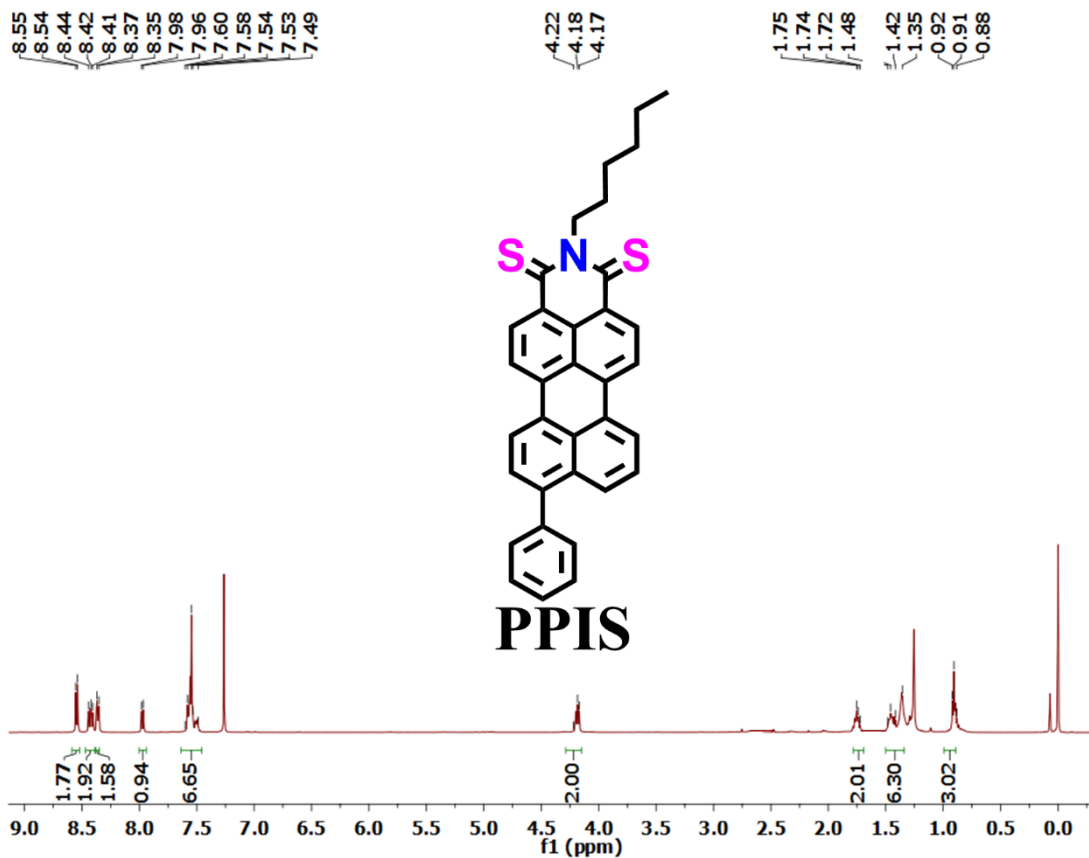


Figure A5.38. ¹H NMR spectra of PPIS.

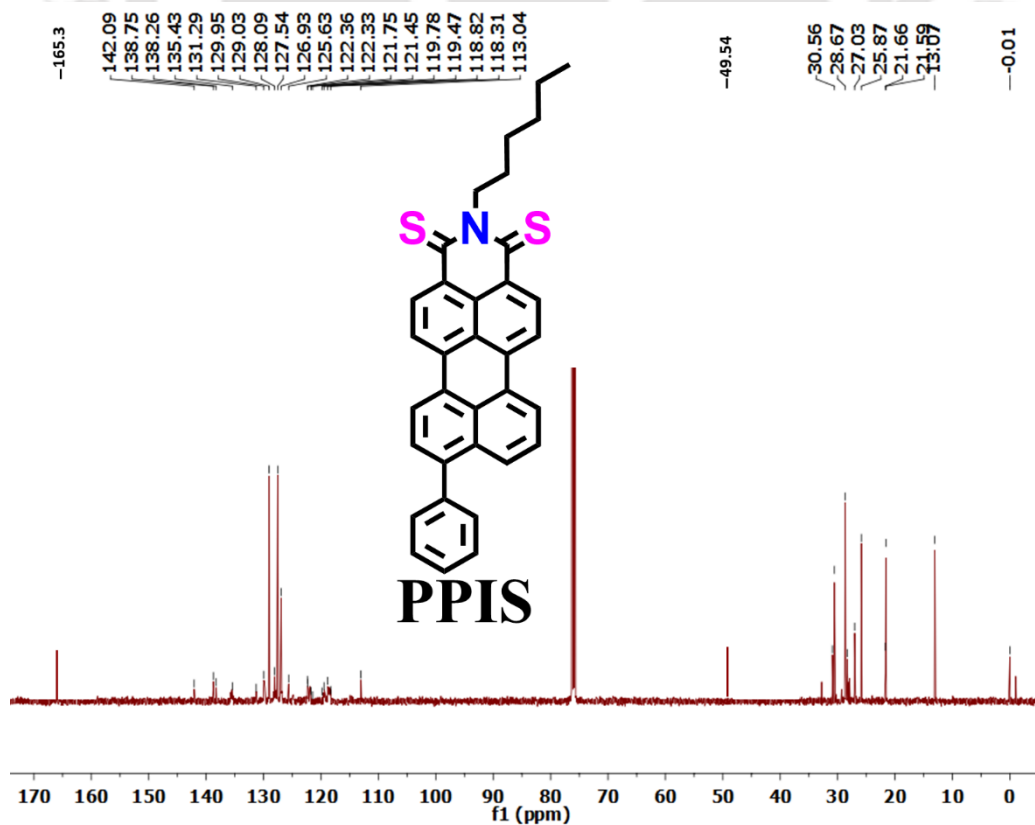


Figure A5.39. ^{13}C NMR spectra of PPIS.

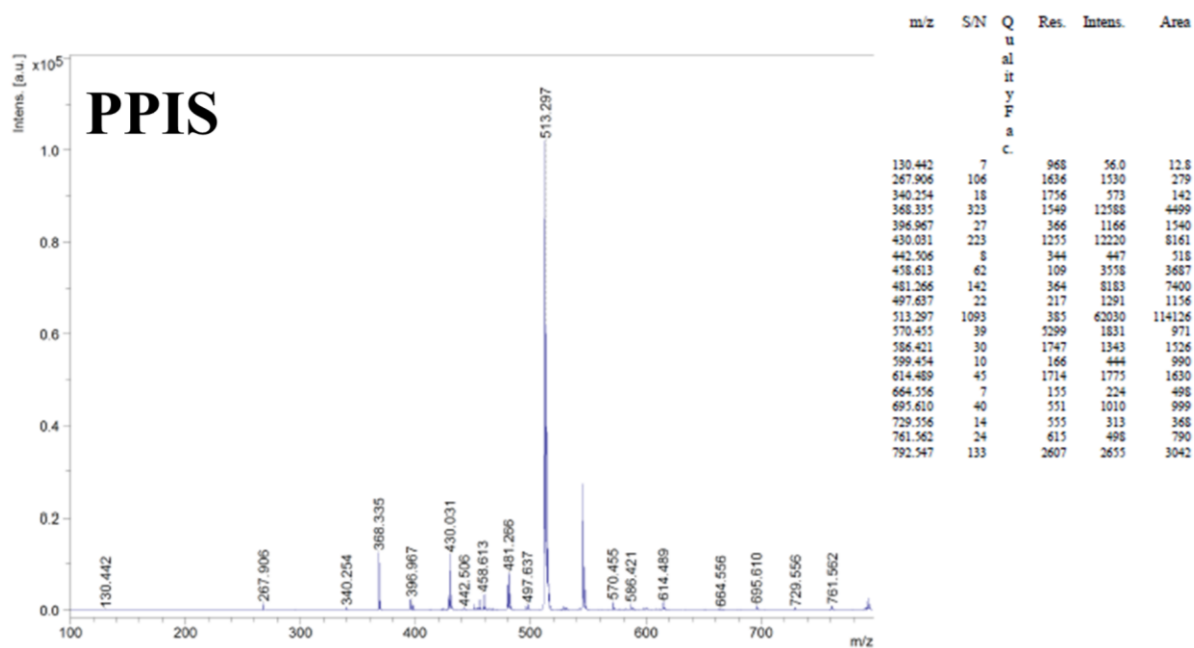


Figure A5.40. Maldi-TOF spectra of PPIS.



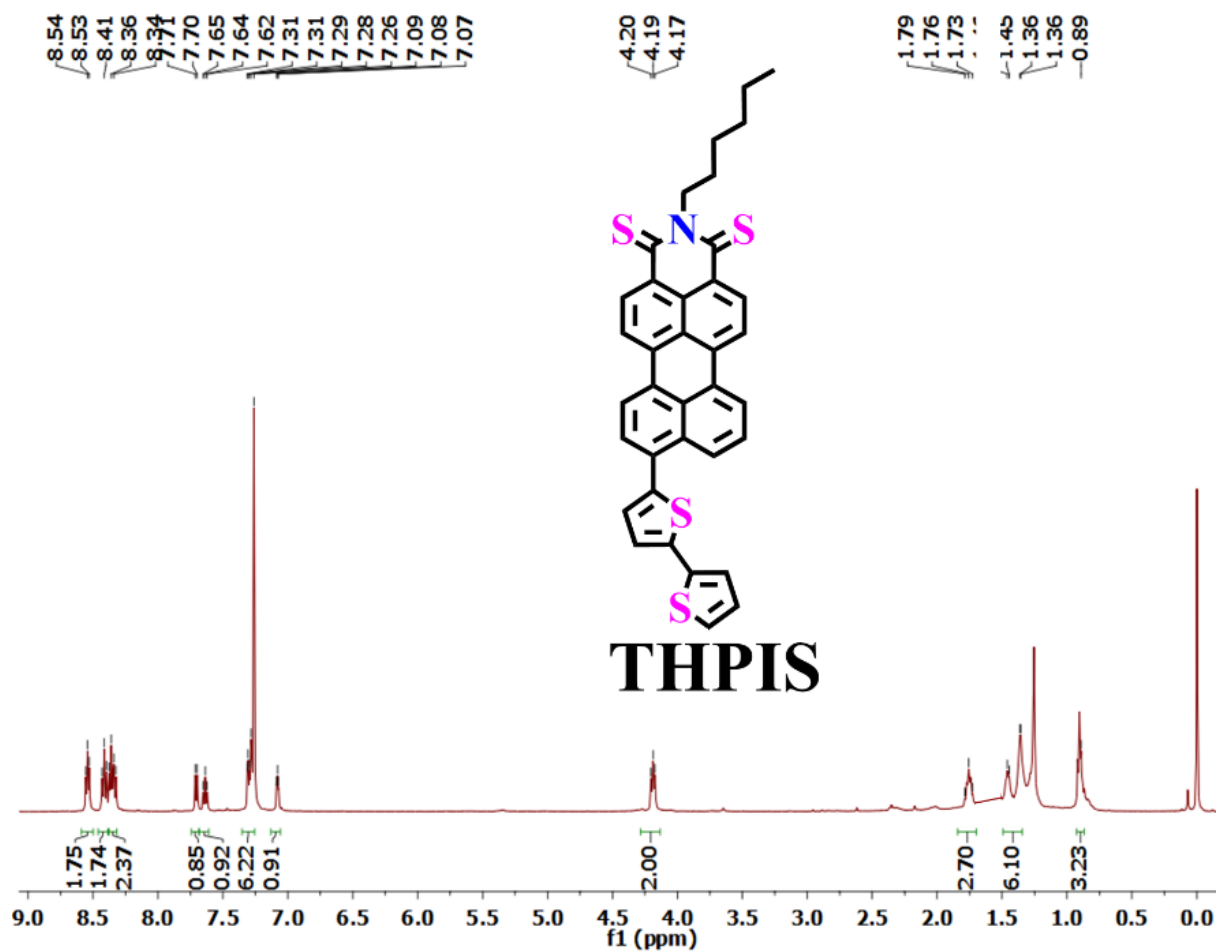


Figure A5.41. ^1H NMR spectra of THPIS.

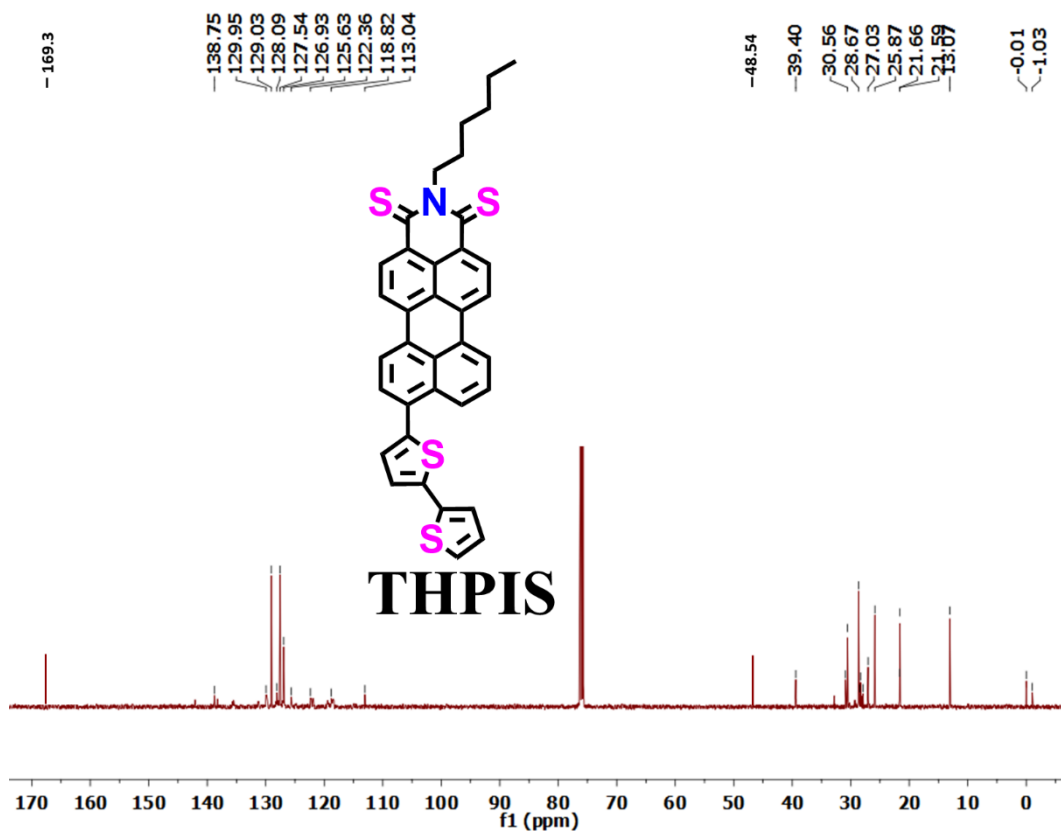


Figure A5.42. ^{13}C NMR spectra of THPIS.

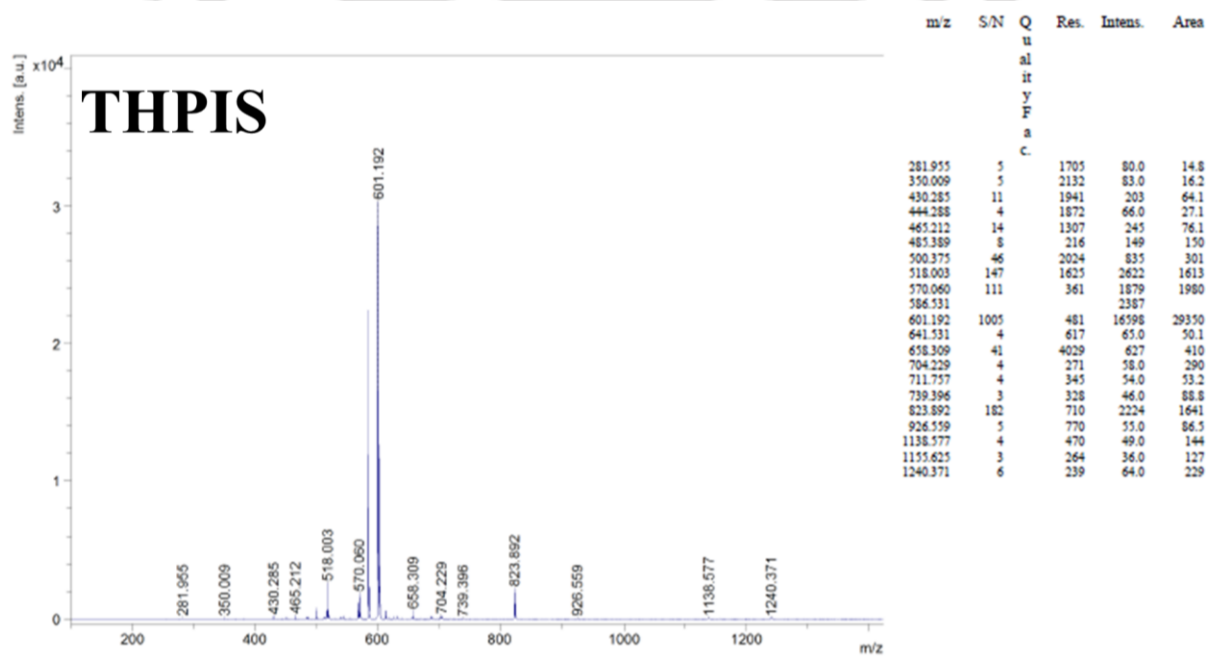


Figure A5.43. Maldi-TOF spectra of THPIS.

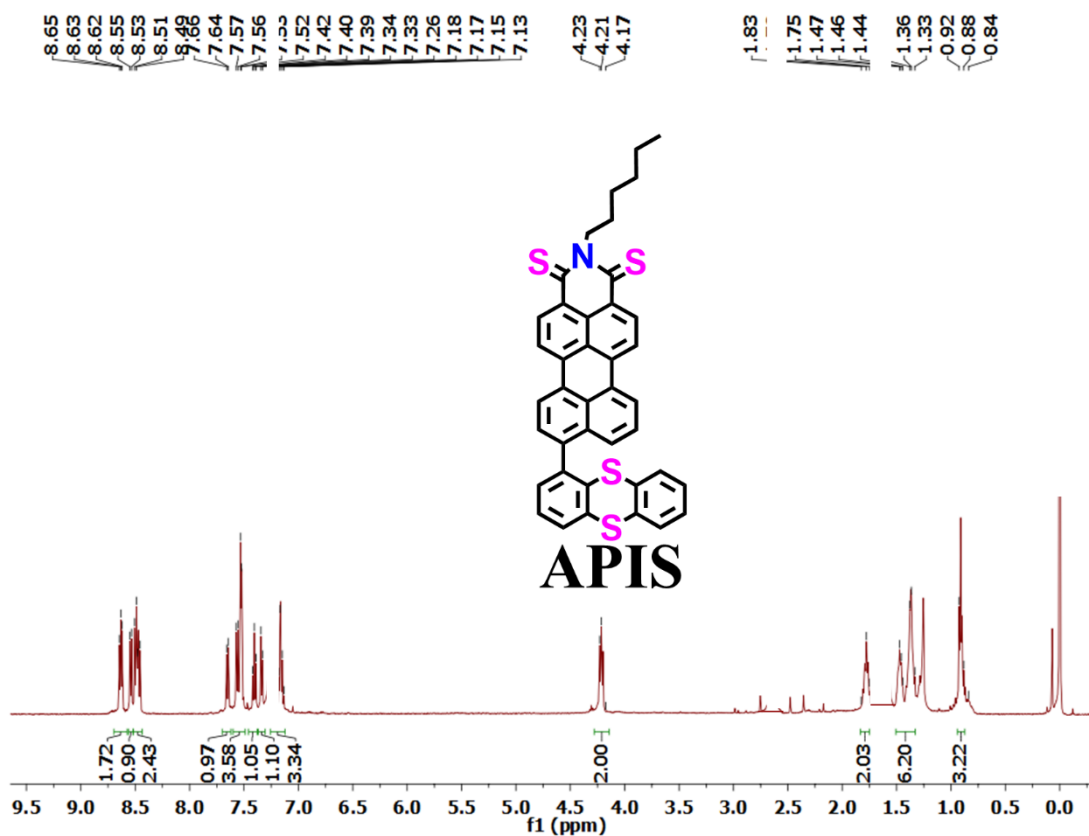


Figure A5.44. ¹H NMR spectra of APIS.

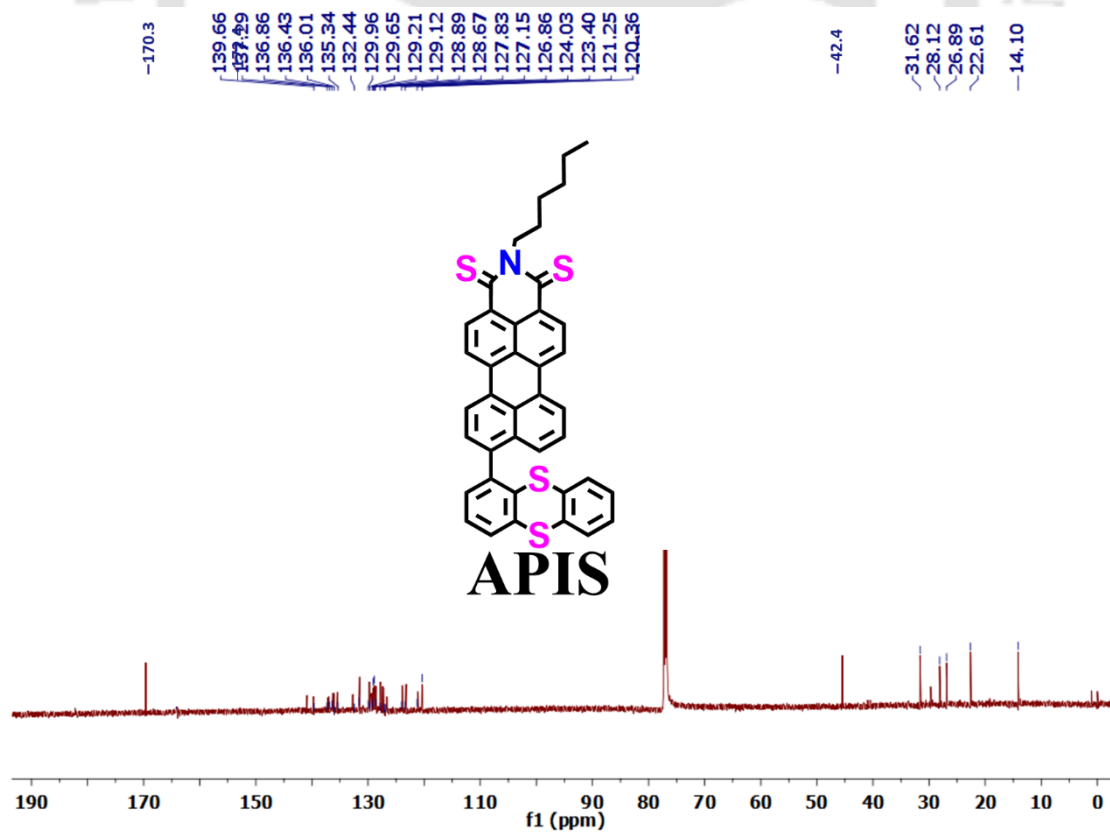


Figure A5.45. ¹³C NMR spectra of APIS.

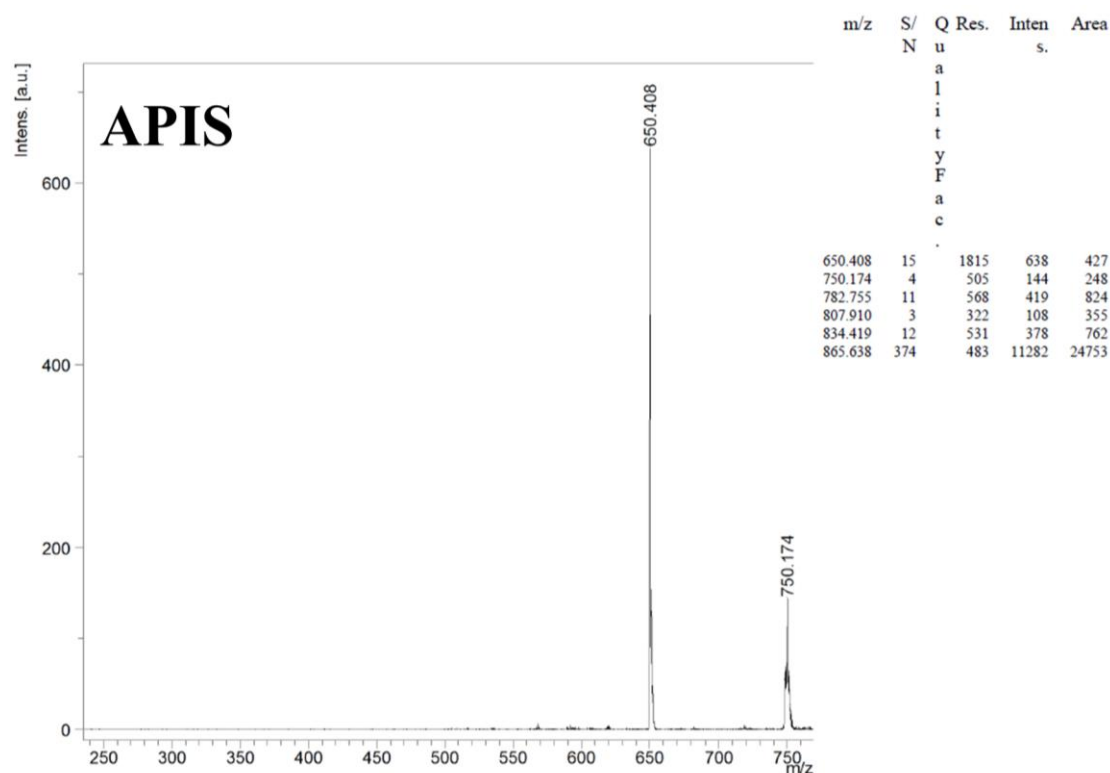


Figure A5.46. Maldi-TOF spectra of APIS.

References

- (1) Becke, A. D. Density-Functional Thermochemistry. III. The Role of Exact Exchange. *J. Chem. Phys.* **1993**, *98*, 5648-5652.
- (2) Frisch, M. J.; Trucks, G. W.; Schlegel, H. B.; Scuseria, G. E.; Robb, M. A.; Cheeseman, J. R.; Scalmani, G.; Barone, V.; Mennucci, B.; Petersson, G. A.; Nakatsuji, H.; Caricato, M.; Li, X.; Hratchian, H. P.; Izmaylov, A. F.; Bloino, J.; Zheng, G.; Sonnenberg, J. L.; Hada, M.; Ehara, M.; Toyota, K.; Fukuda, R.; Hasegawa, J.; Ishida, M.; Nakajima, T.; Honda, Y.; Kitao, O.; Nakai, H.; Vreven, T.; Montgomery, J. A.; Jr., Peralta, J. E.; Ogliaro, F.; Bearpark, M.; Heyd, J. J.; Brothers, E.; Kudin, K. N.; Staroverov, V. N.; Kobayashi, R.; Normand, J.; Raghavachari, K.; Rendell, A.; Burant, J. C.; Iyengar, S. S.; Tomasi, J.; Cossi, M.; Rega, N.; Millam, J. M.; Klene, M.; Knox, J. E.; Cross, J. B.; Bakken, V.; Adamo, C.; Jaramillo, J.; Gomperts, R.; Stratmann, R. E.; Yazyev, O.; Austin, A. J.; Cammi, R.; Pomelli, C.; Ochterski, J. W.; Martin, R. L.; Morokuma, K.; Zakrzewski, V. G.; Voth, G. A.; Salvador, P.; Dannenberg, J. J.; Dapprich, S.; Daniels, A. D.; Farkas, O.; Foresman, J. B.; Ortiz, J. V.; Cioslowski, J.; Fox, D. J. *Gaussian 09, Revision A.02*, Gaussian, Inc., Wallingford CT, **2009**.
- (3) Neese, F. Software Update: The ORCA Program System, Version 4.0. *WIREs Comp. Mol. Sci.* **2018**, *8*, 1327.
- (4) Neese, F. Software Update: The ORCA Program System-Version 5.0. *WIREs Comp. Mol. Sci.* **2022**, *12*, 1606.

- (5) Wang, D.; Lee, M. M. S.; Shan, G.; Kwok, R. T. K.; Lam, J. W. Y.; Su, H.; Cai, Y.; Tang, B. Z.; Highly Efficient Photosensitizers with Far-Red/Near-Infrared Aggregation-Induced Emission for in Vitro and in Vivo Cancer Theranostics. *Adv. Mater.* **2018**, *30*, 1802105.
- (6) Wu, W.; Mao, D.; Xu, S.; Panahandeh-Fard, M.; Duan, Y.; Hu, F.; Kong, D.; Liu, B. Precise Molecular Engineering of Photosensitizers with Aggregation-Induced Emission over 800 nm for Photodynamic Therapy. *Adv. Funct. Mater.* **2019**, *29*, 1901791.
- (7) Shi, X.; Sung, S. H. P.; Chau, J. H. C.; Li, Y.; Liu, Z.; Kwok, R. T. K.; Liu, J.; Xiao, P.; Zhang, J.; Liu, B.; Lam, J. W. Y.; Tang, B. Z. Killing G (+) or G (-) Bacteria? The Important Role of Molecular Charge in AIE-Active Photosensitizers. *Small Methods* **2020**, *4*, 2000046.
- (8) Li, Y.; Zhang, W.; Niu, J.; Chen, Y. Mechanism of Photogenerated Reactive Oxygen Species and Correlation with the Antibacterial Properties of Engineered Metal-Oxide Nanoparticles. *ACS Nano* **2012**, *6*, 5164-5173.
- (9) Xiong, Y.; Zhao, Z.; Zhao, W.; Ma, H.; Peng, Q.; He, Z.; Zhang, X.; Chen, Y.; He, X.; Lam, J. W. Y.; Tang, B. Z. Designing Efficient and Ultralong Pure Organic Room-Temperature Phosphorescent Materials by Structural Isomerism. *Angew. Chem., Int. Ed.* **2018**, *57*, 7997-8001.
- (10) Liu, Z.; Zou, H.; Zhao, Z.; Zhang, P.; Shan, G.-G.; Kwok, R. T. K.; Lam, J. W. Y.; Zheng, L.; Tang, B. Z. Tuning Organelle Specificity and Photodynamic Therapy Efficiency by Molecular Function Design. *ACS Nano* **2019**, *13*, 11283-11293.
- (11) Yang, Z.; Zhang, Z.; Lei, Z.; Wang, D.; Ma, H.; Tang, B. Z. Precise Molecular Engineering of Small Organic Phototheranostic Agents Toward Multimodal Imaging-Guided Synergistic Therapy. *ACS Nano* **2021**, *15*, 7328-7339.
- (12) Wang, X.; Song, Y.; Pan, G.; Han, W.; Wang, B.; Cui, L.; Ma, H.; An, Z.; Xie, Z.; Xu, B.; Tian, W. Exploiting Radical-Pair Intersystem Crossing for Maximizing Singlet Oxygen Quantum Yields in Pure Organic Fluorescent Photosensitizers. *Chem. Sci.* **2020**, *11*, 10921-10927.
- (13) Wang, Z.; Ma, L.; Zhao, H.; Wan, Y.; Zhang, X.-F.; Li, Y.; Kuang, Z.; Xia, A. Spin-Orbit Charge-Transfer Intersystem Crossing in Heavy-Atom-Free Orthogonal Covalent Boron-Dipyrromethene Heterodimers. *Phys. Chem. Chem. Phys.* **2023**, *25*, 24386-24394.
- (14) Schmidt, K.; Brovelli, S.; Coropceanu, V.; Beljonne, D.; Cornil, J.; Bazzini, C.; Caronna, T.; Tubino, R.; Meinardi, F.; Shuai, Z.; Brédas, J.-L. Intersystem Crossing Processes in Nonplanar Aromatic Heterocyclic Molecules. *J. Phys. Chem. A* **2007**, *111*, 10490-10499.
- (15) Barman, D.; Iyer, P. K. Aggregation-Induced Delayed Fluorescence and Phosphorescence from Hot Excitons via Suppression of Kasha's Rule in a Stimuli-Active Molecular Rotor. *J. Phys. Chem. C* **2023**, *127*, 2694-2704.

Future Aspects and Thesis Overview

Naphthalimides (**NI**) and Perylenimides (**PI**) materials are well-known acceptors and have been extensively studied in multiple platforms over the last several decades. They have been received as a significant interest among the scientific community due to its accepting nature and high fluorescence quantum yield. The NIs and specially PIs AIEgens highlight a new class of luminogens with huge promises for various practical application. TPE and HPS are well-established standard and efficient luminogenic core, whereas TPA opens a new luminogenic core in this area. Various research group have been actively participating in this field and developed a large number of AIE/AIEE-active materials with their wide variety of applications.

NI luminogens have been extensively explored over the years after the first discovery of its due to its easy and simple synthetic route. The **NI** luminogens exhibits considerable attention in the supramolecular self-assembly studies, sensors and biological applications. Although, **PI** luminogens has been less explored after first report of its in this area of sensing and biological applications owing to its synthetic requirements, **PI** materials has been extensively studied in the field of light-emitting diode and solar cells in compared to **NI** derivatives. **NI** and **PI** luminogens are promising candidate for long-term bio-imaging and tracking in depth owing to its photostability, biocompatibility and condensed state emissive characteristics. More importantly, **PI** luminogens could be substituted the **NI** luminogens due to its higher wavelength region absorption and emission properties compared to **NI** AIEgens, and its condensed state luminescence characteristics very easily fine-tuned upto NIR/IR region by simply tweaking of the π - π stacking interactions among the PI cores by structural perturbation at their molecular level. The asymmetric and electron withdrawing properties as well as prone to π - π stacking interactions of the **NI** and **PI** have been recognized to have unique and distinct structure-property relationships. The structural conformation of the asymmetric **NI** and **PI** materials could be easily regulated by easily tweaking its π - π stacking interactions with extend their diverse applications towards many unexplored promises.

In this research area, different new strategies have been developed to switch ACQ/AIE phenomenon in **NI** and **PI** derivatives. This research work focused on the systematic tailoring and construction of the condensed state emission of the **NI** and PI by basically structural manipulation particularly. In addition, Supramolecular-assembly in **NIs** and PIs have been tuned in **NIs** by simply judicious structural perturbation. Since, the photophysical properties and supramolecular-assembly behavior greatly controlled by the intermolecular packing orientations of the **NI** and PI by the distinct magnitude of electronic constrains of

the attached units. This strategy could be huge possibilities to monitor the biomedical applications of distinct self-assembly spontaneously achieved from the similar electronic motifs. Along with the distinct supramolecular assembly and condensed state properties, the photosensitizer characteristics of the **NI** and **PI** luminogens serves as a very promising candidates in image-guided photodynamic therapy towards cancer cell and various pathogens. Besides, NIR AIE **PI** PS could be emerge as a great potential for the win-win cooperation in the application of the biomedical fields.

The content of the thesis report entitled “**Naphthalimide and Perylenimide Luminogens: Structure-Property Relationships for Sensing and Biomedical Applications**” has been divided into five chapters as summarized below:

Chapter 1 briefly describes the need and discovery of condensed state emission as well as types and mechanistic aspects of condensed state emission. This chapter demonstrates the importance, potential applications and structural modulation in naphthalimide and perylenimide luminogens as well as the concluding statement on this thesis work.

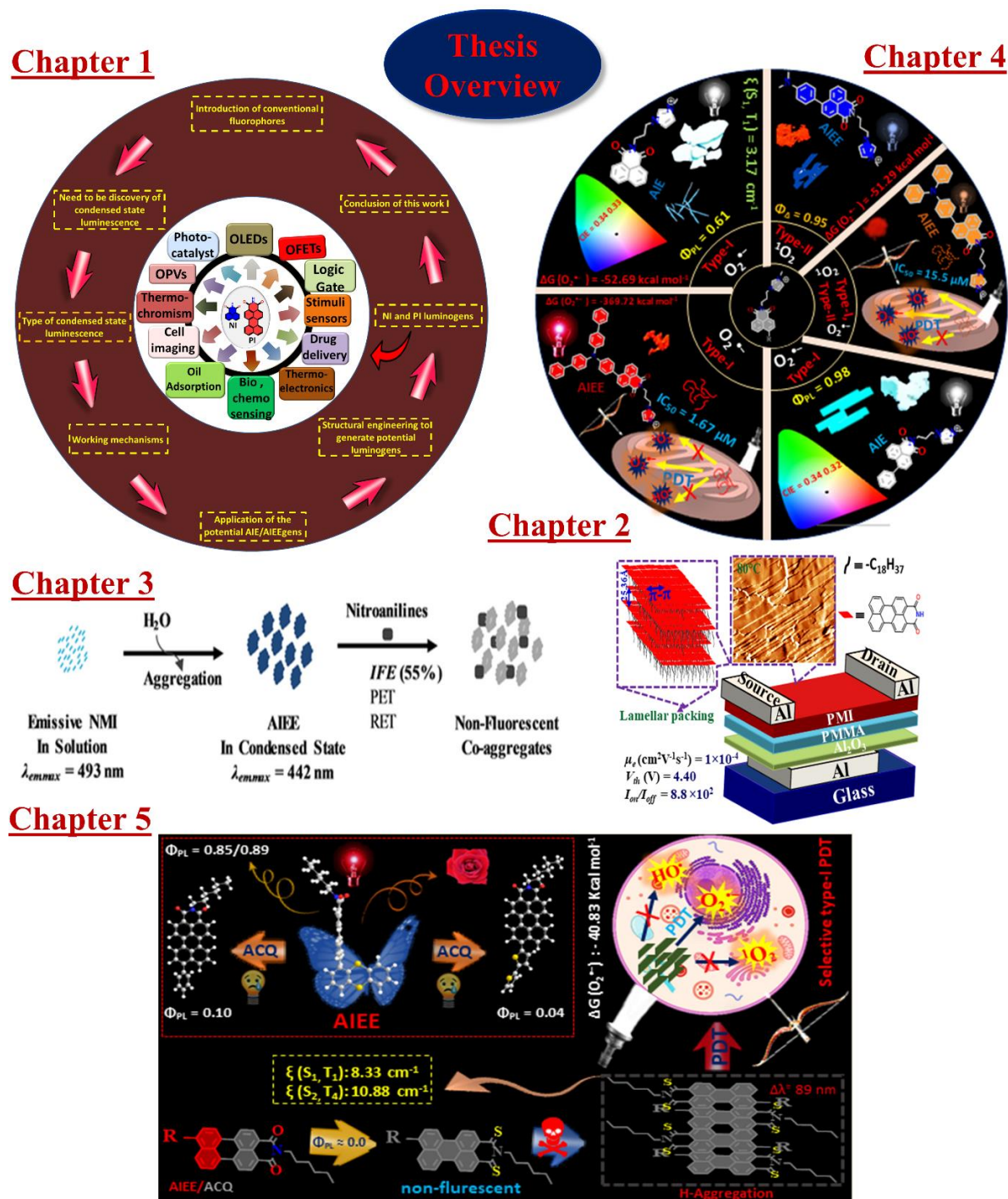
Chapter 2 demonstrates the influence of the pendant non-conjugated chain effect in perylenimide on the electronic, thermal, photophysical along with their morphology in their condensed state. This chapter also includes the OFET characteristics of the perylenimide comprising of the long pendant alkyl chain.

Chapter 3 provides condensed state luminescence characteristics and supramolecular-assembly behaviors of the naphthalene substituted in naphthalimide. This chapter also unveils the 4-nitroaniline (class III toxic pesticides) detection on multiple platform, which includes in aqueous media and the cost-effective simple and portable whatman paper test strips based on-site solid state detection. The sensing mechanisms involved the receptor free inner filter effect (IFE).

Chapter 4 This chapter suggests the simple and precise molecular engineering of donor functional group with targeting imidazole group serves condensed state emission and supramolecular-assembly along with their highly ROS generation characteristics could be provide a new tool for the development of the new generation materials for the diverse futuristic application.

Chapter 5 We demonstrated the novel yet facile design strategy for the ACQ-to-AIEE transformation by simply tweaking the conformation into the functional group in **PNI** as well as second comprehensive structural design of thiobased PS through S-atom engineering at carbonyl position in **PNI (PNIS)** with excellent potential in PDT in cancer cell.

The thesis concludes distinct design strategies with fine-tuned condensed state characteristics, and photosensitizing properties with brief future possibilities that could be the promising tool for the small molecule based traditional fluorophores towards many unexplored potentials.



Thesis Overview: Developed new design strategies with fine-tuned condensed state photophysical properties and supramolecular-assembly behavior in traditional fluorophores, which has been used to detect various toxic elements in aqueous media. Besides, the distinct photosensitizer properties in NI and PI luminogens could be

emerge as the promising route for the PDT in cancer and towards pathogens, as well as it opens up diversified technological application.



Publications

First authors

1. Khatun, M.N.; Tanwar, A.S.; Meher, N.; Iyer, P.K.* An Unprecedented Blueshifted Naphthalimide AIEEgen for Ultrasensitive Detection of 4-Nitroaniline in Water via "Receptor-Free" IFE Mechanism. *Chem. Asian J.* **2019**, *14*, 4725 - 4731. [IF: 4.89]
2. Khatun, M.N.; Dey, A.; Meher, N.; Iyer, P.K.* Non-conjugated alkyl Chain engineering to Fine-Tune the Morphologies in Perylenemonoimides for the Fabrication of the OFET device. *ACS Appl. Electron. Mater.* **2021**, *3*, 3575-3587. [IF: 4.89]
3. Khatun, M.N.; Nandy, S.; Kumar, S.; Iyer, P.K.* Solid-State White Light Emission, Excimer-based Photosensitization, and Type 1 Mitochondrion-Targeted Image-Guided Cancer Theranostics (*Revision Submitted*)
4. Khatun, M.N.; Nandy, S.; Roy, H.; Ghosh, S.; Kumar, S.; Iyer, P.K.* Sulphur-Atom Positional Engineering in Perylenimide: Structure-Property Relationships and H-aggregation-Directed Type-I Photodynamic Therapy. DOI <https://doi.org/10.1039/D4SC01180E> (*Chemical Science*). [IF:9.8]
5. Khatun, M.N.; Nandy, S.; Kumar, S.; Iyer, P.K.* Molecular Engineering of Peryleneimides for Enhanced NIR-Active AIE Luminescence in the Condensed State: Effective Free Radical Photosensitizer for Synergistic Image-Guided Photodynamic Therapy in Cancer Cells. (*Revision Submitted*)
6. Khatun, M.N.; Nandy, S.; Kumar, S.; Iyer, P.K.* Enhanced Ring Expansion Modulation of Peryleneimides for Efficient Photosensitization in Cancer Cell Ablation. (*Under communication*)
7. Khatun, M.N.; Meher, N.; Paroi, R.; Iyer, P. K.* Alteration of Alkyl Chain Length: a Key Parameter to Modulate the Condensed State Intermolecular Stacking Interactions and Photophysical Properties. (*Under communication*)
8. Khatun, M.N.; Adil, L.R.; Iyer, P.K.* Harnessing Naphthalimides for Enhanced Condensed State Luminescence: Highly Efficient Type 1 Fluorescence for Guided Bacterial Ablation. (*Under preparation*)

Co-authors

1. Tanwar, A.S.; Khatun, M.N.; Chanu, M.A.; Iyer, P.K.* Water-Soluble Conjugated Polyelectrolyte for Selective and Sensitive Detection of Carcinogenic Chromium (VI). *Analyst*, **2023**, *148*, 6011-6019 [IF: 5.2]
2. Dhama, S.; Sengupta, Chaitrali.; Khatun, M. N.; Iyer, P. K.*; Pandey, R. * Ultrafast spectroscopic studies on excited state dynamics of different alkyl substituted perylene monoimides in solution and thin film. *Phys. Chem. Chem. Phys.*, **2024**, *26*, 15600-15610 [IF: 4.1]

Review articles

1. Barman, D.; Narang, K.; Parui, R.; Zehra, N.; Khatun, M. N.; Adil, L. R.; Iyer, P.K.* Review on recent trends and prospects in π -conjugated luminescent aggregates for biomedical applications. *Aggregate*. **2022**, *3*, 172. [IF: 18.8]

Book chapters

1. Bhosale, R.S.; Singh, V.; Progress in Molecular Biology and Translational Science, ed. Zehra, N.; A.S.; Khatun, M.N.; Adil, L.R. Iyer, P.K.* Chapter 6-AIE active polymers for biological applications *Elsevier*. **2021**,185, 137-177. [IF: 4.02]
2. Dave, S.; Das, j.; Ghosh, S.; Advanced Nanomaterials for Point of Care Diagnosis and Therapy, ed. Adil, L.R.; Parui, R.; Khatun, M.N.; Chanu, M.A.; Iyer, P.K.* Chapter 7-Nanomaterials for Sensors: Synthesis and Applications. *Elsevier*. **2022**, 121-168 [IF: 5.5]
3. Selvasembian, R.; Thokchom, B.; Singh, P.; Jawad, A. H.; Gwenzi, W. Remediation of Heavy Metals: Sustainable Technologies and Recent Advances ed. Khatun, M.N.; Chanu, M.A.; Sharma, S.; Zehra, N.; Iyer, P.K.* Chapter 13-Nanotechnologically synthesized polymeric materials for the adsorption of heavy metals. *Wiley ISBN*: 978-1-119-85358-9. [IF:4.0].
4. Vallejos, S.; Trigo, M.; Garcia, J.M.; Sensory polymers: from their design to practical applications, ed. Khatun, M.N.; Chanu, M.A.; Ghosh, P; Barman, D.; Adil, L.R.; Iyer, P.K.* Chapter 12-Sensors based on Polymer nanomaterials. Elsevier. 1st Edition - August 1, 2024, **ISBN**: 9780443134074. [IF: 4.1]

Patents

1. Khatun, M.N.; Iyer, P.K. Novel Naphthalimided Ionic Core Derivatives and Synthesis Method Thereof. TEMP/E1/103941/2023-KOL (Indian Patent Submitted)
2. Khatun, M.N.; Iyer, P.K. Novel Thioperylenimides Derivatives and Synthesis Method Thereof. TEMP/E1/80303/2023-KOL (Indian patent Submitted)
3. Khatun, M.N.; Iyer, P.K. An emerging molecular engineering in peryleneimides boost its NIR-active AIE luminescence characteristics in condensed state: effective free radical photosensitizer for synergistic image-guided photodynamic therapy in cancer cell. TEMP/E-1/90403/2023-KOL (Indian Patent Submitted)

Awards and achievement

1. The 2022-2023 Best Paper Award: "Review on recent trends and prospects in π -conjugated luminescent aggregates for biomedical applications": Debasish Barman, Kavita Narang, Retwik Parui, Nehal Zehra, Mst Nasima Khatun, Laxmi Raman Adil, Parameswar Krishnan Iyer*: provide by Ben Zhong Tang Editor-in-Chief, Aggregate, 10th January 2024.
2. **Secured 2nd Position** in Aliah University in Chemistry Hons (2013) with **CGPA 8.3**
3. **Secured 2nd Position** in Aliah University in Medicinal Chemistry (2015) with **CGPA 8.3**
4. Qualified Graduate Aptitude Test in Engineering (GATE) in 2017
5. Qualified Intern with **CGPA 8.1**
6. Qualified Higher Secondary with CGPA 8.0
7. Received merit cum means S w a m i V i v e k a n a n d a Scholarship for Higher secondary with **CGPA 8.1** in 2009
8. Received merit cum means minority scholarship for Under graduation with **CGPA 8.0** (Hons) in 2010
9. Received merit cum means minority scholarship for Under graduation with **CGPA 7.3** (Hons) in 2011
10. Received merit cum means minority scholarship for first year in Under graduation with **CGPA 9.9** (Hons) in 2012
11. Received merit cum means minority scholarship for first year in Under graduation with **CGPA 8.6** (Hons)

in 2013

12. Received Merit cum means **Swami Vivekananda Scholarship** for undergraduate in 2013 with **CGPA 8.3**
13. Received Merit cum means **Swami Vivekananda Scholarship** from for University Postgraduate in 2014 with **CGPA 8.3**.

Conferences

1. Attended the 5th International Conference on Advance Nanomaterials and Nanotechnology held during December 08- 11, 2017 organized by Centre for Nanotechnology, Indian Institute of Technology Guwahati.
2. Attended the International Conference on Synthetic Potent Molecule and Its Applications (ICSPMIA) held during October 30-31, 2018 organized by department of chemistry, SMIT (Sikkim Manipal Institute of Technology).
3. Presented poster in the 6th International Conference on Advance Nanomaterials and Nanotechnology held during December 08-11, 2019 organized by Centre for Nanotechnology, Indian Institute of Technology Guwahati.
4. Presented poster in the 26th CRSI National Symposiums in Chemistry (CRSI-NSC)-2020, during February 07-09, 2020 organized by department of chemistry, VIT vellore. during February 07-09, 2020 organized by department of chemistry, VIT vellore.
5. Presented poster the 7th International Conference on Advance Nanomaterials and Nanotechnology held during December 08-11, 2021 organized by Centre for Nanotechnology, Indian Institute of Technology Guwahati.
6. Oral presentation on North-East Research Conclave (NERC) held during May, 20-22, 2022 organized by Science, Technology and Climate Change Dept. & Dept. of Education, Govt. of Assam, Indian Institute of Technology Guwahati
7. Poster presentation on Frintier on Chemical Sciences (FICS) held during December 2-4, 2022, organized by department of chemistry, Indian Institute of Technology Guwahati.
8. Poster presentation on Research Industrial Conclave (RIC) held during May 14-16, 2023, organized by department of chemistry, Indian Institute of Technology Guwahati.

Vitae

Mst Nasima Khatun was Born in West Bengal, India. She earned her Bachelor of Science in Chemistry (Hons.) from Aliah University, followed by the completion of her Master of Science in Medicinal Chemistry from the same institution in respectively. In 2017, she embarked on her doctoral journey as a PhD student in the Department of Chemistry at the Indian Institute of Technology Guwahati, under the guidance of Prof. Parameswar K. Iyer. Her research trajectory commenced with a focus on pioneering naphthalimide and perylenimide based condensed state emitting materials, a pursuit ignited by her profound interest in sensing and biomedical applications. Her investigations delve deep into the intricacies of intermolecular interactions, which fundamentally govern the photophysical attributes and supramolecular self-assembly properties of these materials. She concentrated on formulating diverse design approaches for creating distinct reactive oxygen species (ROS) with exceptional efficiency in quantum yield. Additionally, She investigated the manipulation of molecular structures to control the generation of specific ROS types, encompassing both type-I and type-II ROS. To encapsulate, her doctoral endeavors have notably enriched comprehension and potential applications of these organic compounds within the biomedical domain, specifically in photodynamic anticancer therapy. The thorough explorations undertaken in her research set a path for future strides in designing and leveraging these luminogens across a broad spectrum of pragmatic uses. Beyond this, her scholarly pursuits encompass a fascination for elucidating the potentials of small molecules, conjugated polymers, and covalent organic frameworks in the realm of luminogenic materials. These explorations traverse a wide spectrum, encompassing fields such as potential biological applications, diverse spectroscopic techniques, and extensive engagement in theoretical calculations.